

Proton-Coupled Electron Transfer in Nitrogen Fixation

Thesis by
Matthew J. Chalkley

In Partial Fulfillment of the Requirements for
the degree of
Doctor of Philosophy

The Caltech logo, featuring the word "Caltech" in a bold, orange, sans-serif font, centered within a light orange rectangular background.

CALIFORNIA INSTITUTE OF TECHNOLOGY
Pasadena, California

2020
Defended: January 17, 2020

© 2020

Matthew J. Chalkley
ORCID: 0000-0002-0484-7335

All rights reserved

ACKNOWLEDGEMENTS

At this critical waypoint in my chemistry journey, I want to reach back in time and thank some of the important people who influenced me to start on this path. Firstly, a thank you to two high school science teachers, Dr. Sohn and Mr. Smith, who with their excellent teaching helped to arouse my interest in science. Also, I want to thank the New Jersey Governor's School in the Sciences, which was an amazing experience and gave me a lot of confidence with respect to pursuing chemistry in college. At Yale, I joined the lab of Professor Nilay Hazari after my freshman year. This is one of those fortuitous life decisions that one can only credit chance for. Nilay is an incredibly generous mentor and friend. He taught me so much and allowed me a remarkable amount of freedom to explore. I continue to benefit tremendously from his advice and imagine that this will always be the case. Nilay also attracted a remarkable group of people to the lab, who I also want to thank. These include Professor Eddie Luzik and Dr. Damian Hruszkewycz, who did much of my hands-on training and welcomed me into the group. Members who joined the lab later including Louise Guard, Heewon Suh, and Amymarie Bartholomew, also became friends. The larger chemistry community at Yale was also an incredibly welcoming environment and I have been lucky to cross paths multiple times with a number of chemists I first met at Yale: Patrick Melvin, Irene Cai, Graham Dobereiner, Nathan Schley, Alissa Hare, and James Blakemore. I was also lucky enough to make non-chemistry friends at Yale. Despite the fact that I have not seen most of them as often as I have hoped in the past five years, through skype and phone calls I have been able to enjoy their company. So thank you to all of these friends and others who have stayed in touch over the years via Skype and phone calls.

After Yale, I spent a year in Germany in the lab of Professor Karsten Meyer. I'm grateful for that opportunity to experience a different culture, both in the laboratory and in general, during my time there. I also met a number of students (Dominik and Mario), post-docs (Pete) and visitors (Donald), who helped me to integrate into the group and enjoy my year there.

Arriving at Caltech, I was fortunate to be able to join the lab of Professor Jonas Peters. Jonas has pushed me throughout my Ph.D. to choose scientific problems more carefully, to consider them more deeply, and to communicate them more coherently; for this, I am very grateful. I also believe that we have a relatively unique rapport that has allowed us to work effectively together. Most importantly though, I have always trusted that Jonas was there to support me, and I believe that if you can find that in a Ph.D. advisor you are very lucky. Furthermore, Jonas has also built a tremendous environment to do science in. The people and the resources of the Peters lab and Caltech at large are hard to match. At the beginning of my Ph.D., I received invaluable mentorship from Jon Rittle and Gaël Ung. In addition to these two, I landed in an office with Tanvi Ratani and Mark Nesbit, who I am sure answered more than their fair share of questions. I hope that I have been able to pay back this help to newly joined group members, who have become my officemates in the years since (Kumiko, Jian, Patricia, Teddy, Pablo, Emily, Tucker, and Nick). The support staff who run the facilities/operations at Caltech are consistently excellent. I want to thank in particular Julianne Just, who does so much to keep the Peters' group running, and Mike Takase, who has been a friendly face ever since I first met him at Yale.

I did a lot of collaborative work at Caltech. This started with two papers that I co-authored with Trevor del Castillo and Ben Matson. These papers really re-oriented the way I was thinking about science and formed a springboard for the work that I would do going forward. That I am still excited by the hypothesis that we formulated several years ago now is a testament to its strength (or maybe my myopic nature). Subsequently, I worked on a paper with Paul Oyala. In hindsight, this project looks very straightforward, but it took a long time for us to gain the first foothold of understanding and so I want to thank him for his persistence in working to solve this problem with me. Thank you to Marcus Drover, who I hope has forgiven me for accidentally committing us both to writing a Chemical Reviews article with Jonas. Most recently, I have been incredibly lucky to get to work with Pablo Garrido-Barros. Pablo has already taught me so much and our current project would not have been possible without his expertise and eternal optimism. I also want to thank Dirk Schild, with whom I was a teaching assistant for Ch 153b, and Nik Thompson, with whom I worked closely on both Mössbauer spectroscopy and nuclear resonance vibrational spectroscopy

over the years. Both were also always eager to chat about chemistry and have given formative input over the years.

I have also gotten valuable input from my committee members: Professor Theodor Agapie, Professor Tom Miller, and Professor Harry Gray. They always came ready with comments and questions to my meetings which helped to push me to do better. They also provided important support and guidance towards building the next phase of my chemistry career. I have also gotten support and guidance from the Resnick Institute, most typically in the form of advice or help offered by Heidi Rusina and Neil Fromer. The Resnick Institute is already a great organization that brings together many scientists on campus, and I am excited to see how it will grow in the future. I also received generous financial support from both the NSF Graduate Research Fellowship and the Caltech Center for Environmental Microbial Interactions (CEMI). The latter of these was particularly patient in putting up with my completely non-microbial work.

I have not had many hobbies over the years at Caltech, but one of them was playing soccer. In my earlier years this was with Gaël, Trevor, Javier Fajardo, Josh Buss, Kyle Horak, Davide Lionetti, and others less familiar to the Caltech community. At the end of my Caltech experience, I have been grateful to again play soccer this time with Pablo, Nick Watkins, Heejun Lee, Alonso Rosas, Mike Zott, and others. I was also involved with volunteering with the RISE program at Caltech Y and want to thank all those who made that possible.

This leaves my family to thank. As always, my parents have been an incredible support to me over the past years. Despite the increased distance, they have remained an ever-present part of my life sharing in my frustrations and joys. I think of how lucky I am to have them as my parents regularly and love them very much. During my Ph.D., we have added Grace to our family. In the time that I have been in graduate school, Grace has completed medical school, (almost) completed residency, and is now interviewing to become an attending physician. I'm so proud of her. Alongside all her own accomplishments, she has spent endless time listening to me talk about my chemistry and experience at Caltech. She and my parents know far more about PCET, metallocenes, nitrogen fixation, Mössbauer, and

all the other topics that you will read about in the coming chapters than they ever could have expected or wanted. So thank you so much to them and to all of the other people mentioned above, without whom this thesis would never have happened.

ABSTRACT

This thesis focuses on the management of protons and electrons in the formation of X–H bonds. In our pursuit of better understanding this process, we have been particularly interested in the nitrogen fixation reaction (N₂-to-NH₃) because of the high number of protons and electrons involved in this conversion (6) and the significant difficulty of functionalizing N₂. The first chapter introduces the important themes of this thesis: (i) multiple bonding, (ii) proton-coupled electron transfer, (iii) overpotential in N₂ fixation, and (iv) selectivity in N₂ fixation. The second chapter discusses the bonding of an iron complex with a small molecule (NO) and how this bonding is key to activating the small molecule for reactivity. The third chapter looks at how employing a new proton and electron source allows an Fe catalyst to achieve improved selectivity and turnover number for the reduction of N₂ to NH₃ despite a lowered overpotential relative to previous reactions. It also raises the hypothesis that this is possible due to proton-coupled electron transfer mediated by a metallocene. The fourth chapter studies the effect of acid strength on N₂ fixation selectivity and demonstrates circumstantial evidence for the involvement of a decamethylcobaltocene (Cp*₂Co) in the formation of N–H bonds via proton-coupled electron transfer. It also highlights how the addition of co-catalytic [Cp*₂Co]⁺ to electrochemical experiments with our Fe catalyst enabled truly electrocatalytic N₂ fixation for the first time. The fifth chapter provides both atomistic detail on the protonation reactivity of Cp*₂Co and experimentally verifies the prediction that this species would be an extremely strong hydrogen-atom donor. It also develops a conceptual framework to explain the uniquely weak C–H bonds both homolytic and heterolytic that result from metallocene protonation and discusses their potential to play a role in not only the hydrogen evolution reaction (HER), but also the N₂ fixation reaction. In the final chapter, we develop a synthetic route to a base appended cobaltocene. We demonstrate that this second-generation cobaltocene can, unlike the first generation, serve as a net hydrogen-atom donor under electrocatalytic conditions. As a demonstration of the utility of this, we use the base-appended cobaltocene for the selective, proton-coupled reduction of ketones to pinacols via a rate-determining concerted proton-electron transfer.

PUBLISHED CONTENT AND CONTRIBUTIONS

Chalkley, M. J.; Peters, J. C. A Triad of Highly Reduced, Linear Iron Nitrosyl Complexes: $\{\text{FeNO}\}^{8-10}$. *Angew. Chem. Int. Ed.* **2016**, *128*, 12174. doi:10.1002/anie.201605403.

M.J.C. designed and performed all experiments. M.J.C. and J.C.P. wrote the manuscript.

Chalkley, M. J.;[†] Del Castillo, T. J.;[†] Matson, B. D.;[†] Roddy, J. P.; Peters, J. C. Catalytic N_2 -to- NH_3 Conversion by Fe at Lower Driving Force: A Proposed Role for Metallocene-Mediated PCET. *ACS Cent. Sci.* **2017**, *3*, 217. doi:10.1021/acscentsci.7b00014.

[†]These authors contributed equally.

M.J.C. performed catalytic runs and freeze-quench spectroscopic measurements. M.J.C. helped to develop the PCET hypothesis and write the manuscript.

Chalkley, M. J.;[†] Del Castillo, T. J.;[†] Matson, B. D.;[†] Peters, J. C. Fe-Mediated Nitrogen Fixation with a Metallocene Mediator: Exploring pK_a Effects and Demonstrating Electrocatalysis. *J. Am. Chem. Soc.* **2018**, *140*, 6122. doi:10.1021/jacs.8b02335.

[†]These authors contributed equally.

M.J.C. performed the pK_a study, the freeze-quench spectroscopic measurements, and the stoichiometric reactivity. M.J.C. helped to write the manuscript.

Chalkley, M. J.; Oyala, P. H.; Peters, J. C. Cp^* Noninnocence Leads to a Remarkably Weak C–H Bond via Metallocene Protonation. *J. Am. Chem. Soc.* **2019**, *141*, 4721. doi:10.1021/jacs.9b00193.

M.J.C. performed all synthesis, quantum chemical calculations, and spectroscopic measurements, other than pulse EPR data. M.J.C. helped to interpret pulse EPR data. M.J.C. wrote the manuscript.

TABLE OF CONTENTS

Chapter 1. Introduction.....	1
1.1 Opening Remarks	2
1.2 Multiple Bonding	6
1.3 Proton-Coupled Electron Transfer:.....	9
1.4 Overpotential in Nitrogen Fixation.....	11
1.5 Selectivity in Nitrogen Fixation Catalysis.....	13
1.6 Chapter Summaries	15
1.7 References	17
Chapter 2. A Triad of Highly-Reduced, Linear Iron Nitrosyls: {Fe(NO)}⁸⁻¹⁰	21
2.1 Introduction	22
2.2 Results.....	23
2.2.1 Synthesis of {Fe(NO)} ⁸⁻¹⁰	23
2.2.2 Characterization and Electronic Structure of {Fe(NO)} ⁸⁻¹⁰	24
2.3 Conclusion.....	32
2.4 References	33
Chapter 3. Catalytic N₂-to-NH₃ Conversion by Fe at Lower Driving Force: A Proposed Role for Metallocene-Mediated PCET	36
3.1 Introduction	37
3.2 Results.....	40
3.2.1 Catalytic N ₂ RR at Lowered Overpotential.....	40
3.2.2 Mechanism of N ₂ RR Catalysis with (P ₃ ^B)Fe	42
3.2.3 PCET from a Protonated Metallocene.....	48
3.3 Discussion.....	52
3.4 Conclusion	53
3.5 References	54
Chapter 4. Fe-Mediated Nitrogen Fixation with a Metallocene Mediator: Exploring pK_a Effects and Demonstrating Electrocatalysis	58
4.1 Introduction	59

4.2 Results and Discussion.....	62
4.2.1 Effect of pK_a on the Selectivity of N_2 Fixation by $[(P_3^B)Fe]^+$	62
4.2.2 Computational Studies on Cp^*_2Co Protonation and N–H Bond Formation...	67
4.2.3 Electrocatalytic N_2 Fixation with $[(P_3^B)Fe]^+$	73
4.3 Conclusion	81
4.4 References	82
Chapter 5. Cp* Non-innocence Leads to a Remarkably Weak C–H Bond via Metallocene Protonation.....	86
5.1 Introduction	87
5.2 Results.....	90
5.2.1 Pulse Electron Paramagnetic Resonance Spectroscopy on Protonated Cp^*_2Co	90
5.2.2 Stereochemical Assignment of Cp^*_2Co Protonation	95
5.2.3 Thermochemical Measurements Relevant to Cp^*_2Co Protonation.....	99
5.3 Discussion.....	103
5.4 Conclusion.....	107
5.5 References	108
Chapter 6. Metallocenes: Beyond Electron Transfer to Proton-Coupled Electron Transfer	113
6.1 Introduction	114
6.2 Results.....	117
6.2A Mechanism of Electrocatalytic HER by $[Cp_2Co]^+$	117
6.2B Synthesis of a Brønsted Base-Appended Cobaltocene	119
6.2C Thermochemical Properties of a Brønsted Base-Appended Cobaltocene.....	122
6.2D Electrochemical behavior of $(Cp)Co(Cp^N)$ with Excess Acid.....	124
6.2E Electrochemical Behavior in the Presence of a Hydrogen Atom Acceptor...	125
6.3 Discussion.....	131
6.4 Conclusion:	135
6.5 References:	136
Appendix A. Supplementary Information for Chapter 2	141

Appendix B. Supplementary Information for Chapter 3	178
Appendix C. Supplementary Information for Chapter 4	213
Appendix D. Supplementary Information for Chapter 5	251
Appendix E. Supplementary Information for Chapter 6	304

LIST OF FIGURES

Figure 1.1: Depiction of the active site of the FeMo nitrogenase.....	3
Figure 1.2: Molecular nitrogen fixation catalysts used in this thesis.....	4
Figure 1.3: Cooperative binding of N ₂ via lone-pair donation from N ₂ and π-backdonation.....	6
Figure 1.4: (top) Mo and W complexes promote the functionalization of N ₂ and its conversion to NH ₃ . ¹⁵ (bottom) Mo complex that binds N ₂ and then cleaves it to form to Mo(N) complexes. ¹⁶	7
Figure 1.5: Comparison of the electronic structure of Fe complexes in C ₃ and C ₄ symmetry.....	8
Figure 1.6: Canonical examples of hydrogen atom transfer (HAT), concerted-proton electron transfer (CPET), and multi-site proton-coupled electron transfer (MS-PCET).	10
Figure 1.7: (left) The square scheme that relates the stepwise ET-PT and PT-ET pathway to the PCET pathway. (right) Definition of C _G	11
Figure 1.8: Calculated gas-phase bond dissociation enthalpies (BDEs) for intermediates of potential relevance to nitrogen fixation. ³²	12
Figure 1.9: The possible pathways for background HER and hypothesized N-H bond forming reactions via H• or H ⁻ transfer.....	15
Figure 2.1: Synthetic route for {(P ₃ ^B)Fe(NO)} ⁸⁻¹⁰	23
Figure 2.2: Variable scan rate cyclic voltammograms in 0.1 M [TBA][BAr ^F ₄] THF of the {(P ₃ ^B)Fe(NO)} ^{8/9} and {(P ₃ ^B)Fe(NO)} ^{9/10} redox couples.....	24
Figure 2.3: IR spectra for {(P ₃ ^B)Fe(NO)} ⁸⁻¹⁰ highlighting the NO stretch.....	25
Figure 2.4: X-ray crystal structures of {(P ₃ ^B)Fe(NO)} ⁸⁻¹⁰	26
Figure 2.5: Experimental bond lengths from X-ray crystallography and Wiberg bond indices from DFT.....	26
Figure 2.6: Zero-field Mössbauer spectra of {(P ₃ ^B)Fe(NO)} ⁸⁻¹⁰	28
Figure 2.7: Density-corrected room temperature (red) and cryogenic (black) UV-Vis spectra of {(P ₃ ^B)Fe(NO)} ⁹ in 2-MeTHF highlighting the region that demonstrates vibronic coupling.....	30

Figure 2.8: CW X-band EPR spectrum of $\{(P_3^B)Fe(NO)\}^9$	31
Figure 2.9: A molecular orbital diagram for $\{(P_3^B)Fe(NO)\}^9$	32
Figure 3.1: Summary of conditions used for catalytic N_2 -to- NH_3 conversion by $[(P_3^B)Fe]^+$ highlighting the estimated driving force ($\Delta\Delta H_f$)......	39
Figure 3.2: Mössbauer spectrum at 80 K with 50 mT applied parallel field of a freeze-quenched catalytic reaction (54 equiv Cp^*Co , 108 equiv $[Ph_2NH_2][OTf]$, 1 equiv $[(P_3^B)^{57}Fe]^+$) after five minutes of reaction time.	44
Figure 3.3: DFT calculations regarding the interaction of metallocenes and acids relevant to nitrogen fixation catalysis.	49
Figure 3.4: X-band 77 K powder EPR spectrum (red) and simulation (blue) of the isolated purple precipitate (assigned as endo- and $[(Cp^*)Co(exo-\eta^4-C_5Me_5H)]^+$) from reaction between Cp^*Co and HOTf at $-78^\circ C$	51
Figure 4.1: Electrosynthetic cycle for the formation of NH_3 from N_2 by a Chatt-type W-phosphine complex. ¹⁹	60
Figure 4.2. Effect of acid strength on the percentage of electrons being used to form NH_3 and H_2	64
Figure 4.3: The kinetics and thermodynamics of protonation of Cp^*Co for three acids from different catalytic efficiency regimes.....	70
Figure 4.4: The calculated thermodynamics and kinetics of synchronous PCET and fully asynchronous PCET (PT-ET), between $(P_3^B)Fe(NNH)$ and $[(Cp^*)Co(exo-\eta^4-C_5Me_5H)][OTf]$ to generate $(P_3^B)Fe(NNH_2)$	72
Figure 4.5: Cyclic voltammograms of relevance to electrocatalytic N_2 fixation in the with co-catalytic $[(P_3^B)Fe]^+$ and $[Cp^*Co]^+$	75
Figure 5.1: Reaction pathways to consider for protonated Cp^*Co species, illustrating both undesired HER and possible N–H bond forming steps relevant to N_2RR	89
Figure 5.2: Pseudomodulated ²⁴ Q-band ESE-detected EPR spectra of the reaction of Cp^*Co with HOTf (black traces), and DOTf (blue traces) measured at 10 K (top traces) and 6 K (bottom traces).	91
Figure 5.3: a) Q-band Davies ENDOR spectra at 10 K and b) narrow Q-band Davies ENDOR spectra at 10 K. c) Q-band Davies ENDOR spectra at 6 K and d) narrow Q-band Davies ENDOR spectra at 6 K. Data from the reaction with HOTf (black) and DOTf (blue) are shown.....	93

- Figure 5.4:** Comparison of Q-band HYSSCORE spectra acquired at the center of the EPR spectrum of the *endo*- (left) and *exo*- (right) protonated Cp*₂Co species generated via reaction with DOTf (top panels) and HOTf (2nd panels from top). 94
- Figure 5.5:** (top) X-Band CW EPR spectrum of the reaction of Cp*₂Co with HOTf (black) and its simulation (red). (bottom) X-Band CW EPR spectrum of the reaction of Cp*₂Co with HNTf₂ (black) and its simulation (red). 97
- Figure 5.6:** a) DFT optimized structures for the isomers of protonated Cp*₂Co. The predicted $A(^1\text{H})$ values for the protons circled in red. b) X-ray crystal structure of (Cp*)Co(*exo*- η^4 -C₅Me₅H). Thermal ellipsoids are shown at 50% probability. c) Experimentally derived ¹H hyperfine parameters for the *endo*- and *exo*-isomers of protonated Cp*₂Co. 98
- Figure 5.7:** Proposed mechanism for the oxidation of (Cp*)Co(*exo*- η^4 -C₅Me₅D) with HBAR^F₄. 99
- Figure 5.8:** Cyclic voltammograms of the [(Cp*)Co(*exo*- η^4 -C₅Me₅H)]⁺⁰ 100
- Figure 5.9:** Thermochemistry of neutral and cationic (Cp*)Co(*exo*- η^4 -C₅Me₅H). 102
- Figure 5.10:** (left) A comparison of the experimental BDFE_{C-H} for a variety of related Cp*Co-species, demonstrating the importance of aromaticity and electron count in predicting the stability of the indicated C-H bond. (right) A comparison of computational BDFE_{C-H} values for a redox series of [(Cp*)Ni(*exo*- η^4 -C₅Me₅H)]ⁿ⁺. 106
- Figure 6.1:** Overview of PCET for the functionalization of unsaturated substrates. 117
- Figure 6.2:** Cyclic voltammetry relevant to HER by [Cp₂Co]⁺ 118
- Figure 6.3:** Scheme describing the synthesis of the Brønsted base appended cobaltocenes. 120
- Figure 6.4:** X-ray structure of (Cp)Co(Cp^N), [(Cp)Co(Cp^N)]⁺, and [(Cp)Co(Cp^{NH})]²⁺ with counteranions and solvent omitted for clarity. Ellipsoids shown at 50% probability. 120
- Figure 6.5:** Spectroscopic data for [(Cp)Co(Cp^{NH})]⁺. 121
- Figure 6.6:** Variable scan rate CVs of 1 mM [(Cp)Co(Cp^{NH})]²⁺ and 1 mM Fc in 100 mM [TBA][PF₆] solution of acetonitrile at a boron-doped diamond working electrode. 123
- Figure 6.7:** Thermochemistry of [(Cp)Co(Cp^{N(H)})]ⁿ⁺ in acetonitrile. 124

- Figure 6.8:** (left) Cyclic voltammogram of $(\text{Cp})\text{Co}(\text{Cp}^{\text{N}})$ in the presence of 100 mM of $[\text{}^4\text{-CNPhNH}_3][\text{OTf}]$ in 200 mM $[\text{TBA}][\text{PF}_6]$ DME at 10 mV/s with the acid background subtracted. (right) Spin density plot of $[(\text{Cp})\text{Co}(\text{Cp}^{\text{NH}})][\text{OTf}]$ at an isovalue of 0.04 demonstrating that the N–H bond is entirely decoupled from the spin density. 125
- Figure 6.9:** DFT calculated thermodynamics of PT, ET, and PCET for the reaction of acetophenone with the $[(\text{Cp})\text{Co}(\text{Cp}^{\text{NH}})]^+$ 126
- Figure 6.10:** Time course of the current (I) and charge (Q) in a CPE experiment at -1.45 V 128
- Figure 6.11:** (left) Cyclic voltammograms of 1 mM $[(\text{Cp})\text{Co}(\text{Cp}^{\text{N}})][\text{OTf}]$ at 10 mV/s in the presence of 100 mM $[\text{}^4\text{-CNPhNH}_3][\text{OTf}]$ and the presence (red) and absence (blue) of 50 mM acetophenone. (right) Plot of the dependence of the plateau current on the ketone concentration with a line of best fit. 130
- Figure 6.12:** (left) Plateau current dependence on the concentration of $[(\text{Cp})\text{Co}(\text{Cp}^{\text{N}})][\text{OTf}]$ in the reaction with 100 mM $[\text{}^4\text{-CNPhNH}_3][\text{OTf}]$ and 50 mM acetophenone in a 200 mM $[\text{TBA}][\text{PF}_6]$ solution of DME at 100 mV/s. (right) Repeated cyclic voltammograms in 200 mM $[\text{TBA}][\text{PF}_6]$ DME solution of $[(\text{Cp})\text{Co}(\text{Cp}^{\text{NH}})][\text{OTf}]_2$ at 100 mV/s with increasing equivalents of acetophenone (0 to 50 mM). 131
- Figure A.1:** The ^1H NMR spectrum (500 MHz) of $\{(\text{P}_3^{\text{B}})\text{Fe}(\text{NO})\}^8$ at room temperature in THF- d_8 149
- Figure A.2:** The ^1H NMR spectrum (500 MHz) of $\{(\text{P}_3^{\text{B}})\text{Fe}(\text{NO})\}^8$ at -78 °C in THF- d_8 149
- Figure A.3:** The ^{31}P NMR spectrum (161.9 MHz) of $\{(\text{P}_3^{\text{B}})\text{Fe}(\text{NO})\}^8$ at room temperature in THF- d_8 150
- Figure A.4:** The ^{31}P NMR spectrum (202.4 MHz) of $\{(\text{P}_3^{\text{B}})\text{Fe}(\text{NO})\}^8$ at -78 °C in THF- d_8 150
- Figure A.5:** The ^{11}B NMR spectrum (128.3 MHz) of $\{(\text{P}_3^{\text{B}})\text{Fe}(\text{NO})\}^8$ at room temperature in THF- d_8 151
- Figure A.6:** The ^{19}F NMR spectrum (376.3 MHz) of $\{(\text{P}_3^{\text{B}})\text{Fe}(\text{NO})\}^8$ at room temperature in THF- d_8 151
- Figure A.7:** The ^{13}C NMR spectrum (100.6 MHz) of $\{(\text{P}_3^{\text{B}})\text{Fe}(\text{NO})\}^8$ at room temperature in THF- d_8 152
- Figure A.8:** The ^1H NMR spectrum (400 MHz) of $\{(\text{P}_3^{\text{B}})\text{Fe}(\text{NO})\}^9$ at room temperature in C_6D_6 152

Figure A.9: The ^1H NMR spectrum (500 MHz) of $\{(\text{P}_3^{\text{B}})\text{Fe}(\text{NO})\}^{10}$ at room temperature in THF- d_8 .	153
Figure A.10: The ^1H NMR spectrum (500 MHz) of $\{(\text{P}_3^{\text{B}})\text{Fe}(\text{NO})\}^{10}$ at $-78\text{ }^\circ\text{C}$ in THF- d_8 .	153
Figure A.11: The ^{31}P NMR spectrum (202.4 MHz) of $\{(\text{P}_3^{\text{B}})\text{Fe}(\text{NO})\}^{10}$ at $-78\text{ }^\circ\text{C}$ in THF- d_8 .	154
Figure A.12: The ^{11}B NMR spectrum (128.3 MHz) of $\{(\text{P}_3^{\text{B}})\text{Fe}(\text{NO})\}^{10}$ at room temperature in THF- d_8 .	154
Figure A.13: The ^{13}C NMR spectrum (125.7 MHz) of $\{(\text{P}_3^{\text{B}})\text{Fe}(\text{NO})\}^{10}$ at $-78\text{ }^\circ\text{C}$ in THF- d_8 .	155
Figure A.14: Thin-film IR Absorption spectrum of $\{(\text{P}_3^{\text{B}})\text{Fe}(\text{NO})\}^8$.	155
Figure A.15: Thin-film IR Absorption spectrum of $\{(\text{P}_3^{\text{B}})\text{Fe}(\text{NO})\}^9$.	156
Figure A.16: Thin-film IR Absorption spectrum of $\{(\text{P}_3^{\text{B}})\text{Fe}(\text{NO})\}^{10}$.	156
Figure A.17: UV/Visible spectra of $\{(\text{P}_3^{\text{B}})\text{Fe}(\text{NO})\}^8$ in 2-MeTHF.	157
Figure A.18: UV/Visible spectra of $\{(\text{P}_3^{\text{B}})\text{Fe}(\text{NO})\}^{10}$ in 2-MeTHF.	157
Figure A.19: The 80 K, zero field ^{57}Fe Mössbauer of $\{(\text{P}_3^{\text{B}})\text{Fe}(\text{NO})\}^8$ as a microcrystalline solid suspended in a boron nitride matrix.	160
Figure A.20: The 80 K, zero field ^{57}Fe Mössbauer of $\{(\text{P}_3^{\text{B}})\text{Fe}(\text{NO})\}^8$ as a powder suspended in a boron nitride matrix.	161
Figure A.21: The 80 K, zero field ^{57}Fe Mössbauer of a 2mM solution of $\{(\text{P}_3^{\text{B}})^{57}\text{Fe}(\text{NO})\}^8$ in 2-MeTHF.	161
Figure A.22: The 80 K, zero field ^{57}Fe Mössbauer of $\{(\text{P}_3^{\text{B}})\text{Fe}(\text{NO})\}^9$ as a microcrystalline solid suspended in a boron nitride matrix.	161
Figure A.23: The 80 K, zero field ^{57}Fe Mössbauer of $\{(\text{P}_3^{\text{B}})\text{Fe}(\text{NO})\}^{10}$ as a microcrystalline solid suspended in a boron nitride matrix.	162
Figure A.24: The 80 K, zero field ^{57}Fe Mössbauer of $\{(\text{P}_3^{\text{B}})\text{Fe}(\text{NO})\}^{10}$ as a powder suspended in a boron nitride matrix.	162
Figure A.25: The 80 K, zero field ^{57}Fe Mössbauer of a 2 mM solution of $\{(\text{P}_3^{\text{B}})^{57}\text{Fe}(\text{NO})\}^{10}$ in THF.	163
Figure A.26: The 80 K, 50 mT parallel field ^{57}Fe Mössbauer of a 2mM solution of $\{(\text{P}_3^{\text{B}})^{57}\text{Fe}(\text{NO})\}^{10}$ in THF.	163

Figure A.27: The 80 K, 50 mT perpendicular field ^{57}Fe Mössbauer of a 2mM solution of $\{(\text{P}_3^{\text{B}})^{57}\text{Fe}(\text{NO})\}^{10}$ in THF.	164
Figure A.28: The 80 K, 50 mT parallel field Mössbauer of $[(\text{P}_3^{\text{B}})\text{Fe}(\text{N}_2)]^-$ $[(\text{P}_3^{\text{B}})\text{Fe}(\text{N}_2)][\text{Na}(12\text{-crown-}4)_2]$ as a powder suspended in a boron-nitride matrix.	164
Figure A.29: Scan rate dependence of the $\{(\text{P}_3^{\text{B}})\text{Fe}(\text{NO})\}^{8/9}$ couple in a THF solution of 100 mM $[\text{TBA}][\text{PF}_6]$ under argon.	165
Figure A.30: Scan rate dependence of the $\{(\text{P}_3^{\text{B}})\text{Fe}(\text{NO})\}^{9/10}$ couple in a THF solution of 100 mM $[\text{TBA}][\text{PF}_6]$ under argon.	165
Figure A.31: Cyclic voltammetry data at 100 mV s^{-1} for $\{(\text{P}_3^{\text{B}})\text{Fe}(\text{NO})\}^8$ in a THF solution of 100 mM $[\text{TBA}][\text{BArF}]$ under N_2	166
Figure A.32: X-Band EPR spectrum of $\{(\text{P}_3^{\text{B}})\text{Fe}(\text{NO})\}^9$ in 2-MeTHF at 7 K and its simulation.	169
Figure A.33: A molecular orbital diagram for $\{(\text{P}_3^{\text{B}})\text{Fe}(\text{NO})\}^8$	174
Figure A.34: A molecular orbital diagram for $\{(\text{P}_3^{\text{B}})\text{Fe}(\text{NO})\}^{10}$	175
Figure A.35: A molecular orbital diagram for $\{(\text{P}_3^{\text{B}})\text{Fe}(\text{NO})\}^9$	176
Figure B.1: ^1H NMR spectrum (300 MHz, $\text{DMSO-}d_6$) of $[\text{N}_2\text{NH}_4][\text{Cl}]$ produced from catalytic N_2 -to- NH_3 conversion conducted with $[(\text{P}_3^{\text{B}})\text{Fe}]^+$ catalyst, 54 equiv Cp^*Co , and 108 equiv $[\text{Ph}_2^{15}\text{NH}_2][\text{OTf}]$ under an atmosphere of $^{14}\text{N}_2$	186
Figure B.2: Mössbauer spectrum collected on $[(\text{P}_3^{\text{B}})^{57}\text{Fe}]^+$ that was used for the Mössbauer experiments conducted in this paper.	192
Figure B.3: Mössbauer spectrum collected from a reaction freeze quenched after 5 minutes between $\text{P}_3^{\text{B}}\text{Fe}^+$ and excess Cp^*Co (20 equiv).	193
Figure B.4: Mössbauer spectrum collected from a reaction freeze quenched after 5 minutes between $\text{P}_3^{\text{B}}\text{Fe}^+$ and excess Cp^*Cr (20 equiv).	194
Figure B.5: Mossbauer spectrum collected from a catalytic reaction freeze quenched after 5 minutes.	195
Figure B.6: Mössbauer spectrum collected from a catalytic reaction freeze quenched after 30 minutes.	196
Figure B.7: The X-band EPR spectrum in a 2-MeTHF glass of 2.3 mM $[(\text{P}_3^{\text{B}})\text{Fe}(\text{N}_2)][\text{Na}(12\text{-crown-}4)_2]$ at 77K.	199
Figure B.8: The X-band EPR spectrum in Et_2O of 2.3 mM $[(\text{P}_3^{\text{B}})\text{Fe}][\text{BAr}^{\text{F}}_4]$ at 77 K.	200

- Figure B.9:** The X-band EPR spectrum in Et₂O of 46 mM Cp*₂Co at 77K. 200
- Figure B.10:** The X-band EPR spectrum in Et₂O (1 mL) of the reaction between [(P₃^B)Fe]⁺ (3.5 mg, 0.0023 mmol) and Cp*₂Co (15.2 mg, 0.046 mmol) stirred for 5 minutes at -78 °C then rapidly frozen to 77 K..... 201
- Figure B.11:** The X-band EPR spectrum in Et₂O (1 mL) of the reaction between [(P₃^B)Fe]⁺ (3.5 mg, 0.0023 mmol) and Cp*₂Co (40.3 mg, 0.124 mmol) and [Ph₂NH₂][OTf] (79.4 mg, 0.248 mmol) stirred for 5 minutes at -78 °C then rapidly frozen to 77 K..... 201
- Figure B.12:** 77 K X-band EPR spectrum of a toluene solution of Cp*₂Co (green), 77 K powder X-Band EPR spectrum of the purple solid isolated from the reaction of Cp*₂Co and HOTf as described in **Section B2.2** (red), and 77 K powder X-Band EPR spectrum after annealing the EPR tube RT for two hours (blue). 203
- Figure B.13:** Powder EPR spectrum at 77 K for the reaction of HOTf and Cp*₂Co and its simulation..... 204
- Figure B.14:** Comparison of the EPR spectra obtained using HOTf and DOTf in the reaction with Cp*₂Co. 205
- Figure B.15:** EPR spectrum obtained when reacting DOTf with Cp*₂Co and its simulation..... 205
- Figure B.16:** Calculated BDE vs literature BDE for the species shown in **Table B.13**.... 209
- Figure B.17:** Activation barrier for PCET reactions between selected (P₃^B)Fe(N_xH_y) species (as labeled, total spin-state of the surface in parenthesis) with [(Cp*)Co(η⁴-C₅Me₅H)]⁺ as a function of outer-sphere reorganization energy. 210
- Figure C.1:** Comparison of catalyzed and uncatalyzed H₂ evolution from 2,6-dichloroanilinium triflate and Cp*₂Co at early time points. 222
- Figure C.2:** Mössbauer spectrum collected from a reaction freeze quenched after stirring for 5 minutes at -78 °C in 1 mL of Et₂O between [P₃^B(⁵⁷Fe)N₂][Na(Et₂O)₃] and excess 2,6-[^{2,6}-ClPhNH₃][OTf] (50 equiv). 223
- Figure C.3:** The continuous wave, X-band EPR at 77K in Et₂O of reaction mixtures freeze-quenched after five minutes. In red is the reaction of [(P₃^B)Fe(N₂)][Na(Et₂O)₃] with 50 equiv of [^{2,6}-ClPhNH₃][BAr^F₄] clearly demonstrating the formation of [(P₃^B)Fe(NNH₂)][BAr^F₄].¹⁸ In green is reaction of [(P₃^B)Fe(N₂)][Na(Et₂O)₃] with 50 equiv of [^{2,6}-ClPhNH₃][OTf] in which the small residual species is neither the starting material ([P₃^B)Fe(N₂)][Na(Et₂O)₃) or the desired product ([P₃^B)Fe(NNH₂)][OTf]). 226

- Figure C.4:** In blue is the continuous wave, X-band EPR spectrum at 77K of a reaction mixture of 50 equiv $[^{2,6}\text{-ClPhNH}_3][\text{BAr}^{\text{F}}_4]$ with $[(\text{P}_3^{\text{B}})\text{Fe}(\text{N}_2)][\text{Na}(12\text{-crown-4})_2]$ quenched with liquid nitrogen after 5 minutes. 227
- Figure C.5:** Cyclic voltammograms of 0.5 mM $[(\text{P}_3^{\text{B}})\text{Fe}][\text{BAr}^{\text{F}}_4]$ at varied scan rates (left) and plot of peak current versus square root of scan rate for each feature (right) showing linear dependence in all cases. 235
- Figure C.6:** Cyclic voltammograms of 0.5 mM $[(\text{P}_3^{\text{B}})\text{Fe}][\text{BAr}^{\text{F}}_4]$ (red trace) and $[(\text{P}_3^{\text{B}})\text{Fe}][\text{BAr}^{\text{F}}_4]$ with 10 equiv of tetrabutylammonium trifluoromethanesulfonate ($[\text{TBA}][\text{OTf}]$) (blue and gray traces). 235
- Figure C.7:** $\text{BDFE}_{\text{calc}}$ and BDFE_{lit} plotted for species of known $\text{BDFE}_{\text{E-H}}$. Line of best fit is shown. 239
- Figure C.8:** Cyclic voltammograms of 5 mM $[\text{Ph}_2\text{NH}_2][\text{OTf}]$ (gray trace) and 5 mM $[\text{per-}^{2,6}\text{-ClPhNH}_3][\text{OTf}]$ (red trace)..... 242
- Figure C.9:** XPS survey scan of a section of a glassy carbon plate which was not exposed to the working chamber solution during a 15 hour bulk electrolysis in the presence of $[(\text{P}_3^{\text{B}})\text{Fe}][\text{BAr}^{\text{F}}_4]$, $[\text{Cp}^*\text{Co}][\text{BAr}^{\text{F}}_4]$, $[\text{Ph}_2\text{NH}_2][\text{OTf}]$ and N_2 at -2.1 V (vs $\text{Fc}^{+/0}$)..... 245
- Figure C.10:** XPS survey scan of a section of a glassy carbon plate which was exposed to the working chamber solution during a 15 hour bulk electrolysis in the presence of $[(\text{P}_3^{\text{B}})\text{Fe}][\text{BAr}^{\text{F}}_4]$, $[\text{Cp}^*\text{Co}][\text{BAr}^{\text{F}}_4]$, $[\text{Ph}_2\text{NH}_2][\text{OTf}]$ and N_2 at -2.1 V (vs $\text{Fc}^{+/0}$)..... 247
- Figure D.1:** a) HYSORE powder patterns 256
- Figure D.2:** ^1H NMR spectrum (400 MHz, C_6D_6 , 25 °C) of $(\text{Cp}^*)\text{Co}(\text{exo-}\eta^4\text{-C}_5\text{Me}_5\text{H})$.. 262
- Figure D.3:** ^1H -COSY NMR spectrum (400 MHz, C_6D_6 , 25 °C) of $(\text{Cp}^*)\text{Co}(\text{exo-}\eta^4\text{-C}_5\text{Me}_5\text{H})$ 263
- Figure D.4:** ^{13}C NMR spectrum (100 MHz, C_6D_6 , 25 °C) of $(\text{Cp}^*)\text{Co}(\text{exo-}\eta^4\text{-C}_5\text{Me}_5\text{H})$. 263
- Figure D.5:** ^1H NMR spectrum (400 MHz, C_6D_6 , 25 °C) of $(\text{Cp}^*)\text{Co}(\text{exo-}\eta^4\text{-C}_5\text{Me}_5\text{D})$.. 264
- Figure D.6:** $^2\text{H}\{^1\text{H}\}$ NMR spectrum (61.42 MHz, 90% C_6H_6 :10% C_6D_6 , 25 °C) of $(\text{Cp}^*)\text{Co}(\text{exo-}\eta^4\text{-C}_5\text{Me}_5\text{D})$ 265
- Figure D.7:** $^{13}\text{C}\{^1\text{H}\}$ NMR spectrum (100 MHz, C_6D_6 , 25 °C) of $(\text{Cp}^*)\text{Co}(\text{exo-}\eta^4\text{-C}_5\text{Me}_5\text{D})$ 265
- Figure D.8:** ^1H NMR spectrum (400 MHz, C_6D_6 , 25 °C) of $(\text{Cp}^*)\text{Co}(\text{exo-}\eta^4\text{-C}_5\text{Me}_5^{13}\text{Me})$ 266

Figure D.9: ^{13}C NMR spectrum (100 MHz, C_6D_6 , 25 °C) $(\text{Cp}^*)\text{Co}(\text{exo-}\eta^4\text{-C}_5\text{Me}_5^{13}\text{Me})$	266
Figure D.10: Reaction of $(\text{Cp}^*)\text{Co}(\text{exo-}\eta^4\text{-C}_5\text{Me}_5\text{H})$ with $^{4\text{MeO}}\text{TEMPO}$	267
Figure D.11: ^1H NMR spectrum (400 MHz, $\text{MeCN-}d_3$, RT) of the reaction between $(\text{Cp}^*)\text{Co}(\text{exo-}\eta^4\text{-C}_5\text{Me}_5\text{H})$ and $^{4\text{MeO}}\text{TEMPO}$	268
Figure D.12: Zoomed in view of the ^1H NMR (500 MHz, C_7D_8 , -78 °C) of the reaction between $(\text{Cp}^*)\text{Co}(\text{exo-}\eta^4\text{-C}_5\text{Me}_5\text{H})$ and 2 equivalents of $^{4\text{MeO}}\text{TEMPO}$	269
Figure D.13: ^1H NMR spectrum (500 MHz, C_7D_8 , RT) of the reaction between Cp^*_2Co and $^{4\text{MeO}}\text{TEMPO}$	270
Figure D.14: ^1H NMR spectrum (500 MHz, C_7D_8 , -78 °C) of the reaction between Cp^*_2Co and $^{4\text{MeO}}\text{TEMPO}$	271
Figure D.15: Reaction scheme of Cp^*_2Co with $^{4\text{MeO}}\text{TEMPO}$	271
Figure D.16: ^{13}C NMR spectrum (125 MHz, C_7D_8 , -78 °C) of between Cp^*_2Co and $^{4\text{MeO}}\text{TEMPO}$	272
Figure D.17: Zoomed in data from the ^1H -ROESY NMR (500 MHz, C_7D_8 , -78 °C) of the reaction between Cp^*_2Co and $^{4\text{MeO}}\text{TEMPO}$	273
Figure D.18: ^1H NMR spectrum (400 MHz, C_7D_8 , RT) of the reaction between octamethylcobaltocene (4 mg, 0.013 mmol, 1 eq) and $^{4\text{MeO}}\text{TEMPO}$ (2.5 mg, 0.013 mmol, 1 eq).....	273
Figure D.19: ^1H NMR (400 MHz, $\text{MeCN-}d_3$, RT) of the reaction of $(\text{Cp}^*)\text{Co}(\text{exo-}\eta^4\text{-C}_5\text{Me}_5\text{H})$ with one atmosphere of CO_2	275
Figure D.20: ^1H NMR (400 MHz, $\text{MeCN-}d_3$, RT) of the reaction of $(\text{Cp}^*)\text{Co}(\text{exo-}\eta^4\text{-C}_5\text{Me}_5\text{H})$ with 4 equivalents of $[\text{Pt}(\text{dmpe})_2][\text{PF}_6]_2$	276
Figure D.21: $^{31}\text{P}\{^1\text{H}\}$ NMR (162 MHz, $\text{MeCN-}d_3$, RT) of the reaction of $(\text{Cp}^*)\text{Co}(\text{exo-}\eta^4\text{-C}_5\text{Me}_5\text{H})$ with 4 equivalents of $[\text{Pt}(\text{dmpe})_2][\text{PF}_6]_2$	276
Figure D.22: Q-band inversion recovery traces of <i>endo</i> - (black) and <i>exo</i> -isomers (red) of Cp^*_2Co protonation	277
Figure D.23: Pseudomodulated Q-band ESE-EPR spectrum at 10 K of a coal standard sample	278
Figure D.24: X-Band CW EPR spectrum (blue) at 77 K in the solid state of the precipitate from the reaction of bis(trifluoromethanesulfonyl)imide with Cp^*_2Co at -78 °C in toluene.....	281

- Figure D.25:** A comparison of the 77 K, X-band EPR spectra of solid samples of $[(\text{Cp}^*)\text{Co}(\text{exo-}\eta^4\text{-C}_5\text{Me}_5\text{H})][\text{BArF}]$ (blue) and $[(\text{Cp}^*)\text{Co}(\text{exo-}\eta^4\text{-C}_5\text{Me}_5\text{D})][\text{BArF}]$ (orange).282
- Figure D.26:** A depiction of our mechanistic proposal to account for observations upon the reaction of $(\text{Cp}^*)\text{Co}(\text{exo-C}_5\text{Me}_5\text{D})$ with HBAr^{F}_4283
- Figure D.27:** A comparison of the data to the simulation (green) for the 77 K, X-band EPR spectra of solid samples of $[(\text{Cp}^*)\text{Co}(\text{exo-}\eta^4\text{-C}_5\text{Me}_5\text{H})][\text{BArF}]$ (blue) and $[(\text{Cp}^*)\text{Co}(\text{exo-}\eta^4\text{-C}_5\text{Me}_5\text{D})][\text{BArF}]$ (orange).284
- Figure D.28:** X-Band CW EPR spectrum (blue) at 77 K in the solid state of the precipitate from the reaction of trifluoromethanesulfonic acid with Cp^*_2Co at $-78\text{ }^\circ\text{C}$ in toluene.285
- Figure D.29:** Cyclic voltammogram of $(\text{Cp}^*)\text{Co}(\eta^4\text{-C}_5\text{Me}_6)$ at room temperature.285
- Figure D.30:** Scan rate dependence of the $[(\text{Cp}^*)\text{Co}(\eta^4\text{-C}_5\text{Me}_6)]^{+/0}$ at room temperature 286
- Figure D.31:** Cyclic voltammograms of $(\text{Cp}^*)\text{Co}(\text{exo-}\eta^4\text{-C}_5\text{Me}_5\text{H})$ at room temperature286
- Figure D.32:** Cyclic voltammograms of $(\text{Cp}^*)\text{Co}(\text{exo-}\eta^4\text{-C}_5\text{Me}_5\text{H})$ at room temperature at different scan rates in a butyronitrile solution of 0.4 M $[\text{TBA}][\text{PF}_6]$287
- Figure D.33:** Cyclic voltammograms of $(\text{Cp}^*)\text{Co}(\text{exo-}\eta^4\text{-C}_5\text{Me}_5\text{H})$ at $-78\text{ }^\circ\text{C}$ 288
- Figure D.34:** Comparison of cyclic voltammograms taken at room temperature ($\sim 22\text{ }^\circ\text{C}$) and at $-78\text{ }^\circ\text{C}$288
- Figure D.35:** Cyclic voltammograms of Cp^*_2Co at room temperature289
- Figure D.36:** Thin film IR spectra of $(\text{Cp}^*)\text{Co}(\text{exo-}\eta^4\text{-C}_5\text{Me}_5\text{H})$ (blue) and $(\text{Cp}^*)\text{Co}(\text{exo-}\eta^4\text{-C}_5\text{Me}_5\text{D})$ (orange).291
- Figure D.37:** Solution state IR spectra of $(\text{Cp}^*)\text{Co}(\text{exo-}\eta^4\text{-C}_5\text{Me}_5\text{H})$ (blue) and $(\text{Cp}^*)\text{Co}(\text{exo-}\eta^4\text{-C}_5\text{Me}_5\text{D})$ (orange) in C_6D_6292
- Figure D.38:** Thin film IR spectrum of the reaction between $(\text{Cp}^*)\text{Co}(\text{exo-}\eta^4\text{-C}_5\text{Me}_5\text{H})$ and CO_2 demonstrating the formation of $[\text{Cp}^*_2\text{Co}][\text{HCO}_2]$292
- Figure D.39:** Measured thermochemical parameters in acetonitrile. Potentials in V vs $\text{Fc}^{+/0}$293
- Figure D.40:** Describes the process of determining the C–H BDFE in $[(\text{Cp}^*)\text{Co}(\text{exo-}\eta^4\text{-C}_5\text{Me}_5\text{H})]^+$ using the measured hydricity of $(\text{Cp}^*)\text{Co}(\text{exo-}\eta^4\text{-C}_5\text{Me}_5\text{H})$ and the redox potential of $(\text{Cp}^*)\text{Co}(\text{exo-}\eta^4\text{-C}_5\text{Me}_5\text{H})$293

- Figure D.41:** Describes the process of determining the C–H BDFE in $[(\text{Cp}^*)\text{Co}(\text{exo-}\eta^4\text{-C}_5\text{Me}_5\text{H})]^+$ using the measured BDFE C–H of $(\text{Cp}^*)\text{Co}(\text{exo-}\eta^4\text{-C}_5\text{Me}_5\text{H})$ and the redox potential of $(\text{Cp}^*)\text{Co}(\text{exo-}\eta^4\text{-C}_5\text{Me}_5\text{H})$ and Cp^*_2Co 294
- Figure E.1:** ^1H NMR spectrum of $\text{Cp}(\eta^4\text{-C}_5\text{H}_5\text{PhNMe}_2)\text{Co}$ in C_6D_6 , 400 MHz, 298 K. ... 313
- Figure E.2:** $^{13}\text{C}\{^1\text{H}\}$ NMR spectrum of $\text{Cp}(\eta^4\text{-C}_5\text{H}_5\text{PhNMe}_2)\text{Co}$ in C_6D_6 , 100 MHz, 298 K. 314
- Figure E.3:** ^1H NMR spectrum of $(\text{Cp})\text{Co}(\text{Cp}^{\text{N}})$ in CD_3CN , 400 MHz, 298 K. 314
- Figure E.4:** ^1H NMR spectrum of $[(\text{Cp})\text{Co}(\text{Cp}^{\text{N}})][\text{OTf}]$ in CD_3CN , 400 MHz, 298 K. ... 315
- Figure E.5:** ^{19}F NMR spectrum of $[(\text{Cp})\text{Co}(\text{Cp}^{\text{N}})][\text{OTf}]$ in CD_3CN , 376 MHz, 298 K. ... 315
- Figure E.6:** $^{13}\text{C}\{^1\text{H}\}$ NMR spectrum of $[(\text{Cp})\text{Co}(\text{Cp}^{\text{N}})][\text{OTf}]$ in CD_3CN , 100 MHz, 298 K. 316
- Figure E.7:** ^1H NMR spectrum of $[(\text{Cp})\text{Co}(\text{Cp}^{\text{NH}})][\text{OTf}]_2$ in CD_3CN , 400 MHz, 298 K. 316
- Figure E.8:** ^{19}F NMR spectrum of $[(\text{Cp})\text{Co}(\text{Cp}^{\text{NH}})][\text{OTf}]_2$ in CD_3CN , 376 MHz, 298 K. 317
- Figure E.9:** $^{13}\text{C}\{^1\text{H}\}$ NMR spectrum of $[(\text{Cp})\text{Co}(\text{Cp}^{\text{NH}})][\text{OTf}]_2$ in CD_3CN , 100 MHz, 298 K. 317
- Figure E.10:** UV-Vis spectrum at room temperature for $[(\text{Cp})\text{Co}(\text{Cp}^{\text{NH}})][\text{OTf}]_2$ in 2-MeTHF:THF solution (4:1). 318
- Figure E.11:** UV-Vis spectra of the reaction of trifluoromethanesulfonimide and $(\text{Cp})\text{Co}(\text{Cp}^{\text{N}})$ at $-130\text{ }^\circ\text{C}$ in 2 UV-Vis spectrum in 2-MeTHF:THF solution (4:1) 318
- Figure E.12:** UV-Vis spectrum at room temperature for $[(\text{Cp})\text{Co}(\text{Cp}^{\text{NH}})][\text{OTf}]_2$ in acetonitrile. 319
- Figure E.13:**(blue) X-band EPR spectrum of a 1 mM solution of $(\text{Cp})\text{Co}(\text{Cp}^{\text{N}})$ in a 2-methyltetrahydrofuran glass at 77 K. 319
- Figure E.14:** (blue) X-band EPR spectrum of a 1 mM solution of $[(\text{Cp})\text{Co}(\text{Cp}^{\text{NH}})][\text{OTf}]$ in a 2-methyltetrahydrofuran glass at 77 K generated via protonation of $(\text{Cp})\text{Co}(\text{Cp}^{\text{N}})$. (red) X-band EPR spectrum of a 1 mM solution of $[(\text{Cp})\text{Co}(\text{Cp}^{\text{NH}})][\text{OTf}]$ in frozen acetonitrile at 77 K generated via reduction of $[(\text{Cp})\text{Co}(\text{Cp}^{\text{NH}})][\text{OTf}]_2$ 321
- Figure E.15:** IR spectrum of $[(\text{Cp})\text{Co}(\text{Cp}^{\text{NH}})][\text{OTf}]_2$ in a KBr pellet. Weak N–H vibration is evident at 3430 cm^{-1} 322

- Figure E.16:** Variable scan rate cyclic voltammograms with a glassy carbon working electrode of a 1 mM solution of the $(\text{Cp})\text{Co}(\text{Cp}^{\text{N}})^{+/0}$ in acetonitrile with 100 mM [TBA][PF₆]. 324
- Figure E.17:** Variable scan rate cyclic voltammograms with a glassy carbon working electrode of a 1 mM solution of the $[(\text{Cp})\text{Co}(\text{Cp}^{\text{N}})]^{2+/+}$ in acetonitrile with 100 mM [TBA][PF₆]. 324
- Figure E.18:** Variable scan rate cyclic voltammograms with a boron doped diamond working electrode of a 1 mM solution of $[(\text{Cp})\text{Co}(\text{Cp}^{\text{NH}})]\text{[OTf]}_2$ and 1 mM solution of ferrocene in acetonitrile with 100 mM [TBA][PF₆]. 325
- Figure E.19:** Cyclic voltammogram of a glassy carbon working electrode of a 1 mM solution of the $(\text{Cp})\text{Co}(\text{Cp}^{\text{N}})^{+/0}$ in DME with 100 mM [TBA][PF₆]. 325
- Figure E.20:** Cathodic scan of CV's at 100 mV/s of different concentrations of $[(\text{Cp})\text{Co}(\text{Cp}^{\text{N}})]\text{[OTf]}$ on a BDD working electrode of a DME solution of 100 mM [⁴CNPhNH₃][OTf], 50 mM acetophenone, and 200 mM [TBA][PF₆]. 326
- Figure E.21:** Plot of plateau current (-1.314 V vs Fc⁺⁰) against concentration of $[(\text{Cp})\text{Co}(\text{Cp}^{\text{N}})]\text{[OTf]}$ for the CV's shown in **Figure E.20** with a line of best fit. 326
- Figure E.22:** Cathodic scan of CV's at 10 mV/s of different concentrations of acetophenone on a BDD working electrode of a DME solution of 100 mM [⁴CNPhNH₃][OTf], 1 mM $[(\text{Cp})\text{Co}(\text{Cp}^{\text{N}})]\text{[OTf]}$, and 200 mM [TBA][PF₆]. 327
- Figure E.23:** Plot of plateau current (-1.314 V vs Fc⁺⁰) against concentration of acetophenone for the CV's shown in **Figure E.22** with a line of best fit. 327
- Figure E.24:** Comparison of CV's on BDD working electrode at 10 mV/s with 1 mM $[(\text{Cp})\text{Co}(\text{Cp}^{\text{N}})]\text{[OTf]}$, 100 mM [⁴CNPhNH₃][OTf], and 200 mM [TBA][PF₆] with variable amount of acetophenone (0 mM, blue) vs (50 mM, red). 328
- Figure E.25:** Differential pulse voltammogram of a DME solution containing 1 mM ferrocene, 1 mM $[(\text{Cp})\text{Co}(\text{Cp}^{\text{N}})]\text{[OTf]}$, 50 mM acetophenone, and 200 mM [TBA][PF₆]. 328
- Figure E.26:** CV at 100 mV/s of a DME solution containing 1 mM ferrocene, 1 mM $[(\text{Cp})\text{Co}(\text{Cp}^{\text{N}})]\text{[OTf]}$, 50 mM acetophenone, and 200 mM [TBA][PF₆]. 329
- Figure E.27:** 400 MHz ¹H NMR spectrum of 4-chloroaniline (⁴-ClPhNH₂) in MeCN-*d*₃ at room temperature. 334
- Figure E.28:** 400 MHz ¹H NMR spectrum of 4-chloroanilinium triflate ($[\text{Cp}^{\text{N}}\text{PhNH}_3]^+\text{[OTf]}^-$) in MeCN-*d*₃ at room temperature. 335

Figure E.29: 400 MHz ^1H NMR spectrum of 2-chloroaniline ($^{2-^{35}\text{Cl}}\text{PhNH}_2$) in $\text{MeCN-}d_3$ at room temperature.....	335
Figure E.30: 400 MHz ^1H NMR spectrum of 2-chloroanilinium triflate ($^{2-^{35}\text{Cl}}\text{PhNH}_3$)[OTf] in $\text{MeCN-}d_3$ at room temperature.	336
Figure E.31: 400 MHz ^1H NMR spectra of titration experiments of $[(\text{Cp})\text{Co}(\text{Cp}^{\text{NH}})]$ [OTf] $_2$ with 4-chloroaniline in $\text{MeCN-}d_3$ at room temperature.....	337
Figure E.32: 400 MHz ^1H NMR spectra of titration experiments of $[(\text{Cp})\text{Co}(\text{Cp}^{\text{NH}})]$ [OTf] $_2$ with 4-chloroaniline in $\text{MeCN-}d_3$ at room temperature.....	338
Figure E.33: 400 MHz ^1H NMR spectra of titration experiments of $[(\text{Cp})\text{Co}(\text{Cp}^{\text{NH}})]$ [OTf] $_2$ with 2-chloroaniline in $\text{MeCN-}d_3$ at room temperature.....	339
Figure E.34: Thermochemical relationships in acetonitrile for cobaltocene species in this study.....	341
Figure E.35: Calibration curve used for GC-TCD detection of H_2	343
Figure E.36: Calibration curve used for GC-FID quantification of pinacol (2,3-diphenylbutanediol).	343
Figure E.37: Calibration curve used for GC-FID quantification of ketone (acetophenone).....	344
Figure E.38: CV's relevant to the set-up of Entry 1 in Table E.14	345
Figure E.39: Current (left axis) and charge passed (right axis) with respect to time during the CPE experiment.....	346
Figure E.40: Negative first derivative of DPV taken after the CPE experiment (Table E.14 , Entry 1).	346
Figure E.41: First derivative of DPV taken after the CPE experiment (Table E.14 , Entry 1).	347
Figure E.42: XPS of the BDD electrode in the Co 2p region	347
Figure E.43: XPS of the BDD electrode in the S 2p region, showing no evidence of S deposition after the CPE experiment (Table E.14 , Entry 1). Sulfur is found in both the triflate counteranion and the tosic acid.....	348
Figure E.44: XPS of the BDD electrode in the N 1s region	348
Figure E.45: CV's relevant to the set-up of Entry 2 in Table E.14	349

Figure E.46: Current (left axis) and charge passed (right axis) with respect to time during the CPE experiment (Table E.14 , Entry 2).	349
Figure E.47: Negative first derivative of DPV taken after the CPE experiment (Table E.14 , Entry 2).	350
Figure E.48: First derivative of DPV taken after the CPE experiment (Table E.14 , Entry 2).	350
Figure E.49: CV's relevant to the set-up of Entry 3 in Table E.14	351
Figure E.50: Current (left axis) and charge passed (right axis) with respect to time during the CPE experiment (Table E.14 , Entry 3).	351
Figure E.51: Negative first derivative of DPV taken after the CPE experiment (Table E.14 , Entry 4)	352
Figure E.52: CV's relevant to the set-up of Entry 4 in Table E.14	352
Figure E.53: Current (left axis) and charge passed (right axis) with respect to time during the CPE experiment (Table E.14 , Entry 4).	353

LIST OF EQUATIONS

Eq 1.1) $\eta = E_{\text{app}} - E_{\text{min}}$	12
Eq 1.2) $\text{BDFE}_{\text{eff}} = 1.37 \times \text{p}K_{\text{a}} + 23.06 \times E^{\circ} + C_{\text{G}}$	13
Eq 1.3) $\Delta\Delta G_{\text{f}} = 3 \times (\text{BDFE}(\text{H}_2)/2 - \text{BDFE}_{\text{eff}})$	13
Eq 1.4) $\text{BDE}_{\text{eff}} = 1.37 \times \text{p}K_{\text{a}} + 23.06 \times E^{\circ} + C_{\text{H}}$	13
Eq 1.5) $\Delta\Delta H_{\text{f}} = 3 \times (\text{BDE}(\text{H}_2)/2 - \text{BDE}_{\text{eff}})$	13
Eq 3.1) $\text{BDE}_{\text{eff}} = 1.37 \times \text{p}K_{\text{a}} + 23.06 \times E^{\circ} + C_{\text{h}}$	39
Eq 3.2) $\Delta\Delta H_{\text{f}} = 3 \times (\text{BDE}_{\text{eff}} - \text{BDE}(\text{H}_2)/2)$	39
Eq 3.3) $(\text{P}_3^{\text{B}})\text{Fe}(\text{N}_2) + \text{e}^{-} \rightarrow [(\text{P}_3^{\text{B}})\text{Fe}(\text{N}_2)]^{-}$	46
Eq 3.4) $[(\text{P}_3^{\text{B}})\text{Fe}(\text{N}_2)]^{-} + \text{H}^{+} \rightarrow (\text{P}_3^{\text{B}})\text{Fe}(\text{NNH})$	46
Eq 3.5) $(\text{P}_3^{\text{B}})\text{Fe}(\text{N}_2) + \text{H}^{+} \rightarrow [(\text{P}_3^{\text{B}})\text{Fe}(\text{NNH})]^{+}$	46
Eq 3.6) $[(\text{P}_3^{\text{B}})\text{Fe}(\text{NNH})]^{+} + \text{e}^{-} \rightarrow (\text{P}_3^{\text{B}})\text{Fe}(\text{NNH})$	46
Eq 3.7) $(\text{P}_3^{\text{B}})\text{Fe}(\text{N}_2) + \text{H}\cdot \rightarrow (\text{P}_3^{\text{B}})\text{Fe}(\text{NNH})$	46
Eq 3.8) $(\text{P}_3^{\text{B}})\text{Fe}(\text{N}_2) + [(\text{Cp}^*)\text{Co}(\eta^4\text{-C}_5\text{Me}_5\text{H})]^{+} \rightarrow (\text{P}_3^{\text{B}})\text{Fe}(\text{NNH}) + [(\text{Cp}^*)_2\text{Co}]^{+}$	52
Eq 4.1) $[(\text{P}_3^{\text{B}})\text{Fe}(\text{N}_2)]^{-} + \text{H}^{+} \rightarrow (\text{P}_3^{\text{B}})\text{Fe}(\text{NNH})$	66
Eq 4.2) $(\text{P}_3^{\text{B}})\text{Fe}(\text{NNH}) + \text{H}^{+} \rightarrow [(\text{P}_3^{\text{B}})\text{Fe}(\text{NNH}_2)]^{+}$	66
Eq 4.3) $(\text{P}_3^{\text{B}})\text{Fe}(\text{NNH}) \rightarrow (\text{P}_3^{\text{B}})\text{Fe}(\text{N}_2) + 1/2 \text{H}_2$	66
Eq 4.4) $\text{PhNH}_2 + [^{2,6\text{-Cl}}\text{PhNH}_3]^{+} \rightarrow [\text{PhNH}_3]^{+} + ^{2,6\text{-Cl}}\text{PhNH}_2$	68
Eq 4.5) $\text{p}K_{\text{a}}([\text{PhNH}_3^{+}]) = -\Delta G_{\text{a}}/(2.303 \times \text{RT}) + \text{p}K_{\text{a}}([^{2,6\text{-Cl}}\text{PhNH}_3]^{+})$	68
Eq 4.6) $\text{PhNH}_2 + [^{2,6\text{-Cl}}\text{PhNH}_3][\text{OTf}] \rightarrow [\text{PhNH}_3][\text{OTf}] + ^{2,6\text{-Cl}}\text{PhNH}_2$	68
Eq 4.7) $\text{p}K_{\text{d}}([\text{PhNH}_3][\text{OTf}]) = -\Delta G_{\text{d}}/(2.303 \times \text{RT}) + \text{p}K_{\text{a}}([^{2,6\text{-Cl}}\text{PhNH}_3]^{+})$	68
Eq 4.8) $K_{\text{eq}} = ([[(^{\text{R}}\text{PhNH}_2\text{-}(\text{Cp}^*)\text{Co}(\text{exo-}\eta^4\text{-C}_5\text{Me}_5\text{H}))][\text{OTf}]])/$	69
Eq 4.9) $(\text{P}_3^{\text{B}})\text{Fe}(\text{NNH}) + [(\text{Cp}^*)\text{Co}(\text{exo-}\eta^4\text{-C}_5\text{Me}_5\text{H})][\text{OTf}] \rightarrow$	71
Eq 4.10) $(\text{P}_3^{\text{B}})\text{Fe}(\text{NNH}) + [(\text{Cp}^*)\text{Co}(\text{exo-}\eta^4\text{-C}_5\text{Me}_5\text{H})][\text{OTf}] \rightarrow$	71

Eq 4.11) $[(P_3^B)Fe(NNH_2)][OTf] + Cp^*_2Co \rightarrow (P_3^B)Fe(NNH_2) + [Cp^*_2Co][OTf] \dots$	71
Eq 5.1) $(Cp^*)Co(exo-\eta^4-C_5Me_5H) + {}^4MeO\text{TEMPO}\cdot \rightarrow Cp^*_2Co + {}^4MeO\text{TEMPO-H} \dots$	102
Eq 5.2) $Cp^*_2Co + {}^4MeO\text{TEMPO}\cdot \rightarrow (Cp^*)Co(\eta^4-C_5Me_4CH_2) + {}^4MeO\text{TEMPO-H} \dots$	102
Eq 6.1) $BDFE = 1.37 \times pK_a + 23.06 \times E^0 + C_G \dots$	123
Eq 6.2) $BDFE_{\text{eff}} = 1.37 \times pK_a(\text{acid}) + 23.06 \times E^0(\text{reductant}) + C_G \dots$	132
Eq 6.3) $E_{\text{onset}} (\text{vs NHE}) = -0.99 + 0.60 \times \text{pH} \dots$	134
Eq B.1) $\Delta G_{\text{solv}} \approx E_{\text{soln}} - E_{\text{gas}} \dots$	182
Eq B.2) $G_{\text{soln}} = G_{\text{gas}} + \Delta G_{\text{solv}} \dots$	182
Eq B.3) $\Delta G = -nFE^0 \dots$	182
Eq B.4) $\Delta G = \Delta H - T\Delta S \dots$	207
Eq B.5) $\Delta H = \text{BDE}(H_2) - 2 \times \text{BDE}([(Cp^*)Co(\eta^4-C_5Me_5H)]^+) \dots$	207
Eq B.6) $T\Delta S = T\Delta S_H - 2 \times T\Delta S_H = -T\Delta S_H = -4.6 \text{ kcal mol}^{-1} \dots$	207
Eq B.7) $105.8 \text{ kcal mol}^{-1} - 2 \times \text{BDE}([(Cp^*)Co(\eta^4-C_5Me_5H)]^+) + 4.6 \text{ kcal mol}^{-1} \dots$	207
Eq B.8) $\therefore \text{BDE}([(Cp^*)Co(\eta^4-C_5Me_5H)]^+) < 50.6 \text{ kcal mol}^{-1} \dots$	207
Eq C.1) $\Delta G_{\text{solv}} \approx E_{\text{soln}} - E_{\text{gas}} \dots$	216
Eq C.2) $G_{\text{soln}} = G_{\text{gas}} + \Delta G_{\text{solv}} \dots$	216
Eq C.3) $\Delta G = -nFE^0 \dots$	216
Eq C.4) $\lambda_{\text{is,PT/PCET}} = \sum_j (f_j^i f_j^p) / (f_j^i + f_j^p) \times \Delta q_j^2 \dots$	236
Eq C.5) $\lambda_{\text{os,PCET}} = \lambda_{\text{os,PT}} + \lambda_{\text{os,ET}} - (\lambda_{\text{os,PT}} * \lambda_{\text{os,ET}}) \cos(\theta) \dots$	237
Eq C.6) $k_{\text{bi}} = K_A * k_{\text{uni}} \dots$	237
Eq C.7) $[{}^{2,6-Cl}PhNH_3][OTf] + Cp^*_2Co \rightarrow (Cp^*)Co(exo-\eta^4-C_5Me_5H)-OTf + \dots$	237
Eq C.8) $[{}^{2,6-Me}PhNH_3][OTf] + Cp^*_2Co \rightarrow (Cp^*)Co(exo-\eta^4-C_5Me_5H)-OTf + \dots$	238
Eq C.9) $[{}^{4-OMe}PhNH_3][OTf] + Cp^*_2Co \rightarrow (Cp^*)Co(exo-\eta^4-C_5Me_5H)-OTf + \dots$	238
Eq C.10) $(P_3^B)Fe(NNH) + [(Cp^*)Co(exo-\eta^4-C_5Me_5H)][OTf] \rightarrow \dots$	238
Eq C.11) $[(P_3^B)Fe(NNH_2)][OTf] + Cp^*_2Co \rightarrow (P_3^B)Fe(NNH_2) + [Cp^*_2Co][OTf] \dots$	238

Eq C.12) $(P_3^B)Fe(NNH) + [(Cp^*)Co(exo-\eta^4-C_5Me_5H)][[OTf] \rightarrow$	238
Eq C.13) $pK_a(THF) = 0.78 \times pK_a(MeCN) - 0.52$	247
Eq C.14) $pK_a(THF) = 1.19 \times pK_a(H_2O) + 2.13$	247
Eq D.1) $v_{\pm} = A/2 \pm v_N $	254
Eq D.2) $v_{\pm, ml} = v_N \pm 3P(2m_l - 1)/2 $	254
Eq D.3) $H = \mu_B B_0 gS + \mu_{NG} B_0 I + hSAI + hIPI$	256
Eq D.4) $P = P_{xx}000P_{yy}000P_{zz} = e2Qq/h4I(2I - 1) - (1 - \eta)000 - (1 + \eta)0002$	257
Eq D.5) $e^2qQ/h = 2I(2I - 1)P_{zz}$	257
Eq D.6) $\eta = (P_{xx} - P_{yy})/P_{zz}$	257
Eq D.7) $M_z = 0, T \approx \ln(2) \times T_1'$	278
Eq D.8) $\Delta G = (G(X\bullet) + G(H\bullet)) - G(X-H)$	296
Eq D.9) $BDFE = 0.996 \times \Delta G + 4.376$	296
Eq E.1) $CS_{Co} = CS_{NH} \times y + CS_N \times (1 - y)$	330
Eq E.2) $CS_{Acid/Base} = CS_{Acid} \times y + CS_{Base} \times (1 - y)$	330
Eq E.3) $[Acid] = y \times Integral$	330
Eq E.4) $K_{eq} = ([Acid][[(Cp)Co(Cp^N)]^+]) / ([Base][[(Cp)Co(Cp^{NH})]^{2+}]$	330
Eq E.5) $\Delta G = RT \times \ln(K_{eq})$	330
Eq E.6) $pK_a([(Cp)Co(Cp^{NH})]^{2+}) = Reference + \Delta G/1.37$	330
Eq E.7) $BDFE = 1.37 \times pK_a + 23.06 \times E^{\circ}_1 + C_G$	340
Eq E.8) $BDFE_1 = 1.37 \times 8.6 + 23.06 \times -1.21 + 54.9$	340
Eq E.9) $BDFE_1 = 38.8 \text{ kcal} \cdot \text{mol}^{-1}$	340
Eq E.10) $BDFE = 1.37 \times pK_a + 23.06 \times E^{\circ}_2 + C_G$	340
Eq E.11) $BDFE_2 = 1.37 \times 8.6 + 23.06 \times 0.54 + 54.9$	340
Eq E.12) $BDFE_2 = 79.1 \text{ kcal} \cdot \text{mol}^{-1}$	340

Eq E.13) $\Delta G(\text{H}^-) = 1.37 \times \text{p}K_{\text{a}} + 23.06 \times E^{\circ}_1 + 23.06 \times E^{\circ}_2 + C_{\text{Hyd}}$	340
Eq E.14) $\Delta G(\text{H}^-) = 1.37 \times 8.6 + 23.06 \times 0.54 + 23.06 \times -1.21 + 79.6$	340
Eq E.15) $\Delta G(\text{H}^-) = 75.9 \text{ kcal} \cdot \text{mol}^{-1}$	340
Eq E.16) $\text{BDFE} = 1.37 \times \text{p}K_{\text{a}} + 23.06 \times E^{\circ}_3 + C_{\text{G}}$	340
Eq E.17) $\text{p}K_{\text{a}} = (\text{BDFE} - 23.06 \times E^{\circ} - C_{\text{G}}) / 1.37$	340
Eq E.18) $\text{p}K_{\text{a}} = (38.8 - 23.06 \times -1.35 - 54.9) / 1.37$	340
Eq E.19) $\text{p}K_{\text{a}} = 11.0$	340

LIST OF TABLES

Table 3.1: N ₂ -to-NH ₃ Conversion with (P ₃ ^E)M Complexes (M = Fe, Co).....	41
Table 3.2: Calculated pK _a Values and BDEs of Selected Species	46
Table 4.1. Literature and calculated pK _a values and efficiencies observed in catalytic N ₂ -to-NH ₃ conversion.....	64
Table 4.2. Yields and Faradaic Efficiencies of NH ₃ from CPE Experiments with [(P ₃ ^B)Fe] ⁺	76
Table 6.1. Results from CPE experiments on a DME solution of 200 mM [TBA][PF ₆], 100 mM tosic acid, 50 mM acetophenone at -1.45 V vs Ag ⁺⁰	127
Table A.1: Comparison of selected data for {(P ₃ ^B)Fe(NO)} ⁹ and [Cr(CN) ₅ (NO)] ³⁻¹⁸	158
Table A.2: X-ray parameters for {(P ₃ ^B)Fe(NO)} ⁹ , and {(P ₃ ^B)Fe(NO)} ¹⁰	166
Table A.3: X-ray parameters for {(P ₃ ^B)Fe(NO)} ⁸	168
Table A.4: A comparison of calculated (BP86, low-spin) and experimental bond parameters	171
Table A.5: Spin ladder energies for different functionals for {(P ₃ ^B)Fe(NO)} ⁸⁻¹⁰ . Broken symmetry solutions in which an S = 1 NO ⁻ unit is antiferromagnetically coupled to the metal are indicated by BS.	171
Table A.6: Calculated Mössbauer parameters for the spin ladder of {(P ₃ ^B)Fe(NO)} ⁸⁻¹⁰ ..	173
Table A.7: Comparison of crystallographically determined bond lengths and Wiberg Bond Indices for {(P ₃ ^B)Fe(NO)} ⁸⁻¹⁰	175
Table B.1: UV-vis quantification results for standard NH ₃ generation experiments with [(P ₃ ^B)Fe] ⁺	184
Table B.2: UV-vis quantification results for standard NH ₃ generation experiments with (P ₃ ^{Si})Fe(N ₂).....	185
Table B.3: UV-vis quantification results for standard NH ₃ generation experiments with [(P ₃ ^B)Co(N ₂)] ⁻	185
Table B.4: UV-vis quantification results for standard NH ₃ generation experiments with (P ₃ ^{Si})Co(N ₂).....	186

Table B.5: UV-vis quantification results for NH ₃ generation experiments with [(P ₃ ^B)Fe] ⁺ , with reloading.....	187
Table B.6: Time-resolved H ₂ quantification for the reaction of Cp* ₂ Co and acid in Et ₂ O at -78 °C in the absence of an Fe precatalyst	188
Table B.7: Fit parameters for [(P ₃ ^B) ⁵⁷ Fe] ⁺	192
Table B.8: Simulation parameters for Mossbauer spectrum in Figure B.3	193
Table B.9: Simulation parameters for Mossbauer spectrum in Figure B.4	195
Table B.10: Simulation parameters for Mossbauer spectrum in Figure B.5	196
Table B.11: Simulation parameters for Mossbauer spectrum in Figure B.6	197
Table B.12: A comparison of the <i>g</i> -tensors for the authentic sample of [(P ₃ ^B)Fe(N ₂)] ⁻ (Figure B.7), the freeze quench of the reaction with the reductant (Figure B.10), the freeze quench of the catalytic reaction mixture (Figure B.11).....	202
Table B.13: Calculated Δ <i>H</i> values and literature BDE values used for BDE calibration.	208
Table B.14: Calculated entropy (<i>S</i>) for selected XH and X• species	209
Table B.15: Calculated Reorganization Energies, Free-Energies of Reaction and Activation Barriers for Selected PCET Reactions.....	210
Table C.1: NMR quantification results for standard NH ₃ generation experiments with [(P ₃ ^B)Fe][BAr ^F ₄].....	219
Table C.24: Data for Background H ₂ Quantification Experiments	220
Table C.25: Time points for catalyzed H ₂ evolution from 2,6-dichloroanilinium triflate and Cp* ₂ Co.....	221
Table C.26: Time points for uncatalyzed H ₂ evolution from 2,6-dichloroanilinium triflate and Cp* ₂ Co.....	221
Table C.5: Simulation parameters for Mossbauer spectrum in Figure C.2	224
Table C.6: Comparative NH ₃ and H ₂ Yields for [^{2,6-Cl} PhNH ₃][OTf] and [^{2,6-Cl} PhNH ₃][BAr ^F ₄].....	228
Table C.7: Controlled Potential Electrolysis Data.....	232
Table C.8: Overview of Parameters Used to Calculate Kinetic Barriers.....	238

Table C.9: Data used to generate the plot and line of best fit shown in Figure C.7 .	239
Table C.10: Calculated Reduction Potentials of Selected Species	240
Table C.11: pK_a values of anilinium acids in different solvents	247
Table D.1: Simulation parameters derived from the ENDOR, HYSCORE, and CW-EPR spectroscopy.	279
Table D.2: Crystallographic details for $(Cp^*)Co(exo-\eta^4-C_5Me_5H)$ and $(Cp^*)Co(\eta^4-C_5Me_6)$	289
Table D.3: Thermochemistry for the structures optimized with different functionals.	294
Table D.4: Thermochemistry for the different potential isomers of neutral, H-functionalized Co species.	295
Table D.5: Thermochemistry for the different potential isomers resulting from the protonation of $(Cp^*)Co(exo-\eta^4-C_5Me_5H)$	295
Table D.6: Gas phase Gibbs Free Energies for species necessary for determining the thermochemical parameters.	297
Table D.7: Particular thermochemical properties of interest.....	297
Table D.8: Effect of functional on structure optimization.....	298
Table D.9: Effect of functional on the calculation of EPR parameters.....	298
Table D.10: Higher level EPR calculations.	300
Table E.1: X-ray crystallography details for $(Cp)Co(Cp^N)$, $[(Cp)Co(Cp^{NH})][OTf]$, and $[(Cp)Co(Cp^N)][OTf]$	322
Table E.2: NMR shifts of pure compounds used in the pK_a determination experiments..	330
Table E.3: NMR data for the cobalt center during titration of $[(Cp)Co(Cp^{NH})][OTf]_2$ with 4-chloroaniline	330
Table E.4: NMR data for the aniline/anilinium during titration of $[(Cp)Co(Cp^{NH})][OTf]_2$ with 4-chloroaniline.....	331
Table E.5: Equilibrium Constants derived from data in Table E.3 and Table E.4	331
Table E.6: NMR data for the cobalt center during second titration of $[(Cp)Co(Cp^{NH})][OTf]_2$ with 4-chloroaniline.....	332

Table E.7: NMR data for the aniline/anilinium during second titration of [(Cp)Co(Cp ^{NH})](OTf) ₂ with 4-chloroaniline	332
Table E.8: Equilibrium Constants derived from data in Table E.6 and Table E.7	332
Table E.9: NMR data for the cobalt center during titration of [(Cp)Co(Cp ^{NH})](OTf) ₂ with 2-chloroaniline	333
Table E.10: NMR data for the aniline/anilinium during titration of [(Cp)Co(Cp ^{NH})](OTf) ₂ with 4-chloroaniline.....	333
Table E.11: Equilibrium Constants derived from data in Table E.9 and Table E.10	333
Table E.12: Final equilibrium constants from data in Table E.5 , Table E.8 , and Table E.11	334
Table E.13: DFT calculated thermochemical parameters for parent cobaltocene and base-appended cobaltocenes	341
Table E.14: Results from CPE experiments under the standard conditions described using the procedures described in Sections E.1.5 and E.1.6	344

NOMENCLATURE

A. Hyperfine tensor

a_{iso} . Isotropic hyperfine value

ADP. Adenosine diphosphate

ATP. Adenosine triphosphate.

Avg. Average

[BAr^F₄]⁻. Tetrakis-(3,5-bis(trifluoromethyl)phenyl)borate

BDD. Boron-doped diamond

BDE. Bond dissociation enthalpy

BDFE. Bond dissociation free energy

B₀. Magnetic Field

BS. Broken symmetry

C_G. Thermodynamic constant accounting for the free energy of forming H• from H⁺ and e⁻

C_H. Thermodynamic constant accounting for the enthalpy of forming H• from H⁺ and e⁻

cm⁻¹. Wavenumbers

Cp. Cyclopentadienide

Cp₂Co. Cobaltocene

Cp₂Fe. Ferrocene

Cp₂Ni. Nickelocene

Cp*. Pentamethylcyclopentadienide

Cp*₂Co. Decamethylcobaltocene

Cp*₂Cr. Decamethylchromocene

- Cp*₂Ni.** Decamethylnickelocene
- CPE.** Controlled potential electrolysis
- CPET.** Concerted proton electron transfer
- CW.** Continuous wave
- CV.** Cyclic voltammogram
- °C.** Degrees Celsius
- δ.** Isomer shift
- Δ_{eq.}** Quadrupole splitting
- ΔΔG_{f.}** Excess energy relative to the free energy of formation
- ΔG.** Gibbs free energy
- ΔG[‡].** Gibbs free energy of the transition state
- ΔG_{f.}** Gibbs free energy of formation
- ΔG(H⁻).** Gibbs free energy of hydricity
- ΔG_{solv.}** Free energy of solvation
- ΔS.** Change in entropy
- ΔΔH_{f.}** Change in enthalpy of formation
- DFT.** Density functional theory
- dmpe.** Dimethylphosphinoethane
- DMSO.** Dimethylsulfoxide
- depe.** Diethylphosphinoethane
- DME.** Dimethoxyethane
- DNA.** Deoxyribose nucleic acid

DOTf. Deuterium-labeled trifluoromethanesulfonic acid

e. Electron charge

E. Reduction potential

e⁻. Electron

EC. Electrochemical-chemical

efg. Electric field gradient

E_g. Gas phase internal energy

ENDOR. Electron nuclear double resonance

Eq. Equation

equiv. Equivalent

EPR. Electron paramagnetic resonance

ESE. Electron spin echo

E_{soln.} Solution phase internal energy

ET. Electron transfer

Et₂O. Diethyl ether

eV. Electron volt

η. Overpotential

η. Rhombicity

F. Faraday's constant

Fc. Ferrocene

FE. Faradaic efficiency

⁴MeO•TEMPO•. 4-methoxy-2,2,6,6-tetramethyl-1-piperidinyloxy

4-MeO[•]TEMPO-H. 1-hydroxy,4-methoxy-2,2,6,6-tetramethyl-1-piperidine

GC. Glassy carbon

g_n. Nuclear g-value

G_{gas}. Gas phase free energy

G_{soln}. Solution phase free energy

h. Planck's constant

H[•]. Hydrogen atom

H⁻. Hydride

H⁺. Proton

¹H. Hydrogen

²H. Deuteron

HAT. Hydrogen atom transfer

HER. Hydrogen evolution reaction

HIPTN₃N. [(3,5-(2,4,6-ⁱPr₃C₆H₂)₂C₆H₃NCH₂CH₂)₃N]³⁻

HNTf₂. Bistrifluoromethanesulfonimide

HOTf. Trifluoromethanesulfonic acid

HYSCORE. Hyperfine sub-level correlation

I. Nuclear spin

IR. Infrared

IRC. Internal reaction coordinate

K. Kelvin

kcal. Kilocalorie

K_{eq} . Equilibrium constant

k_{rel} . Relative rate constant

KC₈. Potassium Graphite

λ . Wavelength

λ_{os} . Outer sphere reorganization energy

Me. Methyl

MeCN. Acetonitrile

MeCy. Methylcyclohexane

MHz. Megahertz

μ_{B} . Bohr magneton

μ_{N} . Nuclear magneton

μL . Microliters

μmol . Micromoles

mL. Milliliters

mm. Millimeters

mol. Moles

ms. Milliseconds

MSE. Mean signed error

mT. Milliteslas

MUE. Mean unsigned error

mV. Millivolts

MS-PCET. Multi-site proton-coupled electron transfer

- NADH.** Nicotinamide adenine dinucleotide
- NADPH.** Nicotinamide adenine dinucleotide phosphate
- n.** Number of moles
- nm.** Nanometers
- NMR.** Nuclear magnetic resonance
- NQI.** Nuclear quadrupole interaction
- ns.** Nanosecond
- N₂RR.** Nitrogen reduction reaction
- v.** Frequency
- ν_N .** Larmor frequency
- [OTf]⁻.** Trifluoromethanesulfonate
- P.** Nuclear quadrupole interaction
- PCET.** Proton-coupled electron transfer
- [PF₆]⁻.** Hexafluorophosphate
- Ph.** Phenyl
- [Ph₂NH₂]⁺.** Diphenylammonium
- Pi.** Phosphate
- PT.** Proton transfer
- P₃^B.** Tris(o-diisopropylphosphinophenyl)-borane
- P₃^{Si}.** Tris(o-diisopropylphosphinophenyl)-silyl
- q.*** Electric field gradient
- Q.*** Electric quadrupolar moment

R. Gas constant

RF. Radio frequency

RNA. Ribose nucleic acid

[^RPhNH₃]⁺. Anilinium substituted on the phenyl ring by an R group

rpm. Rotations per minute

s. Seconds

S. Electron spin

SOMO. Singly occupied molecular orbital

srt. Shot repetition time

T. Temperature

T. Anisotropic hyperfine tensor

τ. Fixed delay time

T₁'. Apparent relaxation rate

[TBA]⁺. Tetrabutylammonium

^tBu. Tert-butyl

THF. Tetrahydrofuran

2-MeTHF. 2-methyltetrahydrofuran

UV-Vis. Ultraviolet-visible

V. Volt

XRD. X-ray diffraction

XPS. X-ray photoelectron spectroscopy

XSEDE. Xtreme Science and Engineering Discovery Environment

Chapter 1.
Introduction

1.1 Opening Remarks

This thesis concerns itself with the proton-coupled reduction of dinitrogen (N_2) to ammonia (NH_3). Throughout the following chapters you will see this process referred to as nitrogen fixation, N_2 -to- NH_3 conversion, and the nitrogen reduction reaction (N_2RR). This reaction has motivated this work because of its critical importance to human and environmental health. Although dinitrogen is the largest component of our atmosphere (~80%) and is a key component of many biomolecules (*i.e.*, DNA, RNA, amino acids, etc.), it cannot be directly incorporated into these biomolecules but must first be fixed into a chemically reactive form, NH_3 .¹ Biologically this fixation is achieved by a highly conserved family of nitrogenase enzymes which feature, I would argue, the most complicated transition metal architectures known in biology (**Figure 1.1**). Metalloenzymes typically operate at low overpotential and with high selectivity, and thus the significant excess energetic demand (fixation of 1 N_2 requires the hydrolysis of 14 ATP) and the poor selectivity (under typical conditions ~2 equivalents of H_2 are produced for every NH_3) demonstrates both the significant challenge presented by this reaction and its critical importance to the organism(s).² Energy demand and selectivity of N_2RR will form key threads through this work.

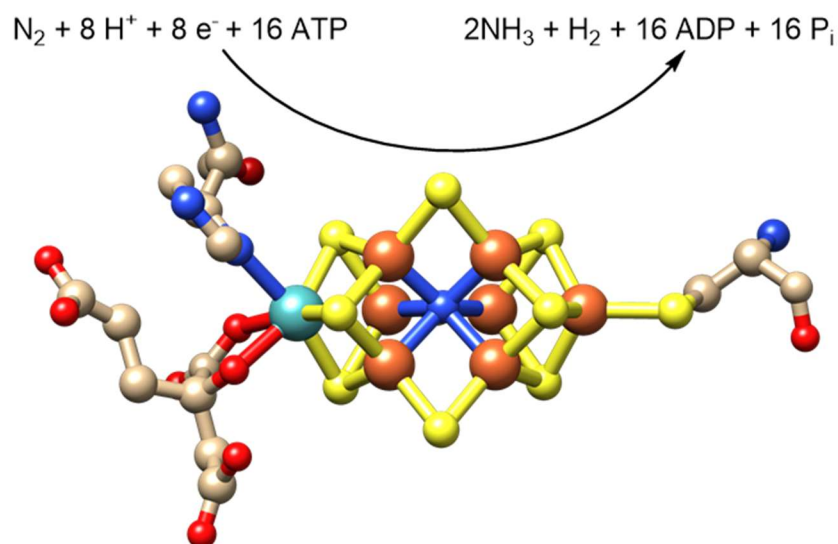


Figure 1.1: Depiction of the active site of the FeMo nitrogenase (PDB: 1M1N)³ with the idealized stoichiometry for biological nitrogen fixation.²

Industrially, nitrogen fixation is (almost) exclusively achieved through the Haber-Bosch process in which NH_3 is formed via the high-temperature and high-pressure combination of H_2 with N_2 on an Fe surface in the presence of promoters. The increased access to fixed nitrogen provided by the discovery of Haber-Bosch in the early 20th century truly transformed the world.⁴ It resulted not only in us fundamentally altering the global biogeochemical nitrogen cycle, but also, via the population boom it enabled, the carbon cycle. The environmental consequences of the disruption of these key biogeochemical cycles will continue to play out for millennia.⁵

The importance of nitrogen fixation would easily motivate study of either of these two globally-important NH_3 -producing systems, biological or industrial. The nitrogen fixing system that we have chosen to study is far removed from both of these in both its atomistic structure and its practicality, although certain design elements are drawn from the active site

cluster in biological nitrogenases. These design elements include the metal identity (Fe), the symmetry (threefold), and the flexible anchoring atom (**Figure 1.2**). Nonetheless, the catalyst is clearly bio-inspired rather than bio-mimetic. One of the key analogies to the biological system is our choice to use protons and electrons (rather than H_2) to reduce N_2 . Indeed, the work presented here is largely focused on the mechanisms by which protons and electrons can be combined to form N–H (or O–H) bonds.

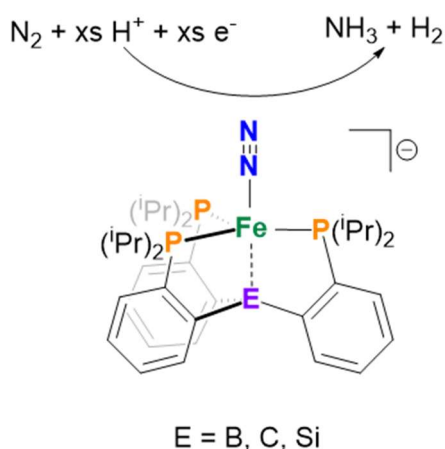


Figure 1.2: Molecular nitrogen fixation catalysts used in this thesis. They feature three in-plane phosphine donors and a variable anchoring atom, E (E = B, C, Si). The ratio of NH_3 to H_2 depends on the exact conditions (*i.e.*, temperature, solvent, acid, reductant).

We have chosen to study the mechanism of X–H bond formation, because we anticipate that combining protons with electrons for X–H bond formation will be one of the defining chemical challenges of the coming decades.⁶ Humans have long used X–H bonds to store, transport, and release energy. Indeed, it is the abundance of energy-rich C–H bonds in biomass such as wood, coal, or oil that makes them such an excellent source of energy: dense and easily-controlled. As energy is increasingly derived from renewable sources such as solar, wind, and hydro, the relevant energy currency will increasingly be electrons. Only by pairing these electrons with protons to form new energy-rich X–H bonds will we be able

to match the benefits in terms of storage, transportation, and controlled release that characterize our current carbon-based fuel cycle.⁷

The conversion of N_2 to NH_3 is thus a fertile training ground for the chemist, as it requires the coordination of 6 protons and 6 electrons to form the energy-rich N–H bonds. For reactions of biogeochemical relevance, this is matched only by sulfite (SO_3^{2-}) reduction to sulfide (S^{2-})⁸ and nitrite (NO_2^-) reduction to ammonia.⁹ Furthermore, no substrate is as resistant to initial functionalization as N_2 . N_2 has an electron affinity lower than that of the noble gases. It has a proton affinity less than methane.¹⁰ N_2 is so unreactive that the addition of a free hydrogen radical to form NNH , the first intermediate of nitrogen fixation, is unfavorable.¹¹ Thus understanding the mechanism by which we can use transition metals in the presence of protons and electrons to functionalize N_2 is a useful whetstone for the chemist interested in the problem of X–H bond formation. Furthermore, NH_3 is a promising fuel candidate with high energy-density, well-developed infrastructure for transportation, and the potential to be carbon-free.¹²

Rather than reviewing a history of molecular species for nitrogen fixation, I will now attempt to sketch out the ideas that have animated my thesis work. In doing so, I hope to pull together some threads that might otherwise seem unrelated to the reader. Naturally, this logic is being applied with the benefit of hindsight and I will inevitably engage in some degree of *ex post facto* rationalization, in order to improve coherence. However, I hope that this exercise will help to inform anyone who would endeavor to read this thesis in its entirety.

1.2 Multiple Bonding

The challenge of functionalizing N_2 can be restated in terms of the high strength of the $N\equiv N$ triple bond. The perfect energy match and overlap of the two nitrogen atoms make their bonding interactions very strong and consequently the anti-bonding interactions very high in energy.¹⁰ Thus, efforts to activate N_2 typically take advantage of transition metals. Considering only the most common case of N_2 binding (terminal and end-on), the transition metal accepts electron density from the poorly basic N-lone pair. This interaction only minimally perturbs the $N\equiv N$ bonding, as can be surmised from the small change in stretching frequency and bond length observed in formally “ σ -only” N_2 -adducts. Rather, activation of the $N\equiv N$ bond is primarily achieved via π -backdonation from the metal center. This backdonation into the π^* orbitals of the N_2 moiety serves to reduce the N–N bond order with a concomitant increase in the M–N bond order. Nonetheless, most M– N_2 complexes are best described as containing a M–N single bond and an $N\equiv N$ triple bond. However, this backdonation increases the negative charge density at the distal nitrogen atom enhancing its basicity and pre-arranges the M–N multiple bonding interactions that will emerge upon functionalization (Figure 1.3).¹³

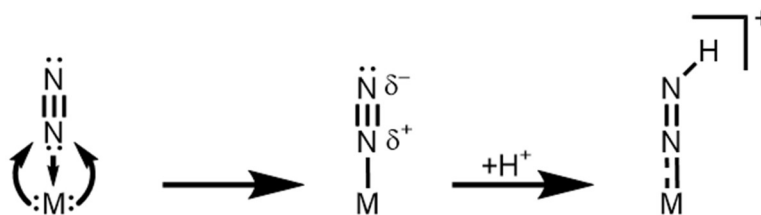


Figure 1.3: Cooperative binding of N_2 via lone-pair donation from N_2 and π -backdonation. This polarizes the N_2 molecule and primes it for protonation at N_β .

Upon protonation the $N\equiv N$ bond order is reduced to 2. This reduced bond order is compensated for (at least in part) by enhanced M–N bonding. Typically the M–N bonding

does not fully compensate for the reduction in N–N bond order and thus the resultant N–H bonds have bond dissociation free energies (BDFEs) that are far weaker than typical N–H bonds ($\leq 50 \text{ kcal mol}^{-1}$ compared to $\sim 100 \text{ kcal mol}^{-1}$) and thus these species are prone to loss of $\frac{1}{2} \text{ H}_2$ to reform the N_2 complex.¹⁴ Considering the significance of M–N bond order for facilitating $\text{N}\equiv\text{N}$ bond disruption, it becomes clear why most N_2 -cleavage and functionalization reactions have been performed with heavier, earlier metals, such as Mo, which due to their more extensive d-orbitals better activate N_2 via backdonation. Indeed, examples of N_2 protonation reactions and N_2 cleavage reactions were both first discovered with Mo (Figure 1.5).^{15,16}

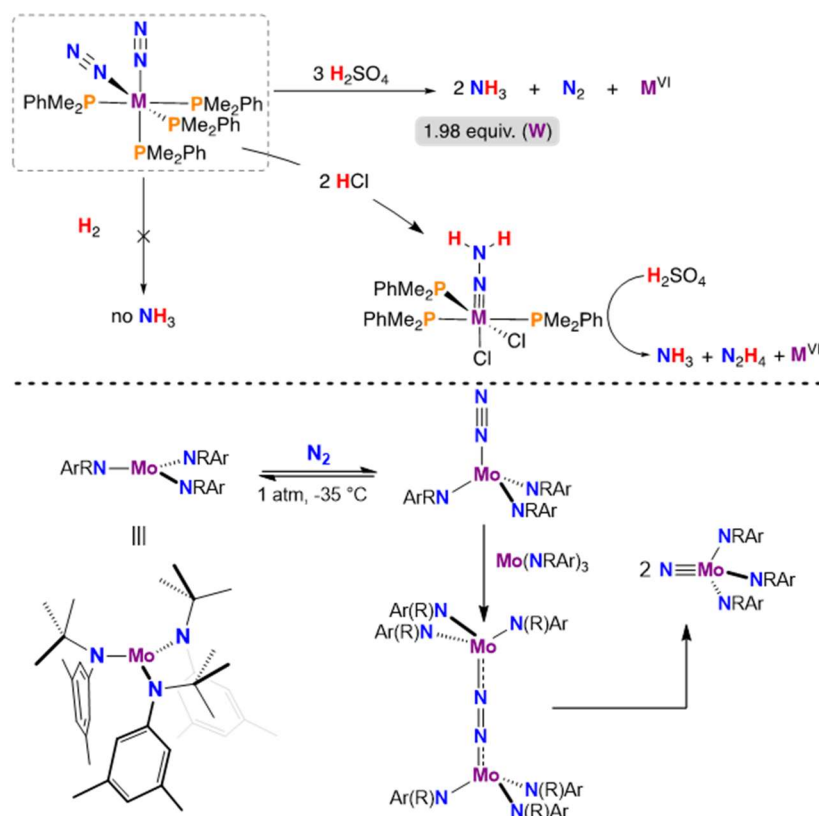


Figure 1.4: (top) Mo and W complexes promote the functionalization of N_2 and its conversion to NH_3 .¹⁵ (bottom) Mo complex that binds N_2 and then cleaves it to form to Mo(N) complexes.¹⁶

For our metal of interest, Fe, the breakthrough in terms of productive N_2 -functionalization reactions came upon lowering the symmetry from fourfold to threefold (Figure 1.5).^{17,18} In doing so, an additional d-orbital becomes formally non-bonding. This facilitates the formation of lower-valent Fe centers (Fe^I and Fe^0), thereby enhancing the π -backbonding and, consequently, the nucleophilicity of the distal nitrogen atom (N_β).¹⁹

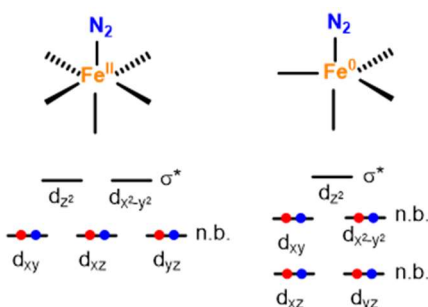


Figure 1.5: Comparison of the electronic structure of Fe complexes in C_3 and C_4 symmetry. (left) In C_4 symmetry only Fe^{II} is accessible. By going to the C_3 symmetry (right), an extra non-bonding orbital becomes available and so the Fe^0 oxidation state is accessible and more activated N_2 complexes are accessible. Bonding interactions described here are ignoring π -interactions.

The unusual stability of the complexes presented in Chapter 2 and their electronic structure is a direct consequence of this reduction from fourfold to threefold symmetry. Although these complexes are iron nitrosyls ($Fe-NO$) rather than $Fe-N_2$ complexes, the same electronic structure arguments apply. Indeed, NO^+ , the canonical resonance form assigned to linear $Fe-NO$ complexes such as these, is isoelectronic with N_2 .

Given the importance of porphyrinic iron nitrosyl complexes, $Fe-NO$ complexes have traditionally been studied in fourfold symmetry.²⁰ In that symmetry, reduction of $Fe-NO$ complexes to lower valent states leads to occupation of d_{z2} resulting in the bending of the $Fe-NO$ ligand and in turn promoting reactivity at the proximal nitrogen (N_α). In threefold symmetry, we see sequential occupation of a d_{xy} -type orbital (defining the xy plane to be that

formed by the three equatorial donors). As we would expect, upon addition of electrons into this orbital the Fe becomes more reduced and consequently the π -backbonding (with the nitrosyl) increases as measured via vibrational spectroscopy and corroborated via density functional theory (DFT). The minimal perturbation of isomer shift in the Mössbauer spectrum further highlights the high covalency of the system that allows electrons to be distributed onto the ligand platform. Similar results have been observed for other redox series of NO complexes in threefold symmetry.^{21,22}

In this way, the electronic structure promoted by three-fold symmetry provides a means of achieving low-valent Fe. In turn the Fe redistributes the electron density to the ligand platform via backdonation. In the case of both nitrosyl and dinitrogen complexes this leads to a build-up of metal-ligand multiple bonding character with N_α , the attenuation of the ligand-ligand multiple bonding (N–N or N–O), and the enhanced electron density at the distal-atom all prime the small molecule for the formation of X–H bonds via protonation.

1.3 Proton-Coupled Electron Transfer:

Considering the mechanism of formation for an X–H bond one can consider three limiting mechanisms. Two stepwise pathways, either electron transfer followed by proton transfer (ET-PT) or proton transfer followed by electron transfer (PT-ET), are possible. Alternatively, a concerted step, namely a proton-coupled electron transfer (PCET), is possible. While PT-ET and ET-PT pathways have been long discussed in the context of nitrogen fixation and discussion of PCET mechanisms for N–H bond formation have taken place in the context of late nitrogen fixation intermediates,^{23–25} such pathways were essentially overlooked in the discussion of forming early N_2 fixation intermediates during catalysis.

PCET comes in many flavors, which I will define briefly here as a reference for the reader (**Figure 1.6**).^{26,27} The simplest is the hydrogen atom transfer (HAT) in which both the proton and electron derive from the same orbital. Abstracting by one degree, one arrives at concerted-proton electron transfer (CPET), in which the proton and electron are derived from different orbitals in the same molecule or derived from the same orbital but travel to two different receptor orbitals in the same molecule. Taking the PCET concept to its limit, one arrives at multi-site proton-coupled electron transfer (MS-PCET). In this extreme, the proton and electron originate from different molecules; nonetheless their movement remains concerted. Throughout this thesis, we will conservatively refer to all reactions involving the concerted movement of protons and electrons as PCET, although deeper study would reveal the particular flavor of each.

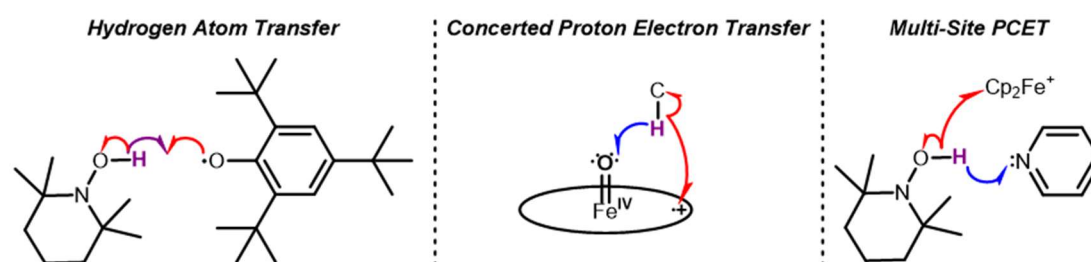


Figure 1.6: Canonical examples of hydrogen atom transfer (HAT), concerted-proton electron transfer (CPET), and multi-site proton-coupled electron transfer (MS-PCET).

Physical organic chemists long ago realized that the homolytic X–H bond strengths of relevance to PCET reactions could be more readily evaluated via measurement of pK_a and E° values and then an application of Hess’s law (**Figure 1.7**).²⁸ This provided a technically more straightforward approach to measuring homolytic bond strengths given the frequent solution instability of radicals formed via $H\cdot$ loss. These concepts, which have now been

employed far beyond their initial home in physical organic chemistry,^{29–31} will prove to be an invaluable tool in much of the work in this thesis, particularly Chapters 5 and 6.

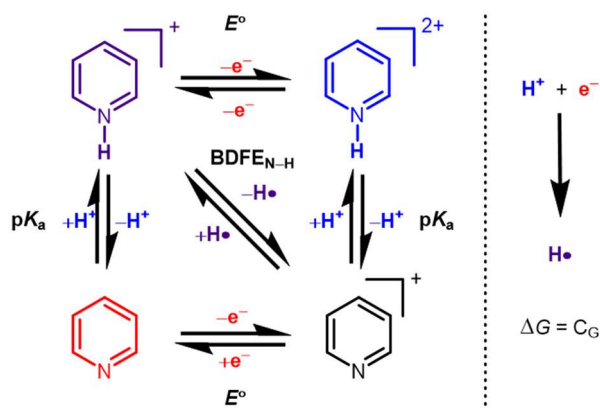


Figure 1.7: (left) The square scheme that relates the stepwise ET-PT and PT-ET pathway to the PCET pathway. (right) Definition of C_G

1.4 Overpotential in Nitrogen Fixation

Zooming out, the proton-coupled reduction of any small molecule (*e.g.*, N_2 , O_2 , CO_2 , etc.) requires the formation of a series of $X-H$ bonds. In our case, we use a proton (H^+) source and an electron (e^-) source, which together are able to form new $X-H$ bonds. The strength of the acid is defined by its pK_a ; the strength of the reductant is defined by its E° .

The various intermediates of a small molecule reduction pathway (*i.e.*, N_2 -to- NH_3) have different intrinsic $X-H$ bond strengths. In the case of nitrogen fixation, the $N-H$ bond strengths generally increase throughout the pathway until the final, thermodynamic product, NH_3 , is formed (Figure 1.8).³² An ideal catalyst would thus, from a thermodynamic perspective, (de)stabilize the various intermediates so that each of the $N-H$ bond strength are equal.

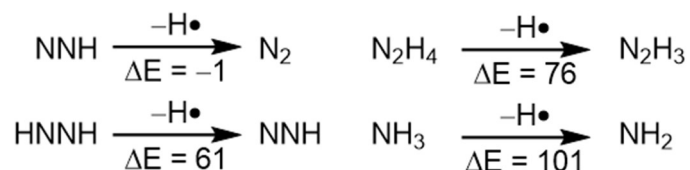


Figure 1.8: Calculated gas-phase bond dissociation enthalpies (BDEs) for intermediates of potential relevance to nitrogen fixation.³²

Naturally, no ideal nitrogen fixing catalyst has been uncovered, so being able to define the (thermodynamic) shortcomings of the various catalysts becomes important in terms of measuring progress within the field. In the proton-coupled reduction of most small molecules, overpotentials are calculated by defining an operating pK_a for the system which in turn defines a thermodynamic potential E_{\min} . The overpotential is then the difference between E_{applied} and E_{\min} and thus is defined as a voltage (**Eq 1.1**). This approach is popular in the electrocatalytic nitrogen fixation field, particularly in papers discussing heterogeneous electrocatalysts.³³

$$\text{Eq 1.1) } \eta = E_{\text{app}} - E_{\min}$$

Within the field of homogeneous nitrogen fixation catalysis, a complementary approach to defining the overpotential has become popular. This approach uses as a point of comparison not E_{\min} but rather the ΔG_f .^{24,34,35} For NH_3 , the ΔG_f is defined as the combination of $1/2 \text{ N}_2$ with $3/2 \text{ H}_2$. Thus, formally each N–H bond in the NH_3 can be thought of as being formed from $\text{H}\bullet$ derived from H_2 . One can therefore compare the energy of forming $\text{H}\bullet$ from H_2 (*i.e.*, the homolytic bond strength of H_2) with that supplied by the reaction, defined as the effective bond dissociation free energy (BDFE_{eff}) of the hypothetical $\text{H}\bullet$ formed from a combination of the H^+ and e^- source.¹¹ This value can be evaluated from the pK_a and the E_{app} via **Error! Reference source not found.** or **Error! Reference source not found.**, where C_G

and C_H are thermodynamic constants that account for the energy or enthalpy of formation of H^\bullet from H^+ and e^- in a particular solvent, respectively. This difference between these energies is then multiplied by three to give the $\Delta\Delta G_f$ in terms of energy per mol (

). The same approach can be used in enthalpic terms with bond dissociation enthalpies (BDEs, **Error! Reference source not found.**) to generate the $\Delta\Delta H_f$ (**Error! Reference source not found.**).

$$\text{Eq 1.2) } BDFE_{\text{eff}} = 1.37 \times pK_a + 23.06 \times E^\circ + C_G$$

$$\text{Eq 1.3) } \Delta\Delta G_f = 3 \times (BDFE(H_2)/2 - BDFE_{\text{eff}})$$

$$\text{Eq 1.4) } BDE_{\text{eff}} = 1.37 \times pK_a + 23.06 \times E^\circ + C_H$$

$$\text{Eq 1.5) } \Delta\Delta H_f = 3 \times (BDE(H_2)/2 - BDE_{\text{eff}})$$

One of the key insights of this thesis was recognizing that the hypothetical H^\bullet represented by the $BD(F)E_{\text{eff}}$ could potentially represent a chemical species that was forming in solution and actually reacting via PCET. This idea is hinted at in **Chapters 3 and 4** and then fully realized in **Chapter 5**.

1.5 Selectivity in Nitrogen Fixation Catalysis

One of the reasons that the direct reaction of proton and electron sources to form a PCET donor had been overlooked for so long was that this reaction was believed to solely contribute to the undesirable background hydrogen evolution reaction (HER). One of the challenges of any proton-coupled reduction of a small molecule is selectivity. Selectivity problems can come in several varieties: product selectivity (*i.e.*, fixation of N_2 to NH_3 or to

N₂H₄), small molecule selectivity (*i.e.*, in atmosphere there is N₂, O₂, and CO₂ which could all be reduced), and small molecule vs H⁺ reduction. This thesis will not touch on either of the first two problems although both pose interesting challenges in the context of developing nitrogen fixation catalysis. However, the issue of selectivity for fixed nitrogen products vs H₂ plays a focus of the **Chapters 3 and 4**.

H₂ formation can either be mediated by the catalyst via a variety of mechanisms^{14,36} or formed directly via a reaction between the acid and reductant. Indeed, we and others have observed H₂ formation from direct reaction of the acid and reductant in the absence of the catalyst on the same time scale as the N₂ fixation reaction, suggesting the kinetic competence of the background HER reaction. This background HER must necessarily proceed via multiple steps given it necessitates the combination of two protons and two electrons. Thus, the chemical identity of the acid and reductant is going to, in turn, impact the identity and reactivity of the intermediates on this background HER pathway.

Reaction of the acid and reductant will typically generate a species that is a powerful PCET reagent ($\text{BDFE}_{\text{X-H}} \leq 50 \text{ kcal mol}^{-1}$). This species can potentially transfer H• to form a desired X–H bond or react with itself in a bimolecular fashion to release H₂. One-electron reduction of this species would result in an intermediate with hydridic characteristics. Again this species could react in a productive fashion (*i.e.*, to form N–H bonds) or it could release H₂ upon protonation.

In theory the intermediates on the background HER pathway provide access to reactive modalities that have traditionally not been considered in nitrogen fixation (H• or H⁻ transfer). Productive N–H bond formation from these intermediates can thus both enhance NH₃ formation and suppress H₂ formation. These concepts animate the work in **Chapter 6**

where we use a synthetic strategy to prevent reduction of a protonated metallocene to a hydridic species, thereby allowing us to electrochemically generate a strong PCET donor.

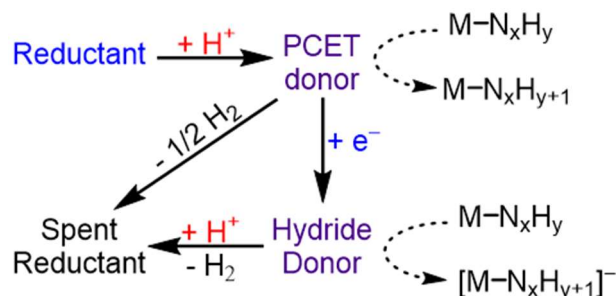


Figure 1.9: The possible pathways for background HER and hypothesized N-H bond forming reactions via $\text{H}\cdot$ or H^- transfer shown with solid and dotted arrows respectively.

1.6 Chapter Summaries

The intellectual motivation of each of the chapters is alluded to in the above paragraphs. Here, I will provide a succinct summary of the means by which we interrogated these concepts.

In **Chapter 2**, we synthesize a redox series of trisphosphine borane (P_3^{B}) iron-supported nitrosyl complexes. These complexes are unusual in their highly reduced state and their retention of a linear Fe-N-O unit. We use spectroscopic methods (Mössbauer, infrared, ultraviolet-visible, and electron paramagnetic resonance) to interrogate the electronic structure of these complexes, which are further verified with density functional theory (DFT).³⁷

In **Chapter 3**, we develop new conditions for the reduction of N_2 -to- NH_3 using (P_3^{B})Fe. These new conditions utilize a metallocene reductant (Cp^*_2Co , Cp^* = pentamethylcyclopentadienide) and an anilinium acid ($[\text{RPhNH}_3]^+$, R = substitution on the phenyl ring). With this acid and reductant, we can use the same catalyst, in the same solvent,

at the same temperature and pressure to achieve higher turnover numbers and improved selectivity compared to previous results.^{38,39} The milder nature of the reagents mean that the $BDFE_{\text{eff}}$ is higher, indirectly suggesting that PCET mechanisms might be accessible. This hypothesis is further supported by DFT calculations demonstrating that metallocene protonation leads to very reactive PCET reagents.³⁴ We believe that this mechanism may be operative in a number of N_2 -fixing systems that operate at high-efficiency with metallocenes.^{40,41}

In **Chapter 4**, we studied the effect of varying the acid pK_a on the selectivity for NH_3 formation vs H_2 formation with $(P_3^B)Fe$. Circumstantial evidence in support of PCET mechanisms under catalytic conditions was derived from stoichiometric reactions and calculations. Furthermore, we found that although Cp^*_2Co on its own cannot reduce N_2 -to- NH_3 , using it as a co-catalyst in the presence of $(P_3^B)Fe$ boosted the yield of NH_3 in electrode-mediated nitrogen fixation reactions into the clearly catalytic regime. This provided the first bona fide example of electrocatalytic N_2 fixation and provided further circumstantial evidence of a role for Cp^*_2Co in mediating productive N–H bond formation.⁴²

In **Chapter 5**, we provide definitive experimental evidence for the protonation of Cp^*_2Co via continuous-wave (CW) electron paramagnetic resonance (EPR) spectroscopy and pulse-EPR spectroscopy. We also use thermochemical techniques to validate the very weak C–H bond formed upon protonation of Cp^*_2Co that we had predicted computationally. We provide a framework for understanding why these bonds are ~ 70 kcal mol⁻¹ weaker than typical C–H bonds and thus very strong H^\bullet donors. We also demonstrate that this H^\bullet donor could be readily converted into an H^- donor by one-electron reduction. We believe that this work has significant implications for reconsidering the interplay between the background

HER reaction and productive X–H bond forming reactions during the proton-coupled reduction of small molecules generally.⁴³

In **Chapter 6**, we confirm that the mechanism of electrocatalytic proton reduction by $[\text{Cp}_2\text{Co}]^+$ (Cp = cyclopentadienide) proceeds via an ECEC-mechanism in which it is initially reduced to Cp_2Co , followed by protonation (presumably on the Cp ring), then reduction leads to a hydridic species from which H_2 is released via protonation.. In order to develop a metallocene based system that would access $\text{H}\cdot$ reactivity under electrocatalytic conditions, we synthetically append a Brønsted basic moiety to the Cp_2Co . By directing protonation to this remote Brønsted basic site rather than the Cp ring, we prevent further reduction. Thus, the molecule must either bimolecularly eliminate H_2 , which is slow, or transfer $\text{H}\cdot$ to an acceptor. We take advantage of this to achieve the electrocatalytic reduction of ketones to pinacols. Mechanistic evidence from cyclic voltammetry indicates that this reaction proceeds via a rate-limiting PCET step and generates a synthetically useful neutral ketyl radical.

1.7 References

- (1) Stein, L. Y.; Klotz, M. G. *Curr. Biol.* **2016**, *26*, R94–R98.
- (2) Hoffman, B. M.; Lukoyanov, D.; Yang, Z. Y.; Dean, D. R.; Seefeldt, L. C. *Chem. Rev.* **2014**, *114*, 4041–4062.
- (3) Einsle, O.; Tezcan, F. A.; Andrade, S. L. A.; Schmid, B.; Yoshida, M.; Howard, J. B.; Rees, D. C. *Science* **2002**, *297*, 1696–1700.
- (4) Leigh, G. J. *Catalysts for Nitrogen Fixation: Nitrogenases, Relevant Chemical Models and Commercial Processes*; Smith, B. E., Richards, R. L., Newton, W. E., Eds.;

Nitrogen Fixation: Origins, Applications, and Research Progress; Springer Netherlands: Dordrecht, 2004; pp 33–54.

- (5) Erisman, J. W.; Sutton, M. A.; Galloway, J.; Klimont, Z.; Winiwarter, W. *Nat. Geosci.* **2008**, *1*, 636–639.
- (6) Chen, J. G.; Crooks, R. M.; Seefeldt, L. C.; Bren, K. L.; Bullock, R. M.; Darensbourg, M. Y.; Holland, P. L.; Hoffman, B.; Janik, M. J.; Jones, A. K.; et al. *Science* **2018**, *360*, 873–879.
- (7) Detz, R. J.; Reek, J. N. H.; Zwaan, B. C. C. van der. *Energy Environ. Sci.* **2018**, *11*, 1653–1669.
- (8) Parey, K.; Schiffer, A.; Steuber, J.; Fritz, G.; Ermler, U.; Kroneck, P. M. *Handbook of Metalloproteins*; American Cancer Society, 2010.
- (9) Maia, L. B.; Moura, J. J. G. *Chem. Rev.* **2014**, *114*, 5273–5357.
- (10) Bazhenova, T. A.; Shilov, A. E. *Coord. Chem. Rev.* **1995**, *144*, 69–145.
- (11) Warren, J. J.; Tronic, T. A.; Mayer, J. M. *Chem. Rev.* **2010**, *110*, 6961–7001.
- (12) Valera-Medina, A.; Xiao, H.; Owen-Jones, M.; David, W. I. F.; Bowen, P. J. *Progress in Energy and Combustion Science* **2018**, *69*, 63–102.
- (13) Burford, R. J.; Fryzuk, M. D. *Nat. Rev. Chem.* **2017**, *1*, 1–13.
- (14) Matson, B. D.; Peters, J. C. *ACS Cat.* **2018**, *8*, 1448–1455.
- (15) Chatt, J.; Heath, G. A.; Richards, R. L. *J. Chem. Soc., Chem. Commun.* **1972**, No. 18, 1010–1011.
- (16) Laplaza, C. E.; Cummins, C. C. *Science* **1995**, *268*, 861–863.
- (17) Moret, M. E.; Peters, J. C. *J. Am. Chem. Soc.* **2011**, *133*, 18118–18121.
- (18) Lee, Y.; Mankad, N. P.; Peters, J. C. *Nat. Chem.* **2010**, *2*, 558–565.

- (19) Del Castillo, T. J.; Thompson, N. B.; Suess, D. L. M.; Ung, G.; Peters, J. C. *Inorg. Chem.* **2015**, *54*, 9256–9262.
- (20) Lehnert, N.; Scheidt, W. R.; Wolf, M. W. *Nitrosyl Complexes in Inorganic Chemistry, Biochemistry and Medicine II*; Mingos, D. M. P., Ed.; Structure and Bonding; Springer: Berlin, Heidelberg, 2014; pp 155–223.
- (21) Speelman, A. L.; White, C. J.; Zhang, B.; Alp, E. E.; Zhao, J.; Hu, M.; Krebs, C.; Penner-Hahn, J.; Lehnert, N. *J. Am. Chem. Soc.* **2018**, *140*, 11341–11359.
- (22) Keilwerth, M.; Hohenberger, J.; Heinemann, F. W.; Sutter, J.; Scheurer, A.; Fang, H.; Bill, E.; Neese, F.; Ye, S.; Meyer, K. *J. Am. Chem. Soc.* **2019**, *141*, 17217–17235.
- (23) Scepaniak, J. J.; Vogel, C. A.; Khusniyarov, M. M.; Heinemann, F. W.; Meyer, K.; Smith, J. M. *Science* **2011**, *331*, 1049–1052.
- (24) Pappas, I.; Chirik, P. J. *J. Am. Chem. Soc.* **2016**, *138*, 13379–13389.
- (25) MacLeod, K. C.; McWilliams, S. F.; Mercado, B. Q.; Holland, P. L. *Chem. Sci.* **2016**, *7*, 5736–5746.
- (26) Huynh, M. H. V.; Meyer, T. J. *Chem. Rev.* **2007**, *107*, 5004–5064.
- (27) Darcy, J. W.; Koronkiewicz, B.; Parada, G. A.; Mayer, J. M. *Acc. Chem. Res.* **2018**, *51*, 2391–2399.
- (28) Friedrich, L. E. *J. Org. Chem.* **1983**, *48*, 3851–3852.
- (29) Miller, D. C.; Tarantino, K. T.; Knowles, R. R. *Top. Curr. Chem.* **2016**, *30*, 374–432.
- (30) Saouma, C. T.; Richard, S.; Smolders, S.; Delley, M. F.; Ameloot, R.; Vermoortele, F.; De Vos, D. E.; Mayer, J. M. *J. Am. Chem. Soc.* **2018**, *140*, 16184–16189.
- (31) Valdez, C. N.; Schimpf, A. M.; Gamelin, D. R.; Mayer, J. M. *J. Am. Chem. Soc.* **2016**, *138*, 1377–1385.

- (32) Siegbahn, P. E. M.; Westerberg, J.; Svensson, M.; Crabtree, R. H. *J. Phys. Chem. B* **1998**, *102*, 1615–1623.
- (33) Lindley, B. M.; Appel, A. M.; Krogh-Jespersen, K.; Mayer, J. M.; Miller, A. J. M. *ACS Energy Lett.* **2016**, *1*, 698–704.
- (34) Chalkley, M. J.; Del Castillo, T. J.; Matson, B. D.; Roddy, J. P.; Peters, J. C. *ACS Cent. Sci.* **2017**, *3*, 217–223.
- (35) Ashida, Y.; Arashiba, K.; Nakajima, K.; Nishibayashi, Y. *Nature* **2019**, *568*, 536–540.
- (36) Benedek, Z.; Papp, M.; Oláh, J.; Szilvási, T. *Inorg. Chem.* **2019**.
- (37) Chalkley, M. J.; Peters, J. C. *Angew. Chem. Int. Ed.* **2016**, *55*, 11995–11998.
- (38) Anderson, J. S.; Rittle, J.; Peters, J. C. *Nature* **2013**, *501*, 84–87.
- (39) Del Castillo, T. J.; Thompson, N. B.; Peters, J. C. *J. Am. Chem. Soc.* **2016**, *138*, 5341–5350.
- (40) Yandulov, D. V.; Schrock, R. R. *Science* **2003**, *301*, 76–78.
- (41) Arashiba, K.; Miyake, Y.; Nishibayashi, Y. *Nat. Chem.* **2010**, *3*, 120–125.
- (42) Chalkley, M. J.; Del Castillo, T. J.; Matson, B. D.; Peters, J. C. *J. Am. Chem. Soc.* **2018**, *140*, 6122–6129.
- (43) Chalkley, M. J.; Oyala, P. H.; Peters, J. C. *J. Am. Chem. Soc.* **2019**, *141*, 4721–4729.

Chapter 2.

A Triad of Highly-Reduced, Linear Iron Nitrosyls: $\{\text{Fe}(\text{NO})\}^{8-10}$

Adapted from:

Chalkley, M. J.; Peters, J. C.

Angew. Chem. Int. Ed. **2016**, *55*, 11995–11998.

DOI: 10.1002/anie.201605403

2.1 Introduction

Due to the prevalence of both heme and non-heme iron nitrosyls in biology,^{1,2} iron model complexes bearing nitrosyl ligands have been the subject of study for decades.³ Iron nitrosyl complexes are frequently characterized by their Enemark-Feltham number, which is the sum of the Fe d-electrons and NO π^* electrons. Many examples of $\{\text{Fe}(\text{NO})\}^6$ and $\{\text{Fe}(\text{NO})\}^7$ complexes are known^{4,5} and, more recently, several $\{\text{Fe}(\text{NO})\}^8$ complexes have been thoroughly characterized.⁶⁻¹¹ However, $\{\text{Fe}(\text{NO})\}^9$ complexes are unknown, and the unique properties of the only known example of an $\{\text{Fe}(\text{NO})\}^{10}$ complex, $[\text{Fe}(\text{CO})_3(\text{NO})]^-$, prompted its reinvestigation in 2014 by Plietker and coworkers.^{12,13} The activated NO stretching frequency (1647 cm^{-1}) and long N–O bond (1.212 \AA) but linear Fe–N–O angle (180°) observed in this complex stand in contrast to the iron nitrosyl literature, where high Enemark-Feltham numbers are associated with a bent geometry.⁶⁻¹¹ Therefore, we sought to investigate the Fe–NO unit under local three-fold symmetry on a ligand platform that would engender strong Fe–N multiple bonding while also providing redox flexibility. With this in mind, we pursued the synthesis of a series of Fe–NO complexes supported by a tris(phosphine)borane (P_3^{B}) ligand ().¹⁴ Herein we report the synthesis of a monoiron-mononitrosyl complex that has been crystallographically characterized across three oxidation states, including highly unusual examples of $\{\text{Fe}(\text{NO})\}^9$ and $\{\text{Fe}(\text{NO})\}^{10}$ complexes. These nitrosyl complexes are distinct in their retention of a strictly linear Fe–N–O unit across the series; a high degree of covalency facilitates this atypical structural behavior. Similar results have been observed recently for a Fe–NO unit supported by four N-heterocyclic carbene ligands.¹⁵

2.2 Results

2.2.1 Synthesis of $\{(P_3^B)Fe(NO)\}^{8-10}$

In our exploration of Fe–N₂ chemistry, the P₃^B ligand has demonstrated the ability to support strong Fe–N π-bonding, while geometric (and electronic) flexibility of the Fe–B interaction allows for stabilization of highly reduced Fe species. Given that (P₃^B)Fe(N₂) has an irreversible oxidation event that causes dissociation of the N₂ ligand to generate [(P₃^B)Fe]⁺, we hypothesized that nitrosonium hexafluorophosphate ([NO][PF₆]) could serve both to oxidize (P₃^B)Fe(N₂) and to act as a source of in situ nitric oxide to bind Fe.¹⁶ Successful isolation of the $\{(P_3^B)Fe(NO)\}^8$ cation as its [BAR^F₄][−] salt (after salt metathesis with [Na][BAR^F₄]; BAR^F₄ = B(3,5-(CF₃)₂-C₆H₃)₄) proved viable (). The cyclic

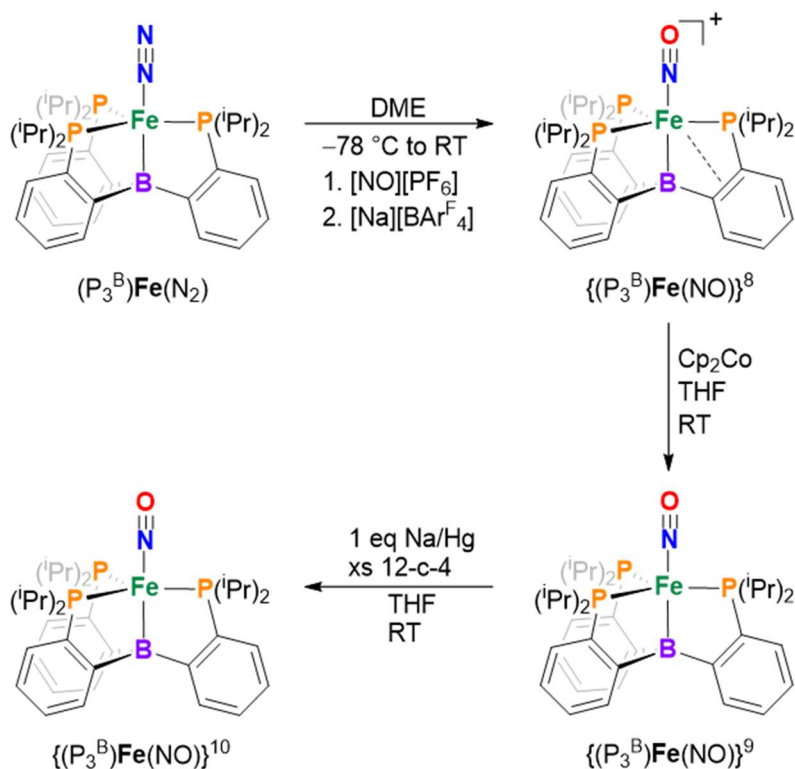


Figure 2.1: Synthetic route for $\{(P_3^B)Fe(NO)\}^{8-10}$.

voltammetry of $\{(P_3^B)Fe(NO)\}^8$ (**Figure 2.2**) demonstrated both a quasi-reversible reduction at -0.56 V vs. $Fc^{+/0}$ and a second, fully reversible feature at -1.97 V vs. $Fc^{+/0}$. We attribute these redox features to the $\{Fe(NO)\}^{8/9}$ and $\{Fe(NO)\}^{9/10}$ couples, respectively. Synthetic generation of neutral $\{(P_3^B)Fe(NO)\}^9$ via cobaltocene reduction of $\{(P_3^B)Fe(NO)\}^8$, and anionic $\{(P_3^B)Fe(NO)\}^{10}$ by Na/Hg reduction of $\{(P_3^B)Fe(NO)\}^9$, provided the desired $\{(P_3^B)Fe(NO)\}^{8-10}$ series (). In contrast to most other reports of highly reduced Fe–NO complexes,^{6–11,17} these three species are stable both in solution and in the solid state at room temperature under an inert atmosphere.

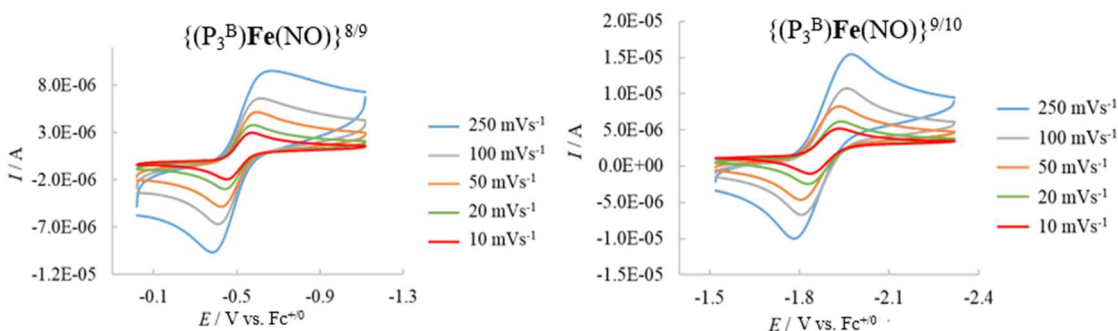


Figure 2.2: Variable scan rate cyclic voltammograms in 0.1 M [TBA][BAR^F₄] THF of the $\{(P_3^B)Fe(NO)\}^{8/9}$ and $\{(P_3^B)Fe(NO)\}^{9/10}$ redox couples on the left and right respectively.

2.2.2 Characterization and Electronic Structure of $\{Fe(NO)\}^{8-10}$

The infrared spectra of $\{(P_3^B)Fe(NO)\}^{8-10}$ demonstrate an approximately 100 cm^{-1} decrease in the stretching frequency of the NO bond upon each successive reduction (**Figure 2.3**). This behaviour is reminiscent of that seen in transition metal complexes of π -accepting ligands such as N_2 and CO .^{16,18} However, this behaviour stands in contrast to that of most previously characterized iron nitrosyls, which more typically show much larger changes (between $200\text{-}350\text{ cm}^{-1}$) in the NO stretching frequency per unit change in their of Enemark-Feltham number.^{6,11} This observation suggested to us that the Fe–NO

linkage remains linear throughout the redox series described here, behaviour that is rare in redox series of metal nitrosyls.^{4,5} The crystal structures of $\{(P_3^B)Fe(NO)\}^{8-10}$ confirm that the Fe–N–O angle is highly linear in each complex: $175.8(3)^\circ$ in $\{(P_3^B)Fe(NO)\}^8$, $176.18(6)^\circ$ in $\{(P_3^B)Fe(NO)\}^9$, and $179.05(12)^\circ$ in $\{(P_3^B)Fe(NO)\}^{10}$.

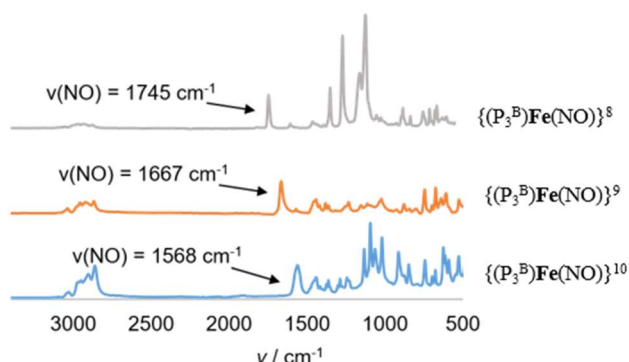


Figure 2.3: IR spectra for $\{(P_3^B)Fe(NO)\}^{8-10}$ highlighting the NO stretch.

The crystal structures¹⁹ (**Figure 2.4**) of $\{(P_3^B)Fe(NO)\}^{8-10}$ further reveal that the only significant ligand rearrangement across the series is the presence of an intramolecular η^4 -BCCP interaction in $\{(P_3^B)Fe(NO)\}^8$. Variable temperature 1H and ^{31}P NMR experiments indicate that this interaction is maintained in solution. In contrast, both $\{(P_3^B)Fe(NO)\}^9$ and $\{(P_3^B)Fe(NO)\}^{10}$ demonstrate approximate three-fold symmetry both in solution and in the solid state. Although Fe–N–O linearity is maintained, the N–O bond does lengthen about 0.03 \AA upon each reduction, in agreement with the activation observed by IR spectroscopy. Although the Fe–N bond distance remains fairly constant (**Figure 2.5**), the Wiberg bond indices (**Figure 2.5**) find that the Fe–N bond order increases slightly from $\{(P_3^B)Fe(NO)\}^8$ to $\{(P_3^B)Fe(NO)\}^{10}$ with a concomitant decrease in the N–O bond order.^{20,21} In addition to Fe–N bonding, the Wiberg Bond Index finds significant Fe–O

bonding (bond order of ~ 0.5). This through bonding interaction has been previously interpreted as indicative of a highly covalent interaction.²⁰ Although the Fe–B bond

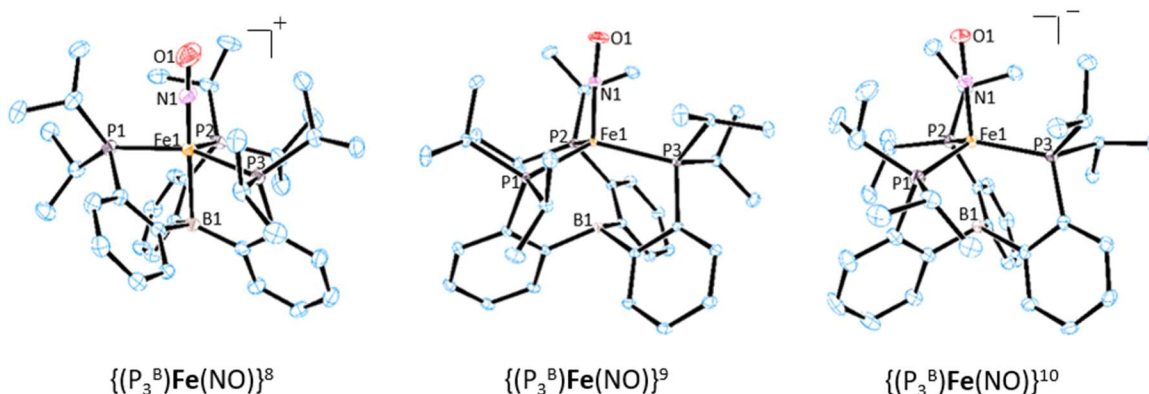


Figure 2.4: X-ray crystal structures of $\{(P_3^B)Fe(NO)\}^{8-10}$ with hydrogens and counteranions omitted for clarity. Fe is orange, phosphorus is purple, nitrogen is pink, oxygen is red, boron is brown, and carbon is blue.

distance increases with reduction, suggestive of a weakening Fe–B interaction, the boron does become more pyramidalized, which agrees with both the DFT calculations (*vide infra*) and the ^{11}B NMR spectra, and suggests increased Fe–B bonding upon reduction. Finally, the Fe–P distances are significantly shorter in $\{(P_3^B)Fe(NO)\}^{10}$ than in both $\{(P_3^B)Fe(NO)\}^8$, and $\{(P_3^B)Fe(NO)\}^9$, potentially suggestive of increased Fe–P backbonding in the most reduced species.

Compound	Fe-N Bond Length (Å)	Fe-B Bond Length (Å)	N-O Bond Length (Å)	Expt. $\nu(NO)$ (cm^{-1})	Fe-N Bond Order	Fe-O Bond Order	Fe-B Bond Order	N-O Bond Order	Calc. $\nu(NO)$ (cm^{-1})
$\{(P_3^B)Fe(NO)\}^8$	1.655(3)	2.311(3)	1.160(4)	1745	1.5166	.4981	.3558	1.8163	1756
$\{(P_3^B)Fe(NO)\}^9$	1.6712(5)	2.4451(6)	1.1901(7)	1667	1.5958	.5156	.4402	1.7244	1696
$\{(P_3^B)Fe(NO)\}^{10}$	1.6505(13)	2.4455(16)	1.2207(16)	1568	1.7049	.4832	.4708	1.6260	1614

Figure 2.5: Experimental bond lengths from X-ray crystallography and Wiberg bond indices from DFT, along with a comparison of experimental and computational NO stretching frequencies.

Mössbauer spectroscopy has been frequently employed in the study of iron nitrosyl complexes as an experimental probe of the relative state of oxidation of the iron center.^{6,11,13,15,17,22,23} Typically octahedral $\{\text{FeNO}\}^6$ complexes have isomer shifts between 0.0 and 0.05 mm s⁻¹, $\{\text{FeNO}\}^7$ complexes have isomer shifts between 0.25 and 0.33 mm s⁻¹ and $\{\text{FeNO}\}^8$ complexes have isomer shifts between 0.4 and 0.5 mm s⁻¹. These significant changes in the isomer shift occur despite NO-centered reduction, as the decreasing ability of the NO ligand to accept electron density through backbonding leads the Fe-center to become more electron rich.⁶ For the high-spin, pseudo-*C*₃ $\{\text{FeNO}\}^{6-8}$ recently reported by Lehnert and coworkers, even larger changes in isomer shift (~0.4 mm s⁻¹) per unit reduction are observed. These authors suggest that such a large shift is indicative of metal-centered reduction.²²

The zero-field, 80 K Mössbauer spectra of $\{(\text{P}_3^{\text{B}})\text{Fe}(\text{NO})\}^{8-10}$ (**Figure 2.6**) show only very minimal changes in the isomer shift as a function of the overall redox state. The linear and therefore strongly π -bonded NO ligand enforces low-spin configurations for all three redox states, leading to short metal–ligand bonds and correspondingly low isomer shifts.²⁴ These low isomer shifts are consistent with the behavior we have observed in other highly-reduced $(\text{P}_3^{\text{B}})\text{Fe}$ complexes, related tris(phosphine)silyl supported Fe complexes, and a very recently reported series of linear $\{\text{FeNO}\}^{6-8}$ with four N-heterocyclic carbene ligands.^{15,18,25,26} Even within this context, the $\{(\text{P}_3^{\text{B}})\text{Fe}(\text{NO})\}$ system is remarkable for the minimal change in isomer shift observed across the redox series; this suggests a high degree of metal–ligand covalency that buffers against any buildup of electron density on the iron center upon successive reductions. The nitrosyl ligand enhances the already strong covalency between the Fe and the P_3^{B} ligand, which we have previously noted leads to a

non-classical relationship between isomer shift and redox state in these species. Low-spin complexes of these types feature low isomer shifts regardless of formal oxidation state.²⁶

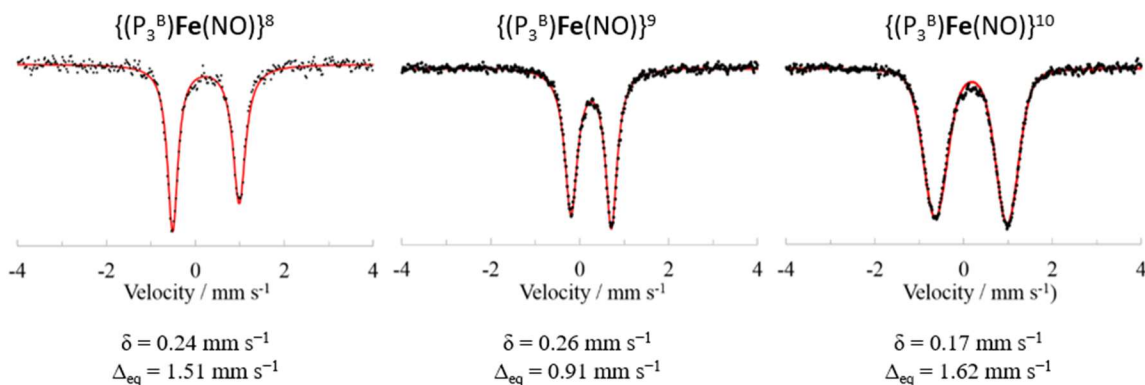


Figure 2.6: Zero-field Mössbauer spectra of $\{(P_3^B)Fe(NO)\}^{8-10}$ obtained as microcrystalline material suspended in a boron nitride matrix at 80 K. Data is shown as black dots and the simulation with the isomer shift (δ) and quadrupole splitting (Δ_{eq}) given below shown as a red line.

The electronic structures of metal nitrosyls are still debated,²⁷ but linear NO complexes are most commonly described by a π -accepting NO^+ resonance form. In $Fe-(NO^+)$ complexes, the $\nu(NO)$ stretching frequency is typically found between 1900 and 2000 cm^{-1} .^[19] There are also cases where a linear nitrosyl is considered to be a π -donating NO^- ligand.^[4e,6b] These two limiting resonance forms indicate formal charge transfer either from the NO to the metal or from the metal to the NO. To help determine which, if either, of these limiting cases more accurately describes the complexes featured herein, we draw comparisons to the known dinitrogen (N_2 is isolobal to NO^+) and imido (NR is isolobal to NO^-) complexes of the $(P_3^B)Fe$ scaffold.^{15,18,25,26} Relative to the $(P_3^B)Fe(NO)$ complexes, the $(P_3^B)Fe(N_2)$ complexes have longer $Fe-N$ (~ 1.78 Å) distances and shorter $Fe-B$ distances (~ 1.3 Å), suggesting a weaker π -interaction between the Fe and the N_2 ligand and

more σ -backdonation into the borane. For comparison, the Wiberg bond index calculation for $[(P_3^B)Fe(N_2)]^-$ (isoelectronic to $\{(P_3^B)Fe(NO)\}^9$) provides an Fe–B bond order of 0.5526 compared to 0.4402 and an Fe–N bond order of 0.9796 compared to 1.5958. In contrast, the $(P_3^B)Fe(NR)$ (R = adamantyl or 4-methoxyphenyl) complexes have similarly short Fe–N (1.66 Å) distances but much longer Fe–B (2.6–2.8 Å) distances, arising from a distortion to a more tetrahedral symmetry at iron that further enhances Fe–N π -bonding, and a more electron poor Fe center with minimal backdonation into the borane. For comparison, the Wiberg bond index calculation for $(P_3^B)Fe(NAd)$ (Ad = adamantyl) (isoelectronic to $\{(P_3^B)Fe(NO)\}^9$) provides an Fe–B bond order of 0.2718 compared to 0.4402 and an Fe–N bond order of 1.7980 compared to 1.5958. It therefore seems apparent that neither limiting scenario (Fe–(NO⁺) vs Fe–(NO[−])) reliably describes the bonding situation observed in the $\{(P_3^B)Fe(NO)\}^{8-10}$ series. A description of the entire ligand sphere about the iron center as covalent seems more appropriate than descriptions that imply significant charge transfer.

This covalent description is further supported by the cryogenic-temperature (−180 °C) UV-vis spectrum of $\{(P_3^B)Fe(NO)\}^9$ (Figure 2.7). Upon cooling, a vibronic progression with spacing of 452, 457, 476, 509, 499 cm^{-1} emerges on the electronic transition centered at 521 nm. To our knowledge, a related vibronic progression has been observed in only one other M–NO system in the cryogenic electronic spectrum of $[Cr(CN)_5(NO)]^{3-}$, characterized by Gray and coworkers in 1966. In that case, the electronic transition featuring the vibronic progression was centered at 470 nm and was attributed to a transition from a metal-based d_{xy} or $d_{x^2-y^2}$ orbital into a Cr–N π^* orbital. Although this

previous study investigated a series of isoelectronic, pentacyano metal ($M = V, Cr, Mn, Fe$) nitrosyl complexes, only $[Cr(CN)_5(NO)]^{3-}$ revealed this vibronic progression upon cooling. The orbital contribution from Cr and NO π^* to the Cr–N π^* orbital was deduced to be nearly equal, leading the authors to posit that this might be requisite for the observation of vibronic coupling.²⁸ Likewise, cooling of $\{(P_3^B)Fe(NO)\}^8$ and $\{(P_3^B)Fe(NO)\}^{10}$, which exhibit absorption features at a similar wavelength, does not lead to the emergence of any vibronic coupling. Due to the similarities in M–N–O angle, N–O distance, and $\nu(NO)$ of $[Cr(CN)_5(NO)]^{3-}$ and $\{(P_3^B)Fe(NO)\}^9$, and the observation that the calculated d_{xy} -Fe–N π^* gap (SOMO-LUMO gap) in $\{(P_3^B)Fe(NO)\}^9$ is 520 nm, we also assign this absorption feature to a d_{xy} -M–N π^* transition.²⁹ Based on our own observations, those of Gray and coworkers, and the paucity of metal–NO complexes demonstrating such vibronic coupling, it appears that vibronic coupling of this type is only (albeit not necessarily) observed in highly covalent, linear M–NO units.

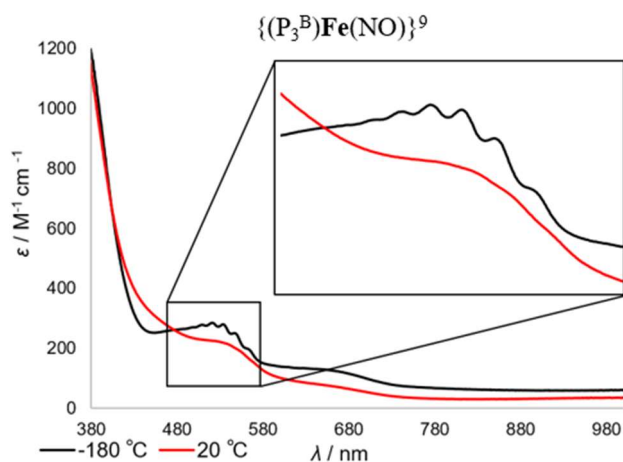


Figure 2.7: Density-corrected room temperature (red) and cryogenic (black) UV-Vis spectra of $\{(P_3^B)Fe(NO)\}^9$ in 2-MeTHF highlighting the region that demonstrates vibronic coupling.

The solution magnetic susceptibility of $\{(P_3^B)Fe(NO)\}^9$ is $1.7\mu_B$ (C_6D_6 , RT), consistent with an $S = \frac{1}{2}$ species. The X-band EPR spectrum of $\{(P_3^B)Fe(NO)\}^9$ (**Figure 2.8**) shows a nearly axial signal with significant g anisotropy and broad features. We favor an electronic structure consistent with a description in which the SOMO consists of an iron d-orbital that is primarily of d_{xy} or $d_{x^2-y^2}$ parentage, akin to ferrocenium.³⁰ Unrestricted DFT

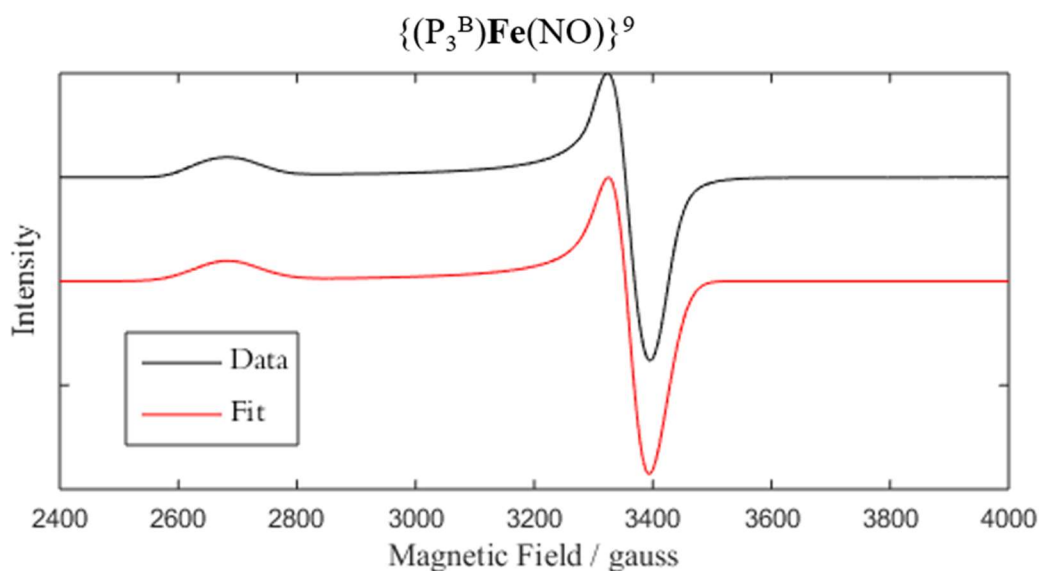


Figure 2.8: CW X-band EPR spectrum of $\{(P_3^B)Fe(NO)\}^9$ at 77 K in a 2-MeTHF glass (black) and its simulation (red). Simulation parameters: $g = [2.50048, 1.99439, 1.96918]$ and $HStrain = [450.420, 159.384, 205.277]$.

calculations using BP86/def2-TZVPP (Fe, B, P, N, O) and 631-G(d) (C, H)³¹⁻³⁵ reproduce the structure of $\{(P_3^B)Fe(NO)\}^9$ well and support this description (**Figure 2.9**). Broken symmetry calculations, in which an $S = 1$ NO^- is antiferromagnetically coupled to a metal center, are often used in the case of linear M–NO complexes.²⁷ Attempts to optimize such wavefunctions with BP86 led to their collapse back to the low-spin wavefunction. Calculations using B3LYP were observed to converge broken symmetry wavefunctions, but

this functional predicted the ground states to be intermediate spin, rather than the observed low-spin.

2.3 Conclusion

The collective data presented here lend support to an electronic description of $\{(P_3^B)Fe(NO)\}^{8-10}$ in which reduction of the system across the Enemark-Feltham numbers from 8 to 9 and 9 to 10 occurs in primarily Fe-based orbitals that are orthogonal to both the

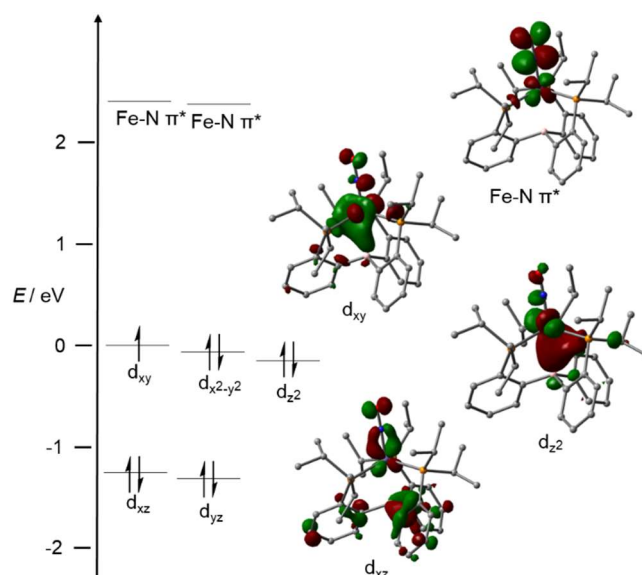


Figure 2.9: A molecular orbital diagram for $\{(P_3^B)Fe(NO)\}^9$. The energies given are relative to the SOMO which was set to be 0 eV. The molecular orbitals depicted (Isovalue = 0.05) are from the α -spin manifold as are the energies. The energy and appearance of the β -spin orbitals are similar.

Fe–NO π -bonds and the Fe–B σ -bond. However, as the Fe becomes more electron rich, backbonding into the NO, σ -backbonding into the borane, and presumably π -backbonding into the phosphines all become stronger, leading to very little overall change in the electron density at the Fe-center (*i.e.*, its relative state of oxidation.)

This high degree of covalency, particularly in the Fe–NO bond but also between the Fe and the P_3^B ligand, leads to the atypical maintenance of a linear Fe–N–O geometry upon

successive reductions, and appears to be key to the ability of the P_3^B ligand to support an Fe–NO unit across three redox states. Finally, trigonal symmetry, rather than tetragonal symmetry, gives rise to an additional non-bonding orbital, providing access to unusually high Enemark-Feltham numbers (8, 9, and 10).

2.4 References

- (1) Pacher, P.; Beckman, J. S.; Liaudet, L. *Physiol. Rev.* **2007**, *87*, 315–424.
- (2) Tennyson, A. G.; Lippard, S. J. *Chem. Biol. (Oxford, U.K.)* **2011**, *18*, 1211–1220.
- (3) Enemark, J. H.; Feltham, R. D. *Coord. Chem. Rev.* **1974**, *13*, 339–406.
- (4) Hayton, T. W.; Legzdins, P.; Sharp, W. B. *Chem. Rev.* **2002**, *102*, 935–992.
- (5) Wright, A. M.; Hayton, T. W. *Comments Inorg. Chem.* **2012**, *33*, 207–248.
- (6) Serres, R. G.; Grapperhaus, C. A.; Bothe, E.; Bill, E.; Weyhermüller, T.; Neese, F.; Wieghardt, K. *J. Am. Chem. Soc.* **2004**, *126*, 5138–5153.
- (7) Pellegrino, J.; Bari, S. E.; Bikiel, D. E.; Doctorovich, F. *J. Am. Chem. Soc.* **2010**, *132*, 989–995.
- (8) Sanders, B. C.; Patra, A. K.; Harrop, T. C. *J. Inorg. Biochem.* **2013**, *118*, 115–127.
- (9) Goodrich, L. E.; Roy, S.; Alp, E. E.; Zhao, J.; Hu, M. Y.; Lehnert, N. *Inorg. Chem.* **2013**, *52*, 7766–7780.
- (10) Speelman, A. L.; Lehnert, N. *Angew. Chem. Int. Ed.* **2013**, *52*, 12283–12287.
- (11) Hu, B.; Li, J. *Angew. Chem. Int. Ed.* **2015**, *54*, 10579–10582.
- (12) Hieber, W.; Beutner, K. *Z. Naturforsch., B: Anorg. Chem., Org. Chem., Biochem., Biophys., Biol.* **1960**, *15*, 323–324.

- (13) Klein, J. E. M. N.; Miehlich, B.; Holzwarth, M. S.; Bauer, M.; Milek, M.; Khusniyarov, M. M.; Knizia, G.; Werner, H.-J.; Plietker, B. *Angew. Chem. Int. Ed.* **2014**, *53*, 1790–1794.
- (14) Bontemps, S.; Bouhadir, G.; Dyer, P. W.; Miqueu, K.; Bourissou, D. *Inorg. Chem.* **2007**, *46*, 5149–5151.
- (15) Kupper, C.; Rees, J. A.; Dechert, S.; DeBeer, S.; Meyer, F. *J. Am. Chem. Soc.* **2016**, *138*, 7888–7898.
- (16) Moret, M.-E.; Peters, J. C. *Angew. Chem. Int. Ed.* **2011**, *50*, 2063–2067.
- (17) Patra, A. K.; Dube, K. S.; Sanders, B. C.; Papaefthymiou, G. C.; Conradie, J.; Ghosh, A.; Harrop, T. C. *Chem. Sci.* **2012**, *3*, 364–369.
- (18) Lee, Y.; Mankad, N. P.; Peters, J. C. *Nat. Chem.* **2010**, *2*, 558–565.
- (19) CCDC 1481636 ($\{(P_3^B)Fe(NO)\}^8$), 1481637 ($\{(P_3^B)Fe(NO)\}^9$), and 1481638 ($\{(P_3^B)Fe(NO)\}^{10}$) contain the supplementary crystallographic data for this paper. These data can be obtained free of charge from The Cambridge Crystallographic Data Centre via www.ccdc.cam.ac.ukj/data_request/cif.
- (20) Sizova, O. V.; Sokolov, A. Yu.; Skripnikov, L. V.; Baranovski, V. I. *Polyhedron* **2007**, *26*, 4680–4690.
- (21) Moret, M. E.; Peters, J. C. *J. Am. Chem. Soc.* **2011**, *133*, 18118–18121.
- (22) Speelman, A. L.; Zhang, B.; Krebs, C.; Lehnert, N. *Angew. Chem. Int. Ed.* **2016**, *55*, 6685–6688.
- (23) Zhang, Y.; Oldfield, E. *J. Am. Chem. Soc.* **2004**, *126*, 9494–9495.

- (24) Gütlich, P.; Bill, E.; Trautwein, A. X. *Mössbauer Spectroscopy and Transition Metal Chemistry: Fundamentals and Applications*; Springer-Verlag: Berlin Heidelberg, 2011.
- (25) Anderson, J. S.; Cutsail, G. E.; Rittle, J.; Connor, B. A.; Gunderson, W. A.; Zhang, L.; Hoffman, B. M.; Peters, J. C. *J. Am. Chem. Soc.* **2015**, *137*, 7803–7809.
- (26) Del Castillo, T. J.; Thompson, N. B.; Peters, J. C. *J. Am. Chem. Soc.* **2016**, *138*, 5341–5350.
- (27) Tomson, N. C.; Crimmin, M. R.; Petrenko, T.; Rosebrugh, L. E.; Sproules, S.; Boyd, W. C.; Bergman, R. G.; DeBeer, S.; Toste, F. D.; Wieghardt, K. *J. Am. Chem. Soc.* **2011**, *133*, 18785–18801.
- (28) Manoharan, P. T.; Gray, H. B. *Inorg. Chem.* **1966**, *5*, 823–839.
- (29) Enemark, J. H.; Quinby, M. S.; Reed, L. L.; Steuck, M. J.; Walthers, K. K. *Inorg. Chem.* **1970**, *9*, 2397–2403.
- (30) Sohn, Y. S.; Hendrickson, D. N.; Gray, H. B. *J. Am. Chem. Soc.* **1970**, *92*, 3233–3234.
- (31) Hehre, W. J.; Ditchfield, R.; Pople, J. A. *J. Chem. Phys.* **1972**, *56*, 2257–2261.
- (32) Perdew, J. P. *Phys. Rev. B* **1986**, *33*, 8822–8824.
- (33) Becke, A. D. *Phys. Rev. A* **1988**, *38*, 3098–3100.
- (34) Schäfer, A.; Horn, H.; Ahlrichs, R. *J. Chem. Phys.* **1992**, *97*, 2571–2577.
- (35) Weigend, F.; Ahlrichs, R. *Phys. Chem. Chem. Phys.* **2005**, *7*, 3297–3305.

Chapter 3.

Catalytic N₂-to-NH₃ Conversion by Fe at Lower Driving Force: A Proposed Role for Metallocene-Mediated PCET

Adapted from:

Chalkley, M. J.; Del Castillo, T. J.; Matson, B. D.; Roddy, J. P.; Peters, J. C.
ACS Cent. Sci. **2017**, *3*, 217–223.
DOI: 10.1021/acscentsci.7b00014

3.1 Introduction

The reduction of N_2 to NH_3 is critical for life and is performed on a massive scale both industrially and biologically.¹ The high stability of the $\text{N}\equiv\text{N}$ triple bond necessitates catalysts and high-energy reagents/conditions to achieve the desired transformation.² Synthetic studies of catalytic N_2 -to- NH_3 conversion by model complexes are of interest to constrain hypotheses concerning the mechanism/s of biological (or industrial) N_2 -fixation and to map fundamental catalyst design principles for multi-electron reductive transformations.^{3,4} Interest in Fe model systems that catalyze N_2 -to- NH_3 conversion has grown in part due to the postulate that one or more Fe centers in the FeMo-cofactor of FeMo-nitrogenase may serve as the site of N_2 binding and activation during key bond-breaking and -making steps.⁵ Previous examples of synthetic molecular Fe catalysts that mediate N_2 -to- NH_3 conversion operate with high driving force, relying on a very strong acid ($\text{p}K_{\text{a}}$ ca. 0) and reductant ($E^\circ < -3.0$ V vs $\text{Fc}^{+/0}$).⁶⁻⁹ In contrast, several Mo catalysts have been shown to facilitate N_2 -to- NH_3 conversion with significantly lower driving force¹⁰⁻¹³ and one Fe catalyst has been recently¹⁰⁻¹³ reported to facilitate N_2 -to- N_2H_4 conversion at lower driving force.¹⁴ There is thus interest in exploring the viability of Fe-mediated catalytic N_2 -to- NH_3 conversion under less forcing conditions from a practical perspective and to continue assessing these systems as functional models of biological nitrogenases, in which 8 ATP are consumed per NH_3 formed leading to a driving force of 58 kcal/mol.² Herein we demonstrate that catalytic conversion of N_2 to NH_3 by $[(\text{P}_3^{\text{B}})\text{Fe}]^+$ (P_3^{B} = tris(*o*-diisopropylphosphinophenyl)borane) can be achieved with a significantly lower driving force by coupling Cp^*Co with $[\text{Ph}_2\text{NH}_2]^+$ or $[\text{PhNH}_3]^+$ (**Figure 3.1**). Such conditions

additionally afford unusually high selectivity and catalytic turnover for NH_3 . It was similarly observed that this reagent combination with $(\text{depe})_2\text{Fe}(\text{N}_2)$ likewise provides high selectivity for N_2H_4 .¹⁴ We note that the use of milder reagents as reductant (E°) and acid ($\text{p}K_a$), as compared to previous Fe-mediated N_2 -to- NH_3 conversion, engenders a higher effective bond dissociation enthalpy (BDE_{eff} , **Error! Reference source not found.**),¹⁵ which in turn lowers the enthalpic driving force ($\Delta\Delta H_f$, **Error! Reference source not found.**), as discussed in Chapter 1. Furthermore, this higher BDE_{eff} suggests access to proton-coupled electron transfer (PCET) pathways (*e.g.*, $\text{FeN}_2 + \text{H}\cdot \rightarrow \text{FeN}_2\text{H}$) in addition to electron transfer (ET)/proton transfer (PT) pathways, thus enhancing overall catalytic efficiency. Theoretical considerations, including DFT calculations, and experimental details are discussed that suggest the viability of a decamethylcobaltocene-mediated PCET pathway in this system; by extension we suggest metallocene-mediated (*e.g.*, Cp^*Cr) PCET pathways may be operative in previously studied Mo and Fe N_2 -fixing systems that use metallocene reductants.^{10–14}

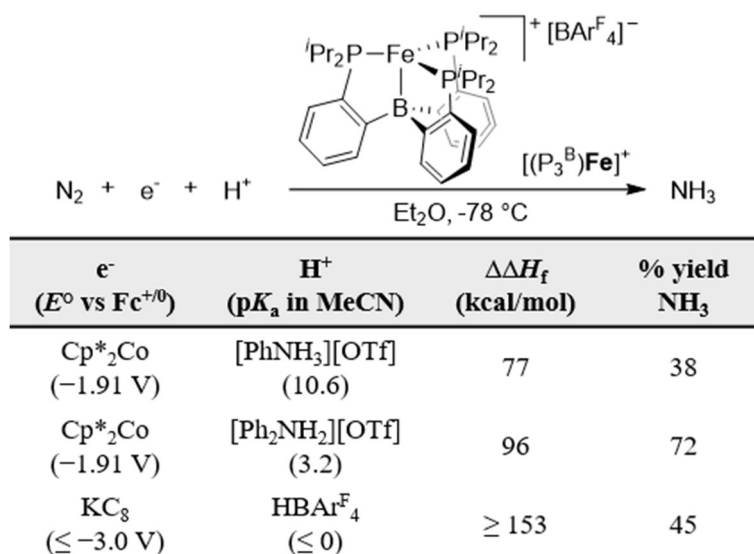


Figure 3.1: Summary of conditions used for catalytic N_2 -to- NH_3 conversion by $[(\text{P}_3^{\text{B}})\text{Fe}]^+$ highlighting the estimated driving force ($\Delta\Delta H_f$).^{6,16}

$$\text{Eq 3.1) } \text{BDE}_{\text{eff}} = 1.37 \times \text{p}K_a + 23.06 \times E^\circ + C_h$$

$$\text{Eq 3.2) } \Delta\Delta H_f = 3 \times (\text{BDE}_{\text{eff}} - \text{BDE}(\text{H}_2)/2)$$

Various observations of $(\text{P}_3^{\text{B}})\text{Fe}$ complexes in the presence of acids and reductants suggested that this system might be capable of N_2 -to- NH_3 conversion with lower driving force than that originally reported. Accordingly, we had observed that the treatment of $[(\text{P}_3^{\text{B}})\text{Fe}(\text{N}_2)]^-$ with KC_8 and weaker acids ($\text{p}K_a > 0$) led to greater than stoichiometric NH_3 formation (*e.g.*, under unoptimized conditions [2,6-dimethylanilinium][OTf] afforded 2.1 equiv NH_3 per Fe).¹⁷ Similarly, the treatment of $[(\text{P}_3^{\text{B}})\text{Fe}(\text{N}_2)]^-$ with $[\text{H}(\text{OEt}_2)_2][\text{BAr}^{\text{F}_4}]$ (HBAr^{F_4} , BAr^{F_4} = tetrakis(3,5-bis(trifluoromethyl)phenyl)borate) and weaker reductants led to modest yields of NH_3 . For example, under unoptimized conditions we had observed that decamethylcobaltocene (Cp^*_2Co) and HBAr^{F_4} afforded 0.6 equiv NH_3 per Fe.^{16,17} Most recently, an apparent catalytic response was observed during a cyclic voltammetry experiment at the $[(\text{P}_3^{\text{B}})\text{Fe}(\text{N}_2)]^{0/-}$ couple (-2.1 V vs $\text{Fc}^{+/0}$) upon addition of excess HBAr^{F_4}

under an N₂ atmosphere. Electrolytic NH₃ generation by [(P₃^B)Fe]⁺ was observed at -2.4 V vs Fc⁺⁰ in Et₂O,²³ and Na/Hg (-2.4 V vs Fc⁺⁰ in THF)¹⁶ could instead be used for N₂-to-NH₃ conversion catalysis (albeit less selectively and with low turnover). Finally, mixing [(P₃^B)Fe]⁺ with Cp*₂Co in Et₂O at -78 °C under N₂ generates some [(P₃^B)Fe(N₂)]⁻ as observed by freeze-quench X-band EPR and Mössbauer spectroscopy, suggesting that Cp*₂Co is, in principle, a sufficiently strong reductant to trigger N₂RR catalysis by [(P₃^B)Fe]⁺.

3.2 Results

3.2.1 Catalytic N₂RR at Lowered Overpotential

Treatment of [(P₃^B)Fe]⁺ with Cp*₂Co and [Ph₂NH₂][OTf], [Ph₂NH₂][BAr^F₄], or [PhNH₃][OTf] in Et₂O at -78 °C under an N₂ atmosphere affords catalytic yields of NH₃ (**Table 3.1**). Notably, the highest selectivity for NH₃ obtained among this series (72% at standard substrate loading; Entry 1) is significantly improved compared to all previously described (molecular) Fe catalysts for N₂-to-NH₃ conversion.^{6-9,14,16} Tripling the initial substrate loading (Entry 2) nearly triples the NH₃ production with only modest loss in efficiency for NH₃ (63 ± 2%). Preliminary attempts to further increase the initial substrate loading have led to substantially decreased efficiency (Entry 3). However, substrate reloading experiments (Entries 4 and 5) maintain greater than 50% efficiency for NH₃ overall; a turnover number for NH₃ generation via two reloadings has been achieved as high as 89 in a single run (84 ± 8 equiv NH₃ per Fe; Entry 5). This is an unusually high turnover number for a molecular N₂-to-NH₃ conversion catalyst under any conditions.¹⁴ In catalytic runs performed with labeled [Ph₂¹⁵NH₂][OTf] under an atmosphere of natural

abundance $^{14}\text{N}_2$ the production of exclusively $^{14}\text{NH}_3$ is observed, demonstrating that the NH_3 formed during catalysis is derived from N_2 and not degradation of the acid.

The use of the more soluble acid $[\text{Ph}_2\text{NH}_2][\text{BAr}^{\text{F}}_4]$ (Entry 6) provides significantly lower, but still catalytic, yields of NH_3 . This more soluble acid presumably increases background reactivity with Cp^*Co . Perhaps more significantly, $[\text{PhNH}_3][\text{OTf}]$ is a considerably weaker acid than $[\text{Ph}_2\text{NH}_2][\text{OTf}]$ (**Figure 3.1**), but still provides substantial catalytic yields of NH_3 (Entries 7 and 8), at efficiencies that compare well with those obtained previously using HBAr^{F}_4 and KC_8 despite a difference in driving force of nearly 100 kcal/mol.¹⁶

Table 3.1: N_2 -to- NH_3 Conversion with $(\text{P}_3^{\text{E}})\text{M}$ Complexes ($\text{M} = \text{Fe}, \text{Co}$)

	Catalyst	Cp^*Co (equiv)	Acid (equiv)	Acid	Equiv NH_3/Fe	% Yield NH_3/e^-
1	$[(\text{P}_3^{\text{B}})\text{Fe}]^+$	54	108	$[\text{Ph}_2\text{NH}_2][\text{OTf}]$	12.8 ± 0.5	72 ± 3
2	$[(\text{P}_3^{\text{B}})\text{Fe}]^+$	162	322	$[\text{Ph}_2\text{NH}_2][\text{OTf}]$	34 ± 1	63 ± 2
3	$[(\text{P}_3^{\text{B}})\text{Fe}]^+$	322	638	$[\text{Ph}_2\text{NH}_2][\text{OTf}]$	26.7 ± 0.9	25 ± 1
4 ^a	$[(\text{P}_3^{\text{B}})\text{Fe}]^+$	$[162]\times 2$	$[322]\times 2$	$[\text{Ph}_2\text{NH}_2][\text{OTf}]$	56 ± 9	52 ± 9
5 ^a	$[(\text{P}_3^{\text{B}})\text{Fe}]^+$	$[162]\times 3$	$[322]\times 3$	$[\text{Ph}_2\text{NH}_2][\text{OTf}]$	84 ± 8	52 ± 5
6	$[(\text{P}_3^{\text{B}})\text{Fe}]^+$	54	108	$[\text{Ph}_2\text{NH}_2][\text{BAr}^{\text{F}}_4]$	8 ± 1	42 ± 6
7	$[(\text{P}_3^{\text{B}})\text{Fe}]^+$	54	108	$[\text{PhNH}_3][\text{OTf}]$	7 ± 1	38 ± 7
8	$[(\text{P}_3^{\text{B}})\text{Fe}]^+$	162	322	$[\text{PhNH}_3][\text{OTf}]$	16 ± 3	29 ± 4
9	$(\text{P}_3^{\text{Si}})\text{Fe}(\text{N}_2)$	54	108	$[\text{Ph}_2\text{NH}_2][\text{OTf}]$	1.2 ± 0.1	6 ± 1
10	$[(\text{P}_3^{\text{B}})\text{Co}(\text{N}_2)]^-$	54	108	$[\text{Ph}_2\text{NH}_2][\text{OTf}]$	1.1 ± 0.4	6 ± 2

11	(P ₃ ^{Si})Co(N ₂)	54	108	[Ph ₂ NH ₂][OTf]	0 ± 0	0 ± 0
----	--	----	-----	---	-------	-------

The catalyst, acid, Cp*₂Co, and Et₂O were sealed in a vessel at -196 °C under an N₂ atmosphere followed by warming to -78 °C and stirring. Yields are reported as an average of at least 2 runs. ^aFor these experiments, the reaction was allowed to proceed for 3 hours at -78 °C before cooling to -196 °C and furnished with additional substrate and solvent

We also screened several related phosphine-ligated, (P₃^E)M(N₂) (M = Fe, Co; E = B, Si) complexes^{18,19} under the optimized reaction conditions with [Ph₂NH₂][OTf] and Cp*₂Co (Entries 9–11) but found that none of these other systems were competent catalysts at these loadings. While we anticipate other catalyst systems for N₂-to-NH₃ conversion may yet be found that function under the conditions described herein,¹⁴ certain features of the (P₃^B)Fe system correlate with unusually productive catalysis.¹⁹

3.2.2 Mechanism of N₂RR Catalysis with (P₃^B)Fe

Also significant is that when [(P₃^B)Fe]⁺ is loaded with 322 equiv [Ph₂NH₂][OTf] and 162 equiv Cp*₂Co in Et₂O at -78 °C, modest levels of N₂H₄ are detected (< 1 equiv per Fe).^{9,14} We had previously reported that catalytic N₂ reduction with KC₈ and HBAr^F₄ yielded no detectable hydrazine, but observed that if hydrazine was added at the outset of a catalytic run, it was consumed.⁶ When 5 equiv of N₂H₄ were added at the beginning of a catalytic run (again with 322 equiv [Ph₂NH₂][OTf] and 162 equiv Cp*₂Co), only 0.22 equiv of N₂H₄ (4.4% recovery) remained after workup. This result indicates that liberated hydrazine can also be reduced or disproportionated under the present conditions or that the work-up

conditions convert N_2H_4 to NH_3 . That N_2H_4 is detected to any extent in the absence of initially added N_2H_4 under these conditions indicates that a late N–N cleavage mechanism to produce NH_3 (*e.g.*, alternating or hybrid cross-over) is accessible.^{4,20,21} A recent report by Ashley and coworkers describes a phosphine-supported Fe system for which catalytic hydrazine formation is kinetically dominant.¹⁴ Whether such a pathway is kinetically dominant in this system is as yet unclear.^{16,22}

The $(\text{P}_3^{\text{B}})\text{Fe}$ speciation under turnover conditions was probed via freeze-quench Mössbauer spectroscopy.¹⁶ The Mössbauer spectrum of a catalytic reaction mixture after five minutes of reaction time (

Figure 3.2) reveals the presence of multiple species featuring well-resolved sets of quadrupole doublets. The spectrum is satisfactorily simulated with $(\text{P}_3^{\text{B}})\text{Fe}(\text{N}_2)$ ($\delta = 0.55$ mm/s, $\Delta E_{\text{Q}} = 3.24$ mm/s, 32%;

Figure 3.2 green), $[(\text{P}_3^{\text{B}})\text{Fe}(\text{N}_2)]^-$ ($\delta = 0.40$ mm/s, $\Delta E_{\text{Q}} = 0.98$ mm/s, 26%;

Figure 3.2 blue),¹⁶ an unknown, likely P_3^{B} -metallated Fe species ($\delta = 0.42$ mm/s, $\Delta E_{\text{Q}} = 1.84$ mm/s, 18%;

Figure 3.2 yellow), and a final species that is modeled with $\delta = 0.96$ mm/s and $\Delta E_{\text{Q}} = 3.10$ mm/s (24%;

Figure 3.2 orange). The presence of $[(\text{P}_3^{\text{B}})\text{Fe}(\text{N}_2)]^-$ was confirmed by freeze-quench EPR spectroscopy experiments. The broad nature of this last signal (

Figure 3.2 orange) and its overlap with other features in the spectrum prevents its precise assignment, but its high isomer shift and large quadrupole splitting are suggestive of a tetrahedral, $S = 2$ Fe(II) complex, which have distinct Mössbauer properties.^{23,24} The

Mössbauer spectrum of a catalytic reaction mixture after 30 minutes was also analyzed.

The spectrum still shows $(P_3^B)Fe(N_2)$ (53%), the same unknown $(P_3^B)Fe$ species (18%), and again a tetrahedral, high-spin Fe(II) component (22%). However, $[(P_3^B)Fe]^+$ is now present ($\delta = 0.75$ mm/s, $\Delta E_Q = 2.55$ mm/s, 8%) and $[(P_3^B)Fe(N_2)]^-$ is no longer observed.

The reloading experiments described above provide strong evidence that “ $(P_3^B)Fe$ ” species represent an “active catalyst” population; interpretation of the relative speciation via spectroscopy should hence bear on the mechanism of the overall catalysis.

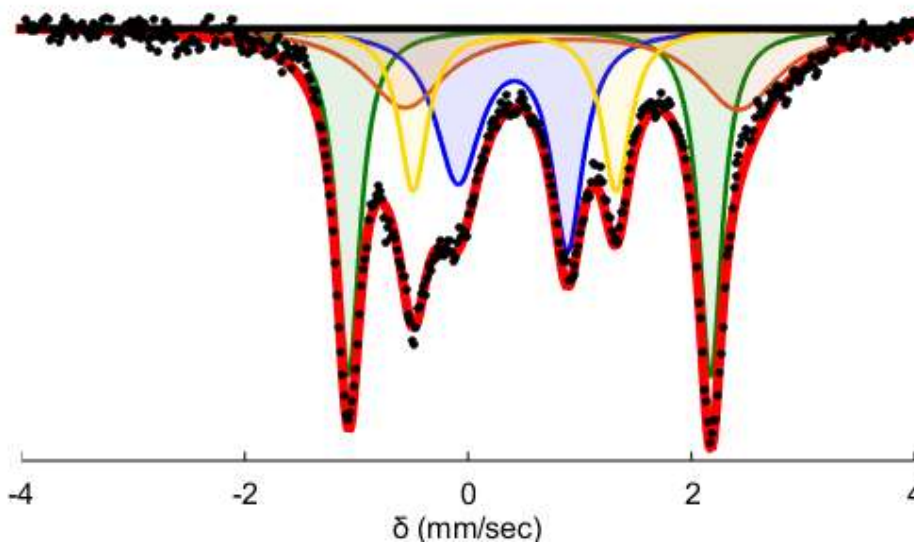


Figure 3.2: Mössbauer spectrum at 80 K with 50 mT applied parallel field of a freeze-quenched catalytic reaction (54 equiv Cp^*Co , 108 equiv $[Ph_2NH_2][OTf]$, 1 equiv $[(P_3^B)^{57}Fe]^+$) after five minutes of reaction time.

The appearance of a presumed high-spin ($S = 2$), tetrahedral Fe(II) species during catalysis (ca. 25%) might arise via dechelation of a phosphine arm. This species could represent an off-path state, or a downstream deactivation product. Interestingly, under the present catalytic conditions we do not observe the borohydrido-hydrido species $(P_3^B)(\mu-$

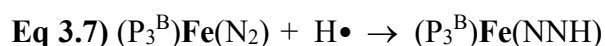
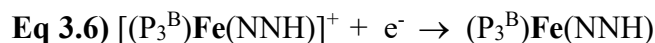
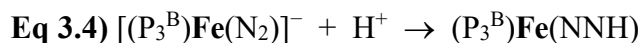
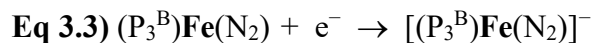
H)Fe(H)(L) ($\text{L} = \text{N}_2$ or H_2); this species was postulated to be an off-path resting state during N_2 -to- NH_3 conversion catalysis using HBAr^{F_4} and KC_8 and was the major component observed at early times (ca. 60% at 5 min).¹⁶ It therefore appears that a larger fraction of the “ $(\text{P}_3^{\text{B}})\text{Fe}$ ” species are in a catalytically on-path state at early reaction times under these new catalytic conditions.

Additionally, the presence of a significant degree of $[(\text{P}_3^{\text{B}})\text{Fe}(\text{N}_2)]^-$ (

Figure 3.2) at an early time point is distinct from conditions with HBAr^{F_4} and KC_8 .¹⁶ This observation is consistent with the notion that protonation of $[(\text{P}_3^{\text{B}})\text{Fe}(\text{N}_2)]^-$ is slowed under the present conditions, likely as a result of the insolubility of the triflate salt $[\text{Ph}_2\text{NH}_2][\text{OTf}]$ and its attenuated acidity relative to HBAr^{F_4} ,^{25–27} Clearly, differences in the rates of key elementary steps under the new conditions described here may lead to new mechanistic scenarios for N_2 -to- NH_3 conversion.

The improved catalytic efficiency at significantly lower driving force warrants additional consideration. When using HBAr^{F_4} and KC_8 we have previously suggested that protonation of $[(\text{P}_3^{\text{B}})\text{Fe}(\text{N}_2)]^-$, which itself can be generated by reduction of $(\text{P}_3^{\text{B}})\text{Fe}(\text{N}_2)$, to produce $(\text{P}_3^{\text{B}})\text{Fe}(\text{NNH})$ is a critical first step; $(\text{P}_3^{\text{B}})\text{Fe}(\text{NNH})$ can then be trapped by acid to produce spectroscopically observable $[(\text{P}_3^{\text{B}})\text{Fe}(\text{NNH}_2)]^+$.²² These steps, shown in **Error! Reference source not found.** and **Error! Reference source not found.** represent an ET-PT pathway. A PT-ET pathway, where $(\text{P}_3^{\text{B}})\text{Fe}(\text{N}_2)$ is sufficiently basic to be protonated to generate $[(\text{P}_3^{\text{B}})\text{Fe}(\text{NNH})]^+$ as a first step, followed by ET, is also worth considering (**Error! Reference source not found., Error! Reference source not found.**) A direct PCET pathway (**Error! Reference source not found.**) where H-atom delivery to $(\text{P}_3^{\text{B}})\text{Fe}(\text{N}_2)$ occurs, thus

obviating the need to access either $[(P_3^B)Fe(N_2)]^-$ or $[(P_3^B)Fe(NNH)]^+$, needs also to be considered.



Initial PT to $(P_3^B)Fe(N_2)$ to generate $[(P_3^B)Fe(NNH)]^+$ (**Error! Reference source not found.**) is unlikely under the present conditions due to the high predicted acidity of $[(P_3^B)Fe(NNH)]^+$ ($pK_a = -3.7$; estimated via DFT); efficient generation of such a species seems implausible for acids whose pK_a 's are calculated at 1.4 ($Ph_2NH_2^+$) and 6.8 ($PhNH_3^+$) in Et_2O (**Table 3.2**). We note that $[Ph_2NH_2][OTf]$ does not react productively with $(P_3^B)Fe(N_2)$ at -78 °C in Et_2O , as analyzed by Mössbauer spectroscopy.

Table 3.2: Calculated pK_a Values and BDEs of Selected Species

Species	$^a pK_a$	BDE (kcal/mol)
$[Ph_2NH_2]^+$	1.4	-
$[PhNH_3]^+$	6.8	-
Lutidinium	14.5	-
$[(Cp^*)Co(endo-\eta^4-C_5Me_5H)]^+$	16.8	31
$[(Cp^*)Co(exo-\eta^4-C_5Me_5H)]^+$	16.8	31

$[(\text{Cp}^*)\text{Cr}(\text{endo-}\eta^4\text{-C}_5\text{Me}_5\text{H})]^+$	17.3	37
$[(\text{Cp}^*)\text{Cr}(\text{exo-}\eta^4\text{-C}_5\text{Me}_5\text{H})]^+$	12.1	30
$[(\text{P}_3^{\text{B}})\text{Fe}(\text{NNH})]^+$	-3.7	-
$(\text{P}_3^{\text{B}})\text{Fe}(\text{NNH})$	38.7	35
$[(\text{P}_3^{\text{B}})\text{Fe}(\text{NNH}_2)]^+$	14.4	51
$(\text{P}_3^{\text{B}})\text{Fe}(\text{NNH}_2)$	-	47
$(\text{HIPTN}_3\text{N})\text{Mo}(\text{NNH})$	-	51

^apK_a values were calculated in Et₂O and reported relative to (Et₂O)₂H⁺.

To analyze these potential pathways DFT calculations were performed using the M06-L²⁸ functional with a def2-TZVP basis set on Fe and a def2-SVP basis set on all other atoms.²⁹ This computational method was selected on the basis that it reproduced the experimentally-derived BDE's of related N-H bonds on the (P₃^{Si})Fe platform.³⁰ We were particularly interested in accurate calculation of the BDE's because the DFT-calculated BDE_{N-H} for (P₃^B)Fe(NNH) (35 kcal/mol; **Table 3.2**) is larger than the effective BDE (**Error! Reference source not found.**) of either Cp*₂Co/Ph₂NH₂⁺ or Cp*₂Co/PhNH₃⁺ (25 and 31 kcal/mol, respectively). This suggests that PCET (**Error! Reference source not found.**) is plausible on thermodynamic grounds. Given that we have employed Cp*₂Co in this study, and that metallocenes generally (*i.e.*, Cp₂Co, Cp*₂Co and Cp*₂Cr) have been effective in other N₂-fixing molecular catalyst systems,¹⁰⁻¹⁴ we have explored via DFT several putative metallocene-derived PCET reagents. Independent studies of H₂ evolution from cobaltocene

have invoked a protonated cobaltocene intermediate.^{31–33} The observation of a background H₂ evolution reaction (HER) when employing metallocene reductants, but in the absence of an N₂-to-NH₃ conversion catalyst, suggests that metallocene protonation is kinetically competent.^{10,34,35} Based on the analysis we describe below, we propose that protonated metallocenes may serve as discrete and highly active H• sources for PCET.

3.2.3 PCET from a Protonated Metallocene

We find that the formation of *endo*- and [(Cp*)Co(*exo*-η⁴-C₅Me₅H)]⁺ are predicted to be thermodynamically favorable via protonation of Cp*₂Co by either [Ph₂NH₂]⁺ or [PhNH₃]⁺ (–21 and –13 kcal/mol, respectively; **Figure 3.3A**). Efforts to optimize a Co–H species led to migration of the hydrogen to the ring; however, transition metal hydride radical cations are also known to display PCET behavior.³⁶ We have calculated the BDE_{C–H}'s for both *endo*- and [(Cp*)Co(*exo*-η⁴-C₅Me₅H)]⁺ as 31 kcal/mol (**Figure 3.3B**; **Table 3.2**),

indicating that they must be among the strongest PCET reagents accessible in this catalyst cocktail. Indeed, they would be among the strongest PCET reagents known.¹⁵

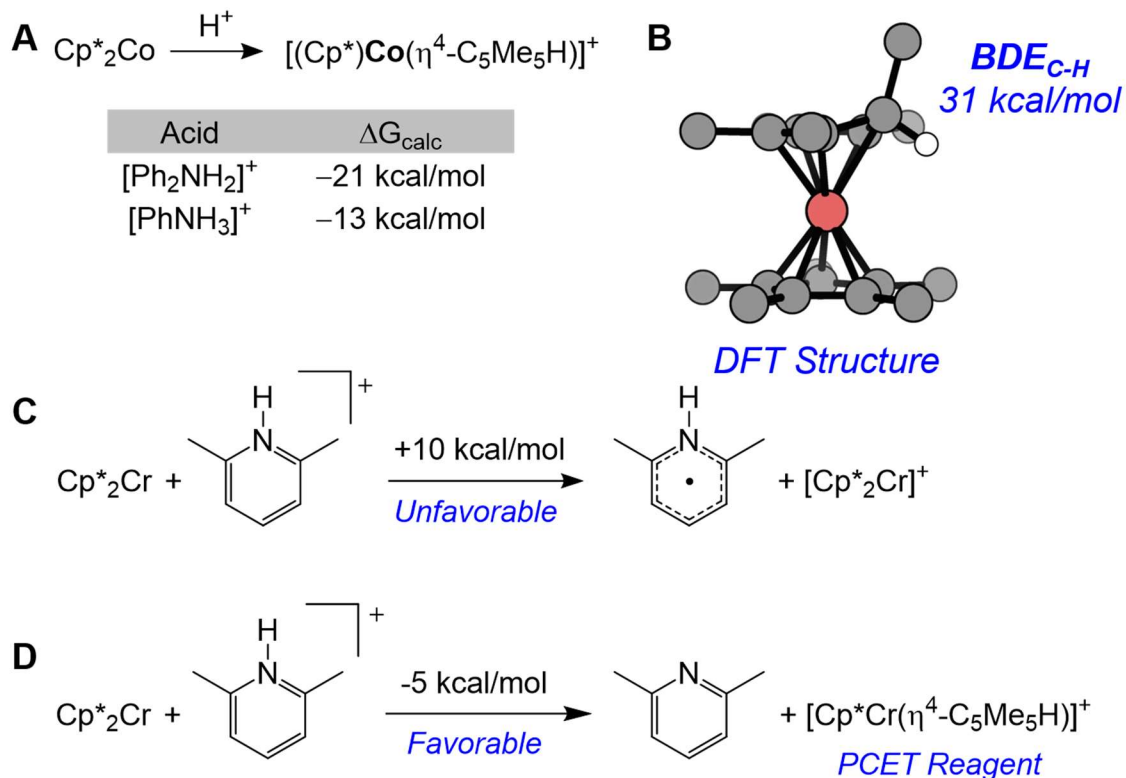


Figure 3.3: DFT calculations regarding the interaction of metallocenes and acids relevant to nitrogen fixation catalysis. (A) Calculated free-energy changes for the protonation of Cp^*_2Co . (B) DFT optimized structure of $[(\text{Cp}^*)\text{Co}(\textit{endo}\text{-}\eta^4\text{-C}_5\text{Me}_5\text{H})]^+$ (methyl protons omitted for clarity). (C) The unfavorable reduction of 2,6-lutidinium by Cp^*_2Cr with the calculated free energy change. (D) The favorable protonation of Cp^*_2Cr by lutidinium with the calculated free energy change.

We anticipate these species would be extremely unstable in solution and hence difficult to detect in situ, but via trapping in the solid state by rapid precipitation from toluene we have isolated a species whose EPR data and chemical behavior are consistent with $[(\text{Cp}^*)\text{Co}(\eta^4\text{-C}_5\text{Me}_5\text{H})][\text{OTf}]$. Accordingly, slow addition of a toluene solution of Cp^*_2Co at -78°C to triflic acid (HOTf) leads to the instantaneous precipitation of a purple solid that can be isolated at low temperature. The purple solid can be characterized at 77 K by powder EPR

spectroscopy via its highly structured signal. By contrast, at this temperature $S = \frac{1}{2}$ Cp^*_2Co does not display a discernable EPR signal. The new signal shows strong Co hyperfine coupling and significant g-anisotropy, consistent with a new $S = \frac{1}{2}$ cobalt species (**Figure 3.4**). Furthermore, the resulting EPR signal is slightly perturbed when this purple solid is instead generated from the reaction between deuterated triflic acid (DOTf) and Cp^*_2Co , suggesting that the acidic proton is directly associated with the new Co species and consistent with its assignment as a protonated decamethylcobaltocene species. Close inspection of these spectra indicate they likely represent a mixture of two signals arising from similar Co-containing complexes. This observation is fully consistent with the presence of both *endo*- and $[(\text{Cp}^*)\text{Co}(\textit{exo}\text{-}\eta^4\text{-C}_5\text{Me}_5\text{H})]^+$, as is to be expected given they are predicted to be nearly isoenergetic. Allowing the purple precipitate to warm to room temperature either as a solid or a stirred suspension in toluene leads to the formation of H_2 and $[\text{Cp}^*_2\text{Co}]^+$.

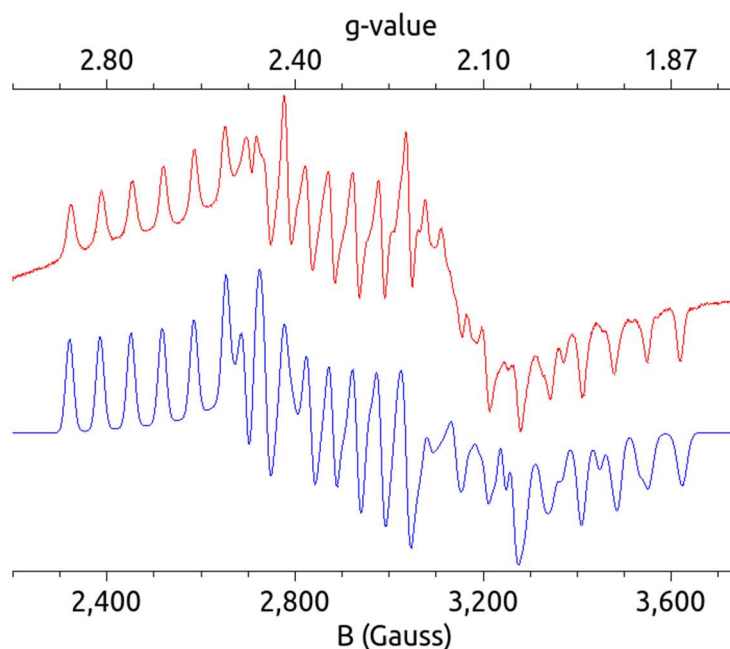


Figure 3.4: X-band 77 K powder EPR spectrum (red) and simulation (blue) of the isolated purple precipitate (assigned as endo- and $[(\text{Cp}^*)\text{Co}(\text{exo-}\eta^4\text{-C}_5\text{Me}_5\text{H})]^+$) from reaction between Cp^*Co and HOTf at -78°C . Simulation parameters are $g_1 = [2.63\ 2.345\ 1.984]$, $A_{1,\text{Co}} = [248\ 160\ 187]$ MHz, $lw_1 = 1$ MHz, $\text{HStrain}_1 = [60\ 50\ 60]$ MHz, $\text{Weight}_1 = 1$; $g_2 = [2.347\ 2.1\ 1.982]$, $A_{2,\text{Co}} = [200\ 50\ 110]$ MHz, $lw_2 = 1$, $\text{HStrain}_2 = [40\ 40\ 40]$ MHz, $\text{Weight}_2 = 0.2$.

To better understand the potential role of PCET in N_2 -to- NH_3 conversion catalysis by $(\text{P}_3^{\text{B}})\text{Fe}$, we have additionally calculated the N–H bond strengths (Table 2) of several early stage candidate intermediates, including the aforementioned $(\text{P}_3^{\text{B}})\text{Fe}(\text{NNH})$ (35 kcal/mol), $[(\text{P}_3^{\text{B}})\text{Fe}(\text{NNH}_2)]^+$ (51 kcal/mol), and $(\text{P}_3^{\text{B}})\text{Fe}(\text{NNH}_2)$ (47 kcal/mol). We conclude that PCET from $[(\text{Cp}^*)\text{Co}(\text{exo-}\eta^4\text{-C}_5\text{Me}_5\text{H})]^+$ to generate intermediates of these types is thermodynamically favorable in each case. Although the dissolution equilibria and kinetics of the insoluble reagents used complicate analysis of the kinetics of individual ET, PT, and PCET steps, the low activation barriers ($\Delta G^\ddagger < 9$ kcal/mol) calculated for all proposed PCET reactions are consistent with these reactions being kinetically accessible. To generate the first

and most challenging intermediate (**Error! Reference source not found.**), the enthalpic driving force for PCET is estimated at ~ 4 kcal/mol ($\Delta G_{\text{calc}} = -9$ kcal/mol). This driving force of PCET steps increases sharply as further downstream Fe-N_xH_y intermediates are considered. Given that the Marcus cross-relation between driving force and reaction kinetics has been shown to hold quite well for many PCET reactions this suggests that these reactions would also be kinetically accessible.³⁹⁻⁴¹



3.3 Discussion

Given the prevalence of metallocene reductants in N₂-to-NH₃ (or -N₂H₄) conversion,¹⁰⁻¹⁴ especially for the well-studied Mo catalyst systems, it is worth considering metallocene-mediated PCET more generally. For instance, a role for ET/PT steps (or conversely PT/ET) in N₂-to-NH₃ conversion catalyzed by (HIPTN₃N)Mo (HIPTN₃N = [(3,5-(2,4,6-*i*Pr₃C₆H₂)₂C₆H₃NCH₂CH₂)₃N]³⁻, a bulky triamidoamine ligand) has been frequently posited.⁴⁰⁻⁴⁴ But PCET steps may play a critical role, too. In the latter context, we note reports from Schrock and coworkers that have shown both acid and reductant are required to observe productive reactivity with (HIPTN₃N)Mo(N₂). These observations are consistent with PCET to generate (HIPTN₃N)Mo(NNH).⁴⁴ A PCET scenario has been discussed in this general context of N₂-to-NH₃ conversion, where a lutidinyl radical intermediate formed via ET from Cp*₂Cr has been suggested as a PCET reagent that can be generated in situ.^{34,45} However, our own calculations predict that the lutidinyl radical should be uphill with Cp*₂Cr as the reductant ($\Delta G_{\text{calc}} = +10$ kcal/mol; Figure 3C). Although estimates of the reduction potential of pyridinium radicals has been controversial, this

calculation is consistent with previous findings.^{46,47} We instead propose protonation of Cp^*_2Cr by the lutidinium acid as more plausible ($\Delta G_{\text{calc}} = -5.3$ kcal/mol; Figure 3D) to generate a highly reactive decamethylchromocene-derived PCET reagent.

While N–H bond strengths have not been experimentally determined for the $(\text{HIPTN}_3\text{N})\text{Mo}$ -system, using published data we deduce the N–H bond of $(\text{HIPTN}_3\text{N})\text{Mo}(\text{NNH})$ to be ca. 49 kcal/mol, and we calculate it via DFT with a truncated HIPTN_3N ligand to be 51 kcal/mol.^{34,44} The $\text{BDE}_{\text{N-H}}$ for this Mo diazenido species is hence much larger than we predict for $(\text{P}_3^{\text{B}})\text{Fe}(\text{NNH})$ (35 kcal/mol), perhaps accounting for its higher stability.⁴⁴ A PCET reaction between $[(\text{Cp}^*)\text{Cr}(\textit{endo}\text{-}\eta^4\text{-C}_5\text{Me}_5\text{H})]^+$ ($\text{BDE}_{\text{calc}} = 37$ kcal/mol) and $(\text{HIPTN}_3\text{N})\text{Mo}(\text{N}_2)$ to generate $(\text{HIPTN}_3\text{N})\text{Mo}(\text{NNH})$ and $[\text{Cp}^*_2\text{Cr}]^+$ would be highly exergonic. Furthermore, we predict a similarly weak $\text{BDE}_{\text{C-H}}$ for Cp-protonated cobaltocene, $[(\text{Cp})\text{Co}(\eta^4\text{-C}_5\text{H}_6)]^+$ ($\text{BDE}_{\text{calc}} = 35$ kcal/mol). These considerations are consistent with the reported rapid formation of $(\text{HIPTN}_3\text{N})\text{Mo}(\text{NNH})$ using either Cp^*_2Cr or Cp_2Co in the presence of lutidinium acid.

3.4 Conclusion

To close, we have demonstrated catalytic N_2 -to- NH_3 conversion by $[(\text{P}_3^{\text{B}})\text{Fe}]^+$ at a much lower driving force (nearly 100 kcal/mol) than originally reported via combination of a weaker reductant (Cp^*_2Co) and acid ($[\text{Ph}_2\text{NH}_2][\text{OTf}]$ or $[\text{Ph}_3\text{NH}][\text{OTf}]$). Significantly improved efficiency for NH_3 formation is observed (up to 72% at standard substrate loading), and by reloading additional substrate at low temperature a turnover number that is unusually high for a synthetic molecular catalyst (84 ± 8 equiv NH_3 per Fe) has been achieved. Freeze-quench Mössbauer spectroscopy under turnover conditions reveals

differences in the speciation of $(P_3^B)Fe$ compared to previous studies with $HBAr^F_4$ and KC_8 , suggesting changes in the rates of key elementary steps. Using DFT calculations we have considered the viability of a decamethylcobaltocene-mediated PCET pathway as an additional contributor to the previously formulated ET-PT and PT-ET pathways. Based on our calculations, we propose that protonated metallocenes should serve as discrete, very reactive PCET reagents in N_2 -to- NH_3 conversion catalysis. Furthermore, we present preliminary experimental data that suggest protonated decamethylcobaltocene can be accessed synthetically and that such a species may be a potent PCET reagent. Indeed, the achievement of high efficiency for N_2 -to- NH_3 conversion by both $(P_3^B)Fe$ and various Mo catalysts that benefit from metallocene reductants raises the intriguing possibility that metallocene-based PCET reactivity is a potentially widespread and overlooked mechanism. Efforts are underway to experimentally probe such pathways.

3.5 References

- (1) Smil, V. MIT Press: Cambridge, MA, 2001.
- (2) van der Ham, C. J. M.; Koper, M. T. M.; Hetterscheid, D. G. H. *Chem. Soc. Rev.* **2014**, *43*, 5183–5191.
- (3) Shaver, M. P.; Fryzuk, M. D. *Adv. Synth. Catal.* **2003**, *345*, 1061–1076.
- (4) MacLeod, K. C.; Holland, P. L. *Nat. Chem.* **2013**, *5*, 559–565.
- (5) Hoffman, B. M.; Lukoyanov, D.; Yang, Z. Y.; Dean, D. R.; Seefeldt, L. C. *Chem. Rev.* **2014**, *114*, 4041–4062.
- (6) Anderson, J. S.; Rittle, J.; Peters, J. C. *Nature* **2013**, *501*, 84–87.
- (7) Creutz, S. E.; Peters, J. C. *J. Am. Chem. Soc.* **2014**, *136*, 1105–1115.

- (8) Ung, G.; Peters, J. C. *Angew. Chem. Int. Ed.* **2015**, *54*, 532–535.
- (9) Kuriyama, S.; Arashiba, K.; Nakajima, K.; Matsuo, Y.; Tanaka, H.; Ishii, K.; Yoshizawa, K.; Nishibayashi, Y. *Nat. Commun.* **2016**, *7*, 12181–12189.
- (10) Yandulov, D. V.; Schrock, R. R. *Science* **2003**, *301*, 76–78.
- (11) Arashiba, K.; Miyake, Y.; Nishibayashi, Y. *Nat. Chem.* **2010**, *3*, 120–125.
- (12) Kuriyama, S.; Arashiba, K.; Nakajima, K.; Tanaka, H.; Kamaru, N.; Yoshizawa, K.; Nishibayashi, Y. *J. Am. Chem. Soc.* **2014**, *136*, 9719–9731.
- (13) Arashiba, K.; Kinoshita, E.; Kuriyama, S.; Eizawa, A.; Nakajima, K.; Tanaka, H.; Yoshizawa, K.; Nishibayashi, Y. *J. Am. Chem. Soc.* **2015**, *137*, 5666–5669.
- (14) Hill, P. J.; Doyle, L. R.; Crawford, A. D.; Myers, W. K.; Ashley, A. E. *J. Am. Chem. Soc.* **2016**, *138*, 13521–13524.
- (15) Warren, J. J.; Tronic, T. A.; Mayer, J. M. *Chem. Rev.* **2010**, *110*, 6961–7001.
- (16) Del Castillo, T. J.; Thompson, N. B.; Peters, J. C. *J. Am. Chem. Soc.* **2016**, *138*, 5341–5350.
- (17) Anderson, J. S. phd, California Institute of Technology, 2014.
- (18) Whited, M. T.; Mankad, N. P.; Lee, Y. H.; Oblad, P. F.; Peters, J. C. *Inorg. Chem.* **2009**, *48*, 2507–2517.
- (19) Del Castillo, T. J.; Thompson, N. B.; Suess, D. L. M.; Ung, G.; Peters, J. C. *Inorg. Chem.* **2015**, *54*, 9256–9262.
- (20) Dilworth, M. J.; Eady, R. R. *Biochem. J.* **1991**, *277*, 465–468.
- (21) Rittle, J.; Peters, J. C. *J. Am. Chem. Soc.* **2016**, *138*, 4243–4248.
- (22) Anderson, J. S.; Cutsail, G. E.; Rittle, J.; Connor, B. A.; Gunderson, W. A.; Zhang, L.; Hoffman, B. M.; Peters, J. C. *J. Am. Chem. Soc.* **2015**, *137*, 7803–7809.

- (23) Gütlich, P.; Bill, E.; Trautwein, A. X. *Mössbauer Spectroscopy and Transition Metal Chemistry: Fundamentals and Applications*; Springer-Verlag: Berlin Heidelberg, 2011.
- (24) Daifuku, S. L.; Kneebone, J. L.; Snyder, B. E. R.; Neidig, M. L. *J. Am. Chem. Soc.* **2015**, *137*, 11432–11444.
- (25) Garrido, G.; Rosés, M.; Ràfols, C.; Bosch, E. *J. Solution Chem.* **2008**, *37*, 689–700.
- (26) Kaljurand, I.; Kütt, A.; Sooväli, L.; Rodima, T.; Mäemets, V.; Leito, I.; Koppel, I. A. *J. Org. Chem.* **2005**, *70*, 1019–1028.
- (27) Hamashima, Y.; Somei, H.; Shimura, Y.; Tamura, T.; Sodeoka, M. *Org. Lett.* **2004**, *6*, 1861–1864.
- (28) Zhao, Y.; Truhlar, D. G. *J. Chem. Phys.* **2006**, *125*, 194101.
- (29) Weigend, F.; Ahlrichs, R. *Phys. Chem. Chem. Phys.* **2005**, *7*, 3297–3305.
- (30) Rittle, J.; Peters, J. C. *J. Am. Chem. Soc.* **2017**, *139*, 3161–3170.
- (31) Koelle, U.; Infelta, P. P.; Graetzel, M. *Inorg. Chem.* **1988**, *27*, 879–883.
- (32) Pitman, C. L.; Finster, O. N. L.; Miller, A. J. M. *Chem. Commun.* **2016**, *52*, 9105–9108.
- (33) Quintana, L. M. A.; Johnson, S. I.; Corona, S. L.; Villatoro, W.; Goddard, W. A.; Takase, M. K.; VanderVelde, D. G.; Winkler, J. R.; Gray, H. B.; Blakemore, J. D. *Proc. Natl. Acad. Sci. U.S.A.* **2016**, *113*, 6409–6414.
- (34) Munisamy, T.; Schrock, R. R. *Dalton Trans.* **2011**, *41*, 130–137.
- (35) Weare, W. W.; Dai, X.; Byrnes, M. J.; Chin, J. M.; Schrock, R. R.; Müller, P. *Proc. Natl. Acad. Sci. U.S.A.* **2006**, *103*, 17099–17106.
- (36) Hu, Y.; Shaw, A. P.; Estes, D. P.; Norton, J. R. *Chem. Rev.* **2016**, *116*, 8427–8462.

- (37) Roth, J. P.; Yoder, J. C.; Won, T.-J.; Mayer, J. M. *Science* **2001**, *294*, 2524–2526.
- (38) Mayer, J. M.; Rhile, I. J. *Biochim. Biophys. Acta-Bioenerg.* **2004**, *1655*, 51–58.
- (39) Hammes-Schiffer, S. *Acc. Chem. Res.* **2001**, *34*, 273–281.
- (40) Studt, F.; Tucek, F. *Angew. Chem. Int. Ed.* **2005**, *44*, 5639–5642.
- (41) Reiher, M.; Le Guennic, B.; Kirchner, B. *Inorg. Chem.* **2005**, *44*, 9640–9642.
- (42) Studt, F.; Tucek, F. *J. Comput. Chem.* **2006**, *27*, 1278–1291.
- (43) Thimm, W.; Gradert, C.; Broda, H.; Wennmohs, F.; Neese, F.; Tucek, F. *Inorg. Chem.* **2015**, *54*, 9248–9255.
- (44) Yandulov, D. V.; Schrock, R. R. *Inorg. Chem.* **2005**, *44*, 1103–1117.
- (45) Pappas, I.; Chirik, P. J. *J. Am. Chem. Soc.* **2016**, *138*, 13379–13389.
- (46) Yan, Y.; Zeitler, E. L.; Gu, J.; Hu, Y.; Bocarsly, A. B. *J. Am. Chem. Soc.* **2013**, *135*, 14020–14023.
- (47) Keith, J. A.; Carter, E. A. *J. Am. Chem. Soc.* **2012**, *134*, 7580–7583.

Chapter 4.

Fe-Mediated Nitrogen Fixation with a Metallocene Mediator:

Exploring pK_a Effects and Demonstrating Electrocatalysis

Adapted from:

Chalkley, M. J.; Del Castillo, T. J.; Matson, B. D.; Peters, J. C.

J. Am. Chem. Soc. **2018**, *140*, 6122–6129.

DOI: 10.1021/jacs.8b02335

4.1 Introduction

There has been substantial recent progress in the development of soluble, well-defined molecular catalysts for N₂-to-NH₃ conversion, commonly referred to as the nitrogen reduction reaction (N₂RR).¹⁻¹⁰ Nevertheless, a significant and unmet challenge is to develop molecular catalysts, and conditions, compatible with electrocatalytic N₂RR. Progress in this area could have both fundamental and practical benefits, including access to informative in situ mechanistic studies via electrochemical techniques, and an electrochemical means to translate solar or otherwise derived chemical currency (H⁺/e⁻) into NH₃. The latter goal, which has been the subject of numerous studies using heterogeneous catalysts, is key to the long-term delivery of new ammonia synthesis technologies for fertilizer and/or fuel.^{11,12}

Many soluble coordination complexes are now known that electrocatalytically mediate the hydrogen evolution reaction (HER),^{13,14} the carbon dioxide reduction reaction (CO₂RR),¹⁵⁻¹⁷ and the oxygen reduction reaction (O₂RR).¹⁸ The study of such systems has matured at a rapid pace in recent years, coinciding with expanded research efforts towards solar-derived fuel systems. In this context, it is noteworthy how little corresponding progress has been made towards the discovery of soluble molecular catalysts that mediate electrocatalytic N₂RR. To our knowledge, only two prior systems address this topic directly.¹⁹⁻²²

More than three decades ago, Pickett and coworkers reported that a Chatt-type tungsten-hydrazido(2-) complex could be electrochemically reduced to release ammonia (and trace hydrazine), along with some amount of a reduced tungsten-dinitrogen product (; the latter species serves as the source of the tungsten-hydrazido(2-) complex (via its protonation by acid)).¹⁹ By cycling through such a process, an electrochemical, but not an

electrocatalytic, synthesis of ammonia was demonstrated. Indeed, efforts to demonstrate electrocatalysis with this and related systems instead led to substoichiometric NH_3 yields.^{20,21}

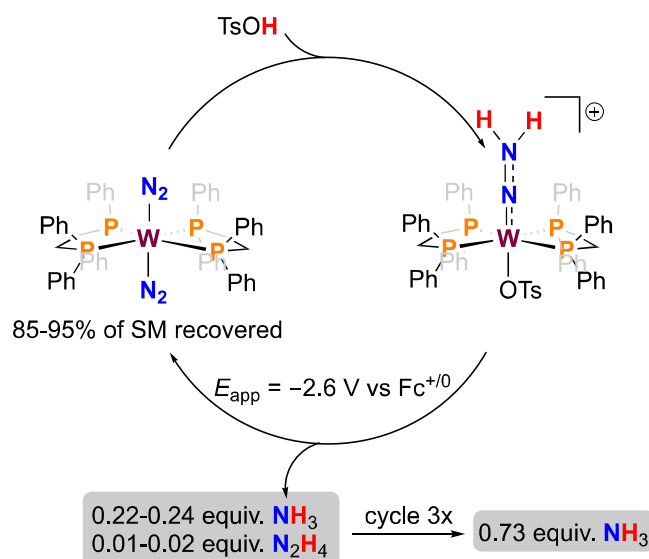


Figure 4.1: Electrocatalytic cycle for the formation of NH_3 from N_2 by a Chatt-type W-phosphine complex.¹⁹

An obvious limitation to progress in electrochemical N_2RR by molecular systems concerns the small number of synthetic N_2RR catalysts that have been available for study; it is only in the past five years that sufficiently robust catalyst systems have been identified to motivate such studies. In addition, the conditions that have to date been employed to mediate N_2RR have typically included non-polar solvents, such as heptane, toluene, and diethyl ether (Et_2O),^{1-8,10} that are not particularly well-suited to electrochemical studies owing to the lack of compatible electrolytes.

Nevertheless, several recent developments, including ones from our lab, point to the likelihood that iron (and perhaps other) molecular coordination complexes may be able to mediate electrocatalytic N_2RR in organic solvent. Specifically, our lab recently reported that a tris(phosphine)borane iron complex, $[(\text{P}_3^{\text{B}})\text{Fe}]^+$, that is competent for catalytic N_2RR with

chemical reductants, can also mediate electrolytic N₂-to-NH₃ conversion,²² with the available data (including that presented in this study) pointing to bona fide electrocatalysis in Et₂O.

Focusing on the [(P₃^B)Fe]⁺ catalytic N₂RR system, a development germane to the present study was its recently discovered catalysis with reagents milder than those that had been originally employed.³ Decamethylcobaltocene (Cp*₂Co) and diphenylammonium acid are effective for N₂RR catalysis; these reagents give rise to fast, and also quite selective (> 70% NH₃), N₂RR catalysis at low temperature and ambient pressure in ethereal solvent. In addition, based on preliminary spectroscopic evidence and density functional theory (DFT) predictions, it appears that a protonated metallocene species, [(Cp*)Co(η⁴-C₅Me₅H)]⁺, may be an important intermediate of N₂RR catalysis under such conditions. Indeed, we have suggested that [(Cp*)Co(η⁴-C₅Me₅H)]⁺ may serve as a proton-coupled-electron-transfer (PCET) donor (BDE_{C-H}(calc) = 31 kcal mol⁻¹), thereby mediating net H-atom transfers to generate N-H bonds during N₂RR.²³ The presence of a metallocene mediator might, we therefore reasoned, enhance N₂RR during electrocatalysis.

We present here a study of the effect of pK_a on the selectivity of [(P₃^B)Fe]⁺ for N₂RR vs HER. By using substituted anilinium acids, we are able to vary the acid pK_a over 9 orders of magnitude and find that the selectivity is highly correlated with the pK_a. In our efforts to investigate the origin of the observed pK_a effect, we found, to our surprise, that in stoichiometric reactions, the catalytically competent anilinium triflate acids are unable to facilitate productive N-H bond formation with early-stage N₂-fixation intermediates. We therefore hypothesize that the formation of a protonated metallocene species, [(Cp*)Co(η⁴-C₅Me₅H)]⁺, plays a critical role in N-H bond-forming reactions, either via PCET, PT, or a

combination of both during N₂RR catalysis. DFT studies support this hypothesis and also establish that the observed p*K*_a correlation with N₂RR selectivity can be explained by the varying ability of the acids to protonate Cp*₂Co. The suggested role of this protonated metallocene intermediate in N–H bond forming reactions led us to test the effect of [Cp*₂Co]⁺ as an additive in the electrolytic synthesis of NH₃ mediated by [(P₃^B)Fe]⁺. We find that the addition of co-catalytic [Cp*₂Co]⁺ enhances the yield of NH₃ without decreasing the Faradaic efficiency (FE), and furnishes what is to our knowledge the first unambiguous demonstration of electrocatalytic N₂RR mediated by a soluble, molecular coordination complex.

4.2 Results and Discussion

4.2.1 Effect of p*K*_a on the Selectivity of N₂ Fixation by [(P₃^B)Fe]⁺

In our recent study on the ability of [(P₃^B)Fe]⁺ to perform N₂RR with Cp*₂Co as the chemical reductant,²³ we found that there was a marked difference in efficiency for NH₃ generation with diphenylammonium triflate ([Ph₂NH₂][OTf]) versus anilinium triflate ([PhNH₃][OTf]). In that study, we posited that this difference could arise from several possibilities, including the differential solubility, sterics, or p*K*_a's of these acids.²³ To investigate the last possibility, we have studied the efficiency of the catalysis by quantifying the NH₃ and H₂ produced when using substituted anilinium acids with different p*K*_a values (**Table 4.1**). The table is organized in increasing acid strength, from [⁴-OMePhNH₃][OTf] as the weakest acid to the perchlorinated derivative ([^{per-Cl}PhNH₃][OTf]) as the strongest. Importantly, good total electron yields (85.8 ± 3.3) were obtained in all cases. As can be seen from the table, the NH₃ efficiencies are found to be strongly correlated with p*K*_a. In some cases, the p*K*_a of a particular anilinium acid was already

known in THF, in which case this value was used. In cases where the pK_a has not been reported in THF a literature procedure was used to appropriately convert the pK_a from the solvent in which it was measured into a value for THF.²⁴

In particular, a comparison of the efficiency for NH_3 with the pK_a of the anilinium acid used gives rise to four distinct activity regimes (**Table 4.1, Figure 4.2**). One regime that is completely inactive for N_2RR , but active for HER, is defined by the weakest acid, [⁴-OMePhNH₃][OTf] ($pK_a = 8.8$). Consistent with this observation is that efforts to use other weak, non anilinium acids such as benzylammonium triflate (pK_a in THF of 13.2) and collidinium triflate (pK_a in THF of 11.2) also led to no observed NH_3 formation. With stronger anilinium acids, a gradual increase in observed NH_3 yields, coupled with a decrease in H_2 yield comprises the second regime ([PhNH₃][OTf], $pK_a = 7.8$; [^{2,6}-MePhNH₃][OTf], $pK_a = 6.8$; [²-ClPhNH₃][OTf], $pK_a = 5.6$). Yet stronger acids, [^{2,5}-ClPhNH₃][OTf] ($pK_a = 4.3$), [^{2,6}-ClPhNH₃][OTf] ($pK_a = 3.4$), and [^{2,4,6}-ClPhNH₃][OTf] ($pK_a = 2.1$), constitute another, most active N_2RR regime, one in which the H_2 yields are nearly invariant. These results are consistent with our previous observation with [Ph₂NH₂][OTf] (pK_a of 3.2 in THF) yielding $72 \pm 3\%$ NH_3 ; H_2 yields were not measured in that study.²³ The highest selectivity for N_2RR ($77.5 \pm 3.8\%$) was observed using [^{2,5}-ClPhNH₃][OTf] as the acid. A final regime of very low N_2RR activity is encountered with [^{per}-ClPhNH₃][OTf] ($pK_a = 1.3$) as the acid. We suspect this last acid undergoes unproductive reduction via ET, thereby short-circuiting N_2RR . The only other N_2RR system for which this type of acid-dependent correlation has been systematically studied is the enzyme MoFe-nitrogenase.²⁵ In some other reports on N_2RR by

molecular catalysts, efficiencies for NH_3 have been reported for several acids, but typically these acids span only a small $\text{p}K_a$ range, electron yields are inconsistent, and variations are not explained.^{2,26} As shown in **Figure 4.2**, the N_2RR vs HER activity of $[(\text{P}_3^{\text{B}})\text{Fe}]^+$ as a function of acid strength, is, in broad terms, similar to the behavior of the enzyme²⁵ across a wide pH range.

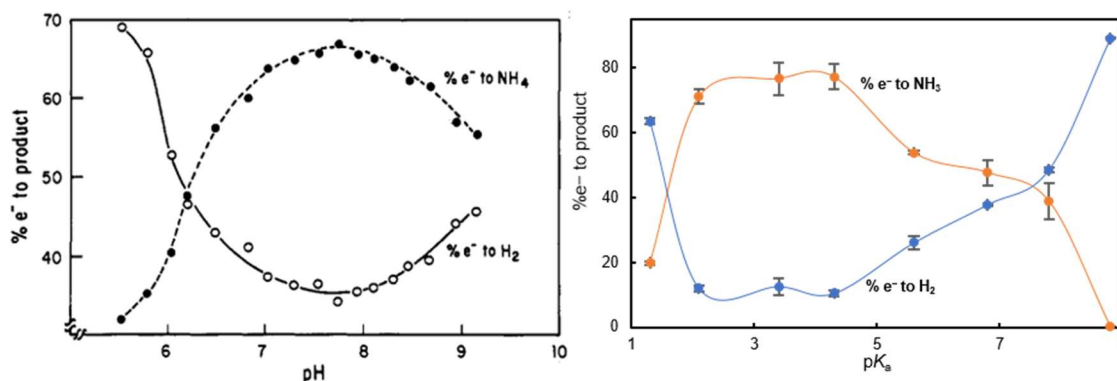


Figure 4.2. Effect of acid strength on the percentage of electrons being used to form NH_3 and H_2 . (left) Selectivity of the FeMo-nitrogenase in *A. vinelandi* at different pH values. Reprinted with permission from Pham, D. N.; Burgess, B. K. *Biochemistry* **1993**, 32, 13725-13731. Copyright 1993 American Chemical Society.²⁵ (right) Selectivity of $[(\text{P}_3^{\text{B}})\text{Fe}]^+$ at different $\text{p}K_a$ values.

Table 4.1. Literature and calculated $\text{p}K_a$ values and efficiencies observed in catalytic N_2 -to- NH_3 conversion

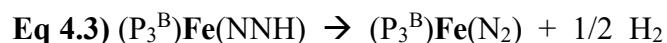
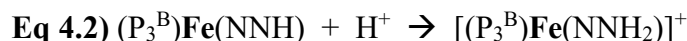
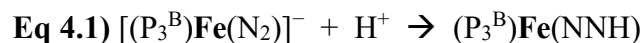
	$\text{p}K_a^{\text{exp}}$ (THF)	$\text{p}K_a^{\text{calc}}$ (298 K) ^a	$\text{p}K_d^{\text{calc}}$ (195 K) ^b	Equiv of NH_3/Fe	% yield of NH_3/e^-	% yield of H_2/e^- ^c	Total Yield/ e^-
$[\text{}^4\text{-OMePhNH}_3]^+$	8.8	9.6	15.7	0.04 ± 0.01	0.2 ± 0.1	89.1 ± 0.2	89.3
$[\text{PhNH}_3]^+$	7.8	7.7	13.8	7.3 ± 0.1	40.4 ± 0.5	48.6 ± 0.7	87.5
$[\text{}^{2,6}\text{-MePhNH}_3]^+$	6.8	7.3	13.2	8.6 ± 0.7	47.5 ± 4.0	37.8 ± 0.2	85.6

$[(\text{Cp}^*)\text{Co}(\text{exo-}\eta^4\text{-C}_5\text{Me}_5\text{H})]^+$	N/A	9.2	11.8	—	—	—	—
$[\text{2-ClPhNH}_3]^+$	5.6	5.6	6.0	10.7 ± 0.1	53.9 ± 0.4	26.1 ± 1.9	80.0
$[\text{2,5-Cl}_2\text{PhNH}_3]^+$	4.3	4.0	5.0	13.9 ± 0.7	77.5 ± 3.8	10.5 ± 1.1	87.7
$[\text{2,6-Cl}_2\text{PhNH}_3]^+$	3.4	3.4	3.4	13.8 ± 0.9	76.7 ± 4.9	12.6 ± 2.5	89.3
$[\text{2,4,6-Cl}_3\text{PhNH}_3]^+$	2.1	2.7	1.8	12.8 ± 0.4	70.9 ± 2.2	12.0 ± 0.8	83.1
$[\text{per-Cl}_5\text{PhNH}_3]^+$	1.3	0.8	0.4	3.6 ± 0.1	19.9 ± 0.5	63.5 ± 1.1	83.5

$[\text{4-OMePhNH}_3]^+$ = 4-methoxyanilinium; $[\text{PhNH}_3]^+$ = anilinium; $[\text{2,6-Me}_2\text{PhNH}_3]^+$ = 2,6-dimethylanilinium; $[\text{2-ClPhNH}_3]^+$ = 2-chloroanilinium; $[\text{2,5-Cl}_2\text{PhNH}_3]^+$ = 2,5-dichloroanilinium; $[\text{2,6-Cl}_2\text{PhNH}_3]^+$ = 2,6-dichloroanilinium; $[\text{2,4,6-Cl}_3\text{PhNH}_3]^+$ = 2,4,6-trichloroanilinium; $[\text{per-Cl}_5\text{PhNH}_3]^+$ = 2,3,4,5,6-pentachloroanilinium. ^aAcidities calculated at 298 K in THF and referenced to the known literature value for $[\text{2,6-Cl}_2\text{PhNH}_3]^+$. ^bAll species calculated as the ion-paired $[\text{OTf}]^-$ species in Et₂O at 195 K and referenced to the known literature value for $[\text{2,6-Cl}_2\text{PhNH}_3][\text{OTf}]$ in THF.

In a previous study of Cp*₂Co-mediated N₂RR by $[(\text{P}_3^{\text{B}})\text{Fe}]^+$,²³ we identified that $[(\text{P}_3^{\text{B}})\text{Fe}(\text{N}_2)]^-$ forms under the catalytic conditions. Earlier studies on the reactivity of $[(\text{P}_3^{\text{B}})\text{Fe}(\text{N}_2)]^-$ with an excess of soluble acids, including HOTf and $[\text{H}(\text{OEt}_2)_2][\text{BAr}^{\text{F}}_4]$ (HBAr^{F}_4 , BAr^{F}_4 = tetrakis(3,5-bis(trifluoromethyl)phenyl)borate), at -78 °C in Et₂O, established rapid formation of the doubly protonated species, $[(\text{P}_3^{\text{B}})\text{Fe}(\text{NNH}_2)]^+$.²⁷ Recent computational work from our group suggests that, under catalytic conditions with a soluble acid, different efficiencies for N₂RR (versus HER) by $(\text{P}_3^{\text{E}})\text{Fe}$ catalysts (E = B, C, Si) are likely correlated to the rate of formation and consumption of early N₂RR intermediates (i.e., $(\text{P}_3^{\text{E}})\text{Fe}(\text{NNH})$ and $[(\text{P}_3^{\text{E}})\text{Fe}(\text{NNH}_2)]^{+/0}$).²⁸ Thus, we were interested in the reactivity of these anilinium triflate acids with $[(\text{P}_3^{\text{B}})\text{Fe}(\text{N}_2)]^-$, reasoning they may show differential efficiency in the formation of $[(\text{P}_3^{\text{B}})\text{Fe}(\text{NNH}_2)]^+$.

To our surprise, a freeze-quench EPR spectrum of the reaction of excess [^{2,6}-^{Cl}PhNH₃][OTf] (high N₂RR efficiency regime) at -78 °C in Et₂O with [(P₃^B)Fe(N₂)]⁻ does not show any [(P₃^B)Fe(NNH₂)]⁺. Freeze-quench Mössbauer analysis shows the formation of the oxidized products (P₃^B)Fe(N₂) and [(P₃^B)Fe]⁺, but nothing assignable to [(P₃^B)Fe(NNH₂)]⁺. Analysis of such a reaction for NH₃ or N₂H₄ after warming to room temperature shows no fixed-N products. The observation of exclusive oxidation, rather than productive N-H bond formation, is analogous to what is observed upon addition of 1 equiv of a soluble acid (HBAr^F₄ or HOTf) to [(P₃^B)Fe(N₂)]⁻. We have previously suggested that if unstable (P₃^B)Fe(NNH) is formed (**Error! Reference source not found.**) without excess acid to trap it as the more stable [(P₃^B)Fe(NNH₂)]⁺ (**Error! Reference source not found.**), then it can decay bimolecularly with the loss of 1/2 H₂ to form (P₃^B)Fe(N₂), a net oxidation (**Error! Reference source not found.**).



The low solubility of the anilinium triflate acids studied herein, under the catalytically relevant conditions (1 mL Et₂O, -78 °C), likely leads to a similar scenario, despite the excess employed; consequently, (P₃^B)Fe(NNH) that is generated is not efficiently captured by acid, leading instead to bimolecular H₂ loss. In accord with this idea, a freeze-quench EPR spectrum of the addition of 50 equiv of [^{2,6}-^{Cl}PhNH₃][BAr^F₄], a far more ether-soluble derivative of the same anilinium, to [(P₃^B)Fe(N₂)]⁻ shows [(P₃^B)Fe(NNH₂)]⁺ formation, and the detection of fixed-N products upon warming (0.20 ± 0.04 equiv NH₃ per Fe).

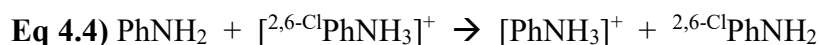
These observations must be reconciled with the seemingly contradictory observation that comparatively efficient N₂RR catalysis is observed when [^{2,6}-C^lPhNH₃][OTf], and other anilinium triflate acids, are employed under catalytic conditions. For example, [Ph₂NH₂][OTf] leads to better efficiency for NH₃ formation versus [Ph₂NH₂][BAr^F₄] (72 ± 3% and 42 ± 6%, respectively). A key difference between the stoichiometric reactions described above, and the catalytic reaction, is the presence of Cp*₂Co in the latter.

We have suggested that Cp*₂Co can be protonated under the catalytic reaction conditions, to form [(Cp*)Co(η⁴-C₅Me₅H)]⁺,²³ which may then play a role in N–H bond forming steps. Recent results on a Cr–N₂ species also support the role of PCET in the formation of early-stage N₂ fixation intermediates in the presence of collidinium triflate and a cobaltocene.²⁹ The results presented here (and below) suggest that such a mechanism is not only plausible, but is likely necessary, to explain the observed catalytic results with anilinium triflate acids. Given the effect of pK_a on the efficiency for N₂RR, we now hypothesize that this effect can arise from the relative energetics and rates of Cp*₂Co protonation by the different anilinium triflate acids.

4.2.2 Computational Studies on Cp*₂Co Protonation and N–H Bond Formation

To investigate the kinetics and thermodynamics of Cp*₂Co protonation by anilinium triflate acids we turned to a computational study. DFT-D₃³⁰ calculations were undertaken at the TPSS/def2-TZVP(Fe); def2-SVP^{31,32} level of theory, as has been previously demonstrated is capable of not only reproducing crystallographic details but also experimentally measured singlet-triplet gaps, reduction potentials, and N–H BDFE's on the (P₃^E)Fe platforms.²⁸ The free energy of H⁺ exchange (ΔG_a) was calculated for all of the

anilinium acids used (representative example shown in **Error! Reference source not found.**), and also for $[(\text{Cp}^*)\text{Co}(\text{exo-}\eta^4\text{-C}_5\text{Me}_5\text{H})]^+$, in Et₂O at 298 K. These free energies were then used to determine the acid pK_a 's, with inclusion of a term to reference them to the literature pK_a value for $[\text{}^{2,6}\text{-ClPhNH}_3][\text{OTf}]$ at 298 K in THF (**Error! Reference source not found.**).



$$\text{Eq 4.5) } pK_a([\text{PhNH}_3^+]) = -\Delta G_a/(2.303 \times RT) + pK_a([\text{}^{2,6}\text{-ClPhNH}_3]^+)$$

Because we presume that variable triflate hydrogen bonding effects (0.5-10 kcal mol⁻¹) are likely to be important under the catalytic conditions (low temperature and low polarity solvent), we additionally calculated the free energy for net HOTf exchange reactions (ΔG_d) at 195 K in Et₂O (representative example shown in **Error! Reference source not found.**). The free energies of these reactions can then be used to determine a pK_d , referenced to the pK_a value for $[\text{}^{2,6}\text{-ClPhNH}_3][\text{OTf}]$ at 298 K in THF, for ease of comparison (**Error! Reference source not found.**). Hereafter, we use these pK_d values for discussion, but we note that use of the pK_a values instead does not substantively alter the conclusions drawn.



$$\text{Eq 4.7) } pK_d([\text{PhNH}_3][\text{OTf}]) = -\Delta G_d/(2.303 \times RT) + pK_a([\text{}^{2,6}\text{-ClPhNH}_3]^+)$$

Calculations of the pK_d of all of the relevant species (Table 4.1) shows that the pK_d of $[(\text{Cp}^*)\text{Co}(\text{exo-}\eta^4\text{-C}_5\text{Me}_5\text{H})][\text{OTf}]$ ($pK_d^{\text{calc}} = 11.8$; Table 4.1) falls within the range of the anilinium acids studied ($0.4 \leq pK_d^{\text{calc}} \leq 15.7$), suggesting there should be a significant acid

dependence on the kinetics and thermodynamics of Cp*₂Co protonation. To better elucidate the differences in Cp*₂Co protonation between the acids studied, we investigated the kinetics of protonation for three acids, [2,6-ClPhNH₃][OTf] (high selectivity; pK_d^{calc} = 3.4), [2,6-MePhNH₃][OTf] (modest selectivity; pK_d^{calc} = 13.2), and [4-OMePhNH₃][OTf] (poor selectivity; pK_d^{calc} = 15.8).

Transition states for Cp*₂Co protonation were located for all three acids. To confirm that these transition states accurately reflect proton transfer, internal reaction coordinates (IRC) were followed to determine the reactant (IRC-A) and product (IRC-B) minima (Figure 4.3). These minima represent hydrogen bonded arrangements of the reactants and products. Protonation is found to have only a moderate barrier (ΔG^\ddagger in kcal mol⁻¹) in all three cases: ([4-OMePhNH₃][OTf], +4.5; [2,6-MePhNH₃][OTf], +3.8; [2,6-ClPhNH₃][OTf], +1.3). This suggests that Cp*₂Co protonation is kinetically accessible in all cases, in agreement with the experimental observation of background HER with each of these acids.

The small differences in rate, and the large variance in the equilibrium constant K_{eq} defined in Eq 4.8, points to a significant difference in the population of protonated metallocene, [(Cp*)Co(*exo*- η^4 -C₅Me₅H)][OTf], for these anilinium acids during catalysis.

$$\text{Eq 4.8 } K_{eq} = \frac{([\text{RPhNH}_2\text{-(Cp}^*\text{)Co}(\textit{exo}\text{-}\eta^4\text{-C}_5\text{Me}_5\text{H})][\text{OTf}]])}{([\text{RPhNH}_3\text{-Cp}^*\text{}_2\text{Co}][\text{OTf}]])}$$

We reason that the low solubility of the anilinium triflate acids, and the low catalyst concentration (2.3 mM (P₃^B)Fe), leads to a scenario in which the interaction between the acid and the Cp*₂Co, the latter being present in excess relative to the iron catalyst (measured solubility of Cp*₂Co at -78 °C in Et₂O is ~ 6 mM), significantly affects the overall kinetics

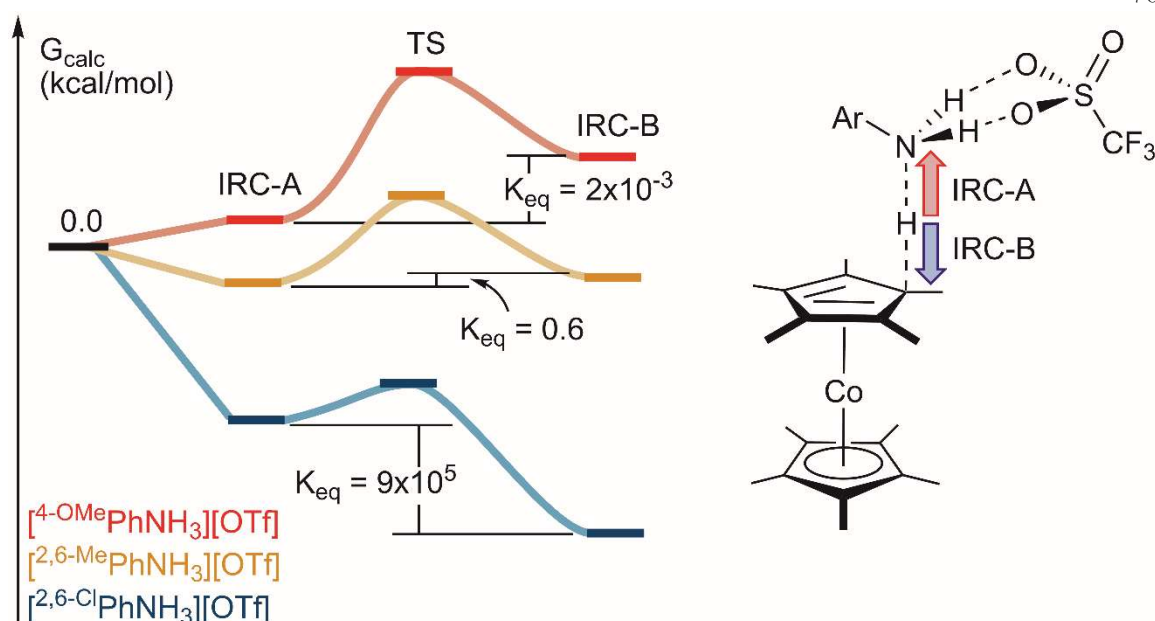


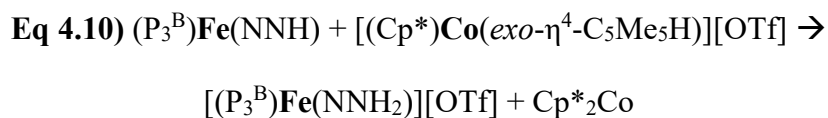
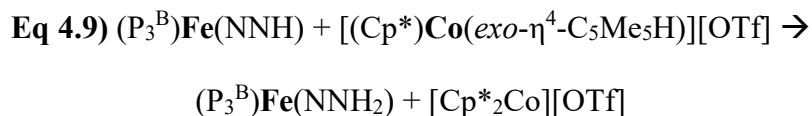
Figure 4.3: The kinetics and thermodynamics of protonation of Cp^*Co for three acids from different catalytic efficiency regimes ($[\text{4-OMePhNH}_3][\text{OTf}]$ = poor selectivity); $[\text{2,6-MePhNH}_3][\text{OTf}]$ = modest selectivity; $[\text{2,6-ClPhNH}_3][\text{OTf}]$ = high selectivity).

of productive N–H bond formation. As such, the difference in $[(\text{Cp}^*)\text{Co}(\text{exo-}\eta^4\text{-C}_5\text{Me}_5\text{H})][\text{OTf}]$ concentration and formation rate should relate to, and likely dominate, the origin of the observed $\text{p}K_{\text{a}}$ effect. This explanation, rather than one that involves differences in rates for the direct interaction of a given $(\text{P}_3^{\text{B}})\text{Fe}(\text{N}_x\text{H}_y)$ species with an anilinium acid, better captures the collected data available.

$[(\text{Cp}^*)\text{Co}(\text{exo-}\eta^4\text{-C}_5\text{Me}_5\text{H})][\text{OTf}]$, characterized by a very weak C–H bond, should be a strong PCET donor, and we presume it serves such a role under the catalytic conditions being discussed herein. Its reactions with $(\text{P}_3^{\text{B}})\text{Fe}(\text{N}_x\text{H}_y)$ intermediates may occur in a synchronous fashion, akin to HAT, as DFT calculations suggest that in almost all cases the $(\text{P}_3^{\text{B}})\text{Fe}(\text{N}_x\text{H}_y)$ intermediates have stronger N–H bonds than the C–H bond in $[(\text{Cp}^*)\text{Co}(\text{exo-}\eta^4\text{-C}_5\text{Me}_5\text{H})]^+$. Asynchronous reactions more akin to a PT-ET reaction are likely also possible because in cases where the basicity of $(\text{P}_3^{\text{B}})\text{Fe}(\text{N}_x\text{H}_y)$ has been evaluated, they are

predicted to be readily protonated by $[(\text{Cp}^*)\text{Co}(\text{exo-}\eta^4\text{-C}_5\text{Me}_5\text{H})]^+$. The reactivity of ring-functionalized Cp* rings has been discussed previously in the context of electrocatalytic HER by 4d and 5d metals but via a mechanism of hydride transfer rather than PCET.^{33–35} So while multiple N–H bond forming mechanisms must be considered, the evidence suggests that a PCET reaction with $[(\text{Cp}^*)\text{Co}(\text{exo-}\eta^4\text{-C}_5\text{Me}_5\text{H})][\text{OTf}]$, plays a critical role in productively trapping the highly reactive first fixed intermediate, $(\text{P}_3^{\text{B}})\text{Fe}(\text{NNH})$ (Figure 4.4), before it can bimolecularly release H_2 (Eq 4.9). Productive N–H bond formation via PCET with models of late-stage N_2 fixation intermediates (*i.e.*, $\text{M}\equiv\text{N}$ or $\text{M}-\text{NH}_2$) has been observed previously,^{36–39} but examples with early-stage N_2 fixation intermediates are lacking, so we investigated this reaction in more detail via DFT.

Both a synchronous PCET ($\Delta G_{\text{PCET}} = -17.3 \text{ kcal mol}^{-1}$; Eq 4.9) and a fully asynchronous net-PCET path ($\Delta G_{\text{PT}} = -5.7 \text{ kcal mol}^{-1}$, $\Delta G_{\text{ET}} = -11.6 \text{ kcal mol}^{-1}$; Eq 4.10 and Eq 4.11), are predicted to be thermodynamically favorable.



To evaluate the kinetics of these reactions the Marcus theory expressions⁴⁰ and the Hammes-Schiffer method⁴¹ were used to approximate relative rates of bimolecular ET and

PCET. We find that there is a slight kinetic preference for the fully synchronous PCET reaction ($k_{\text{rel}}^{\text{PCET}} \sim 3 \times 10^3 \text{ M}^{-1} \text{ s}^{-1}$) compared to the fully asynchronous PT-ET reaction ($k_{\text{rel}}^{\text{PT-ET}} \approx k_{\text{rel}}^{\text{ET}} \equiv 1 \text{ M}^{-1} \text{ s}^{-1}$; **Figure 4.4**) assuming in that case that ET is rate limiting based on lower reorganization energies and barriers for PT than ET.

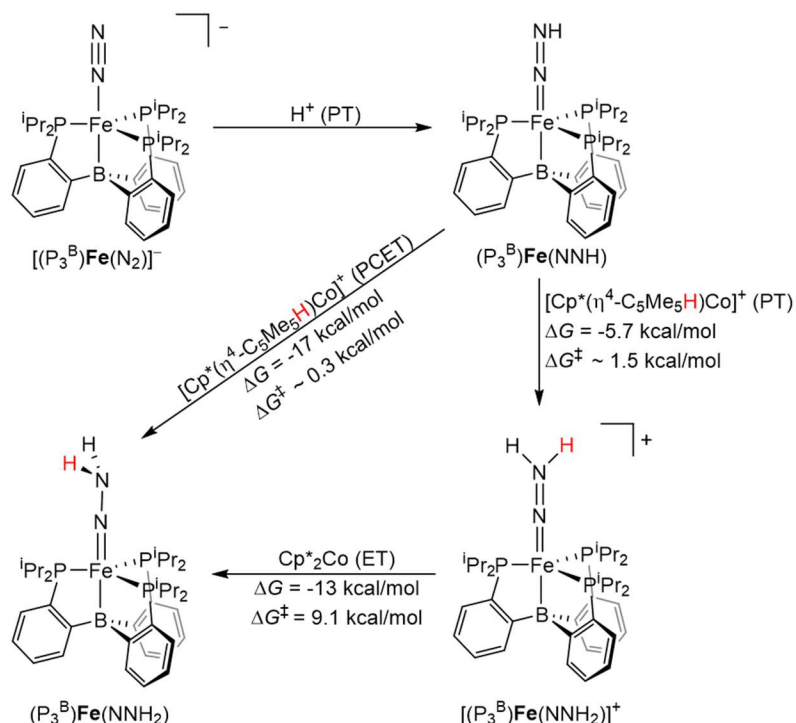


Figure 4.4: The calculated thermodynamics and kinetics of synchronous PCET and fully asynchronous PCET (PT-ET), between $(P_3^B)Fe(NNH)$ and $[(Cp^*)Co(\textit{exo}-\eta^4-C_5Me_5H)] [OTf]$ to generate $(P_3^B)Fe(NNH_2)$.

The above discussion leads to the conclusion that the efficiency for NH_3 formation in this system is coupled to the kinetics and/or thermodynamics of the reaction between the anilinium triflate acid and the Cp^*_2Co reductant. This conclusion is counterintuitive, as the protonation of Cp^*_2Co is also the requisite first step for background HER.⁴² The fact that a key HER intermediate can be intercepted and used for productive N_2RR steps is an important

design principle for such catalysis. Similar design strategies are currently being used to repurpose molecular cobalt HER catalysts for the reduction of unsaturated substrates.⁴³

Efforts are often undertaken to suppress background reactivity between acid and reductant in catalytic N₂RR systems.^{1,2} We were hence particularly interested to explore whether the inclusion of a metallocene co-catalyst, in this case Cp*₂Co, might improve the yield, and/or the Faradaic efficiency (FE), for N₂RR versus HER, in controlled potential electrolysis (CPE) experiments with [(P₃^B)Fe]⁺ under N₂.

4.2.3 Electrocatalytic N₂ Fixation with [(P₃^B)Fe]⁺

To set the context for this section of the present study, we had shown previously that ~ 2.2 equiv NH₃ per Fe could be generated via controlled potential electrolysis (CPE; -2.3 V vs Fc⁺⁰) at a reticulated vitreous carbon working electrode, using [(P₃^B)Fe]⁺ as the (pre)catalyst in the presence of HBAr^F₄ (50 equiv) at -45 °C under an atmosphere of N₂. This yield of NH₃ corresponded to a ~ 25% FE²² which, while modest in terms of overall chemoselectivity, compares very favorably to FE's most typically reported for heterogeneous electrocatalysts for N₂RR that operate below 100 °C (< 2%), although some recently reported studies have reported heterogeneous systems with significantly improved yields (> 10% FE).^{11,12}

To further explore the possibility of using [(P₃^B)Fe]⁺ as an electrocatalyst for N₂RR, various conditions were surveyed to determine whether enhanced yields of NH₃ could be obtained from CPE experiments. For example, various applied potentials were studied (ranging from -2.1 to -3.0 V vs Fc⁺⁰), the concentrations of [(P₃^B)Fe]⁺ and HBAr^F₄ were varied, the ratio of acid to catalyst was varied, and the rate at which acid was delivered to the system was varied (*e.g.*, initial full loadings, batch-wise additions, reloadings, or continuous

slow additions). None of these studies led to substantial improvement in N₂RR; in all cases, < 2.5 equiv of NH₃ was obtained per Fe. Attempts to vary the ratio of the electrode surface area to the working compartment solution volume, either by employing smaller cell geometries or by using different morphologies of glassy carbon as the working electrode (*e.g.*, reticulated porous materials of different pore density or plates of different dimensions), also failed to provide substantial improvement in NH₃ yield. The replacement of HBAr^F₄, the original acid used in our electrolysis studies,²² by 50 equiv of [Ph₂NH₂][OTf] led to similar yields of NH₃ (Table 4.2, entry 1).

We next investigated the effect of [Cp*₂Co]⁺ as an additive on the electrolysis/electrocatalysis. Traces of relevant cyclic voltammograms (Figure 4.5) collected with glassy carbon as the working electrode in Et₂O under glovebox atmosphere N₂ at -35 °C are provided. Background traces including only [Ph₂NH₂][OTf] are present in both panels (gray traces, Figure 4.5). [Cp*₂Co]⁺ (yellow trace, Figure 4.5A), [Cp*₂Co]⁺ with the addition of ten equiv of [Ph₂NH₂][OTf] (green trace, Figure 4.5A), [(P₃^B)Fe]⁺ (dark blue trace, Figure 4.5B), [(P₃^B)Fe]⁺ with the addition of ten equiv of [Ph₂NH₂][OTf] (light blue trace, Figure 4.5B), and [(P₃^B)Fe]⁺ with the addition of one equiv of [Cp*₂Co]⁺ and ten equiv of [Ph₂NH₂][OTf] (red traces, Figure 4.5).

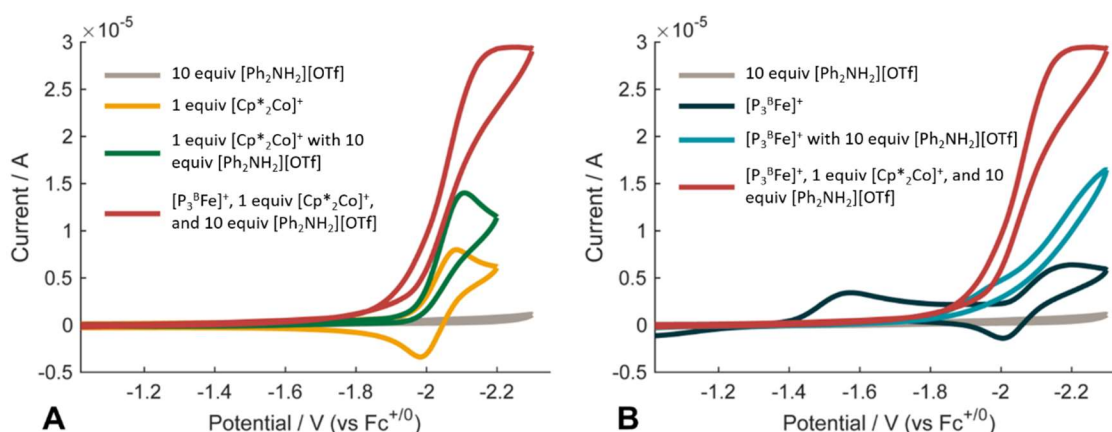
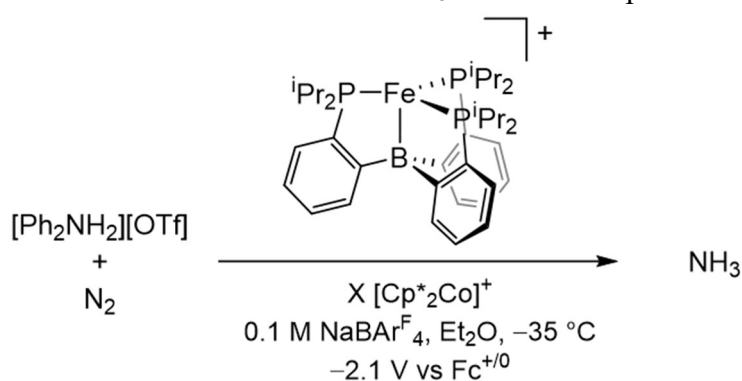


Figure 4.5: Cyclic voltammograms of relevance to electrocatalytic N_2 fixation in the with co-catalytic $[(\text{P}_3^{\text{B}})\text{Fe}]^+$ and $[\text{Cp}^*_2\text{Co}]^+$. **A)** 10 equiv $[\text{Ph}_2\text{NH}_2][\text{OTf}]$ (gray trace), 1 equiv $[\text{Cp}^*_2\text{Co}][\text{BAR}^{\text{F}_4}]$ ($[\text{Cp}^*_2\text{Co}]^+$) (yellow trace), 1 equiv $[\text{Cp}^*_2\text{Co}]^+$ with 10 equiv $[\text{Ph}_2\text{NH}_2][\text{OTf}]$ (green trace), and $[(\text{P}_3^{\text{B}})\text{Fe}]^+$ with 1 equiv of $[\text{Cp}^*_2\text{Co}]^+$ and 10 equiv $[\text{Ph}_2\text{NH}_2][\text{OTf}]$ (red trace). **B)** 10 equiv $[\text{Ph}_2\text{NH}_2][\text{OTf}]$ (gray trace), $[(\text{P}_3^{\text{B}})\text{Fe}]^+$ (dark blue trace), $[(\text{P}_3^{\text{B}})\text{Fe}]^+$ with 10 equiv $[\text{Ph}_2\text{NH}_2][\text{OTf}]$ (light blue trace), and $[(\text{P}_3^{\text{B}})\text{Fe}]^+$ with 1 equiv of $[\text{Cp}^*_2\text{Co}]^+$ and 10 equiv $[\text{Ph}_2\text{NH}_2][\text{OTf}]$ (red trace). All voltammograms are collected in 0.1 M $\text{NaBAR}^{\text{F}_4}$ solution in Et_2O at -35°C using a glassy carbon working electrode, and externally referenced to the $\text{Fc}^{+/0}$ couple. Scan rate is 100 mV/s.

The cyclic voltammogram of $[\text{Cp}^*_2\text{Co}]^+$ is shown in **Figure 4.5A** (yellow trace), displaying the reversible $[\text{Cp}^*_2\text{Co}]^{+/0}$ couple at -2.0 V. The addition of $[\text{Ph}_2\text{NH}_2][\text{OTf}]$ to $[\text{Cp}^*_2\text{Co}]^+$ causes an increase in current at this potential, consistent with HER catalyzed by $[\text{Cp}^*_2\text{Co}]^+$ (green trace, **Figure 4.5A**). **Figure 4.5B** provides the cyclic voltammogram of $[(\text{P}_3^{\text{B}})\text{Fe}]^+$ in the absence (dark blue trace, showing previously assigned and quasi-reversible $[(\text{P}_3^{\text{B}})\text{Fe}(\text{N}_2)]^{0/-}$ couple at ~ -2.1 V) and in the presence (light blue trace) of $[\text{Ph}_2\text{NH}_2][\text{OTf}]$.⁴⁴ The latter is indicative of modest HER and N_2RR . Also evident upon the addition of acid is the disappearance of a wave corresponding to the $[(\text{P}_3^{\text{B}})\text{Fe}]^{+/0}$ couple at ~ -1.6 V. This wave, in the absence of acid, is broad and shows a large peak-to-peak separation, likely due to the presence of both $[(\text{P}_3^{\text{B}})\text{Fe}]^+$ and $[(\text{P}_3^{\text{B}})\text{Fe}(\text{N}_2)]^+$ in solution at -35°C . The addition of a large excess of $[\text{Ph}_2\text{NH}_2][\text{OTf}]$ presumably results in triflate binding (to

generate $(P_3^B)Fe(OTf)$, thereby attenuating the waves associated with the reduction of $[(P_3^B)Fe]^+$ and $[(P_3^B)Fe(N_2)]^+$. The red trace of **Figure 4.5A** is reproduced in **Figure 4.5B** to illustrate the marked increase in current observed when Cp^*_2Co is added.

Table 4.2. Yields and Faradaic Efficiencies of NH_3 from CPE Experiments with $[(P_3^B)Fe]^+$



Entry	Equiv $[Cp^*_2Co]^+$	Equiv NH_3 (per Fe)	Equiv NH_3 (per Co)	NH_3 FE (%)
1	0	2.6 ± 0.3^d	—	24 ± 5
2 ^a	0	2.6 ± 0.6	—	18 ± 1
3		4.0 ± 0.6	4.0 ± 0.6	28 ± 5
4	5	4.0 ± 0.6^d	0.8 ± 0.1	25 ± 3
5 ^a	5	5.5 ± 0.9^e	1.1 ± 0.2	19 ± 1
6	10	4 ± 1	0.4 ± 0.1	24 ± 7
7 ^b	5	1.9 ± 0.2	0.4 ± 0.1	10 ± 1
8 ^c	5	0.9 ± 0.4	0.2 ± 0.1	6 ± 3

All CPE experiments conducted at $-2.1 V$ vs $Fc^{+/0}$ with $0.1 M NaBAR^F_4$ in Et_2O as solvent at $-35\ ^\circ C$ under an N_2 atmosphere, featuring a glassy carbon plate working electrode, $Ag^{+/0}$ reference couple isolated by a CoralPorTM frit referenced externally to $Fc^{+/0}$, and a solid sodium auxiliary electrode. Working and auxiliary chambers separated by a sintered glass frit. Averages represent two runs unless noted. ^aAfter initial electrolysis with 50 equiv $[Ph_2NH_2][OTf]$, an additional 50 equiv $[Ph_2NH_2][OTf]$ in $0.1 M NaBAR^F_4 Et_2O$ solution was

added to the working chamber, via syringe through a rubber septum, followed by additional CPE at -2.1 V vs $\text{Fc}^{+/0}$. The listed Equiv NH_3 (per Fe or Co) for these runs is the total yield from both electrolysis experiments. ^b $[\text{PhNH}_3][\text{OTf}]$ employed as the acid. ^c $[\text{PhNH}_3][\text{OTf}]$ employed as the acid. ^dAverage of three runs. ^eAverage of five runs.

CPE studies were undertaken to characterize the reduction products associated with the red trace at ~ -2.1 V vs $\text{Fc}^{+/0}$. These studies employed a glassy carbon plate electrode, a $\text{Ag}^{+/0}$ reference electrode that was isolated by a CoralPorTM frit and referenced externally $\text{Fc}^{+/0}$ redox couple, and a solid sodium auxiliary electrode. The latter was used to avoid excessive, non-productive redox cycling between the working and auxiliary chambers. Unless otherwise noted, CPE experiments were performed at -2.1 V versus $\text{Fc}^{+/0}$, with 0.1 M NaBARF_4 as the ether-soluble electrolyte, under a glovebox N_2 atmosphere at -35 °C. The electrolysis was continued until the current had dropped to 1% of the initial current measured, or until 21.5 hours had passed.

CPE experiments were conducted with the inclusion of 0, 1, 5, and 10 equiv of $[\text{Cp}^*\text{Co}]^+$ with respect to $[(\text{P}_3^{\text{B}})\text{Fe}]^+$, using excess $[\text{Ph}_2\text{NH}_2][\text{OTf}]$ as the acid. In the absence of added $[\text{Cp}^*\text{Co}]^+$, a significant amount of NH_3 was generated (2.6 ± 0.3 equiv per Fe, **Table 4.2**, entry 1), consistent with the previous finding that, in the presence of a strong acid, $[(\text{P}_3^{\text{B}})\text{Fe}]^+$ can electrolytically mediate N_2 -to- NH_3 conversion.²² Notably, when a CPE experiment that did not include $[\text{Cp}^*\text{Co}]^+$ was reloaded with additional acid after electrolysis and electrolyzed again, the total yield of NH_3 (2.6 ± 0.6 equiv NH_3 per Fe, **Table 4.2**, entry 2) did not improve.

We found that inclusion of 1.0 equiv of $[\text{Cp}^*\text{Co}]^+$ enhanced the NH_3 yield, by a factor of ~ 1.5 (**Table 4.2**, entry 3) without decreasing the FE. The data provide a total yield,

with respect to both Fe and Co, that confirms modest but unequivocal N_2RR electrocatalysis. In single run experiments, the highest NH_3 yield in the absence of $[Cp^*_2Co]^+$ was 2.8 equiv, compared with 4.4 equiv in the presence of 1 equiv of $[Cp^*_2Co]^+$. Conversely, the lowest single run NH_3 yield in the absence of $[Cp^*_2Co]^+$ was 2.3 equiv, compared with 3.5 equiv in the presence of 1 equiv of $[Cp^*_2Co]^+$.

Increasing the amount of added $[Cp^*_2Co]^+$ did not affect the NH_3 yield (Table 4.2, entry 4). However, the addition of a second loading of $[Ph_2NH_2][OTf]$ following the first electrolysis (Table 4.2, entry 5), followed by additional electrolysis, led to an improved yield of NH_3 , suggesting that some active catalyst is still present after the first run.^{22,23} Even higher $[Cp^*_2Co]^+$ loading did not lead to higher NH_3 yields (Table 4.2, entry 6).

CPE of $[(P_3^B)Fe]^+$ in the presence of $[Cp^*_2Co]^+$ was also explored with other acids. Replacing $[Ph_2NH_2][OTf]$ in these experiments with $[^{2,6-Cl}PhNH_3][OTf]$ led to lower yields of NH_3 , and with $[PhNH_3][OTf]$ even lower yields of NH_3 were observed (Table 4.2, entries 7 and 8 respectively). The lower, but nonzero, yield of NH_3 provided by $[PhNH_3][OTf]$ in these CPE experiments is consistent with chemical trials employing various acids (*vide supra*) and can be rationalized by the relative pK_a of the acids (Table 4.1). The intermediate yield of NH_3 provided by $[^{2,6-Cl}PhNH_3][OTf]$ in these CPE experiments is less consistent with simple pK_a considerations, suggesting that additional factors are at play, perhaps including the relative stability of the acid or conjugate base to electrolysis.

To probe whether electrode-immobilized iron might contribute to the N_2RR electrocatalysis, X-ray photoelectron spectroscopy (XPS) was used to study the electrode. After a standard CPE experiment with $[(P_3^B)Fe]^+$, 5 equiv of $[Cp^*_2Co]^+$, and 50 equiv

[Ph₂NH₂][OTf], the electrode was removed, washed with fresh 0.1 M NaBAr^F₄ Et₂O solution, then fresh Et₂O, and probed by XPS. A *very low* coverage of Fe (< 0.3 atom % Fe) was detected in the post-electrolysis material; no Fe was detected on a segment of the electrode which was not exposed to the electrolytic solution. This observation implies a detectable but likely small degree of degradation of [(P₃^B)Fe]⁺ over the course of a 15 hour CPE experiment. Worth noting is that no Co was detected on the post-electrolysis electrode. This may be consistent with the known stability of metallocenes and the recently discovered stability of protonated-Cp* ligands on Rh.⁴⁵

To test whether the small amount of deposited Fe material might be catalytically active for N₂RR, following a standard CPE experiment the electrode was removed from the cold electrolysis solution, washed with fresh 0.1 M NaBAr^F₄ Et₂O at -35 °C (the electrode itself was maintained at -35 °C at all times), and then used for an additional CPE experiment, under identical conditions except that [(P₃^B)Fe]⁺ was excluded. This CPE experiment yielded no detectable NH₃. The charge passed, and H₂ yield, were very similar to a “no [(P₃^B)Fe]⁺” control experiment conducted with a freshly cleaned electrode. Accordingly, a CPE experiment in the absence of [(P₃^B)Fe]⁺ demonstrated that [Cp*₂Co]⁺ serves as an effective electrocatalyst for HER with [Ph₂NH₂][OTf] as the acid source, but does not catalyze the N₂RR reaction (0% FE for NH₃, 75% FE for H₂). This background HER, and the observed catalytic response to the addition of [Ph₂NH₂][OTf] at the [Cp*₂Co]⁺⁰ couple, provides circumstantial evidence for the formation of a protonated decamethylcobaltocene intermediate, [(Cp*)Co(η⁴-C₅Me₅H)]⁺, on a timescale similar to that of the N₂RR mediated by [(P₃^B)Fe]⁺.

To probe whether the sodium auxiliary electrode used in the CPE experiments might play a non-innocent role as a chemical reductant, a standard CPE experiment with $[(P_3^B)Fe]^+$, 5 equiv $[Cp^*_2Co]^+$, and 50 equiv $[Ph_2NH_2][OTf]$ was assembled, but was left to stir at $-35\text{ }^\circ\text{C}$ for 43 hours without an applied potential bias. This experiment yielded 0.3 equiv NH_3 (relative to Fe), suggesting that background N_2RR due to the sodium auxiliary electrode is very minor.

To ensure the NH_3 produced was derived from the N_2 atmosphere during these electrolysis experiments, as opposed to degradation of the anilinium acid used, a standard CPE experiment using $[(P_3^B)Fe]^+$, 5 equiv $[Cp^*_2Co]^+$, and 50 equiv of $[Ph_2^{15}NH_2][OTf]$ was performed. Only $^{14}NH_3$ product was detected.

We also sought to compare the chemical N_2RR catalysis efficiency of the $[(P_3^B)Fe]^+$ catalyst under conditions similar to those used for electrocatalysis. Hence, chemical catalysis with $[(P_3^B)Fe]^+$, employing Cp^*_2Co as a reductant and $[Ph_2NH_2][OTf]$ as the acid at $-35\text{ }^\circ\text{C}$ instead of the more typical temperature of $-78\text{ }^\circ\text{C}$, in a $0.1\text{ M NaBAR}^F_4\text{ Et}_2\text{O}$ solution, afforded lower yields of NH_3 (1.8 ± 0.7 equiv of NH_3 per Fe) than the yields observed via electrolysis with $[Cp^*_2Co]^+$ as an additive. The lower yields of NH_3 in these chemical trials, compared with our previously reported conditions (12.8 ± 0.5 equiv of NH_3 per Fe at $-78\text{ }^\circ\text{C}$),²³ may be attributable to increased competitive HER resulting from a more solubilizing medium ($0.1\text{ M NaBAR}^F_4\text{ Et}_2\text{O}$ vs pure Et_2O) and a higher temperature ($-35\text{ }^\circ\text{C}$ vs $-78\text{ }^\circ\text{C}$).²³ These results suggest that an electrochemical approach to NH_3 formation can improve performance, based on selectivity for N_2RR , of a molecular catalyst under comparable conditions.

4.3 Conclusion

Herein we described the first systematic pK_a studies on a synthetic nitrogen fixation catalyst and find a strong correlation between pK_a and N_2RR vs HER efficiency. Chemical studies reveal that, on their own, the anilinium triflate acids employed in the catalysis are unable to generate the N–H bonds of early-stage N_2RR intermediates such as $[(P_3^B)Fe(NNH_2)]^+$. We propose that the insolubility of these triflate acids prevents the sufficiently rapid proton transfer necessary to capture the critical but unstable first fixed intermediate, $(P_3^B)Fe(NNH)$. Under catalytic conditions, we believe that the presence of the metallocene reductant (Cp^*_2Co) is essential, as this species can be protonated in situ to form $[(Cp^*)Co(exo-\eta^4-C_5Me_5H)]^+$, which in turn is effective in N–H bond formation with early intermediates. This leads to the intriguing conclusion that an intermediate of the background HER pathway is redirected for productive N_2RR chemistry during catalysis.

DFT studies illustrate that the pK_a effect on the N_2RR efficiency may be explained by the variation in the kinetics and thermodynamics of Cp^*_2Co protonation by the different acids. Investigation of the reactivity of $[(Cp^*)Co(exo-\eta^4-C_5Me_5H)]^+$ with the $(P_3^B)Fe(NNH)$ intermediate revealed that PCET reactivity, both synchronous or fully asynchronous, is favorable and may proceed with only a small barrier, suggesting that $(P_3^B)Fe(NNH)$ can be rapidly trapped by $[(Cp^*)Co(exo-\eta^4-C_5Me_5H)]^+$. We suspect $[(Cp^*)Co(exo-\eta^4-C_5Me_5H)]^+$ is likely involved in a variety of N–H bond forming reactions during the overall catalysis, including reactions with late-stage nitrogen fixation intermediates.

Despite the fact that $[Cp^*_2Co]^+$ itself catalyzes HER under the conditions employed for electrocatalytic N_2RR , we found that its inclusion in CPE experiments containing $[(P_3^B)Fe]^+$ and acid under an N_2 atmosphere led to modest improvements in the overall

catalytic yield of NH₃. This system represents the first unambiguous example of electrocatalytic N₂RR mediated by a soluble, molecular coordination complex.

4.4 References

- (1) Yandulov, D. V.; Schrock, R. R. *Science* **2003**, *301*, 76–78.
- (2) Arashiba, K.; Miyake, Y.; Nishibayashi, Y. *Nat. Chem.* **2010**, *3*, 120–125.
- (3) Anderson, J. S.; Rittle, J.; Peters, J. C. *Nature* **2013**, *501*, 84–87.
- (4) Ung, G.; Peters, J. C. *Angew. Chem. Int. Ed.* **2015**, *54*, 532–535.
- (5) Kuriyama, S.; Arashiba, K.; Nakajima, K.; Matsuo, Y.; Tanaka, H.; Ishii, K.; Yoshizawa, K.; Nishibayashi, Y. *Nat. Commun.* **2016**, *7*, 12181–12189.
- (6) Kuriyama, S.; Arashiba, K.; Tanaka, H.; Matsuo, Y.; Nakajima, K.; Yoshizawa, K.; Nishibayashi, Y. *Angew. Chem. Int. Ed.* **2016**, *55*, 14291–14295.
- (7) Hill, P. J.; Doyle, L. R.; Crawford, A. D.; Myers, W. K.; Ashley, A. E. *J. Am. Chem. Soc.* **2016**, *138*, 13521–13524.
- (8) Buscagan, T. M.; Oyala, P. H.; Peters, J. C. *Angew. Chem. Int. Ed.* **2017**, *56*, 6921–6926.
- (9) Wickramasinghe, L. A.; Ogawa, T.; Schrock, R. R.; Müller, P. *J. Am. Chem. Soc.* **2017**, *139*, 9132–9135.
- (10) Fajardo Jr., J.; Peters, J. C. *J. Am. Chem. Soc.* **2017**, *139*, 16105–16108.
- (11) Shipman, M. A.; Symes, M. D. *Catal. Today* **2017**, *286*, 57–68.
- (12) Kyriakou, V.; Garagounis, I.; Vasileiou, E.; Vourros, A.; Stoukides, M. *Catal. Today* **2017**, *286*, 2–13.
- (13) McKone, J. R.; Marinescu, S. C.; Brunschwig, B. S.; Winkler, J. R.; Gray, H. B. *Chem. Sci.* **2014**, *5*, 865–878.

- (14) Bullock, R. M.; Appel, A. M.; Helm, M. L. *Chem. Commun.* **2014**, *50*, 3125–3143.
- (15) Benson, E. E.; Kubiak, C. P.; Sathrum, A. J.; Smieja, J. M. *Chem. Soc. Rev.* **2008**, *38*, 89–99.
- (16) Appel, A. M.; Bercaw, J. E.; Bocarsly, A. B.; Dobbek, H.; DuBois, D. L.; Dupuis, M.; Ferry, J. G.; Fujita, E.; Hille, R.; Kenis, P. J. A.; et al. *Chem. Rev.* **2013**, *113*, 6621–6658.
- (17) Francke, R.; Schille, B.; Roemelt, M. *Chem. Rev.* **2018**, *118*, 4631–4701.
- (18) Zhang, W.; Lai, W.; Cao, R. *Chem. Rev.* **2017**, *117*, 3717–3797.
- (19) Pickett, C. J.; Talarmin, J. *Nature* **1985**, *317*, 652–653.
- (20) Pickett, C. J.; Ryder, K. S.; Talarmin, J. *J. Chem. Soc., Dalton Trans.* **1986**, *7*, 1453–1457.
- (21) Becker, J. Y.; Avraham, S. *J. Electroanal. Chem.* **1990**, *280*, 119–127.
- (22) Del Castillo, T. J.; Thompson, N. B.; Peters, J. C. *J. Am. Chem. Soc.* **2016**, *138*, 5341–5350.
- (23) Chalkley, M. J.; Del Castillo, T. J.; Matson, B. D.; Roddy, J. P.; Peters, J. C. *ACS Cent. Sci.* **2017**, *3*, 217–223.
- (24) Garrido, G.; Rosés, M.; Ràfols, C.; Bosch, E. *J. Solution Chem.* **2008**, *37*, 689–700.
- (25) Pham, D. N.; Burgess, B. K. *Biochemistry* **1993**, *32*, 13725–13731.
- (26) Weare, W. W.; Dai, X.; Byrnes, M. J.; Chin, J. M.; Schrock, R. R.; Müller, P. *Proc. Natl. Acad. Sci. U.S.A.* **2006**, *103*, 17099–17106.
- (27) Anderson, J. S.; Cutsail, G. E.; Rittle, J.; Connor, B. A.; Gunderson, W. A.; Zhang, L.; Hoffman, B. M.; Peters, J. C. *J. Am. Chem. Soc.* **2015**, *137*, 7803–7809.
- (28) Matson, B. D.; Peters, J. C. *ACS Cat.* **2018**, *8*, 1448–1455.

- (29) Kendall, A. J.; Johnson, S. I.; Bullock, R. M.; Mock, M. T. *J. Am. Chem. Soc.* **2018**, *140*, 2528–2536.
- (30) Grimme, S.; Antony, J.; Ehrlich, S.; Krieg, H. *J. Chem. Phys.* **2010**, *132*, 154104–154119.
- (31) Tao, J.; Perdew, J. P.; Staroverov, V. N.; Scuseria, G. E. *Phys. Rev. Lett.* **2003**, *91*, 146401–146404.
- (32) Weigend, F.; Ahlrichs, R. *Phys. Chem. Chem. Phys.* **2005**, *7*, 3297–3305.
- (33) Pitman, C. L.; Finster, O. N. L.; Miller, A. J. M. *Chem. Commun.* **2016**, *52*, 9105–9108.
- (34) Quintana, L. M. A.; Johnson, S. I.; Corona, S. L.; Villatoro, W.; Goddard, W. A.; Takase, M. K.; VanderVelde, D. G.; Winkler, J. R.; Gray, H. B.; Blakemore, J. D. *Proc. Natl. Acad. Sci. U.S.A.* **2016**, *113*, 6409–6414.
- (35) Peng, Y.; Ramos-Garces, M. V.; Lionetti, D.; Blakemore, J. D. *Inorg. Chem.* **2017**, *56*, 10824–10831.
- (36) Scepaniak, J. J.; Young, J. A.; Bontchev, R. P.; Smith, J. M. *Angew. Chem. Int. Ed.* **2009**, *48*, 3158–3160.
- (37) Pappas, I.; Chirik, P. J. *J. Am. Chem. Soc.* **2015**, *137*, 3498–3501.
- (38) MacLeod, K. C.; McWilliams, S. F.; Mercado, B. Q.; Holland, P. L. *Chem. Sci.* **2016**, *7*, 5736–5746.
- (39) Lindley, B. M.; Bruch, Q. J.; White, P. S.; Hasanayn, F.; Miller, A. J. M. *J. Am. Chem. Soc.* **2017**, *139*, 5305–5308.
- (40) Marcus, R. A. *J. Chem. Phys.* **1956**, *24*, 966–978.

- (41) Iordanova, N.; Decornez, H.; Hammes-Schiffer, S. *J. Am. Chem. Soc.* **2001**, *123*, 3723–3733.
- (42) Koelle, U.; Infelta, P. P.; Graetzel, M. *Inorg. Chem.* **1988**, *27*, 879–883.
- (43) Call, A.; Casadevall, C.; Acuña-Parés, F.; Casitas, A.; Lloret-Fillol, J. *Chem. Sci.* **2017**, *8*, 4739–4749.
- (44) Moret, M.-E.; Peters, J. C. *Angew. Chem. Int. Ed.* **2011**, *50*, 2063–2067.
- (45) Henke, W. C.; Lionetti, D.; Moore, W. N. G.; Hopkins, J. A.; Day, V. W.; Blakemore, J. D. *ChemSusChem* **2017**, *10*, 4589–4598.

Chapter 5.
Cp* Non-innocence Leads to a Remarkably Weak C–H Bond
via Metallocene Protonation

Adapted from:
Chalkley, M. J.; Oyala, P. H.; Peters, J. C.
J. Am. Chem. Soc. **2019**, *141*, 4721–4729.
DOI: 10.1021/jacs.9b00193

5.1 Introduction

Metallocenes such as ferrocene, chromocene, and cobaltocene have enjoyed a privileged role in the development of organometallic chemistry and serve as useful reagents owing to their high compositional stabilities and accessible redox couples.^{1,2} Indeed, many chemists first encounter metallocenes in the context of their one-electron redox chemistry, with the $[\text{Cp}_2\text{Fe}]^{+/0}$, $[\text{Cp}_2\text{Cr}]^{+/0}$, and $[\text{Cp}_2\text{Co}]^{+/0}$ couples, and those of their related permethylated variants, being some of the most commonly exploited in all of synthetic chemistry.³

An area where divalent metallocene reductants (e.g., Cp^*_2Cr , Cp^*_2Co) have been proven particularly effective is catalytic N_2 -to- NH_3 conversion (N_2RR).⁴⁻⁶ Schrock first identified their utility in this context via the discovery of a molybdenum tris(amido)amine ($(\text{HIPTN}_3\text{N})\text{Mo}$, $\text{HIPTN}_3\text{N} = [(3,5-(2,4,6\text{-}^i\text{Pr}_3\text{C}_6\text{H}_2)_2\text{C}_6\text{H}_3\text{NCH}_2\text{CH}_2)_3\text{N}]^{3-}$) N_2RR catalyst system employing lutidinium as the acid and Cp^*_2Cr as the reductant.⁴ Since that discovery, other labs have exploited related cocktails that pair a metallocene reductant with an acid to drive N_2RR using a range of metal catalysts, with selectivities and turnover numbers that continue to improve.⁵⁻⁹

The protonation chemistry of metallocenes is well studied, especially among Group 8^{10,11} and 10^{12,13} metallocenes. Related studies on more reducing Group 6 and 9 metallocenes (e.g., Cp^*_2Cr , Cp_2Co , Cp^*_2Co), which are relevant to the aforementioned proton-coupled reduction of N_2 , have been much more limited. While studies have shown that the release of H_2 is highly favorable on both thermodynamic and kinetic grounds,¹⁴ protonated Group 6 and 9 metallocene intermediates have not been reliably identified and

characterized. It has been presumed that the direct reactions of acids with reducing metallocenes are deleterious to selectivity for N_2RR versus H_2 generation.^{4,15,16}

Our lab became interested in metallocenes following the observation that Cp^*_2Co could serve as the electron source for Fe-mediated N_2RR in the presence of anilinium acids and an iron catalyst, $(P_3^B)Fe$ ($P_3^B = \text{tris}(o\text{-diisopropylphosphinophenyl})\text{-borane}$).^{8,9} Indeed, the selectivity for N_2RR under these conditions proved far more efficient for NH_3 formation (up to 78%) than our originally published conditions using KC_8 and $[H(OEt)_2][BAr^F_4]$ ($HBar^F_4$, $BAr^F_4 = \text{tetrakis}(3,5\text{-bis}(\text{trifluoromethyl})\text{phenyl})\text{borate}$).^{17,18} However, contrary to our mechanistic experiments with $HBar^F_4$, reaction of $[(P_3^B)Fe(N_2)]^-$ with anilinium triflate acids led neither to the observation of relevant intermediates (e.g., $[(P_3^B)Fe(NNH_2)]^+$) in freeze-quench spectroscopic methods, nor to the observation of fixed-N products upon annealing.^{9,19,20}

The apparent need for both acid and reductant to be present to achieve productive N–H bond formation is reminiscent of Schrock and coworkers' observations when attempting to functionalize $(HIPTN_3N)Mo(N_2)$ with catalytically relevant reagents.²¹ In both cases, we have hypothesized that metallocene-mediated proton-coupled electron transfer reactions may play a key role in N–H bond-forming steps.^{8,9,22} Furthermore, given the ubiquity of these metallocene reagents in N_2RR , we wondered whether metallocene-mediated N–H bond forming steps might provide a contributing, or even dominant, mechanistic pathway.

Density functional theory (DFT) studies by our group supported the notion that protonation of metallocenes such as Cp^*_2Co or Cp^*_2Cr by catalytically relevant acids is

thermodynamically favorable. To our surprise, these DFT studies also predicted that ring protonation is thermodynamically favored versus protonation at the metal (to form a metal hydride).⁸ Such selectivity would contrast with the classic case of ferrocene, where protonation at Fe has been firmly established.^{10,23} The Cp*₂Co and Cp*₂Cr ring-protonated species are predicted to have remarkably weak C–H bond dissociation enthalpies (BDE <37 kcal mol⁻¹), which should in turn make them excellent PCET donors.^{8,9} These observations intimate that protonated metallocene intermediates might thereby offer viable pathways for N–H bond formation via PCET (or even hydride transfer; *vide infra*), in addition to the more commonly presumed pathway for deleterious H₂ evolution (**Figure 5.1**).

Figure 5.1: Reaction pathways to consider for protonated Cp*₂Co species, illustrating both undesired HER and possible N–H bond forming steps relevant to N₂RR.

We previously reported preliminary investigations into the protonation of Cp*₂Co. In brief, slow addition of a toluene solution of Cp*₂Co to a vigorously stirred suspension of trifluoromethanesulfonic acid (HOTf) in toluene at –78 °C led to precipitation of a purple solid that could be isolated via filtration. On the basis of the X-band continuous wave (CW) electron paramagnetic resonance (EPR) spectrum (77 K, Figure 4) of the solid, we speculated that it was a protonated Cp*₂Co species.⁸ Herein, we undertake the rigorous characterization of the protonation products of Cp*₂Co using pulse EPR techniques, and provide unequivocal evidence for the assignment of the ring protonated isomers [(Cp*)Co(*exo/endo*-η⁴-C₅Me₅H)]⁺. Variable temperature Q-Band (34 GHz) pulse EPR spectroscopy, in conjunction with DFT predictions, are key to enabling the assignment. We

also demonstrate that *exo*-protonation can be favored when using a bulkier acid. Of further interest, we provide physical data to experimentally assess the C–H bond dissociation free energy (BDFE_{C–H}) for [(Cp*)Co(*exo*-η⁴-C₅Me₅H)]⁺, which support our earlier DFT predictions that it has an exceptionally weak C–H bond (**Figure 5.1**). This behavior should not be limited to the present protonated metallocene, and we thus outline a general approach to understanding the reactivity of arene-protonated metal species.

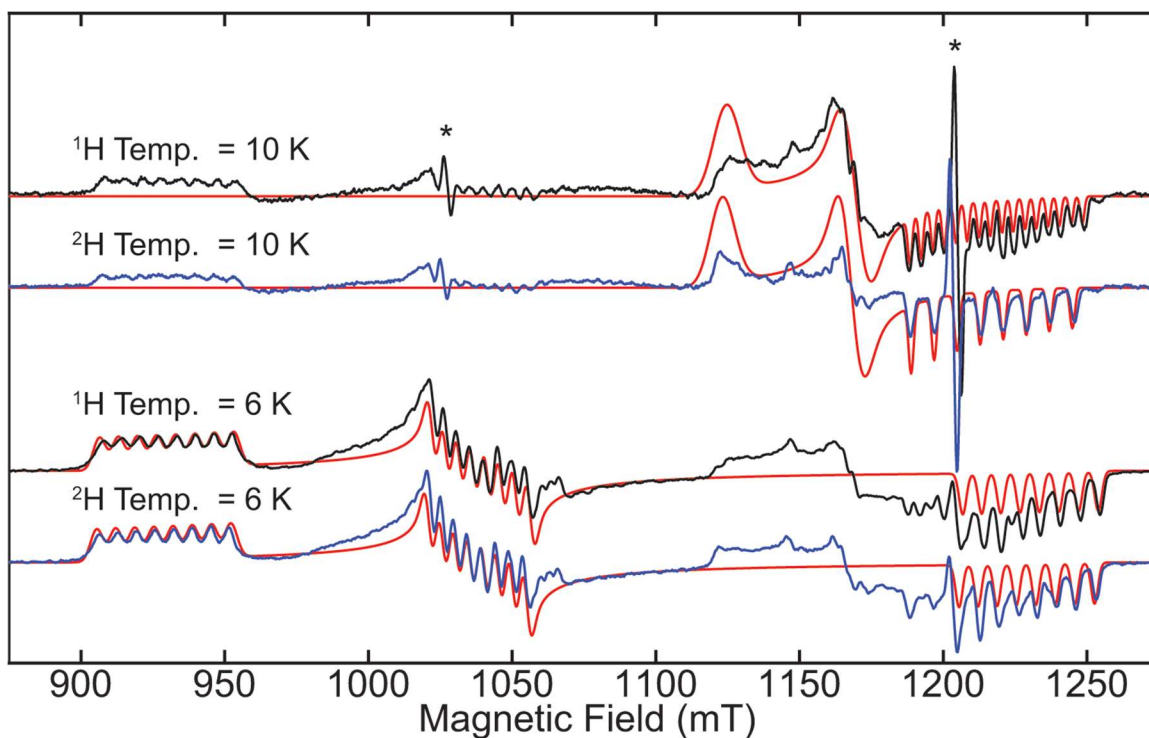
5.2 Results

5.2.1 Pulse Electron Paramagnetic Resonance Spectroscopy on Protonated Cp*₂Co

To interrogate the reaction of Cp*₂Co with HOTf, we employed Q-band pulse EPR experiments at very low temperatures. Electron spin-echo (ESE) detected, field-swept spectra at Q-band, performed at 6 K and 10 K, clearly identify the presence of two different species with dramatically different **g**-anisotropy in the precipitated solid (**Figure 5.2**). Fortuitously, measurement of the approximate spin-lattice relaxation rates via inversion recovery reveals that the two species have significantly different *T*₁' times. The species with higher **g**-anisotropy (**g** = [2.625, 2.349, 1.984]) exhibits a much shorter *T*₁' than the species exhibiting a narrower spectrum (**g** = [2.170, 2.085, 2.005]), even at 6 K. This difference in relaxation rates becomes more dramatic upon warming the sample to 10 K; at this temperature, *T*₁' for the species with high **g**-anisotropy is short enough to greatly diminish its electron-nuclear double resonance (ENDOR) response relative to the other species, even at magnetic fields with significant spectral overlap. Thus, the signals arising

from these two species in pulse EPR experiments can be largely isolated by recording spectra at these two different temperatures (6 K and 10 K; **Figure 5.2**).

Figure 5.2: Pseudomodulated²⁴ Q-band ESE-detected EPR spectra of the reaction of Cp*₂Co with HOTf (black traces), and DOTf (blue traces) measured at 10 K (top traces) and 6 K (bottom traces). Simulations for each species are displayed in red. The **g**-values and ¹H hyperfine coupling is in **Figure 5.6c**. Furthermore, for the species with larger **g**-anisotropy a ⁵⁹Co coupling used was [245, 155, 187] MHz, $e^2qQ/h = 170$ MHz, $\eta < 0.1$. For the species with smaller **g**-anisotropy, a ⁵⁹Co coupling of [15, 15, 225] MHz was used. The sharp signals with asterisks above them are due to a background signal arising from a component of the EPR cavity.



For the narrower, more slowly relaxing species, a comparison of the Q-band ESE-detected EPR spectra from the reaction of Cp*₂Co with HOTf and DOTf shows a clear change, from 16 resolved splittings centered at 1270 mT, to the 8 lines expected for a large hyperfine coupling to an $I = 7/2$ ⁵⁹Co nucleus ($A(^{59}\text{Co})_{10\text{ K}} = [15, 15, 225]$ MHz). This observation indicates that, at least at the orientation corresponding to **g**₃, there is a single

^1H nucleus with a hyperfine coupling of approximately $\frac{1}{2}$ of the magnitude of the ^{59}Co hyperfine coupling.

Analysis of the field-dependent ^1H ENDOR (**Figure 5.3a-b**) at 10 K, with corroboration from ^2H hyperfine sub-level correlation (HYSCORE) spectra (**Figure 5.4**) of each respective species, allows determination of the full hyperfine tensor of this acid-derived proton: $A(^1\text{H})_{10\text{K}} = [106.5, 112.5, 108.2]$ MHz, with $a_{\text{iso}} = 109.1$ MHz. Comparing this value to that known for the hydrogen atom (1420 MHz) indicates that approximately $0.08 e^-$ are localized on this proton.²⁵ The amount of spin density localized on this proton is unusually large, even when compared with highly reactive, paramagnetic transition metal hydrides.²⁶

Characterization of the species with greater g -anisotropy was targeted by performing analogous experiments at 6 K. In this case, the Q-band ESE-detected EPR spectra for this species in samples generated with HOTf and DOTf are indistinguishable, indicating that the ^1H hyperfine coupling to the acid-derived proton is small in comparison to the ^{59}Co hyperfine and the inhomogeneous line broadening. This was confirmed via field-dependent ENDOR (**Figure 5.3c-d**) and HYSCORE (**Figure 5.4**) spectra acquired at

6 K, which reveal a single acid-derived proton coupling of $A(^1\text{H})_{6\text{K}} = [19.0, 15.0, 19.5]$

MHz, $a_{\text{iso}} = 17.8$ MHz.

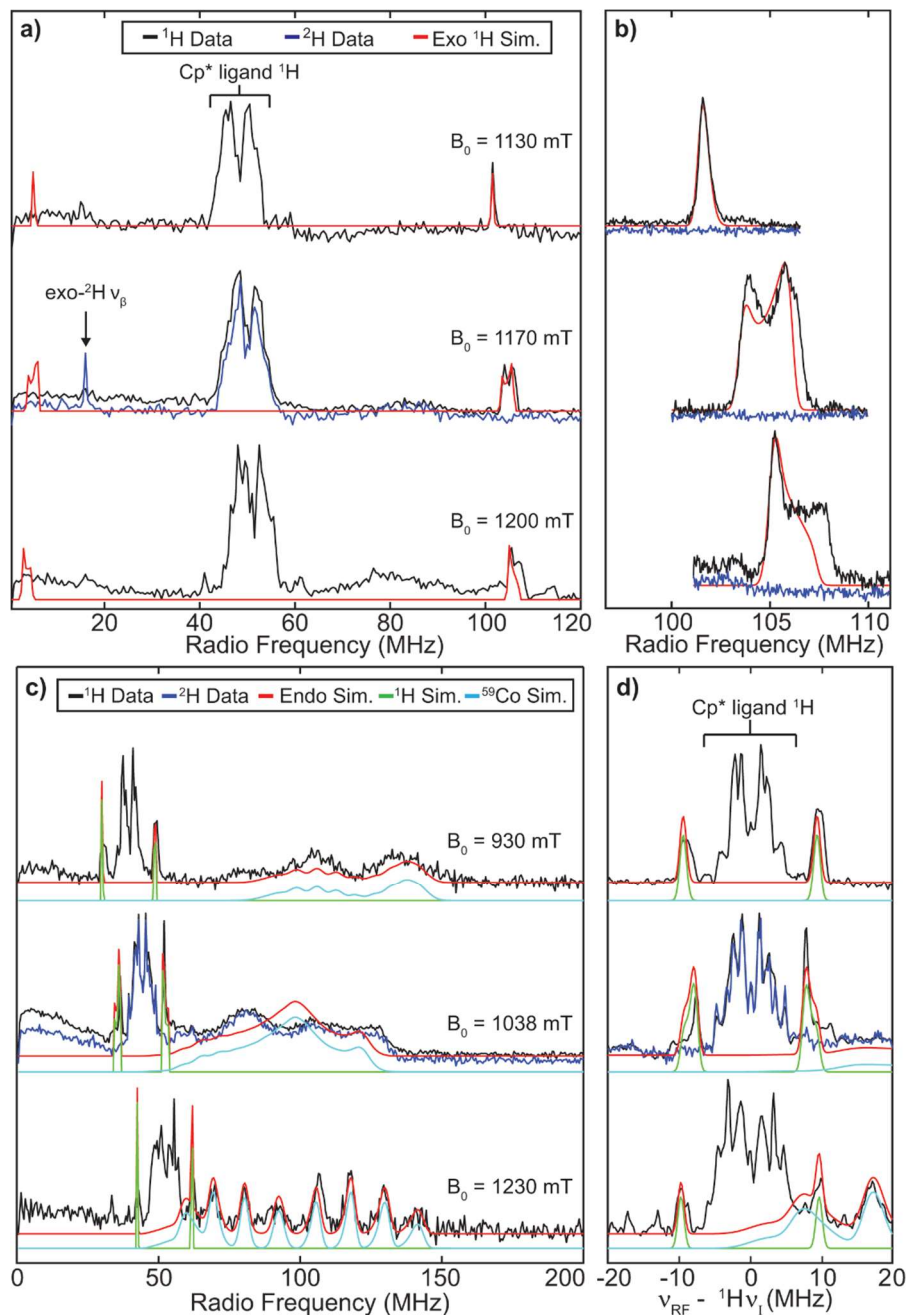


Figure 5.3: a) Q-band Davies ENDOR spectra at 10 K and b) narrow Q-band Davies ENDOR spectra at 10 K. c) Q-band Davies ENDOR spectra at 6 K and d) narrow Q-band Davies ENDOR spectra at 6 K. Data from the reaction with HOTf (black) and DOTf (blue) are shown. A simulation (red) is given and in the spectra at 6 K the simulation is further decomposed into the components for the ^1H simulation (green) and the ^{59}Co simulation (light blue).

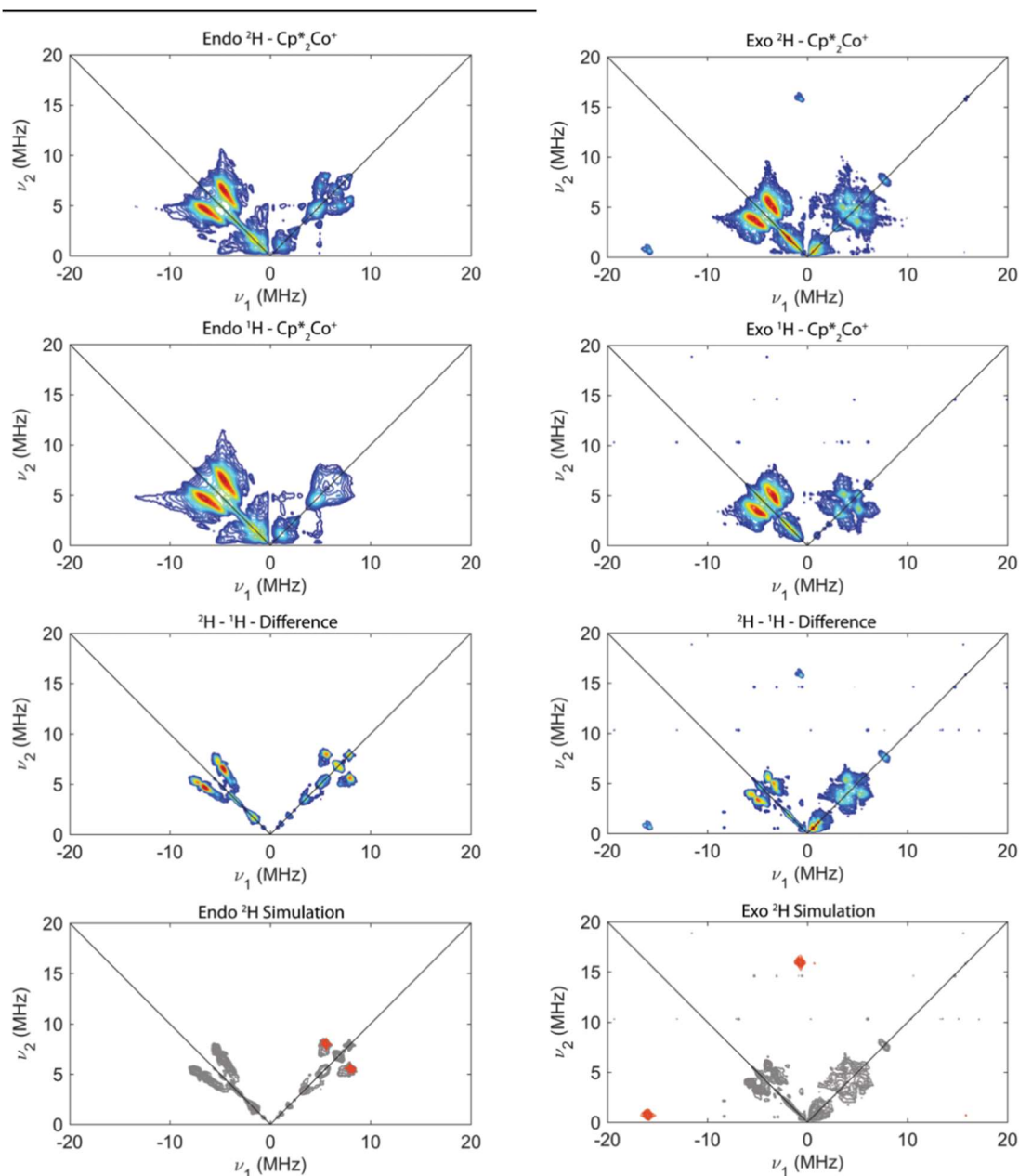


Figure 5.4: Comparison of Q-band HYSCORE spectra acquired at the center of the EPR spectrum of the *endo*- (left) and *exo*- (right) protonated Cp^*_2Co species generated via reaction with DOTF (top panels) and HOTF (2nd panels from top). To minimize the intensity of the features centered at 5 MHz in the $(-, +)$ quadrant common to both isotopologues, the $^2\text{H}-^1\text{H}$ difference spectrum is shown third from the top. Simulations of the ^2H hyperfine couplings derived from the ^1H couplings determined via ENDOR for the *endo*- and *exo*-species are overlaid in red over the difference spectra, which are plotted in grey.

Additionally, features from ^{59}Co ($A(^{59}\text{Co})_{6\text{K}} = [245, 160, 187]$ MHz) are observable in the ENDOR spectra at all fields, which is likely due to the more isotropic nature of the coupling symmetry of this species in comparison to the species with smaller g -anisotropy. In the ENDOR acquired at 1230 mT, additional splittings due to the ^{59}Co nuclear quadrupole interaction are resolved. Simulations of these ENDOR spectra indicate a quadrupole coupling constant of $e^2qQ/h = 170$ MHz, with negligible electric field gradient rhombicity ($\eta < 0.1$). These values are very similar to those reported for Cp_2Co^+ ($e^2qQ/h = 171.5$ MHz and $\eta = 0$), as previously determined by nuclear quadrupole resonance.²⁷ This suggests that protonation results in only a relatively minor perturbation of the environment around Co.

5.2.2 Stereochemical Assignment of Cp^*_2Co Protonation

Notably, both of the proton hyperfine coupling tensors are highly isotropic in nature, with only small anisotropic components ($T(^1\text{H})_{10\text{K}} = [-2.6, 3.4, -0.9]$ MHz; $T(^1\text{H})_{6\text{K}} = [1.2, -2.8, 1.7]$ MHz). To evaluate possible chemical assignments for these observations, DFT calculations were performed to optimize the structure of the three plausible protonation isomers (i.e., *Co-H*, *exo-C-H*, and *endo-C-H*) and then single point calculations were performed to predict the relevant hyperfine tensors (**Figure 5.6a**). Different functionals (TPSS,²⁸ TPSSH,²⁸ BP86,^{29,30} B3LYP^{29,31–33}) were used for both the optimization and also the single point calculation to determine the hyperfine coupling. In all cases, similar T -tensors and the highly disparate magnitude of the a_{iso} for the *endo*- and *exo*-functionalized species were observed (*vide supra*). Consistent with previous experimental observations for paramagnetic transition metal hydrides, DFT predicts the

Co–H isomer to have a large, roughly axial dipolar coupling tensor ($T(^1\text{H})_{\text{Co-H}} = [34.1, -20.7, -12.9]$).^{34,35} Furthermore, the predicted a_{iso} value for the Co–H of -50 MHz is inconsistent with our experimental EPR data for the protonated species. In contrast, the hyperfine coupling tensor for both *exo*- and *endo*-isomers are predicted to be far more isotropic ($T(^1\text{H})_{\text{exo-C-H}} = [-2.4, 3.8, -1.4]$ MHz and $T(^1\text{H})_{\text{endo-C-H}} = [-3.1, 8.7, -5.6]$ MHz), consistent with the available EPR data. Importantly, our DFT calculations also predict that the two ring-protonated isomers have very different a_{iso} values, with the *exo*-isomer predicted to have $a_{\text{iso}} = 119$ MHz and the *endo*-isomer predicted to have $a_{\text{iso}} = 31$ MHz. Thus, we assign the species with small **g**-anisotropy to be the *exo*-isomer and that with large **g**-anisotropy to be the *endo*-isomer.

Assuming this assignment is correct then, on the basis of the recorded CW EPR spectra, the *endo*-isomer is formed in higher yield with HOTf (**Figure 5.5**, top). We wondered whether it might be possible to achieve preferential *exo*-functionalization by using a bulkier acid. Indeed, we have found that slow addition of a toluene solution of Cp^*_2Co at -78 °C to a rapidly stirred suspension of the more sterically encumbered bis(trifluoromethane)sulfonimide (HNTf_2) in toluene also precipitates a purple solid (**Figure 5.5**, bottom). Analysis of this solid by CW X-Band EPR at 77 K reveals a near complete inversion of the protonation-site selectivity suggesting that with the smaller HOTf, *endo*-protonation is preferred (**Figure 5.6a**), but with the bulkier HNTf_2 , steric clash with the opposite Cp^* ring leads to *exo*-protonation being favored (**Figure 5.6b**). We believe that both of the protonation reactions are under kinetic control due to the rapid precipitation upon proton transfer.

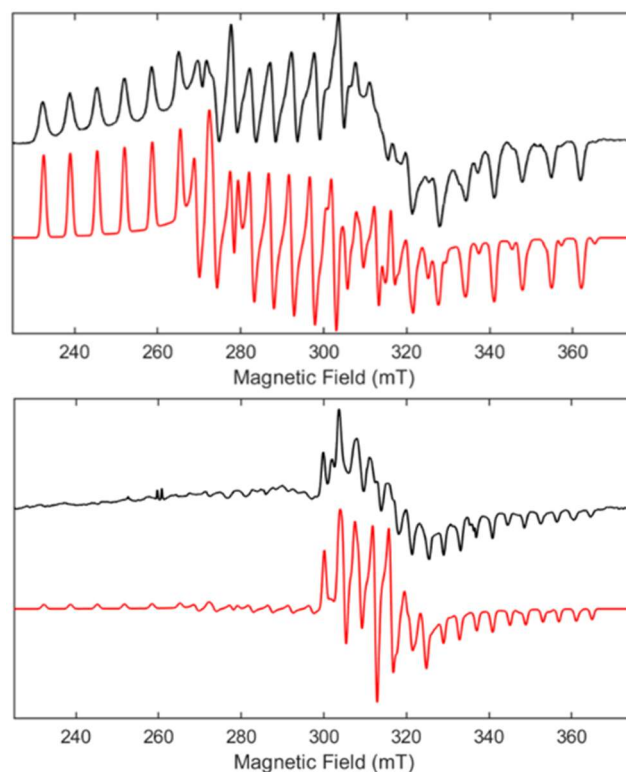


Figure 5.5: (top) X-Band CW EPR spectrum of the reaction of Cp^*_2Co with HOTf (black) and its simulation (red). (bottom) X-Band CW EPR spectrum of the reaction of Cp^*_2Co with HNTf_2 (black) and its simulation (red). The simulations are generated using the same parameters except for the weighting of the two species. For the top simulation it is 10:1 *endo:exo* and in the bottom simulation it is 3:10 *endo:exo*.

Further chemical confirmation of the protonation site was obtained by pre-functionalization of the Cp^* ring. Taking a cue from classic literature, we noted that Wilkinson and coworkers previously characterized a far more stable, neutral ring-functionalized species, $(\text{Cp})\text{Co}(\eta^4\text{-C}_5\text{H}_6)$.³⁶ By analogy to their approach, we generated $(\text{Cp}^*)\text{Co}(\textit{exo}\text{-}\eta^4\text{-C}_5\text{Me}_5\text{H})$ in moderate yield via the reaction of $[\text{Cp}^*_2\text{Co}]^+$ with excess tetrabutylammonium borohydride in refluxing THF. The stereospecificity of *exo*-functionalization could be confirmed in the solid state by XRD analysis (**Figure 5.6b**) and in solution via NMR spectroscopy.

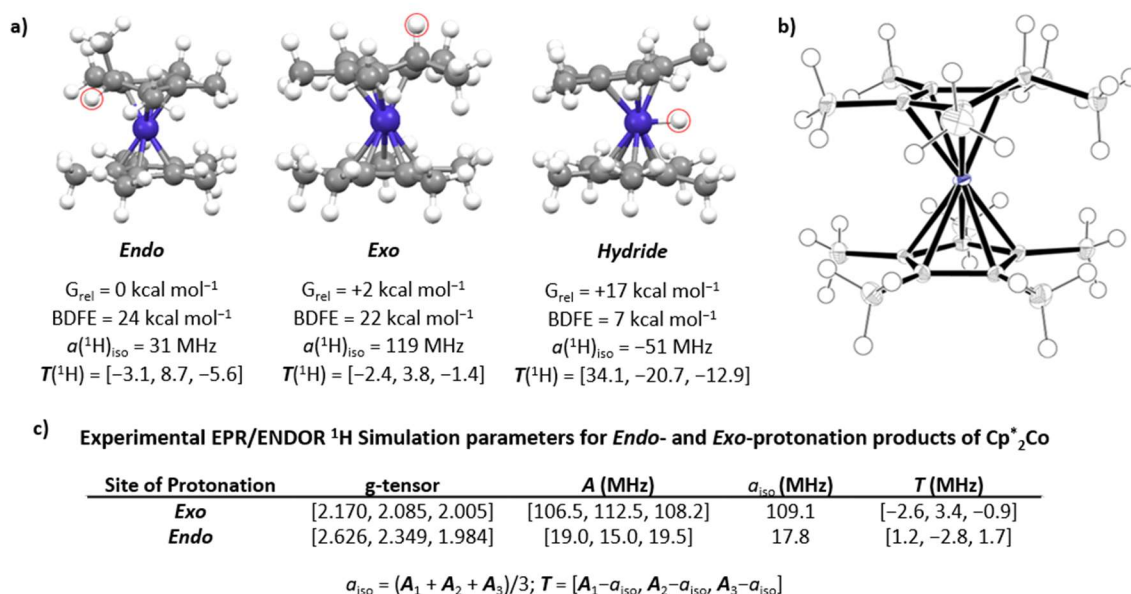


Figure 5.6: a) DFT optimized structures for the isomers of protonated Cp^*_2Co . The predicted $A(^1\text{H})$ values for the protons circled in red. b) X-ray crystal structure of $(\text{Cp}^*)\text{Co}(\text{exo-}\eta^4\text{-C}_5\text{Me}_5\text{H})$. Thermal ellipsoids are shown at 50% probability. c) Experimentally derived ^1H hyperfine parameters for the *endo*- and *exo*-isomers of protonated Cp^*_2Co .

Although our efforts to use common oxidants (*i.e.*, Fc^+ , Ag^+) to affect the electron transfer were unsuccessful, we found that $(\text{Cp}^*)\text{Co}(\text{exo-}\eta^4\text{-C}_5\text{Me}_5\text{H})$ could be oxidized by reaction with HBAr^{F_4} at $-78 \text{ }^\circ\text{C}$ in pentane. The purple precipitate was analyzed by X-Band CW EPR and, as expected, demonstrated only the signal that we had assigned to the *exo*-isomer. To confirm that the strongly coupled proton observed derived from our pre-functionalized ring and not the acid, $(\text{Cp}^*)\text{Co}(\text{exo-}\eta^4\text{-C}_5\text{Me}_5\text{D})$ was reacted with HBAr^{F_4} . Only the formation of $[(\text{Cp}^*)\text{Co}(\text{exo-}\eta^4\text{-C}_5\text{Me}_5\text{D})]^+$ was detected by EPR (**Figure 5.7**).

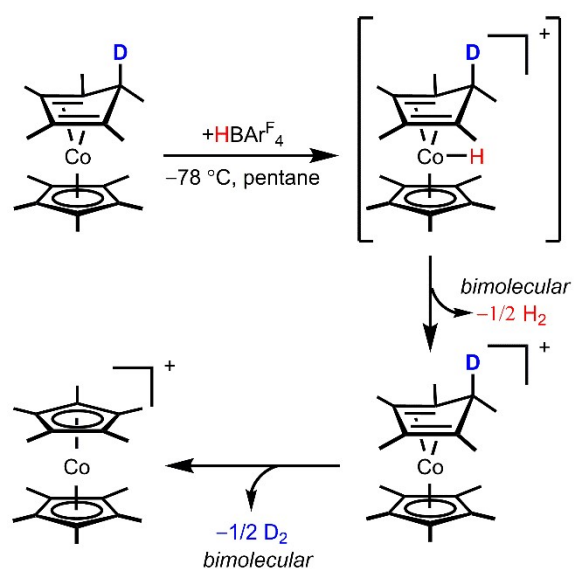


Figure 5.7: Proposed mechanism for the oxidation of $(\text{Cp}^*)\text{Co}(\text{exo-}\eta^4\text{-C}_5\text{Me}_5\text{D})$ with HBAr^{F}_4 .

5.2.3 Thermochemical Measurements Relevant to Cp^*_2Co Protonation

We were also interested in experimentally validating the DFT-predicted thermochemical properties of these species. The high kinetic instability of $[(\text{Cp}^*)\text{Co}(\text{endo/exo-}\eta^4\text{-C}_5\text{Me}_5\text{H})]^+$ in solution precludes direct measurement of the thermochemical properties that we have predicted by DFT. Of particular interest is experimental validation of a remarkably weak $\text{BDFE}_{\text{C-H}}$. We therefore turned to the neutral species $(\text{Cp}^*)\text{Co}(\text{exo-}\eta^4\text{-C}_5\text{Me}_5\text{H})$ as a means to indirectly measure pertinent thermochemical properties for $[(\text{Cp}^*)\text{Co}(\text{exo-}\eta^4\text{-C}_5\text{Me}_5\text{H})]^+$.

One important parameter in this regard is the $[(\text{Cp}^*)\text{Co}(\text{exo-}\eta^4\text{-C}_5\text{Me}_5\text{H})]^{+/0}$ redox couple. In cyclic voltammograms (CVs) of $(\text{Cp}^*)\text{Co}(\text{exo-}\eta^4\text{-C}_5\text{Me}_5\text{H})$, obtained at typical scan rates (0.01 to 1.0 V s^{-1}) at room temperature in butyronitrile, only an irreversible oxidation is observed. Continuing to scan these voltammograms further in the cathodic direction leads to the observation of the fully reversible $[\text{Cp}^*_2\text{Co}]^{+/0}$ couple (Figure 5.8, top),

consistent with the loss of 0.5 equivalents of H_2 , as expected from $[(\text{Cp}^*)\text{Co}(\text{exo-}\eta^4\text{-C}_5\text{Me}_5\text{H})]^+$ in solution. By scanning rapidly ($>10 \text{ V s}^{-1}$) at room temperature (Figure 5.8, bottom), or alternatively by cooling the reaction mixture to $-78 \text{ }^\circ\text{C}$, voltammograms with appreciable reversibility could be obtained, from which E^0 could be determined to be $-0.62 \text{ V vs Fc}^{+/0}$ (Figure 5.9). Butyronitrile was used in this study, because potentials in this solvent have been shown to be similar to those in acetonitrile, and it enables low-temperature electrochemistry, which was useful for verifying the oxidation potential.^{37,38}

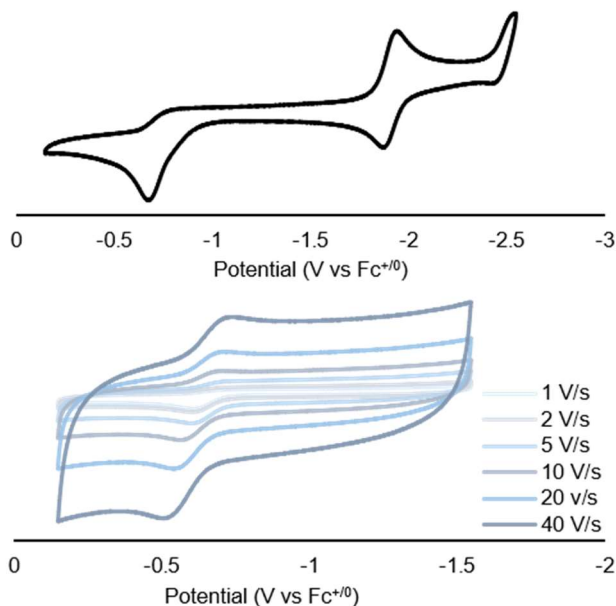


Figure 5.8: Cyclic voltammograms of the $[(\text{Cp}^*)\text{Co}(\text{exo-}\eta^4\text{-C}_5\text{Me}_5\text{H})]^{+/0}$ couple at room temperature in a 0.4 M $[\text{TBA}][\text{PF}_6]$ solution of butyronitrile. (top) Scan showing that the oxidation of $(\text{Cp}^*)\text{Co}(\text{exo-}\eta^4\text{-C}_5\text{Me}_5\text{H})^0$ leads to the emergence of the $[\text{Cp}^*_2\text{Co}]^{+/0}$ couple. (bottom) Variable scan rate measurements on the $[(\text{Cp}^*)\text{Co}(\text{exo-}\eta^4\text{-C}_5\text{Me}_5\text{H})]^{+/0}$ feature.

To further confirm this value, the methylated derivative, $(\text{Cp}^*)\text{Co}(\eta^4\text{-C}_5\text{Me}_6)$, was prepared.¹³ The oxidation event for this species is reversible.³⁹ This result is consistent with the significantly higher kinetic barrier anticipated for $\text{Me}\cdot$ loss/transfer compared to $\text{H}\cdot$

loss/transfer. In acetonitrile, the E^0 we measure for $[(\text{Cp}^*)\text{Co}(\text{C}_5\text{Me}_6)]^{+/0}$ is -0.61 V vs $\text{Fc}^{+/0}$, in good agreement with our experimental data for the $[(\text{Cp}^*)\text{Co}(\text{exo-}\eta^4\text{-C}_5\text{Me}_5\text{H})]^{+/0}$ couple.

An estimate of the hydricity ($\Delta G(\text{H}^-)$) of $(\text{Cp}^*)\text{Co}(\text{exo-}\eta^4\text{-C}_5\text{Me}_5\text{H})$ provides another useful parameter. Dissolution of $(\text{Cp}^*)\text{Co}(\text{exo-}\eta^4\text{-C}_5\text{Me}_5\text{H})$ in $\text{MeCN-}d_3$ and reaction with 1 atm of CO_2 or with excess $[\text{Pt}(\text{dmpe})_2]^{2+}$ ($\text{dmpe} = 1,2\text{-dimethylphosphinoethane}$), leads in both cases to quantitative hydride transfer. From this observation we can determine a lower bound for the hydricity of $(\text{Cp}^*)\text{Co}(\text{exo-}\eta^4\text{-C}_5\text{Me}_5\text{H})$ ($\Delta G(\text{H}^-) < 41$ kcal mol $^{-1}$; **Figure 5.9**).⁴⁰ This is in good agreement with our DFT prediction of $\Delta G(\text{H}^-) = 37$ kcal mol $^{-1}$ for this species. The C–H bond of $(\text{Cp}^*)\text{Co}(\text{exo-}\eta^4\text{-C}_5\text{Me}_5\text{H})$ is thus about 15 kcal mol $^{-1}$ more hydridic than the C–H bonds in the common biological hydride donors NADH and NADPH.⁴¹ These observations hint at the possibility that, at least in principle, species such as $(\text{Cp}^*)\text{Co}(\text{exo-}\eta^4\text{-C}_5\text{Me}_5\text{H})$ could mediate hydride transfer steps relevant to N_2RR , such as that shown in **Figure 5.1**.

In an attempt to estimate the homolytic C–H bond strength (BDFE) of $(\text{Cp}^*)\text{Co}(\text{exo-}\eta^4\text{-C}_5\text{Me}_5\text{H})$, it was reacted with excess 4-methoxy-2,2,6,6-tetramethyl-1-piperidinyloxy (${}^{4\text{-MeO}}\text{TEMPO}\bullet$). To our surprise, two equivalents of ${}^{4\text{-MeO}}\text{TEMPO-H}$ were formed. The first equivalent derives from the expected H-atom abstraction to form Cp^*_2Co , providing an upper limit to the $\text{BDFE}_{\text{exo-C-H}} < 65$ kcal mol $^{-1}$ (**Error! Reference source not found., Figure 5.9**). The second ${}^{4\text{-MeO}}\text{TEMPO-H}$ equiv is derived from a second H-atom abstraction step between ${}^{4\text{-MeO}}\text{TEMPO}\bullet$ and Cp^*_2Co (**Error! Reference source not found.**). This generates the known fulvene complex, $(\text{Cp}^*)\text{Co}(\text{exo-}\eta^4\text{-C}_5\text{Me}_4\text{CH}_2)$.⁴² These

observations are consistent with our $\text{BDFE}_{\text{C-H}}$ predictions for the C–H bond in both $(\text{Cp}^*)\text{Co}(\text{exo-}\eta^4\text{-C}_5\text{Me}_5\text{H})$ and Cp^*_2Co (53 and 62 kcal/mol, respectively).



With this thermochemical data for $(\text{Cp}^*)\text{Co}(\text{exo-}\eta^4\text{-C}_5\text{Me}_5\text{H})$ in hand, it is possible to constrain the $\text{BDFE}_{\text{C-H}}$ for $[(\text{Cp}^*)\text{Co}(\text{exo-}\eta^4\text{-C}_5\text{Me}_5\text{H})]^+$. Using the bound established for the $\text{BDFE}_{\text{C-H}}$ for neutral $(\text{Cp}^*)\text{Co}(\text{exo-}\eta^4\text{-C}_5\text{Me}_5\text{H})$, we can establish an upper limit for the $\text{BDFE}_{\text{C-H}}$ of $[(\text{Cp}^*)\text{Co}(\text{exo-}\eta^4\text{-C}_5\text{Me}_5\text{H})]^+$ of 34 kcal mol⁻¹. But using the upper limit determined for the $\Delta G(\text{H}^-)$ of $(\text{Cp}^*)\text{Co}(\text{exo-}\eta^4\text{-C}_5\text{Me}_5\text{H})$ allows us to place an even lower upper limit for $\text{BDFE}([(Cp^*)Co(exo-\eta^4-C_5Me_5H)]^+)$ of <29 kcal mol⁻¹. This experimental upper limit predicted from the solution phase data is in reasonable agreement with our gas-phase DFT prediction of 23 kcal mol⁻¹, thus confirming that the C–H bond of $[(\text{Cp}^*)\text{Co}(\text{exo-}\eta^4\text{-C}_5\text{Me}_5\text{H})]^+$ is extremely weak.

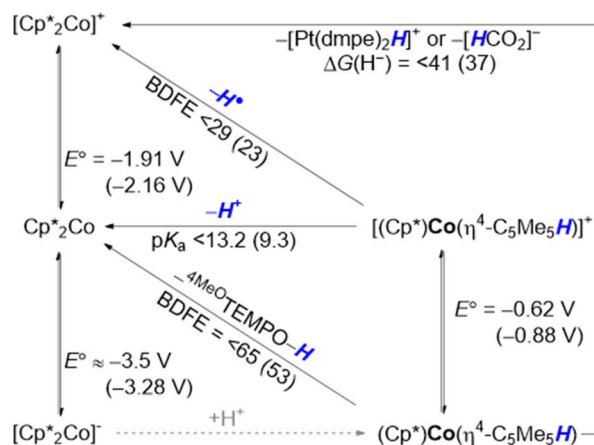


Figure 5.9: Thermochemistry of neutral and cationic $(\text{Cp}^*)\text{Co}(\text{exo-}\eta^4\text{-C}_5\text{Me}_5\text{H})$. Computational values are shown in parentheses. Thermodynamic quantities are in kcal mol⁻¹ and potentials are against $\text{Fc}^{+/0}$.

5.3 Discussion

It is well established that group 8 metallocenes form metal hydrides upon protonation.^{10,11,23} In the case of ferrocene, computational trajectories have been used to argue that there is fast exchange between a terminal hydride and a hydride that forms an agostic interaction with the Cp ring.^{43,44} In contrast, neutral group 10 metallocenes (Cp_2Ni and Cp^*_2Ni), and the isoelectronic $[\text{Cp}_2\text{Co}]^-$, are known to undergo *exo*-protonation of the ring.^{12,13,45} Here we find that, consistent with the near isoenergetic protonation predicted by DFT, Cp^*_2Co undergoes both *exo*- and *endo*-protonation on the ring. This result provides a distinct example of a metallocene that undergoes non-specific protonation. Furthermore, the protonation selectivity can be altered by changing the steric profile of the acid.

We suspect that formation of the *exo*-isomer is likely critical to observing productive PCET reactions in N_2RR mediated by the $(\text{P}_3^{\text{B}})\text{Fe}$ -system, as this isomer provides significantly less steric shielding for the reactive $\text{H}\cdot$. Given the steric profile of the catalytically relevant acids that we and others have used (e.g., anilinium and pyridinium),⁴⁻⁹ we expect that *exo*-protonation is far more likely under N_2RR conditions. Indeed, we have calculated only small barriers ($\Delta G^\ddagger < 5 \text{ kcal mol}^{-1}$) for the *exo*-protonation of Cp^*_2Co by substituted anilinium triflate acids.⁹ Facile *endo*-protonation by these acids is inconsistent with simple space-filling models.

Although Cp^* is most typically considered to be an innocent ligand, evidence continues to emerge that it can be involved in the management of protons. In addition to the well-established protonation of Cp^*_2Ni ,^{13,46} several half-sandwich Rh complexes have recently been reported to form Cp^*-H linkages following reductive elimination of a $\text{Rh}-\text{H}$.

In these cases, the Cp*–H bond has been directly implicated in H[−] transfer, either to H⁺ or to NAD⁺.^{47–49}

The present study illustrates that Cp*–H linkages are not limited to H[−] transfer pathways. Rather, the type of reactivity can be predicted by the tendency of the metal center to achieve a closed-shell, 18e[−] d⁶ configuration. Thus, the d⁷ Co center in [(Cp*)Co(*exo*-η⁴-C₅Me₅H)]⁺ should favor a one electron process (H• transfer), while the d⁸ Co center in (Cp*)Co(*exo*-η⁴-C₅Me₅H) should favor a two electron process (H[−] transfer), akin to those observed for the aforementioned d⁸ Rh centers.

In this work, we have derived a BDFE for three different C–H bonds relevant to decamethylcobaltocene [(Cp*)Co(*exo*-η⁴-C₅Me₅H)]⁺, (Cp*)Co(*exo*-η⁴-C₅Me₅H), and (Cp*)Co(η⁵-C₅Me₄CH₂H) (**Figure 5.10**). All of these bonds are weak, but that in [(Cp*)Co(*exo*-η⁴-C₅Me₅H)]⁺ is significantly weaker than the other two. This can be readily explained in terms of the two primary factors affecting the stability of the starting and product complexes: aromaticity and electron count. In the case of H-atom abstraction from (Cp*)Co(*exo*-η⁴-C₅Me₅H) or from a methyl substituent in Cp*₂Co, these factors offset one another to provide a weak, but not an exceptionally weak, BDFE_{C–H}. For (Cp*)Co(*exo*-η⁴-C₅Me₅H), H-atom abstraction aromatizes the Cp* ring, offset by the formation of a 19e[−] center (**Figure 5.10**). On the other hand, in Cp*₂Co, H-atom abstraction transforms the 19e[−] center to an 18e[−] center, but the Cp* ring is dearomatized (**Figure 5.10**). Only in the case of [(Cp*)Co(*exo*-η⁴-C₅Me₅H)]⁺ are both stabilizing factors driving formation of the product. H-atom abstraction affords aromatic, 18e[−] Cp*₂Co⁺, and correspondingly the C–H bond is remarkably weak (BDFE <29 kcal mol^{−1}, **Figure 5.10**).

Reagents with such weak X–H bonds have been sought due to their utility in organic synthesis for the stepwise reduction of unsaturated substrates, such as olefins, ketones, aldehydes, esters, and enamines via H• transfer.^{50,51} Traditional strategies for developing such reagents have focused on reactive metal hydrides, for which the M• product of an overall hydrogen atom transfer is stabilized by dimerization via M–M bond formation, and/or the formation of bridging carbonyl products.⁵² Another strategy has involved the coordination of substrates that contain otherwise strong X–H bonds to a highly reducing, but nonetheless oxophilic/azaphilic, metal centers, resulting in remarkable weakening of the X–H bond.⁵³ One system where this phenomenon has proven particularly effective for engendering synthetically useful PCET reactions is SmI₂–H₂O, in which coordination of H₂O to Sm^{II} has been estimated to result in an O–H bond weakening of almost 100 kcal mol⁻¹.^{54–57}

The present study presents the protonation of Cp*₂Co to form [(Cp*)Co(*exo*-η⁴-C₅Me₅H)]⁺ as a distinct and promising strategy for developing extremely strong PCET donors. In general, this strategy involves coupling a d⁷ (or d⁴) metal ion to a dearomatized arene ligand. Given the prevalence of sandwich and half-sandwich complexes in organometallic chemistry, it is likely that as yet unrecognized examples of such PCET reagents already exist or are readily accessible.

[(Cp*)Ni(*exo*-η⁴-C₅Me₅H)]²⁺ provides one such example. Electrochemical oxidation of the stable [(Cp*)Ni(*exo*-η⁴-C₅Me₅H)]⁺ to [(Cp*)Ni(*exo*-η⁴-C₅Me₅H)]²⁺ leads to rapid generation of [Cp*₂Ni]²⁺ on the CV time scale. This transformation was originally proposed to occur via H⁺ loss followed by e⁻ loss.⁵⁸ Alternatively, we suspect that, in analogy to

$[(\text{Cp}^*)\text{Co}(\text{exo-}\eta^4\text{-C}_5\text{Me}_5\text{H})]^+$, this transformation may occur via rapid $\text{H}\cdot$ loss. In contrast, electrochemical reduction of the cation $[(\text{Cp}^*)\text{Ni}(\text{exo-}\eta^4\text{-C}_5\text{Me}_5\text{H})]^+$ to $(\text{Cp}^*)\text{Ni}(\text{exo-}\eta^4\text{-C}_5\text{Me}_5\text{H})$ is fully reversible on the CV time scale.⁵⁸

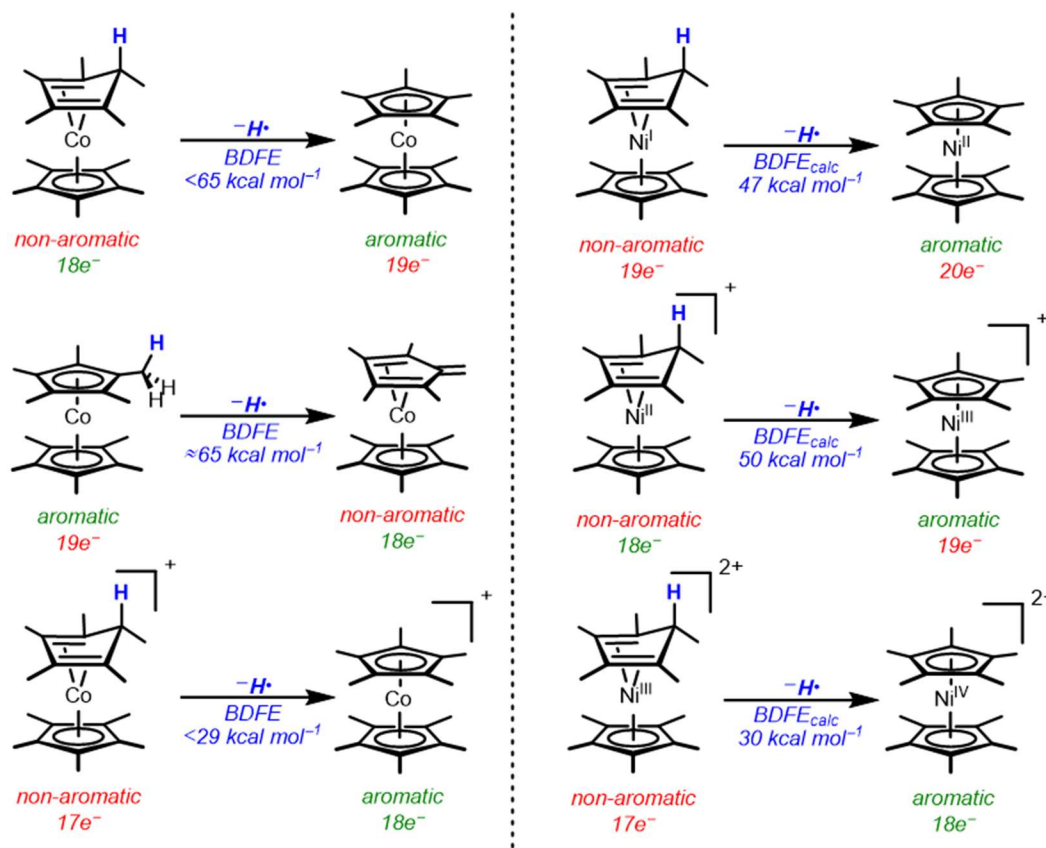


Figure 5.10: (left) A comparison of the experimental $\text{BDFE}_{\text{C-H}}$ for a variety of related Cp*Co-species, demonstrating the importance of aromaticity and electron count in predicting the stability of the indicated C–H bond. (right) A comparison of computational $\text{BDFE}_{\text{C-H}}$ values for a redox series of $[(\text{Cp}^*)\text{Ni}(\text{exo-}\eta^4\text{-C}_5\text{Me}_5\text{H})]^{n+}$.

These results emphasize that the electron count of the metal center, instead of its reducing power, can be a good predictor of the reactivity. Indeed, our DFT calculations and the relative experimental stability of $(\text{Cp}^*)\text{Ni}(\text{exo-}\eta^4\text{-C}_5\text{Me}_5\text{H})$ and $[(\text{Cp}^*)\text{Ni}(\text{exo-}\eta^4\text{-C}_5\text{Me}_5\text{H})]^+$ suggest that even though $\text{H}\cdot$ loss involves formal oxidation of the metal center the d^9 Ni^I and d^8 Ni^{II} species are less prone to PCET reactivity. However, upon oxidation to

the $d^7 \text{Ni}^{\text{III}}$ species, the C–H bond is weakened by approximately 20 kcal mol^{-1} . This weakening is due to the high stability of the $18e^-$, $d^6 [\text{Cp}^*_2\text{Ni}]^{2+}$ product resulting from net hydrogen atom transfer.

5.4 Conclusion

We have demonstrated using pulse EPR spectroscopy, supported by DFT calculations, that for Cp^*_2Co the Cp^* ring is the site of protonation. Both ring-protonated isomers (*endo* and *exo*) can be formed and observed, with the selectivity being determined by the bulk of the acid. For the *exo*-species, we were able to use the one-electron reduced, neutral congener, $(\text{Cp}^*)\text{Co}(\textit{exo}\text{-}\eta^4\text{-C}_5\text{Me}_5\text{H})$, to verify our DFT prediction that the protonated species, $[(\text{Cp}^*)\text{Co}(\textit{exo}\text{-}\eta^4\text{-C}_5\text{Me}_5\text{H})]^+$, has a remarkably weak C–H bond ($<29 \text{ kcal mol}^{-1}$). This is consistent with the suggestion that it may serve as a PCET donor in catalytic N_2RR in which it is generated in situ.

The facile protonation of Cp^*_2Co to generate $[(\text{Cp}^*)\text{Co}(\textit{exo}\text{-}\eta^4\text{-C}_5\text{Me}_5\text{H})]^+$ points to a more general strategy for developing conceptually related, strong PCET donors. Such strategies would complement current approaches for the development of PCET reagents, which rely on creating weak M–H bonds or coordination-induced weakening of O–H or N–H bonds.

We have also shown that $[(\text{Cp}^*)\text{Co}(\textit{exo}\text{-}\eta^4\text{-C}_5\text{Me}_5\text{H})]^+$ can be converted from a PCET donor to a strong hydride donor by one electron reduction, as demonstrated by the capacity of $(\text{Cp}^*)\text{Co}(\textit{exo}\text{-}\eta^4\text{-C}_5\text{Me}_5\text{H})$ to convert CO_2 to formate. This observation highlights the dual potential for metallocenes to mediate both hydride transfer and PCET steps during the proton-coupled reduction of small molecule substrates (**Figure 5.1**). Both

types of reactivity differ from the canonical role associated with metallocenes as electron transfer reagents.

5.5 References

- (1) Wilkinson, G.; Rosenblum, M.; Whiting, M. C.; Woodward, R. B. *J. Am. Chem. Soc.* **1952**, *74*, 2125–2126.
- (2) Stepnicka, P. John Wiley & Sons, Ltd: Chichester, England, 2008.
- (3) Geiger, W. E. *Organometallics* **2007**, *26*, 5738–5765.
- (4) Yandulov, D. V.; Schrock, R. R. *Science* **2003**, *301*, 76–78.
- (5) Arashiba, K.; Miyake, Y.; Nishibayashi, Y. *Nat. Chem.* **2010**, *3*, 120–125.
- (6) Hill, P. J.; Doyle, L. R.; Crawford, A. D.; Myers, W. K.; Ashley, A. E. *J. Am. Chem. Soc.* **2016**, *138*, 13521–13524.
- (7) Arashiba, K.; Eizawa, A.; Tanaka, H.; Nakajima, K.; Yoshizawa, K.; Nishibayashi, Y. *Bull. Chem. Soc. Jpn.* **2017**, *90*, 1111–1118.
- (8) Chalkley, M. J.; Del Castillo, T. J.; Matson, B. D.; Roddy, J. P.; Peters, J. C. *ACS Cent. Sci.* **2017**, *3*, 217–223.
- (9) Chalkley, M. J.; Del Castillo, T. J.; Matson, B. D.; Peters, J. C. *J. Am. Chem. Soc.* **2018**, *140*, 6122–6129.
- (10) Curphey, T. J.; Santer, J. O.; Rosenblum, M.; Richards, J. H. *J. Am. Chem. Soc.* **1960**, *82*, 5249–5250.
- (11) Liles, D. C.; Shaver, A.; Singleton, E.; Wiege, M. B. *J. Organomet. Chem.* **1985**, *288*, c33–c36.
- (12) Court, T. L.; Werner, H. *J. Organomet. Chem.* **1974**, *65*, 245–251.

- (13) Koelle, U.; Khouzami, F. *Angew. Chem. Int. Ed.* **1980**, *19*, 640–641.
- (14) Koelle, U.; Infelta, P. P.; Graetzel, M. *Inorg. Chem.* **1988**, *27*, 879–883.
- (15) Weare, W. W.; Dai, X.; Byrnes, M. J.; Chin, J. M.; Schrock, R. R.; Müller, P. *Proc. Natl. Acad. Sci. U.S.A.* **2006**, *103*, 17099–17106.
- (16) Kuriyama, S.; Arashiba, K.; Nakajima, K.; Tanaka, H.; Kamaru, N.; Yoshizawa, K.; Nishibayashi, Y. *J. Am. Chem. Soc.* **2014**, *136*, 9719–9731.
- (17) Anderson, J. S.; Rittle, J.; Peters, J. C. *Nature* **2013**, *501*, 84–87.
- (18) Del Castillo, T. J.; Thompson, N. B.; Peters, J. C. *J. Am. Chem. Soc.* **2016**, *138*, 5341–5350.
- (19) Anderson, J. S.; Cutsail, G. E.; Rittle, J.; Connor, B. A.; Gunderson, W. A.; Zhang, L.; Hoffman, B. M.; Peters, J. C. *J. Am. Chem. Soc.* **2015**, *137*, 7803–7809.
- (20) Thompson, N. B.; Green, M. T.; Peters, J. C. *J. Am. Chem. Soc.* **2017**, *139*, 15312–15315.
- (21) Yandulov, D. V.; Schrock, R. R. *Inorg. Chem.* **2005**, *44*, 1103–1117.
- (22) Wickramasinghe, L. A.; Schrock, R. R.; Tsay, C.; Müller, P. *Inorg. Chem.* **2018**, *57*, 15566–15574.
- (23) Malischewski, M.; Seppelt, K.; Sutter, J.; Heinemann, F. W.; Dittrich, B.; Meyer, K. *Angew. Chem. Int. Ed.* **2017**, *56*, 13372–13376.
- (24) Hyde, J. S.; Pasenkiewicz-Gierula, M.; Jesmanowicz, A.; Antholine, W. E. *Appl. Magn. Reson.* **1990**, *1*, 483–496.
- (25) Wittke, J. P.; Dicke, R. H. *Phys. Rev.* **1956**, *103*, 620–631.
- (26) Hu, Y.; Shaw, A. P.; Estes, D. P.; Norton, J. R. *Chem. Rev.* **2016**, *116*, 8427–8462.
- (27) Brown, T. L. *Acc. Chem. Res.* **1974**, *7*, 408–415.

- (28) Tao, J.; Perdew, J. P.; Staroverov, V. N.; Scuseria, G. E. *Phys. Rev. Lett.* **2003**, *91*, 146401–146404.
- (29) Becke, A. D. *Phys. Rev. A* **1988**, *38*, 3098–3100.
- (30) Perdew, J. P. *Phys. Rev. B* **1986**, *33*, 8822–8824.
- (31) Lee, C.; Yang, W.; Parr, R. G. *Phys. Rev. B* **1988**, *37*, 785–789.
- (32) Miehlich, B.; Savin, A.; Stoll, H.; Preuss, H. *Chemical Physics Letters* **1989**, *157*, 200–206.
- (33) Becke, A. D. *J. Chem. Phys.* **1993**, *98*, 5648–5652.
- (34) Harmer, J.; Finazzo, C.; Piskorski, R.; Ebner, S.; Duin, E. C.; Goenrich, M.; Thauer, R. K.; Reiher, M.; Schweiger, A.; Hinderberger, D.; et al. *J. Am. Chem. Soc.* **2008**, *130*, 10907–10920.
- (35) Kinney, R. A.; Saouma, C. T.; Peters, J. C.; Hoffman, B. M. *J. Am. Chem. Soc.* **2012**, *134*, 12637–12647.
- (36) Green, M. L. H.; Pratt, L.; Wilkinson, G. *J. Chem. Soc.* **1959**, *0*, 3753–3767.
- (37) Izutsu, K. *Handbook of Reference Electrodes*; Inzelt, G., Lewenstam, A., Scholz, F., Eds.; Springer: Berlin, Heidelberg, 2013; pp 145–187.
- (38) Van Duyne, R. P.; Reilly, C. N. *Anal. Chem.* **1972**, *44*, 142–152.
- (39) Koelle, U. *Inorg. Chim. Acta* **1981**, *47*, 13–18.
- (40) Wiedner, E. S.; Chambers, M. B.; Pitman, C. L.; Bullock, R. M.; Miller, A. J. M.; Appel, A. M. *Chem. Rev.* **2016**, *116*, 8655–8692.
- (41) Ilic, S.; Alherz, A.; Musgrave, C. B.; Glusac, K. D. *Chem. Soc. Rev.* **2018**, *47*, 2809–2836.
- (42) Ohki, Y.; Murata, A.; Imada, M.; Tatsumi, K. *Inorg. Chem.* **2009**, *48*, 4271–4273.

- (43) Bühl, M.; Grigoleit, S. *Organometallics* **2005**, *24*, 1516–1527.
- (44) Sharma, N.; Ajay, J. K.; Venkatasubbaiah, K.; Lourderaj, U. *Phys. Chem. Chem. Phys.* **2015**, *17*, 22204–22209.
- (45) Geiger, W. E.; Bowden, W. L.; El Murr, N. *Inorg. Chem.* **1979**, *18*, 2358–2361.
- (46) Werner, H.; Demberger, Th. *J. Organomet. Chem.* **1980**, *198*, 97–103.
- (47) Pitman, C. L.; Finster, O. N. L.; Miller, A. J. M. *Chem. Commun.* **2016**, *52*, 9105–9108.
- (48) Quintana, L. M. A.; Johnson, S. I.; Corona, S. L.; Villatoro, W.; Goddard, W. A.; Takase, M. K.; VanderVelde, D. G.; Winkler, J. R.; Gray, H. B.; Blakemore, J. D. *Proc. Natl. Acad. Sci. U.S.A.* **2016**, *113*, 6409–6414.
- (49) Johnson, S. I.; Gray, H. B.; Blakemore, J. D.; Goddard, W. A. *Inorg. Chem.* **2017**, *56*, 11375–11386.
- (50) Crossley, S. W. M.; Obradors, C.; Martinez, R. M.; Shenvi, R. A. *Chem. Rev.* **2016**, *116*, 8912–9000.
- (51) Gentry, E. C.; Knowles, R. R. *Acc. Chem. Res.* **2016**, *49*, 1546–1556.
- (52) Hartung, J.; Norton, J. R. *Catalysis without Precious Metals*; Bullock, R. M., Ed.; WILEY-VCH Verlag GmbH & Co., 2010; pp 1–21.
- (53) Cuerva, J. M.; Campaña, A. G.; Justicia, J.; Rosales, A.; Oller-López, J. L.; Robles, R.; Cárdenas, D. J.; Buñuel, E.; Oltra, J. E. *Angew. Chem. Int. Ed.* **2006**, *45*, 5522–5526.
- (54) Chciuk, T. V.; Flowers, R. A. *J. Am. Chem. Soc.* **2015**, *137*, 11526–11531.
- (55) Chciuk, T. V.; Anderson, W. R.; Flowers, R. A. *J. Am. Chem. Soc.* **2016**, *138*, 8738–8741.

- (56) Chciuk, T. V.; Anderson, W. R.; Flowers, R. A. *J. Am. Chem. Soc.* **2018**, *140*, 15342–15352.
- (57) Kolmar, S. S.; Mayer, J. M. *J. Am. Chem. Soc.* **2017**, *139*, 10687–10692.
- (58) Kölle, U.; Khouzami, F.; Lueken, H. *Chem. Ber.* **1982**, *115*, 1178–1196.

Chapter 6.
Metalloenes: Beyond Electron Transfer to
Proton-Coupled Electron Transfer

6.1 Introduction

The high stability of the bis-cyclopentadienyl (Cp) ligand framework has allowed a remarkable number of metallocenes (Cp_2M) to be isolated, often in multiple redox states $[\text{Cp}_2\text{M}]^{n+}$ making many of these reagents useful as electron transfer reagents. Indeed, the $[\text{Cp}_2\text{Fe}]^{0/+}$ redox couple is the canonical example of a reversible electron transfer in organometallic chemistry. The bis-cyclopentadienyl scaffold also stabilizes formally electron excessive ($>18e^-$) complexes such as Cp_2Co that are strong reductants. Indeed, our group first became interested in metallocenes, when we discovered that permethylated cobaltocene, Cp^*_2Co , is an efficient electron donor for the reduction of N_2 -to- NH_3 in the presence of a trisphosphine borane Fe species, $(\text{P}_3^{\text{B}})\text{Fe}$, and excess diphenylammonium or anilinium acids. Under such conditions high selectivity for NH_3 was attainable (up to 80%),^{1,2} akin to results from other groups with Mo ^{3,4} and Fe .⁵ We hypothesized that given the ubiquity of metallocenes in high-efficiency N_2 -fixation catalysis that Cp^*_2Co or related reducing metallocenes (*e.g.*, Cp_2Co or Cp^*_2Cr) were not only serving as electron transfer reagents, but could also be protonated to generate species with weak C–H bonds that would therefore be strong PCET reagents.¹ Significant circumstantial evidence from stoichiometric experiments and theory suggested that such species had a role in N–H bond forming reactions during nitrogen fixation both chemical and electrochemical.² We ultimately found conditions under which, we could characterize the highly reactive protonated Cp^*_2Co via its precipitation at low temperature and the employ of solid-state pulse electron paramagnetic resonance (EPR) spectroscopy. Consistent with our calculations, we found that Cp^*_2Co underwent protonation on the Cp^* ring to form $[(\text{Cp}^*)\text{Co}(\textit{endo/exo}\text{-}\eta^4\text{-C}_5\text{Me}_5\text{H})]^+$ with the *endo*- vs *exo*-selectivity determined by the steric bulk of the acid. This allowed us to use the much more stable

$(\text{Cp}^*)\text{Co}(\text{exo-}\eta^4\text{-C}_5\text{Me}_5\text{H})$ to indirectly verify our hypothesis that the protonated Cp^*_2Co is a strong hydrogen atom donor ($\text{BDFE}_{\text{C-H}} < 29 \text{ kcal mol}^{-1}$).⁶

In our efforts to study electrocatalytic nitrogen fixation, we had observed that the addition of co-catalytic $[\text{Cp}^*_2\text{Co}]^+$ to controlled potential electrolyses (CPEs) containing $[(\text{P}_3^{\text{B}})\text{Fe}]^+$, N_2 , and excess diphenylammonium boosted the yield of NH_3 from the electrocatalytic (2.6 \pm 0.3 equiv per Fe) to the electrocatalytic regime (4.0 \pm 0.6 equiv per Fe and Co). This was despite the fact that CPE experiments of $[\text{Cp}^*_2\text{Co}]^+$ under an N_2 atmosphere in the presence of excess acid do not reveal the formation of any NH_3 only H_2 . Probing the $[\text{Cp}^*_2\text{Co}]^{+/0}$ couple by cyclic voltammetry (CV) reveals that it becomes irreversible and shows moderate current enhancement upon the addition of diphenylammonium, consistent with catalytic HER.² Although these data suggest that under electrocatalytic conditions in the presence of excess acid, the strong hydrogen atom donors $[(\text{Cp}^*)\text{Co}(\text{endo/exo-}\eta^4\text{-C}_5\text{Me}_5\text{H})]^+$ could be formed, it remained unclear whether such a species built up in such a way that might allow it to react via H-atom donation. Instead, it might be that Cp^*_2Co , an electron donor ($E^0 = -1.91 \text{ V vs Fc}^{+/0}$ in MeCN), or that $(\text{Cp}^*)\text{Co}(\text{endo/exo-}\eta^4\text{-C}_5\text{Me}_5\text{H})$, a hydride donor ($\Delta G(\text{H}^-) < 41 \text{ kcal mol}^{-1}$ in MeCN), was the kinetically relevant species under these conditions.

We were interested in the active species, because there are a paucity of examples of species that provide access to freely diffusing strong H-atom donors ($\text{BDFE}_{\text{X-H}} < 50 \text{ kcal mol}^{-1}$) without rapidly evolving H_2 under electrocatalytic conditions. This contrasts with the many organic or organometallic species that under reductive conditions in the presence of

acid provide access to freely diffusing electron donors^{7,8} or freely diffusing hydride donors.⁹⁻¹¹ Indeed, freely diffusing electron donors are frequently employed as redox mediators^{7,8} while freely diffusing hydride donors are involved in many proton-coupled reductions.⁹⁻¹¹ This led us to believe that freely diffusing strong PCET reagents would be similarly useful. Weak PCET reagents ($BDFE_{X-H} > 50 \text{ kcal mol}^{-1}$) have already found utility as co-catalysts in the electrocatalytic reduction of O_2 to H_2O .^{12,13} An electrochemical means of generating a strong net H-atom donors would be complementary to photochemical strategies using acids and Rh or Ir photoreductants,¹⁴⁻¹⁶ and chemical strategies that use Sm^{II} -aquo complexes¹⁷⁻¹⁹ or $M-H$ species derived from the reaction of M^{II} salts ($M^{II} = Mn, Fe, Co$) with silanes and alcohols^{20,21} that have been exploited for organic synthesis. Strong PCET donors are particularly useful for the functionalization of unsaturated substrates, because hydrogen-atom donation cleaves a π -bond; the resultant $X-H$ bond is consequently weakened by the α -radical. Although challenging to generate, this radical intermediate has proven highly synthetically versatile allowing for hydrofunctionalization reactions, non-syn hydrogenations, and three-component couplings.²⁰

Although, we ultimately uncovered that parent cobaltocenes are not suitable for the electrocatalytic generation of strong PCET donors, we demonstrate a simple synthetic strategy for modifying them to achieve this goal. We characterize this novel PCET donor via chemical and electrochemical means and demonstrate the utility of this new, base-appended cobaltocene in the electrocatalytic proton-coupled reduction of ketones to pinacols.

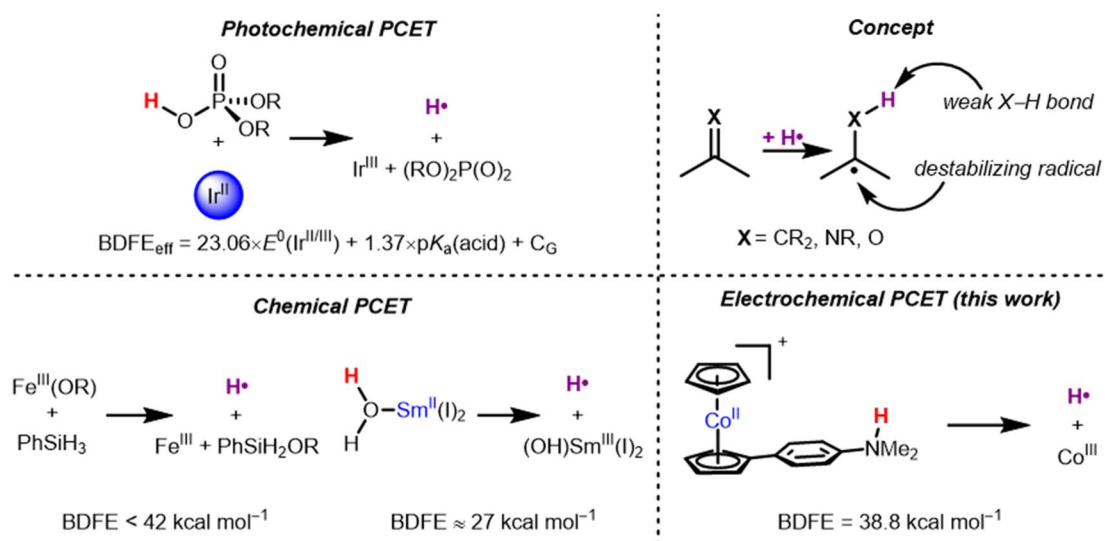


Figure 6.1: Overview of PCET for the functionalization of unsaturated substrates. (top left) The combination of phosphoric acids and iridium photoreductants have been shown to be strong PCET donors.^{15,16} (bottom left) The combination of silanes and Fe^{III} alkoxides^{20,21} and Sm^{II} with water have been shown to generate strong PCET donors.^{17–19,22} (top right) PCET to an unsaturated organic substrate results in a new X–H bond that is unusually weak due to the α -radical. (bottom right) A novel, strong PCET donor synthesized and characterized herein suitable for the electrocatalytic reduction of ketones to pinacols.

6.2 Results

6.2A Mechanism of Electrocatalytic HER by [Cp₂Co]⁺

DFT calculations suggest that much like Cp*₂Co, Cp₂Co should undergo ring-protonation to form a species that is a strong PCET reagent (BDFE_{calc} = 33.8 kcal mol⁻¹). Cyclic voltammograms of 1 mM [Cp₂Co]⁺ at 10 mV/s with a boron-doped diamond (BDD) working electrode in the presence of 100 equiv of 4-cyanoanilinium ([^{4-CN}PhNH₃]⁺) in a 200 mM [TBA][PF₆] solution of DME demonstrate an irreversible wave at the [Cp₂Co]⁺⁰ couple. This feature is indicative of electrocatalytic HER, albeit the shallow slope and minimal current enhancement suggest slow catalysis. Measurement of the HER current at different concentrations of [Cp₂Co]⁺ are consistent with a reaction that is first order in Co (Figure 6.2). Increasing the scan rate to 100 mV/s leads to enhanced reversibility at the

$[\text{Cp}_2\text{Co}]^{+/0}$ couple (**Figure 6.2**), rather than at the $[(\text{Cp})\text{Co}(\eta^4\text{-C}_5\text{H}_6)]^{+/0}$ couple ($E^0 = -0.33 \text{ V vs Fc}^{+/0}$) indicating that the rate-determining step (RDS) in the HER cycle is the initial protonation of Cp_2Co . These data are consistent with previous pulse radiolytic measurements of HER by Cp_2Co .²³ Given the facile reduction of the cobaltocene protonation product, $[(\text{Cp})\text{Co}(\eta^4\text{-C}_5\text{H}_6)]^+$, at -1.33 V ($\Delta G(\text{ET}) = -23 \text{ kcal mol}^{-1}$), it seems likely that the electrocatalytic HER follows a traditional ECEC mechanism, but the current data are not definitive on this issue. Regardless, although protonation of cobaltocene (and Cp^*_2Co) generates a strong PCET donor, they are not suitable as electrocatalytic PCET mediators under our envisioned CPE conditions (negative applied bias, excess acid, *vide infra*).

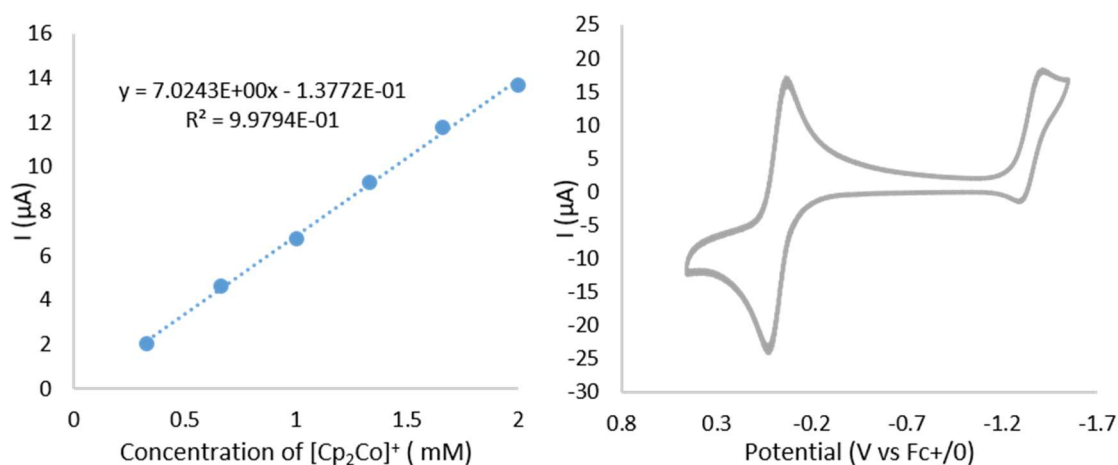


Figure 6.2: Cyclic voltammetry relevant to HER by $[\text{Cp}_2\text{Co}]^+$ (left) Line of best fit for relationship between the plateau current and $[\text{Cp}_2\text{Co}]^+$ concentration in the HER reaction at a BDD electrode in DME with 100 mM $[\text{}^4\text{-CNPhNH}_3][\text{OTf}]$ and 200 mM $[\text{TBA}][\text{PF}_6]$ at 10 mV/s. (right) CV of $[\text{Cp}_2\text{Co}]^+$ at a BDD electrode in DME with 100 mM $[\text{}^4\text{-CNPhNH}_3][\text{OTf}]$ and 200 mM $[\text{TBA}][\text{PF}_6]$ at 100 mV/s demonstrating significant reversibility at the $[\text{Cp}_2\text{Co}]^{+/0}$ couple.

This lack of suitability emerges from two problems. The first is that protonation of the Cp ligand is slow. This is consistent with a large body of physical organic literature

demonstrating that (de)protonations at carbon are slow relative to those at nitrogen or oxygen.²⁴ Secondly, protonation of the Cp (or Cp*) ligand results in the formation of an electron-accepting diolefinic ligand which makes subsequent reduction more favorable. This effect has been discussed in the context of half-sandwich (Cp*)**Rh** complexes that undergo ring-protonation.²⁵ We anticipated that by synthetically appending a Brønsted base to the cobaltocene, we would both accelerate the rate of protonation and retain the bis-Cp ligand framework thereby disfavoring a second reduction by avoiding formation of an electron-accepting diolefin ligand.

6.2B Synthesis of a Brønsted Base-Appended Cobaltocene

Unlike with ferrocene,²⁶ there are relatively few synthetic strategies for elaborating cobaltocenes. One strategy that has been successfully used is the addition of aryllithium reagents to $[\text{Cp}_2\text{Co}]^+$ to generate an *exo*-substituted cyclopentadienyl cyclopentadiene Co complex from which a hydride can often be extracted to yield the desired, mono-substituted cobaltocenium in reasonable yields.^{27,28} Addition of a THF solution of 4-lithio-N,N-dimethylaniline to a stirred suspension of $[\text{Cp}_2\text{Co}][\text{PF}_6]$ in THF at $-78\text{ }^\circ\text{C}$ led to the desired nucleophilic addition product (**Figure 6.3**). Although hydride abstraction from this species was unsuccessful, reflux of this species in 5:1 methylcyclohexane:benzene led to the formal loss of $1/2\text{ H}_2$ and rearomatization of the Cp ring yielding $(\text{Cp})\text{Co}(\text{Cp}^{\text{N}})$ (Cp^{N} = 4-cyclopentadienyl-N,N-dimethylaniline, **Figure 6.3**). This species was readily oxidized to $[(\text{Cp})\text{Co}(\text{Cp}^{\text{N}})][\text{OTf}]$ by reaction with AgOTf at room temperature (**Figure 6.3**). This oxidized species is readily protonated by HOTf in DME to form $[(\text{Cp})\text{Co}(\text{Cp}^{\text{NH}})][\text{OTf}]_2$ (Cp^{NH} = 4-cyclopentadienyl-N,N-dimethylanilinium, **Figure 6.3**). X-ray structures of

$(\text{Cp})\text{Co}(\text{Cp}^{\text{N}})$, $[(\text{Cp})\text{Co}(\text{Cp}^{\text{N}})]^+$, $[(\text{Cp})\text{Co}(\text{Cp}^{\text{NH}})]^{2+}$ confirm that, as hoped, the primary coordination sphere is minimally perturbed by redox or protonation (**Figure 6.4**).

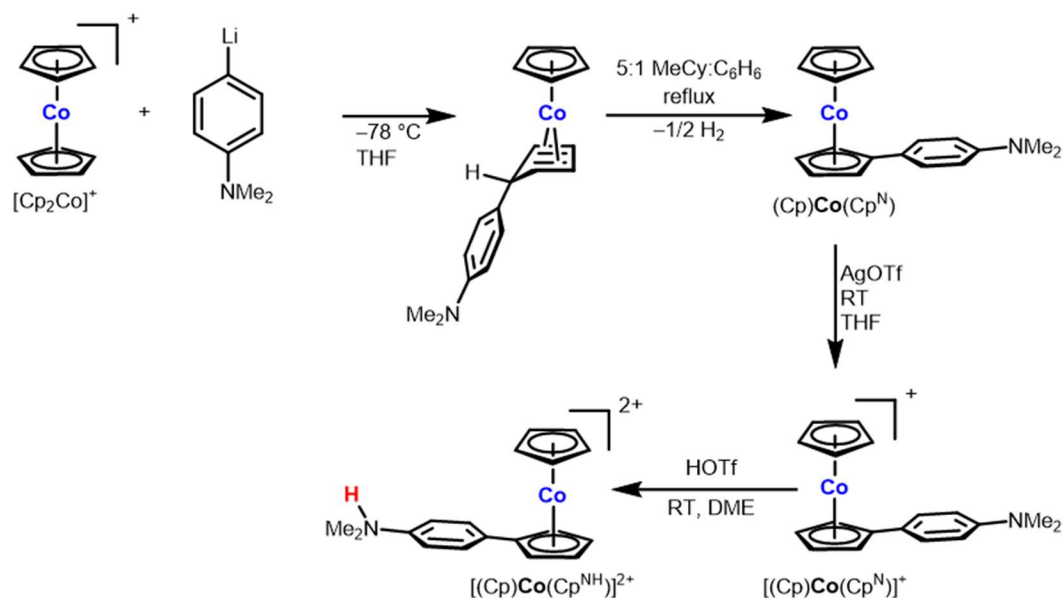


Figure 6.3: Scheme describing the synthesis of the Brønsted base appended cobaltocenes.

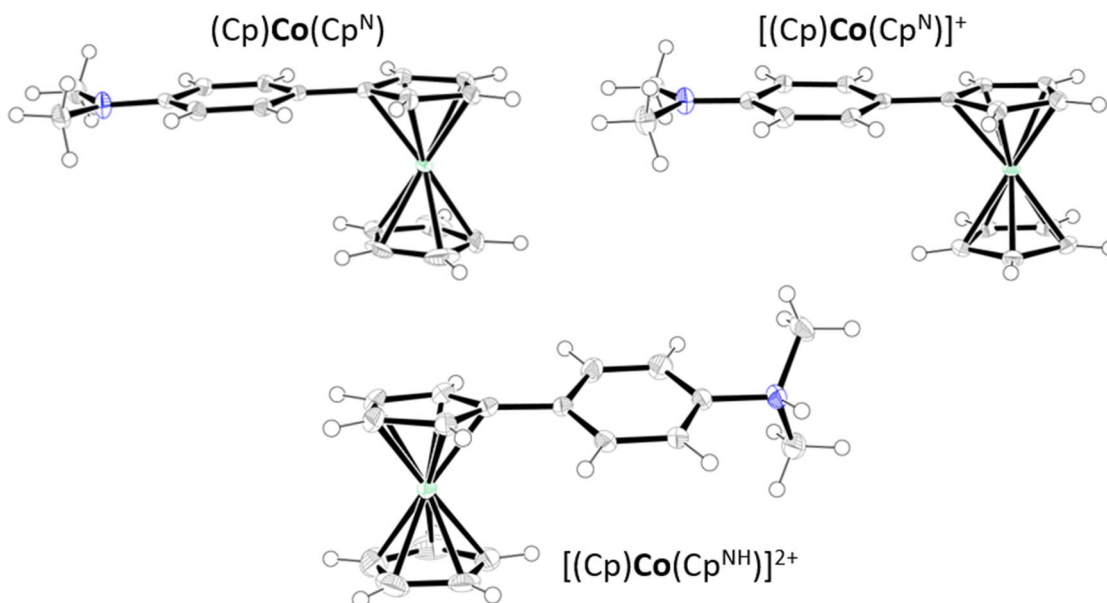


Figure 6.4: X-ray structure of $(\text{Cp})\text{Co}(\text{Cp}^{\text{N}})$, $[(\text{Cp})\text{Co}(\text{Cp}^{\text{N}})]^+$, and $[(\text{Cp})\text{Co}(\text{Cp}^{\text{NH}})]^{2+}$ with counteranions and solvent omitted for clarity. Ellipsoids shown at 50% probability.

With these complexes in hand, we assessed our ability to chemically access our desired PCET donor, $[(\text{Cp})\text{Co}(\text{Cp}^{\text{NH}})]^+$. Continuous-wave X-band electron paramagnetic resonance spectroscopy at 77 K of rapidly freeze quenched reaction mixtures (**Figure 6.5**) of either $[(\text{Cp})\text{Co}(\text{Cp}^{\text{NH}})]^{2+}$ with SmI_2 or $(\text{Cp})\text{Co}(\text{Cp}^{\text{N}})$ with trifluoromethanesulfonimide led to the observation of the same EPR signal. The signal is best fit with a roughly axial g-tensor with g-values at or below the free-electron value ($g = [2.056, 1.994, 1.791]$) consistent with other d^9 metallocenes²⁹ and distinct from the g-tensors we observed for *endo*- and *exo*-protonation of the Cp* ring in decamethylcobaltocene.⁶ We thus assign this species to be $[(\text{Cp})\text{Co}(\text{Cp}^{\text{NH}})]^+$. UV-Vis spectroscopy of the reaction of $(\text{Cp})\text{Co}(\text{Cp}^{\text{N}})$ with trifluoromethanesulfonimide at -130 °C in 4:1 2-MeTHF:THF demonstrates isobestic behavior, consistent with the formation of a single product (**Figure 6.5**). Warming of these reactions to room temperature ultimately led to decomposition to form $[(\text{Cp})\text{Co}(\text{Cp}^{\text{N}})]^+$ consistent with the high thermodynamic driving force for formal H_2 loss.

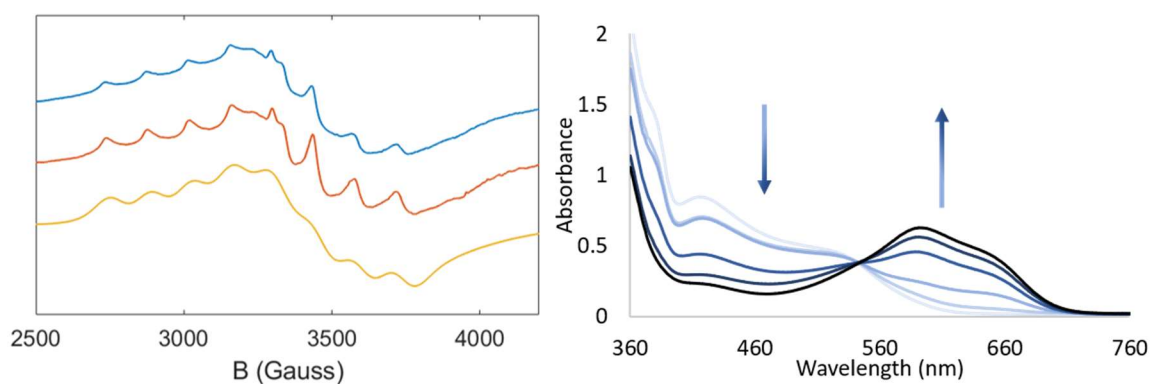


Figure 6.5: Spectroscopic data for $[(\text{Cp})\text{Co}(\text{Cp}^{\text{NH}})]^+$. (left) Freeze-quench EPR data for $[(\text{Cp})\text{Co}(\text{Cp}^{\text{NH}})]^+$ formed either via the reduction of $[(\text{Cp})\text{Co}(\text{Cp}^{\text{NH}})]^{2+}$ with SmI_2 (blue) or the protonation of $(\text{Cp})\text{Co}(\text{Cp}^{\text{N}})$ with bistrifluoromethanesulfonimide (red) and their simulation (orange). (right) UV-Vis spectroscopy for the reaction of $(\text{Cp})\text{Co}(\text{Cp}^{\text{N}})$ with 1.5 equiv of bistrifluoromethanesulfonimide in 4:1 2-MeTHF:THF at -130 °C.

6.2C Thermochemical Properties of a Brønsted Base-Appended Cobaltocene

We next set out to perform thermochemical experiments in order to confirm that $[(\text{Cp})\text{Co}(\text{Cp}^{\text{NH}})]^+$ is indeed a strong PCET donor. The electrochemical properties of $[(\text{Cp})\text{Co}(\text{Cp}^{\text{N}})]^+$ were evaluated in a 100 mM [TBA][PF₆] acetonitrile solution on a glassy carbon working electrode. A cyclic voltammogram revealed a reversible reduction to $(\text{Cp})\text{Co}(\text{Cp}^{\text{N}})$ at -1.35 V vs $\text{Fc}^{+/0}$, a minimal perturbation from the $[\text{Cp}_2\text{Co}]^{+/0}$ couple ($E^0 = -1.33$ V vs $\text{Fc}^{+/0}$). Also apparent is a pseudo-reversible oxidation to $[(\text{Cp})\text{Co}(\text{Cp}^{\text{N}})]^{2+}$ at 0.52 V vs $\text{Fc}^{+/0}$, which we assign to an N-centered oxidation on the basis of the similar oxidation potential for N,N-dimethylaniline (0.38 V vs $\text{Fc}^{+/0}$ in acetonitrile).³⁰ The enhanced reversibility of this peak relative to that of parent N,N-dimethylaniline suggests that the cobaltocenium substituent helps to stabilize the resultant aminium radical. We also observe a pseudo-reversible reduction at ~ -2.25 V vs $\text{Fc}^{+/0}$ to form $[(\text{Cp})\text{Co}(\text{Cp}^{\text{N}})]^-$; this redox feature is fully reversible in DME (-2.42 V vs $\text{Fc}^{+/0}$) consistent with observations of the $[\text{Cp}_2\text{Co}]^{0/-}$ couple.³¹

To ascertain the $\text{p}K_{\text{a}}$ of $[(\text{Cp})\text{Co}(\text{Cp}^{\text{NH}})]^{2+}$, ¹H NMR spectra in MeCN-*d*₃ were recorded of titration experiments with aniline bases. In particular, titration experiments with ⁴-ClPhNH₂ ($\text{p}K_{\text{a}}([\text{}^4\text{-ClPhNH}_3]^+) = 9.60$)³² and ²-ClPhNH₂ ($\text{p}K_{\text{a}}([\text{}^2\text{-ClPhNH}_3]^+) = 7.86$)³³ reveal that the $\text{p}K_{\text{a}}$ of $[(\text{Cp})\text{Co}(\text{Cp}^{\text{NH}})]^{2+}$ is 8.86 ± 0.02 . The enhanced acidity relative to N,N-dimethylanilinium ($\text{p}K_{\text{a}} = 11.4$)³³ is consistent with the introduction of the electron-withdrawing cobaltocenium at the para-position.

Oxidative scans of $[(\text{Cp})\text{Co}(\text{Cp}^{\text{NH}})]^{2+}$ in 100 mM $[\text{TBA}][\text{PF}_6]$ do not lead to the observation of any waves before the solvent window, consistent with our above assignment of the $[(\text{Cp})\text{Co}(\text{Cp}^{\text{N}})]^{2+/+}$ couple to an N-centered oxidation. Cathodic scans of $[(\text{Cp})\text{Co}(\text{Cp}^{\text{NH}})]^{2+}$ lead to the observation of a fully reversible wave ($E_{\text{red}} = -1.20$ V vs $\text{Fc}^{+/0}$) at moderate scan rates 100-1000 mV/s (**Figure 6.6**). With the collected data, we can determine the N–H BDFE of $[(\text{Cp})\text{Co}(\text{Cp}^{\text{NH}})]^+$, to be $38.8 \text{ kcal mol}^{-1}$ (**Figure 6.7, Eq 6.1**) satisfying one of our criteria for a strong PCET donor ($\text{BDFE} < 50 \text{ kcal mol}^{-1}$).

$$\text{Eq 6.1) BDFE} = 1.37 \times \text{p}K_{\text{a}} + 23.06 \times E^0 + C_{\text{G}}$$

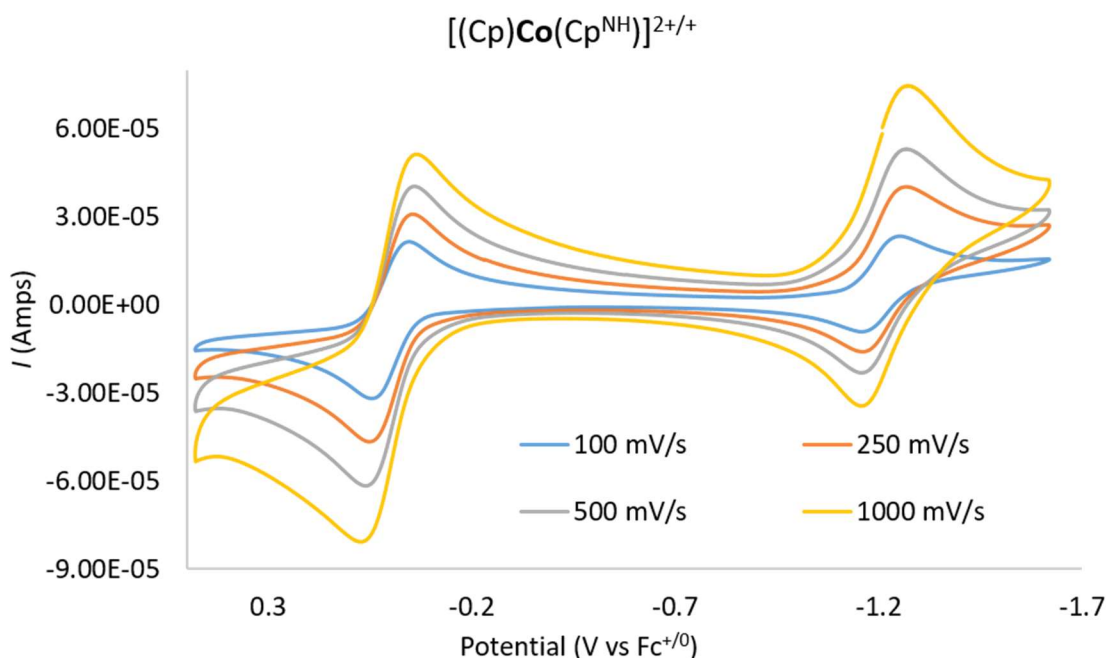


Figure 6.6: Variable scan rate CVs of 1 mM $[(\text{Cp})\text{Co}(\text{Cp}^{\text{NH}})]^{2+}$ and 1 mM Fc in 100 mM $[\text{TBA}][\text{PF}_6]$ solution of acetonitrile at a boron-doped diamond working electrode.

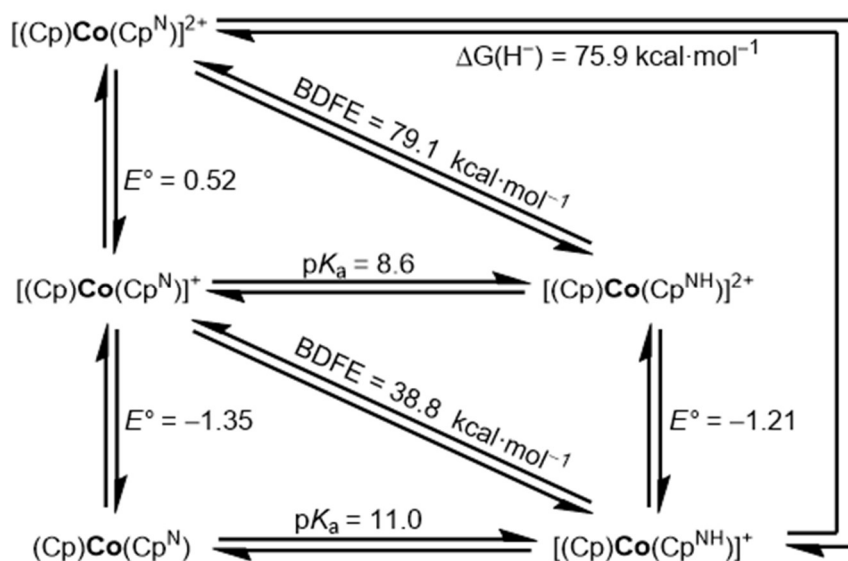


Figure 6.7: Thermochemistry of $[(\text{Cp})\text{Co}(\text{Cp}^{\text{N}(\text{H})})]^{n+}$ in acetonitrile. Potentials are in V vs $\text{Fc}^{+/0}$.

6.2D Electrochemical behavior of $(\text{Cp})\text{Co}(\text{Cp}^{\text{N}})$ with Excess Acid

Addition of 1 mmol of $[(\text{Cp})\text{Co}(\text{Cp}^{\text{N}})]^+$ to a DME solution containing 100 mM $[\text{Cp}^{\text{N}}\text{PhNH}_3][\text{OTf}]$ leads to instantaneous formation of $[(\text{Cp})\text{Co}(\text{Cp}^{\text{NH}})]^{2+}$ consistent with their respective $\text{p}K_{\text{a}}$'s in acetonitrile (7.0 vs 8.6). Notably protonation is the slow step in Cp_2Co -mediated HER. Here the Co species is protonated even before reduction, nonetheless these CV's demonstrate appreciable reversibility even at 10 mV/s (**Figure 6.8**). Thus, $[(\text{Cp})\text{Co}(\text{Cp}^{\text{NH}})]^+$ is an even worse HER catalyst than Cp_2Co presumably because further protonation or reduction is unfavorable under these conditions and thus the only mechanism for HER is bimolecular. Potentially, the slow bimolecular H_2 evolution is due to the electronically decoupled nature of the Co center and the N–H bond (**Figure 6.8**). These data suggest that we have developed a species that met all of the criteria we had established for an electrocatalytic, strong PCET donor: 1) slow HER catalyst, 2) X–H bond strength of less

than 50 kcal mol⁻¹, and 3) H• transfer is the thermodynamically preferred mode of reactivity as opposed to H⁺ or H⁻ transfer (**Figure 6.7**).

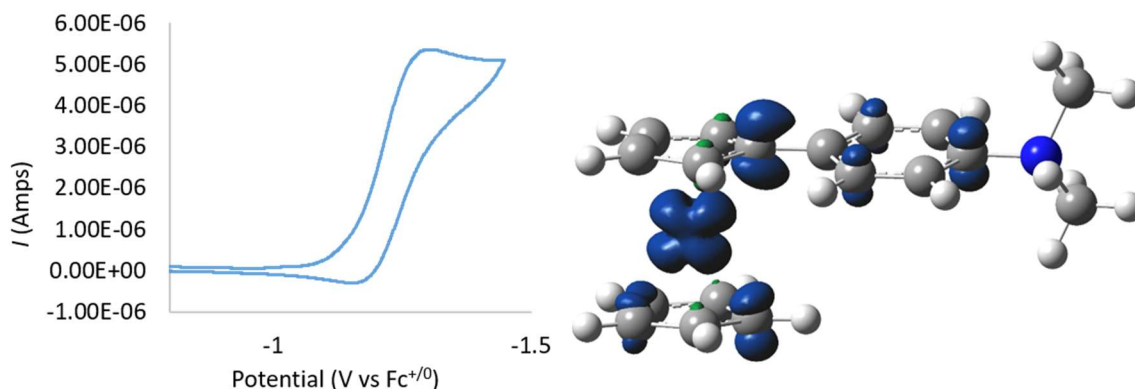


Figure 6.8: (left) Cyclic voltammogram of (Cp)Co(Cp^N) in the presence of 100 mM of [4⁻CNPhNH₃][OTf] in 200 mM [TBA][PF₆] DME at 10 mV/s with the acid background subtracted. (right) Spin density plot of [(Cp)Co(Cp^{NH})] [OTf] at an isovalue of 0.04 demonstrating that the N–H bond is entirely decoupled from the spin density.

6.2E Electrochemical Behavior in the Presence of a Hydrogen Atom Acceptor

To explore the possibility of electrocatalytic PCET, we sought out a model substrate for which thermodynamics favored a PCET pathway. DFT calculations suggest that acetophenone is an ideal substrate. The calculated O–H bond strength of the radical intermediate is well-matched to that of our catalyst (BDFE_{O–H} = 38.7 kcal mol⁻¹, ΔG(PCET) = 0 kcal mol⁻¹), while both the ET to form the ketyl anion (ΔG(ET) = +26 kcal mol⁻¹) and PT to form the oxonium (ΔG(PT) = +19 kcal mol⁻¹) are significantly uphill (**Figure 6.9**). These calculated energies for electron transfer and proton transfer are consistent with the known experimental reduction potential and pK_a of acetophenone.^{34,35} We were particularly interested in this substrate because recently it has been demonstrated that photochemical PCET strategies are a means of selectively forming pinacol products at potentials much more mild than traditional, ET routes.^{36,37}

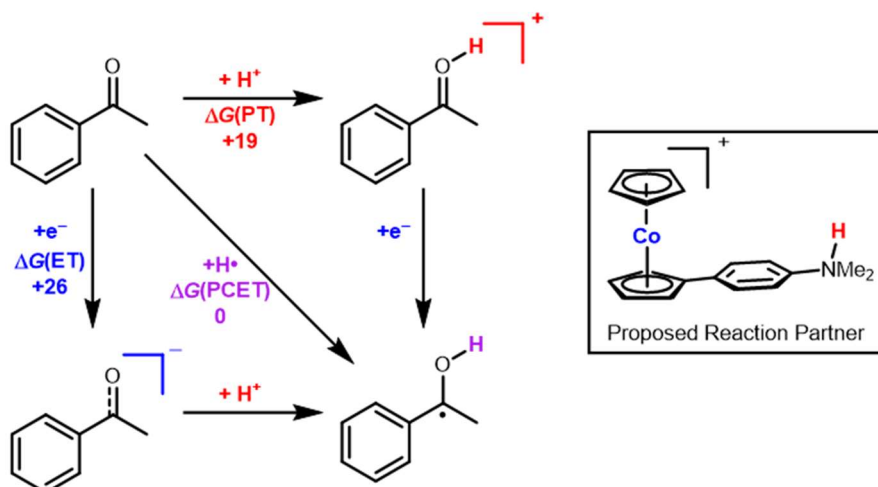


Figure 6.9: DFT calculated thermodynamics of PT, ET, and PCET for the reaction of acetophenone with the $[(\text{Cp})\text{Co}(\text{Cp}^{\text{NH}})]^+$.

To test the suitability of acetophenone as a hydrogen-atom acceptor, we added 12 equiv of the ketone to the aforescribed solution containing 1 mM $[(\text{Cp})\text{Co}(\text{Cp}^{\text{NH}})]\text{[OTf]}$, 100 mM $[\text{}^4\text{CNPhNH}_3]\text{[OTf]}$, and 200 mM $[\text{TBA}]\text{[PF}_6]$. Cyclic voltammograms at 100 mV/s after the addition of the ketone lead to the observation of enhanced current (180% increase) and the complete loss of reversibility indicating a catalytic reaction. Control CV's without $[(\text{Cp})\text{Co}(\text{Cp}^{\text{N}})]\text{[OTf]}$ do reveal slightly enhanced current densities relative to the background HER reaction but significantly less than the catalytic reaction at the relevant potential. To interrogate the product of these CV experiments, we performed CPE experiments. Optimization of the CPE conditions ultimately led us to the use of a one-compartment cell with tosic acid ($\text{p}K_{\text{a}}$ of 8.45 in MeCN),³⁸ and a glassy-carbon counter electrode. The one-compartment cell was necessary to avoid diffusion of the acetophenone out of the working compartment. The tosic acid was necessary due to undesirable anodic reactivity of the conjugate base of anilinium acids. Lastly, although reasonable results could be obtained with a Pt mesh counter electrode (35.7% FE for pinacol, 38.4% FE for H_2 , **Table 4.1**, Entry 1)

substantially higher turnover number (10.5 vs 41.6) could be achieved with a glassy-carbon counter electrode (**Table 6.1**). This improved performance with a glassy carbon counter electrode could be due to favorable adsorption of the ketone on the Pt electrode, as no ketone was recovered in this experiment despite the lower yield of pinacol.

Table 6.1. Results from CPE experiments on a DME solution of 200 mM [TBA][PF₆], 100 mM tosic acid, 50 mM acetophenone at -1.45 V vs Ag⁺⁰

Catalyst	Counter Electrode	Pinacol Yield	Ketone Recovery	Pinacol TON (FE)	H ₂ Yield (FE)	Q (C)
1 mM [(Cp)Co(Cp ^N)] [OTf]	Pt	22%	5%	11 (36%)	12% (38%)	21
1 mM [(Cp)Co(Cp ^N)] [OTf]	Glassy Carbon	83%	11%	42 (39%)	48% (45%)	72
1 mM [Cp ₂ Co] [PF ₆]	Glassy Carbon	6%	0%	3 (3%)	66% (62%)	72
none	Glassy Carbon	10%	0%	N/A (47%)	1% (8%)	8

Under our optimized conditions (200 mM [TBA][PF₆], 100 mM tosic acid, 50 mM acetophenone, 1 mM [(Cp)Co(Cp^N)] [OTf], BDD working electrode, and glassy carbon counter electrode) a CPE experiment at -1.45 V for ~53 hours with stirring results in the passage of 71.6 Coulombs (**Figure 6.10**). Analysis of the headspace by gas chromatography revealed the formation of H₂ (45.0% FE). Analysis of the solution phase products by comparison of their GC-MS and GC-FID traces to authentic standards after work-up led to

the identification of 83.2% yield for pinacol (39.0% FE) and 10.8% recovery of the ketone (**Table 6.1**, Entry 2). No 1-phenylethanol or other reduction products were identified. Differential pulse voltammograms (DPV's) taken of the bulk solution with a fresh electrode after the CPE experiment reveals redox features assignable to both the reduction and oxidation of $[(\text{Cp})\text{Co}(\text{Cp}^{\text{N}})][\text{OTf}]$. Furthermore, x-ray photoelectron spectroscopy measurements of the BDD electrode surface after the CPE experiment does not reveal the presence of any cobalt. These observations are consistent with catalyst stability under the CPE conditions.

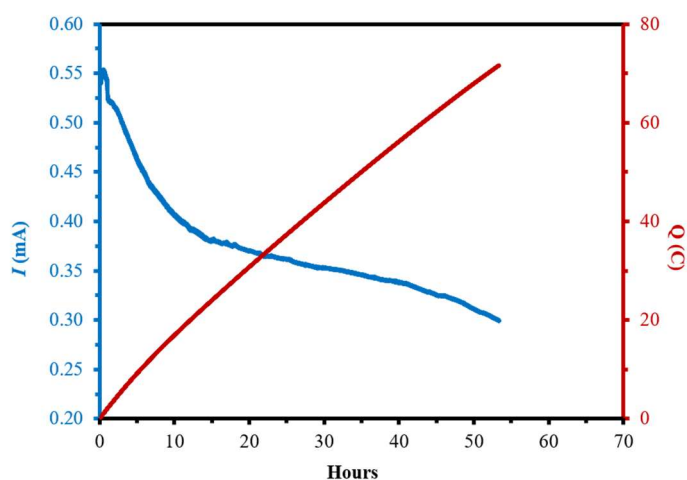


Figure 6.10: Time course of the current (I) and charge (Q) in a CPE experiment at -1.45 V vs $\text{Ag}^{+/0}$ of a 200 mM $[\text{TBA}][\text{PF}_6]$, 100 mM tosic acid, 1 mM $[(\text{Cp})\text{Co}(\text{Cp}^{\text{N}})][\text{OTf}]$ DME solution at a BDD working electrode with a glassy carbon counter electrode, and Ag wire reference electrode.

A CPE experiment for the same amount of time in the absence of our catalyst (**Table 4.1**, Entry 3) reveals minimal pinacol formation (10.4% yield) and H_2 formation (1.0% yield). The low conversion is consistent with the minimal currents observed in the CV experiments. Intriguingly, no ketone is observed suggesting that the ketone may become adsorbed or degraded over long-times in the absence of a catalytic reaction promoting its conversion. A

CPE experiment performed with 1 mM $[\text{Cp}_2\text{Co}][\text{PF}_6]$ (**Table 6.1**, Entry 4) instead of our base-appended cobalt catalyst, revealed slightly enhanced rates for HER (65.8% yield and 62.0% Fe for H_2) and a slight deterioration relative to the background for pinacol formation (5.6%). This is consistent with our hypothesis that the protonated Cp_2Co species is not the predominant reactive species under these conditions.

To mechanistically interrogate the $[(\text{Cp})\text{Co}(\text{Cp}^{\text{N}})]^{2+}$ mediated catalysis, we returned to performing cyclic voltammograms. For mechanistic experiments, we continued to use $[\text{Cp}^{\text{N}}\text{PhNH}_3][\text{OTf}]$, as the similar $\text{p}K_{\text{a}}$ of $[(\text{Cp})\text{Co}(\text{Cp}^{\text{NH}})][\text{OTf}]_2$ and tosic acid (8.6 and 8.45 in MeCN respectively) complicates the analysis due to incomplete protonation of the Co catalyst. Titrating acetophenone into a DME solution of 200 mM $[\text{TBA}][\text{PF}_6]$, 100 mM $[\text{Cp}^{\text{N}}\text{PhNH}_3][\text{OTf}]$, and 1 mM $[(\text{Cp})\text{Co}(\text{Cp}^{\text{N}})][\text{OTf}]$ results in S-shaped CV's with increasing current density (representative CV shown in **Figure 6.11**).³⁹ Plotting the plateau current observed after subtraction of the background current against the concentration of acetophenone reveals a first-order dependence on ketone (**Figure 6.11**).

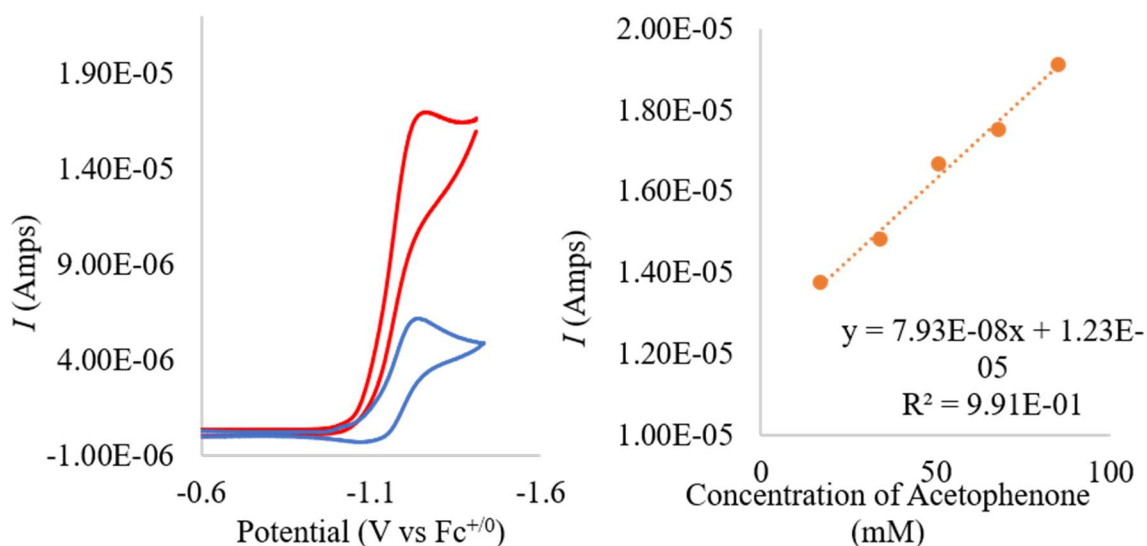


Figure 6.11: (left) Cyclic voltammograms of 1 mM [(Cp)Co(Cp^N)] [OTf] at 10 mV/s in the presence of 100 mM [4-CNPhNH₃] [OTf] and the presence (red) and absence (blue) of 50 mM acetophenone. (right) Plot of the dependence of the plateau current on the ketone concentration with a line of best fit.

Titration of [(Cp)Co(Cp^N)] [OTf] into a DME solution of 100 mM [4-CNPhNH₃] [OTf], 50 mM acetophenone, and 200 mM [TBA] [PF₆] led to observation of a first order dependence on Co concentration. Although these data indicate a rate-limiting reaction between Co and acetophenone, we find that CV's of a DME solution of 1 mM [(Cp)Co(Cp^N)] [OTf] and 50 mM acetophenone in the absence of acid demonstrates no evidence of an interaction between these two species. In contrast, CV's of [(Cp)Co(Cp^{NH})] [OTf]₂ at 100 mV/s in the presence of acetophenone (increasing from 0 to 50 equiv) leads to observation of an increasing amount of the product of H-atom transfer, [(Cp)Co(Cp^N)] [OTf] (**Figure 6.12**), behavior which is not observed in the absence of ketone. Thus, we conclude that the cumulative evidence support a mechanism involving a rate limiting reaction between [(Cp)Co(Cp^{NH})] [OTf] and acetophenone. We suggest that this reaction is a concerted proton-electron transfer (CPET).

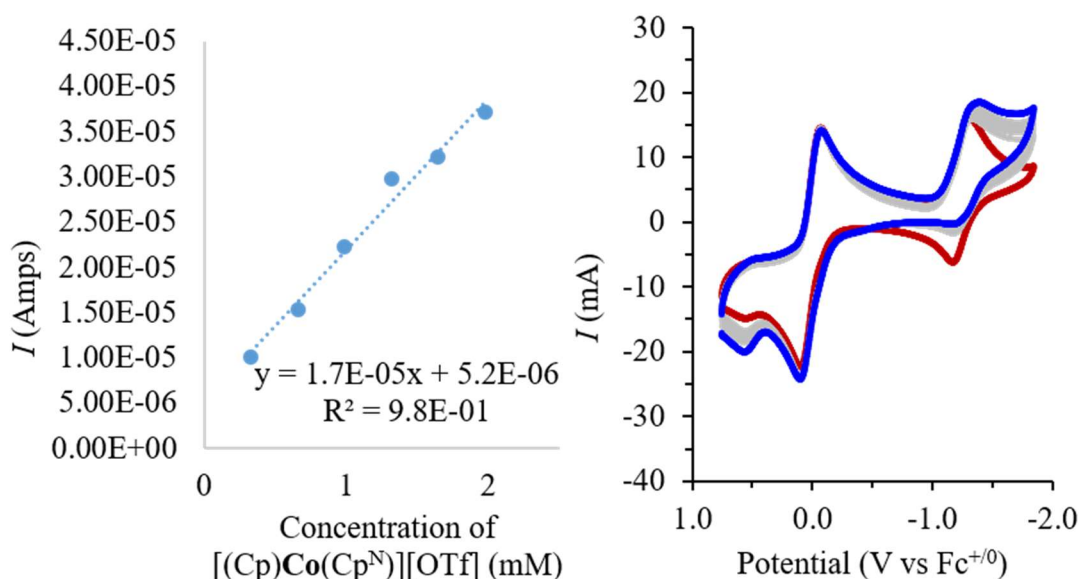


Figure 6.12: (left) Plateau current dependence on the concentration of $[(\text{Cp})\text{Co}(\text{Cp}^{\text{N}})]\text{[OTf]}$ in the reaction with 100 mM $[\text{}^4\text{-CNPhNH}_3]\text{[OTf]}$ and 50 mM acetophenone in a 200 mM $[\text{TBA}]\text{[PF}_6\text{]}$ solution of DME at 100 mV/s. (right) Repeated cyclic voltammograms in 200 mM $[\text{TBA}]\text{[PF}_6\text{]}$ DME solution of $[(\text{Cp})\text{Co}(\text{Cp}^{\text{NH}})]\text{[OTf]}_2$ at 100 mV/s with increasing equivalents of acetophenone (0 to 50 mM).

6.3 Discussion

We were interested in the thermochemical consequences of synthetic integration of the cobaltocene moiety with N,N-dimethylanilinium. We find that the $\text{BDFE}_{\text{N-H}}$ of $[(\text{Cp})\text{Co}(\text{Cp}^{\text{NH}})]^{2+}$ ($79.1 \text{ kcal mol}^{-1}$) is in excellent agreement with that of N,N-dimethylanilinium ($\text{BDFE}_{\text{N-H}} = 79 \text{ kcal mol}^{-1}$).^{30,40} While the introduction of the $[\text{Cp}_2\text{Co}]^+$ group at the para-position of the anilinium makes it more acidic ($\text{p}K_{\text{a}}$ of 8.6 vs 11.4), this effect is balanced by the increased oxidation potential (0.52 V vs $\text{Fc}^{+/0}$ vs 0.38 V vs $\text{Fc}^{+/0}$). These data are consistent with the $[\text{Cp}_2\text{Co}]^+$ acting as an innocent, electron-withdrawing substituent in this redox state, although the enhanced stability of $[(\text{Cp})\text{Co}(\text{Cp}^{\text{N}})]^{2+}$ relative to $[\text{N,N-dimethylanilinium}]^+$ suggests some electronic interaction between these species. It also points to the potential utility of $[(\text{Cp})\text{Co}(\text{Cp}^{\text{N}})]^{2+}$ as a hydrogen-atom abstracting reagent

given the similarity of its hydrogen-atom abstracting power to that of 2,4,6-tri-tert-butylphenoxy radical ($\text{BDFE}_{\text{O-H}}(2,4,6\text{-tri-tert-butylphenol}) = 77.1 \text{ kcal mol}^{-1}$ in MeCN).⁴⁰

One electron reduction of $[(\text{Cp})\text{Co}(\text{Cp}^{\text{NH}})]^{2+}$ attenuates the $\text{BDFE}_{\text{N-H}}$ by 40 kcal mol^{-1} . The $\text{BDFE}_{\text{N-H}}$ of $[(\text{Cp})\text{Co}(\text{Cp}^{\text{NH}})]^+$ is thus not well-predicted by that of the parent anilinium but rather by the effective BDFE ($\text{BDFE}_{\text{eff}} = 37.9 \text{ kcal mol}^{-1}$, **Eq 6.2**) of its constituent elements, namely cobaltocene ($E^0(\text{reductant}) = -1.33 \text{ V vs Fc}^{+/0}$) and N,N-dimethylanilinium ($\text{p}K_{\text{a}}(\text{acid}) = 11.4$).⁴⁰ This suggests that although the loci of electron donation has changed from being the aniline to the Co, the thermochemical properties of the constituent elements are again only minimally perturbed by synthetic integration. Density functional theory calculations with the TPSS functional,⁴¹ the def2-tzvp basis set,^{42,43} Grimme-d3 dispersion correction,⁴⁴ and SMD⁴⁵ solvation in acetonitrile also predict the homolytic bond strength of both species well, $\text{BDFE}_{\text{calc}} = 75.8$ and $38.5 \text{ kcal mol}^{-1}$ respectively. The ready prediction of the $\text{BDFE}_{\text{N-H}}$ both by effective BDFE calculations and by DFT is promising for the development of future catalytic systems with targeted H-atom donor strengths.

$$\text{Eq 6.2) } \text{BDFE}_{\text{eff}} = 1.37 \times \text{p}K_{\text{a}}(\text{acid}) + 23.06 \times E^0(\text{reductant}) + C_{\text{G}}$$

The importance of the BDFE in determining the reactivity is demonstrated by the selective proton-coupled reduction of acetophenone to its pinacol in CPE experiments. Thermodynamic considerations and mechanistic data derived from CV experiments strongly support the active mechanism to be a rate-limiting CPET from $[(\text{Cp})\text{Co}(\text{Cp}^{\text{NH}})]^+$ to acetophenone to generate the neutral ketyl radical ($\text{BDFE}_{\text{calc}} = 38.7 \text{ kcal mol}^{-1}$). This

demonstrates that the base-appended cobaltocene is able to take advantage of the inherent reversible electron-transfer properties and the kinetically facile protonation of anilines and harness them to achieve a thermodynamically challenging CPET reaction.

The proton-coupled reduction of acetophenone directly on metal electrodes has been extensively studied.⁴⁶⁻⁵⁰ In general, metals with a low-overpotential for hydrogen evolution (*i.e.*, Pt) preferentially hydrogenate the substrate to the alcohol.^{48,51} For metals with high-overpotential for HER, such as Hg, more complicated and sometimes contradictory results have been observed, but at least some pinacol product is always observed.^{46,47,50,52,53} Summarized here are the clear results from the literature and how they compare to our own observations of Co-mediated pinacolization. Firstly, with Hg, at low-pH values the reduction of the acetophenone is proton-coupled and thus pH-dependent (**Eq 6.3**).⁴⁷ In contrast, the onset potential in our system is neither pH- (or pK_a -) dependent but is rather fixed by the $[(Cp)Co(Cp^{NH})]^{2+/+}$ redox couple. This is highlighted by the fact that we observe catalysis upon the addition of cobalt even though the relevant cobalt species, $[(Cp)Co(Cp^{NH})]^+$ is four orders of magnitude less acidic than the acid that was already present, $[^{4-CN}PhNH_3]^+$ ($pK_a = 11.0$ and 7.0 respectively). Secondly, the pinacolization reaction at a Hg electrode is second-order in acetophenone indicating a rate-determining step coupling step. In our case, the reaction is first order in $[(Cp)Co(Cp^N)][OTf]$ and acetophenone, which we interpret as resulting from a rate-limiting proton-coupled electron transfer step. Lastly, it has been established that at the potentials relevant to Hg-mediated electropinacolization reactions that aromatic ketones are strongly adsorbed to Hg electrodes.⁵⁴⁻⁵⁶ This is consistent with results on the proton-coupled electrode-mediated reduction of ketones with other metals,^{50,51} and the

strongly sterically-dependent onset potential observed for differently substituted phenyl ketones. In our case, we believe that the reaction is happening in the homogeneous phase, consistent with the 1:1 ratio of diastereomers that we are observing, which is typically not the case in surface-mediated pinacolizations.^{52,54}

$$\text{Eq 6.3) } E_{\text{onset}} (\text{vs NHE}) = -0.99 + 0.60 \times \text{pH}$$

While the overall transformation mediated by our catalyst and a Hg pool electrode are similar, we believe that the comparison is illustrative. Firstly, the mechanistic differences observed support our contention that we are performing a Co-mediated CPET reaction in the homogeneous phase. Secondly, we anticipate that the mechanistic differences identified in this first study will position us to develop reactions that are not accessible directly on a mercury electrode. Adsorption on Hg is exquisitely sensitive to both sterics and electronics,^{53,55} so it is likely that many ketones would not be suitable for that reaction, although studies on the scope of the electropinacolization reaction are very limited. Furthermore, the necessity of adsorbing a substrate to the electrode may prevent hydrofunctionalization or three-component coupling reactions that are potentially accessible to the freely diffusing radical, such observations have been made previously in related electrohydrodimerization reactions.⁵⁶ Lastly, with a Hg electrode, the proton-coupled reduction of a substrate relies on pre-association of the acid with the substrate, and, thus, proton-coupled electron transfer reactivity to substrates lacking polar motifs, such as olefins, is not observed.⁵⁷ In our case, the acid and electron are co-localized by the cobalt catalyst

suggesting that we may also be able to mediate the proton-coupled reduction of non-polar unsaturated moieties.

6.4 Conclusion:

Herein, we expanded upon our interest in metallocenes as mediators of electrocatalytic reactions. In particular, we uncovered that although protonated cobaltocenes are strong proton-coupled electron transfer donors upon protonation,⁶ which we^{1,2} and others⁵⁸ have suggested could be relevant to N–H bond formation during chemical nitrogen fixation reactions, they are likely not relevant under electrocatalytic conditions due to slow protonation of the Cp(*) ring. Furthermore, protonation to form the PCET donor (*i.e.*, [(Cp)Co(η^4 -C₅H₆)]⁺) results in a species that is rapidly reduced by the electron to a species whose preferred mechanism of reaction is as a hydride donor. This is not a unique mechanism; indeed, many organometallic species undergo ECEC mechanisms for HER. In contrast, relatively few are able to access EC (or CE) mechanisms that produce stable, strong hydrogen-atom donors ($\text{BDFE}_{\text{X-H}} < 50 \text{ kcal mol}^{-1}$). As such, we became interested in synthetic modifications that would both kinetically accelerate protonation of the cobaltocene and prevent its further reduction to a hydridic species.

To this end, we synthetically append an aniline base to cobaltocenium. Now, protonation no longer requires reduction instead readily occurring in the Co^{III} state. Furthermore, by effectively decoupling protonation from the primary coordination sphere, a second reduction to form a hydridic species (*i.e.*, an ECE mechanism) is no longer favorable. Instead, as desired, the aniline-protonated, Co^{II} species, [(Cp)Co(Cp^{NH})]⁺, is a strong H-atom

donor ($\text{BDFE}_{\text{N-H}} = 38.8 \text{ kcal mol}^{-1}$) that is fairly stable under reductive conditions despite the high thermodynamic driving force for HER and the presence of excess protons and electrons. CPE experiments in the presence of excess acid and acetophenone form the pinacolization product selectively demonstrating the potential of this catalyst as a PCET mediator. Mechanistic information gleaned from cyclic voltammetry indicate a first-order reaction in cobalt and acetophenone, which is dependent on formation of $[(\text{Cp})\text{Co}(\text{Cp}^{\text{NH}})]^+$. These data point at a rate-limiting CPET to acetophenone.

On the basis of these data and known reactions,^{20,56} we believe that this catalyst will now provide access to electrocatalytic hydrofunctionalization or three-component cross coupling reactions preceding via carbon-centered radicals derived from the CPET to unsaturated substrates. Furthermore, given the growing acknowledgment of the role of strong PCET donors in nitrogen fixation catalysis^{1,2,6,59,60} and the demonstrated utility of PCET mediators as co-catalysts in electrocatalytic O_2 -reduction,^{12,13} we believe that similar cobalt catalysts may have a role as co-catalysts in the proton-coupled reduction of small molecules.

6.5 References:

- (1) Chalkley, M. J.; Del Castillo, T. J.; Matson, B. D.; Roddy, J. P.; Peters, J. C. *ACS Cent. Sci.* **2017**, *3*, 217–223.
- (2) Chalkley, M. J.; Del Castillo, T. J.; Matson, B. D.; Peters, J. C. *J. Am. Chem. Soc.* **2018**, *140*, 6122–6129.
- (3) Yandulov, D. V.; Schrock, R. R. *Science* **2003**, *301*, 76–78.
- (4) Arashiba, K.; Miyake, Y.; Nishibayashi, Y. *Nat. Chem.* **2010**, *3*, 120–125.

- (5) Hill, P. J.; Doyle, L. R.; Crawford, A. D.; Myers, W. K.; Ashley, A. E. *J. Am. Chem. Soc.* **2016**, *138*, 13521–13524.
- (6) Chalkley, M. J.; Oyala, P. H.; Peters, J. C. *J. Am. Chem. Soc.* **2019**, *141*, 4721–4729.
- (7) Francke, R.; Little, R. D. *Chem. Soc. Rev.* **2014**, *43*, 2492–2521.
- (8) Oh, Y.; Hu, X. *Chem. Soc. Rev.* **2013**, *42*, 2253–2261.
- (9) Taheri, A.; Berben, L. A. *Chem. Commun.* **2016**, *52*, 1768–1777.
- (10) Bullock, R. M.; Appel, A. M.; Helm, M. L. *Chem. Commun.* **2014**, *50*, 3125–3143.
- (11) Kang, P.; Chen, Z.; Brookhart, M.; Meyer, T. J. *Top. Catal.* **2015**, *58*, 30–45.
- (12) Gerken, J. B.; Stahl, S. S. *ACS Cent. Sci.* **2015**, *1*, 234–243.
- (13) Anson, C. W.; Stahl, S. S. *J. Am. Chem. Soc.* **2017**, *139*, 18472–18475.
- (14) Tarantino, K. T.; Liu, P.; Knowles, R. R. *J. Am. Chem. Soc.* **2013**, *135*, 10022–10025.
- (15) Rono, L. J.; Yayla, H. G.; Wang, D. Y.; Armstrong, M. F.; Knowles, R. R. *J. Am. Chem. Soc.* **2013**, *135*, 17735–17738.
- (16) Qiu, G.; Knowles, R. R. *J. Am. Chem. Soc.* **2019**, *141*, 2721–2730.
- (17) Chciuk, T. V.; Flowers, R. A. *J. Am. Chem. Soc.* **2015**, *137*, 11526–11531.
- (18) Chciuk, T. V.; Anderson, W. R.; Flowers, R. A. *J. Am. Chem. Soc.* **2018**, *140*, 15342–15352.
- (19) Chciuk, T. V.; Anderson, W. R.; Flowers, R. A. *J. Am. Chem. Soc.* **2016**, *138*, 8738–8741.
- (20) Crossley, S. W. M.; Obradors, C.; Martinez, R. M.; Shenvi, R. A. *Chem. Rev.* **2016**, *116*, 8912–9000.
- (21) Kim, D.; Rahaman, S. M. W.; Mercado, B. Q.; Poli, R.; Holland, P. L. *J. Am. Chem. Soc.* **2019**, *141*, 7473–7485.

- (22) Kolmar, S. S.; Mayer, J. M. *J. Am. Chem. Soc.* **2017**, *139*, 10687–10692.
- (23) Koelle, U.; Infelta, P. P.; Graetzel, M. *Inorg. Chem.* **1988**, *27*, 879–883.
- (24) Henderson, R. A. *Angew. Chem., Int. Ed. Engl.* **1996**, *35*, 946–967.
- (25) Peng, Y.; Ramos-Garces, M. V.; Lionetti, D.; Blakemore, J. D. *Inorg. Chem.* **2017**, *56*, 10824–10831.
- (26) Stepnicka, P. John Wiley & Sons, Ltd: Chichester, England, 2008.
- (27) El Murr, N. *J. Organomet. Chem.* **1981**, *208*, C9–C11.
- (28) Pauson, P. L. *Encyclopedia of Reagents for Organic Synthesis*; American Cancer Society, 2001.
- (29) Robbins, J. L.; Edelstein, N.; Spencer, B.; Smart, J. C. *J. Am. Chem. Soc.* **1982**, *104*, 1882–1893.
- (30) Liu, W.-Z.; Bordwell, F. G. *J. Org. Chem.* **1996**, *61*, 4778–4783.
- (31) Geiger, W. E. *J. Am. Chem. Soc.* **1974**, *96*, 2632–2634.
- (32) Garrido, G.; Rosés, M.; Ràfols, C.; Bosch, E. *J. Solution Chem.* **2008**, *37*, 689–700.
- (33) Kaljurand, I.; Kütt, A.; Sooväli, L.; Rodima, T.; Mäemets, V.; Leito, I.; Koppel, I. A. *J. Org. Chem.* **2005**, *70*, 1019–1028.
- (34) Loutfy, R. O.; Loutfy, R. O. *Tetrahedron* **1973**, *29*, 2251–2252.
- (35) Arnett, E. M.; Quirk, R. P.; Larsen, J. W. *J. Am. Chem. Soc.* **1970**, *92*, 3977–3984.
- (36) Nakajima, M.; Fava, E.; Loescher, S.; Jiang, Z.; Rueping, M. *Angew. Chem. Int. Ed.* **2015**, *54*, 8828–8832.
- (37) Caron, A.; Morin, É.; Collins, S. K. *ACS Catal.* **2019**, *9*, 9458–9464.
- (38) Eckert, F.; Leito, I.; Kaljurand, I.; Kütt, A.; Klamt, A.; Diedenhofen, M. *J. Comput. Chem.* **2009**, *30*, 799–810.

- (39) Costentin, C.; Drouet, S.; Robert, M.; Savéant, J.-M. *J. Am. Chem. Soc.* **2012**, *134*, 11235–11242.
- (40) Warren, J. J.; Tronic, T. A.; Mayer, J. M. *Chem. Rev.* **2010**, *110*, 6961–7001.
- (41) Tao, J.; Perdew, J. P.; Staroverov, V. N.; Scuseria, G. E. *Phys. Rev. Lett.* **2003**, *91*, 146401–146404.
- (42) Weigend, F.; Ahlrichs, R. *Phys. Chem. Chem. Phys.* **2005**, *7*, 3297–3305.
- (43) Weigend, F. *Phys. Chem. Chem. Phys.* **2006**, *8*, 1057–1065.
- (44) Grimme, S.; Antony, J.; Ehrlich, S.; Krieg, H. *J. Chem. Phys.* **2010**, *132*, 154104–154119.
- (45) Marenich, A. V.; Cramer, C. J.; Truhlar, D. G. *J. Phys. Chem. B* **2009**, *113*, 6378–6396.
- (46) Brennan, M. P. J.; Brown, O. R. *J. Chem. Soc., Faraday Trans. 1* **1973**, *69*, 132–142.
- (47) Elving, P. J.; Leone, J. T. *J. Am. Chem. Soc.* **1958**, *80*, 1021–1029.
- (48) Bondue, C. J.; Koper, M. T. M. *J. Am. Chem. Soc.* **2019**, *141*, 12071–12078.
- (49) Lopez-Ruiz, J. A.; Andrews, E.; Akhade, S. A.; Lee, M.-S.; Koh, K.; Sanyal, U.; Yuk, S. F.; Karkamkar, A. J.; Derewinski, M. A.; Holladay, J.; et al. *ACS Catal.* **2019**, *9*, 9964–9972.
- (50) Rudd, E. J.; Conway, B. E. *Trans. Faraday Soc.* **1971**, *67*, 440–457.
- (51) Yue, Y.-N.; Wu, D.; Zeng, S.; Yang, M.-P.; Wang, H.; Lu, J.-X. *New J. Chem.* **2017**, *41*, 7853–7856.
- (52) Bewick, A.; P. Cleghorn, H. *Journal of the Chemical Society, Perkin Transactions 2* **1973**, *0*, 1410–1413.

- (53) Tilborg, W. J. M. van; Dekker, L. J. G.; Smit, C. J. *Recl. Trav. Chim. Pays-Bas* **1978**, *97*, 321–326.
- (54) Stocker, J. H.; Jenevein, R. M. *J. Org. Chem.* **1968**, *33*, 294–297.
- (55) Blomgren, E.; Bockris, J. O.; Jesch, C. *J. Phys. Chem.* **1961**, *65*, 2000–2010.
- (56) Nielsen, M. F.; Utley, J. H. P. *Organic Electrochemistry*; Marcel Dekker: New York, NY, 1999; pp 795–882.
- (57) Laitinen, H. A.; Wawzonek, S. *J. Am. Chem. Soc.* **1942**, *64*, 1765–1768.
- (58) Bruch, Q. J.; Connor, G. P.; Chen, C.-H.; Holland, P. L.; Mayer, J. M.; Hasanayn, F.; Miller, A. J. M. *J. Am. Chem. Soc.* **2019**, *141*, 20198–20208.
- (59) Ashida, Y.; Arashiba, K.; Nakajima, K.; Nishibayashi, Y. *Nature* **2019**, *568*, 536–540.
- (60) Munisamy, T.; Schrock, R. R. *Dalton Trans.* **2011**, *41*, 130–137.

APPENDIX A.
Supplementary Information for Chapter 2

Adapted from:
Chalkley, M. J.; Peters, J. C.
Angew. Chem. Int. Ed. **2016**, *55*, 11995–11998.
DOI: 10.1002/anie.201605403

A.1 Experimental Details

A.1.1 General Considerations

All manipulations were carried out using standard Schlenk or glovebox techniques under an N₂ atmosphere. Unless otherwise noted, solvents were deoxygenated and dried by thoroughly sparging with N₂ gas followed by passage through an activated alumina column in the solvent purification system by SG Water, USA LLC. Non-halogenated solvents were tested with a standard purple solution of sodium benzophenone ketyl in tetrahydrofuran in order to confirm effective oxygen and moisture removal. All reagents were purchased from commercial vendors and used without further purification unless otherwise stated. (P₃^B)Fe(N₂),¹ and [TBA][BAr^F₄]² were synthesized via known literature procedures. Deuterated solvents were purchased from Cambridge Isotope Laboratories, Inc. C₆D₆ was degassed and stored over activated 3 Å molecular sieves prior to use, and THF-*d*₈ was dried with NaK and vac-transferred into a dry vessel. Elemental analysis for {(P₃^B)Fe(NO)}⁸ was performed by Midwest Microlab, LLC, Indianapolis, IN, and elemental analysis for {(P₃^B)Fe(NO)}⁹⁻¹⁰ was performed by the Beckman Institute Elemental Analysis facility at California Institute of Technology. ¹H and ¹³C NMR chemical shifts are reported in ppm relative to tetramethylsilane, using residual solvent resonances as internal standards. ³¹P NMR chemical shifts are reported in ppm relative to 85% aqueous H₃PO₄. ¹¹B NMR chemical shifts are reported in ppm relative to a 15% solution of BF₃·OEt₂ in CDCl₃. Solution phase magnetic measurements were performed by the method of Evans.³ Solid IR measurements were obtained on a Bruker Alpha spectrometer equipped with a diamond ATR probe.

A.1.2 EPR Spectroscopy

X-band EPR spectra were obtained on a Bruker EMX spectrometer on 2-5 mM solutions prepared as frozen glasses in 2-methyltetrahydrofuran (2-MeTHF). Samples were collected at powers ranging from 20 μ W to 15 mW and modulation amplitudes of 1-5 Gauss. Spectra were simulated using the EasySpin⁴ suite of programs with Matlab 2013.

A.1.3 Optical Spectroscopy

Measurements were taken on a Cary 50 UV/Visible spectrophotometer using a 1 cm quartz cell connected to a round-bottom flask and sealed with a Teflon stopcock. Variable temperature measurements were collected with a Unisoku CoolSpek cryostat mounted within the Cary spectrophotometer. Density corrections were applied using literature temperature vs. density data available for 2-MeTHF.⁵

A.1.4 X-ray Crystallography

XRD studies were carried out at the Beckman Institute Crystallography Facility on a Bruker Kappa Apex II diffractometer (Mo K α radiation). Structures were solved using SHELXS or SHELXT and refined against F^2 on all data by full-matrix least squares with SHELXL.⁶ The crystals were mounted on a glass fiber under Paratone N oil.

A.1.5 Electrochemistry

Electrochemical measurements were carried out in a thick-walled one-component electrochemical cell fitted with a Teflon stopcock and tungsten leads protruding from the top of apparatus. A CD instruments 600B electrochemical analyzer was used for data collection. A freshly-polished glassy carbon electrode was used as the working electrode, a platinum wire was used as the auxiliary electrode, and a silver wire as a reference

electrode. The analyte was used in 1 mM concentration. After the desired scans were completed, ferrocene (1 mM) was added to serve as an internal reference. All reported potentials are referenced to the ferrocene couple, Fc/Fc⁺.

A.1.6 ⁵⁷Fe Mössbauer Spectroscopy

Spectra were recorded on a spectrometer from SEE Co (Edina, MN) operating in the constant acceleration mode in a transmission geometry. The sample was kept in an SVT-400 cryostat from Janis (Wilmington, MA). The quoted isomer shifts are relative to the centroid of the spectrum of a metallic foil of α -Fe at room temperature. Solid samples were prepared by grinding crystalline material and then mounted in a Delrin cup fitted with a screw-cap as a boron nitride pellet. Data analysis was performed using the program WMOSS (www.wmoss.org) and quadrupole doublets were fit to Lorentzian lineshapes except where noted.

A.1.7 Density Functional Theory Calculations

Optimizations were performed using the ORCA program.⁷ Frequency calculations were performed using the Gaussian 09 program. Gas-phase structures were optimized using the crystal structure coordinates as the input. The BP86^{8,9} and B3LYP¹⁰ functional with the 6-31G(d) basis set was used on C and H,¹¹ and the def2-TZVPP basis set was used on P, B, Fe, N, and O.^{12,13} That optimized structures represented true stationary points was checked by doing a single-point frequency calculations on the optimized structure, which in all cases revealed no negative frequencies or one negative frequency that was small (≥ -30 cm⁻¹) and weak. Bond indices were calculated using the built-in Wiberg Bond Index algorithm in Gaussian 09. Broken symmetry solutions were found by first optimizing the high spin

wavefunction and then using the Flip Spin keyword in ORCA to find and optimize a broken symmetry solution. Mössbauer parameters were calculated by doing a single point calculation on the BP86 optimized structure using TPSSH¹⁴ and CP(PPP) on Fe;¹⁵ def2-TZVP on P, B, and N;^{12,13} and def2-SVP on C and H.¹⁶ The obtained density was converted to an isomer shift using the calibration constant obtained by Neese and coworkers for this functional.¹⁷

A.2 Synthetic Procedures:

$\{(P_3^B)Fe(NO)\}^8$ -A vial containing $[NO][PF_6]$ (11.4 mg, 0.065 mmol, 1.0 eq.) and a stir bar was chilled to $-78\text{ }^\circ\text{C}$. A suspension of $(P_3^B)Fe(N_2)$ (45.0 mg, 0.067 mmol, 1.02 eq.) in DME (3 mL) was chilled to $-78\text{ }^\circ\text{C}$. Using a syringe the suspension of $(P_3^B)Fe(N_2)$ was added in one portion to the stirring $[NO][PF_6]$. This mixture was then immediately capped and allowed to stir at $-78\text{ }^\circ\text{C}$ for a half hour before being warmed to room temperature. It was then stirred at room temperature for an additional half hour to yield a black solution. The solvent was removed under reduced pressure, and the oily solid was washed with pentane (3 x 1 mL), ether (3 x 1 mL) and benzene (3 x 1 mL). The residual solid was dissolved in THF and filtered through celite. The THF solution was then layered with benzene, and precipitated by slow diffusion of pentane overnight. This yielded crystalline purple material of $[(P_3^B)Fe(NO)][PF_6]$ (not characterized due to its very poor solubility after recrystallization) which was then suspended in Et_2O (2 mL) and stirred with NaBARF (0.95 eq.) overnight. The ether was then filtered to remove salts and the solvent was removed in vacuo. The purple solid is then dissolved in minimal THF and pentane was allowed to diffuse in yielding purple crystals of $\{(P_3^B)Fe(NO)\}^8$ overnight (yield = 41.1 mg, 41%).

^1H NMR (RT, THF- d_8 , 400 MHz): δ = 7.80 (11 H, br s, Ar- H), 7.68-7.48 (10 H, m, Ar- H), 7.27 (3 H, d, $^3\text{J}(\text{H-H})$ = 7.2 Hz, Ar- H), 2.86 (3 H, m, PCH), 1.73 (9 H, m), 1.58 (9 H, 'dd' $^4\text{J}(\text{P-H})$ = 14.5 Hz and $^3\text{J}(\text{H-H})$ = 7.0 Hz, PCHCH $_3$), 1.02 (9 H, 'dd' $^4\text{J}(\text{P-H})$ = 14.5 Hz and $^3\text{J}(\text{H-H})$ = 6.3 Hz, PCHCH $_3$), 0.81 (3 H, br s, PCH), 0.71 (9 H, 'dd' $^4\text{J}(\text{P-H})$ = 12.0 Hz and $^3\text{J}(\text{H-H})$ = 6.4 Hz, PCHCH $_3$). ^1H NMR (-78 °C, THF- d_8 , 500 MHz): δ = 8.17 (2 H, 't' $^3\text{J}(\text{H-H})$ = 8.9 Hz, Ar- H), 7.99 (2 H, br s, Ar- H), 7.90 (8 H, s, BArF- H), 7.74 (4 H, s, BArF- H), 7.54 (2 H, br s, Ar- H), 7.49 (2 H, br s, Ar- H), 7.34 (2 H, br s, Ar- H), 7.30 (1 H, br s, Ar- H), 6.88 (1 H, br s, Ar- H), 3.62 (1 H, br s, PCH), 3.41 (1 H, br s, PCH), 3.06 (1 H, br s, PCH), 2.33 (1 H, br s, PCH), 1.94 (4 H, br s, PCHCH $_3$), 1.89-1.77 (4 H, m, PCHCH $_3$), 1.60 (3 H, br s, PCHCH $_3$), 1.51 (3 H, br s, PCHCH $_3$), 1.42 (3 H, d $^3\text{J}(\text{H-H})$ = 15.7 Hz, PCHCH $_3$), 1.24 (4 H, br s, PCHCH $_3$), 1.11 (6 H, br s, PCHCH $_3$), 0.86 (3 H, d $^3\text{J}(\text{H-H})$ = 12.7 Hz, PCHCH $_3$), 0.55 (3 H, br s, PCHCH $_3$), .47 (3 H, br s, PCHCH $_3$), -0.07 (1 H, br s, PCH), -0.17 (1 H, br s, PCH). ^{31}P NMR (RT, THF- d_8 , 162 MHz): δ = 64.0 (br). ^{31}P NMR (-78 °C, THF- d_8 , 202 MHz): δ = 84.4 (br), 80.0 (br), 19.6 (br). ^{11}B NMR (RT, THF- d_8 , 128 MHz): δ = 36.7 (br, P $_3^{\text{B}}$), -2.0 (sh, BArF). ^{13}C NMR (RT, THF- d_8 , 100 MHz): δ = 164.8 (q, $^2\text{J}(\text{C-B})$ = 29.7 Hz), 139.1 (br), 137.5 (s), 134.3 (d, $^2\text{J}(\text{C-P})$ = 17.3 Hz), 133.2 (br), 131.9 (m), 127.4 (q, $^2\text{J}(\text{C-F})$ = 72.2 Hz), 120.1 (m), 35.0 (d, $^2\text{J}(\text{C-P})$ = 19.0 Hz), 30.6 (d, $^2\text{J}(\text{C-P})$ = 8.9 Hz), 24.8 (d, $^3\text{J}(\text{C-P})$ = 4.2 Hz), 24.0 (s), 23.7 (s), 21.7 (s). ^{19}F NMR (RT, THF- d_8 , 376 MHz): δ = -63.4 (s). IR (Thin Film): 1745 cm^{-1} (ν_{NO}). UV/Vis (2-MeTHF, nm { $\text{cm}^{-1} \text{M}^{-1}$ }): 463 {220}, 565 {350}. Elemental Analysis: theory [C 53.05, H 4.32, N 0.91]; found [C 53.11, H 4.17, N 1.08]

$\{(P_3^B)Fe(NO)\}^9$ -The microcrystalline material, $[(P_3^B)Fe(NO)][PF_6]$, (38.0 mg, 0.046 mmol, 1.0 eq) was suspended in THF (5 mL) and added to a vial containing Cp_2Co (8.7 mg, 0.046 mmol, 1.0 eq.). The suspension was stirred for three hours during which the color of the solution lightened to an orange-pink color. The solvent was then removed under reduced pressure, and the residue was extracted with pentane and filtered through celite. The pentane was then reduced to a minimal volume under reduced pressure and the solvent was allowed to concentrate slowly overnight by slow evaporation into an HMDSO antisolvent at room temperature. The mother liquor was decanted and the solids were washed with HMDSO (3 x 1 mL). This yielded red-brown crystalline material of $\{(P_3^B)Fe(NO)\}^9$ (yield = 21.3 mg, 68%).

1H NMR (C_6D_6 , 400 MHz, RT): 17.48 (3 H), 11.27 (3 H), 8.58 (3 H), 6.11 (3 H), 2.11 (9H), 1.87 (9H), 0.57 (3 H), -1.23 (9H), -2.10 (9 H). μ_{eff} (RT, Evans Method, C_6D_6): $1.7\mu_B$. IR (Thin Film): 1664 cm^{-1} (ν_{NO}). UV/Vis (2-MeTHF, nm $\{cm^{-1}\text{ M}^{-1}\}$): 535 {420}, 916 {180}. Elemental Analysis: theory [C 63.93, H 8.05, N 2.07]; found [63.59, 8.11, 2.18]

$\{(P_3^B)Fe(NO)\}^{10}$ - $[(P_3^B)Fe(NO)][PF_6]$ (66.3 mg, 0.081 mmol, 1.0 eq.) was suspended in THF (10 mL) and added to a vial containing 1% Na/Hg amalgam (3.8 mg of Na, 0.162 mmol, 2.0 eq.). The suspension was stirred at room temperature for four hours yielding a dark red solution. The solvent was removed under reduced pressure, and the residue was extracted with ether (3 x 3 mL) and filtered through celite. The solvent was then evaporated to dryness under reduced pressure. The residue was dissolved in minimal THF (~2 mL) and layered with a 2 mL benzene solution of 12-crown-4 (47 mg, 0.267 mmol, 3.3 eq.). After standing at room temperature overnight, red needles of the desired compound were obtained.

Decanting and washing with minimal ether and then drying yielded $\{(P_3^B)Fe(NO)\}^{10}$ (48 mg, 57 %). The best yields could be obtained using this procedure but reduction of $\{(P_3^B)Fe(NO)\}^9$ with 1 eq. of Na/Hg and the above reported isolation procedure also led reproducibly to pure material.

1H NMR (-78 °C, THF- d_8 , 500 MHz): δ = 7.15 (3 H, br s, Ar-*H*), 7.01 (3 H, br s, Ar-*H*), 6.73 (3 H, br s, Ar-*H*), 6.59 (3 H, br s, Ar-*H*), 3.74 (32 H, s, 12-*c*-4), 2.79 (3 H, br s, PCH), 2.00 (3 H, br s, PCH), 1.52-0.80 (27 H, m, PCHCH₃), -0.43 (9H, s, PCHCH₃). ^{31}P NMR (-78 °C, THF- d_8 , 202 MHz): δ = 88.7 (br). ^{11}B NMR (RT, THF- d_8 , 128 MHz): δ = 19.9 (br). ^{13}C NMR (-78 °C, 126 MHz, THF- d_8 , 100 MHz): δ = 175.9 (br), 146.0, 130.7, 125.2, 124.9, 119.9, 70.4, 65.1, 30.7, 27.6, 20.3, 18.9, 17.2.

At room temperature there is no detectable ^{31}P NMR signal and the 1H NMR spectrum is broadened presumably by the presence of undetectably small amounts of $\{(P_3^B)Fe(NO)\}^9$ that undergoes fast electron transfer with $\{(P_3^B)Fe(NO)\}^{10}$ in solution. Cooling the solution to -78 °C makes this process slower than the NMR time scale allowing 1H and ^{31}P NMR spectra to be obtained.

IR (Thin Film): 1568 cm^{-1} (ν_{NO}). UV/Vis (2-MeTHF, nm $\{cm^{-1} M^{-1}\}$): 314 {11700}, 389 {4000}, 499 {1800}. Elemental Analysis: $\{(P_3^B)Fe(NO)\}^{10} \cdot .5C_6H_6$ theory [C 60.56, H 8.22, N 1.28]; found [C 60.32, H 8.10, N 1.41]

Taking crystalline $\{(P_3^B)FeNO\}^{10}$ and then pulling vacuum on it before dissolution in THF- d_8 leads to the presence of 0.5 equivalents of C₆H₆ as seen in **Figure S9**. The crystal structure of $\{(P_3^B)Fe(NO)\}^{10}$ has two half-occupied benzene molecules present confirming the presence of benzene in crystalline $\{(P_3^B)Fe(NO)\}^{10}$.

A.3 NMR Spectra:

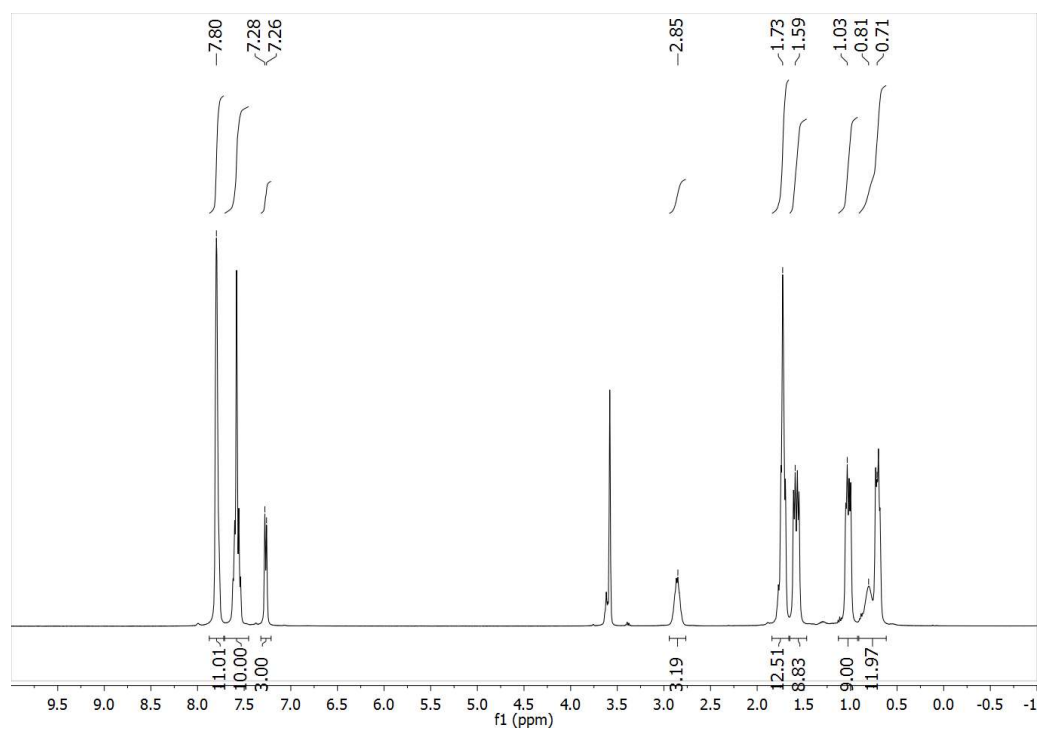


Figure A.1: The ^1H NMR spectrum (500 MHz) of $\{(\text{P}_3^{\text{B}})\text{Fe}(\text{NO})\}_8$ at room temperature in $\text{THF-}d_8$.

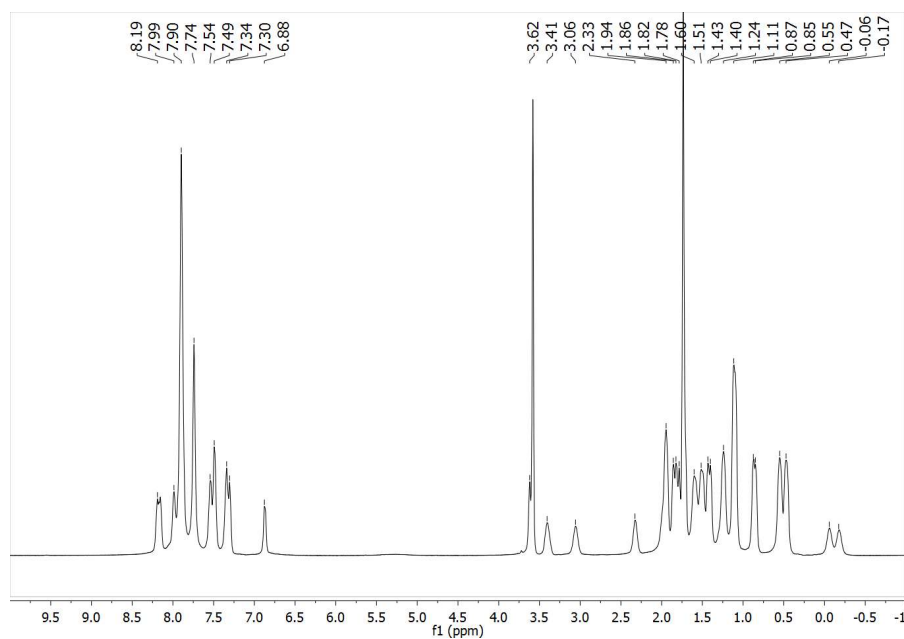


Figure A.2: The ^1H NMR spectrum (500 MHz) of $\{(\text{P}_3^{\text{B}})\text{Fe}(\text{NO})\}_8$ at $-78\text{ }^\circ\text{C}$ in $\text{THF-}d_8$.

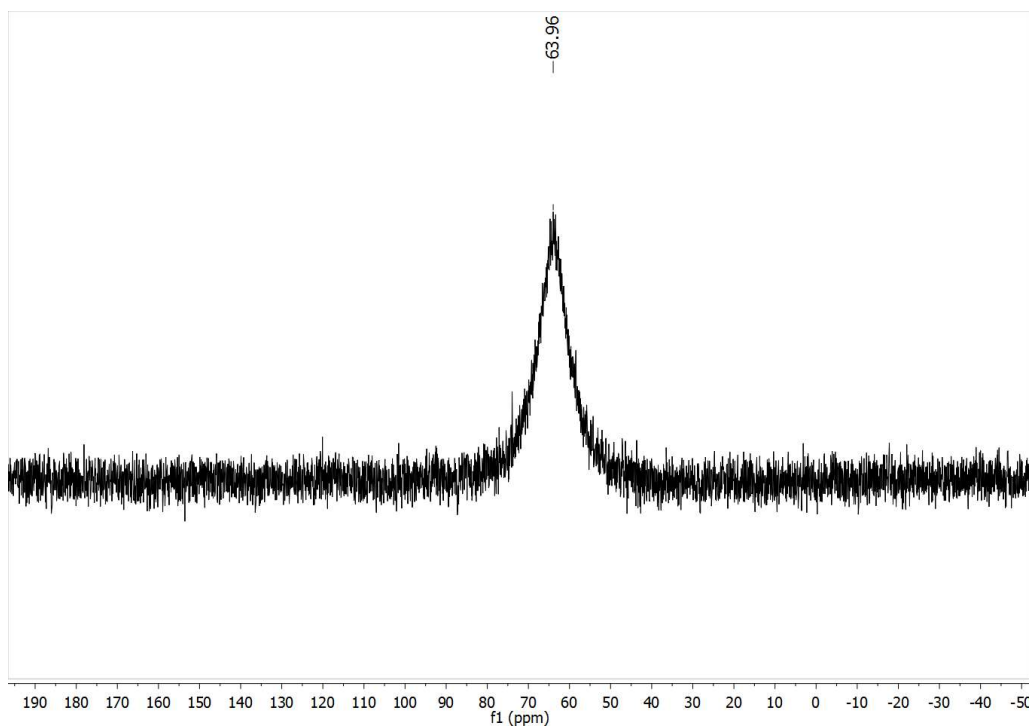


Figure A.3: The ^{31}P NMR spectrum (161.9 MHz) of $\{(\text{P}_3^{\text{B}})\text{Fe}(\text{NO})\}_8$ at room temperature in $\text{THF-}d_8$.

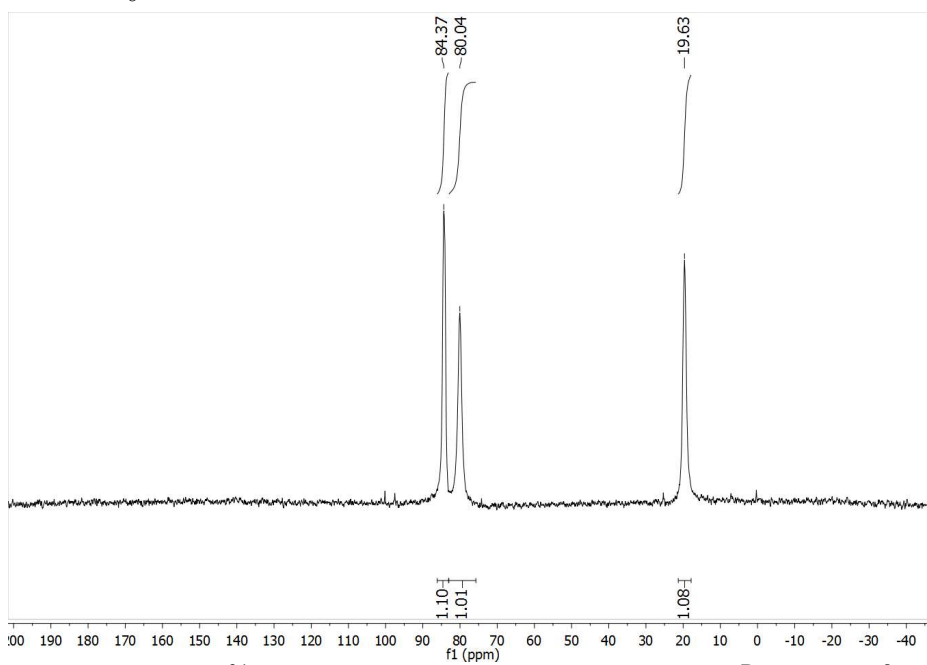


Figure A.4: The ^{31}P NMR spectrum (202.4 MHz) of $\{(\text{P}_3^{\text{B}})\text{Fe}(\text{NO})\}_8$ at -78°C in $\text{THF-}d_8$.

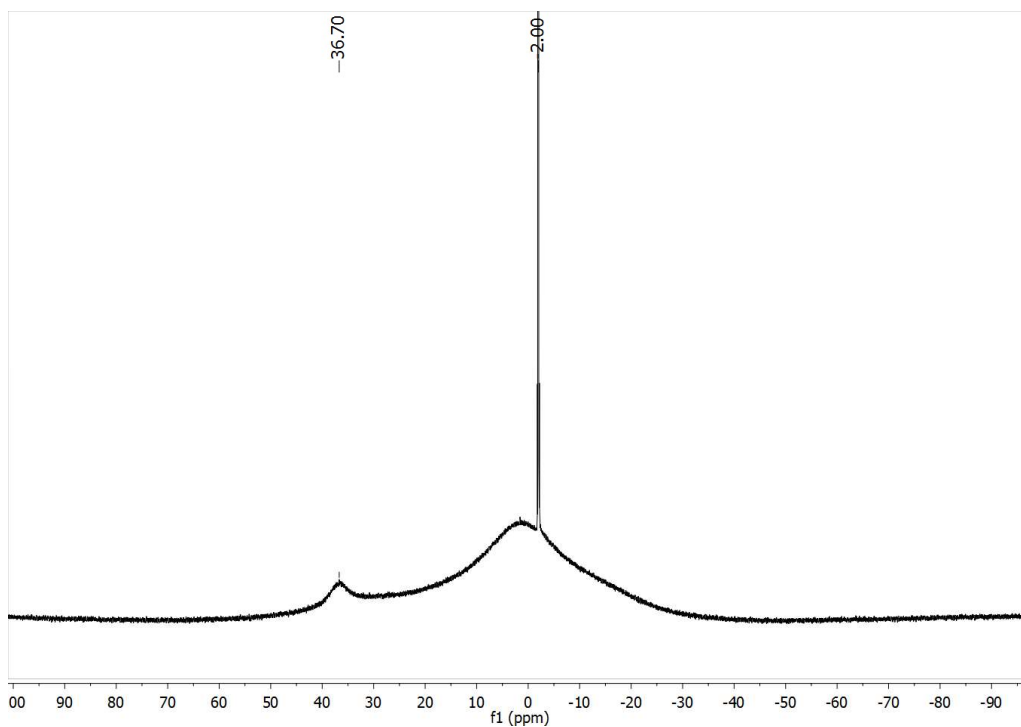


Figure A.5: The ^{11}B NMR spectrum (128.3 MHz) of $\{(\text{P}_3^{\text{B}})\text{Fe}(\text{NO})\}_8$ at room temperature in $\text{THF-}d_8$.

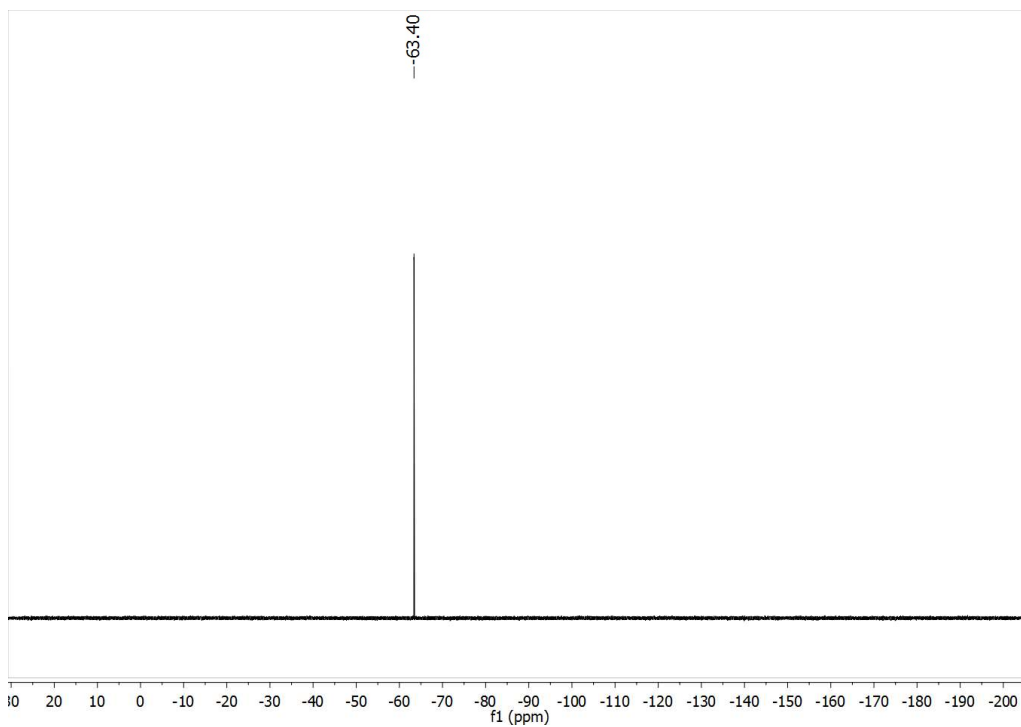


Figure A.6: The ^{19}F NMR spectrum (376.3 MHz) of $\{(\text{P}_3^{\text{B}})\text{Fe}(\text{NO})\}_8$ at room temperature in $\text{THF-}d_8$.

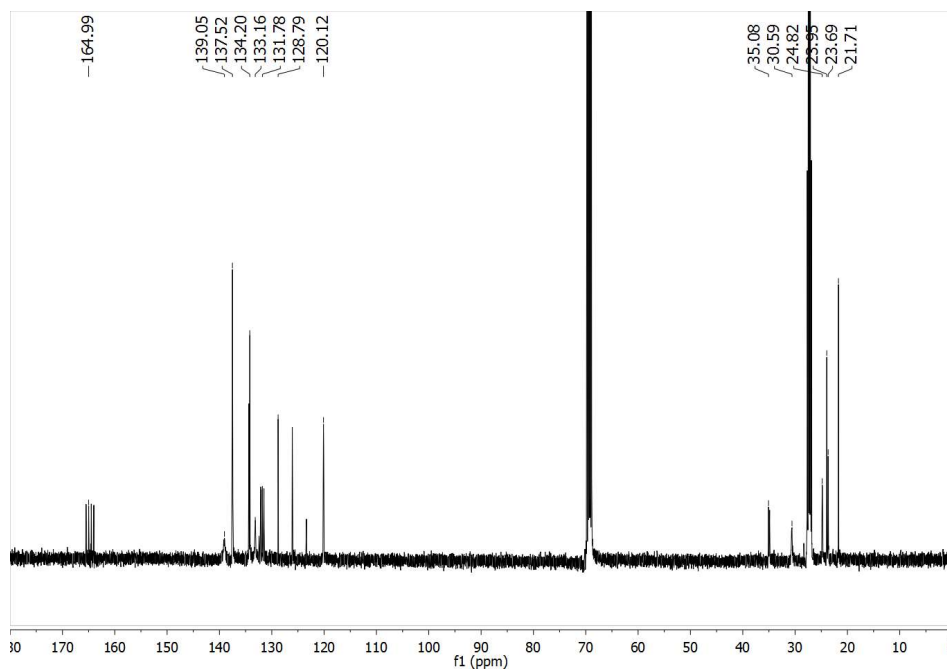


Figure A.7: The ^{13}C NMR spectrum (100.6 MHz) of $\{(\text{P}_3^{\text{B}})\text{Fe}(\text{NO})\}_8$ at room temperature in $\text{THF-}d_8$.

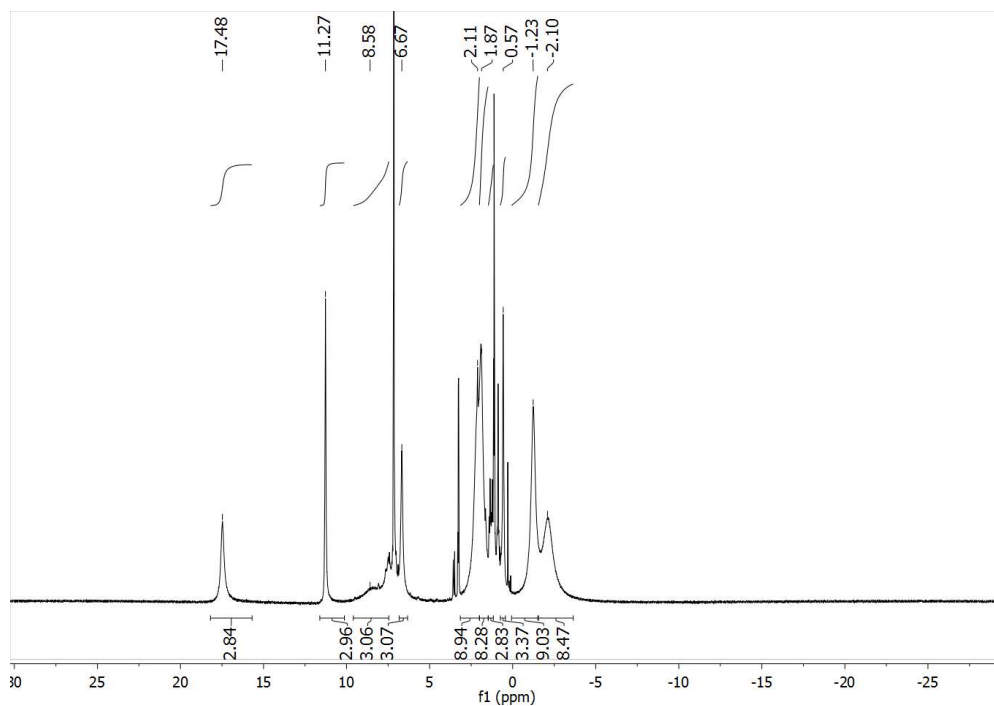


Figure A.8: The ^1H NMR spectrum (400 MHz) of $\{(\text{P}_3^{\text{B}})\text{Fe}(\text{NO})\}_9$ at room temperature in C_6D_6 .

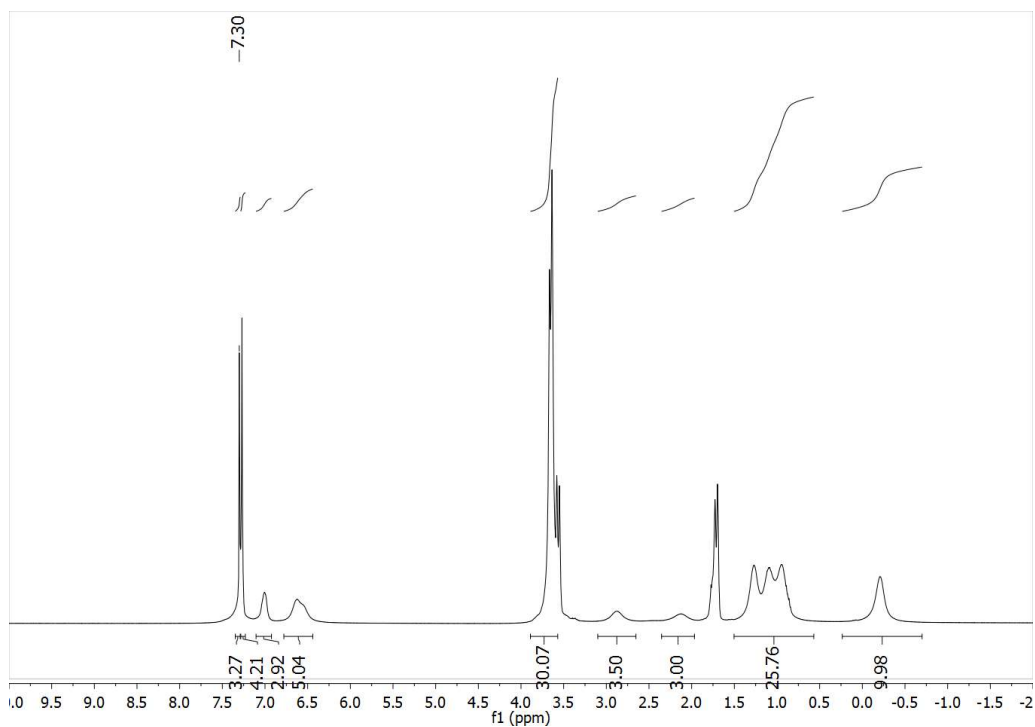


Figure A.9: The ^1H NMR spectrum (500 MHz) of $\{(\text{P}_3^{\text{B}})\text{Fe}(\text{NO})\}^{10}$ at room temperature in $\text{THF-}d_8$.

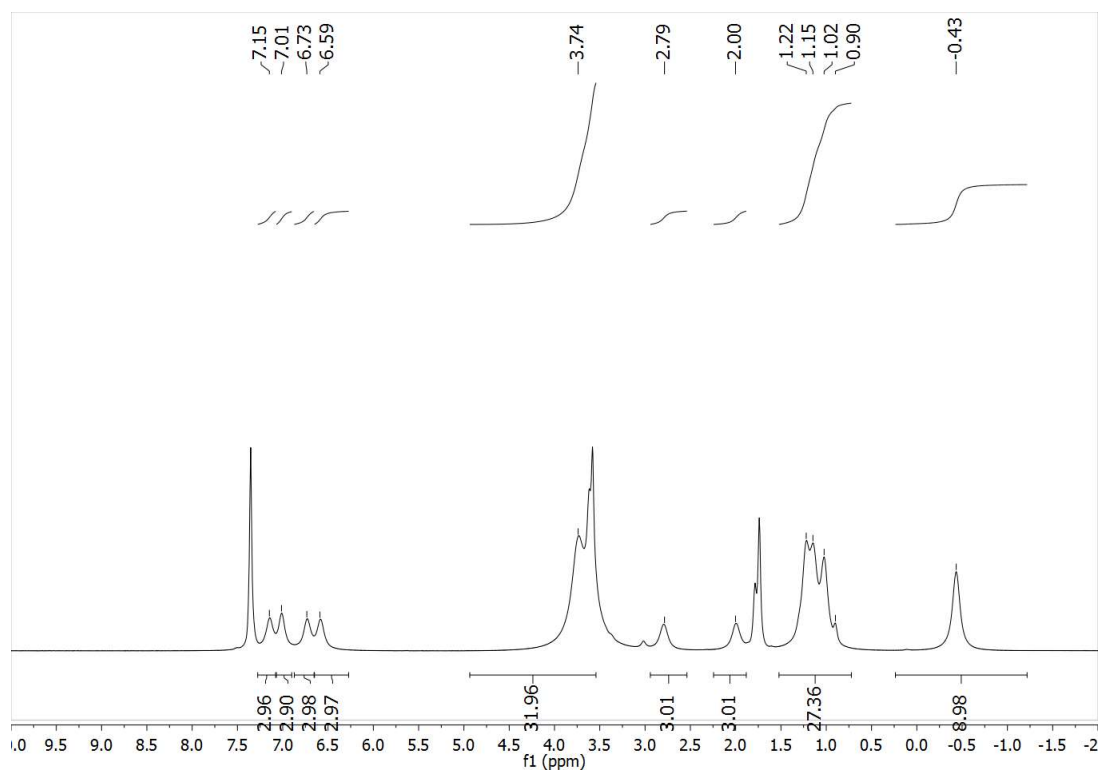


Figure A.10: The ^1H NMR spectrum (500 MHz) of $\{(\text{P}_3^{\text{B}})\text{Fe}(\text{NO})\}^{10}$ at $-78\text{ }^\circ\text{C}$ in $\text{THF-}d_8$.

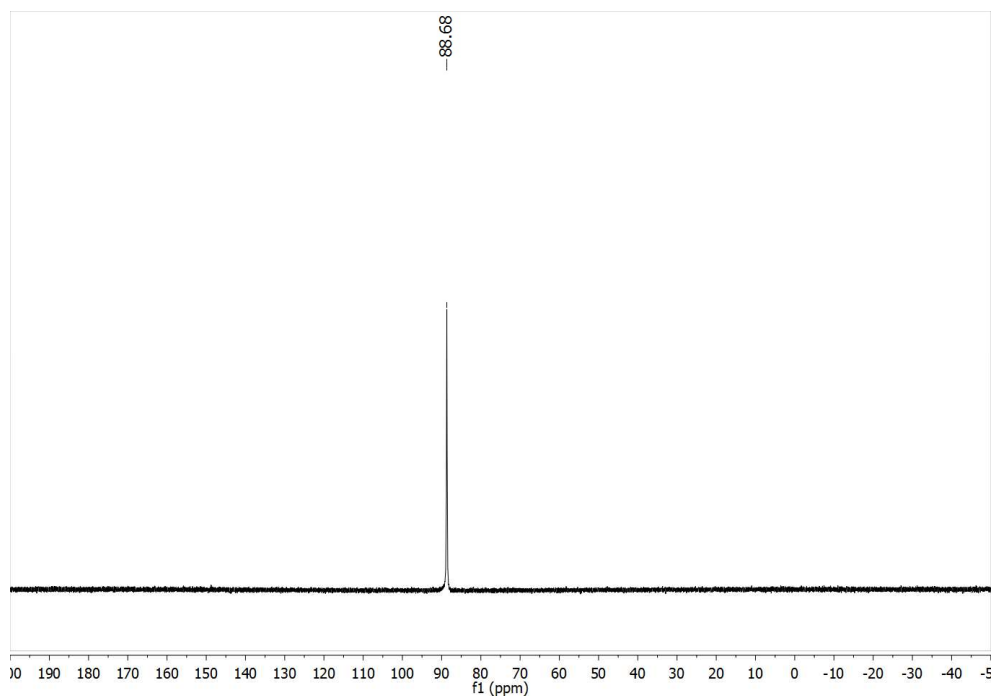


Figure A.11: The ^{31}P NMR spectrum (202.4 MHz) of $\{(\text{P}_3^{\text{B}})\text{Fe}(\text{NO})\}^{10}$ at -78 °C in $\text{THF-}d_8$.

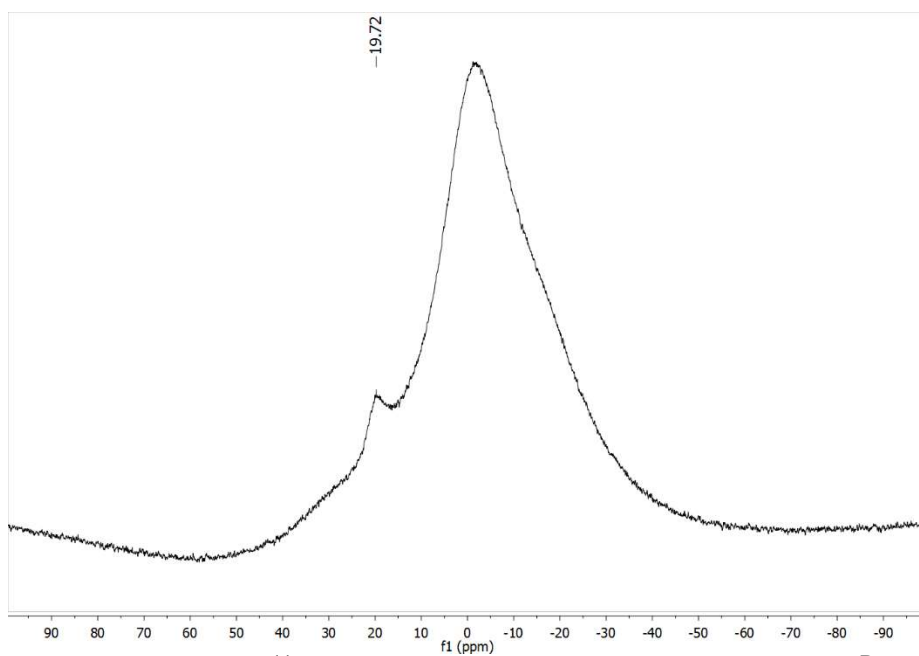


Figure A.12: The ^{11}B NMR spectrum (128.3 MHz) of $\{(\text{P}_3^{\text{B}})\text{Fe}(\text{NO})\}^{10}$ at room temperature in $\text{THF-}d_8$.

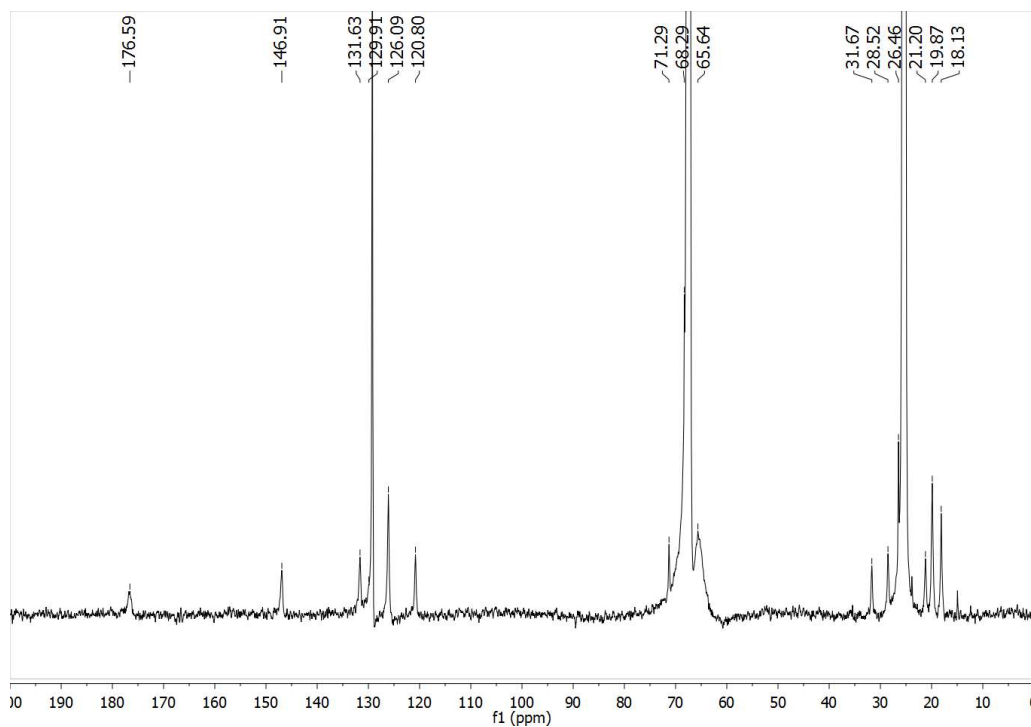


Figure A.13: The ^{13}C NMR spectrum (125.7 MHz) of $\{(\text{P}_3^{\text{B}})\text{Fe}(\text{NO})\}^{10}$ at $-78\text{ }^\circ\text{C}$ in $\text{THF-}d_8$.

A.4 IR Spectra

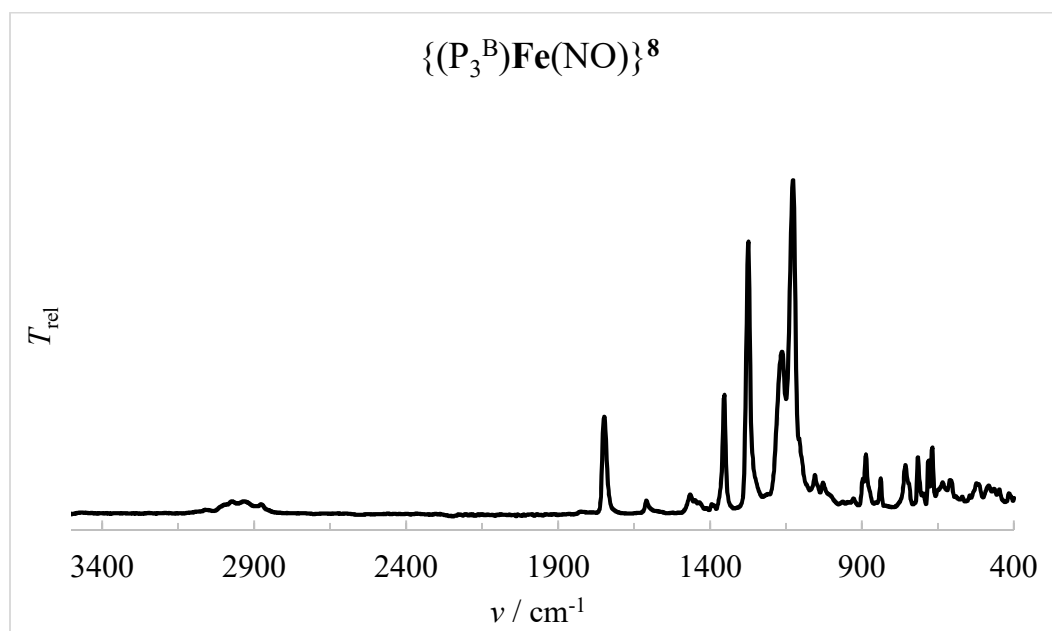


Figure A.14: Thin-film IR Absorption spectrum of $\{(\text{P}_3^{\text{B}})\text{Fe}(\text{NO})\}^8$.

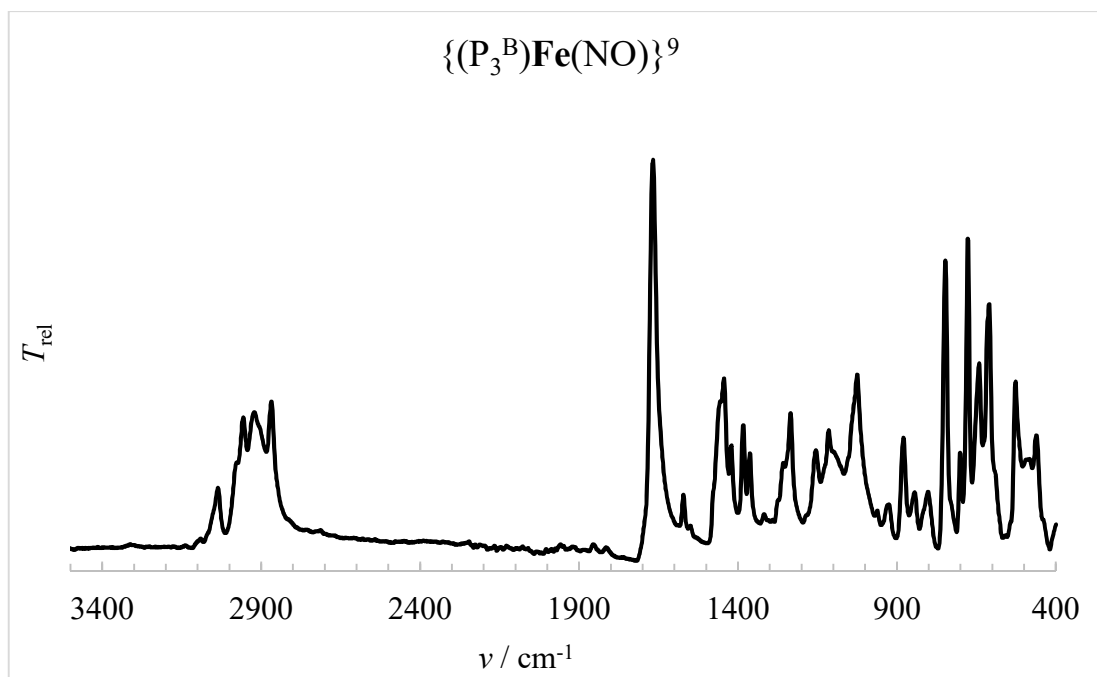


Figure A.15: Thin-film IR Absorption spectrum of $\{(P_3^B)Fe(NO)\}_9$.

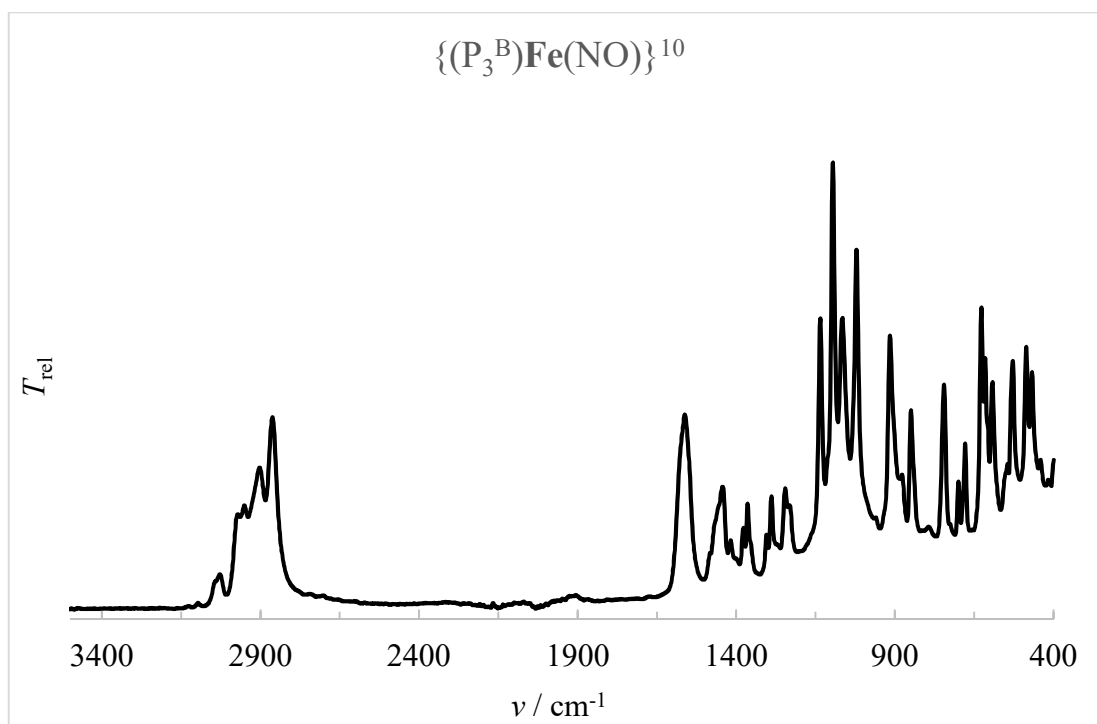


Figure A.16: Thin-film IR Absorption spectrum of $\{(P_3^B)Fe(NO)\}_{10}$.

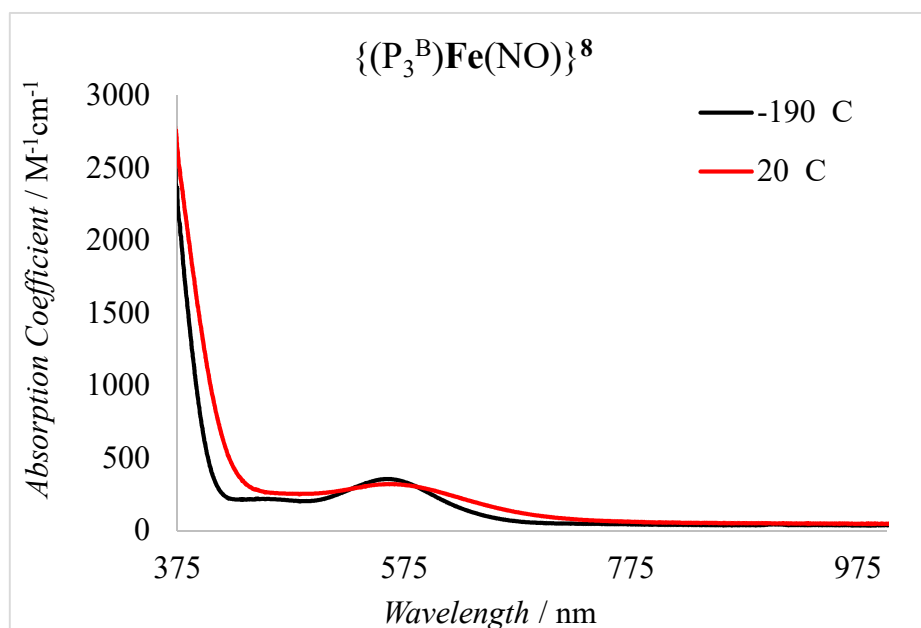
A.5 UV/Visible Spectra

Figure A.17: UV/Visible spectra of $\{(P_3^B)Fe(NO)\}_8$ in 2-MeTHF accounting for changes in density with temperature.^[5]

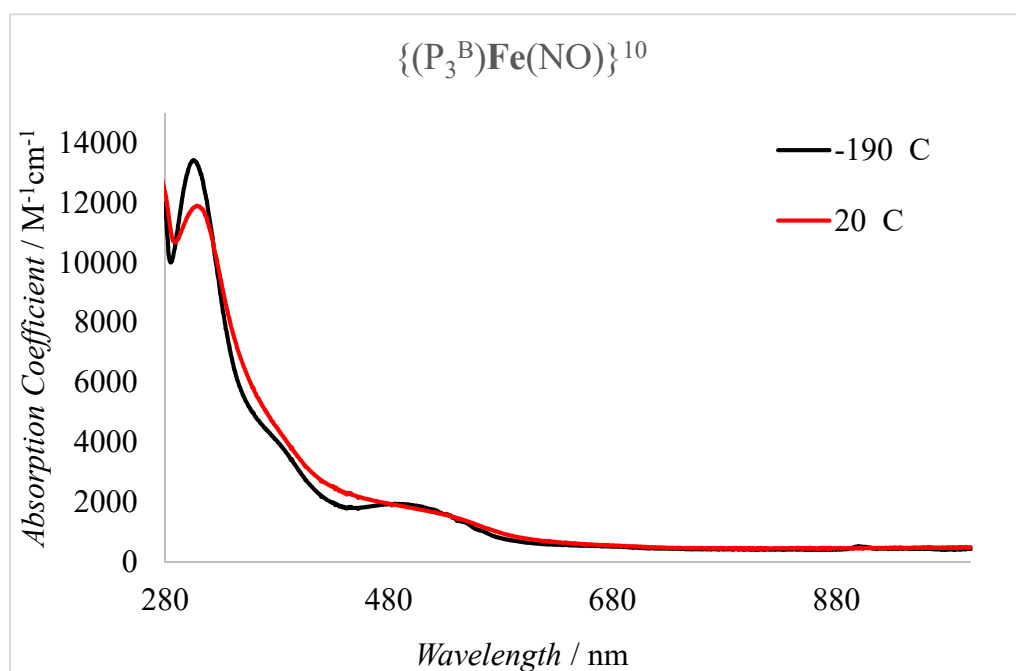


Figure A.18: UV/Visible spectra of $\{(P_3^B)Fe(NO)\}_{10}$ in 2-MeTHF accounting for changes in density with temperature.^[5]

Property	{TPBFeNO} ⁹	[Cr(CN) ₅ (NO)] ³⁻
$\nu(\text{NO})$ (cm ⁻¹)	1667	1645
$d(\text{N-O})$ (Å)	1.1901(7)	1.207(12)
$\angle(\text{M-N-O})$ (°)	176.18(6)	175.6(1)
ϵ_{max} (nm)	521	450

Table A.1: Comparison of selected data for {(P₃^B)Fe(NO)}⁹ and [Cr(CN)₅(NO)]³⁻.¹⁸

A.6 ⁵⁷Fe Mössbauer Spectroscopy

A.6.1 Mössbauer Discussion

There are a variety of mechanisms that can lead to an asymmetric quadrupole doublet arising. The most common cause is the presence of a local magnetic field (usually from the measured iron complex being paramagnetic) that causes a difference in the relaxation rate of the nuclear transitions.¹⁹ However, other mechanisms can cause broad and asymmetric line shapes even in diamagnetic samples particularly when they are measured as crystalline or microcrystalline solids. Such phenomena include the Goldanskii-Kargaryin effect,²⁰ “texture,”²¹ or cosine smearing.²² Despite the appearance of asymmetric line shapes in the crystalline, 80 K, zero field Mössbauer of {(P₃^B)Fe(NO)}⁸ and {(P₃^B)Fe(NO)}¹⁰ we believe that these species are diamagnetic in the solid state. The X-ray structures manifest short metal-ligand bond lengths that are well predicted by DFT calculations with an $S = 0$ ground state. In contrast optimizations from using the crystal structures as input in an $S = 1$ or 2 ground state lead to considerably different structures and higher energies. To further verify that the bulk material was diamagnetic we performed 80 K, zero field Mössbauer on

powdered samples obtained by dissolving crystalline material in THF, evaporating the solvent and then triturating it with pentane. This procedure led to the obtainment of signals with symmetric line shapes and in the case of $\{(P_3^B)Fe(NO)\}^{10}$ significantly sharper line widths.

Furthermore, the spin state of $\{(P_3^B)Fe(NO)\}^8$ and $\{(P_3^B)Fe(NO)\}^{10}$ is known to be $S = 0$ in solution due to the multinuclear NMR data. As such 2 mM THF solutions of ^{57}Fe enriched samples of $\{(P_3^B)Fe(NO)\}^8$ and $\{(P_3^B)Fe(NO)\}^{10}$ were measured in the presence (50 mT) and absence of a magnetic field. These samples also manifested the same isomer shift and quadrupole splitting as the solid samples confirming that the spin state is the same in solution and solid state. In the $\{(P_3^B)^{57}Fe(NO)\}^{10}$ there is the presence of a ~20 % contamination of $[(P_3^B)Fe(N_2)]^-$. This contaminant was verified by the measurement of an independently prepared sample of $[(P_3^B)Fe(N_2)]^-$. As can be seen in the electrochemistry under N_2 (**Figure S32**), addition of excess strong reductant leads to the formation of $[(P_3^B)Fe(N_2)]^-$ from samples of $\{(P_3^B)Fe(NO)\}^8$. Such an issue can be readily avoided on large scale syntheses of $\{(P_3^B)Fe(NO)\}^{10}$ by the use of stoichiometric reducing agent but in the preparation of small amounts of ^{57}Fe enriched material (~ 2 mg) consistent over reduction was observed. However the presence of this impurity does not prevent the observation of symmetric and narrow linewidths for solution state measurements of $\{(P_3^B)Fe(NO)\}^{10}$.

The calculated Mössbauer parameters (**Table S5**) consistently underestimate the isomer shift by ~ 0.08 mm s⁻¹ an error within the standard found by Neese and coworkers.^[16] The predictions of the quadrupole splitting are remarkably accurate within 0.04 mm s⁻¹ in all

cases. These calculations also illustrate the trend discussed in the main text in which lower spin states are associated with low isomer shifts.

A.6.2 Mössbauer Spectra

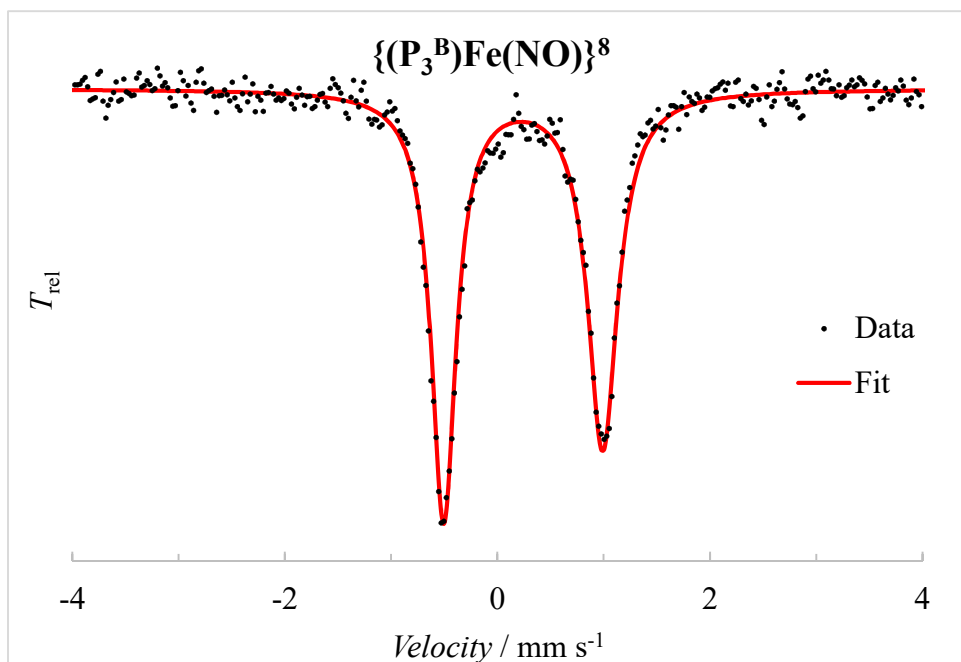


Figure A.19: The 80 K, zero field ^{57}Fe Mössbauer of $\{(P_3^B)Fe(NO)\}^8$ as a microcrystalline solid suspended in a boron nitride matrix. Fit with $\delta = 0.24\ mm\ s^{-1}$, $\Delta E_{eq} = 1.50\ mm\ s^{-1}$, $\Gamma_R = 0.34\ mm\ s^{-1}$, and $\Gamma_L = 0.29\ mm\ s^{-1}$.

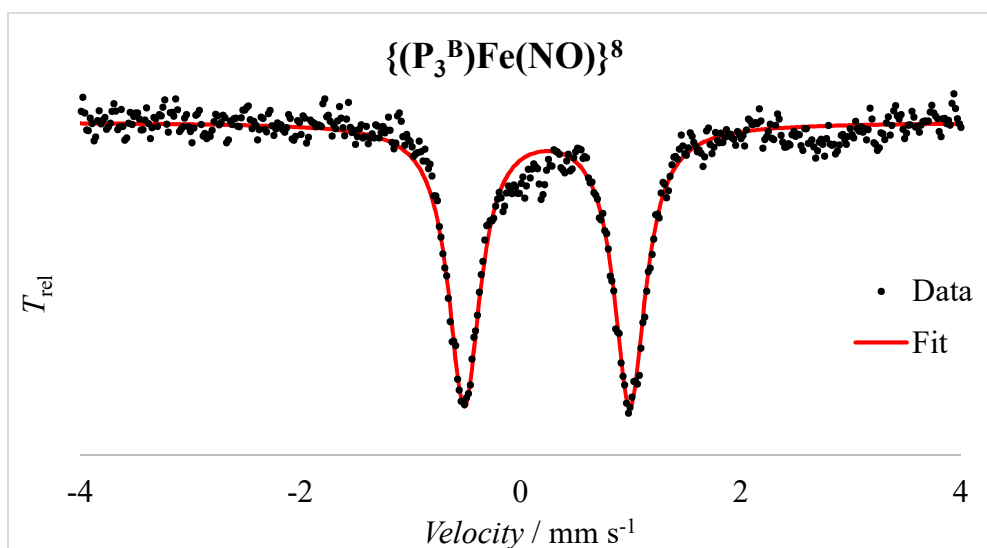


Figure A.20: The 80 K, zero field ^{57}Fe Mössbauer of $\{(\text{P}_3^{\text{B}})\text{Fe}(\text{NO})\}^8$ as a powder suspended in a boron nitride matrix. Fit with $\delta = 0.24 \text{ mm s}^{-1}$, $\Delta E_{\text{q}} = 1.50 \text{ mm s}^{-1}$, $\Gamma_{\text{R}} = 0.34 \text{ mm s}^{-1}$, and $\Gamma_{\text{L}} = 0.34 \text{ mm s}^{-1}$.

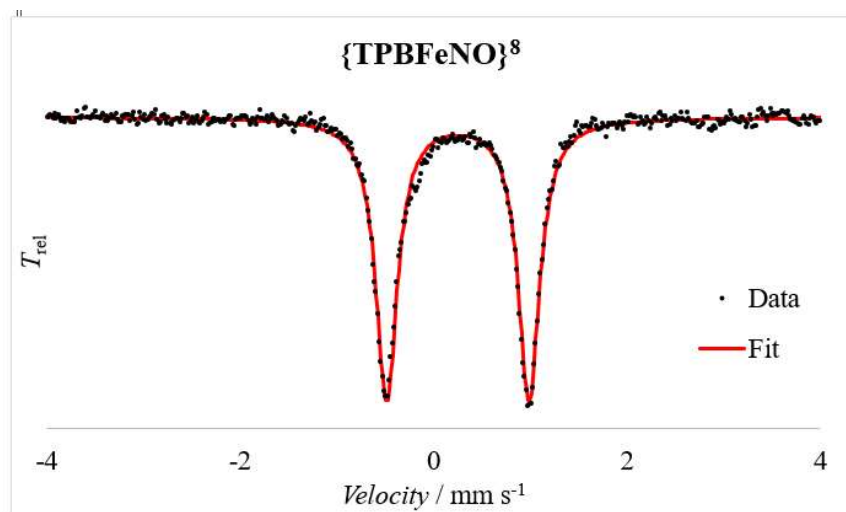


Figure A.21: The 80 K, zero field ^{57}Fe Mössbauer of a 2mM solution of $\{(\text{P}_3^{\text{B}})^{57}\text{Fe}(\text{NO})\}^8$ in 2-MeTHF. Fit with $\delta = 0.25 \text{ mm s}^{-1}$, $\Delta E_{\text{q}} = 1.47 \text{ mm s}^{-1}$, $\Gamma_{\text{R}} = 0.27 \text{ mm s}^{-1}$, and $\Gamma_{\text{L}} = 0.27 \text{ mm s}^{-1}$.

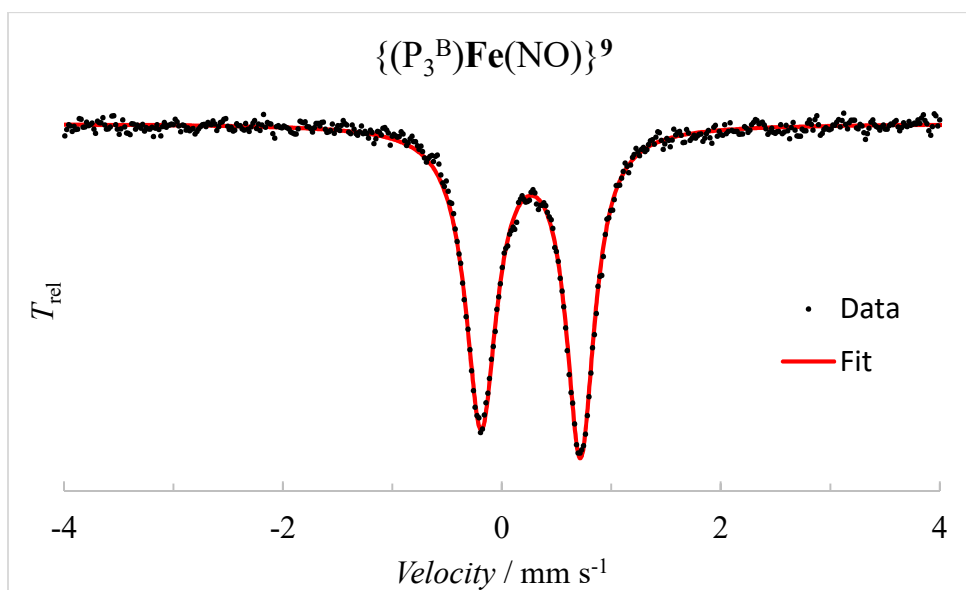


Figure A.22: The 80 K, zero field ^{57}Fe Mössbauer of $\{(\text{P}_3^{\text{B}})\text{Fe}(\text{NO})\}^9$ as a microcrystalline solid suspended in a boron nitride matrix. Fit with $\delta = 0.26 \text{ mm s}^{-1}$, $\Delta E_{\text{q}} = 0.92 \text{ mm s}^{-1}$, $\Gamma_{\text{R}} = 0.34 \text{ mm s}^{-1}$, and $\Gamma_{\text{L}} = 0.31 \text{ mm s}^{-1}$.

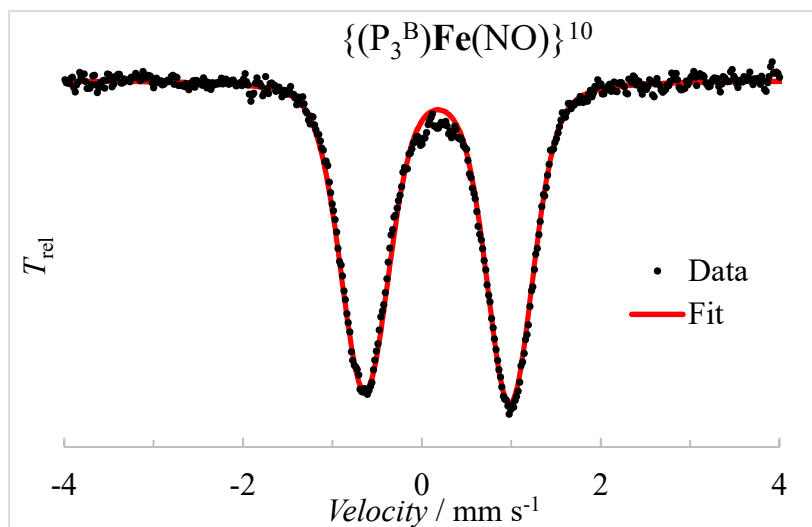


Figure A.23: The 80 K, zero field ^{57}Fe Mössbauer of $\{(\text{P}_3^{\text{B}})\text{Fe}(\text{NO})\}^{10}$ as a microcrystalline solid suspended in a boron nitride matrix. Fit with $\delta = 0.17 \text{ mm s}^{-1}$, $\Delta E_{\text{q}} = 1.62 \text{ mm s}^{-1}$, $\Gamma_{\text{R}} = -0.61 \text{ mm s}^{-1}$, and $\Gamma_{\text{L}} = -0.64 \text{ mm s}^{-1}$. Given the microcrystalline nature of the material a Voigtian distribution was considered to be an appropriate model,^[13,17] and the purity of the material was confirmed by NMR and IR spectroscopy. The most likely impurity would be $\{(\text{P}_3^{\text{B}})\text{Fe}(\text{NO})\}^9$ due to the handling procedure needed to mount the Mössbauer sample, but including a second species with the parameters for $\{(\text{P}_3^{\text{B}})\text{Fe}(\text{NO})\}^9$ leads to that component only representing 1% of the total intensity and no improvement of the fit as judged by the χ^2 -value.

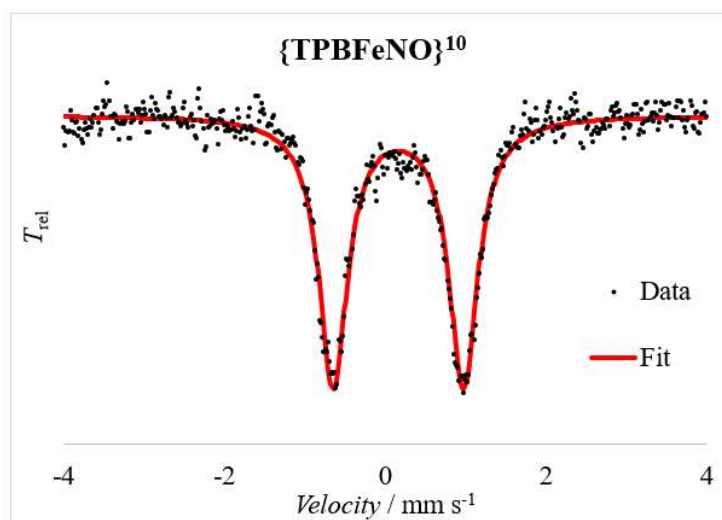


Figure A.24: The 80 K, zero field ^{57}Fe Mössbauer of $\{(\text{P}_3^{\text{B}})\text{Fe}(\text{NO})\}^{10}$ as a powder suspended in a boron nitride matrix. Fit with $\delta = 0.16 \text{ mm s}^{-1}$, $\Delta E_{\text{q}} = 1.62 \text{ mm s}^{-1}$, $\Gamma_{\text{R}} = 0.44 \text{ mm s}^{-1}$, and $\Gamma_{\text{L}} = 0.44 \text{ mm s}^{-1}$.

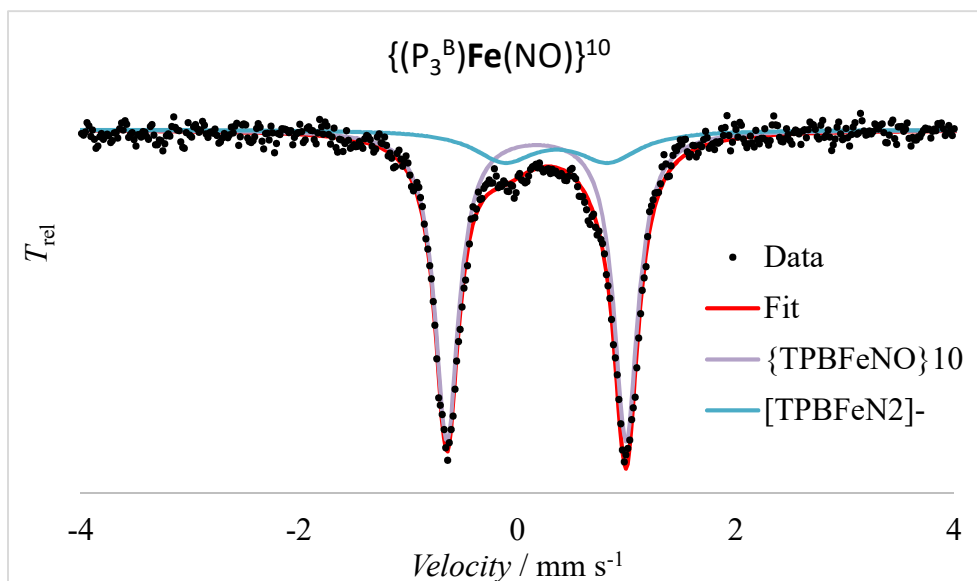


Figure A.25: The 80 K, zero field ^{57}Fe Mössbauer of a 2 mM solution of $\{(\text{P}_3^{\text{B}})^{57}\text{Fe}(\text{NO})\}^{10}$ in THF. Fit for $\{(\text{P}_3^{\text{B}})^{57}\text{Fe}(\text{NO})\}^{10}$ $\delta = 0.17 \text{ mm s}^{-1}$, $\Delta_{\text{Eq}} = 1.64 \text{ mm s}^{-1}$, $\Gamma_{\text{R}} = 0.26 \text{ mm s}^{-1}$, and $\Gamma_{\text{L}} = 0.26 \text{ mm s}^{-1}$ Weight = 0.81. Fit for $[(\text{P}_3^{\text{B}})^{57}\text{Fe}(\text{N}_2)]^-$ $\delta = 0.36 \text{ mm s}^{-1}$, $\Delta_{\text{Eq}} = 0.95 \text{ mm s}^{-1}$, $\Gamma_{\text{R}} = 0.67 \text{ mm s}^{-1}$, and $\Gamma_{\text{L}} = 0.67 \text{ mm s}^{-1}$ Weight = 0.19.

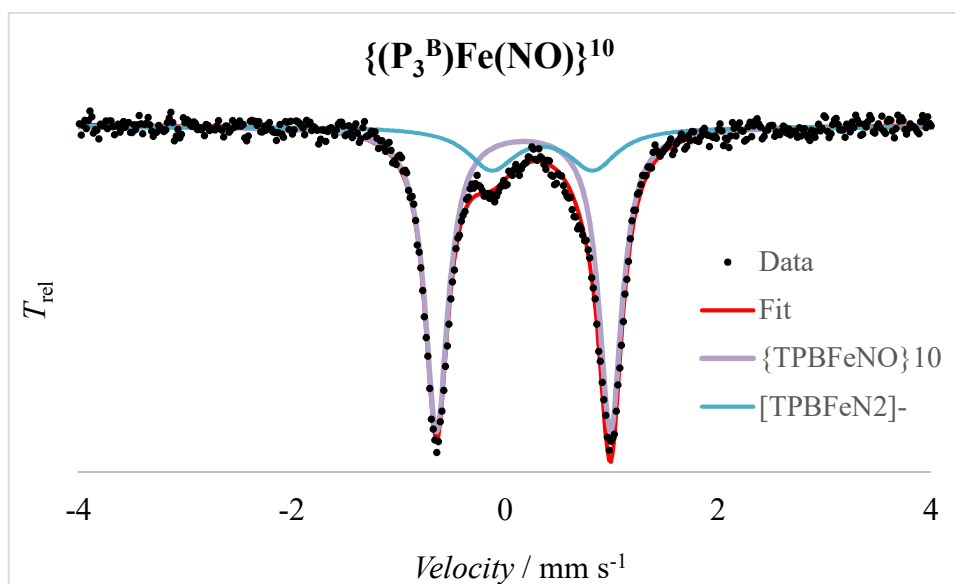


Figure A.26: The 80 K, 50 mT parallel field ^{57}Fe Mössbauer of a 2 mM solution of $\{(\text{P}_3^{\text{B}})^{57}\text{Fe}(\text{NO})\}^{10}$ in THF. Fit for $\{(\text{P}_3^{\text{B}})^{57}\text{Fe}(\text{NO})\}^{10}$ $\delta = 0.17 \text{ mm s}^{-1}$, $\Delta_{\text{Eq}} = 1.64 \text{ mm s}^{-1}$, $\Gamma_{\text{R}} = 0.36 \text{ mm s}^{-1}$, and $\Gamma_{\text{L}} = 0.36 \text{ mm s}^{-1}$ Weight = 0.81. Fit for $[(\text{P}_3^{\text{B}})^{57}\text{Fe}(\text{N}_2)]^-$ $\delta = 0.36 \text{ mm s}^{-1}$, $\Delta_{\text{Eq}} = 0.95 \text{ mm s}^{-1}$, $\Gamma_{\text{R}} = 0.54 \text{ mm s}^{-1}$, and $\Gamma_{\text{L}} = 0.54 \text{ mm s}^{-1}$ Weight = 0.19.

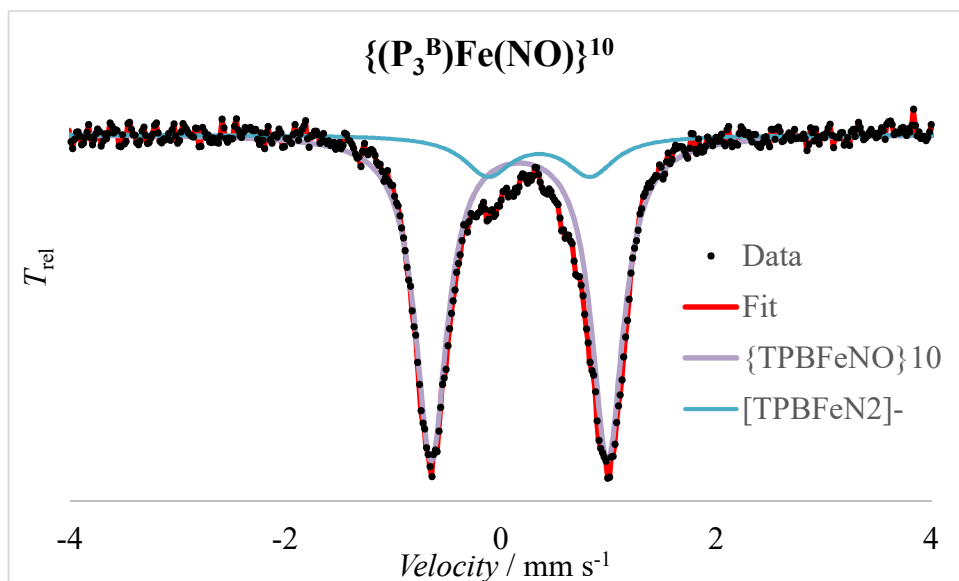


Figure A.27: The 80 K, 50 mT perpendicular field ^{57}Fe Mössbauer of a 2mM solution of $\{(\text{P}_3^{\text{B}})^{57}\text{Fe}(\text{NO})\}^{10}$ in THF. Fit for $\{(\text{P}_3^{\text{B}})^{57}\text{Fe}(\text{NO})\}^{10}$ $\delta = 0.17 \text{ mm s}^{-1}$, $\Delta_{\text{Eq}} = 1.63 \text{ mm s}^{-1}$, $\Gamma_{\text{R}} = 0.26 \text{ mm s}^{-1}$, and $\Gamma_{\text{L}} = 0.26 \text{ mm s}^{-1}$ Weight = 0.78. Fit for $[(\text{P}_3^{\text{B}})^{57}\text{Fe}(\text{N}_2)]^-$ $\delta = 0.36 \text{ mm s}^{-1}$, $\Delta_{\text{Eq}} = 0.95 \text{ mm s}^{-1}$, $\Gamma_{\text{R}} = 0.54 \text{ mm s}^{-1}$, and $\Gamma_{\text{L}} = 0.54 \text{ mm s}^{-1}$ Weight = 0.22.

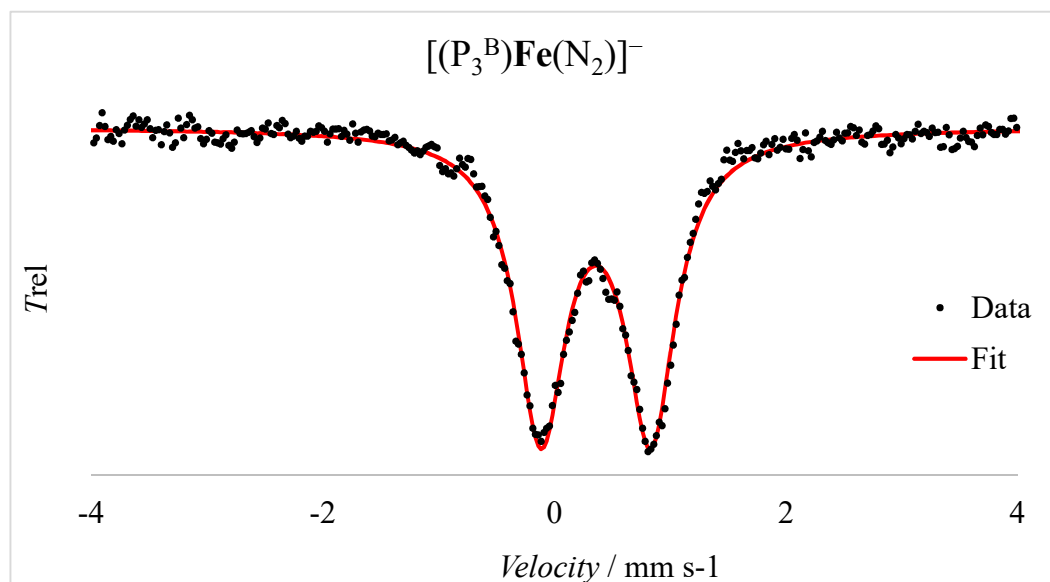


Figure A.28: The 80 K, 50 mT parallel field Mössbauer of $[(\text{P}_3^{\text{B}})^{57}\text{Fe}(\text{N}_2)]^-$ $[(\text{P}_3^{\text{B}})^{57}\text{Fe}(\text{N}_2)][\text{Na}(12\text{-crown-}4)_2]$ as a powder suspended in a boron-nitride matrix. Fit with $\delta = 0.36 \text{ mm s}^{-1}$, $\Delta_{\text{Eq}} = 0.95 \text{ mm s}^{-1}$, $\Gamma_{\text{R}} = 0.52 \text{ mm s}^{-1}$, and $\Gamma_{\text{L}} = 0.52 \text{ mm s}^{-1}$.

A.7 Electrochemistry

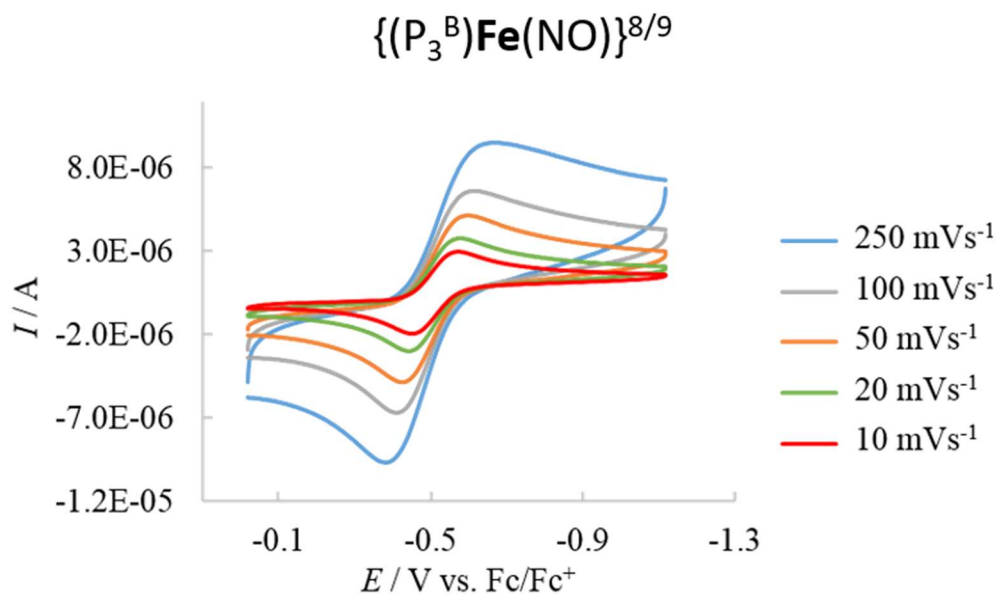


Figure A.29: Scan rate dependence of the $\{(P_3^B)Fe(NO)\}^{8/9}$ couple in a THF solution of 100 mM $[TBA][PF_6]$ under argon.

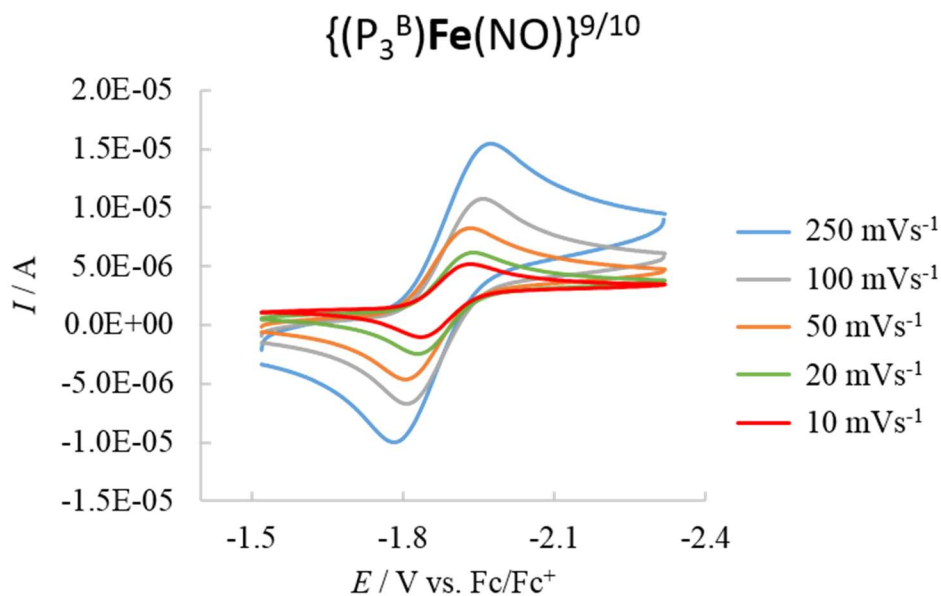


Figure A.30: Scan rate dependence of the $\{(P_3^B)Fe(NO)\}^{9/10}$ couple in a THF solution of 100 mM $[TBA][PF_6]$ under argon.

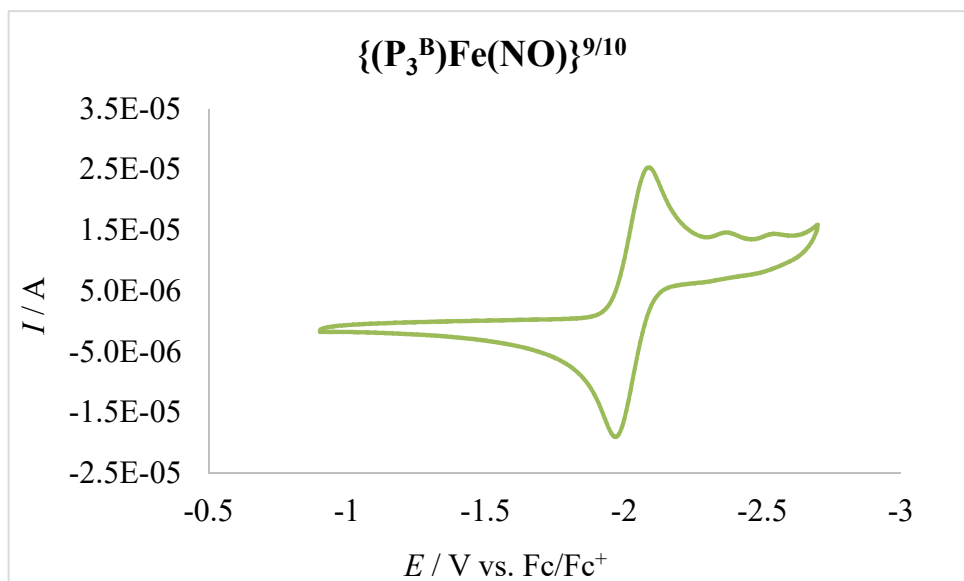


Figure A.31: Cyclic voltammety data at 100 mV s^{-1} for $\{(P_3^B)Fe(NO)\}^8$ in a THF solution of $100 \text{ mM [TBA][BArF]}$ under N_2 .

A.8 X-ray Crystallography

Table A.2: X-ray parameters for $\{(P_3^B)Fe(NO)\}^9$, and $\{(P_3^B)Fe(NO)\}^{10**}$.

Compound	$\{(P_3^B)Fe(NO)\}^9$	$\{(P_3^B)Fe(NO)\}^{10**}$
Chemical Formula	$C_{36}H_{54}FeNOBP_3$	$C_{58}H_{92}FeNO_9NaP_3$
Formula Weight	676.41	1129.89
Crystal System	Triclinic	Monoclinic
Space Group	P-1	C2/c
a [Å]	10.8566(3)	34.611(2)
b [Å]	11.3808(4)	10.8164(7)
c [Å]	15.9526(5)	32.356(2)

α [°]	91.345(2)	90
β [°]	95.217(1)	98.5813 (18)
γ [°]	118.023(1)	90
V [Å ³]	1727.84(10)	11977.5(13)
Z	2	8
D _{calcd} [g cm ⁻³]	1.300	1.253
F ₀₀₀	722.0	4848.0
μ [mm ⁻¹]	0.605	0.393
Temperature [K]	100	100
Wavelength [Å]	0.71073	0.71073
Measured Reflections	29705	22866
Unique Reflections	22786	14652
Data/Restraints/Parameters	22786/0/593	14652/1316/928
R(F) (I>2 σ (I))	0.0353	0.0499
wR(F ²) (all)	0.0790	0.1073
GOOF	1.030	1.013

** Both 12-crown-4 units that encapsulate the Na counterion are rotationally disordered over two positions. As such, restraints (EADP and SAME) have been applied to the smaller component. No changes to the structural parameters of the $\{(P_3^B)Fe(NO)\}^{10-}$ anion of interest occurred due to this process.

Table A.3: X-ray parameters for $\{(P_3^B)Fe(NO)\}^{\delta *}$.

Compound	$\{(P_3^B)Fe(NO)\}^{\delta *}$
Chemical Formula	$C_{68}H_{66}FeNOB_2P_3F_{24}$
Formula Weight	1539.63
Crystal System	Monoclinic
Space Group	$P2_1/c$
a [Å]	20.1940(2)
b [Å]	13.9917(8)
c [Å]	25.7210(14)
α [°]	90
β [°]	109.837(3)
γ [°]	90
V [Å ³]	6836.2(7)
Z	4
D_{calcd} [g cm ⁻³]	1.496
F_{000}	3144.0
μ [mm ⁻¹]	0.400
Temperature [K]	100
Wavelength [Å]	0.71073

Measured Reflections	19288
Unique Reflections	127279
Data/Restraints/Parameters	12729/54/941
R(F) ($I > 2\sigma(I)$)	0.0622
wR(F ²) (all)	0.1854
GOOF	1.037

* There is one highly disordered CF₃ group on the BArF₂₄ counteranion. Modeling this disorder led to no improvement in the $\{(P_3^B)Fe(NO)\}^8$ cation of interest, hence such disorder was not modeled.

A.9 EPR Spectroscopy

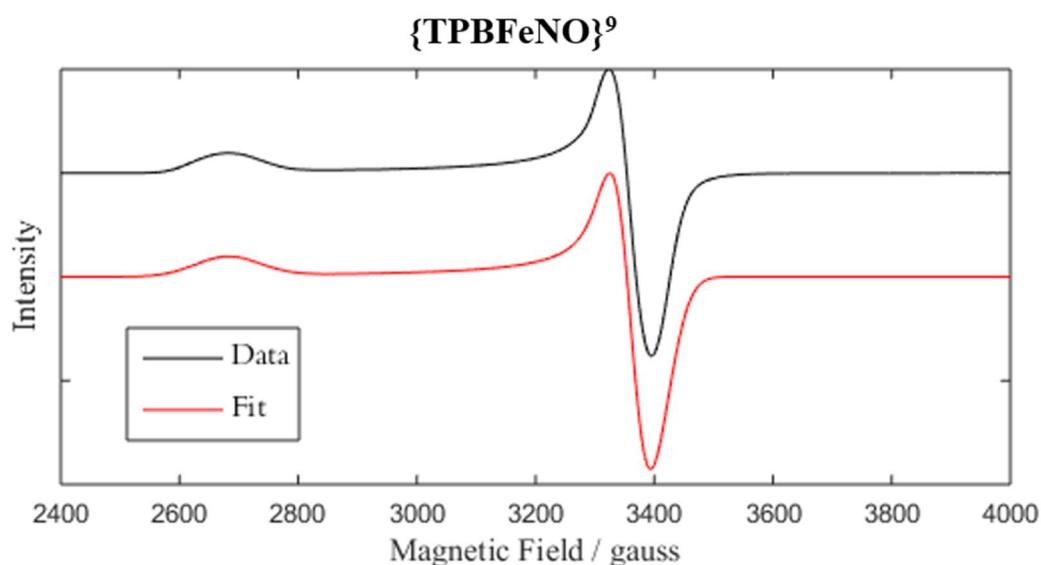


Figure A.32: X-Band EPR spectrum of $\{(P_3^B)Fe(NO)\}^9$ in 2-MeTHF at 7 K and its simulation. The simulation was done using the least-squares fitting program of EasySpin^[4] and produced the following parameters: $g = [2.50048, 1.99439, 1.96918]$ and $HStrain = [450.420, 159.384, 205.277]$.

A.10 DFT Calculations

A.10.1 DFT Discussion

The calculated structures using BP86/def2-TZVVP (Fe, B, P, N, O); 631-G(d) (C, H) led to very good agreement with the experimental values as can be seen in **Table S4**. Higher spin states were also calculated and revealed poor matches to the experimental data (long Fe–P, Fe–N, and N–O bond distances) and bent Fe–N–O angles. They were also notably higher in energy. Attempts to generate broken symmetry solutions using BP86 with $S = 1$ NO \cdot antiferromagnetically coupled to an intermediate spin metal center led to collapse of the wavefunction to the low-spin solution. This is unsurprising because BP86 is a pure functional and as such will favor electron pairing. To find broken symmetry solutions we used B3LYP, which as a hybrid functional should favor such solutions. In these cases broken-symmetry solutions are found, which in all cases are of a similar energy to the standard low-spin calculation. However, these calculations despite using the same basis sets provide both a poorer estimate of the solid state structure and more importantly predict that the triplet ground state for $\{(P_3^B)Fe(NO)\}^8$ is more stable than the singlet ground state by 23.1 kcal mol $^{-1}$ (**Table S4**). This triplet structure fails to capture the η^4 -BCCP interaction that is characteristic of this molecule in the solid state and solution. Therefore we believe that these calculations do not provide as accurate a picture of the electronic structure of these molecules. As such only the BP86 calculations are discussed in Chapter 2.

Table A.4: A comparison of calculated (BP86, low-spin) and experimental bond parameters demonstrating good agreement between optimized gas-phase structures and experimental values from X-ray data for $\{(P_3^B)Fe(NO)\}^8$, $\{(P_3^B)Fe(NO)\}^9$, and $\{(P_3^B)Fe(NO)\}^{10}$.

Metric	$\{TPBFeNO\}^8$ Experimental	$\{TPBFeNO\}^8$ Calculated	$\{TPBFeNO\}^9$ Experimental	$\{TPBFeNO\}^9$ Calculated	$\{TPBFeNO\}^{10}$ Experimental	$\{TPBFeNO\}^{10}$ Calculated
N-O	1.160(4) Å	1.177 Å	1.1901(7) Å	1.1915 Å	1.2207(16) Å	1.2110 Å
Fe-N	1.655(3) Å	1.649 Å	1.6712(5) Å	1.6555 Å	1.6505(13) Å	1.6426 Å
Fe-B	2.311(3) Å	2.314 Å	2.4451(6) Å	2.4121 Å	2.4455(16) Å	2.4530 Å
Fe-P	2.2774(9) Å	2.3053 Å	2.28169(18) Å	2.28327 Å	2.2125(4) Å	2.2297 Å
Fe-P	2.2777(9) Å	2.3085 Å	2.29654(19) Å	2.31773 Å	2.2155(4) Å	“ “
Fe-P	2.2917(8) Å	2.3271 Å	2.34813(18) Å	2.35522 Å	2.2268(4) Å	“ “
P-Fe-P	100.05(3) °	99.07 °	105.897(6) °	106.835 °	115.480(16) °	115.693 °
P-Fe-P	100.50(3) °	101.54 °	110.500(7) °	110.39 °	115.576(16) °	“ “
P-Fe-P	153.72(3) °	153.14 °	125.833(7) °	126.19 °	115.644(15) °	“ “
Fe-N-O	175.8(3) °	175.0 °	176.18(6) °	175.62 °	179.05(12) °	180.00 °
N-Fe-B	175.02(14) °	174.71 °	174.99(2) °	174.53 °	179.21(6) °	180.00 °
Σ (< C-B-C)	349.3(3) °	352.8 °	339.69(5) °	336.49 °	332.18(12) °	331.93 °

A.10.2 DFT Tables

Table A.5: Spin ladder energies for different functionals for $\{(P_3^B)Fe(NO)\}^{8-10}$. Broken symmetry solutions in which an $S = 1$ NO^- unit is antiferromagnetically coupled to the metal are indicated by BS. In all cases attempts to find broken symmetry solutions with BP86 led to collapse of the wavefunction to the electron-paired, low-spin solution. The energies given are relative to the low-spin wavefunction for that functional and species.

Functional	Spin State	Species	Energy (kcal mol ⁻¹)
BP86	$S = 0$	$\{(P_3^B)Fe(NO)\}^8$	0
BP86	$S = 1$	$\{(P_3^B)Fe(NO)\}^8$	3.6
BP86	$S = 2$	$\{(P_3^B)Fe(NO)\}^8$	27.5
B3LYP	$S = 0$	$\{(P_3^B)Fe(NO)\}^8$	0

B3LYP	$S = 1$	$\{(P_3^B)Fe(NO)\}^8$	-23.1
B3LYP	$S = 2$	$\{(P_3^B)Fe(NO)\}^8$	-7.4
B3LYP	BS $S = 0$	$\{(P_3^B)Fe(NO)\}^8$	1.5
BP86	$S = 1/2$	$\{(P_3^B)Fe(NO)\}^9$	0
BP86	$S = 3/2$	$\{(P_3^B)Fe(NO)\}^9$	28.9
BP86	$S = 5/2$	$\{(P_3^B)Fe(NO)\}^9$	53.1
B3LYP	$S = 1/2$	$\{(P_3^B)Fe(NO)\}^9$	0
B3LYP	$S = 3/2$	$\{(P_3^B)Fe(NO)\}^9$	17.5
B3LYP	$S = 5/2$	$\{(P_3^B)Fe(NO)\}^9$	34.5
B3LYP	BS $S = 1/2$	$\{(P_3^B)Fe(NO)\}^9$	0.1
BP86	$S = 0$	$\{(P_3^B)Fe(NO)\}^{10}$	0
BP86	$S = 1$	$\{(P_3^B)Fe(NO)\}^{10}$	25.6
BP86	$S = 2$	$\{(P_3^B)Fe(NO)\}^{10}$	53.4
B3LYP	$S = 0$	$\{(P_3^B)Fe(NO)\}^{10}$	0
B3LYP	$S = 1$	$\{(P_3^B)Fe(NO)\}^{10}$	4.6
B3LYP	$S = 2$	$\{(P_3^B)Fe(NO)\}^{10}$	17.5
B3LYP	BS $S = 0$	$\{(P_3^B)Fe(NO)\}^{10}$	1.8

Table A.6: Calculated Mössbauer parameters for the spin ladder of $\{(P_3^B)Fe(NO)\}^{8-10}$.

Species	Spin State	Isomer Shift ($mm\ s^{-1}$)	Quadrupole Splitting ($mm\ s^{-1}$)
$\{(P_3^B)Fe(NO)\}^8$	$S = 0$	0.19	-1.48
$\{(P_3^B)Fe(NO)\}^8$	$S = 1$	0.23	1.84
$\{(P_3^B)Fe(NO)\}^8$	$S = 2$	0.35	-2.27
$\{(P_3^B)Fe(NO)\}^9$	$S = 0$	0.17	0.87
$\{(P_3^B)Fe(NO)\}^9$	$S = 1$	0.33	1.53
$\{(P_3^B)Fe(NO)\}^9$	$S = 2$	0.47	-2.04
$\{(P_3^B)Fe(NO)\}^{10}$	$S = 0$	0.10	1.68
$\{(P_3^B)Fe(NO)\}^{10}$	$S = 1$	0.33	1.05
$\{(P_3^B)Fe(NO)\}^{10}$	$S = 2$	0.51	-0.44

A.10.3 DFT Orbitals

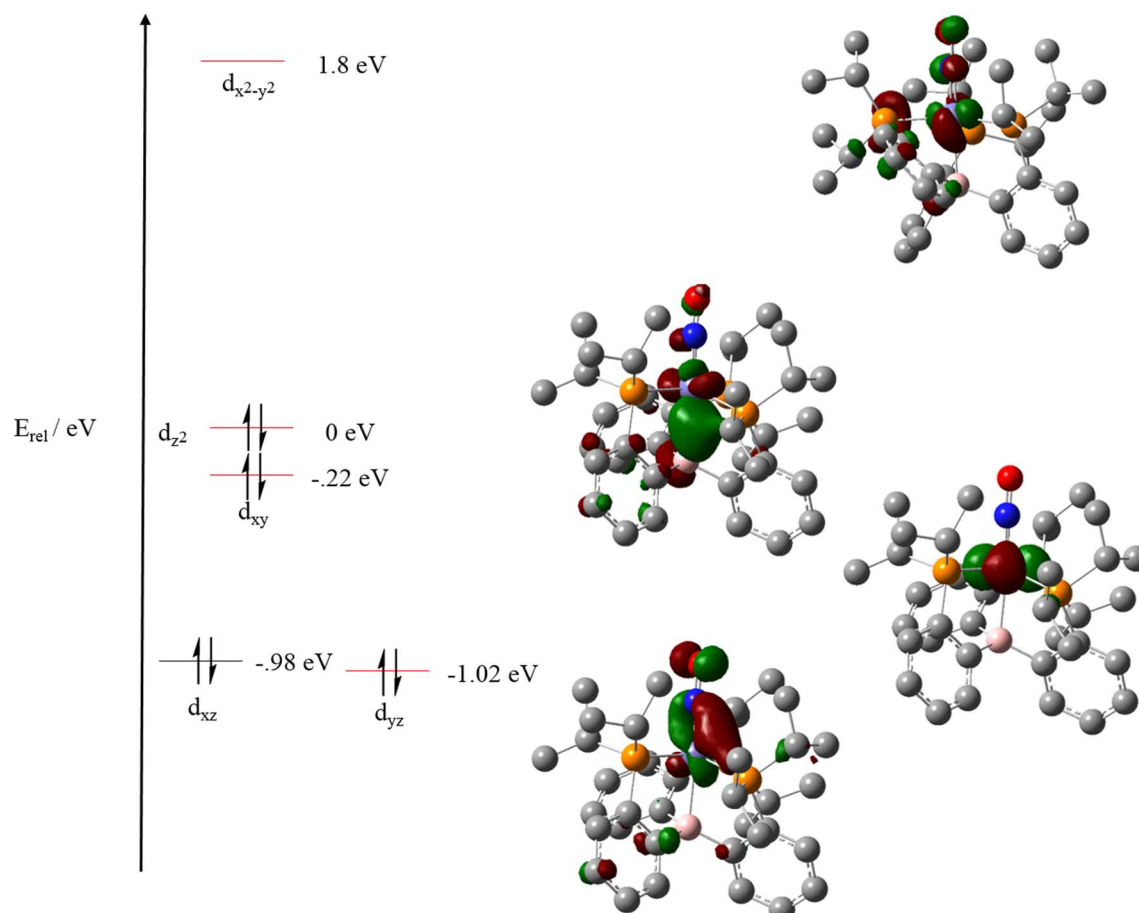


Figure A.33: A molecular orbital diagram for $\{(P_3^B)Fe(NO)\}^8$ picturing select valence orbitals. The orbitals drawn in red correspond to those depicted (isovalue = 0.05) on the right. The orbitals are denoted by their d-orbital parentage. Energies are relative to the HOMO (d_{z^2}) which was set to be 0 eV.

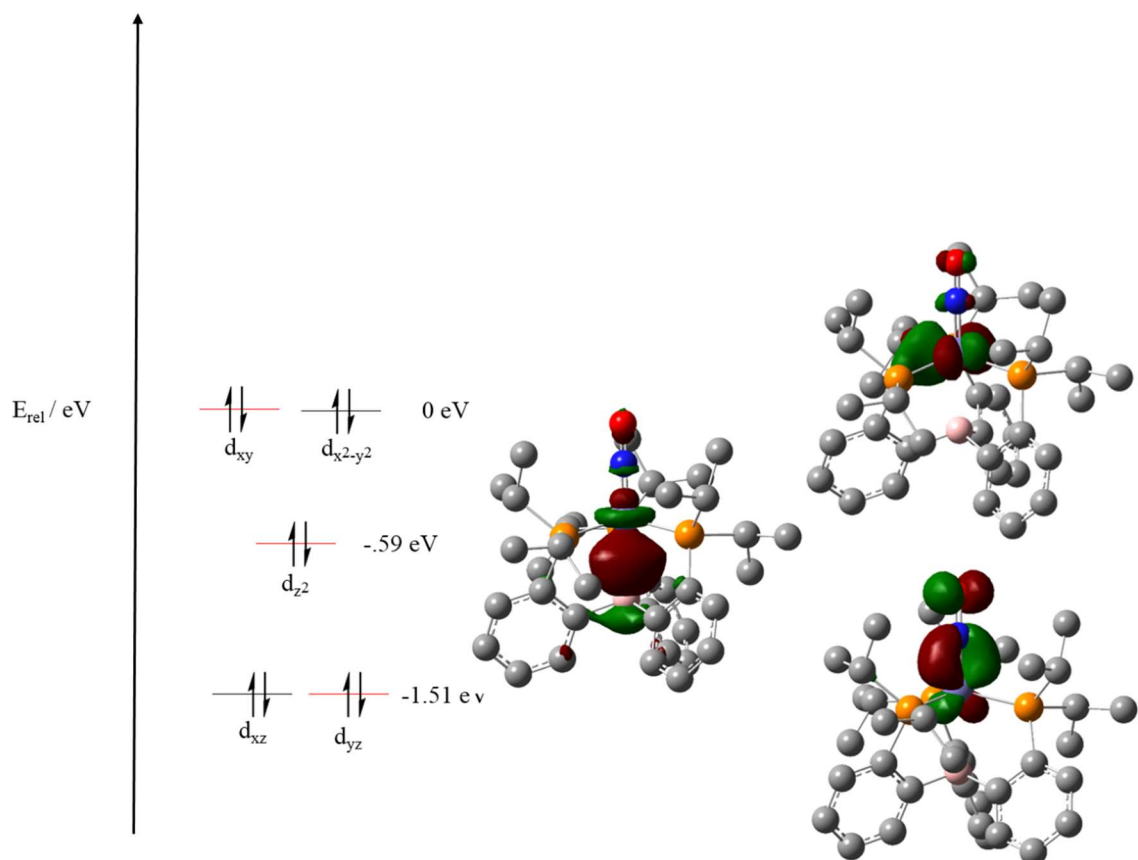


Figure A.34: A molecular orbital diagram for $\{(P_3^B)Fe(NO)\}^{10}$ picturing select valence orbitals. The orbitals drawn in red correspond to those depicted (isovalue = 0.05) on the right. The orbitals are denoted by their d-orbital parentage. Energies are relative to the HOMO (d_{xy}) which was set to be 0 eV.

Table A.7: Comparison of crystallographically determined bond lengths and Wiberg Bond Indices for $\{(P_3^B)Fe(NO)\}^{8-10}$.

Compound	Fe-N Bond Length (Å)	Fe-B Bond Length (Å)	N-O Bond Length (Å)	Expt. $\nu(NO)$ (cm^{-1})	Fe-N Bond Order	Fe-O Bond Order	Fe-B Bond Order	N-O Bond Order	Calc. $\nu(NO)$ (cm^{-1})
$\{TPBFeNO\}^8$	1.655(3)	2.311(3)	1.160(4)	1745	1.5166	.4981	.3558	1.8163	1756
$\{TPBFeNO\}^9$	1.6712(5)	2.4451(6)	1.1901(7)	1667	1.5958	.5156	.4402	1.7244	1696
$\{TPBFeNO\}^{10}$	1.6505(13)	2.4455(16)	1.2207(16)	1568	1.7049	.4832	.4708	1.6260	1614

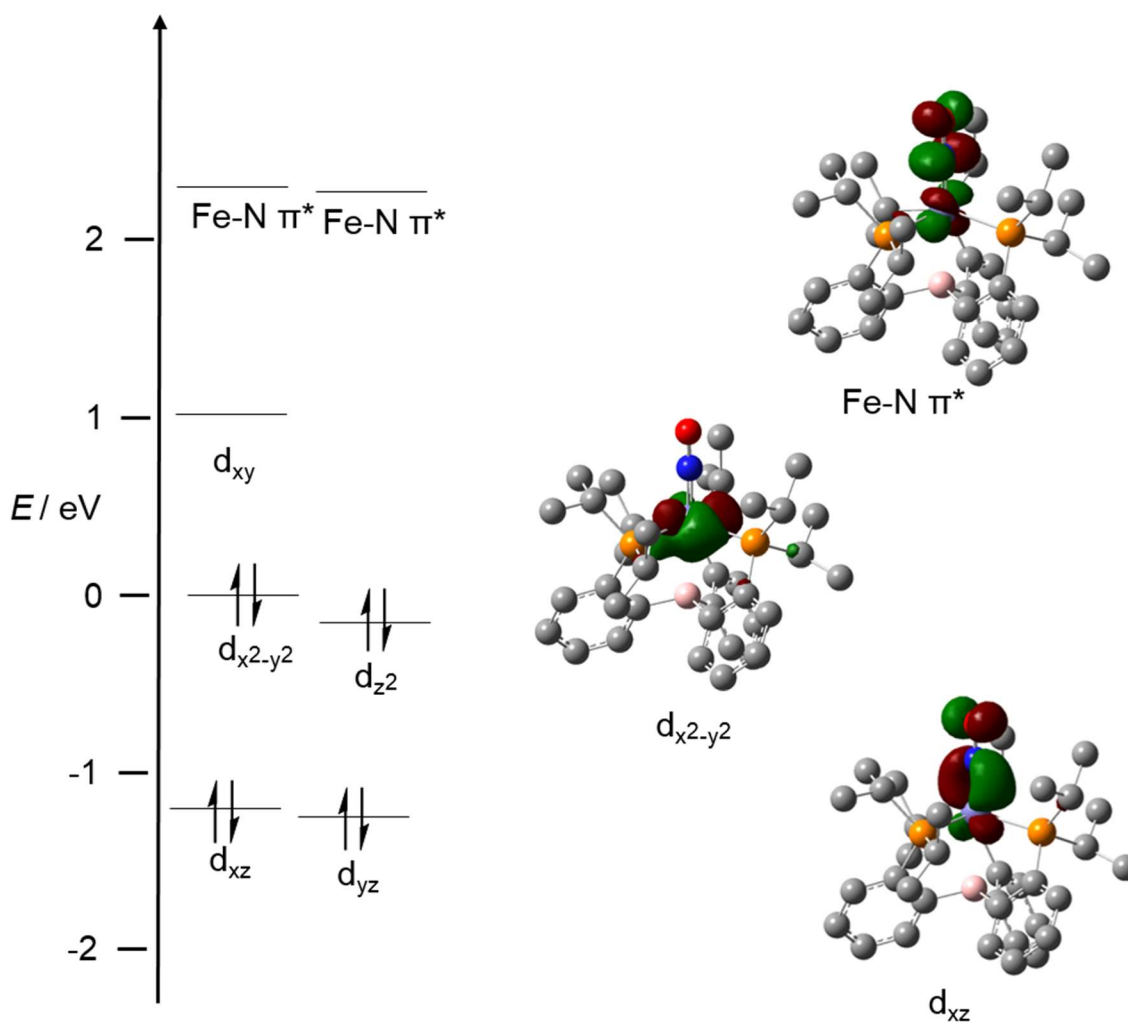


Figure A.35: A molecular orbital diagram for $\{(P_3^B)Fe(NO)\}^9$ picturing selected valence orbitals from the β -spin manifold. The orbitals are denoted with their d-orbital parentage. Energies given are relative to the HOMO ($d_{x^2-y^2}$) for the β -spin set which was set to be 0 eV. The depicted orbitals are shown at an isovalue of 0.05.

A.11 References

- (1) Moret, M.-E.; Peters, J. C. *Angew. Chem. Int. Ed.* **2011**, *50*, 2063–2067.
- (2) Ono, T.; Ohta, M.; Sada, K. *ACS Macro Lett.* **2012**, *1*, 1270–1273.
- (3) Evans, D. F. *J. Chem. Soc.* **1959**, *0*, 2003–2005.
- (4) Stoll, S.; Schweiger, A. *J. Magn. Reson.* **2006**, *178*, 42–55.

- (5) Shinsaka, K.; Gee, N.; Freeman, G. R. *J. Chem. Thermodyn.* **1985**, *17*, 1111–1119.
- (6) Sheldrick, G. M. *Acta Crystallogr., Sect. C: Struct. Chem.* **2015**, *71*, 3–8.
- (7) Neese, F. *Wiley Interdiscip. Rev.: Comput. Mol. Sci.* **2012**, *2*, 73–78.
- (8) Perdew, J. P. *Phys. Rev. B* **1986**, *33*, 8822–8824.
- (9) Becke, A. D. *Phys. Rev. A* **1988**, *38*, 3098–3100.
- (10) Becke, A. D. *J. Chem. Phys.* **1993**, *98*, 5648–5652.
- (11) Hehre, W. J.; Ditchfield, R.; Pople, J. A. *J. Chem. Phys.* **1972**, *56*, 2257–2261.
- (12) Schäfer, A.; Horn, H.; Ahlrichs, R. *J. Chem. Phys.* **1992**, *97*, 2571–2577.
- (13) Weigend, F.; Ahlrichs, R. *Phys. Chem. Chem. Phys.* **2005**, *7*, 3297–3305.
- (14) Tao, J.; Perdew, J. P.; Staroverov, V. N.; Scuseria, G. E. *Phys. Rev. Lett.* **2003**, *91*, 146401–146404.
- (15) Neese, F. *Inorg. Chim. Acta* **2002**, *337*, 181–192.
- (16) Schäfer, A.; Huber, C.; Ahlrichs, R. *J. Chem. Phys.* **1994**, *100*, 5829–5835.
- (17) Römelt, M.; Ye, S.; Neese, F. *Inorg. Chem.* **2009**, *48*, 784–785.
- (18) Enemark, J. H.; Quinby, M. S.; Reed, L. L.; Steuck, M. J.; Walthers, K. K. *Inorg. Chem.* **1970**, *9*, 2397–2403.
- (19) Münck, E. *Physical Methods in Bioinorganic Spectroscopy*; University Science Books: Sausalito, CA, 2000.
- (20) Goldanskii, V. I.; Makarov, E. F.; Khrapov, V. V. *Phys. Lett.* **1963**, *3*, 344–346.
- (21) Grenèche, J. M.; Varret, F. *J. Phys. C: Solid State Phys.* **1982**, *15*, 5333–5344.
- (22) Gütlich, P.; Bill, E.; Trautwein, A. X. *Mössbauer Spectroscopy and Transition Metal Chemistry: Fundamentals and Applications*; Springer-Verlag: Berlin Heidelberg, 2011.

APPENDIX B.
Supplementary Information for Chapter 3

Adapted from:

Chalkley, M. J.; Del Castillo, T. J.; Matson, B. D.; Roddy, J. P.; Peters, J. C.

ACS Cent. Sci. **2017**, *3*, 217–223.

DOI: 10.1021/acscentsci.7b00014

B.1 Experimental Details

B.1.1 General Considerations

All manipulations were carried out using standard Schlenk or glovebox techniques under an N₂ atmosphere. Solvents were deoxygenated and dried by thoroughly sparging with N₂ followed by passage through an activated alumina column in a solvent purification system by SG Water, USA LLC. Non-halogenated solvents were tested with sodium benzophenone ketyl in tetrahydrofuran (THF) in order to confirm the absence of oxygen and water. Deuterated solvents were purchased from Cambridge Isotope Laboratories, Inc., degassed, and dried over activated 3-Å molecular sieves prior to use.

Cp^*Co ,¹ $[(\text{P}_3^{\text{B}})\text{Fe}][\text{BAr}^{\text{F}}_4]$,² $(\text{P}_3^{\text{Si}})\text{Fe}(\text{N}_2)$,³ $[(\text{P}_3^{\text{B}})\text{Co}(\text{N}_2)][\text{Na}(12\text{-crown-}4)_2]$,⁴ $(\text{P}_3^{\text{Si}})\text{Co}(\text{N}_2)$,⁵ $[(\text{P}_3^{\text{B}})\text{Fe}(\text{N}_2)][\text{Na}(12\text{-crown-}4)_2]$,⁶ and $[\text{Ph}_2^{15}\text{NH}_2][\text{OTf}]$ ^{7,8} were prepared according to literature procedures. $\text{Ph}^{15}\text{NH}_2$ was obtained from Sigma-Aldrich, Inc. degassed, and dried over activated 3-Å molecular sieves prior to use. All other reagents were purchased from commercial vendors and used without further purification unless otherwise stated. Diethyl ether (Et₂O) used in the experiments herein was stirred over Na/K (≥ 2 hours) and filtered or vacuum-transferred before use unless otherwise stated.

B.1.2 Physical Methods

¹H chemical shifts are reported in ppm relative to tetramethylsilane, using ¹H resonances from residual solvent as internal standards. IR measurements were obtained as solutions or thin films formed by evaporation of solutions using a Bruker Alpha Platinum ATR spectrometer with OPUS software (solution IR collected in a cell with KBr windows and a 1 mm pathlength). H₂ was quantified on an Agilent 7890A gas chromatograph (HP-

PLOT U, 30 m, 0.32 mm ID; 30 °C isothermal; nitrogen carrier gas) using a thermal conductivity detector.

B.1.3 Mössbauer Spectroscopy

Mössbauer spectra were recorded on a spectrometer from SEE Co. (Edina, MN) operating in the constant acceleration mode in a transmission geometry. The sample was kept in an SVT-400 cryostat from Janis (Wilmington, MA). The quoted isomer shifts are relative to the centroid of the spectrum of a metallic foil of α -Fe at room temperature (RT). Solution samples were transferred to a sample cup and chilled to 77 K inside of the glovebox, and unless noted otherwise, quickly removed from the glovebox and immersed in liquid N₂ until mounted in the cryostat. Data analysis was performed using version 4 of the program WMOSS (www.wmoss.org) and quadrupole doublets were fit to Lorentzian lineshapes. See discussion below for detailed notes on the fitting procedure.

B.1.4 Ammonia and Hydrazine Quantification

Reaction mixtures are cooled to 77 K and allowed to freeze. The reaction vessel is then opened to atmosphere and to the frozen solution is slowly added an excess (with respect to acid) solution of a NaO^tBu solution in MeOH (0.25 mM) over 1-2 minutes. This solution is allowed to freeze, then the headspace of the tube is evacuated and the tube is sealed. The tube is then allowed to warm to RT and stirred at RT for at least 10 minutes. An additional Schlenk tube is charged with HCl (3 mL of a 2.0 M solution in Et₂O, 6 mmol) to serve as a collection flask. The volatiles of the reaction mixture are vacuum transferred at RT into this collection flask. After completion of the vacuum transfer, the collection flask is sealed and warmed to RT. Solvent is removed in vacuo, and the remaining residue is dissolved in H₂O (1 mL). An aliquot of this solution (10–100 μ L) is then analyzed for the presence of NH₃

(present as NH_4Cl) by the indophenol method.⁹ A further aliquot of this solution is analyzed for the presence of N_2H_4 (present as $\text{N}_2\text{H}_5\text{Cl}$) by a standard colorimetric method.¹⁰ Quantification is performed with UV-vis spectroscopy by analyzing absorbance at 635 nm. In this case of runs with $[\text{PhNH}_3][\text{OTf}]$ we found that aniline in the form of anilinium chloride was present in the receiving vessels. The anilinium chloride interfered with the indophenol and hydrazine detection method. Therefore, quantification for NH_3 was performed by extracting the solid residue into 1 mL of $\text{DMSO-}d_6$ that has 20 mmol of trimethoxybenzene as an internal standard. Integration of the ^1H NMR peak observed for NH_4 was then integrated against the two peaks of trimethoxybenzene to quantify the ammonium present. This ^1H NMR detection method was also used to differentiate $[\text{^{14}NH}_4][\text{Cl}]$ and $[\text{^{15}NH}_4][\text{Cl}]$ produced in the control reactions conducted with $[\text{^{15}NPh}_2\text{H}_2][\text{OTf}]$.

B.1.5 EPR Spectroscopy

X-band EPR spectra were obtained on a Bruker EMX spectrometer. Samples were collected at powers ranging from 6-7 mW with modulation amplitudes of 2.00 G, modulation frequencies of 100.00 kHz, over a range of 1800 to 4500 Gauss. Spectra were baseline corrected using the algorithm in SpinCount. EPR spectra were modeled using the easyspin program.¹¹

B.1.6 Density Functional Theory

All stationary point geometries were calculated using DFT with an M06-L functional,¹² a def2-TZVP¹³ basis set on transition metals (Stuttgart ECP¹⁴ was used on Mo atoms) and a def2-SVP¹³ basis set on all other atoms. Calculations were performed, in part, using Xtreme Science and Engineering Discovery Environment (XSEDE) resources.¹⁵

Calculations were performed on the full (P₃^E)Fe scaffolds. Calculations on the (HIPTN₃N)Mo system were performed on a truncated scaffold in which the isopropyl groups were removed (i.e. [$\{3,5-(\text{C}_6\text{H}_4)_2\text{C}_6\text{H}_3\text{NCH}_2\text{CH}_2\}_3\text{N}\}^{3-}$). Geometries were optimized using the NWChem 6.5 package.¹⁶ All single point energy, frequency and solvation energy calculations were performed with the Gaussian09 package. Frequency calculations were used to confirm true minima and to determine gas phase free energy values (G_{gas}). Single point solvation calculations were done using an SMD solvation model with diethyl ether solvent and were used to determine solvated internal energy (E_{soln}). Free energies of solvation were approximated using the difference in gas phase internal energy (E_{gas}) and solvated internal energy (**Eq B.1**) and the free energy of a species in solution was then calculated using the gas phase free energy (G_{gas}) and the free energy of solvation (**Eq B.2**).¹⁷⁻¹⁹ All reduction potentials were calculated referenced to Fc⁺⁰ using the standard Nernst relation (**Eq B.3**).

$$\text{Eq B.1) } \Delta G_{\text{solv}} \approx E_{\text{soln}} - E_{\text{gas}}$$

$$\text{Eq B.2) } G_{\text{soln}} = G_{\text{gas}} + \Delta G_{\text{solv}}$$

$$\text{Eq B.3) } \Delta G = -nFE^0$$

B.1.7 Gas Chromatography

H₂ was quantified on an HP 5890 Series II Plus Gas Chromatograph (nitrogen carrier gas) using a thermal conductivity detector. All measurements were obtained using a 100 μL manual injection and the final value was obtained as an average of two runs.

B.2 Synthetic Details

B.2.1 General Procedure for the Synthesis of the Acids

Prior to use the amine was purified (aniline by distillation and diphenylamine by recrystallization). To a 250 mL round bottom flask in the glovebox was added the amine which was subsequently dissolved in 100 mL of Et₂O (no additional drying with NaK). To this was added dropwise (1 equiv) of HOTf with stirring over five minutes. Immediate precipitation of white solid was observed and the reaction mixture was allowed to stir for one hour at RT. The reaction mixture was then filtered and the resulting white powder was washed with Et₂O (50 mL), pentane (50 mL) and Et₂O again (50 mL). The resulting white microcrystalline material was then dried under vacuum. Yields of greater than 90% of microcrystalline material was obtained in this manner in all cases.

B.2.2 Procedure for Reaction of Cp*₂Co with Acid

A 1 mL solution of HOTf or DOTf (23 μ L, 3.0 equiv) in toluene and a 2 mL solution of Cp*₂Co (40 mg, 1.0 equiv) was chilled to -78 °C for ten minutes in a cold well. With strong stirring the Cp*₂Co solution was added dropwise over ten minutes to the HOTf solution. Purple precipitate could be observed upon the addition of each drop. After the completion of the addition the reaction mixture was allowed to stir for 5 more minutes. The reaction was then vacuum filtered in the cold well through a medium porosity frit to yield a purple solid. This solid was then washed with toluene that had been prechilled to -78 °C (5 mL) and then likewise prechilled pentane (15 mL). After drying on the frit for ten minutes the solid was then transferred to a prechilled vial. The solid was then dried under vacuum for several hours at -78 °C. Exact yields were not obtained due to the solid retaining some solvent even after extended drying at these temperatures; however, the material isolated

reproducibly represents > 75% of the expected chemical yield. All further spectroscopic and reactivity characterization of this material was carried out immediately after its synthesis and with the maintenance of the material at ≤ -78 °C except where specifically noted.

B.3. Ammonia Production and Quantification Studies

B.3.1 Standard NH₃ Generation Reaction Procedure

All solvents are stirred with Na/K for ≥ 2 hours and filtered prior to use. In a nitrogen-filled glovebox, the precatalyst (2.3 μmol) was weighed into a vial.* The precatalyst was then transferred quantitatively into a Schlenk tube using THF. The THF was then evaporated to provide a thin film of precatalyst at the bottom of the Schlenk tube. The tube is then charged with a stir bar and the acid and reductant are added as solids. The tube is then cooled to 77 K in a cold well. To the cold tube is added Et₂O to produce a concentration of precatalyst of 2.3 mM. The temperature of the system is allowed to equilibrate for 5 minutes and then the tube is sealed with a Teflon screw-valve. This tube is passed out of the box into a liquid N₂ bath and transported to a fume hood. The tube is then transferred to a dry ice/acetone bath where it thaws and is allowed to stir at -78 °C for three hours. At this point the tube is allowed to warm to RT with stirring, and stirred at RT for 5 minutes. To ensure reproducibility, all experiments were conducted in 200 mL Schlenk tubes (51 mm OD) using 25 mm stir bars, and stirring was conducted at ~ 900 rpm.

* In cases where less than 2.3 μmol of precatalyst was used stock solutions were used to avoid having to weigh very small amounts.

Table B.1: UV-vis quantification results for standard NH₃ generation experiments with [(P₃^B)Fe]⁺

Entry	[(P ₃ ^B)Fe] ⁺ (μmol)	Acid equiv	Cp* ₂ Co equiv	NH ₄ Cl (μmol)	N ₂ H ₅ Cl (μmol)	Equiv NH ₃ /Fe	% Yield NH ₃ Based on e ⁻
-------	--	---------------	------------------------------	---	---	------------------------------	--

A	2.3	108 ^a	54	31.4	0.0	13.5	75.6
B	2.3	108 ^a	54	28.5	0.0	12.3	68.6
C	2.3	108 ^a	54	29.2	0.0	12.6	70.4
Avg.						12.8 ± 0.5	72 ± 3
D	2.3	322 ^a	162	76.4	2.0	33.0	61.4
E	2.3	322 ^a	162	80.0	0.7	34.5	64.2
Avg.						34 ± 1	63 ± 2
F	2.3	638 ^a	322	60.4	0.5	26.0	24.3
G	2.3	638 ^a	322	63.2	0.3	27.3	25.4
Avg.						26.7 ± 0.9	25 ± 1
H	1.1	108 ^b	54	7.8	0.0	6.9	37.6
I	2.3	108 ^b	54	19.2	0.0	8.3	46.3
Avg.						8 ± 1	42 ± 6
J	2.3	108 ^c	54	17.7	N.D.	7.7	43.1
K	2.3	108 ^c	54	13.8	N.D.	6.0	33.6
Avg.						7 ± 1	38 ± 7
L	2.3	322 ^c	162	39.8	N.D.	17.3	32.0
M	2.3	322 ^c	162	31.9	N.D.	13.9	25.7
Avg.						16 ± 3	29 ± 4

N.D. indicates the value was not determined ^aAcid used is [Ph₂NH₂][OTf] ^bAcid used is [Ph₂NH₂][BAR^F₄] ^cAcid used is [PhNH₃][OTf]

Table B.2: UV-vis quantification results for standard NH₃ generation experiments with (P₃^{Si})Fe(N₂)

Entry	P ₃ ^{Si} FeN ₂ (μmol)	Acid equiv	Cp* ₂ Co equiv	NH ₄ Cl (μmol)	N ₂ H ₅ Cl (μmol)	Equiv NH ₃ /Fe	% Yield NH ₃ Based on e ⁻
A	2.3	108 ^a	54	6.6	0.0	1.7	9.3
B	2.3	108 ^a	54	2.7	0.0	0.7	3.8
Avg.						1.2 ± 0.2	6.5 ± 0.3

^aAcid used is [Ph₂NH₂][OTf]

Table B.3: UV-vis quantification results for standard NH₃ generation experiments with [(P₃^B)Co(N₂)]⁻

Entry	[(P ₃ ^B)Co(N ₂)] ⁻ (μmol)	Acid equiv	Cp* ₂ Co equiv	NH ₄ Cl (μmol)	N ₂ H ₅ Cl (μmol)	Equiv NH ₃ /Co	% Yield NH ₃ Based on e ⁻
A	2.3	108 ^a	54	3.0	0.0	1.3	7.2
B	2.3	108 ^a	54	1.8	0.0	0.8	4.4
Avg.						1.1 ± 0.4	6 ± 2

^aAcid used is [Ph₂NH₂][OTf]

Table B.4: UV-vis quantification results for standard NH₃ generation experiments with (P₃^{Si})Co(N₂)

Entry	(P ₃ ^{Si})Co(N ₂) (μmol)	Acid equiv	Cp* ₂ Co equiv	NH ₄ Cl (μmol)	N ₂ H ₅ Cl (μmol)	Equiv NH ₃ /Fe	% Yield NH ₃ Based on e ⁻
A	2.3	108 ^a	54	0.0	0.0	0.0	0.0
B	2.3	108 ^a	54	0.0	0.0	0.0	0.0
Avg.						0.0	0.0

^aAcid used is [Ph₂NH₂][OTf]

B.3.2 Ammonia production studies with [Ph₂¹⁵NH₂][OTf]

The procedure was the same as the general procedure presented in section 3.1 with 2.3 μmol of P₃^BFe⁺ catalyst, 54 equiv Cp*₂Co, and 108 equiv [Ph₂¹⁵NH₂][OTf]. Product analyzed by ¹H NMR as described in section 1.4 and only the diagnostic triplet of [¹⁴NH₄][Cl] is observed.

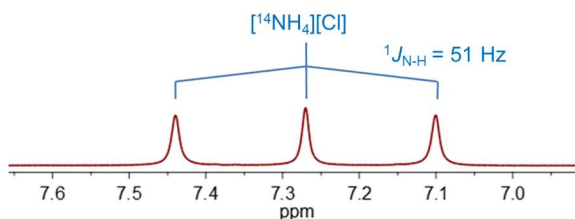


Figure B.1: ¹H NMR spectrum (300 MHz, DMSO-*d*₆) of [¹⁴NH₄][Cl] produced from catalytic N₂-to-NH₃ conversion conducted with [(P₃^B)Fe]⁺ catalyst, 54 equiv Cp*₂Co, and 108 equiv [Ph₂¹⁵NH₂][OTf] under an atmosphere of ¹⁴N₂.

B.3.3 NH₃ Generation Reaction with Periodic Substrate Reloading – Procedure with [(P₃^B)Fe]⁺

All solvents are stirred with Na/K for ≥2 hours and filtered prior to use. In a nitrogen-filled glovebox, the precatalyst (2.3 μmol) was weighed into a vial. The precatalyst was then transferred quantitatively into a Schlenk tube using THF. The THF was then evaporated to provide a thin film of precatalyst at the bottom of the Schlenk tube. The tube is then charged

with a stir bar and the acid and reductant are added as solids. The tube is then cooled to 77 K in a cold well. To the cold tube is added 1 mL of Et₂O. The temperature of the system is allowed to equilibrate for 5 minutes and then the tube is sealed with a Teflon screw-valve. The cold well cooling bath is switched from a N_{2(l)} bath to a dry ice/acetone bath. In the cold well the mixture in the sealed tube thaws with stirring and is allowed to stir at -78 °C for 3 hours. Then, without allowing the tube to warm above -78 °C, the cold well bath is switched from dry ice/acetone to N_{2(l)}. After fifteen minutes the reaction mixture is observed to have frozen, at this time the tube is opened. To the cold tube is added acid (324 equiv) and reductant (162 equiv) as solids. To the tube then 1 additional mL of Na/K-dried Et₂O is added. The cold well cooling bath is switched from a N_{2(l)} bath to a dry ice/acetone bath. In the cold well the mixture in the sealed tube thaws with stirring and is allowed to stir at -78 °C for 3 hours. These reloading steps are repeated the desired number of times. Then the tube is allowed to warm to RT with stirring and stirred at RT for 5 minutes.

Table B.5: UV-vis quantification results for NH₃ generation experiments with [(P₃^B)Fe]⁺, with reloading

Entry	Load #	[(P ₃ ^B)Fe] ⁺ (μmol)	Acid equiv	Cp* ₂ Co equiv	NH ₄ Cl (μmol)	N ₂ H ₅ Cl (μmol)	Equiv NH ₃ /Fe	% Yield Based on H ⁺
A	2	2.3	[322] x2 ^a	[162]x2	115.0	0.1	49.6	46.2
B	2	2.3	[322] x2 ^a	[162]x2	145.6	0.0	62.8	58.5
Avg.							56 ± 9	52 ± 9
C	3	2.3	[322] x3 ^a	[162]x3	182.4	0.3	78.7	48.9
D	3	2.3	[322] x3 ^a	[162]x3	207.3	0.1	89.5	55.5
Avg.							84 ± 8	52 ± 5

^aAcid used is [Ph₂NH₂][OTf]

B.4. Time Resolved H₂ Quantification

Inside of a nitrogen filled glovebox, solid acid (0.248 mmol) and Cp*₂Co (0.124 mmol) are added to a 260 mL glass tube charged with a stir bar. The vessel is sealed with a septum at RT and subsequently chilled to -196 °C in a cold well in the nitrogen filled glovebox. Et₂O (1 mL) is added via syringe into the vessel and completely frozen. The vessel is passed out of the glovebox into a liquid N₂ bath, and subsequently thawed in a dry ice/acetone bath with stirring at ~900 rpm. The timer was started as soon as the vessel was transferred to the dry ice/acetone bath. The headspace of the reaction vessel was periodically sampled with a sealable gas sampling syringe (10 mL), which was loaded into a gas chromatograph, and analyzed for the presence of H_{2(g)}. From these data, the percent H₂ evolved (relative to Cp*₂Co) was calculated, correcting for the vapor pressure of Et₂O and the removed H₂ from previous samplings. Each time course was measured from a single reaction maintained at -78 °C.

Table B.6: Time-resolved H₂ quantification for the reaction of Cp*₂Co and acid in Et₂O at -78 °C in the absence of an Fe precatalyst

Acid	Time (min)	H _{2(g)} (μmol)	% H ₂ Based on Cp* ₂ Co
[Ph ₂ NH ₂][OTf] ^a	10	1.0 ± 0.4	1.6 ± 0.6
	60	2.1 ± 0.6	3 ± 1
[Ph ₂ NH ₂][BAr ^F ₄] ^b	10	3.7 ± 0.1	6.0 ± 0.2
	60	12.7 ± 0.8	21 ± 1

^aAverage of two experiments ^bAverage of three experiments

B.5. Time Resolved NH₃ Quantification

All solvents are stirred with Na/K for ≥2 hours and filtered prior to use. In a nitrogen-filled glovebox, the precatalyst (2.3 μmol) was weighed into a vial. The precatalyst was then transferred quantitatively into a Schlenk tube using THF. The THF was then evaporated to

provide a thin film of precatalyst at the bottom of the Schlenk tube. The tube is then charged with a stir bar and diphenylammonium triflate (108 eq) and decamethylcobaltocene (54 eq) are added as solids. The tube is then cooled to 77 K in a cold well. To the cold tube is added Et₂O to produce a concentration of precatalyst of 2.3 mM. The temperature of the system is allowed to equilibrate for 5 minutes and then the tube is sealed with a Teflon screw-valve. This tube is passed out of the box into a liquid N₂ bath and transported to a fume hood.

For the control reaction at this point a 2.6 M heptane solution of ^tBuLi (2 eq with respect to the acid) was added to the tube under N₂ backflow and the headspace was evacuated. The tube was then allowed to warm to room temperature with stirring and then stirred for a further ten minutes at room temperature. At this point the normal procedure was used to quantify NH₃ and N₂H₄. No NH₃ or N₂H₄ was observed.

To test catalytic activity at five minutes, a tube prepared as described above was allowed to stir for five minutes at -78 °C. At five minutes the tube was frozen in a liquid N₂ bath and allowed to equilibrate for five minutes. Under N₂ backflow a 2.6 M heptane solution of ^tBuLi (2 eq with respect to the acid) was added to the tube. The tube was then sealed and the headspace was evacuated. The reaction mixture was then allowed to warm to room temperature with stirring and then stirred for a further ten minutes at room temperature. At this point the normal procedure was used to quantify NH₃ and N₂H₄. Ammonia (1.2 ± 0.5 eq) was detected. No hydrazine was detected.

B.6. Mössbauer Spectroscopy

B.6.1 General procedure for preparation of rapid-freeze-quench Mössbauer samples of catalytic reaction mixtures using $[(P_3^B)Fe]^+$

All manipulations are carried out inside of a nitrogen filled glovebox. The precatalyst, $[(P_3^B)^{57}Fe][BAr^F_4]$, is weighed into a vial (3.5 mg, 2.3 μ mol) and transferred using THF into a 150 mL Schlenk tube. The solvent is evaporated to form a thin film of the precatalyst and a stir bar is added. The $[Ph_2NH_2][OTf]$ (79.4 mg, 0.248 mmol) and Cp^*Co (40.3 mg, 0.124 mmol) are added to the Schlenk tube as solids. The Schlenk tube is then placed in $N_{2(l)}$ and the temperature is allowed to equilibrate. To the tube 1 mL of Et_2O is added. The tube is then sealed with a Teflon screw tap and transferred to a pre-chilled cold well at $-78\text{ }^\circ C$. The timer is set to zero as soon as the stir bar is freed from the thawing solvent. At the desired time, the tube is opened and the well-stirred suspension is transferred to a Delrin cup pre-chilled to $-78\text{ }^\circ C$ using a similarly pre-chilled pipette. The sample in the Delrin cup is then rapidly frozen in $N_{2(l)}$. At this point the sample, immersed in $N_{2(l)}$, is taken outside of the glovebox and mounted in the cryostat.

B.6.2 General Procedure for Preparation of Rapid-freeze-quench Mössbauer Samples of the Reaction of $[(P_3^B)Fe]^+$ with Reductants

All manipulations are carried out inside of a nitrogen filled glovebox. The precatalyst, $[(P_3^B)^{57}Fe][BAr^F_4]$, is weighed into a vial (3.5 mg, 2.3 μ mol) and .5 mL of THF is added. The solvent is then evaporated to provide a thin film of $[(P_3^B)^{57}Fe][BAr^F_4]$. To this is added the desired reductant as a solid (46.0 μ mol, 20 equiv). This vial is then placed in $N_{2(l)}$ and the temperature is allowed to equilibrate. To this is added 1 mL of NaK-dried Et_2O . The vial is then sealed with a cap and transferred to a pre-chilled cold well at $-78\text{ }^\circ C$. The timer is set

to zero as soon as the stir bar is freed from the thawing solvent. After five minutes using a pre-chilled pipette the well-stirred reaction mixture is transferred to a Delrin cup that has been pre-chilled to $-78\text{ }^{\circ}\text{C}$. The sample in the Delrin cup is then rapidly frozen in $\text{N}_2(l)$. At this point the sample, immersed in $\text{N}_2(l)$, is taken outside of the glovebox and mounted in the cryostat.

B.6.3 General Procedure for Fitting of Rapid-freeze-quench Mössbauer Samples

Data analysis was performed using version 4 of the program WMOSS (www.wmoss.org) and quadrupole doublets were fit to Lorentzian lineshapes. Simulations were constructed from the minimum number of quadrupole doublets required to attain a quality fit to the data (convergence of χ_R^2). Quadrupole doublets were constrained to be symmetric, unless $[(\text{P}_3^{\text{B}})\text{Fe}(\text{N}_2)][\text{Na}(12\text{-crown-}4)_2]$ was included in the model. With $[(\text{P}_3^{\text{B}})\text{Fe}(\text{N}_2)][\text{Na}(12\text{-crown-}4)_2]$ since it is known to have characteristic asymmetry we started with the observed linewidths in the authentic sample and allowed them to then relax. It is known that the exact linewidths are sensitive to the particular sample but the relative line breadth should be fairly constant. Using the non-linear error analysis algorithm provided by WMOSS, the errors in the computed parameters are estimated to be 0.02 mm s^{-1} for δ and 2% for ΔE_{q} . We additionally note that in these spectra the exact percentage contributions given do not represent exact percentages. Particularly for components that represent less than 10% of the overall spectrum, these values are subject to a high degree of uncertainty; however, all of the included components are necessary to generate satisfactory fits of the data and therefore are believed to be present in the reaction mixtures.

B.6.4 Details of Individual RFQ Mossbauer spectra

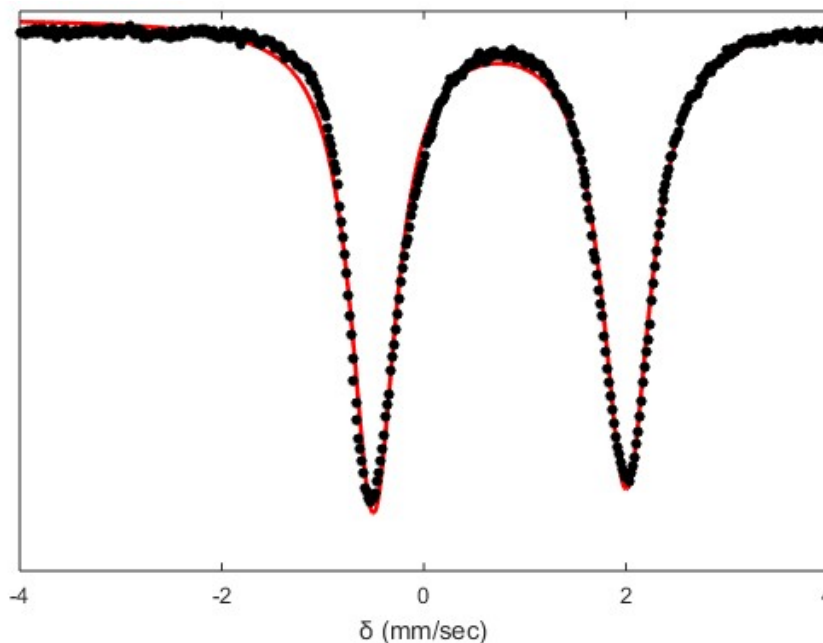


Figure B.2: Mössbauer spectrum collected on $[(P_3^B)^{57}\text{Fe}]^+$ that was used for the Mössbauer experiments conducted in this paper. The parameters used to model this species are well within the experimental error of those used previously to model this species ($\delta = 0.75$ mm/sec, $\Delta E_Q = 2.55$ mm/sec, $\Gamma_r = \Gamma_l = 0.52$ mm/sec).²⁰

Table B.7: Fit parameters for $[(P_3^B)^{57}\text{Fe}]^+$

Component	δ (mm s ⁻¹)	ΔE_Q (mm s ⁻¹)	Linewidths, Γ_L / Γ_R (mm s ⁻¹)
A	0.75 ± 0.02	2.50 ± 0.05	0.54/0.58

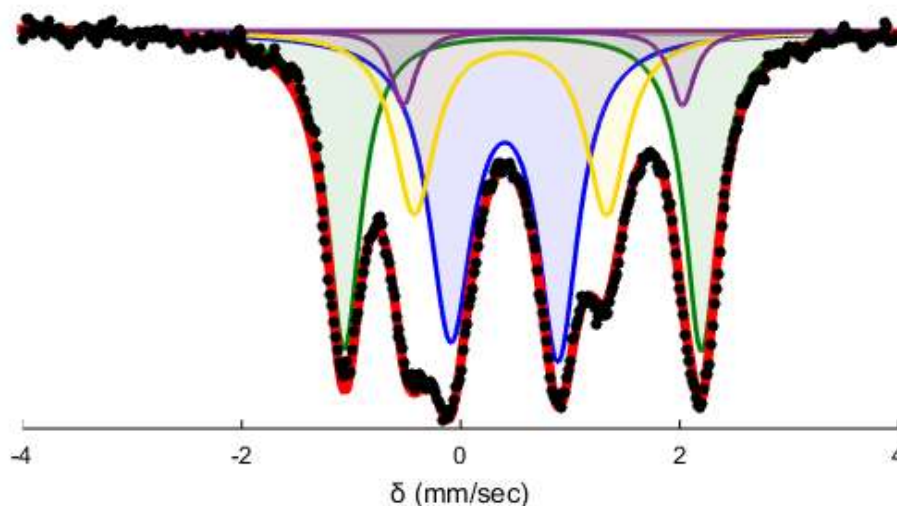


Figure B.3: Mössbauer spectrum collected from a reaction freeze quenched after 5 minutes between $P_3^B Fe^+$ and excess Cp^*Co (20 equiv). Raw data shown as black points, simulation as a solid red line, with components in green, blue, yellow, and purple (see **Table B.8** for parameters). The spectrum was collected at 80 K with a parallel applied magnetic field of 50 mT as a suspension in Et_2O .

Fitting details for **Figure B.3** are as follows: four quadrupole doublets were found to be necessary to obtain an adequate simulation. The simulation parameters are given in **Table B.8**. The two major species in this spectrum are well simulated as $(P_3^B)Fe(N_2)$ and $[(P_3^B)Fe(N_2)]^-$. The residual signal exhibits only two well resolved absorbances but to obtain a good fit with symmetric lineshapes two additional quadrupole doublets were necessary. One of these can be identified as $[(P_3^B)Fe]^+$ based on the asymmetry in the lineshape of the right feature of $[(P_3^B)Fe(N_2)]^-$. The similarity of the other two quadrupole doublets to those identified in the five-minute freeze quench make this a logically consistent fit but one that is not strictly required by the data.

Table B.8: Simulation parameters for Mossbauer spectrum in **Figure B.3**

Component	δ ($mm\ s^{-1}$)	ΔE_Q ($mm\ s^{-1}$)	Linewidths, Γ_L/Γ_R ($mm\ s^{-1}$)	Relative area
A (green)	0.57 ± 0.02	3.26 ± 0.06	0.29/0.29	0.33

B (purple)	0.75 ± 0.02	2.55 ± 0.05	0.27/0.27	0.06
C (yellow)	0.45 ± 0.02	1.76 ± 0.04	0.45/0.45	0.23
D (blue)	0.40 ± 0.02	0.98 ± 0.02	0.48/0.45	0.39

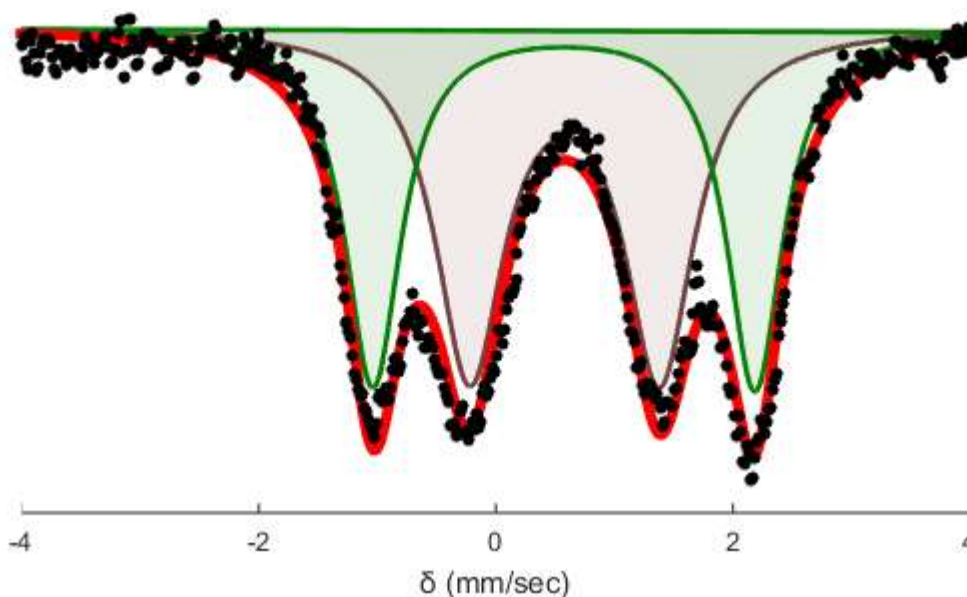


Figure B.4: Mössbauer spectrum collected from a reaction freeze quenched after 5 minutes between $P_3^B Fe^+$ and excess Cp^*Cr (20 equiv). Raw data shown as black points, simulation as a solid red line, with components in green and brown (see Table S9 for parameters). The spectrum was collected at 80 K with a parallel applied magnetic field of 50 mT as a suspension in Et_2O .

Fitting details for **Figure B.4** are as follows: the two well-resolved quadrupole doublets can be simulated. The simulation parameters are given in **Table B.9**. One of the two major species in this spectrum is well simulated as $(P_3^B)Fe(N_2)$. The other feature has a very similar isomer shift but a significantly narrower quadrupole splitting. Given the labile nature of the N_2 ligand this other species may represent a vacant neutral species or a dimeric N_2 bridged species.

Table B.9: Simulation parameters for Mossbauer spectrum in **Figure B.4**

Component	δ (mm s ⁻¹)	ΔE_Q (mm s ⁻¹)	Linewidths, Γ_L/Γ_R (mm s ⁻¹)	Relative area
A (green)	0.57 ± 0.02	3.22 ± 0.06	0.29/0.29	0.46
B (brown)	0.58 ± 0.02	1.60 ± 0.05	0.71/0.71	0.54

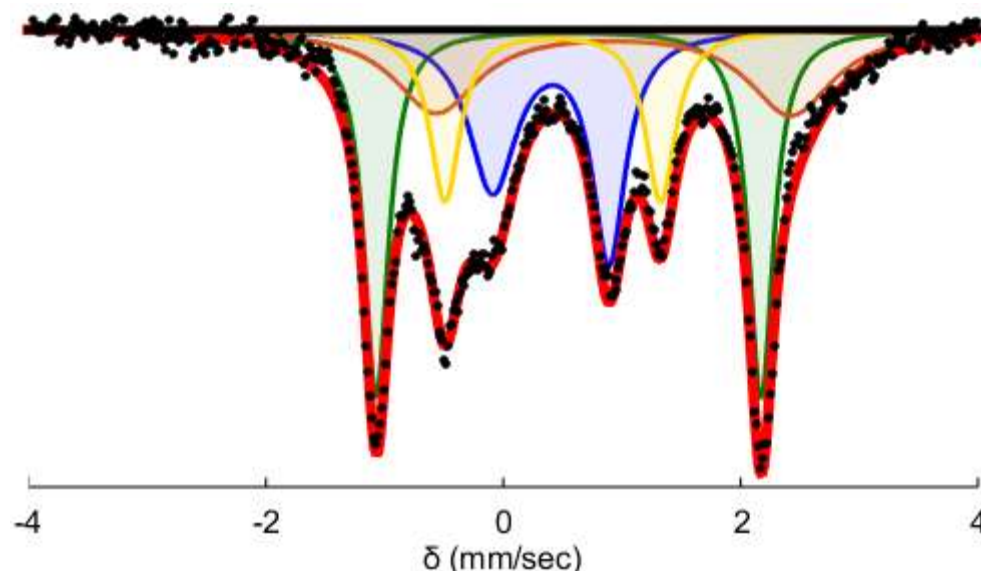


Figure B.5: Mossbauer spectrum collected from a catalytic reaction freeze quenched after 5 minutes. Conditions: $[(P_3^B)^{57}Fe][BArF] = 0.23$ mM, $[Ph_2NH_2][OTf] = 24.8$ mM (108 equiv), and Cp^*_2Co 12.4 mM (54 equiv). Raw data shown as black points, simulation as a solid red line, with components in green, blue, yellow, and orange (see **Table B.10** for parameters). The spectrum was collected at 80 K with a parallel applied magnetic field of 50 mT.

Fitting details for **Figure B.5** are as follows four pairs of quadrupole doublets were found to be necessary to obtain an adequate simulation of these data. The simulation parameters are given in Table S10. The outer pair of sharp features clearly belong to $(P_3^B)Fe(N_2)$. The inner feature is highly suggestive of $[(P_3^B)Fe(N_2)]^-$ the presence of which was confirmed by freeze-quench EPR. The residual then consists of two sharp features which were simulated with the quadrupole doublet in yellow and a broader residual feature that is

captured by the quadrupole doublet in orange. The exact isomer shift and quadrupole splitting of orange is not determined by this model but the one here is representative.

Table B.10: Simulation parameters for Mossbauer spectrum in Figure B.5

Component	δ (mm s ⁻¹)	ΔE_Q (mm s ⁻¹)	Linewidths, Γ_L/Γ_R (mm s ⁻¹)	Relative area
A (green)	0.55 ± 0.02	3.24 ± 0.06	0.25/0.25	0.32
B (blue)	0.40 ± 0.02	0.98 ± 0.02	0.49/0.34	0.26
C (yellow)	0.42 ± 0.02	1.82 ± 0.04	0.31/0.31	0.18
D (orange)	0.93 ± 0.02	2.99 ± 0.06	0.87/0.87	0.24

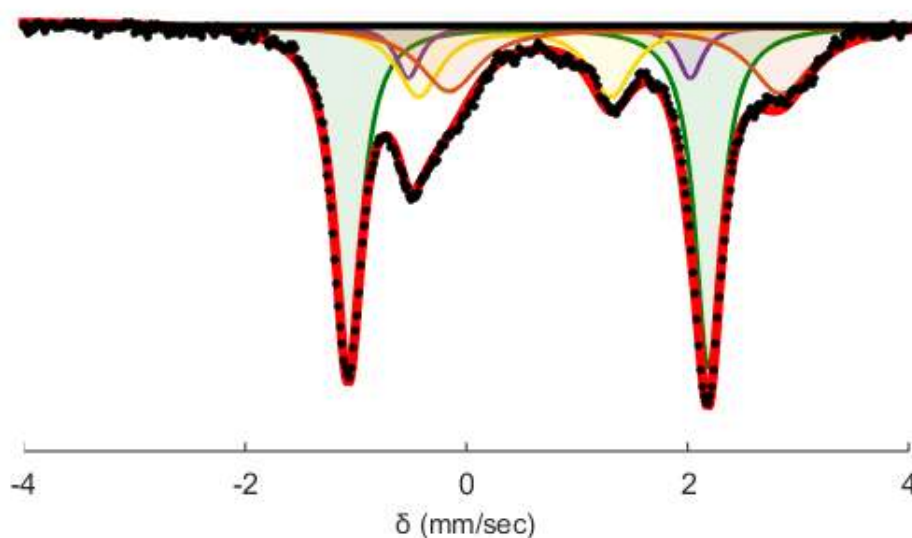


Figure B.6: Mössbauer spectrum collected from a catalytic reaction freeze quenched after 30 minutes. Conditions: $[(P_3^B)^{57}Fe][BArF] = 0.23$ mM, $[Ph_2NH_2][OTf] = 24.8$ mM (108 equiv), and Cp^*_2Co 12.4 mM (54 equiv). Raw data shown as black points, simulation as a solid red line, with components in green, purple, yellow, and orange (see **Table B.11** for parameters). The spectrum was collected at 80 K with a parallel-applied magnetic field of 50 mT.

Fitting details for **Figure B.6** are as follows: four quadrupole doublets were found to be necessary to obtain an adequate simulation. The simulation parameters are given in **Table B.11**. The major species in this spectrum is again well simulated as $(P_3^B)Fe(N_2)$. The residual signal exhibits only three well resolved absorbances. To obtain a good fit with symmetric lineshapes three additional quadrupole doublets were necessary. One of these can be

identified as $[(P_3^B)Fe]^+$ based on the asymmetry in the lineshape of the right feature of $(P_3^B)Fe(N_2)$. The similarity of the other two quadrupole doublets to those identified in the five-minute freeze quench make this a logically consistent fit but one that is not strictly required by the data.

Table B.11: Simulation parameters for Mossbauer spectrum in **Figure B.6**

Component	δ (mm s ⁻¹)	ΔE_Q (mm s ⁻¹)	Linewidths, Γ_L/Γ_R (mm s ⁻¹)	Relative area
A (green)	0.55 ± 0.02	3.24 ± 0.06	0.29/0.29	0.53
B (purple)	0.75 ± 0.02	2.55 ± 0.05	0.27/0.27	0.08
C (yellow)	0.44 ± 0.02	1.74 ± 0.04	0.48/0.48	0.18
D (orange)	1.35 ± 0.02	3.00 ± 0.06	0.67/0.67	0.22

B.7. EPR Spectroscopy

B.7.1 General Procedure for Preparation of Rapid-freeze-quench EPR Samples of Catalytic Reaction Mixtures using $[(P_3^B)Fe]^+$

All manipulations are carried out inside of a nitrogen filled glovebox. The precatalyst, $[(P_3^B)Fe][BARF_4]$, is weighed into a vial (3.5 mg, 2.3 μ mol) and transferred using THF into a 150 mL Schlenk tube. The solvent is evaporated to form a thin film of the precatalyst and a stir bar is added. The $[Ph_2NH_2][OTf]$ (79.4 mg, 0.248 mmol) and Cp^*_2Co (40.3 mg, 0.124 mmol) are added to the Schlenk tube as solids. The Schlenk tube is then placed in $N_{2(l)}$ and the temperature is allowed to equilibrate. To the tube 1 mL of Et_2O is added. The tube is then sealed with a Teflon screw tap and transferred to a pre-chilled cold well at -78 °C. The timer is set to zero as soon as the stir bar is freed from the thawing solvent. At the desired time, the tube is opened and the well-stirred suspension is transferred to an EPR tube that is prechilled to -78 °C using a pipette that has similarly been pre-chilled to -78 °C. The EPR sample is

then rapidly frozen in $N_{2(l)}$. At this point the sample is quickly transferred out of the glovebox and put into $N_{2(l)}$ before it can warm.

B.7.2 General Procedure for Preparation of Rapid-freeze-quench EPR Samples of the Reaction of $[(P_3^B)Fe]^+$ with Reductants

All manipulations are carried out inside of a nitrogen filled glovebox. The precatalyst, $[(P_3^B)Fe][BAr^F_4]$, is weighed into a vial (3.5 mg, 2.3 μ mol) and .5 mL of THF is added. The solvent is then evaporated to provide a thin film of $[(P_3^B)Fe][BAr^F_4]$. To this is added (46.0 μ mol, 20 equiv) of the desired reductant as a solid. This vial is then placed in $N_{2(l)}$ and the temperature is allowed to equilibrate. To this is added 1 mL of NaK-dried Et_2O . The vial is then sealed with a cap and transferred to a pre-chilled cold well at -78 °C. The timer is set to zero as soon as the stir bar is freed from the thawing solvent. At the desired time, the tube is opened and the well-stirred suspension is transferred to an EPR tube that is prechilled to -78 °C using a pipette that has similarly been pre-chilled to -78 °C. The EPR sample is then rapidly frozen in $N_{2(l)}$. At this point the sample is quickly transferred out of the glovebox and put into $N_{2(l)}$ before it can warm.

B.7.3 General Procedure for Preparation of EPR Samples of Cp^*_2Co , $[(P_3^B)Fe][BAr^F_4]$, and $[(P_3^B)Fe(N_2)][Na(12-crown-4)]_2$

The desired species was dissolved in 1 mL of Et_2O at RT and transferred to an EPR tube. The EPR tube was then chilled to -78 °C for five minutes. It was then rapidly frozen by transfer to a bath of $N_{2(l)}$.

B.7.3 Procedure for EPR Characterization of the Reaction of Cp^*_2Co with Acid

The as isolated solid was added to a J-Young or septum-sealed X-Band EPR tube after prechilling both in the cold well to 77 K. Specific experimental details are listed with the accompanying spectra.

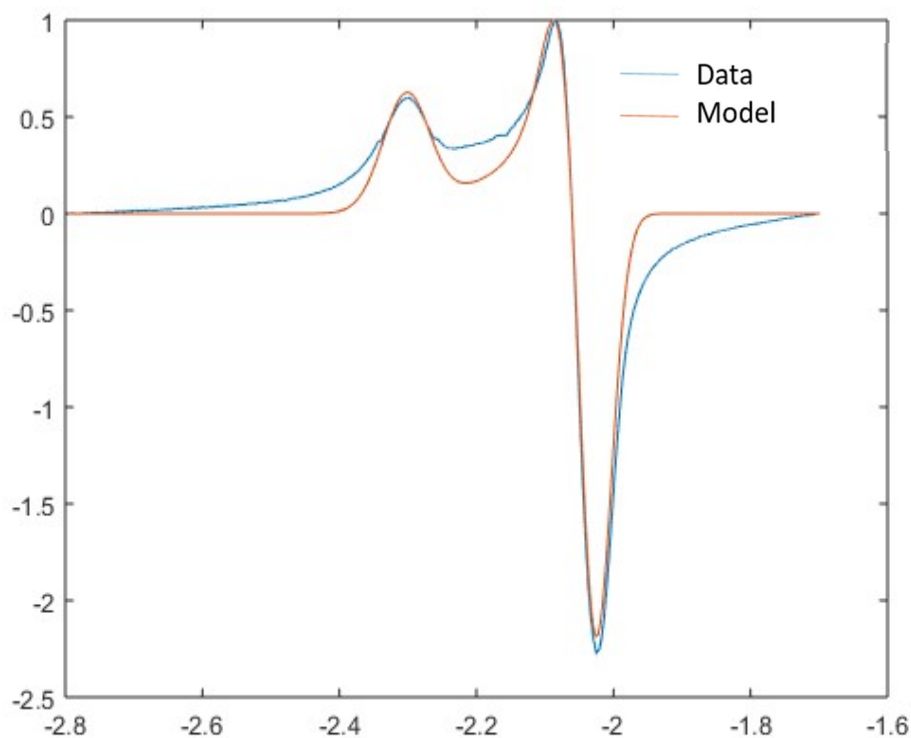


Figure B.7: The X-band EPR spectrum in a 2-MeTHF glass of 2.3 mM $[(\text{P}_3^{\text{B}})\text{Fe}(\text{N}_2)][\text{Na}(12\text{-crown-}4)_2]$ at 77K. Note that the exceeding insolubility of these species when encapsulated in a crown salt prevented its measurement in ether. We note that this species has significantly different parameters than the species in which the Na is not encapsulated with a crown ether and is therefore interacting with the N_2 ligand. We think this species is more representative of what a hypothetical $[(\text{P}_3^{\text{B}})\text{Fe}(\text{N}_2)][\text{Cp}^*_2\text{Co}]$ species would look like if isolated.

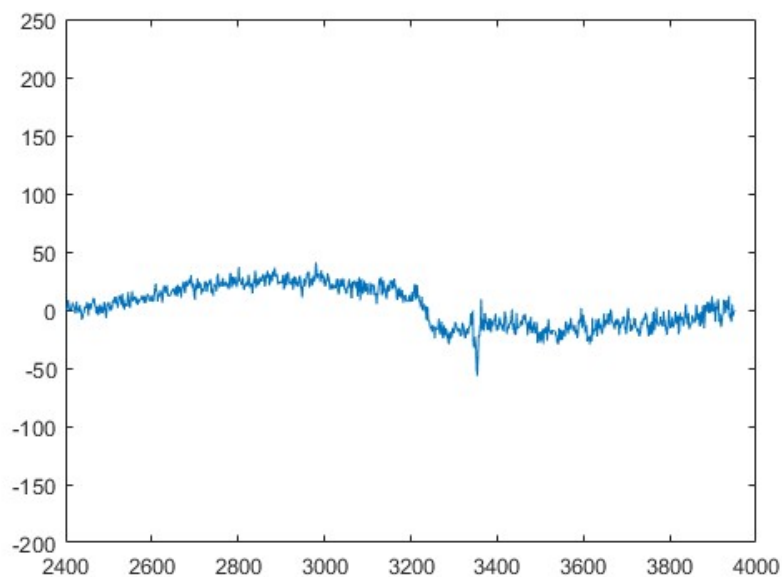


Figure B.8: The X-band EPR spectrum in Et₂O of 2.3 mM [(P₃^B)Fe][BAr^F₄] at 77 K. Note this species is $S = 3/2$. We attribute the extremely weak signal observed here to background signal from the cavity.

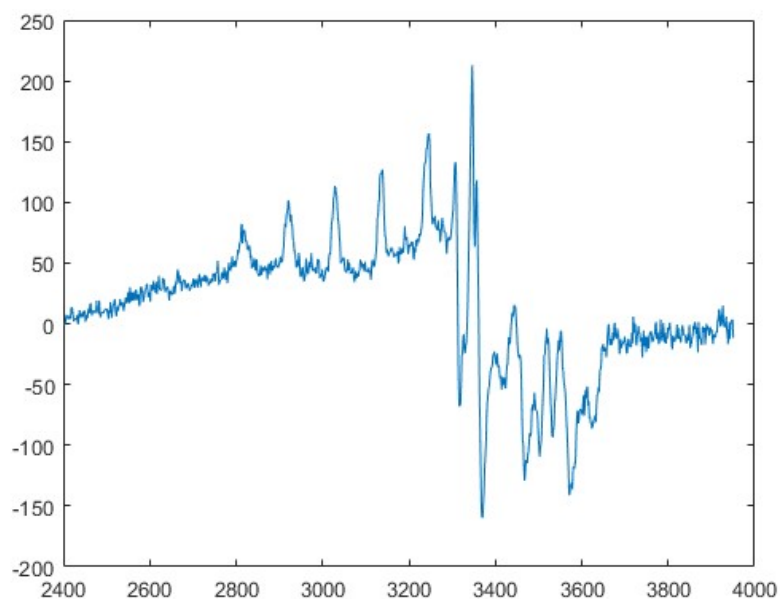


Figure B.9: The X-band EPR spectrum in Et₂O of 46 mM Cp*₂Co at 77K. Decamethylcobaltocene is known to be EPR silent at 77 K²⁴ but at these high concentrations it becomes apparent that there is a small $S = 1/2$ impurity present in this spectrum. This persistent impurity is observable in both freeze quenched reactions of this reductant with [(P₃^B)Fe][BAr^F₄] and in spectra of the freeze quenched catalytic reaction mixtures.

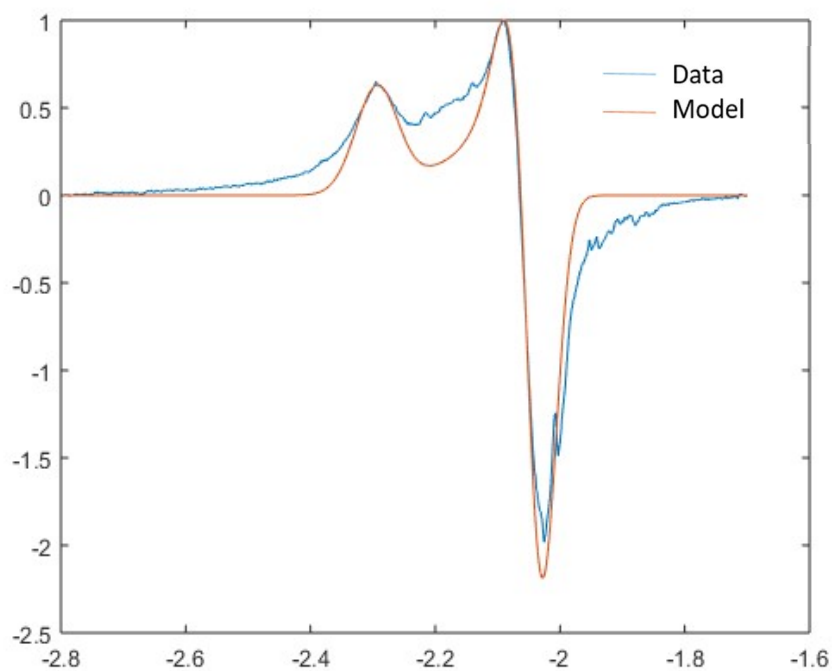


Figure B.10: The X-band EPR spectrum in Et₂O (1 mL) of the reaction between [(P₃^B)Fe]⁺ (3.5 mg, 0.0023 mmol) and Cp*₂Co (15.2 mg, 0.046 mmol) stirred for 5 minutes at -78 °C then rapidly frozen to 77 K.

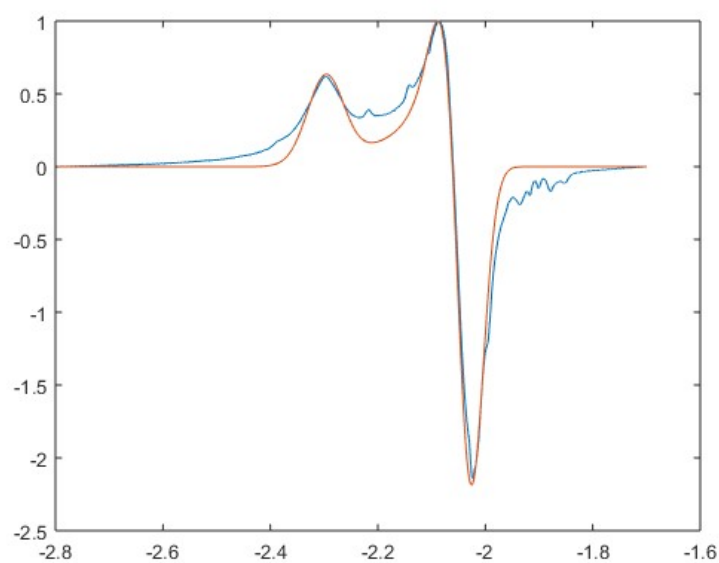


Figure B.11: The X-band EPR spectrum in Et₂O (1 mL) of the reaction between [(P₃^B)Fe]⁺ (3.5 mg, 0.0023 mmol) and Cp*₂Co (40.3 mg, 0.124 mmol) and [Ph₂NH₂][OTf] (79.4 mg, 0.248 mmol) stirred for 5 minutes at -78 °C then rapidly frozen to 77 K.

Table B.12: A comparison of the g -tensors for the authentic sample of $[(P_3^B)Fe(N_2)]^-$ (Figure B.7), the freeze quench of the reaction with the reductant (Figure B.10), the freeze quench of the catalytic reaction mixture (Figure B.11)

Reaction	g_x	g_y	g_z
Figure B.7	2.304	2.048	2.032
Figure B.10	2.295	2.048	2.032
Figure B.11	2.298	2.048	2.032

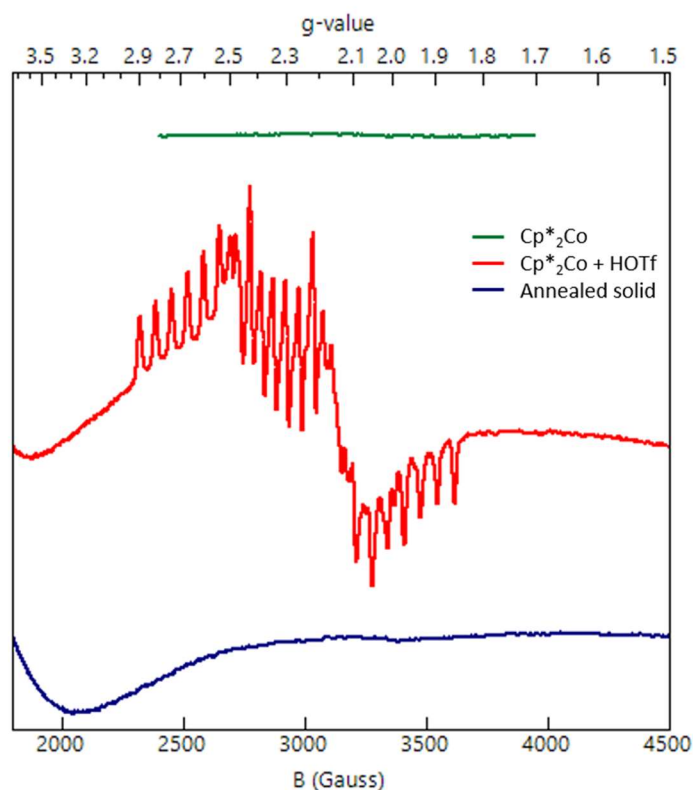
B.7.5 Discussion of the EPR spectra obtained by reacting Cp^*_2Co with Acid

Previous studies have demonstrated that the EPR signal for Cp^*_2Co is only apparent at temperatures below the 77 K used in this study. In line with this expectation the solution spectra of Cp^*_2Co at 77 K do not show any signal (

Figure B.12, green). The 77 K powder, X-band EPR spectrum obtained of the material isolated as described in SI 2.2 (

Figure B.12, red) demonstrates a signal with significant g -anisotropy and Co-hyperfine coupling. Although 1H -hyperfine coupling is not resolved in this spectrum we believe that this is due to the large Co-hyperfine coupling and the significant linewidths observed (Figure B.13). Attempts to obtain narrower linewidths by diluting the solid in KBr did not lead to any observable improvement. However, comparison of the spectrum obtained from reaction of Cp^*_2Co with HOTf and DOTf (Figure B.14) strongly supports the hypothesis that this material represents a protonated Cp^*_2Co . In particular, the narrower lineshapes observed in the reaction with DOTf evidence both that the metallocene has been protonated but also that this proton is strongly coupled to the spin. The narrower line shapes manifest because of the lesser gyromagnetic ratio of 2H compared to 1H confirming that the linewidths in the reaction with HOTf are in part broadened by coupling to the added proton. That the appearance of the extra lines observed in the reaction with DOTf can be well-

simulated simply by dividing the anisotropic strain parameter (HStrain in EasySpin) by the ratio of the ^1H gyromagnetic ratio: ^2H gyromagnetic ratio (~ 6.5) strongly supports this hypothesis (Figure B.15). That two species are present (more obvious in the DOTf reaction due to the sharper lineshapes) is further evidence that these spectra represent *endo*- and *exo*-protonated decamethylcobaltocene $[(\text{Cp}^*)\text{Co}(\eta^4\text{-C}_5\text{Me}_5\text{H})]^+$, as we would expect both the *endo*- and *exo*-protonated isomers to be kinetically and thermodynamically accessible under these conditions, and they should manifest distinct EPR signatures. Although preliminary in nature the observed reactivity of these species (discussed in SI 9.1-9.3) is further evidence



that this material is competent for PCET reactivity as predicted by DFT.

Figure B.12: 77 K X-band EPR spectrum of a toluene solution of Cp^*_2Co (green), 77 K powder X-Band EPR spectrum of the purple solid isolated from the reaction of Cp^*_2Co

and HOTf as described in **Section B2.2** (red), and 77 K powder X-Band EPR spectrum after annealing the EPR tube RT for two hours (blue).

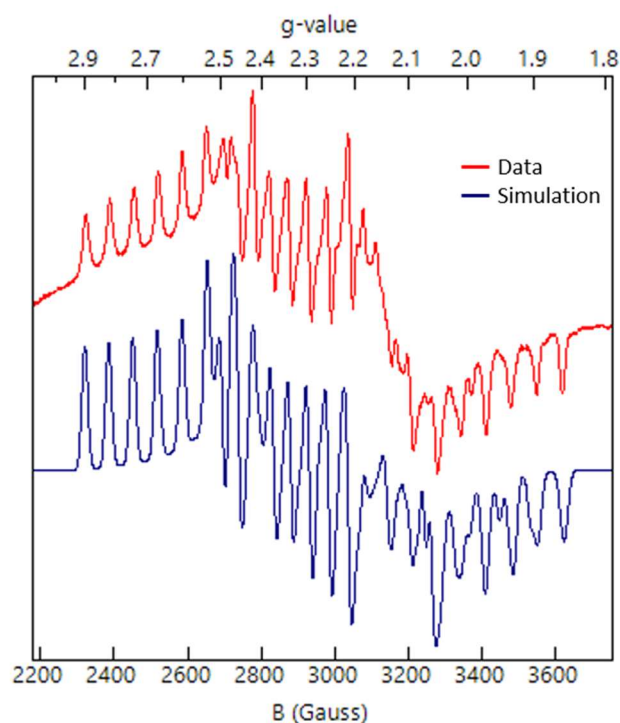
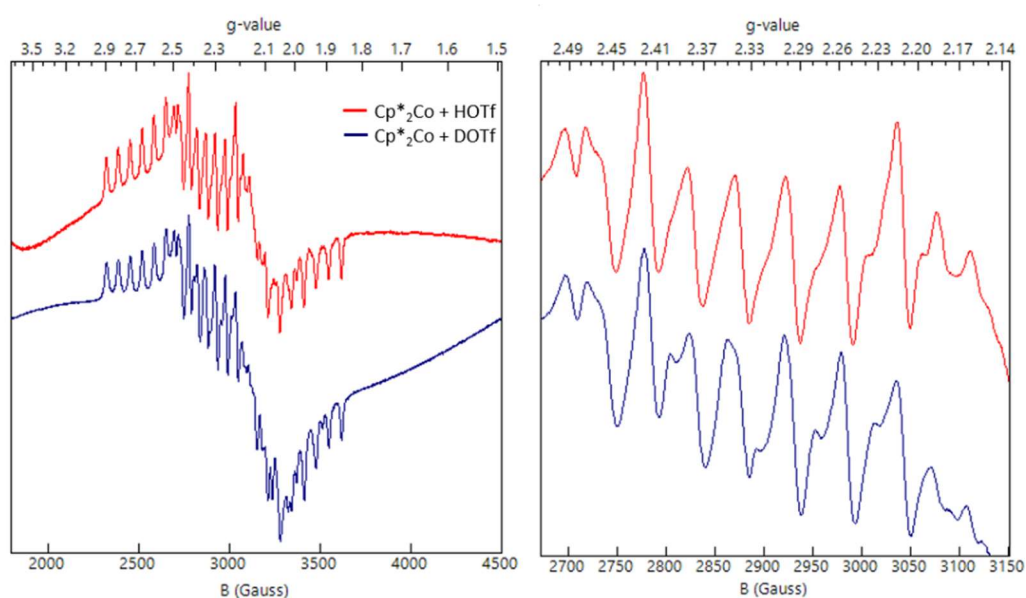


Figure B.13: Powder EPR spectrum at 77 K for the reaction of HOTf and Cp^*_2Co and its simulation. Simulation parameters are $g_1 = [2.63 \ 2.345 \ 1.984]$, $A_{1,\text{Co}} = [248 \ 160 \ 187]$, lw_1



= 1 MHz, $H_{\text{Strain}_1} = [60 \ 50 \ 60]$, $\text{Weight}_1 = 1$; $g_2 = [2.347 \ 2.1 \ 1.982]$, $A_{2,\text{Co}} = [200 \ 50 \ 110]$, $lw_2 = 1$, $H_{\text{Strain}_2} = [40 \ 40 \ 40]$, $\text{Weight}_2 = 0.2$.

Figure B.14: Comparison of the EPR spectra obtained using HOTf and DOTf in the reaction with Cp^*_2Co . The zoomed in spectrum highlights the middle g-value where the differences are most apparent between the two reactions.

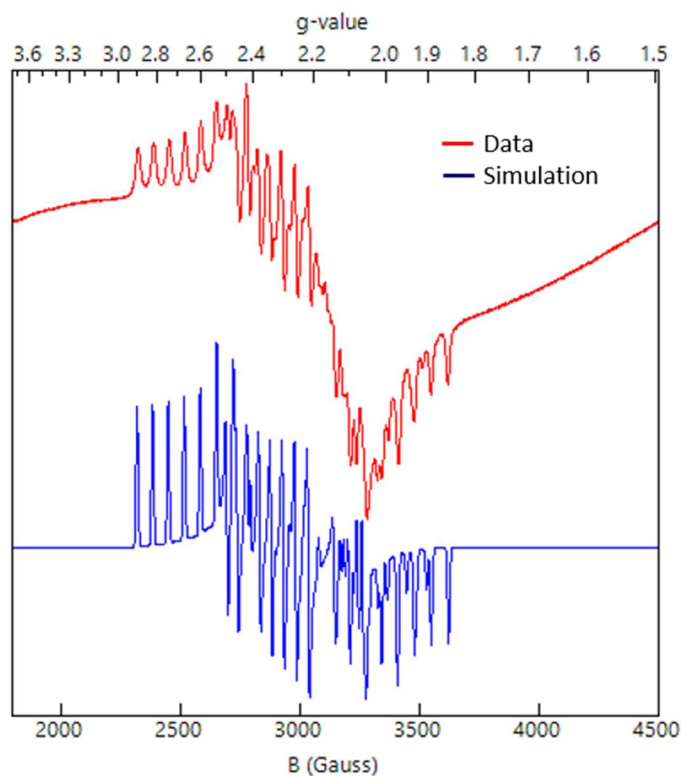


Figure B.15: EPR spectrum obtained when reacting DOTf with Cp^*_2Co and its simulation. Simulation parameters are $g_1 = [2.63 \ 2.345 \ 1.984]$, $A_{1,\text{Co}} = [248 \ 160 \ 187]$, $lw_1 = 1$ MHz, $H_{\text{Strain}_1} = [9.2 \ 7.7 \ 9.2]$, $\text{Weight}_1 = 1$; $g_2 = [2.347 \ 2.1 \ 1.982]$, $A_{2,\text{Co}} = [200 \ 50 \ 110]$, $lw_2 = 1$, $H_{\text{Strain}_2} = [6.2 \ 6.2 \ 6.2]$, $\text{Weight}_2 = 0.2$.

B.8. Reactivity of $[(Cp^*)Co(\eta^4-C_5Me_5H)]^+$

B.8.1 Annealing the Purple Solid

Purple solid isolated as described in **Section B2.2** was placed in an X-band EPR tube at 77 K and sealed with a rubber septum. A 77 K, powder X-band EPR spectrum was then taken to confirm the presence of $[(Cp^*)Co(\eta^4-C_5Me_5H)]^+$. After two hours at room temperature a second 77 K, powder EPR spectrum was taken to confirm the quenching of $[(Cp^*)Co(\eta^4-C_5Me_5H)]^+$. At this point the headspace was analyzed for H₂ via GC (14% yield).

B.8.2 Annealing a Suspension of the Purple Solid in Toluene

Into a 26 mL vial with a septum seal was loaded 2 mL of toluene which was frozen at 77 K. To this purple solid isolated as described in **Section B2.2** was added along with a stir bar. The suspension was stirred for 1 hour at $-78\text{ }^\circ\text{C}$ and then warmed to room temperature and stirred for an additional 15 minutes. At this point the headspace was sampled for H₂ via GC (35% yield). The solvent was then removed and to the yellow residue was added 1,3,5-trimethoxybenzene (1 eq.). The solid was then extracted with *d*₆-acetone and ¹H NMR was obtained. $[Cp^*_2Co]^+$ was observed (>95 % yield).

B.8.3 Upper Bound on Protonated Metallocene BDE

An upper bound for the BDE of the putative protonated metallocene was estimated using the literature BDE value for H₂ (105.8 kcal/mol) in MeCN, as well as the approximation for TΔS_{H•} (4.6 kcal/mol) in MeCN.²⁴ The maximum BDE was then approximated as follows:

$$\text{Eq B.4) } \Delta G = \Delta H - T\Delta S$$

$$\begin{aligned} \text{Eq B.5) } \Delta H &= \text{BDE}(\text{H}_2) - 2 \times \text{BDE}([\text{Cp}^*\text{Co}(\eta^4\text{-C}_5\text{Me}_5\text{H})]^+) \\ &= 105.8 \text{ kcal mol}^{-1} - 2 \text{ BDE}([\text{Cp}^*\text{Co}(\eta^4\text{-C}_5\text{Me}_5\text{H})]^+) \end{aligned}$$

$$\text{Eq B.6) } T\Delta S = T\Delta S_H - 2 \times T\Delta S_H = -T\Delta S_H = -4.6 \text{ kcal mol}^{-1}$$

$$\begin{aligned} \text{Eq B.7) } 105.8 \text{ kcal mol}^{-1} - 2 \times \text{BDE}([\text{Cp}^*\text{Co}(\eta^4\text{-C}_5\text{Me}_5\text{H})]^+) + 4.6 \text{ kcal mol}^{-1} \\ < 0 \text{ kcal mol}^{-1} \end{aligned}$$

$$\text{Eq B.8) } \therefore \text{BDE}([\text{Cp}^*\text{Co}(\eta^4\text{-C}_5\text{Me}_5\text{H})]^+) < 50.6 \text{ kcal mol}^{-1}$$

B.9. Details on DFT Estimates of pK_a and BDE

B.9.1 Computational Estimates of pK_a in Et₂O

The pK_a values in diethyl ether were calculated referenced to [H(OEt₂)₂]⁺ and were predicted on the basis of the free-energy change of the exchange reaction with [H(OEt₂)₂]⁺ and application of Hess' law on the closed chemical cycle. The pK_a of [H(OEt₂)₂]⁺ was defined as 0.0.

B.9.2 Computational Estimates of BDEs

Bond dissociation enthalpies (BDE) of X–H bonds were calculated in the gas-phase using a series of known reference compounds containing M–OH, M–H and M–NH bonds (Table B.13).²⁰ The enthalpy difference between the H-atom donor/acceptor pair was calculated based on the thermochemical information provided by frequency calculations after structure optimizations using the procedure described in the general computational section. A linear plot of ΔH vs BDE_{lit} was generated to form a calibration curve (Figure B.16). BDE predictions were generated by application of the line of best fit to the calculated ΔH of the unknown species. Error were calculated by application of the trend line to the calculated enthalpies of known species and comparison to their literature BDE value.²¹ Errors

are reported as the average of $BDE_{\text{calc}}-BDE_{\text{lit}}$ (mean signed error, MSE) and the average of the absolute values of $BDE_{\text{calc}}-BDE_{\text{lit}}$ (mean unsigned error, MUE). The use of the Bordwell equation for bond dissociation enthalpies is well supported by small $\Delta S_{\text{calc}} = S(X^\bullet) - S(XH)$, as shown in Table S14.

Table B.13: Calculated ΔH values and literature BDE values used for BDE calibration

Species	ΔH_{calc} (kcal mol ⁻¹)	BDE_{lit} (kcal mol ⁻¹)	BDE_{calc} (kcal mol ⁻¹)	Notes
[Cr(H ₂ O) ₅ (OH)] ²⁺	97.735	89	90	ref 21
[Fe(H ₂ O) ₆] ²⁺	77.985	77	75	ref 21
[Cr(H ₂ O) ₅ (OOH)] ²⁺	77.175	79	75	ref 21
[(bim)Fe(N ₂)] ²⁺	69.255	67	68	ref 21
[(P ₃ ^{Si})Fe(CNH)] ⁺	65.905	65	66	ref 21
[(bip)Fe(H)] ²⁺	65.475	62	65	ref 21
[(Tren)Fe(OH)] ²⁻	64.105	66	64	ref 21
(Cp)Fe(CO) ₂ (H)	57.455	56	59	ref 21
(HIPTN ₃ N)Mo(NNH)	47.715	49	51	Truncated; ref 22
[(P ₃ ^{Si})Fe(NNMeH)] ⁺	43.915	48	48	ref 23
(P ₃ ^{Si})Fe(CNH)	38.915	44	44	ref 23
(P ₃ ^{Si})Fe(CNMeH)	34.375	45	40	ref 23
[(P ₃ ^{Si})Fe(CNMeH)] ⁺	32.955	44	39	ref 23
			MSE	-0.9
			MUE	2.1

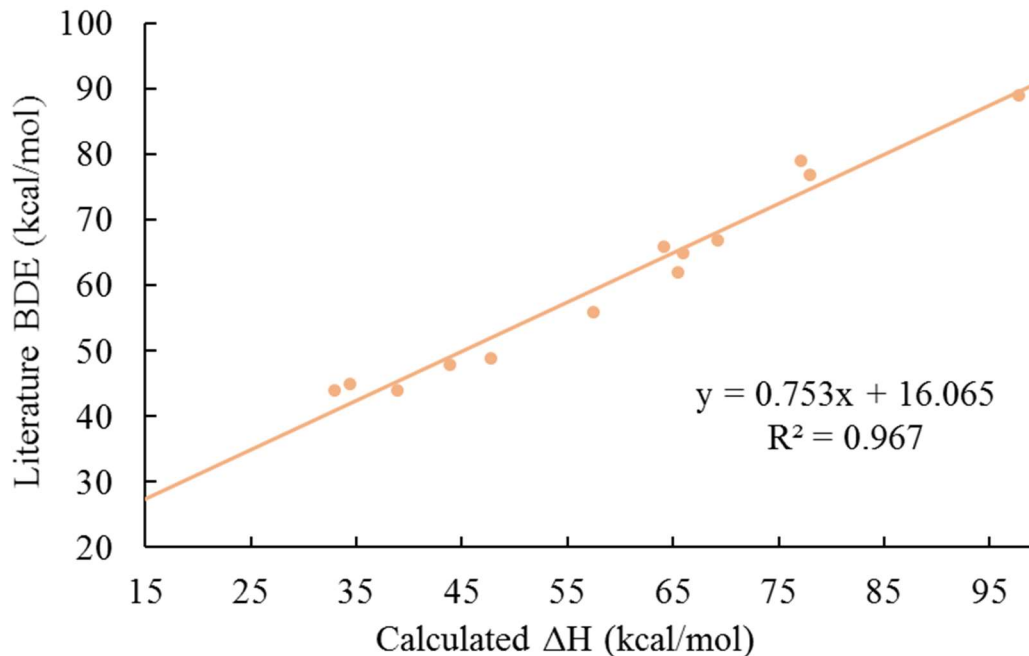


Figure B.16: Calculated BDE vs literature BDE for the species shown in **Table B.13**.

Table B.14: Calculated entropy (S) for selected XH and X• species

Species	$S(X\bullet)$ (cal/mol*K)	$S(XH)$ (cal/mol*K)	ΔS (kcal/mol*K)
$(P_3^B)Fe(NNH)$	271.6	268.9	2.7×10^{-3}
$[(P_3^B)Fe(NNH_2)]^+$	266.3	273.1	-6.8×10^{-3}
$(P_3^B)Fe(NNH_2)$	268.9	281.3	-1.2×10^{-2}
$(Cp^*)Co(\eta^4-C_5Me_5H)]^+$	168.8	162.0	6.6×10^{-3}
$[(Cp^*)Cr(\eta^4-C_5Me_5H)]^+$	159.5	163.4	-3.9×10^{-3}

B.9.3 Estimation of PCET Activation Barriers

Activation barriers were bracketed using the methods developed by the Hammes-Schiffer group. The inner sphere reorganization energy was estimated using force constants for normal modes in the Fe- and Co-coordination sphere.²⁴ The outer sphere reorganization energy (λ_{OS}) was estimated by calculating the outer sphere reorganization energy for a single ET in diethyl ether using the continuum solvation model²⁵ and assuming $\lambda_{OS,PCET} \leq \lambda_{OS,ET}$.²⁴

The activation barrier was plotted as a function of λ_{OS} (**Figure B.17**) to determine a maximum and minimum barrier for each PCET reaction (**Table B.15**).

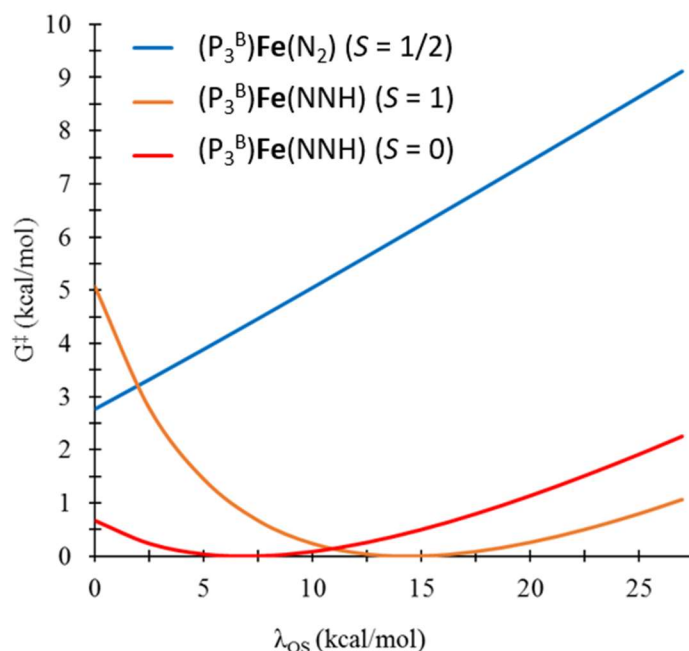


Figure B.17: Activation barrier for PCET reactions between selected $(P_3^B)Fe(N_xH_y)$ species (as labeled, total spin-state of the surface in parenthesis) with $[(Cp^*)Co(\eta^4-C_5Me_5H)]^+$ as a function of outer-sphere reorganization energy.

Table B.15: Calculated Reorganization Energies, Free-Energies of Reaction and Activation Barriers for Selected PCET Reactions

Acceptor	Spin State	Donor	λ_{tot} Range (kcal/mol)	ΔG_{rxn} (kcal/mol)	ΔG^\ddagger Range (kcal/mol)
$(P_3^B)Fe(N_2)$	$S = 1/2$	$[(Cp^*)Co(\eta^4-C_5Me_5H)]^+$	26.1 - 53.5	-9.1	3 - 9
$(P_3^B)Fe(NNH)$	$S = 0$	$[(Cp^*)Co(\eta^4-C_5Me_5H)]^+$	17.7 - 45.1	-24.6	0 - 2
$(P_3^B)Fe(NNH)$	$S = 1$	$[(Cp^*)Co(\eta^4-C_5Me_5H)]^+$	10.2 - 37.6	-24.6	0 - 5

B.10. References

- (1) Robbins, J. L.; Edelstein, N.; Spencer, B.; Smart, J. C. *J. Am. Chem. Soc.* **1982**, *104*, 1882–1893.
- (2) Anderson, J. S.; Moret, M. E.; Peters, J. C. *J. Am. Chem. Soc.* **2013**, *135*, 534–537.

- (3) Mankad, N. P.; Whited, M. T.; Peters, J. C. *Angew. Chem. Int. Ed.* **2007**, *46*, 5768–5771.
- (4) Del Castillo, T. J.; Thompson, N. B.; Suess, D. L. M.; Ung, G.; Peters, J. C. *Inorg. Chem.* **2015**, *54*, 9256–9262.
- (5) Suess, D. L. M.; Tsay, C.; Peters, J. C. *J. Am. Chem. Soc.* **2012**, *134*, 14158–14164.
- (6) Moret, M.-E.; Peters, J. C. *Angew. Chem. Int. Ed.* **2011**, *50*, 2063–2067.
- (7) Melzer, M. M.; Mossin, S.; Dai, X.; Bartell, A. M.; Kapoor, P.; Meyer, K.; Warren, T. H. *Angew. Chem. Int. Ed.* **2010**, *49*, 904–907.
- (8) Vicente, J.; Chicote, M.-T.; Guerrero, R.; Jones, P. G. *J. Chem. Soc., Dalton Trans.* **1995**, *8*, 1251–1254.
- (9) Weatherburn, M. W. *Anal. Chem.* **1967**, *39*, 971–974.
- (10) Watt, G. W.; Chrisp, J. D. *Anal. Chem.* **1952**, *24*, 2006–2008.
- (11) Stoll, S.; Schweiger, A. *J. Magn. Reson.* **2006**, *178*, 42–55.
- (12) Zhao, Y.; Truhlar, D. G. *J. Chem. Phys.* **2006**, *125*, 194101.
- (13) Weigend, F.; Ahlrichs, R. *Phys. Chem. Chem. Phys.* **2005**, *7*, 3297–3305.
- (14) Andrae, D.; Häußermann, U.; Dolg, M.; Stoll, H.; Preuß, H. *Theoret. Chim. Acta* **1990**, *77*, 123–141.
- (15) Towns, J.; Cockerill, T.; Dahan, M.; Foster, I.; Gaither, K.; Grimshaw, A.; Hazelwood, V.; Lathrop, S.; Lifka, D.; Peterson, G. D.; et al. *Comput. Sci. Eng.* **2014**, *16*, 62–74.
- (16) Valiev, M.; Bylaska, E. J.; Govind, N.; Kowalski, K.; Straatsma, T. P.; Van Dam, H. J. J.; Wang, D.; Nieplocha, J.; Apra, E.; Windus, T. L.; et al. *Comput. Phys. Commun.* **2010**, *181*, 1477–1489.

- (17) Ribeiro, R. F.; Marenich, A. V.; Cramer, C. J.; Truhlar, D. G. *J. Phys. Chem. B* **2011**, *115*, 14556–14562.
- (18) Wang, T.; Brudvig, G.; Batista, V. S. *J. Chem. Theory Comput.* **2010**, *6*, 755–760.
- (19) Marten, B.; Kim, K.; Cortis, C.; Friesner, R. A.; Murphy, R. B.; Ringnalda, M. N.; Sitkoff, D.; Honig, B. *J. Phys. Chem.* **1996**, *100*, 11775–11788.
- (20) Anderson, J. S.; Cutsail, G. E.; Rittle, J.; Connor, B. A.; Gunderson, W. A.; Zhang, L.; Hoffman, B. M.; Peters, J. C. *J. Am. Chem. Soc.* **2015**, *137*, 7803–7809.
- (21) Warren, J. J.; Tronic, T. A.; Mayer, J. M. *Chem. Rev.* **2010**, *110*, 6961–7001.
- (22) Yandulov, D. V.; Schrock, R. R. *Inorg. Chem.* **2005**, *44*, 1103–1117.
- (23) Rittle, J.; Peters, J. C. *J. Am. Chem. Soc.* **2017**, *139*, 3161–3170.
- (24) Iordanova, N.; Decornez, H.; Hammes-Schiffer, S. *J. Am. Chem. Soc.* **2001**, *123*, 3723–3733.
- (25) Marcus, R. A. *J. Chem. Phys.* **1956**, *24*, 966–978.

APPENDIX C.
Supplementary Information for Chapter 4

Adapted from:

Chalkley, M. J.; Del Castillo, T. J.; Matson, B. D.; Peters, J. C.
J. Am. Chem. Soc. **2018**, *140*, 6122–6129.
DOI: 10.1021/jacs.8b02335

C.1 Experimental Details

C.1.1 General Considerations

All manipulations were carried out using standard Schlenk or glovebox techniques under an N₂ atmosphere. Solvents were deoxygenated and dried by thoroughly sparging with N₂ followed by passage through an activated alumina column in a solvent purification system by SG Water, USA LLC. Non-halogenated solvents were tested with sodium benzophenone ketyl in tetrahydrofuran (THF) in order to confirm the absence of oxygen and water. Deuterated solvents were purchased from Cambridge Isotope Laboratories, Inc., degassed, and dried over activated 3-Å molecular sieves prior to use.

Cp*₂Co,¹ [(P₃^B)Fe][BAr^F₄],² [(P₃^B)Fe(N₂)] [Na(Et₂O)₃],³ [(P₃^B)Fe(N₂)] [Na(12-crown-4)₂],³ [H(OEt₂)] [BAr^F₄] (HBAr^F₄; BAr^F₄ = tetrakis-(3,5-bis(trifluoromethyl)phenyl)borate),⁴ sodium BAr^F₄ (NaBAr^F₄),⁴ and ¹⁵N-diphenylammonium triflate ([Ph₂¹⁵NH₂][OTf]).^{5,6} Ph¹⁵NH₂ was obtained from Sigma-Aldrich, Inc. degassed, and dried over activated 3-Å molecular sieves prior to use. All other reagents were purchased from commercial vendors and used without further purification unless otherwise stated. Diethyl ether (Et₂O) used in the experiments herein was stirred over Na/K (≥ 2 hours) and filtered or vacuum-transferred before use unless otherwise stated.

C.1.2 Mössbauer Spectroscopy

Mössbauer spectra were recorded on a spectrometer from SEE Co. (Edina, MN) operating in the constant acceleration mode in a transmission geometry. The sample was kept in an SVT-400 cryostat from Janis (Wilmington, MA). The quoted isomer shifts are relative to the centroid of the spectrum of a metallic foil of α-Fe at room temperature (RT). Solution

samples were transferred to a sample cup and chilled to 77 K inside of the glovebox, and unless noted otherwise, quickly removed from the glovebox and immersed in liquid N₂ until mounted in the cryostat. Data analysis was performed using version 4 of the program WMOSS (www.wmoss.org) and quadrupole doublets were fit to Lorentzian lineshapes. See discussion below for detailed notes on the fitting procedure.

C.1.3 Ammonia and Hydrazine Quantification

Reaction mixtures are cooled to 77 K and allowed to freeze. The reaction vessel is then opened to atmosphere and to the frozen solution is slowly added a twofold excess (with respect to acid) solution of a NaO^tBu solution in MeOH (0.25 mM) over 1-2 minutes. This solution is allowed to freeze and a Schlenk tube adapter is added and the headspace of the tube is evacuated. After sealing the tube is then allowed to warm to RT and stirred at RT for at least 10 minutes. An additional Schlenk tube is charged with HCl (3 mL of a 2.0 M solution in Et₂O, 6 mmol) to serve as a collection flask. The volatiles of the reaction mixture are vacuum transferred at RT into this collection flask. After completion of the vacuum transfer, the collection flask is sealed and warmed to RT and stirred vigorously for 10 minutes. Solvent is removed in vacuo, and the remaining residue is dissolved in DMSO-*d*₆ containing 20 mM 1,3,5-trimethoxybenzene as an internal standard. The ammonium chloride is quantified by integration relative to the 1,3,5-trimethoxybenzene internal standard.

C.1.4 EPR Spectroscopy

X-band EPR spectra were obtained on a Bruker EMX spectrometer. Samples were collected at powers ranging from 6-7 mW with modulation amplitudes of 2.00 G, modulation frequencies of 100.00 kHz, over a range of 1800 to 4500 Gauss. Spectra were baseline

corrected using the algorithm in SpinCount. EPR spectra were modeled using the easyspin program.⁷

C.1.5 Density Functional Theory

All stationary point geometries were calculated using DFT-D₃ (Grimmes D₃ dispersion correction)⁸ with an TPSS functional,⁹ a def2-TZVP¹⁰ basis set on transition metals and a def2-SVP⁷ basis set on all other atoms. Calculations were performed, in part, using Xtreme Science and Engineering Discovery Environment (XSEDE) resources.¹¹ Calculations were performed on the full (P₃^B)Fe scaffold. Geometries were optimized using the NWChem 6.5 package.¹² All single point energy, frequency and solvation energy calculations were performed with the ORCA package.¹³ Frequency calculations were used to confirm true minima and to determine gas phase free energy values (G_{gas}). Single point solvation calculations were done using an SMD solvation model^{14,15} with diethyl ether solvent and were used to determine solvated internal energy (E_{soln}). Free energies of solvation were approximated (**Eq C.1**) using the difference in gas phase internal energy (E_{gas}) and solvated internal energy (E_{soln}) and the free energy of a species in solution (G_{soln}) was then calculated (**Eq C.2**) using the gas phase free energy (G_{gas}) and the free energy of solvation (ΔG_{solv}).^{16,17} All reduction potentials were calculated referenced to $\text{Fc}^{+/0}$ and using the standard Nernst relation (**Eq C.3**).

$$\text{Eq C.1) } \Delta G_{\text{solv}} \approx E_{\text{soln}} - E_{\text{gas}}$$

$$\text{Eq C.2) } G_{\text{soln}} = G_{\text{gas}} + \Delta G_{\text{solv}}$$

$$\text{Eq C.3) } \Delta G = -nFE^0$$

C.1.7 Gas Chromatography

H₂ was quantified on an Agilent 7890A gas chromatograph (HP-PLOT U, 30 m, 0.32 mm ID; 30 °C isothermal; nitrogen carrier gas) using a thermal conductivity detector. A 10 mL manual injection was used and integration area was converted to percent H₂ composition by use of a calibration obtained from injection of H₂ solutions in N₂ of known concentration.

C.2 Synthetic Details

C.2.1 Synthesis of Anilinium Triflates

Prior to use the amine was purified (aniline and 2,6-dimethylaniline by distillation and the remaining substituted anilines by sublimation). To a 100 mL round bottom flask in the glovebox was added the desired aniline which was subsequently dissolved in 50 mL of Et₂O (no additional drying with NaK). To this was added dropwise (1 equiv) of HOTf with stirring over five minutes. Immediate precipitation of white solid was observed and the reaction mixture was allowed to stir for thirty minutes. The reaction mixture was then filtered and the resulting white powder was washed with Et₂O (50 mL) and pentane (50 mL). The resulting white microcrystalline material was then dried under vacuum. Yields of greater than 90% of microcrystalline material was obtained in this manner in all cases.

4-methoxyanilinium triflate ($[\text{4-OMePhNH}_3][\text{OTf}]$): ¹H NMR (DMSO-*d*₆, 400 MHz): 7.52 (m, 2 H), 7.28 (m, 2H), 4.30 (br, 3H).

anilinium triflate ($[\text{PhNH}_3][\text{OTf}]$): ¹H NMR (DMSO-*d*₆, 400 MHz): 7.50 (m, 2 H), 7.41 (m, 1H), 7.34 (m, 2H).

2,6-dimethylanilinium triflate ($[\text{2,6-MePhNH}_3][\text{OTf}]$): ¹H NMR (DMSO-*d*₆, 400 MHz): 7.14 (m, 3H), 2.32 (br, 6H).

2-chloroanilinium triflate ($[\text{}^2\text{-ClPhNH}_3][\text{OTf}]$): ^1H NMR (DMSO-*d*₆, 400 MHz):

7.32 (m, 1H), 7.15 (m, 1H), 7.02 (m, 1H), 6.82 (m, 1H).

2,5-chloroanilinium triflate ($[\text{}^{2,5}\text{-ClPhNH}_3][\text{OTf}]$): ^1H NMR (DMSO-*d*₆, 400 MHz):

7.19 (apparent d, 1H, $^3\text{J}(\text{H-H}) = 8.5$ Hz), 6.83 (apparent dd, 1H, $^3\text{J}(\text{H-H}) = 2.5$ Hz, 0.9 Hz), 6.56 (m, 1H).

2,6-chloroanilinium triflate ($[\text{}^{2,6}\text{-ClPhNH}_3][\text{OTf}]$): ^1H NMR (DMSO-*d*₆, 400 MHz):

7.22 (d, 2H, $^3\text{J}(\text{H-H}) = 8.0$ Hz), 6.57 (t, 1H, $^3\text{J}(\text{H-H}) = 8.0$ Hz).

2,4,6-chloroanilinium triflate ($[\text{}^{2,4,6}\text{-ClPhNH}_3][\text{OTf}]$): ^1H NMR (DMSO-*d*₆, 400 MHz): 7.37 (s, 2H).

C.2.2 Preparation of $[\text{Cp}^*_2\text{Co}][\text{BAR}^{\text{F}}_4]$

A RT solution of HBAR^{F}_4 (96.1 mg, 0.095 mmol) in Et_2O (6 mL) is added dropwise to a stirred, RT solution of Cp^*_2Co (32.9 mg, 0.1 mmol) in Et_2O (6 mL). This mixture is allowed to stir 30 min and then reduced to dryness in vacuo. The resulting solid residue is washed with pentane (3 x 2 mL) to yield $[\text{Cp}^*_2\text{Co}][\text{BAR}^{\text{F}}_4]$ as a bright yellow solid (104 mg isolated, 92% yield).

^1H NMR (THF-*d*₈, 300 MHz): δ 7.79 (8H, s, BAR^{F}_4), δ 7.58 (4H, s, BAR^{F}_4), δ 1.75 (30H, s, Cp^*_2Co).

C.3 Ammonia Generation Details

All solvents are stirred with Na/K for ≥ 2 hours and filtered prior to use. In a nitrogen-filled glovebox, the precatalyst (2.3 μmol) was weighed into a vial. The precatalyst was then transferred quantitatively into a long tube with a female 24-40 joint at the top using THF. The THF was then evaporated to provide a thin film of precatalyst at the bottom of tube. The tube is then charged with a stir bar, the acid (108 equiv), and Cp^*_2Co (41.2 mg, 54 equiv) as

solids. The tube is then sealed at RT with a septum that is secured with copper wire (this ensures a known volume of N₂ in the reaction vessel, which is important for H₂ detection). The tube is then chilled to 77 K and allowed to equilibrate for 10 minutes. To the chilled tube is added 1 mL of Et₂O. The temperature of the system is allowed to equilibrate for 5 minutes. This tube is passed out of the box into a liquid N₂ bath and transported to a fume hood. The tube is then transferred to a dry ice/acetone bath where it thaws and is allowed to stir at -78 °C for four hours. At this point the headspace of the tube is sampled with a 10 mL sealable gas syringe which is used to analyze for H₂ by GC. The tube is then allowed to warm to RT with stirring and then stirred at RT for a further ten minutes. At this point the previously described procedure for quantifying ammonia was employed. To ensure reproducibility, all experiments were conducted in 395 mL tubes (51 mm OD) using 25 mm stir bars and stirring was conducted at ~ 650 rpm.

Table C.1: NMR quantification results for standard NH₃ generation experiments with [(P₃^B)Fe][BAr^F₄]

Acid	Integration Relative to Internal Standard	% Yield NH ₃ (error)	% Yield H ₂ (error)
[⁴ -OMePhNH ₃][OTf]	0.01, 0.02	0.2 ± 0.1	89.1 ± 0.2
[PhNH ₃][OTf]	3.42, 3.33	40.4 ± 0.5	48.6 ± 0.7
[^{2,6} -MePhNH ₃][OTf]	4.30, 3.63	47.5 ± 4.0	37.8 ± 0.2
[² -ClPhNH ₃][OTf]	4.98, 4.92	59.3 ± 0.4	26.1 ± 1.9
[^{2,5} -ClPhNH ₃][OTf]	6.78, 6.15	77.5 ± 3.8	10.5 ± 1.1
[^{2,6} -ClPhNH ₃][OTf]	6.81, 6.00	76.7 ± 4.9	12.6 ± 2.5
[^{2,6} -ClPhNH ₃][OTf]*	6.60, 5.81	74.4 ± 4.7	14.2 ± 3.4
[^{2,6} -ClPhNH ₃][BAr ^F ₄]	4.12, 3.0	42.7 ± 6.7	18.8 ± 0.8
[^{2,4,6} -ClPhNH ₃][OTf]	5.73, 6.10	70.9 ± 2.2	12.0 ± 0.8
pentachloroanilinium triflate ([^{per} -ClPhNH ₃][OTf])	1.62, 1.70	19.9 ± 0.5	63.5 ± 1.1

*Run performed with [(P₃^B)Fe(N₂)] [Na(Et₂O)₃] as the precatalyst.

C.4 H₂ Monitoring Details

C.4.1 Standard Background Generation Reaction

All solvents are stirred with Na/K for ≥ 2 hours and filtered prior to use. In a nitrogen-filled glovebox, a long tube with a female 24-40 joint is charged with a stir bar, the acid (108 equiv) and Cp*₂Co (41.2 mg, 54 equiv). The tube is then sealed at RT with a septum that is secured with copper wire. The tube is then chilled to 77 K and allowed to equilibrate for 10 minutes. To the chilled tube is added 1 mL of Et₂O. The temperature of the system is allowed to equilibrate for 5 minutes. This tube is passed out of the box into a liquid N₂ bath and transported to a fume hood. The tube is then transferred to a dry ice/acetone bath where it thaws and is allowed to stir at -78 °C for four hours. At this point the headspace of the tube is sampled with a 10 mL sealable gas syringe which is used to analyze for H₂.

Table C.2: Data for Background H₂ Quantification Experiments

Acid	GC Integration for H ₂	% Yield H ₂
[⁴ -OMePhNH ₃][OTf]	49.8	31.5
[PhNH ₃][OTf]	24.0	15.2
[^{2,6} -MePhNH ₃][OTf]	8.2	5.2
[² -ClPhNH ₃][OTf]	47.2	29.9
[^{2,5} -ClPhNH ₃][OTf]	37.1	23.5
[^{2,6} -ClPhNH ₃][OTf]	77.8	49.2
[^{2,4,6} -ClPhNH ₃][OTf]	34.8	22.0
[^{per} -ClPhNH ₃][OTf]	98.3	62.3

C.4.2 H₂ Evolution Kinetics

All solvents are stirred with Na/K for ≥ 2 hours and filtered prior to use. For the catalyzed run, the precatalyst was then transferred quantitatively into a Schlenk tube using THF. The THF was then evaporated to provide a thin film of precatalyst at the bottom of the long tube with a female 24-40 joint. The tube is then charged with a stir bar and the [^{2,6}-

$^o\text{PhNH}_3][\text{OTf}]$ (77.9 mg, 108 equiv) and Cp^*Co (41.2 mg, 54 equiv) are added as solids.

The tube is then sealed at RT with a septum that is secured with copper wire. The tube is then chilled to 77 K and allowed to equilibrate for 10 minutes. To the chilled tube is added 1 mL of Et_2O . The temperature of the system is allowed to equilibrate for 5 minutes. This tube is passed out of the box into a liquid N_2 bath and transported to a fume hood. The tube is then transferred to a dry ice/acetone bath where it thaws and is allowed to stir at -78°C . As soon as the stir bar is freed from the frozen solution and stirring begins the timing is started. At the time points noted below the headspace was sampled for H_2 with a 10 mL sealable gas syringe.

Table C.3: Time points for catalyzed H_2 evolution from 2,6-dichloroanilinium triflate and Cp^*Co

Time (min)	GC Integration for H_2	% Yield H_2 (error)
5	3.8, 6.4	3.3 ± 0.9
15	11.6, 16.9	9.3 ± 1.8
25	14.7, 26.2	13.4 ± 3.8
35	22.5, 20.8	13.9 ± 0.5

Table C.4: Time points for uncatalyzed H_2 evolution from 2,6-dichloroanilinium triflate and Cp^*Co

Time (min)	GC Integration for H_2	% Yield H_2 (error)
5	3.3, 2.9	2.0 ± 0.1
15	7.0, 6.2	4.3 ± 0.3
25	8.8, 11.1	6.3 ± 0.8
65	20.7, 27.0	14.5 ± 1.7

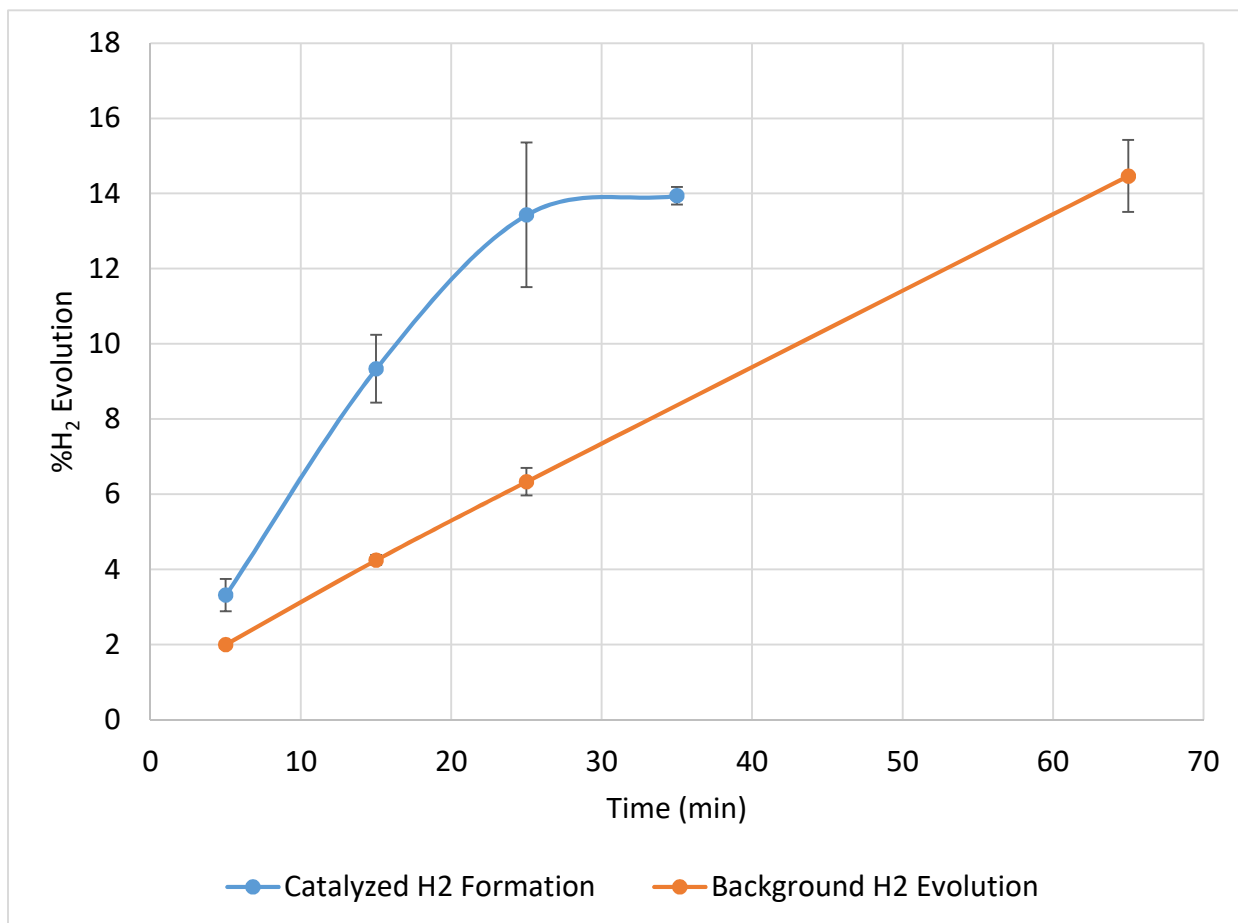


Figure C.1: Comparison of catalyzed and uncatalyzed H₂ evolution from 2,6-dichloroanilinium triflate and Cp*₂Co at early time points.

C.5 Mössbauer Spectroscopy

All solvents are stirred with Na/K for ≥ 2 hours and filtered prior to use. In a nitrogen-filled glovebox, the desired ⁵⁷Fe species (0.0023 mmol) is quantitatively transferred using THF to a vial and then evaporated to yield a thin film. That vial is charged with a small stir bar and the other reagents as solids. The vial is then chilled to 77 K in a liquid nitrogen bath and allowed to equilibrate for five minutes. To the chilled tube is added 1 mL of Et₂O and this allowed to equilibrate for another five minutes. The vial is then transferred to a cold well

that has been pre-cooled for at least fifteen minutes to $-78\text{ }^{\circ}\text{C}$ with a dry ice/acetone bath.

When the stir bar is freed from the frozen solvent and begins to stir the time is started. At the time noted the stirring is stopped and using a prechilled pipette the reaction mixture is transferred in one portion to a pre-chilled Mössbauer cup sitting in a vial. The vial is then placed in a liquid nitrogen bath causing the reaction mixture to freeze in approximately twenty seconds. The Mössbauer cup is then submerged in the liquid nitrogen and then removed from the glovebox and standard procedure is used to mount the sample on the Mössbauer spectrometer.

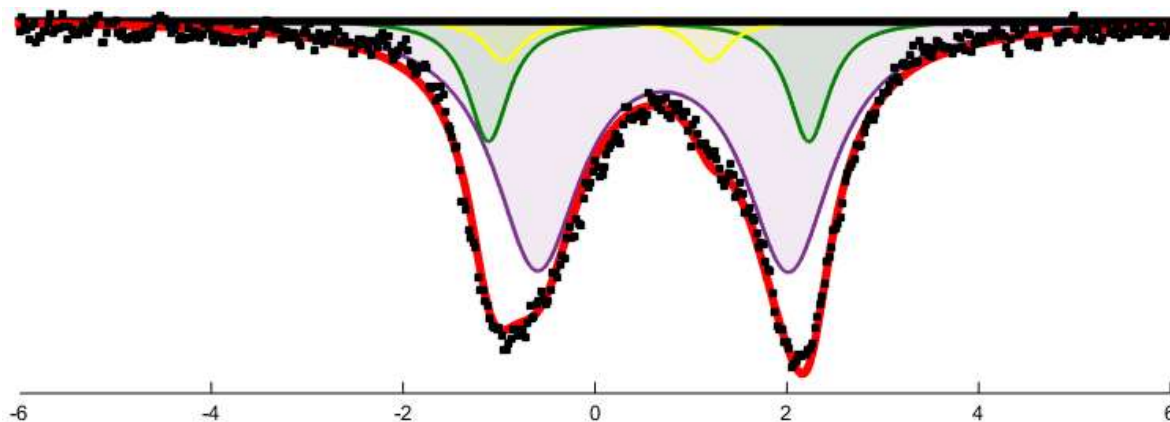


Figure C.2: Mössbauer spectrum collected from a reaction freeze quenched after stirring for 5 minutes at $-78\text{ }^{\circ}\text{C}$ in 1 mL of Et_2O between $[\text{P}_3^{\text{B}}(^{57}\text{Fe})\text{N}_2][\text{Na}(\text{Et}_2\text{O})_3]$ and excess 2,6- $[\text{}^{2,6}\text{-Cl}]\text{PhNH}_3][\text{OTf}]$ (50 equiv). Raw data shown as black points, simulation as a solid red line, with components in green, purple, and yellow (see Table S3 for parameters). The spectrum was collected at 80 K with a parallel applied magnetic field of 50 mT in Et_2O .

Fitting details for **Figure C.2** are as follows: three quadrupole doublets were found to be necessary to obtain an adequate simulation. Although a variety of parameters could potentially simulate the relatively broad absorptions observed here, previous reactivity of $[(\text{P}_3^{\text{B}})\text{Fe}(\text{N}_2)]^-$ with acid¹⁸ suggested that $(\text{P}_3^{\text{B}})\text{Fe}(\text{N}_2)$ and $[(\text{P}_3^{\text{B}})\text{Fe}]^+$ were likely products. Satisfyingly if the known isomer shift and quadrupole splitting for one of those species was fixed during the fitting process and the other components were allowed to refine freely the

other major component was found to be the complementary species.² The third species was always unchanged in these simulations and represents an unknown species. Its presence in the fit is demanded by the inflection point on the more negative side of the right-hand absorbance. Modeling this feature also helps to capture the asymmetry of the left-hand absorbance while using the symmetric line-shapes we expect for $(P_3^B)Fe(N_2)$ (green) and $[(P_3^B)Fe]^+$ (purple). The broad linewidths for $[(P_3^B)Fe]^+$ have been observed previously and may be explained by the existence of unbound and bound varieties of the species with the reaction mixture providing potential ligands such as $[OTf]^-$, $^{2,6-Cl}PhNH_2$, and N_2 .

Table C.5: Simulation parameters for Mossbauer spectrum in **Figure C.2**.

Component	δ (mm s ⁻¹)	ΔE_Q (mm s ⁻¹)	Linewidths, Γ_L/Γ_R (mm s ⁻¹)	Relative area
A (green)	0.58 ± 0.02	3.28 ± 0.07	0.52/0.52	0.26
B (purple)	0.76 ± 0.02	2.57 ± 0.05	1.10/1.10	0.63
C (yellow)	0.13 ± 0.02	2.24 ± 0.04	0.50/0.50	0.11

C.6 EPR Spectroscopy

C.6.1 General Procedure for EPR Spectroscopy

All solvents are stirred with Na/K for ≥ 2 hours and filtered prior to use. In a nitrogen-filled glovebox, the desired Fe species (0.0023 mmol) is quantitatively transferred using THF to a vial and then evaporated to yield a thin film. That vial is charged with a small stir bar and the acid (0.116 mmol, 50 equiv) as solids ($^{2,6-Cl}PhNH_3[OTf]$ or $^{2,6-Cl}PhNH_3[BAr^F_4]$). The vial is then chilled to 77 K in a liquid nitrogen bath and allowed to equilibrate for five minutes. To the chilled tube is added 1 mL of Et₂O (for HOTf 50 equiv have been dissolved in this 1 mL of Et₂O at RT) and this allowed to equilibrate for another five minutes. The vial is then transferred to a cold well that has been pre-cooled for at least fifteen minutes to -78

°C with a dry ice/acetone bath. When the stir bar is freed from the frozen solvent and begins to stir the time is started. The reaction mixture is stirred for five minutes and then stirring is stopped. Using a pre-chilled pipette approximately 0.5 mL of the reaction mixture is rapidly transferred to a pre-chilled X-band EPR tube. The X-band EPR tube is then placed in a liquid nitrogen bath causing the reaction mixture to freeze in approximately twenty seconds. The EPR tube is then sealed and removed from the glovebox in liquid nitrogen.

C.6.2 Comment on Stoichiometric Reactivity

In our attempt to model the catalytic reaction mixture we were interested in the reactivity of $[(P_3^B)Fe(N_2)]^-$ (observed previously both from mixing $[(P_3^B)Fe][BAr^F_4]$ with excess Cp^*_2Co and under the catalytic reaction conditions) with acid. In order to achieve this we wanted to prepare independently known $[(P_3^B)Fe(N_2)]^-$ species to model the proposed catalytic intermediate $[(P_3^B)Fe(N_2)][Cp^*_2Co]$. We chose $[(P_3^B)Fe(N_2)][Na(Et_2O)_3]$ because we believed that its solubility in Et_2O likely modeled that of $[(P_3^B)Fe(N_2)][Cp^*_2Co]$.

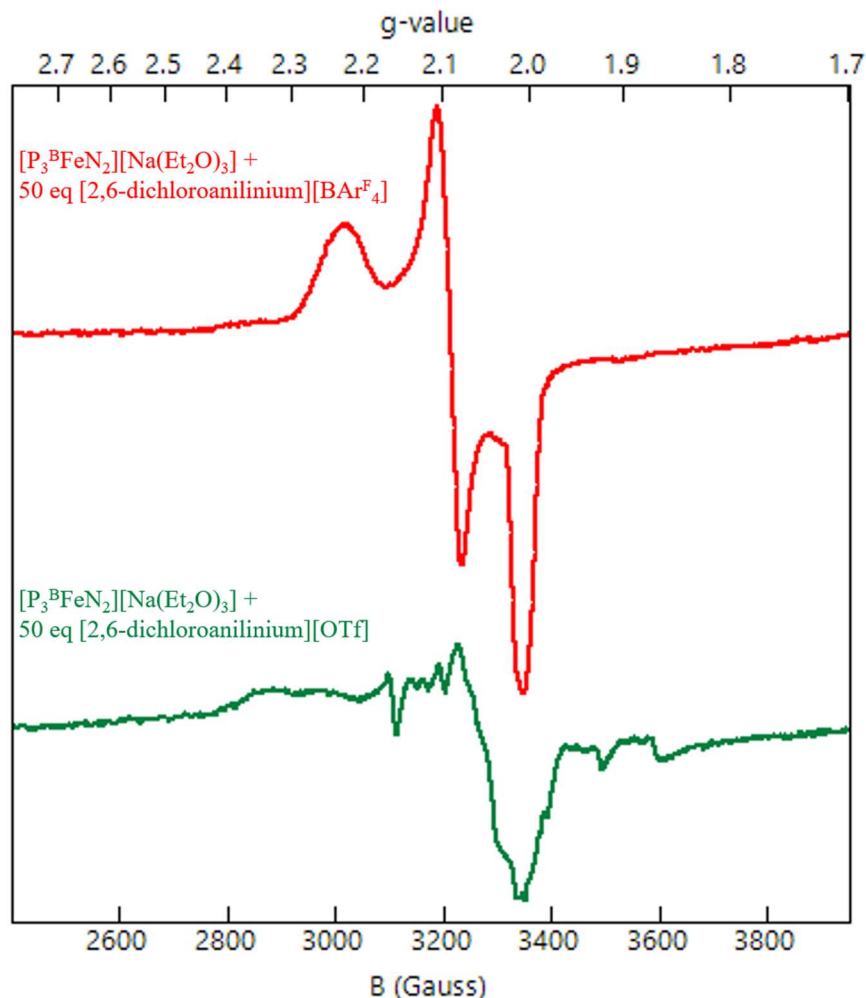


Figure C.3: The continuous wave, X-band EPR at 77K in Et_2O of reaction mixtures freeze-quenched after five minutes. In red is the reaction of $[(\text{P}_3^{\text{B}})\text{Fe}(\text{N}_2)][\text{Na}(\text{Et}_2\text{O})_3]$ with 50 equiv of $[^{2,6\text{-Cl}}\text{PhNH}_3][\text{BAr}^{\text{F}_4}]$ clearly demonstrating the formation of $[(\text{P}_3^{\text{B}})\text{Fe}(\text{NNH}_2)][\text{BAr}^{\text{F}_4}]$.¹⁸ In green is reaction of $[(\text{P}_3^{\text{B}})\text{Fe}(\text{N}_2)][\text{Na}(\text{Et}_2\text{O})_3]$ with 50 equiv of $[^{2,6\text{-Cl}}\text{PhNH}_3][\text{OTf}]$ in which the small residual species is neither the starting material ($[(\text{P}_3^{\text{B}})\text{Fe}(\text{N}_2)][\text{Na}(\text{Et}_2\text{O})_3]$) or the desired product ($[(\text{P}_3^{\text{B}})\text{Fe}(\text{NNH}_2)][\text{OTf}]$). Although we do not know the chemical identity of this species we note that it is very similar to the EPR observed in the reaction of $[(\text{P}_3^{\text{B}})\text{Fe}(\text{N}_2)][\text{Na}(12\text{-crown-4})_2]$ with 1 equiv of HBAr^{F_4} .¹⁹ We hypothesize therefore that it may represent a Fe–H side product.

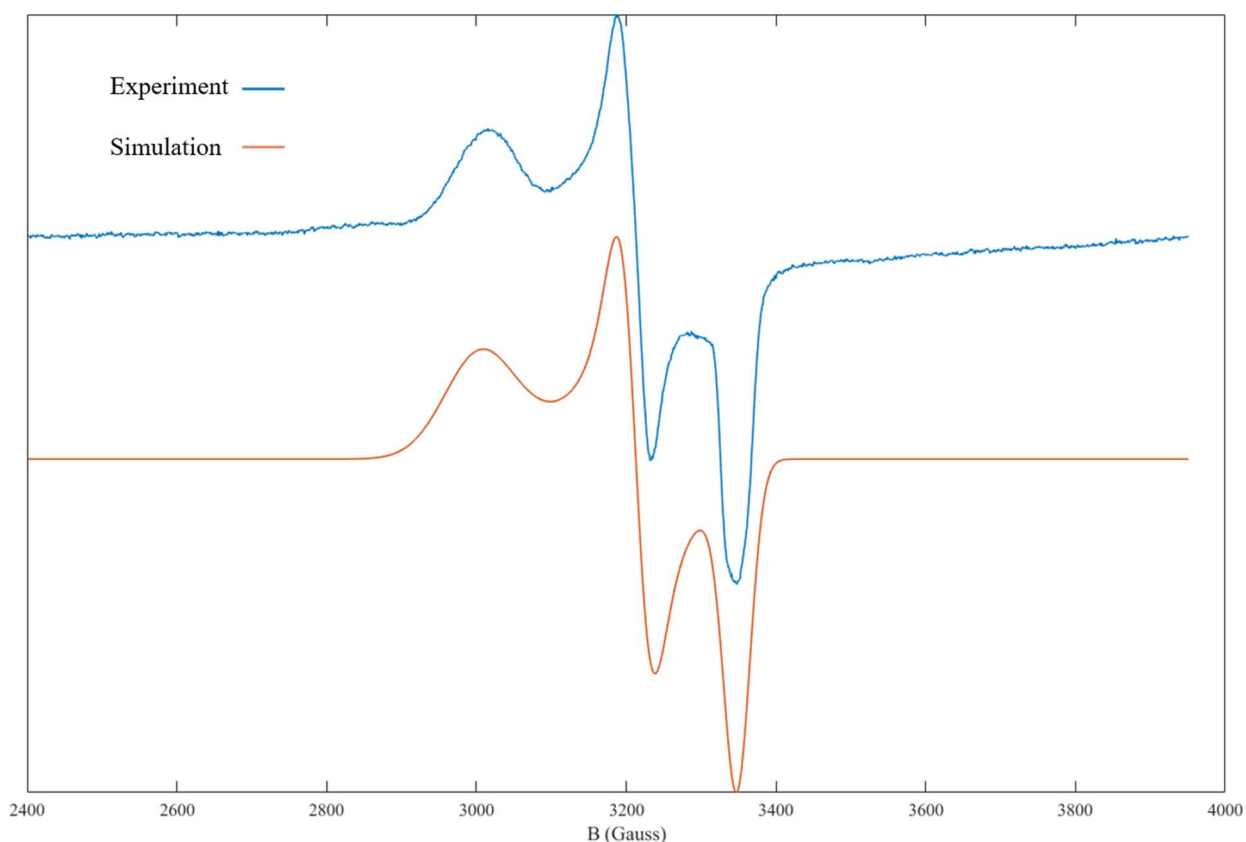


Figure C.4: In blue is the continuous wave, X-band EPR spectrum at 77K of a reaction mixture of 50 equiv $[\text{}^{2,6\text{-Cl}}\text{PhNH}_3][\text{BAr}^{\text{F}}_4]$ with $[(\text{P}_3^{\text{B}})\text{Fe}(\text{N}_2)][\text{Na}(12\text{-crown-4})_2]$ quenched with liquid nitrogen after 5 minutes. In orange is the simulation of this spectrum (fitting details below)

Fitting details for **Figure C.4** are as follows: the parameters used to fit the spectrum were obtained using the esfit application in the easyspin program.²⁰ The fitting program obtains the best fit by minimizing the root mean square deviation from the data.

The data was fit with the following parameters: $g_1 = 2.23899$, $g_2 = 2.09189$, $g_3 = 2.00664$, and a line broadening of 323.8530, 71.2309, and 38.7902 MHz respectively. These parameters represent only a very small perturbation from those used previously to model $[(\text{P}_3^{\text{B}})\text{Fe}(\text{NNH}_2)][\text{BAr}^{\text{F}}_4]$: $g_1 = 2.222$, $g_2 = 2.091$, $g_3 = 2.006$ and a line broadening of 256, 113, and 41 MHz respectively.¹⁹ The slightly broader spectrum observed here precludes resolution of the small phosphorus coupling on g_3 . We believe that this broadening arises

from either the use of a non-glassing solvent (Et₂O vs 2-MeTHF) or via small differences in hydrogen-bonding that arise from the presence of 2,6-dichloroaniline.

C.7 Acid Quench of [(P₃^B)Fe(N₂)]⁻

All solvents are stirred with Na/K for ≥ 2 hours and filtered prior to use. In a nitrogen-filled glovebox, the desired Fe species (2.3 μ mol) was weighed into a vial. The Fe species was then transferred quantitatively into a Schlenk tube using THF. The THF was then evaporated to provide a thin film of Fe species at the bottom of the Schlenk tube. The tube is then charged with a stir bar and acid (0.116 mmol, 50 equiv) as solids 9[^{2,6-Cl}PhNH₃][OTf] or [^{2,6-Cl}PhNH₃][BAr^F₄) is added as a solid. The tube is then sealed at RT with a septum and a Konte's valve that is left partially open. The tube is then chilled to 77 K and allowed to equilibrate for 10 minutes. To the chilled tube is added 1 mL of Et₂O through the septum. The temperature of the system is allowed to equilibrate for 5 minutes and then the Konte's valve is sealed. This tube is passed out of the box into a liquid N₂ bath and transported to a fume hood. The tube is then transferred to a dry ice/acetone bath where it thaws and is allowed to stir at -78 °C for three hours. At the end of the reaction the Konte's valve is opened and the reaction headspace is allowed to equilibrate. At this point the headspace of the tube is sampled with a 10 mL sealable gas syringe which is used to analyze for H₂. The tube is then allowed to warm to RT with stirring and then stirred at RT for a further ten minutes. At this point the previously described procedure for quantifying ammonia was employed.

Table C.6: Comparative NH₃ and H₂ Yields for [^{2,6-Cl}PhNH₃][OTf] and [^{2,6-Cl}PhNH₃][BAr^F₄)

Acid	Yield of NH ₃ (equiv)	% Yield H ₂
[^{2,6-Cl} PhNH ₃][OTf]	0.0 \pm 0.0	43.7 \pm 4.6
[^{2,6-Cl} PhNH ₃][BAr ^F ₄)	0.20 \pm 0.03	37.8 \pm 7.6

C.8 Procedure for Measuring Solubility

To measure the solubility of Cp*₂Co, all solvents are stirred with Na/K for ≥ 2 hours and filtered prior to use. In a nitrogen-filled glovebox, a Schlenk tube is charged with a stir bar and the Cp*₂Co (41.2 mg, 0.125 mmol) is added to the tube. The tube is then chilled to 77 K in a liquid nitrogen bath and allowed to equilibrate for 5 minutes. To the chilled tube is added 1 mL of Et₂O. The temperature of the system is allowed to equilibrate for 5 minutes and then the Schlenk tube is transferred to the cold well which has been prechilled to -78 °C for fifteen minutes. After five minutes of stirring at ~ 620 rpm, the stirring is stopped. With a prechilled pipette the entirety of the reaction mixture is transferred to a similarly prechilled celite pad for filtration. Filtration yielded a pale green solution that was then warmed to RT and the solvent was removed under reduced pressure. The vial was then extracted with a 20 mM solution of 1,3,5-trimethoxybenzene in C₆D₆. The NMR was then measured and the Cp*₂Co signal was integrated relative to the 1,3,5-trimethoxybenzene standard. The accuracy of this integration procedure was confirmed by performing this procedure on a sample of Cp*₂Co that had simply been weighed into a vial. Repetition of this experiment resulted in Cp*₂Co concentrations between 5-6 mM.

To measure the solubility of [^{2,6-Cl}PhNH₃][OTf], all solvents are stirred with Na/K for ≥ 2 hours and filtered prior to use. In a nitrogen-filled glovebox, a Schlenk tube is charged with a stir bar and the [^{2,6-Cl}PhNH₃][OTf] (77.9 mg, 0.250 mmol) is added to the tube. The tube is then chilled to 77 K in a liquid nitrogen bath and allowed to equilibrate for 5 minutes. To the chilled tube is added 1 mL of Et₂O. The temperature of the system is allowed to equilibrate for 5 minutes and then the Schlenk tube is transferred to the cold well which has been prechilled to -78 °C for fifteen minutes. After five minutes of stirring at ~ 620 rpm, the

stirring is stopped. With a prechilled pipette the entirety of the reaction mixture is transferred to a similarly prechilled celite pad for filtration. Filtration yielded a colorless solution that was then warmed to RT and the solvent was removed under reduced pressure. The vial was then extracted with a 20 mM solution of 1,3,5-trimethoxybenzene in THF-*d*₈. The NMR was then measured and the two signals for [^{2,6}-ClPhNH₃][OTf] were integrated relative to the 1,3,5-trimethoxybenzene standard. The result was a [^{2,6}-ClPhNH₃][OTf] concentration of 0.4 mM.

C.9 Controlled Potential Electrolysis and Cyclic Voltammetry Details

C.9.1 General Considerations

All manipulations are carried out in an N₂-filled glove box. For CPE experiments a sealable H-cell consisting of two compartments separated by a fine porosity sintered glass frit is cooled to -35 °C in a cold well and charged with 4 mL (working chamber) and 4 mL (auxiliary chamber) of 0.1 M NaBAR^F₄ solution in Et₂O, the solutions are also cooled to -35 °C and the solution for the working chamber may contain additional chemical components as described below. The working chamber is outfitted with a glassy carbon working electrode, rectangular prismatic in shape with dimensions of 10 mm × 2 mm and submerged in the working chamber solution to a depth of ~ 10 mm. The working chamber is also equipped with a Ag/AgPF₆ in 0.1 M NaBAR^F₄ Et₂O reference electrode isolated by a CoralPorTM frit (obtained from BASi) and referenced externally to Fc⁺⁰. The auxiliary chamber is outfitted with a solid sodium auxiliary electrode (~ 5 mm × ~ 1 mm rectangular prism, submerged to ~ 5 mm). The cell is sealed before electrolysis. The cell is connected to a CH Instruments 600B electrochemical analyzer and controlled potential bulk electrolysis

experiments were performed at $-35\text{ }^{\circ}\text{C}$ with stirring, cold well external bath temperature maintained by a SP Scientific FTS Systems FC100 immersion cooler.

CV experiments are conducted in a single compartment cell cooled to $-35\text{ }^{\circ}\text{C}$ in a cold well in $0.1\text{ M NaBAR}^{\text{F}_4}\text{ Et}_2\text{O}$ solution, again cold well external bath temperature maintained by a SP Scientific FTS Systems FC100 immersion cooler. The working electrode is a glassy carbon disk, the reference electrode is a Ag/AgPF_6 in $0.1\text{ M NaBAR}^{\text{F}_4}\text{ Et}_2\text{O}$ reference electrode isolated by a CoralPor™ frit (obtained from BASi) and referenced externally to $\text{Fc}^{+/0}$, the auxiliary electrode is a platinum wire. Measurements conducted with a CH Instruments 600B electrochemical analyzer

C.9.2 General Methodology for Controlled Potential Electrolysis Experiments

To the working chamber is added 3 mg of $[(\text{P}_3^{\text{B}})\text{Fe}][\text{BAR}^{\text{F}_4}]$ ($2\text{ }\mu\text{mol}$), $100\text{ }\mu\text{mol}$ of acid (e.g. $[\text{Ph}_2\text{NH}_2][\text{OTf}]$), $0\text{-}23.8\text{ mg}$ of $[\text{Cp}^*\text{Co}][\text{BAR}^{\text{F}_4}]$ ($0\text{-}20\text{ }\mu\text{mol}$), and a magnetic stir bar. The cell is held at a working potential of $-2.1\text{ V vs Fc}^{+/0}$ until the current passed in the cell falls to 1% of the initial current pass or until 21.5 hours have passed. After that time the potential bias is removed, the headspace of the cell is sampled with a sealable gas syringe (10 mL), which is immediately analyzed by GC for the presence of H_2 . Then an additional $100\text{ }\mu\text{mol}$ of acid in $2\text{ mL }0.1\text{ M NaBAR}^{\text{F}_4}$ solution in Et_2O is injected through rubber septa into both chambers to sequester NH_3 as $[\text{NH}_4][\text{OTf}]$. The cell is allowed to stir at $-35\text{ }^{\circ}\text{C}$ for 10 minutes and then warmed to RT. The contents of both chambers are then transferred to a Schlenk tube (cell washed with additional Et_2O) and this material is analyzed for NH_3 by base digestion, vacuum transfer of volatiles, and NMR integration as described in section S1.4

C.9.3 Methodology for Controlled Potential Electrolysis Experiments with Reloading of Substrate

To the working chamber is added 3 mg of $[(P_3^B)Fe][BAr^F_4]$ (2 μ mol), 100 μ mol of acid (e.g. $[Ph_2NH_2][OTf]$), 0-23.8 mg of $[Cp^*_2Co][BAr^F_4]$ (0-20 μ mol), and a magnetic stir bar. The cell is held at a working potential of -2.1 V vs $Fc^{+/0}$ until the current passed in the cell falls to 1% of the initial current pass or until 21.5 hours have passed. After that time the potential bias is removed. An additional 100 μ mol of acid in 2 mL 0.1 M $NaBAr^F_4$ solution in Et_2O is then added to the working chamber of the cell via injection through a rubber septum. The cell is then held at a working potential of -2.1 V vs $Fc^{+/0}$ until the current passed in the cell falls to 1% of the initial current pass or until 21.5 hours have passed. After that time the potential bias is removed, the headspace of the cell is sampled with a sealable gas syringe (10 mL), which is immediately analyzed by GC for the presence of H_2 . Then an additional 100 μ mol of acid in 2 mL 0.1 M $NaBAr^F_4$ solution in Et_2O is injected through rubber septa into both chambers of the cell to sequester NH_3 as $[NH_4][OTf]$. The cell is allowed to stir at -35 °C for 10 minutes and then warmed to RT. The contents of both chambers are then transferred to a Schlenk tube (cell washed with additional Et_2O) and this material is analyzed for NH_3 by base digestion, vacuum transfer of volatiles, and NMR integration as described in section S1.4

Table C.7: Controlled Potential Electrolysis Data

Entry	Acid	Equiv $[Cp^*_2Co]$ $[BAr^F_4]$	Time (h)	Charge Passed (C)	Yield of NH_3 (equiv per Fe)	FE NH_3 (%)	FE H_2^a (%)
1	$[Ph_2NH_2][OTf]$	0	42	7.5	2.3	18	80
2	$[Ph_2NH_2][OTf]$	0	63	6.2	2.8	26	25
3	$[Ph_2NH_2][OTf]$	0	43	5.4	2.6	28	53

Avg					2.6 ± 0.3	24 ± 5	
4 ^b	[Ph ₂ NH ₂][OTf]	0	43	7.5	2.2	17	67
5 ^b	[Ph ₂ NH ₂][OTf]	0	43	9.0	3.0	19	22
Avg					2.6 ± 0.6	18 ± 1	
6	[Ph ₂ NH ₂][OTf]	1	17	8.1	4.4	31	56
7	[Ph ₂ NH ₂][OTf]	1	22	8.3	3.5	24	47
Avg					4.0 ± 0.6	28 ± 5	
8	[Ph ₂ NH ₂][OTf]	5	17	8.5	3.9	26	61
9	[Ph ₂ NH ₂][OTf]	5	21	9.1	3.5	22	57
10	[Ph ₂ NH ₂][OTf]	5	22	9.5	4.6	28	27
Avg					4.0 ± 0.6	25 ± 3	
11	[Ph ₂ NH ₂][OTf]	10	21	9.4	3.0	19	64
12	[Ph ₂ NH ₂][OTf]	10	10	10.2	5.1	29	47
Avg					4 ± 1	24 ± 7	
13	[PhNH ₃][OTf]	5	15	9.0	1.2	8	48
14	[PhNH ₃][OTf]	5	22	7.8	0.6	4	35
Avg					0.9 ± 0.4	6 ± 3	
15	[^{2,6} -ClPhNH ₃][OTf]	5	17	10.6	2.0	11	44
16	[^{2,6} -ClPhNH ₃][OTf]	5	17	10.7	1.7	9	41
Avg					1.9 ± 0.2	10 ± 1	
17 ^b	[Ph ₂ NH ₂][OTf]	5	32	17.3	6.1	20	43
18 ^b	[Ph ₂ NH ₂][OTf]	5	22	18.7	6.7	21	32
19 ^b	[Ph ₂ NH ₂][OTf]	5	37	13.7	4.7	20	38
20 ^b	[Ph ₂ NH ₂][OTf]	5	41	15.3	4.8	18	52
21 ^b	[Ph ₂ NH ₂][OTf]	5	43	17.8	5.4	18	31
Avg					5.5 ± 0.9	19 ± 1	
22A ^c	[Ph ₂ NH ₂][OTf]	5	21.5	9.5	4.6	28	27
22B ^c	[Ph ₂ NH ₂][OTf]	5	11.5	9.2	0.0	0	88
23 ^d	[Ph ₂ NH ₂][OTf]	5	16	9.2	0.0	0	75
24 ^e	[Ph ₂ NH ₂][OTf]	5	43	0.0	0.3	N/A	N/A
25 ^f	[Ph ₂ NH ₂][OTf]	Chemical runs	21.5	N/A	1.3	7.8 e ⁻	50 e ⁻
26 ^f	[Ph ₂ NH ₂][OTf]	Chemical runs	21.5	N/A	2.3	13.8 e ⁻	31 e ⁻
Avg					1.8 ± 0.7	11 ± 4	

^aSome ports of the cell are sealed with septa and one of these is pierced before the electrolysis begins to pressure equilibrate the cell as it cools to -35 °C, we note therefore that H₂ gas may escape from the cell particular during long experiments, indeed a test of H₂ retention in the cell under equivalent conditions revealed leakage of H₂ (60% recovery), thus the detected % yield of H₂ reported here should be considered a lower limit. ^bThese experiments were conducted using the reloading protocol as described above. ^cElectrode rinse test as described in main text. ^dControl experiment with no [(P₃^B)Fe][BAR^F₄] included but including a typical loading of 11.9 mg (10 μmol) of [Cp*₂Co][BAR^F₄]. ^eControl experiment in which the cell

with all components, including the sodium auxiliary electrode, was assembled and stirred at $-35\text{ }^{\circ}\text{C}$ for 43 hours but neither a potential bias was applied, nor the working and auxiliary electrodes externally connected. This experiment thus interrogates the ability of the sodium electrode to function as a chemical reductant. ^fChemical catalysis runs at $-35\text{ }^{\circ}\text{C}$ in 0.1 M $\text{NaBAR}^{\text{F}_4}\text{Et}_2\text{O}$ solution with 50 equiv (100 μmol) of Cp^*_2Co included as a chemical reductant as well as $[(\text{P}_3^{\text{B}})\text{Fe}][\text{BAR}^{\text{F}_4}]$ (2 μmol) and 100 μmol of acid ($[\text{Ph}_2\text{NH}_2][\text{OTf}]$).

C.9.4 Control experiment for the possibility of NH_3 being generated in a chemical rather than electrochemical process during acidic workup

As per the general CPE methodologies described in S9.2 and S9.3, after electrolysis additional acid is added to the cell to sequester generated NH_3 as an ammonium salt to facilitate transfer of these materials to a Schlenk tube, ultimately allowing NH_3 quantitation via base digestion and vacuum transfer as described in S1.4. This presents the possibility that electrochemically reduced species formed during electrolysis (e.g., $[(\text{P}_3^{\text{B}})\text{Fe}(\text{N}_2)]^-$ and Cp^*_2Co) could react with this additional acid after the electrolysis was complete to generate NH_3 in a chemical reaction. A control experiment to determine the extent to which this type of reactivity might contribute to the total NH_3 yield observed from the CPE experiments was conducted. The H-cell is assembled via the standard methodology and charged with a typical loading of $[(\text{P}_3^{\text{B}})\text{Fe}][\text{BAR}^{\text{F}_4}]$ (2 μmol) and $[\text{Cp}^*_2\text{Co}][\text{BAR}^{\text{F}_4}]$ (10 μmol , 5 equiv) but without initial acid (i.e., no $[\text{Ph}_2\text{NH}_2][\text{OTf}]$). Electrolysis is then carried out at -2.1 V vs $\text{Fc}^{+/0}$ until the current pass in the cell falls to 1% of the initial current passed (in this case 1.12 C of charge were passed, corresponding to 11.6 μmol of reducing equivalents stored in the system, which approaches the theoretical limit of reducing equivalents that the loading of $[(\text{P}_3^{\text{B}})\text{Fe}][\text{BAR}^{\text{F}_4}]$ (2 μmol) and $[\text{Cp}^*_2\text{Co}][\text{BAR}^{\text{F}_4}]$ (10 μmol) could store) at this potential. This post electrolysis mixture is then treated with acid and analyzed for NH_3 via the standard methodology. This experiment yielded 0.2 equiv NH_3 (relative to Fe) indicating that

chemical N_2RR between electrochemically reduced species during the acidic workup is very minor.

C.9.5 Additional CV Data

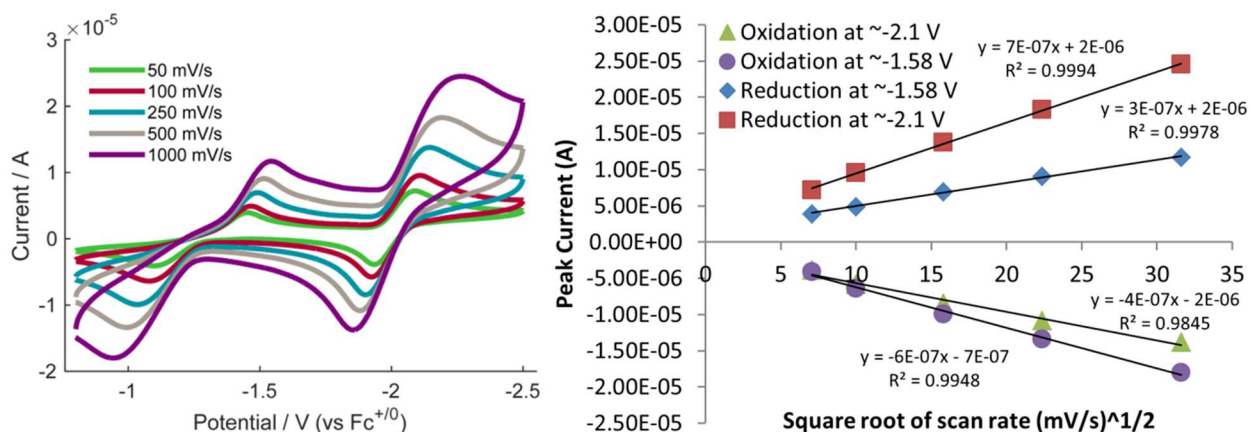


Figure C.5: Cyclic voltammograms of $0.5 \text{ mM } [(P_3^B)Fe][BAR^F_4]$ at varied scan rates (left) and plot of peak current versus square root of scan rate for each feature (right) showing linear dependence in all cases. All spectra are collected in 0.1 M NaBAR^F_4 solution in Et_2O at $-35 \text{ }^\circ\text{C}$ using a glassy carbon working electrode, and externally referenced to the $Fc^{+/0}$ couple.

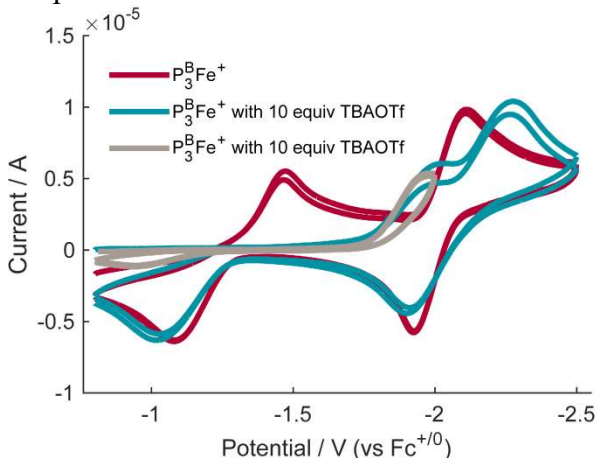


Figure C.6: Cyclic voltammograms of $0.5 \text{ mM } [(P_3^B)Fe][BAR^F_4]$ (red trace) and $[(P_3^B)Fe][BAR^F_4]$ with 10 equiv of tetrabutylammonium trifluoromethanesulfonate ([TBA][OTf]) (blue and gray traces). The traces with [TBA][OTf] show disappearance of a wave corresponding to the $[(P_3^B)Fe]^{+/0}$ couple at $\sim -1.58 \text{ V}$ (present in the red trace). This phenomenon, as in the case with acidic triflate sources as described in the main text, is likely due to triflate binding (to generate $(P_3^B)Fe(OTf)$), thereby attenuating the wave associated with the reduction of $[(P_3^B)Fe]^+$ and $[(P_3^B)Fe(N_2)]^+$. If the scan is stopped and reversed at -2.0 (before the $[(P_3^B)Fe(N_2)]^{0/-}$ couple) no reversibility is observed, consistent with a chemical step (dissociation of triflate) being coupled with this redox event. We note that in

the presence of OTf⁻ it appears that the second reductive feature is also slightly anodically shifted. We believe this to be due to slow N₂ binding kinetics and thus this wave would represent a convolution of the 0/1- reduction processes for both a vacant and an N₂ bound (P₃^B)Fe. All spectra are collected in 0.1 M NaBAR^F₄ solution in Et₂O at -35 °C using a glassy carbon working electrode, and externally referenced to the Fc⁺⁰ couple.

C.10 Computational Details

C.10.1 Calculation of Acid Dissociation Constants

Acid dissociation constants (pK_a and pK_d) were performed were optimized and solvated as discussed in the general methods section. For pK_a values, the ΔG for the exchange of a proton (H⁺) between the acid of interest and ^{2,6}-ClPhNH₂/[^{2,6}-ClPhNH₃]⁺. For pK_d values, the same approach was used except that the net exchange of a HOTf unit was calculated. In all cases the dissociation constant was reference to the literature value for the pK_a of [^{2,6}-ClPhNH₃]⁺ in THF.

C.10.2 Determination of PT, ET and PCET Kinetics

Kinetic barriers for reported for PT, ET and PCET were performed in one of two ways. Internal consistency between the methods was determined where possible. Values are summarized in **Table C.8**.

Method A. Marcus Theory. Standard Marcus theory expressions¹⁹ were used in Method A. Inner sphere reorganization energies for PT or PCET were calculated using the method developed by the group of Hammes-Schiffer (**Error! Reference source not found.**) utilizing the force constants for the reactant (f_j^r) and product (f_j^p) species and the change in equilibrium bond length (Δq_j).²⁰

$$\text{Eq C.4) } \lambda_{\text{is,PT/PCET}} = \sum_j (f_j^r f_j^p) / (f_j^r + f_j^p) \times \Delta q_j^2$$

Outer sphere reorganization energies were calculated using a continuum solvation model for the solvation of a point charge ($\lambda_{\text{os,ET}}$)¹⁹ or a dipole ($\lambda_{\text{os,PT}}$).²⁰⁻²² The $\lambda_{\text{os,PCET}}$ was

approximated using **Eq C.5**, where θ is the angle between the ET and PT vectors.²⁰ It was determined via analysis of the structure of a constrained optimization (in which the Fe–H–Co distance was kept constant) that θ is between 0 and 45°, a range which corresponds to an insignificant variation (less than 0.2 kcal mol⁻¹) in $\lambda_{\text{os,PCET}}$.

$$\text{Eq C.5) } \lambda_{\text{os,PCET}} = \lambda_{\text{os,PT}} + \lambda_{\text{os,ET}} - (\lambda_{\text{os,PT}} * \lambda_{\text{os,ET}}) \cos(\theta)$$

Relative rates for a bimolecular PT/ET vs PCET (k_{bi}) pathway for reaction shown in **Table C.8**, **Eq C.12** were determined via the method outline by the group of Hammes-Schiffer in which the bimolecular rate constant for PT, ET or PCET is approximated by **Eq C.6**.

$$\text{Eq C.6) } k_{\text{bi}} = K_{\text{A}} * k_{\text{uni}}$$

K_{A} represents the pre-arrangement equilibrium constant and k_{uni} represents the unimolecular rate constant for PCET or ET.^{23,25} Along an PT/ET pathway, the barriers calculated suggest that $k^{\text{PT}} > k^{\text{ET}}$. In approximating k_{un} for PCET and ET, we made extensive use of the webPCET portal.²⁴ The electronic coupling for PCET and ET was assumed to be equal. In order to approximate a lower bound for $k^{\text{PCET}}/k^{\text{ET}}$, the pre-arrangement equilibrium (K_{A}) was also assumed to be equal for PCET and ET. We believe this represents a lower bound as the approximation for K_{A} does not include any hydrogen bonding interactions for a PCET pathway.

Method B. Optimization of a 1st Order Saddle Point. PT barriers for the protonation of Cp*₂Co were also found by optimization of a 1st order saddle point. That the optimized structure represented a 1st order saddle point was confirmed with a frequency calculation, which showed only one imaginary frequency.



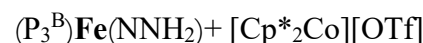
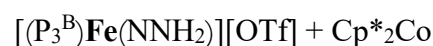
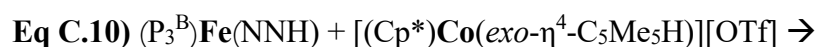


Table C.8: Overview of Parameters Used to Calculate Kinetic Barriers

Reaction	λ_{is}	λ_{os}	Barrier { k_{rel} }	Method
Eq C.7	N/A	N/A	1.3 kcal mol ⁻¹	A
Eq C.7	7.5 kcal mol ⁻¹	6.3 kcal mol ⁻¹	1.3 kcal mol ⁻¹	B
Eq C.8	N/A	N/A	3.8 kcal mol ⁻¹	A
Eq C.8	7.5 kcal mol ⁻¹	6.3 kcal mol ⁻¹	3.6 kcal mol ⁻¹	B
Eq C.9	N/A	N/A	4.5 kcal mol ⁻¹	A
Eq C.9	7.5 kcal mol ⁻¹	6.3 kcal mol ⁻¹	4.8 kcal mol ⁻¹	B
Eq C.10	8.9 kcal mol ⁻¹	6.3 kcal mol ⁻¹	1.5 kcal mol ⁻¹	A
Eq C.11	8.9 kcal mol ⁻¹	25.0 kcal mol ⁻¹	4.1 kcal mol ⁻¹	A ^a
Eq C.12	13.7 kcal mol ⁻¹	0-10 kcal mol ⁻¹	{ $k_{\text{rel}} \equiv 1$ } 0.2 – 0.6 kcal mol ⁻¹ {2000 – 4500}	A

^a The barrier for $[(\text{P}_3^{\text{B}})\text{Fe}(\text{NNH}_2)][\text{OTf}]$ reduction was calculated assuming that rate-determining reduction to $[(\text{P}_3^{\text{B}})\text{Fe}(\text{NNH}_2)][\text{OTf}]^-$ precedes OTf⁻ release.

C.10.3 BDFE Calculations

Bond dissociation free energies (BDFE) of X–H bonds were calculated in the gas-phase using a series of known reference compounds.²⁵ The free-energy difference between

the H-atom donor/acceptor pair was calculated based on the thermochemical information provided by frequency calculations after structure optimizations using the procedure described in the general computational section. A linear plot of ΔG vs $BDFE_{lit}$ was generated to form a calibration curve (**Figure C.7**). BDFE predictions were generated by application of the line of best fit to the calculated ΔG of the unknown species.

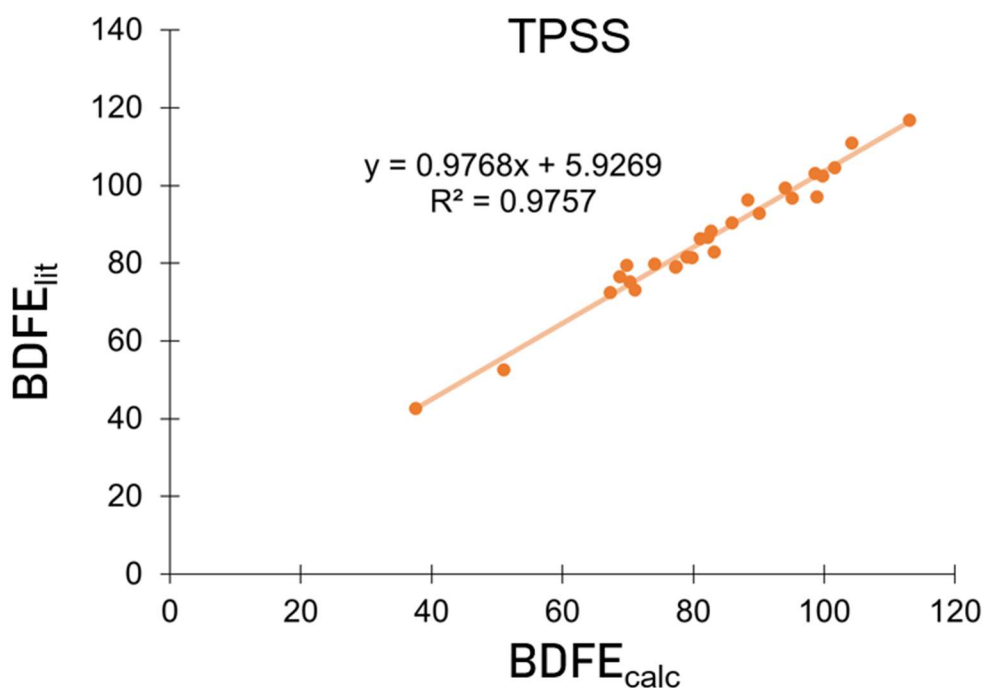


Figure C.7: $BDFE_{calc}$ and $BDFE_{lit}$ plotted for species of known $BDFE_{E-H}$. Line of best fit is shown.

Table C.9: Data used to generate the plot and line of best fit shown in **Figure C.7**

Species	ΔG (E-H) (kcal mol ⁻¹)	ΔG (E [•]) (kcal mol ⁻¹)	ΔG_{calc} (kcal mol ⁻¹)	$BDFE_{E-H}$ (kcal mol ⁻¹)
HOOH	-151.4	-150.8	69.8	79.7
MeOH	-115.6	-115.0	88.3	96.4
EtOOH	-230.0	-229.4	68.7	76.6
H ₂ O	-76.4	-75.7	104.2	111.0
NH ₃	-56.5	-55.8	94.0	99.4
Me ₃ CH	-158.3	-157.6	82.7	88.3

PhOH	-307.2	-306.6	74.0	79.8
Et ₂ NH	-213.6	-212.9	81.0	86.4
NH ₂ NH ₂	-111.8	-111.1	67.3	72.6
[OH] ⁻	-75.7	-75.0	98.6	103.1
PhSH	-630.2	-629.5	70.3	75.3
[NH ₄] ⁺	-56.8	-56.1	113.0	116.9
Me ₂ CH ₂	-119.0	-118.4	85.9	90.4
HC(O)OOH	-264.7	-264.1	82.2	86.8
OOH	-150.8	-150.2	37.5	42.7
C ₆ H ₆	-232.1	-231.4	101.6	104.7
C ₂ H ₄	-78.5	-77.8	99.7	102.5
C ₂ H ₆	-79.7	-79.1	90.0	92.9
PhCH ₃	-271.3	-270.7	79.0	81.6
CH ₄	-40.5	-39.8	95.1	96.8
CpH	-193.9	-193.3	71.0	73.2
EtSH	-477.8	-477.2	77.2	79.1
MeSH	-438.6	-437.9	77.3	79.2
PhNH ₂	-287.4	-286.7	79.8	81.5
NHNH	-110.6	-110.0	51.0	52.6
H ₂ S	-399.3	-398.7	83.1	83.0
H ₂	-1.2	-0.5	98.8	97.2

C.10.4 Calculated Reduction Potentials for Selected [Ar_nNH_(4-n)][OTf] and Ar_nNH_(3-n)

Table C.10: Calculated Reduction Potentials of Selected Species

Species	E° (V vs Fc ⁺⁰)
[^{4-OMe} PhNH ₃][OTf]	-3.8 V
^{4-OMe} PhNH ₂	-3.4 V
[^{2,6-Me} PhNH ₃][OTf]	-3.8 V
[^{2,6-Cl} PhNH ₃][OTf]	-2.4 V

$[\text{}^{2,6\text{-Cl}}\text{PhNH}_3]^+$	-2.0 V
$[\text{Ph}_2\text{NH}_2]^+$	< -2.5 V ^a
Ph_2NH	-3.1 V
$[\text{}^{\text{per-Cl}}\text{PhNH}_3][\text{OTf}]$	-2.0 V
Cp^*_2Co	-2.2 V

^a Potential for the formation of $\text{Ph}_2\text{NH}^\bullet + \text{H}^\bullet$ is reported. No ‘reversible’ minima was found.

C.10.5 Calculated Reduction Potentials for Selected $[\text{Ar}_n\text{NH}_{(4-n)}][\text{OTf}]$ and $\text{Ar}_n\text{NH}_{(3-n)}$

Determining the reduction potential of the acids using electrochemical techniques is challenging due to the significant, electrode catalyzed HER observed upon scanning anodically (see **Figure C.8**). However, as expected due to the lower pK_a of $[\text{}^{\text{per-Cl}}\text{PhNH}_3][\text{OTf}]$ compared to $[\text{Ph}_2\text{NH}_2][\text{OTf}]$ we see an earlier onset of the reduction potential and a higher current density. These processes are likely electrode-mediated and thus do not reflect a pure reduction potential, so to better estimate the outer-sphere reduction potential of the acids employed we have used DFT (**Table C.10**). In many cases, attempts to optimize the one electron reduced species results in a chemical step (*i.e.*, loss of Cl^- or H^\bullet) precluding determination of the reversible redox potential for the system. We are, however, able to find (*in silico*) a well-behaved reduction for $[\text{}^{\text{per-Cl}}\text{PhNH}_3][\text{OTf}]$ of -2.0 V. As a comparison, the high efficiency acid, $[\text{}^{2,6\text{-Cl}}\text{PhNH}_3][\text{OTf}]$, has a reduction potential of -2.4 V. This leads us to believe for $[\text{}^{\text{per-Cl}}\text{PhNH}_3][\text{OTf}]$ rather than engaging in an inner-sphere proton transfer with Cp^*_2Co ($E_{\text{calc}}^0(\text{Cp}^*_2\text{Co}^{0/+}) = -2.18$ V) it is likely that an outer sphere electron transfer occurs first. This change in mechanism would explain the increased H_2 yields and the decreased N_2RR efficiency. In contrast, $[\text{}^{2,6\text{-Cl}}\text{PhNH}_3][\text{OTf}]$ should be resistant to reduction and thus able to protonate the metallocene and engage in the mechanism discussed in **Chapter 4**.

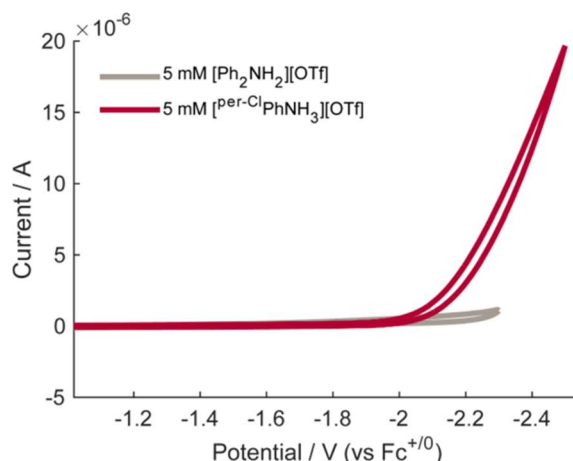


Figure C.8: Cyclic voltammograms of 5 mM $[\text{Ph}_2\text{NH}_2][\text{OTf}]$ (gray trace) and 5 mM $[\text{per-ClPhNH}_3][\text{OTf}]$ (red trace). All spectra are collected in 0.1 M $\text{NaBAR}^{\text{F}_4}$ solution in Et_2O at -35°C using a glassy carbon working electrode and externally referenced to the $\text{Fc}^{+/0}$ couple. Scan rate is 100 mV/s.

C.11 X-ray Photoelectron Spectroscopy Details

The surface composition of the carbon electrode surface after a 15 hour bulk electrolysis in the presence of $[(\text{P}_3^{\text{B}})\text{Fe}][\text{BAR}^{\text{F}_4}]$, $[\text{Cp}^*\text{Co}][\text{BAR}^{\text{F}_4}]$, $[\text{Ph}_2\text{NH}_2][\text{OTf}]$ and N_2 was determined via XPS on a Kratos Axis Nova spectrometer with DLD (Kratos Analytical; Manchester, UK). The excitation source for all analysis was monochromatic $\text{Al K}\alpha_{1,2}$ ($h\nu = 1486.6\text{ eV}$) operating at 10 mA and 15 kV. The X-ray source was directed at 54° with respect to the sample normal. A base pressure of 1×10^{-9} Torr is maintained in the analytical chamber, which rises to 5×10^{-9} Torr during spectral acquisition. All spectra were acquired using the hybrid lens magnification mode and slot aperture, resulting in an analyzed area of $700\ \mu\text{m} \times 400\ \mu\text{m}$. Survey scans were collected using 160 eV pass energy, while narrow region scans used 10 eV; charge compensation via the attached e^- -flood source was not necessary in this study.

Subsequent peak fitting and composition analysis was performed using CasaXPS version 2.3.16 (Casa Software Ltd.; Teignmouth, UK). Energy scale correction for the survey

and narrow energy regions was accomplished by setting the large component in the C 1s spectrum, corresponding to a C 1s C(=C) transition, to 284.8 eV. All components were fit using a Gaussian 30% Lorentzian convolution function. For quantification, Shirley baselines were employed where there was a noticeable change in CPS before and after the peak in the survey spectrum; otherwise, linear was chosen. Atomic percentages were calculated using the CasaXPS packages for regions and/or components and are reported herein. Calculations were performed using region or component areas normalized to relative sensitivity factors specific to the instrument conditions with deconvolution from the spectrometer transmission function.

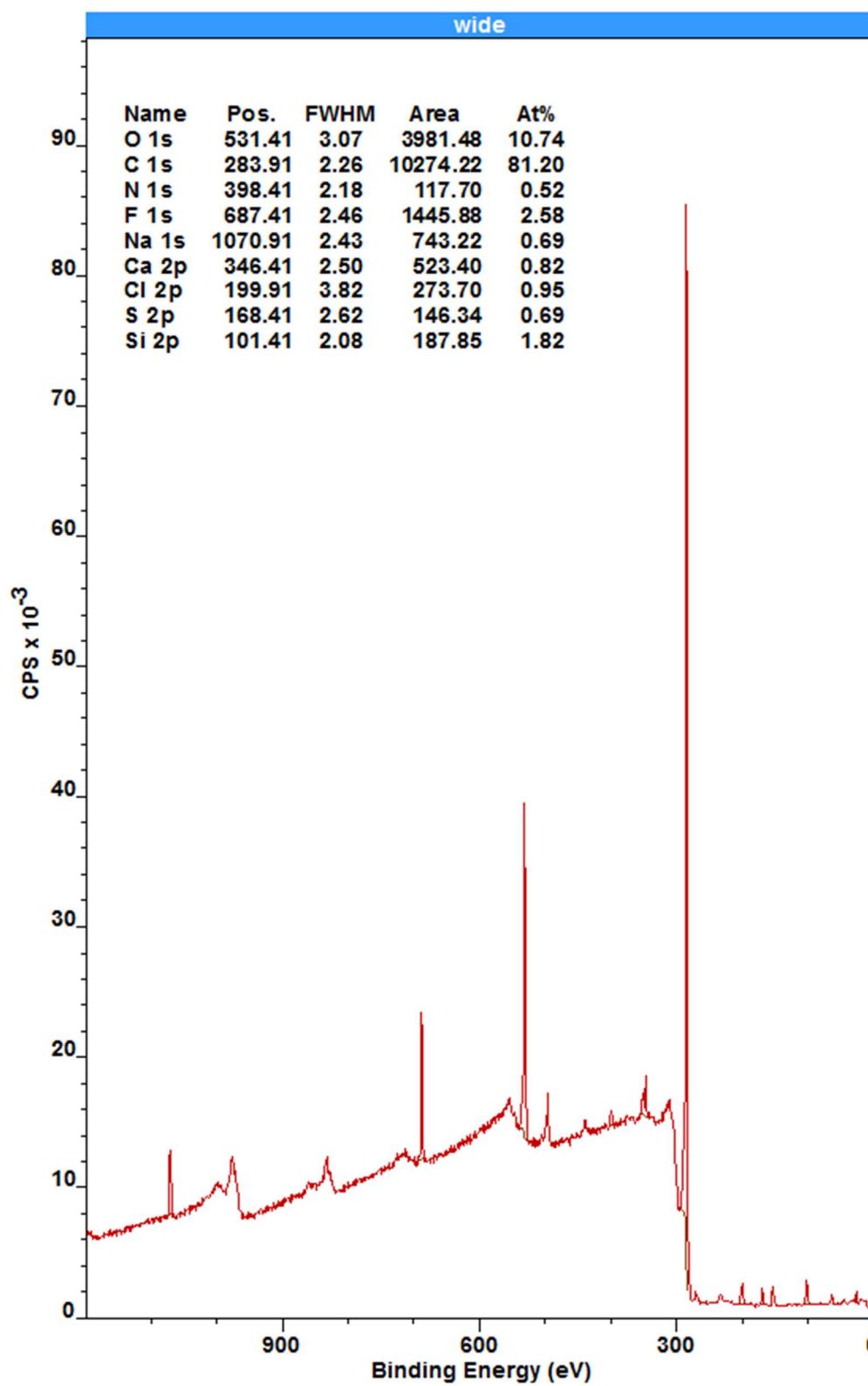


Figure C.9: XPS survey scan of a section of a glassy carbon plate which was not exposed to the working chamber solution during a 15 hour bulk electrolysis in the presence of $[(P_3^B)Fe][BAr^F_4]$, $[Cp^*_2Co][BAr^F_4]$, $[Ph_2NH_2][OTf]$ and N_2 at -2.1 V (vs $Fc^{+/0}$). XPS and Auger peaks are assigned as labeled in the legend, which also includes atomic percentages calculated from component fits from scans of individual XPS regions. This material represents a baseline of the electrode surface composition resulting from cleaning, polishing, and handling prior to CPE experiments and is provided for comparison to a XPS survey scan of a section of the same glassy carbon plate which was exposed to the working chamber solution during a 15 hour bulk electrolysis in the presence of $[(P_3^B)Fe][BAr^F_4]$, $[Cp^*_2Co][BAr^F_4]$, $[Ph_2NH_2][OTf]$ and N_2 at -2.1 V (vs $Fc^{+/0}$) presented in figure S7.

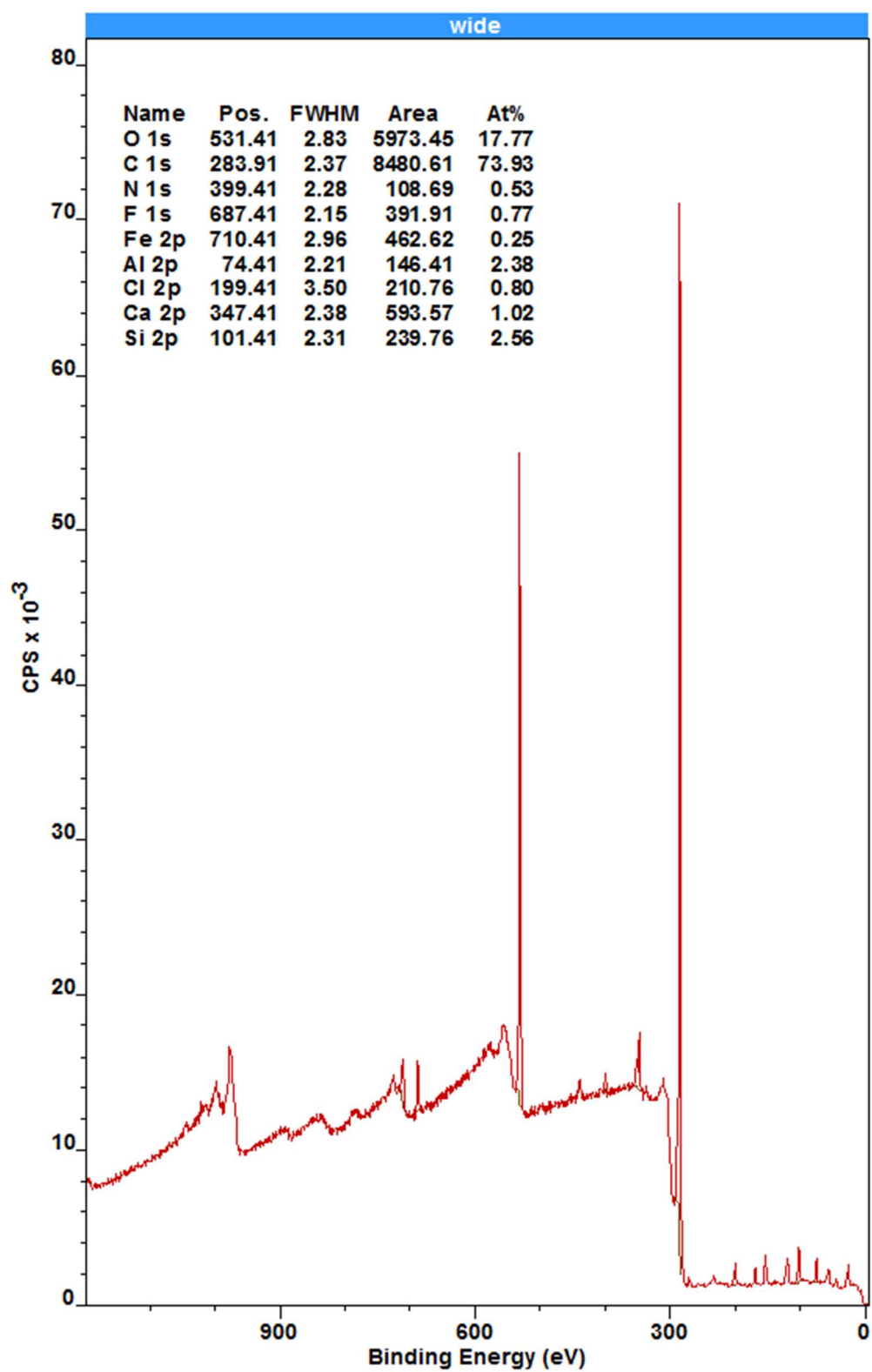


Figure C.10: XPS survey scan of a section of a glassy carbon plate which was exposed to the working chamber solution during a 15 hour bulk electrolysis in the presence of $[(P_3^B)Fe][BAr^F_4]$, $[Cp^*_2Co][BAr^F_4]$, $[Ph_2NH_2][OTf]$ and N_2 at -2.1 V (vs $Fc^{+/0}$) XPS and Auger peaks are assigned as labeled in the legend, which also includes atomic percentages calculated from component fits from scans of individual XPS regions. This material represents a post-electrolysis state of the electrode surface composition for comparison to a XPS survey scan of a section of the same glassy carbon plate which was not exposed to the working chamber solution during a 15 hour bulk electrolysis in the presence of $[(P_3^B)Fe][BAr^F_4]$, $[Cp^*_2Co][BAr^F_4]$, $[Ph_2NH_2][OTf]$ and N_2 at -2.1 V (vs $Fc^{+/0}$) presented in figure S1. Notably this active surface scan reveals a small Fe signal, likely resulting from some degree of decomposition of the $[(P_3^B)Fe][BAr^F_4]$ catalyst over the course of the 15 hour electrolysis; however it is also possible that this small Fe signal is the result of contamination during the handling of the sample. This Fe 2p signal occurs at 710.4 eV, but due to the weak signal intensity it is not possible to confidently assign its oxidation state. Although, the signal does not appear consistent with Fe(0) whose signal is typically around 707 eV; we would also note though that the handling process involves transferring the electrode quickly in air which could result in oxidation of Fe(0) that was present. Also notable is that no new Co signal is observed in the post-electrolysis scan suggesting that $[Cp^*_2Co][BAr^F_4]$ does not decompose to a surface bound Co species in detectable amounts during the electrolysis. Phosphorus is also detectable in the survey scan but the signal is too small for quantitation.

C.12 pK_a Determination Strategy

Bosch et al. published a procedure for converting a pK_a in THF into the equivalent pK_a in different solvents.²⁶ Although not all of the pK_a values have been experimentally determined in THF the values obtained from converting from MeCN or H_2O into a THF value is quite accurate. So we have used these converted values in the text. Where available a number measured in THF has been used, if not the MeCN derived value is used. If neither is available then the H_2O derived value is used.

Solvent conversion equations:

$$\text{Eq C.13 } pK_a(\text{THF}) = 0.78 \times pK_a(\text{MeCN}) - 0.52$$

$$\text{Eq C.14 } pK_a(\text{THF}) = 1.19 \times pK_a(\text{H}_2\text{O}) + 2.13$$

Table C.11: pK_a values of anilinium acids in different solvents

Acid	pK _a in MeCN	pK _a in H ₂ O	Converted pK _a ^a	Experimental pK _a in THF
[⁴ -OMePhNH ₃][OTf]	11.86 ²⁷	5.29 ²⁸	8.8 (8.4)	8.8 ²⁶
[PhNH ₃][OTf]	10.62 ²⁷	4.58 ²⁸	7.8 (7.6)	8.0 ²⁶
[^{2,6} -MePhNH ₃][OTf]	--	3.89 ²⁸	-- (6.8)	
[² -ClPhNH ₃][OTf]	7.86 ²⁷	2.64 ²⁸	5.6 (5.3)	6.0 ²⁶
[^{2,5} -ClPhNH ₃][OTf]	6.21 ²⁹	1.53 ²⁷	4.3 (4.0)	4.5 ²⁶
[^{2,6} -ClPhNH ₃][OTf]	5.06 ²⁷	0.42 ³⁰	3.4 (2.6)	
[^{2,4,6} -ClPhNH ₃][OTf]	--	-0.03 ³⁰	-- (2.1)	
[^{per} -ClPhNH ₃][OTf]	2.35 ²⁹	--	1.3 (--)	
collidinium triflate	14.98 ²⁷	--	11.2 (--)	
benzylammonium triflate	--	9.34 ³¹	-- (13.2)	

^aFirst is listed the value converted from THF and then in parentheses is the value converted from H₂O.

C.13 References

- (1) Robbins, J. L.; Edelstein, N.; Spencer, B.; Smart, J. C. *J. Am. Chem. Soc.* **1982**, *104*, 1882–1893.
- (2) Anderson, J. S.; Moret, M. E.; Peters, J. C. *J. Am. Chem. Soc.* **2013**, *135*, 534–537.
- (3) Moret, M.-E.; Peters, J. C. *Angew. Chem. Int. Ed.* **2011**, *50*, 2063–2067.
- (4) Del Castillo, T. J.; Thompson, N. B.; Peters, J. C. *J. Am. Chem. Soc.* **2016**, *138*, 5341–5350.
- (5) Melzer, M. M.; Mossin, S.; Dai, X.; Bartell, A. M.; Kapoor, P.; Meyer, K.; Warren, T. H. *Angew. Chem. Int. Ed.* **2010**, *49*, 904–907.
- (6) Vicente, J.; Chicote, M.-T.; Guerrero, R.; Jones, P. G. *J. Chem. Soc., Dalton Trans.* **1995**, *8*, 1251–1254.
- (7) Stoll, S.; Schweiger, A. *J. Magn. Reson.* **2006**, *178*, 42–55.
- (8) Grimme, S.; Antony, J.; Ehrlich, S.; Krieg, H. *J. Chem. Phys.* **2010**, *132*, 154104–154119.

- (9) Tao, J.; Perdew, J. P.; Staroverov, V. N.; Scuseria, G. E. *Phys. Rev. Lett.* **2003**, *91*, 146401–146404.
- (10) Weigend, F.; Ahlrichs, R. *Phys. Chem. Chem. Phys.* **2005**, *7*, 3297–3305.
- (11) Towns, J.; Cockerill, T.; Dahan, M.; Foster, I.; Gaither, K.; Grimshaw, A.; Hazlewood, V.; Lathrop, S.; Lifka, D.; Peterson, G. D.; et al. *Comput. Sci. Eng.* **2014**, *16*, 62–74.
- (12) Valiev, M.; Bylaska, E. J.; Govind, N.; Kowalski, K.; Straatsma, T. P.; Van Dam, H. J. J.; Wang, D.; Nieplocha, J.; Apra, E.; Windus, T. L.; et al. *Comput. Phys. Commun.* **2010**, *181*, 1477–1489.
- (13) Neese, F. *Wiley Interdiscip. Rev.: Comput. Mol. Sci.* **2012**, *2*, 73–78.
- (14) Klamt, A.; Schüürmann, G. *J. Chem. Soc., Perkin Trans. 2* **1993**, *5*, 799–805.
- (15) Marten, B.; Kim, K.; Cortis, C.; Friesner, R. A.; Murphy, R. B.; Ringnalda, M. N.; Sitkoff, D.; Honig, B. *J. Phys. Chem.* **1996**, *100*, 11775–11788.
- (16) Ribeiro, R. F.; Marenich, A. V.; Cramer, C. J.; Truhlar, D. G. *J. Phys. Chem. B* **2011**, *115*, 14556–14562.
- (17) Wang, T.; Brudvig, G.; Batista, V. S. *J. Chem. Theory Comput.* **2010**, *6*, 755–760.
- (18) Anderson, J. S.; Cutsail, G. E.; Rittle, J.; Connor, B. A.; Gunderson, W. A.; Zhang, L.; Hoffman, B. M.; Peters, J. C. *J. Am. Chem. Soc.* **2015**, *137*, 7803–7809.
- (19) Marcus, R. A. *J. Chem. Phys.* **1956**, *24*, 966–978.
- (20) Iordanova, N.; Decornez, H.; Hammes-Schiffer, S. *J. Am. Chem. Soc.* **2001**, *123*, 3723–3733.
- (21) Koper, M. T. M. *Chem. Sci.* **2013**, *4*, 2710–2723.
- (22) Onsager, L. *J. Am. Chem. Soc.* **1936**, *58*, 1486–1493.

- (23) Thoss, M.; Evers, F. *J. Chem. Phys.* **2018**, *148*, 030901.
- (24) Hammes-Schiffer, S.; Soudackov, A. V. *J. Phys. Chem. B* **2008**, *112*, 14108–14123.
- (25) Warren, J. J.; Tronic, T. A.; Mayer, J. M. *Chem. Rev.* **2010**, *110*, 6961–7001.
- (26) Garrido, G.; Rosés, M.; Ràfols, C.; Bosch, E. *J. Solution Chem.* **2008**, *37*, 689–700.
- (27) Kaljurand, I.; Kütt, A.; Sooväli, L.; Rodima, T.; Mäemets, V.; Leito, I.; Koppel, I. A. *J. Org. Chem.* **2005**, *70*, 1019–1028.
- (28) Pankratov, A. N.; Uchaeva, I. M.; Doronin, S. Yu.; Chernova, R. K. *J. Struct. Chem.* **2001**, *42*, 739–746.
- (29) Haav, K.; Saame, J.; Kütt, A.; Leito, I. *Eur. J. Org. Chem.* **2012**, *2012*, 2167–2172.
- (30) Liao, K.; Pack, B. W.; Toltl, N. P. *J. Pharm. Biomed. Anal.* **2007**, *44*, 118–126.
- (31) Hall, H. K. *J. Am. Chem. Soc.* **1957**, *79*, 5441–5444.

Appendix D.
Supplementary Information for Chapter 5

D.1 Experimental Details

D.1.1 General Considerations

All manipulations were carried out using standard Schlenk or glovebox techniques under an N₂ atmosphere. Unless otherwise noted, solvents were deoxygenated and dried by thoroughly sparging with N₂ gas followed by passage through an activated alumina column in the solvent purification system by SG Water, USA LLC. Non-halogenated solvents were tested with a standard purple solution of sodium benzophenone ketyl in tetrahydrofuran in order to confirm effective oxygen and moisture removal. All reagents were purchased from commercial vendors and used without further purification unless otherwise stated. Cp*₂Co,¹ (Cp*)Co(η⁴-C₅Me₆),² [H(OEt₂)₂][BAr^F₄] (HBAr^F₄, BAr^F₄ = tetrakis-(3,5-bis(trifluoromethyl)phenyl)borate),³ [Fc][BAr^F₄] (Fc = ferrocenium),⁴ and [TBA][BD₄] (TBA = tetrabutylammonium, BD₄ = borodeuteride)⁵ were synthesized according to a literature procedure. Deuterated solvents were purchased from Cambridge Isotope Laboratories, Inc. C₆D₆ and MeCN-*d*₃ were degassed and stored over activated 3 Å molecular sieves prior to use. Elemental analysis was performed by the Beckman Institute Elemental Analysis facility at California Institute of Technology. ¹H and ¹³C NMR chemical shifts are reported in ppm relative to tetramethylsilane, using residual solvent resonances as internal standards. Solid IR measurements were obtained on a Bruker Alpha spectrometer equipped with a diamond ATR probe.

D.1.2 Continuous Wave EPR Spectroscopy

X-band (9.4 GHz) CW EPR spectra were acquired using a Bruker EMX spectrometer equipped with a Super High-Q (SHQE) resonator using Bruker Win-EPR software (ver. 3.0).

Spectra were acquired at 77 K using a vacuum-insulated quartz liquid nitrogen immersion dewar inserted into the EPR resonator.

D.1.3 Pulse EPR Spectroscopy

All pulse Q-band (34 GHz) electron nuclear double resonance (ENDOR), hyperfine sublevel correlation (HYSCORE), and electron spin echo detected field-swept spectra were acquired using a Bruker ELEXSYS E580 pulse EPR spectrometer equipped with a Bruker D2 resonator. Temperature control was achieved using an ER 4118HV-CF5-L Flexline Cryogen-Free VT cryostat manufactured by ColdEdge equipped with an Oxford Instruments Mercury ITC temperature controller.

Q-band electron spin-echo detected EPR (ESE-EPR) field-swept spectra were acquired using the 2-pulse “Hahn-echo” sequence ($\pi/2 - \tau - \pi - \tau - \text{echo}$) where τ was held constant. Subsequently, each field swept echo-detected EPR absorption spectrum was modified using a pseudo-modulation function to approximate the effect of field modulation and produce the CW-like 1st derivative spectrum.⁶ Specific acquisition parameters: $\pi/2 = 12$ ns; $\pi = 24$ ns; $\tau = 160$ ns (6 K spectra), 600 ns (10 K spectra); shot repetition time (srt) = 5 ms (6 K spectra), 2 ms (10 K spectra).

Q-band inversion recovery experiments were conducted using the pulse sequence $\pi - T - \pi/2 - \tau - \pi - \tau - \text{echo}$, where T is a variable delay and τ is a fixed delay. Specific acquisition parameters: $\pi/2 = 12$ ns; $\pi = 24$ ns; $\tau = 160$ ns

Q-band HYSCORE spectra were acquired using the 4-pulse sequence ($\pi/2 - \tau - \pi/2 - t_1 - \pi - t_2 - \pi/2 - \tau - \text{echo}$), where τ is a fixed delay, and t_1 and t_2 are variable delays independently incremented by Δt_1 and Δt_2 , respectively. Sixteen step phase cycling

was utilized. The time domain spectra were baseline-corrected (third-order polynomial), apodized with a Hamming window function, zero-filled to eight-fold points, and fast Fourier-transformed to yield the frequency domain. For ^2H - ^1H difference spectra, the time domain of the HYSORE spectrum of the ^1H sample was subtracted from that of the ^2H sample, and the same data processing procedure detailed above was used to generate the frequency spectrum.

Q-band ENDOR spectra were acquired using the Davies pulse sequence ($\pi - t_{RF} - \pi_{RF} - t_{RF} - \pi/2 - \tau - \pi - \text{echo}$), where t_{RF} is the delay between MW pulses and RF pulses, π_{RF} is the length of the RF pulse. The RF frequency was randomly sampled during each pulse sequence. Specific acquisition parameters: $\pi/2 = 40$ ns; $\pi_{RF} = 15$ μs ; $t_{RF} = 2$ μs ; $\pi = 80$ ns; $\tau = 300$; shot repetition time (srt) = 5 ms

In general, the ENDOR spectrum for a given nucleus with spin $I = 1/2$ (^1H) coupled to the $S = 1/2$ electron spin exhibits a doublet at frequencies (**Eq D.1**)

$$\text{Eq D.1) } \nu_{\pm} = |A/2 \pm \nu_N|$$

Where ν_N is the nuclear Larmor frequency and A is the hyperfine coupling. For nuclei with $I \geq 1$ (^{14}N , ^2H), an additional splitting of the ν_{\pm} (**Eq D.2**) manifolds is produced by the nuclear quadrupole interaction (P)

$$\text{Eq D.2) } \nu_{\pm, m_I} = |\nu_N \pm 3P(2m_I - 1)/2|$$

In HYSORE spectra, these signals manifest as cross-peaks or ridges in the 2-D frequency spectrum which are generally symmetric about the diagonal of a given quadrant. This technique allows hyperfine levels corresponding to the same electron-nuclear submanifold to be differentiated, as well as separating features from hyperfine couplings

in the weak-coupling regime ($|A| < 2|v_1|$) in the (+,+) quadrant from those in the strong coupling regime ($|A| > 2|v_1|$) in the (-,+) quadrant. The (-,-) and (+,-) quadrants of these frequency spectra are symmetric to the (+,+) and (-,+) quadrants, thus typically only two of the quadrants are typically displayed in literature.

For systems with appreciable hyperfine anisotropy in frozen solutions or solids, HYSORE spectra typically do not exhibit sharp cross peaks, but show ridges that represent the sum of cross peaks from selected orientations at the magnetic field position at which the spectrum is collected. The length and curvature of these correlation ridges allow for the separation and estimation of the magnitude of the isotropic and dipolar components of the hyperfine tensor, as shown in **Figure D.1**.

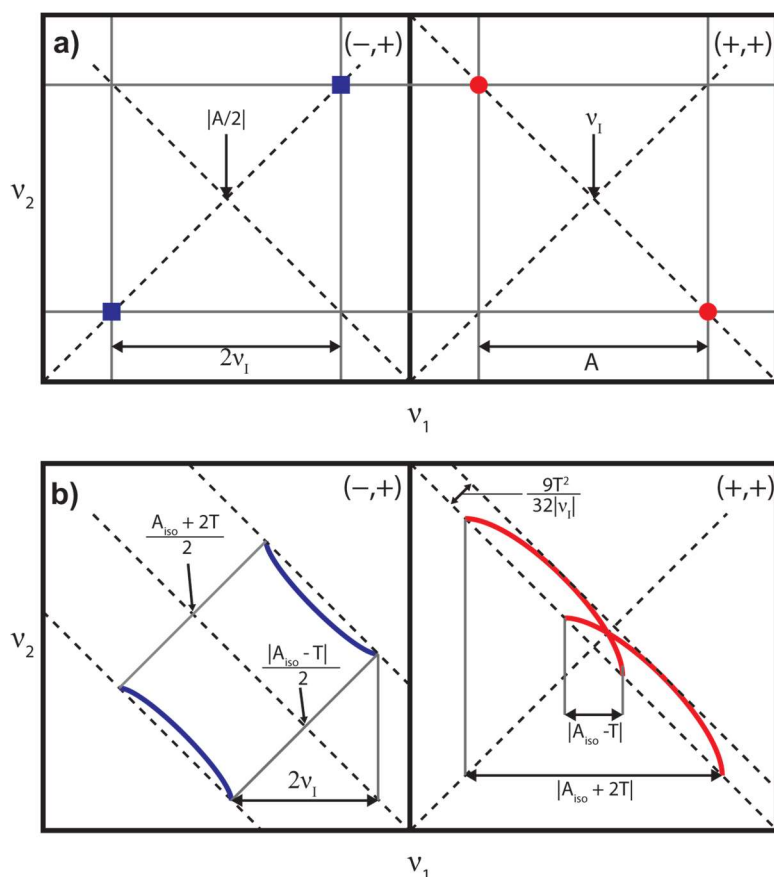


Figure D.1: a) HYSORE powder patterns for an $S = 1/2$, $I = 1/2$ spin system with an isotropic hyperfine tensor A . b) HYSORE powder patterns for an $S = 1/2$, $I = 1/2$ spin system with an isotropic hyperfine tensor which contains isotropic (a_{iso}) and dipolar (T) contributions. Blue correlation ridges represent the strong coupling case; red correlation ridges represent the weak coupling case.

D.1.4 EPR Simulations

All CW and pulse EPR spectra were simulated using the EasySpin⁷ suite of programs with Matlab 2017 using the following Hamiltonian (Eq D.3):

$$\text{Eq D.3) } H = \mu_B B_0 gS + \mu_{NGN} B_0 I + hSAI + hIPI$$

In this expression, the first term corresponds to the electron Zeeman interaction term where μ_B is the Bohr magneton, g is the electron spin g -value matrix with principle components $\mathbf{g} = [g_{xx}, g_{yy}, g_{zz}]$, and \hat{S} is the electron spin operator; the second term corresponds to the

nuclear Zeeman interaction term where μ_N is the nuclear magneton, g_N is the characteristic nuclear g -value for each nucleus (e.g. ^1H , ^2H , ^{31}P) and \hat{I} is the nuclear spin operator; the third term corresponds to the electron-nuclear hyperfine term, where A is the hyperfine coupling tensor with principle components $A = [A_{xx}, A_{yy}, A_{zz}]$; and for nuclei with $I \geq 1$, the final term corresponds to the nuclear quadrupole (NQI) term which arises from the interaction of the nuclear quadrupole moment with the local electric field gradient (efg) at the nucleus, where \mathbf{P} is the quadrupole coupling tensor. In the principle axis system (PAS), \mathbf{P} is traceless and parametrized by the quadrupole coupling constant e^2qQ/h and the asymmetry parameter η such that (**Eq D.4-D.6**):

$$\text{Eq D.4) } \mathbf{P} = \begin{pmatrix} P_{xx} & 0 & 0 \\ 0 & P_{yy} & 0 \\ 0 & 0 & P_{zz} \end{pmatrix} = \frac{e^2qQ/h}{4I(2I-1)} \begin{pmatrix} -(1-\eta) & 0 & 0 \\ 0 & -(1+\eta) & 0 \\ 0 & 0 & 2 \end{pmatrix}$$

$$\text{Eq D.5) } e^2qQ/h = 2I(2I-1)P_{zz}$$

$$\text{Eq D.6) } \eta = (P_{xx} - P_{yy})/P_{zz}$$

The asymmetry parameter may have values between 0 and 1, with 0 corresponding to an electric field gradient with axial symmetry and 1 corresponding to a fully rhombic efg. The orientations between the hyperfine and NQI tensor principle axis systems and the \mathbf{g} -matrix reference frame are defined by the Euler angles (α , β , γ).

D.1.5 X-ray Crystallography

XRD studies were carried out at the Beckman Institute Crystallography Facility on a Bruker Kappa Apex II diffractometer (Mo $K\alpha$ radiation). Structures were solved using SHELXS or SHELXT and refined against F^2 on all data by full-matrix least squares with

SHELXL.⁸ All of the solutions were performed in the Olex2 program.⁹ The crystals were mounted on a glass fiber under Paratone N oil or fluorolube.

D.1.6 Electrochemistry

Electrochemical measurements were carried out in a thick-walled one-component electrochemical cell fitted with a Teflon stopcock and tungsten leads protruding from the top of apparatus. A CH instruments 600B electrochemical analyzer was used for data collection. A freshly-polished glassy carbon electrode was used as the working electrode, a platinum wire was used as the auxiliary electrode, and a silver wire as a reference electrode. The analyte was used in 1 mM concentration. The solvent and the concentration of the electrolyte are noted with the individual voltammograms. After the desired scans were completed, ferrocene (1 mM) was added to serve as an internal reference or the known decamethylcobaltocenium/decamethylcobaltocene couple was used as the internal reference. All reported potentials are referenced to the ferrocenium/ferrocene couple ($\text{Fc}^{+/0}$).

D.1.7 Density Functional Theory Calculations

All calculations were performed using the ORCA 4.0 program.^{10,11} In cases where crystal structures were available these coordinates were used as the input. The calculations were performed using the TPSS (meta-GGA)¹² functional with the def2-SVP basis set was on C and H and the def2-TZVP basis set on Co¹³ and Grimme-d3 dispersion correction.¹⁴ That optimized structures represented true stationary points was checked by doing a single-point frequency calculations on the optimized structure.

For species where calculating the EPR parameters was of interest further calculations were performed in order to verify the robustness of those results. Using the

structures optimized as described above additional optimizations were performed with other functionals: BP86 (GGA),^{15,16} B3LYP (hybrid+GGA),^{15,17,18} and TPSSH (hybrid+meta-GGA).^{12,19} In all cases the ring-functionalized structures were found to be minima by means of a frequency calculation. For the Co–H structures in all cases (except with TPSS) there was a small negative frequency that did involve motion of the Co–H between the top and bottom ring suggesting that with these other functionals that this structure may only be a transition state. This is consistent with our previous observations with M06-L²⁰ where a Co–H structure could not be optimized.²¹ In all cases the thermochemistry was very similar.

EPR parameters for the TPSS-optimized structure were calculated by doing a single point calculation on the optimized structures using CP(PPP)²² on Co and def2-TZVP on C and H with Grid6 and TPSSH as the functional. To check the robustness of this basis set a higher level calculation was also done using CP(PPP) on Co and EPR-III²³ on C and H with grid 7. The results were very similar. Thus the EPR parameters were also calculated using CP(PPP) on Co and def2-TZVP on C and H with TPSS, BP86, and B3LYP. Lastly, the EPR parameters for the structures optimized using TPSSH, BP86, and B3LYP were all calculated via a single point calculation using TPSSH with CP(PPP) on Co and def2-TZVP on C and H with Grid6. See below for a discussion of the results.

For the calculation of thermochemical properties (reduction potential, pK_a , and hydricity) an additional solvation calculation was done using the CPCM solvation model with acetonitrile solvent to determine the solvated internal energy (E_{soln}).^{24–26} Free energies of solvation were approximated using the difference in gas phase internal energy (E_{gas}) and solvated internal energy ($\Delta G_{\text{solv}} \approx E_{\text{soln}} - E_{\text{gas}}$) and the free energy of a species in solution

was then calculated using the gas phase free energy (G_{gas}) and the free energy of solvation ($G_{\text{soln}} = G_{\text{gas}} + \Delta G_{\text{solv}}$).^{27,28} The calculations of BDFE were done without the additional solvation correction as there is no change in charge for either reactants or products and it was found to introduce additional error in previous studies.

D.2 Synthetic Procedures

(Cp*)Co(*exo*- η^4 -C₅Me₅H)-[Cp*₂Co][PF₆] (100.0 mg, 0.21 mmol) was added as a solid to a THF solution (15 mL) of [TBA][BH₄] (271.2 mg, 1.05 mmol, 5.0 equiv) in a Schlenk tube. This reaction was then heated to reflux and allowed to stir overnight. The reaction mixture was cooled to room temperature and the solvent was evaporated. The orange solid was extracted with pentane (8 x 5 mL) and filtered through an alumina plug. The solvent was then removed under reduced pressure to yield an orange solid. X-ray diffraction quality crystals were obtained by slow evaporation of a concentrated pentane solution. (Yield: 40.2 mg, 57.8%).

¹H NMR (RT, C₆D₆, 400 MHz): δ = 2.11 (1H, m, C(H)-CH₃), 1.87 (6H, s, β -CH₃), 1.65 (15H, s, Cp*), 1.42 (3H, d, ⁴J(H-H) = 6.7 Hz, C(H)-CH₃) 0.76 (6H, d, ⁵J(H-H) = 1.2 Hz, α -CH₃). ¹³C{¹H} NMR (RT, C₆D₆, 100 MHz): δ = 87.74, 86.14, 53.21, 51.66, 17.08, 11.39, 10.21, 9.55. IR (Thin Film): 2708 and 2612 cm⁻¹ ($\nu_{\text{C-H}}$ for the ring-bound C-H). UV/Vis (2-MeTHF): nm [cm⁻¹ M⁻¹): 463 [220], 565 [350]. Elemental Analysis: theory [C: 72.71 H: 9.46]; found [C: 72.82, H: 9.64]. See the IR spectra for a further discussion of why two stretches are observed for the C-H mode.

Cp*(*exo*- η^4 -C₅Me₅D)Co-[Cp*₂Co][PF₆] (100 mg, 0.21 mmol) and [TBA][BD₄] (275.4 mg, 1.05 mmol, 5 equiv) were added to a Schlenk tube as solids. A small stir bar and

20 mL of THF were then added. The reaction was then heated to reflux overnight. At this point the solvent was removed *in vacuo* and the solid extracted with (8 x 5 mL) pentane. This material was then filtered through alumina and the solvent was removed under reduced pressure. (Yield: 36.5 mg, 52.0%)

^1H NMR (RT, C_6D_6 , 400 MHz): $\delta = 1.87$ (6H, s, $\beta\text{-CH}_3$), 1.65 (15H, s, Cp*), 1.42 (3H, s, C(D)- CH_3) 0.76 (6H, s, $\alpha\text{-CH}_3$). A small residual peak from the protio-incorporated material can be observed at 2.11 ppm. Integration of this peak suggests that there has been ~95% deuterium incorporation. $^{13}\text{C}\{^1\text{H}\}$ NMR (RT, C_6D_6 , 100 MHz): $\delta = 51.21$ (t, $^2\text{J}(\text{C-D}) = 18.0$ Hz). $^2\text{H}\{^1\text{H}\}$ NMR (RT, 90% C_6H_6 :10% C_6D_6 , 61.42 MHz): $\delta = 2.05$ (s). IR (Thin Film): 2001 and 1957 cm^{-1} ($\nu_{\text{C-D}}$ for the ring-bound C-H).

(Cp*)Co(*exo*- $\eta^4\text{-C}_5\text{Mes}^{13}\text{Me}$)-Cp* $_2$ Co (50 mg, 0.15 mmol) was dissolved in toluene and chilled to -78 °C with stirring. To this was added dropwise ^{13}C -MeOTf (75 mg, 0.45 mmol, 3 eq). The reaction was stirred for one hour at -78 °C followed by warming to room temperature for five hours. The reaction was then filtered to remove [Cp* $_2$ Co][OTf]. The desired product could then be obtained by evaporation. (Yield: 23.1 mg, 87%)

^1H NMR (RT, C_6D_6 , 400 MHz): $\delta = 1.84$ (6H, s), 1.65 (15H, s, Cp*), 1.42 (3H, d, $^3\text{J}(\text{C-H}) = 4.5$ Hz) 0.76 (6H, s), 0.47 (3H, d, $^1\text{J}(\text{C-H}) = 124.4$ Hz). $^{13}\text{C}\{^1\text{H}\}$ NMR (RT, C_6D_6 , 100 MHz): $\delta = 26.38$.

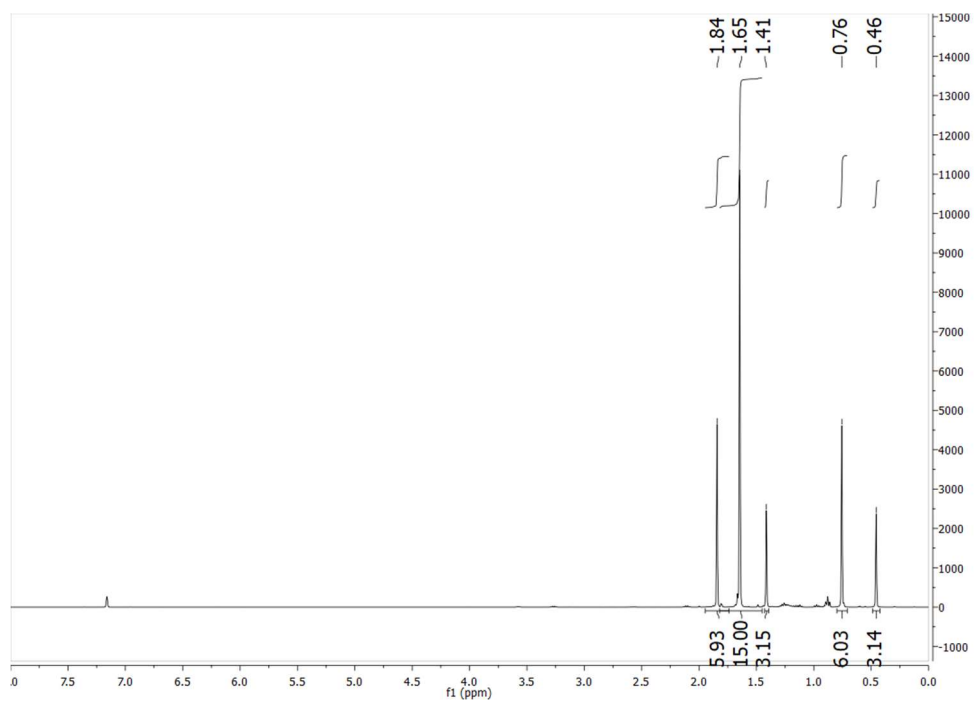
D.3 NMR Characterization of New Species

Figure D.2: ¹H NMR spectrum (400 MHz, C₆D₆, 25 °C) of (Cp*)Co(*exo*-η⁴-C₅Me₅H).

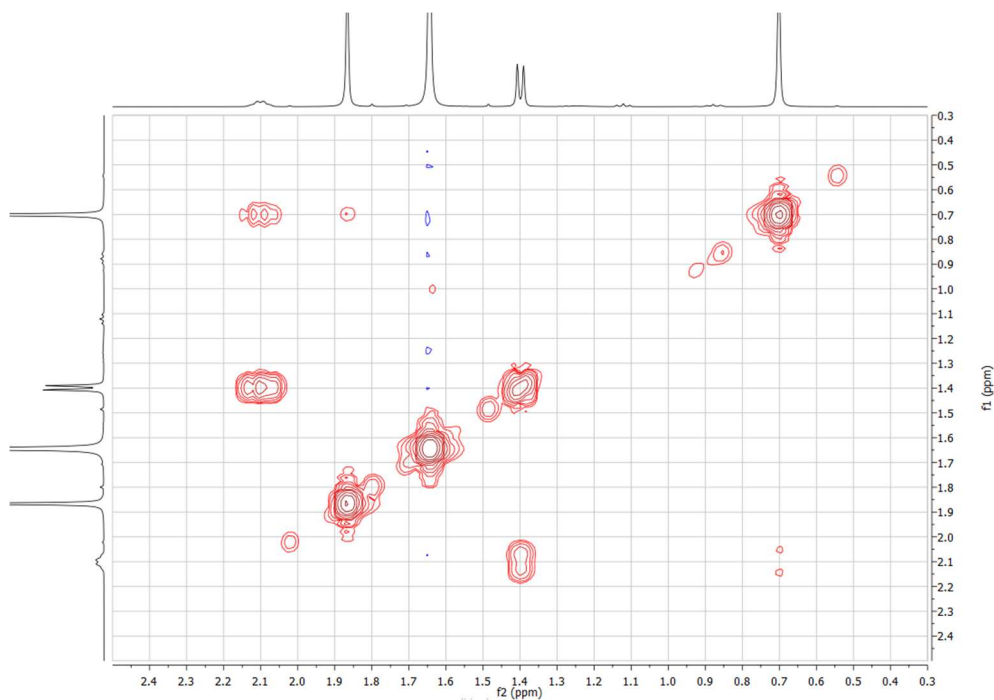


Figure D.3: ^1H -COSY NMR spectrum (400 MHz, C_6D_6 , 25 °C) of $(\text{Cp}^*)\text{Co}(\text{exo-}\eta^4\text{-C}_5\text{Me}_5\text{H})$. This data was used to establish the chemical shift of the Me groups that are α and β to the quaternary carbon.

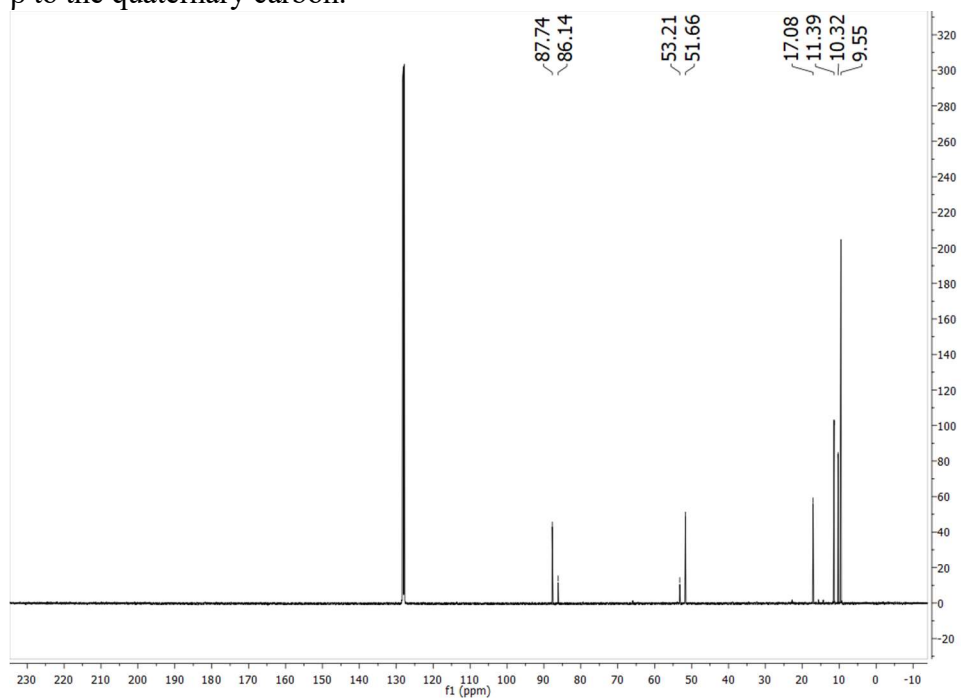


Figure D.4: ^{13}C NMR spectrum (100 MHz, C_6D_6 , 25 °C) of $(\text{Cp}^*)\text{Co}(\text{exo-}\eta^4\text{-C}_5\text{Me}_5\text{H})$.

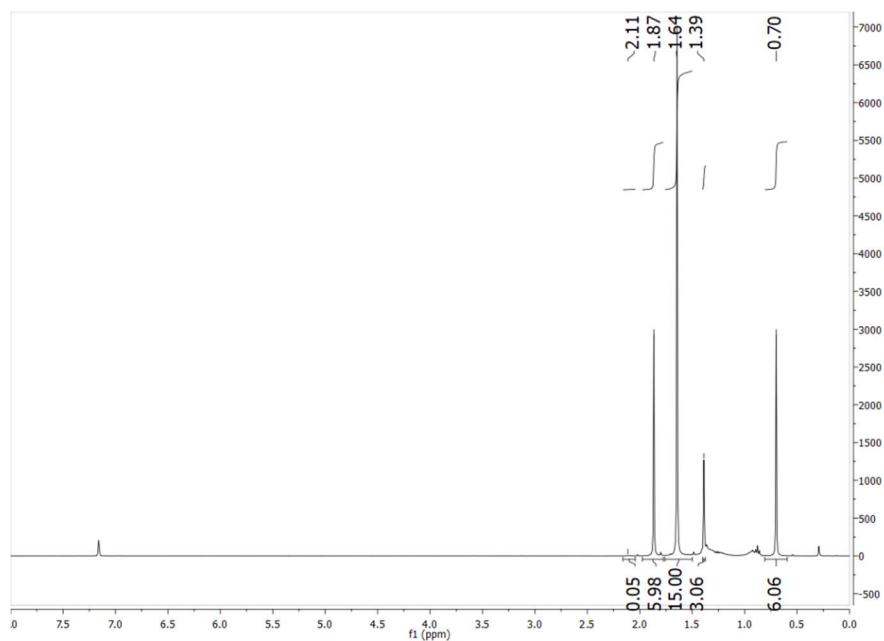


Figure D.5: ¹H NMR spectrum (400 MHz, C₆D₆, 25 °C) of (Cp*)Co(*exo*-η⁴-C₅Me₅D). Integration of the residual ¹H signal at 2.11 indicates approximately 95% deuterium incorporation.

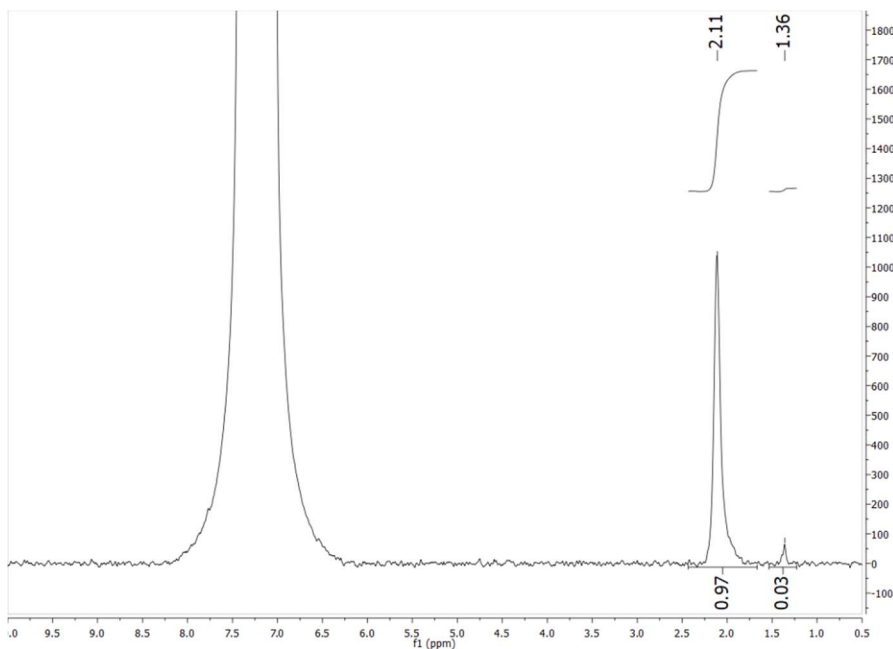


Figure D.6: $^2\text{H}\{^1\text{H}\}$ NMR spectrum (61.42 MHz, 90% C_6H_6 :10% C_6D_6 , 25 °C) of $(\text{Cp}^*)\text{Co}(\text{exo-}\eta^4\text{-C}_5\text{Me}_5\text{D})$. In addition to the expected deuterium incorporation into the *exo*-position it appears that there is also a small amount of deuterium incorporation into the methyl group that is attached to the quaternary carbon.

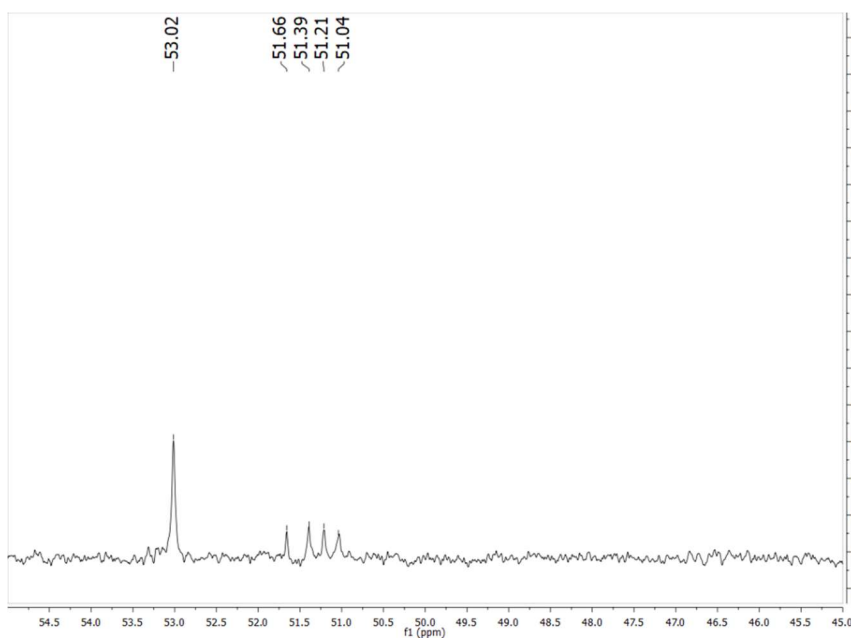


Figure D.7: $^{13}\text{C}\{^1\text{H}\}$ NMR spectrum (100 MHz, C_6D_6 , 25 °C) of $(\text{Cp}^*)\text{Co}(\text{exo-}\eta^4\text{-C}_5\text{Me}_5\text{D})$. Here we can also see a small amount of contamination with the protio species at 51.66. The triplet is centered at 51.21 demonstrating the expected change in chemical shift upon deuteration.

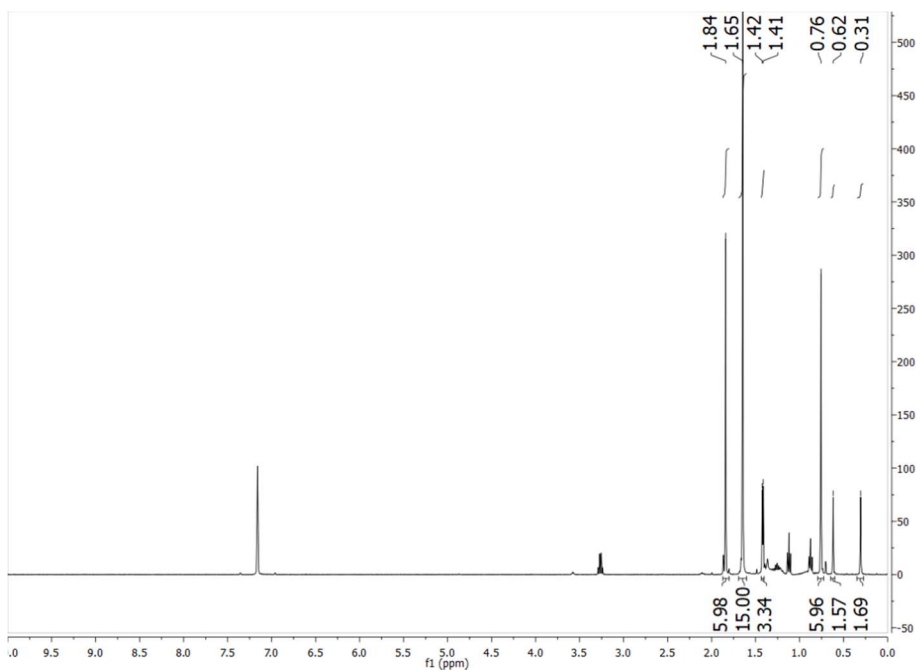


Figure D.8: ¹H NMR spectrum (400 MHz, C₆D₆, 25 °C) of (Cp*)Co(*exo*-η⁴-C₅Me₅¹³Me) demonstrating the ¹³C-¹H coupling evident in the splitting of the peak for the α-protons at 0.46 ppm and the smaller coupling to the γ-protons at 1.41 ppm.

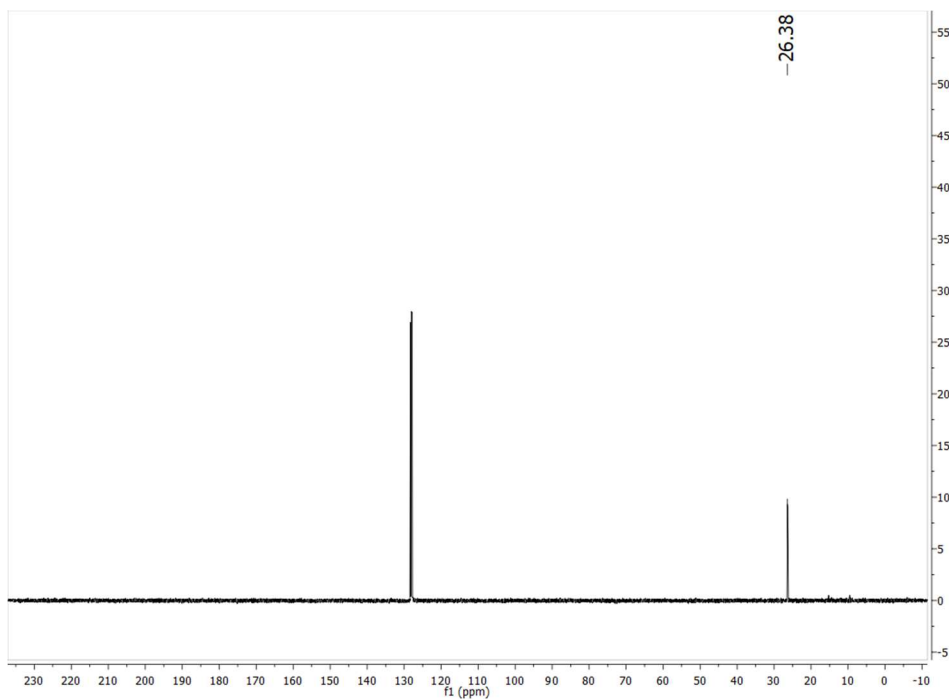


Figure D.9: ¹³C NMR spectrum (100 MHz, C₆D₆, 25 °C) (Cp*)Co(*exo*-η⁴-C₅Me₅¹³Me) highlighting the selective ¹³C incorporation.

D.4 Reactivity of $(\text{Cp}^*)\text{Co}(\text{exo-}\eta^4\text{-C}_5\text{Me}_5\text{H})$

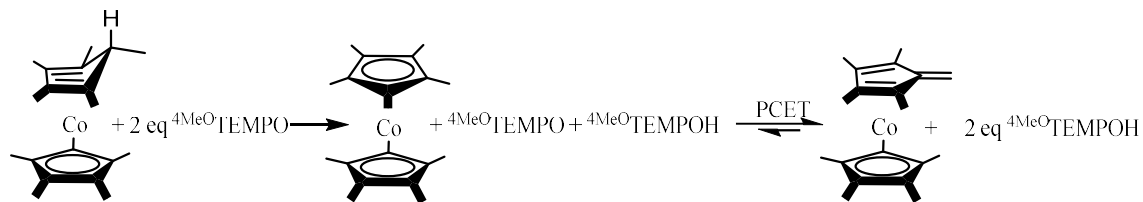


Figure D.10: Reaction of $(\text{Cp}^*)\text{Co}(\text{exo-}\eta^4\text{-C}_5\text{Me}_5\text{H})$ with ${}^4\text{MeO-TEMPO}$.

$(\text{Cp}^*)\text{Co}(\text{exo-}\eta^4\text{-C}_5\text{Me}_5\text{H})$ (1.5 mg, 0.005 mmol, 1 eq) and ${}^4\text{MeO-TEMPO}$ (1.9 mg, 0.010, 2.2 eq) were dissolved in $\text{MeCN-}d_3$. These were then allowed to react at room temperature for thirty minutes with shaking. A ${}^1\text{H}$ NMR was then taken. In this the formation of 2 equivalents of ${}^4\text{MeO-TEMPOH}$ is observed (**Figure D.11**)²⁹ confirmed by integration relative to a benzene internal standard containing 2 equivalents. However, the Co product is unclear. On the basis of reactions performed in toluene, we believe that this is because of the high instability of the fulvene product, $(\text{Cp}^*)\text{Co}(\eta^4\text{-C}_5\text{Me}_4\text{CH}_2)$, in coordinating solvents.

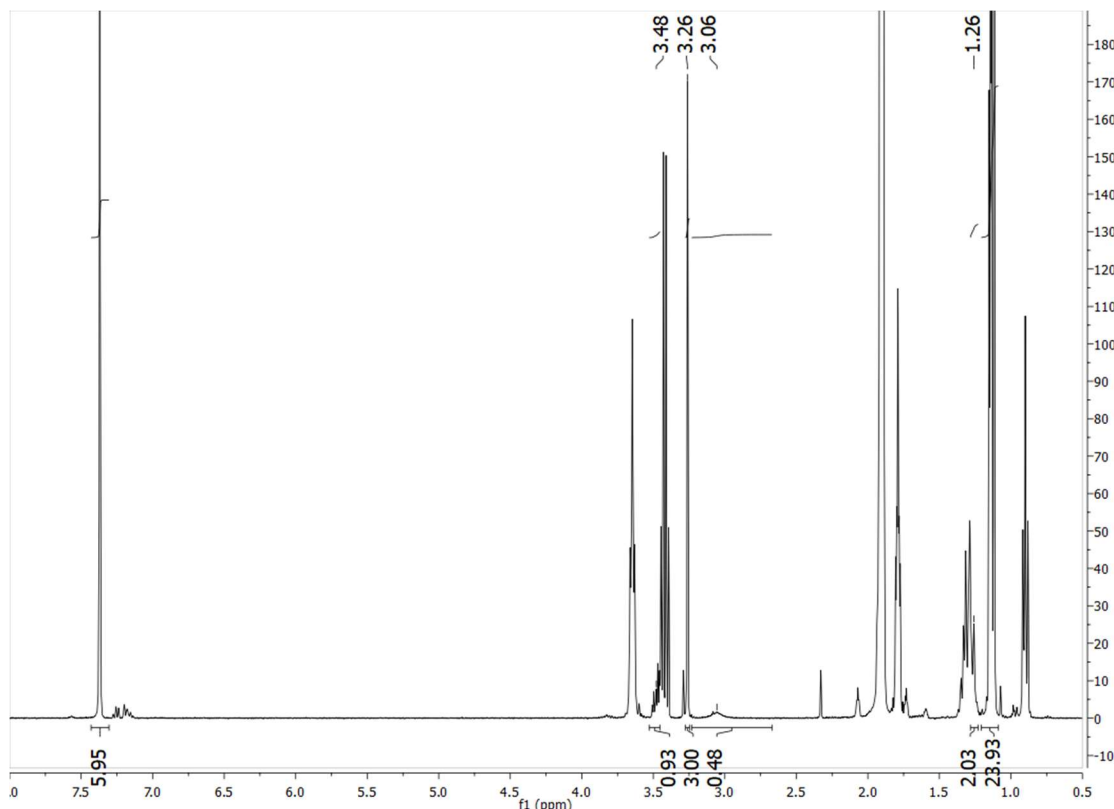


Figure D.11: ^1H NMR spectrum (400 MHz, $\text{MeCN-}d_3$, RT) of the reaction between $(\text{Cp}^*)\text{Co}(\text{exo-}\eta^4\text{-C}_5\text{Me}_5\text{H})$ and ^4MeO TEMPO.

Due to the poor solubility of the reagents in acetonitrile, the limited ability to cool that solvent, and that the NMR chemical shifts of the fulvene complex have only been previously reported in aromatic solvents the reaction was performed again in toluene- d_8 .^{30,31} $(\text{Cp}^*)\text{Co}(\text{exo-}\eta^4\text{-C}_5\text{Me}_5\text{H})$ (4 mg, 0.012 mmol, 1 eq) and ^4MeO TEMPO (4.5 mg, 0.024 mmol, 1 eq) were each dissolved in minimal d_8 -toluene and both added to a J-Young NMR tube (Figure S10). Due to broadening at room temperature the reaction mixture was cooled to -78 $^\circ\text{C}$ and a ^1H (Figure D.12).

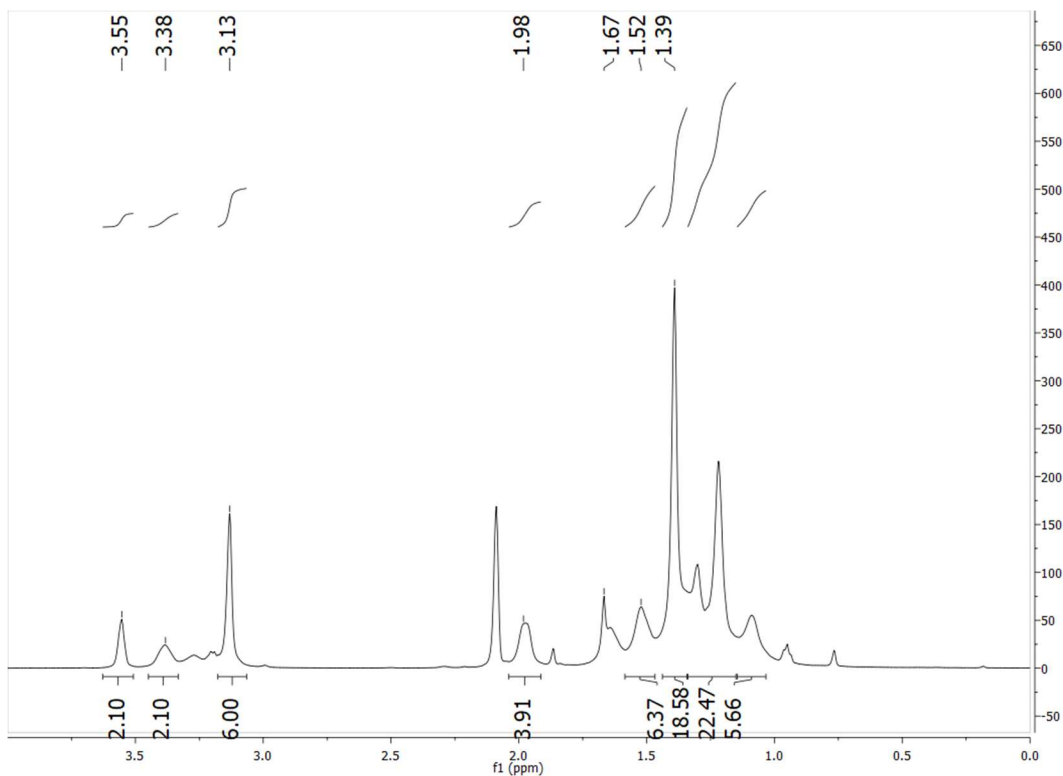


Figure D.12: Zoomed in view of the ^1H NMR (500 MHz, C_7D_8 , $-78\text{ }^\circ\text{C}$) of the reaction between $(\text{Cp}^*)\text{Co}(\text{exo-}\eta^4\text{-C}_5\text{Me}_5\text{H})$ and 2 equivalents of ^4MeO TEMPO demonstrating that two equivalents of ^4MeO TEMPOH are formed for each equivalent of $\text{Cp}^*(\eta^4\text{-C}_5\text{Me}_4\text{CH}_2)\text{Co}$.

As further evidence for the proposed scheme, decamethylcobaltocene (8 mg, 0.024 mmol, 1 eq) and ^4MeO TEMPO (4.5 mg, 0.024 mmol, 1 eq) were each dissolved in minimal d_8 -toluene and both added to a J-Young NMR tube (Figure S13). Due to broadening at room temperature (Figure D.13) the reaction mixture was cooled to $-78\text{ }^\circ\text{C}$ and a ^1H (Figure D.14) and ^{13}C NMR (Figure D.16) were taken. These data are in good agreement with the previously reported spectroscopic data.^{30,31}

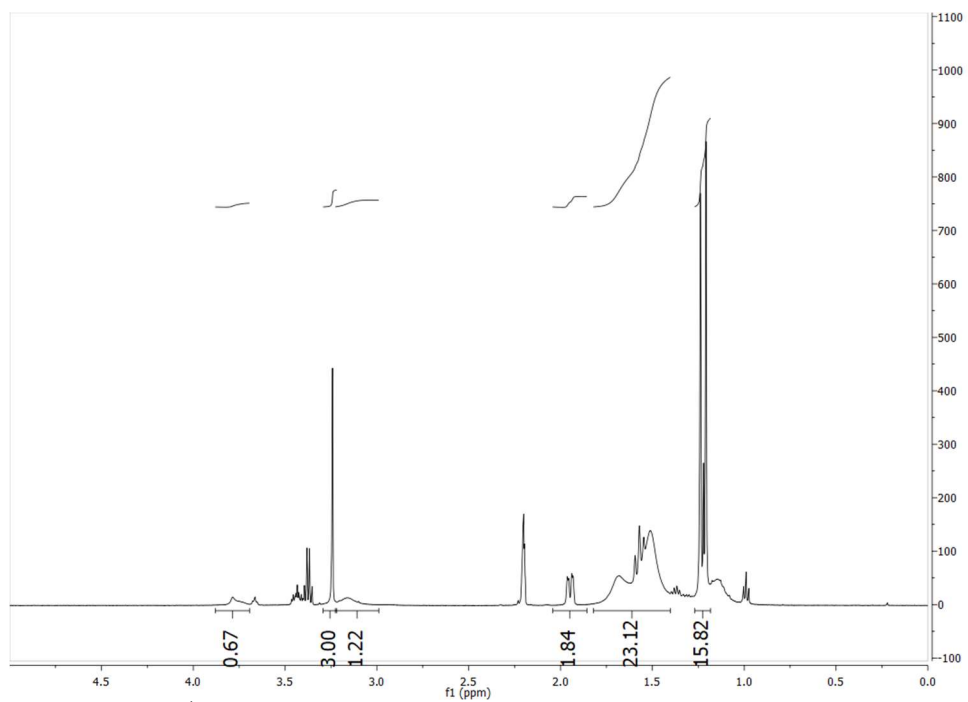


Figure D.13: ^1H NMR spectrum (500 MHz, C_7D_8 , RT) of the reaction between Cp^*_2Co and ^4MeO TEMPO.

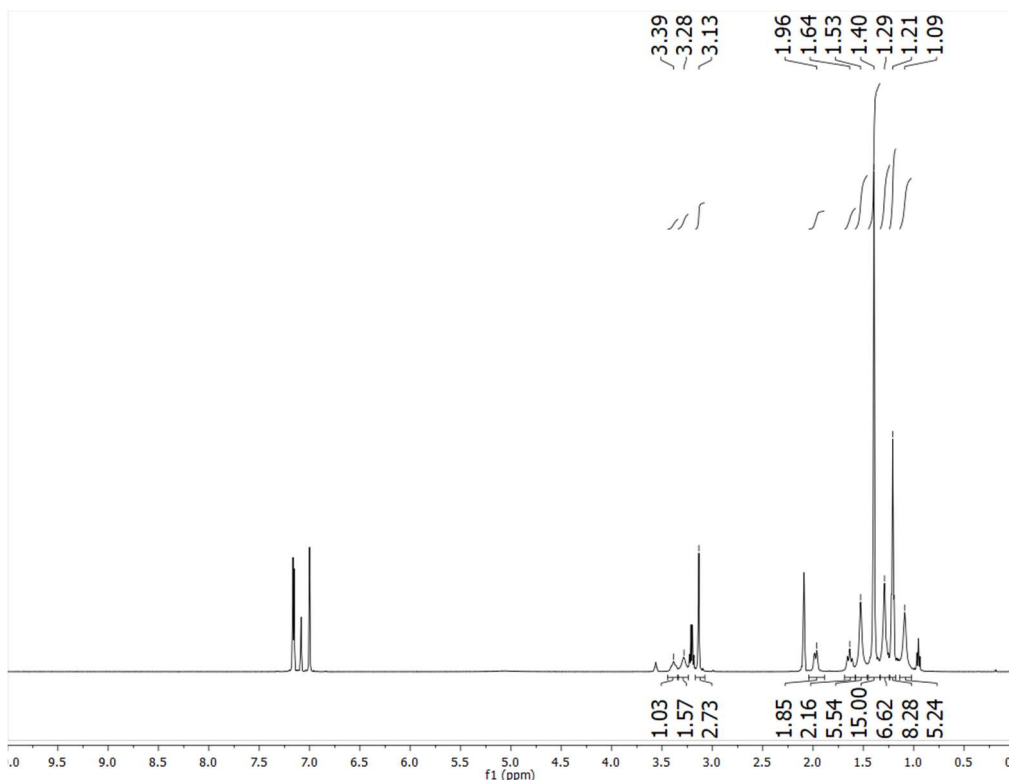


Figure D.14: ^1H NMR spectrum (500 MHz, C_7D_8 , -78°C) of the reaction between Cp^*Co and $^4\text{MeO-TEMPO}$.

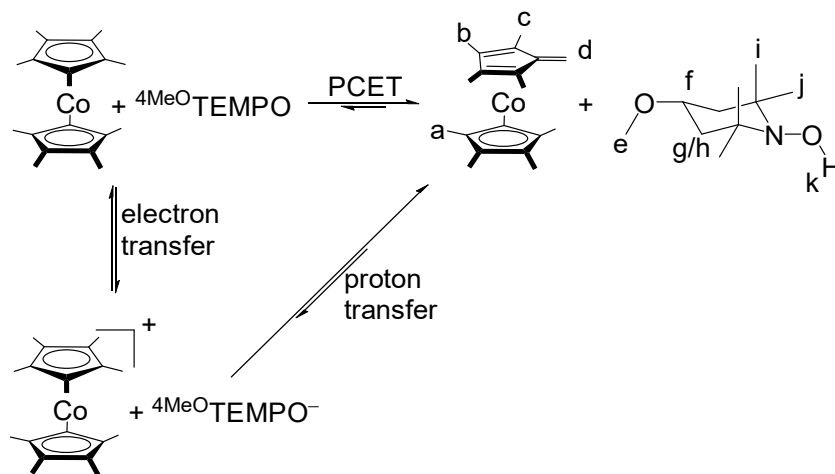


Figure D.15: Reaction scheme of Cp^*Co with $^4\text{-MeO-TEMPO}$ and the left side is labeled with the assignments made in the ^1H NMR based on known spectroscopic properties of these molecules. Both the concerted and separated PCET reaction pathways are possible. The deprotonation of decamethylcobaltocenium by TEMPO^- has been observed previously as part of a more complicated reaction scheme.³¹

^1H NMR ($-78\text{ }^\circ\text{C}$, C_7D_8 , 500 MHz): $\delta = 5.10$ (1H, s, **k**), 3.39 (1H, app t, $^3\text{J}(\text{H-H}) = 11.3$ MHz, **f**), 3.26 (2H, s, **d**), 3.13 (3H, s, **e**), 1.98 (2H, d, $^3\text{J}(\text{H-H}) = 11.3$ Hz, **g/h**), 1.64 (2H, t, $^2\text{J}(\text{H-H}) = 11.2$ MHz, **g/h**), 1.53 (6H, s, **b/c**), 1.40 (15 H, s, **a**), 1.29 (6H, s, **i/j**), 1.21 (6H, s, **i/j**), 1.09 (6H, s, **b/c**).

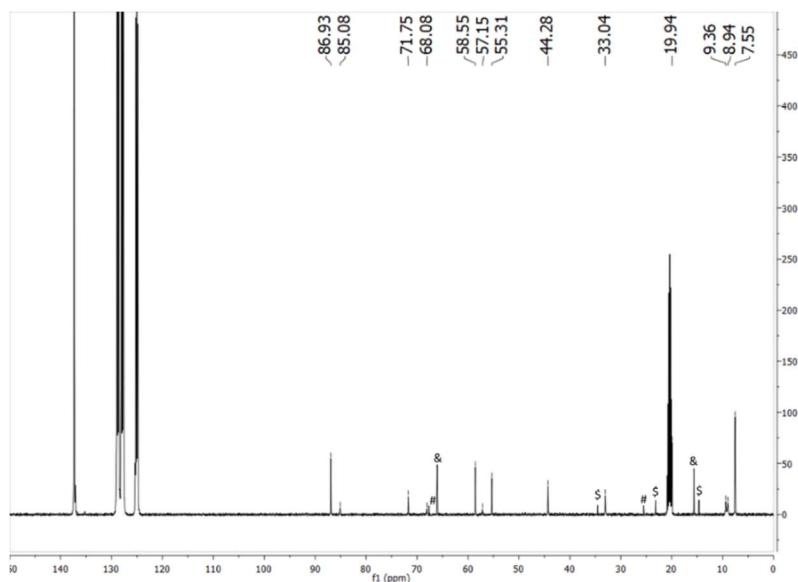


Figure D.16: ^{13}C NMR spectrum (125 MHz, C_7D_8 , $-78\text{ }^\circ\text{C}$) of between Cp^*_2Co and $^4\text{Me}^0\text{TEMPO}$ which demonstrates the formation of $\text{Cp}^*(\eta^4\text{-C}_5\text{Me}_4\text{CH}_2)\text{Co}$ and $^4\text{Me}^0\text{TEMPO-H}$. Residual solvents are indicated with symbols (# = THF, & = diethylether, \$ = pentane).

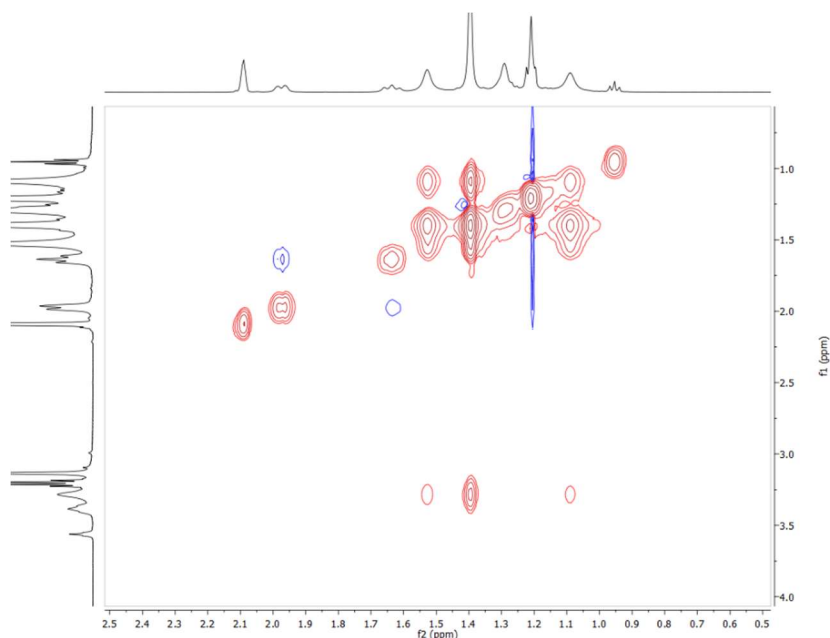


Figure D.17: Zoomed in data from the ¹H-ROESY NMR (500 MHz, C₇D₈, -78 °C) of the reaction between Cp*₂Co and ⁴Me⁰TEMPO.

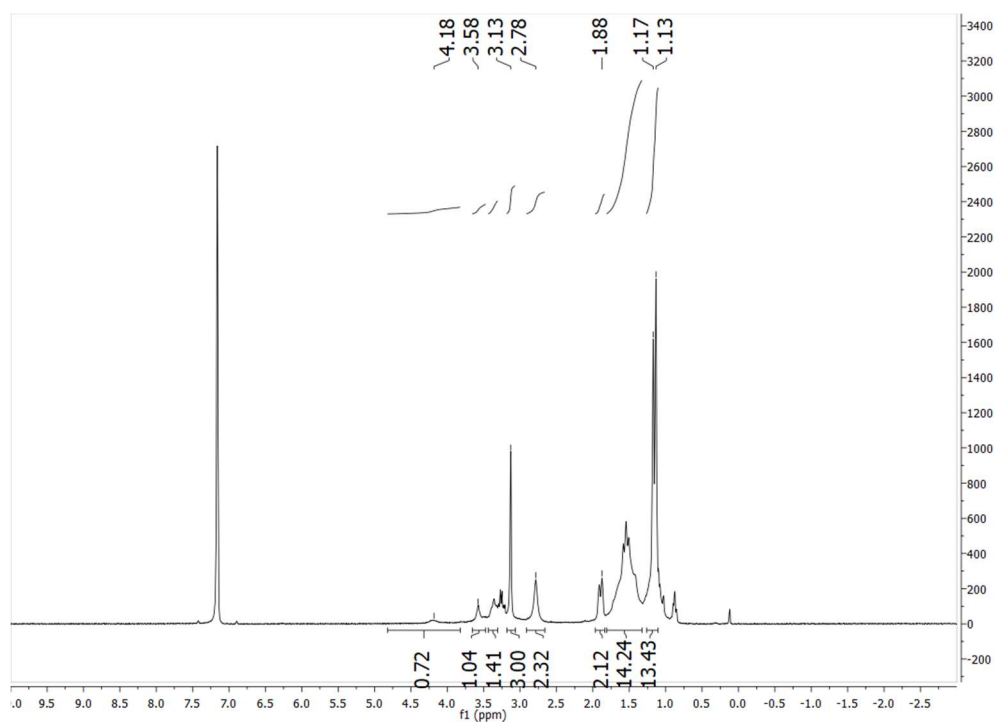


Figure D.18: ¹H NMR spectrum (400 MHz, C₇D₈, RT) of the reaction between octamethylcobaltocene (4 mg, 0.013 mmol, 1 eq) and ⁴Me⁰TEMPO (2.5 mg, 0.013 mmol, 1 eq).

In the ROESY NMR spectrum at $-78\text{ }^{\circ}\text{C}$ (Figure S17), there is clear chemical exchange between the different positions of the fulvene complex. The ROESY experiment is phase-sensitive, so you can observe both the through-space interaction between the axial and equatorial protons on the piperidin-1-oxyl ring, and the exchange coupling between all the positions that originate from the Cp^*_2Co species. The lack of through space interaction between the resonances from the $^4\text{MeO-TEMPO-H}$ and those from the $(\text{Cp}^*)\text{Co}$ -derived fragment suggest that they are not coupled. However, the exchange between the resonances attributed to $(\text{Cp}^*)\text{Co}(\eta^4\text{-C}_5\text{Me}_4\text{CH}_2)$ along with the broadening at room temperature indicates that the reaction between these two is reversible with two possibilities shown in Figure S15. The observation of similar reactivity between $^4\text{MeO-TEMPO}$ and octamethylcobaltocene (Figure S18) biases us towards the latter explanation but does not provide definitive evidence.

This reversibility is not evident in acetonitrile. This may be because the O–H bond is stronger in this more polar solvents due to preferential hydrogen bonding interactions relative to the C–H bond of the methyl in Cp^*_2Co . It has been observed that the O–H bond of TEMPO–H is a little more than 1 kcal mol^{-1} stronger in acetonitrile than in benzene.

Attempts to isolate the fulvene product from this reaction were precluded by the similar solubility of the two products and as had been previously observed, the relative instability of this complex at room temperature.

Reaction of $(\text{Cp}^*)\text{Co}(\textit{exo}\text{-}\eta^4\text{-C}_5\text{Me}_5\text{H})$ with CO_2 is done as follows: $(\text{Cp}^*)\text{Co}(\textit{exo}\text{-}\eta^4\text{-C}_5\text{Me}_5\text{H})$ (2.0 mg, 0.006 mmol) is dissolved in $\text{MeCN-}d_3$ and added to a J-Young NMR

tube. The J-Young tube is freeze-pump-thawed 3x and then backfilled with CO₂ that is passed through a dry-ice/acetonitrile bath to one atmosphere of pressure. The reactions is then rotated for three days and a pale yellow color is obtained. A new ¹H NMR reveals the formation of [Cp*₂Co][HCO₂] (**Figure D.19**). This product can be further confirmed by a thin film IR spectrum of the reaction (**Figure D.38**).

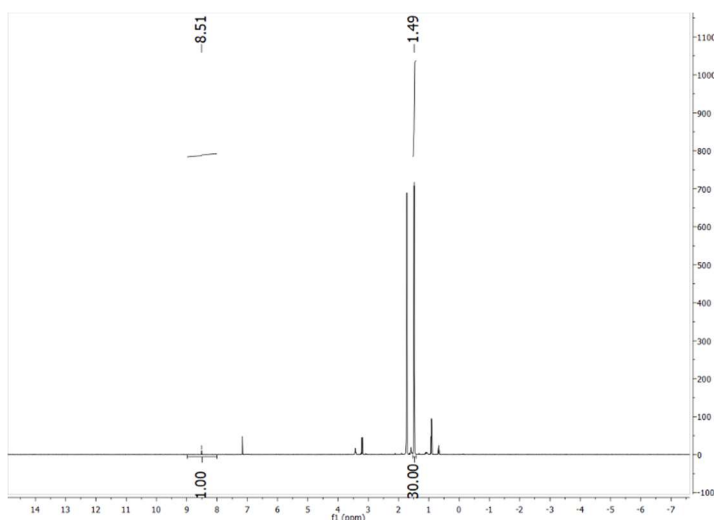


Figure D.19: ¹H NMR (400 MHz, MeCN-*d*₃, RT) of the reaction of (Cp*)Co(*exo-η*⁴-C₅Me₅H) with one atmosphere of CO₂ illustrating the formation of [Cp*₂Co][HCO₂] with the characteristic peak at 8.5 ppm for the formate proton.

Reaction of (Cp*)Co(*exo-η*⁴-C₅Me₅H) with [Pt(dmpe)₂][PF₆]₂ is done as follows: (Cp*)Co(*exo-η*⁴-C₅Me₅H) (1.8 mg, 0.0055 mmol) and [Pt(dmpe)₂][PF₆]₂ (9.0 mg, 0.014 mmol, 4 equiv) are added as solids to a vial. They are then dissolved in MeCN-*d*₃ and added to a J-Young NMR tube. They are then allowed to react for one day after which ¹H NMR (**Figure D.20**) and ³¹P NMR (**Figure D.21**) revealed complete transfer of the hydride to the Pt to form [HPt(dmpe)₂][PF₆] and [Cp*₂Co][PF₆].

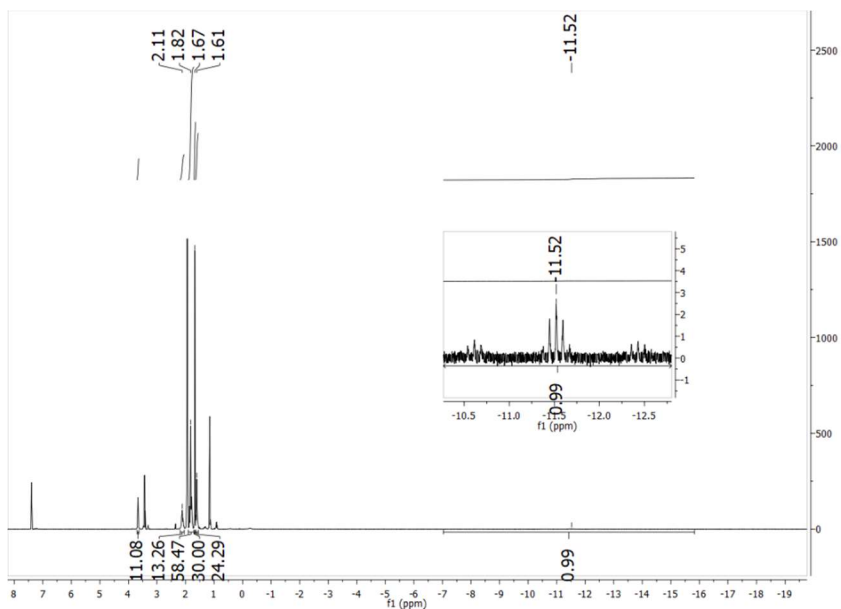


Figure D.20: ^1H NMR (400 MHz, $\text{MeCN-}d_3$, RT) of the reaction of $(\text{Cp}^*)\text{Co}(\text{exo-}\eta^4\text{-C}_5\text{Me}_5\text{H})$ with 4 equivalents of $[\text{Pt}(\text{dmpe})_2][\text{PF}_6]_2$ illustrating the quantitative hydride transfer to form $[\text{HPt}(\text{dmpe})_2][\text{PF}_6]_2$. The signal at 1.82 consists of three different peaks, the methyl protons for the hydride product, the methylene protons for the Pt starting material, and also a residual peak from THF. The inset highlights the formation of the hydride peak.

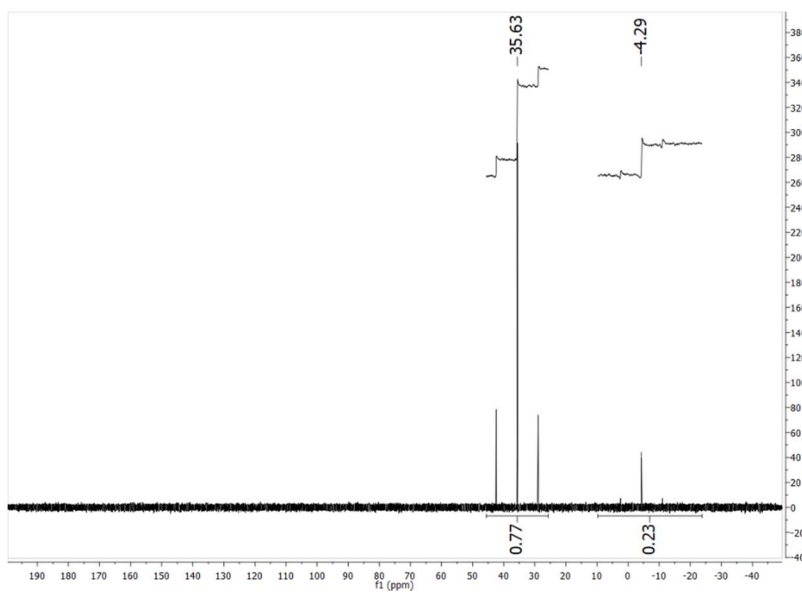


Figure D.21: $^{31}\text{P}\{^1\text{H}\}$ NMR (162 MHz, $\text{MeCN-}d_3$, RT) of the reaction of $(\text{Cp}^*)\text{Co}(\text{exo-}\eta^4\text{-C}_5\text{Me}_5\text{H})$ with 4 equivalents of $[\text{Pt}(\text{dmpe})_2][\text{PF}_6]_2$ illustrating the quantitative hydride transfer to form $[\text{HPt}(\text{dmpe})_2][\text{PF}_6]_2$.

D.5 Pulse EPR Spectroscopy

Samples for pulse EPR spectroscopy were prepared as previously described.²¹

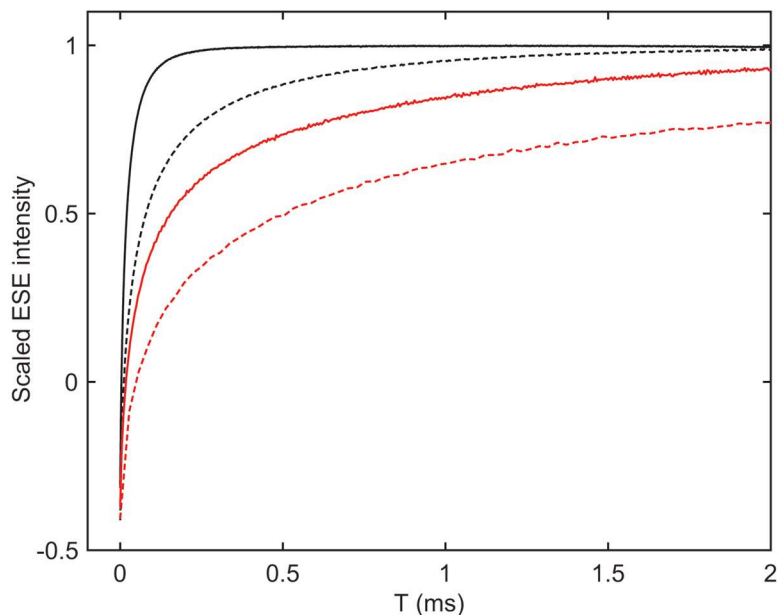


Figure D.22: Q-band inversion recovery traces of *endo*- (black) and *exo*-isomers (red) of Cp^*_2Co protonation acquired at 6 K (dashed lines) and 10 K (solid lines). Data for each species was acquired at the field corresponding to peak spectral intensity for that species. This illustrates the significantly faster relaxation properties of the *endo*-isomer.

Accurate measurement of the T_1' in these species is technically challenging due to their significant g -anisotropy. This is because there are contributions to the relaxation from spectral diffusion in addition to explicit spin-lattice relaxation, as only a very small portion of the EPR spectral envelope is acted upon by the initial inversion pulse. Furthermore, the EPR signals of the *exo*-product, overlap with those of the *endo*-product. Thus a multiexponential function would be necessary to model its inversion recovery data and would thus not be well constrained. Nonetheless, a rough estimate of the T_1' can be obtained without fitting of exponential functions by using **Eq D.8** for the longitudinal magnetization as a function of time in the inversion recovery experiment.

$$\text{Eq D.7) } M_z = 0, T \approx \ln(2) \times T_1'$$

This allows for the following estimates to be made. For the *exo*-species the T_1' is ~ 80 μs at 6 K and ~ 25 μs at 10 K. For the *endo*-species the T_1' is ~ 20 μs at 6 K and ~ 6 μs at 10 K. This clearly illustrates the significant difference observed in the longitudinal relaxation rates of the two species, which enables relatively clean pulse EPR data (particularly in the case of ENDOR) to be collected.

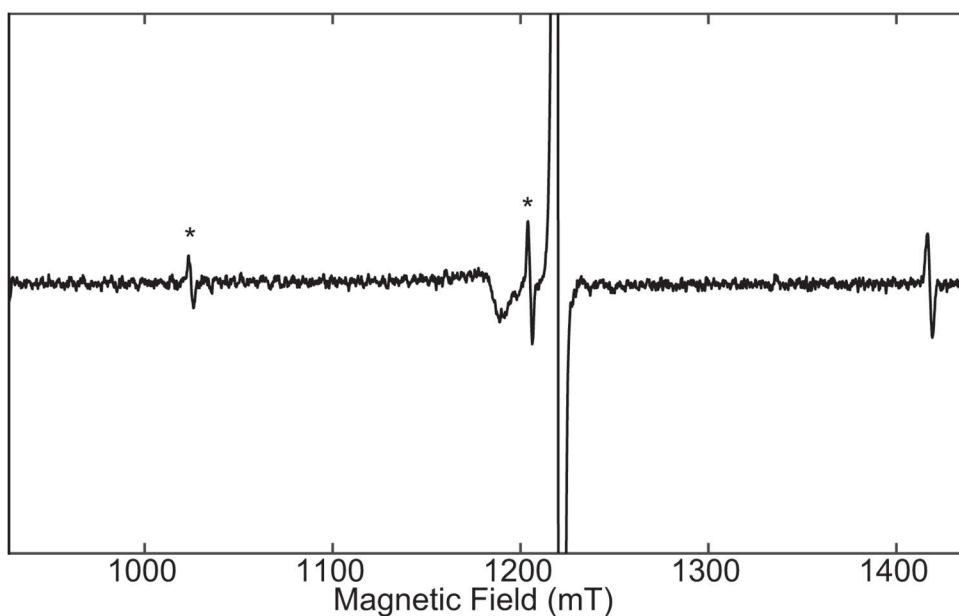


Figure D.23: Pseudomodulated Q-band ESE-EPR spectrum at 10 K of a coal standard sample (seen as an intense, isotropic signal at 1200 mT) using the same Bruker Q-band D2 resonator as in this study. There are additionally three sharp signals present in the background (1025 mT, 1205 mT, and 1418 mT) that arise from a trace paramagnetic species present in a component of the resonator, as well as a broad axial feature from a small amount of Cu(II) at 1184 mT. Two of these sharp background signals, marked with asterisks, are observed in the ESE-EPR spectra acquired at 10 K presented in the main text (Figure 2). The other signal is outside of the measured spectral window in this work. These features are much less intense relative to the signals derived from Cp^*Co -protonation at 6 K and thus are not observed in the spectra acquired at that temperature.

Table D.1: Simulation parameters derived from the ENDOR, HYSCORE, and CW-EPR spectroscopy.

Species	g-tensor	$A(^1\text{H})$ (MHz)	$A(^{59}\text{Co})$ (MHz)	e^2qQ/h for Co (MHz)	η
$[(\text{Cp}^*)\text{Co}(\text{endo-}\text{C}_5\text{Me}_5\text{H})]^+$	[2.626, 2.349, 1.984]	[19.0, 15.0, 19.5]	[245, 155, 187]	170	<0.1
$[(\text{Cp}^*)\text{Co}(\text{exo-}\text{C}_5\text{Me}_5\text{H})]^+$	[2.170, 2.085, 2.005]	[106.5, 112.5, 108.2]	[15, 15, 225]	N.D.	N.D.

D.6 CW EPR Spectroscopy

Experimental details for the reaction of Cp^*_2Co with HOTf have been reported previously²¹ but are repeated here for convenience. A 1 mL solution of HOTf (23 μL , 3.0 eq) in toluene and a 2 mL solution of Cp^*_2Co (40 mg, 1.0 eq) were chilled to $-78\text{ }^\circ\text{C}$ for ten minutes in a cold well. With strong stirring of the HOTf solution, the Cp^*_2Co solution was added dropwise over ten minutes. Purple precipitate could be observed upon the addition of each drop. After the completion of the addition, the reaction mixture was allowed to stir for 5 more minutes. The reaction was then vacuum filtered in the cold well through a medium porosity frit to yield a purple solid. This solid was then washed with toluene that had been prechilled to $-78\text{ }^\circ\text{C}$ (5 mL) and then likewise with prechilled pentane (15 mL). After drying on the frit for ten minutes the solid was then transferred to a prechilled vial. The solid was then dried under vacuum for several hours at $-78\text{ }^\circ\text{C}$. This solid was then transferred to an EPR tube and passed out of the glovebox into a dewar filled with liquid nitrogen.

For reactions with DOTf, the same experimental protocol as above was used with the exception that DOTf was employed and in all cases where toluene had previously been used it was replaced with toluene-*d*₈.

For the reaction of Cp*₂Co with HNTf₂, decamethylcobaltocene (20 mg, 0.061 mmol) was weighed into a 20 mL scintillation vial and dissolved in 5 mL of toluene. Bis(trifluoromethanesulfonyl)imide (HNTf₂) is weighed into a 20 mL scintillation vial and 5 mL of toluene is added and the vial is charged with a stir bar. Both solutions are cooled to -78 °C in the cold well for ten minutes. Then the Cp*₂Co solution is added dropwise to the HNTf₂ solution while it was being vigorously stirred over five minutes. The reaction mixture is allowed to stir for ten minutes during which it turns purple. Prechilled pentane (10 mL) is added to the toluene solution and the reaction is stirred for another five minutes. The reaction mixture is then filtered through a pre-chilled frit. The solid is then washed with pentane (5 x 2 mL). The solid is then transferred to a pre-chilled vial. The solid is then placed under vacuum for three hours to yield a pale purple solid. This solid is then transferred into a pre-chilled EPR tube and the cold well is then switched to a liquid nitrogen bath. The tube is allowed to cool for ten minutes before it is then quickly transferred out of the box and into a dewar with liquid nitrogen (**Figure D.24**).

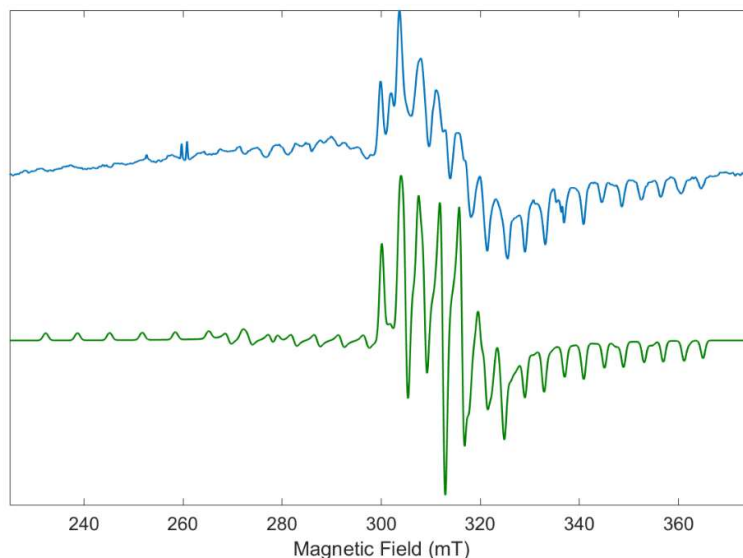


Figure D.24: X-Band CW EPR spectrum (blue) at 77 K in the solid state of the precipitate from the reaction of bis(trifluoromethanesulfon)imide) with Cp^*_2Co at $-78\text{ }^\circ\text{C}$ in toluene. Simulation (green) of this data using the parameters from **Table D.1** with a weight of 0.3 on the *endo-isomer* and a weight of 1.0 on the *exo-isomer*.

Both of the protonation reactions are under kinetic control due to the rapid precipitation upon proton transfer. Thus the relative energies of either the transition state or a pre-equilibrium must be affected by the steric bulk of the acid. We believe that this likely due to a hydrogen bonding interaction between the acid and the π -electrons of the Cp^* ring. Such hydrogen bonds have previously been observed experimentally by IR and NMR for ferrocene,^{32,33} and we have observed computationally the formation of hydrogen bonded interactions between anilinium triflates and Cp^*_2Co preceding proton transfer.³⁴ In this model, the thermodynamics of hydrogen bonding for the smaller HOTf reflect those of the isolated products and thus *endo*-protonation is preferred. With the bulkier HNTf₂, steric clash with the opposite Cp^* ring leads to destabilization of this *endo*-hydrogen bond and thus *exo*-hydrogen bonding and consequently *exo*-protonation is favored.

For oxidation of $(\text{Cp}^*)\text{Co}(\text{exo-}\eta^4\text{-C}_5\text{Me}_5\text{H})$ with HBAr^{F}_4 , $(\text{Cp}^*)\text{Co}(\text{exo-}\eta^4\text{-C}_5\text{Me}_5\text{H})$ (20 mg, 0.061 mmol) was dissolved in pentane and cooled to $-78\text{ }^\circ\text{C}$. It was then added to a 50 mL round bottom flask with a large stir bar that was also chilled to $-78\text{ }^\circ\text{C}$ after it was charged with HBAr^{F}_4 (122.6 mg, 0.12 mmol, 2 equiv.). This was then stirred for several hours during which a pale purple solid was seen to form in the reaction. This can then be filtered through a pre-chilled frit and washed with pre-chilled pentane (5 x 2 mL). The solid was then transferred to a pre-chilled EPR tube. The cold well was then swapped for one that contained liquid nitrogen and the solid was allowed to equilibrate to 77 K. The tube was then quickly passed out of the glovebox into a dewar containing liquid nitrogen (**Figure D.25**). For oxidation of $(\text{Cp}^*)\text{Co}(\text{exo-}\eta^4\text{-C}_5\text{Me}_5\text{D})$ with HBAr^{F}_4 , the same procedure as above was used except now $(\text{Cp}^*)\text{Co}(\text{exo-}\eta^4\text{-C}_5\text{Me}_5\text{D})$ was used (**Figure D.25**).

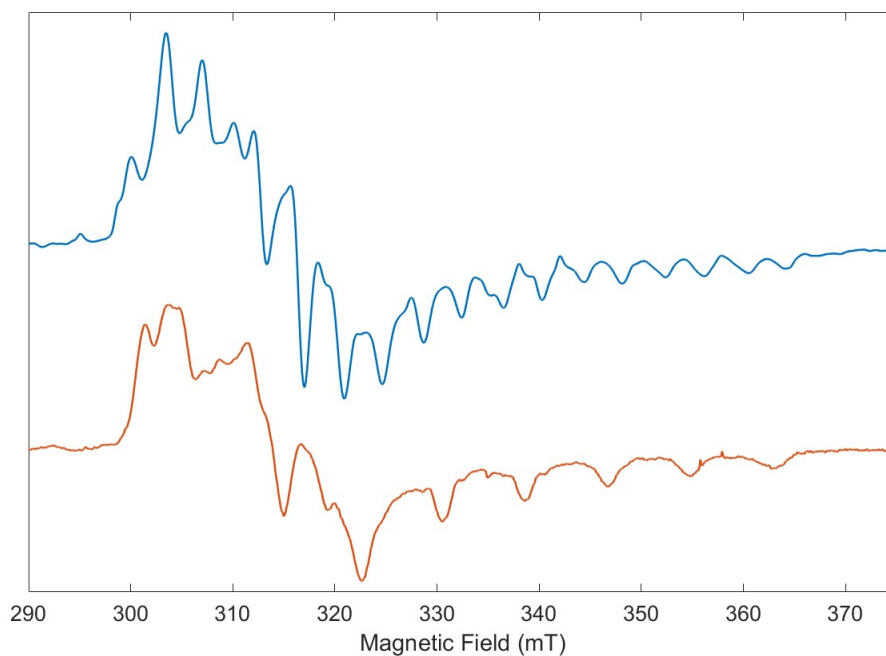


Figure D.25: A comparison of the 77 K, X-band EPR spectra of solid samples of $[(\text{Cp}^*)\text{Co}(\text{exo-}\eta^4\text{-C}_5\text{Me}_5\text{H})][\text{BArF}]$ (blue) and $[(\text{Cp}^*)\text{Co}(\text{exo-}\eta^4\text{-C}_5\text{Me}_5\text{D})][\text{BArF}]$ (orange).

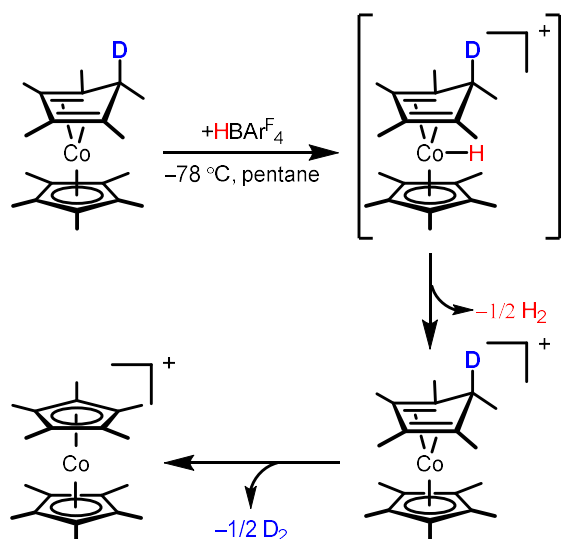


Figure D.26: A depiction of our mechanistic proposal to account for observations upon the reaction of $(\text{Cp}^*)\text{Co}(\text{exo-C}_5\text{Me}_5\text{D})$ with HBAr^{F_4} . Efforts to identify the bracketed $\text{Co}^{\text{III}}\text{-H}$ intermediate at low temperature using NMR spectroscopy always resulted in the sole observation of the terminal oxidation product Cp^*_2Co^+ . However, we believe that formation of this species is reasonable on the basis of DFT which suggests that the most favorable site of protonation (*endo*, *exo*, or Co) is the Co (see Table S5). This proposal is supported by the known protonation of $18e^-$ Cp-Co^I species to form hydrides.^{35,36} DFT calculations suggest that this Co-H bond is homolytically weak ($\text{BDFE}_{\text{Co-H}} = 51 \text{ kcal mol}^{-1}$). Thus it should be able to react with itself or with the starting material to release H₂ or HD bimolecularly and form the experimentally observed product, $[(\text{Cp}^*)\text{Co}(\text{exo-C}_5\text{Me}_5\text{D})\text{Co}]^+$. It is quite possible that the precipitated solid is contaminated with the $\text{Co}^{\text{III}}\text{-H}$ species, which we would also expect to be fairly insoluble under the reaction conditions, but due to the expected diamagnetic nature of this species we would not observe it by EPR techniques.

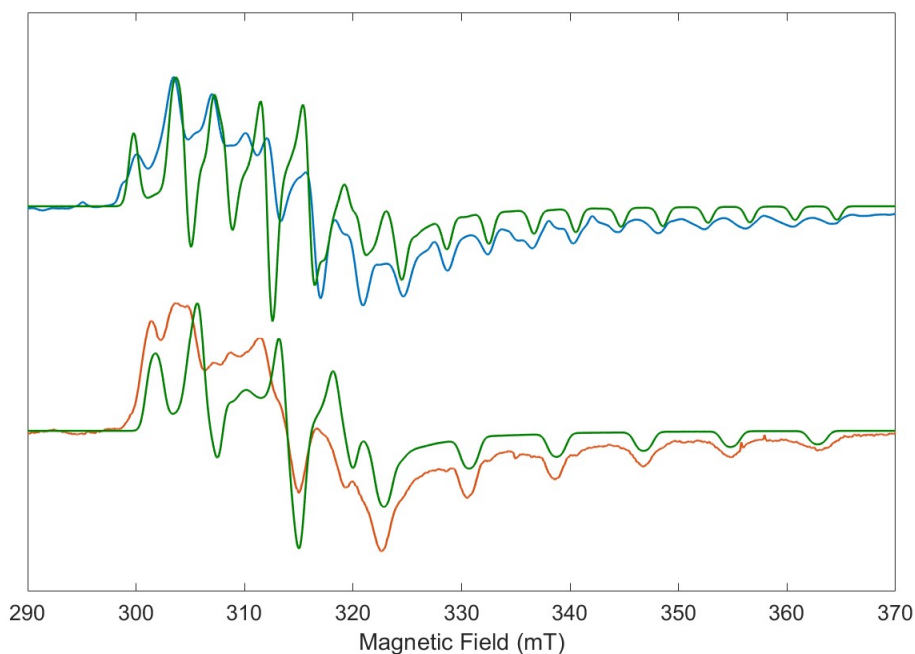


Figure D.27: A comparison of the data to the simulation (green) for the 77 K, X-band EPR spectra of solid samples of $[(\text{Cp}^*)\text{Co}(\text{exo-}\eta^4\text{-C}_5\text{Me}_5\text{H})][\text{BARF}]$ (blue) and $[(\text{Cp}^*)\text{Co}(\text{exo-}\eta^4\text{-C}_5\text{Me}_5\text{D})][\text{BARF}]$ (orange). Simulation parameters are the same in both cases (**Table D.1**

Table) except for $A(^1\text{H})$ being scaled down by the ratio of the gyromagnetic ratio for proton:deuterium (~ 6.5) in the simulation for $[(\text{Cp}^*)\text{Co}(\text{exo-}\eta^4\text{-C}_5\text{Me}_5\text{D})][\text{BARF}]$ (bottom). We believe that the small deviation of the observed EPR spectra from the simulations can be accounted for by the fact that there is likely a significant difference in hydrogen bonding with the $[\text{BARF}_4]^-$ counteranion as compared to the $[\text{OTf}]^-$ counteranion for which the simulation parameters were derived using pulse EPR.

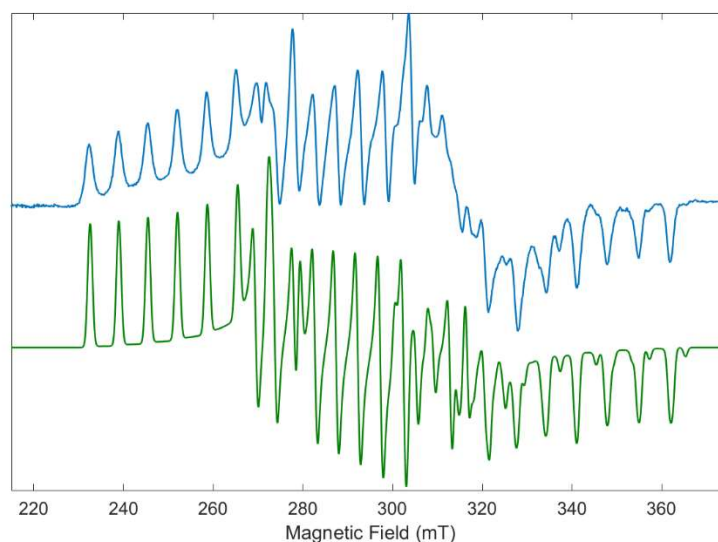


Figure D.28: X-Band CW EPR spectrum (blue) at 77 K in the solid state of the precipitate from the reaction of trifluoromethanesulfonic acid with Cp^*Co at -78°C in toluene.²¹ Simulation (green) of this data using the parameters from **Table D.1**

Table with a weight of 1.0 on the species measured at 6 K (endo) and a weight of 0.1 on the species measured at 10 K (exo).

D.7 Electrochemistry

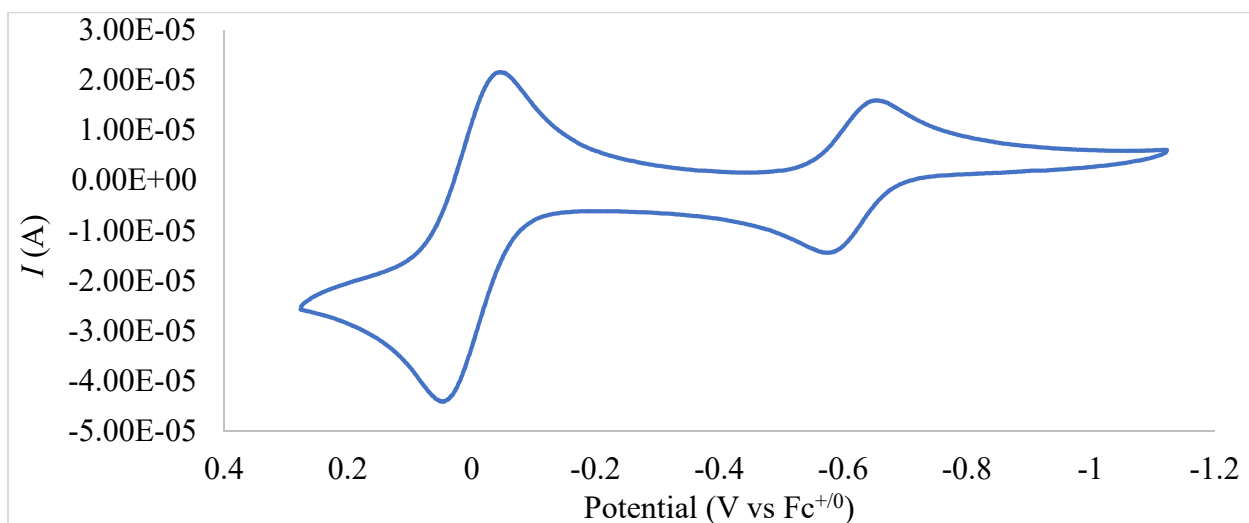


Figure D.29: Cyclic voltammogram of $(\text{Cp}^*)\text{Co}(\eta^4\text{-C}_5\text{Me}_6)$ at room temperature in an acetonitrile solution of 200 mM $[\text{TBA}][\text{PF}_6]$ with ferrocene added as an internal reference. From this a potential of -0.61 V is determined for the $[(\text{Cp}^*)\text{Co}(\eta^4\text{-C}_5\text{Me}_6)]^{0/+}$ couple. This potential is shifted by $\sim 0.05\text{ V}$ from that previously reported in DCM (-0.21 V vs SCE in

DCM and -0.16 V vs SCE in DME.³⁷ This small shift is attributed to going to the more coordinating acetonitrile solvent.

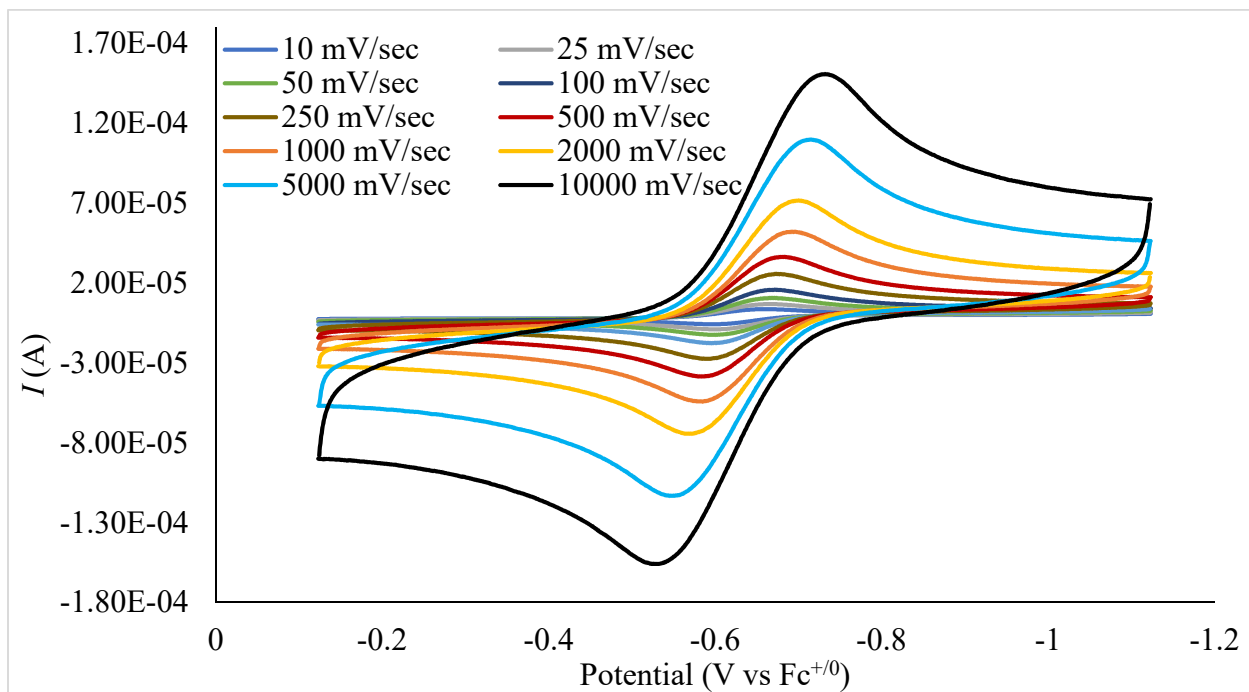


Figure D.30: Scan rate dependence of the $[(\text{Cp}^*)\text{Co}(\eta^4\text{-C}_5\text{Me}_6)]^{+/0}$ at room temperature in an acetonitrile solution of 200 mM $[\text{TBA}][\text{PF}_6]$. This demonstrates the high reversibility of this couple in contrast to what is observed with $(\text{Cp}^*)\text{Co}(\text{exo-}\eta^4\text{-C}_5\text{Me}_5\text{H})$

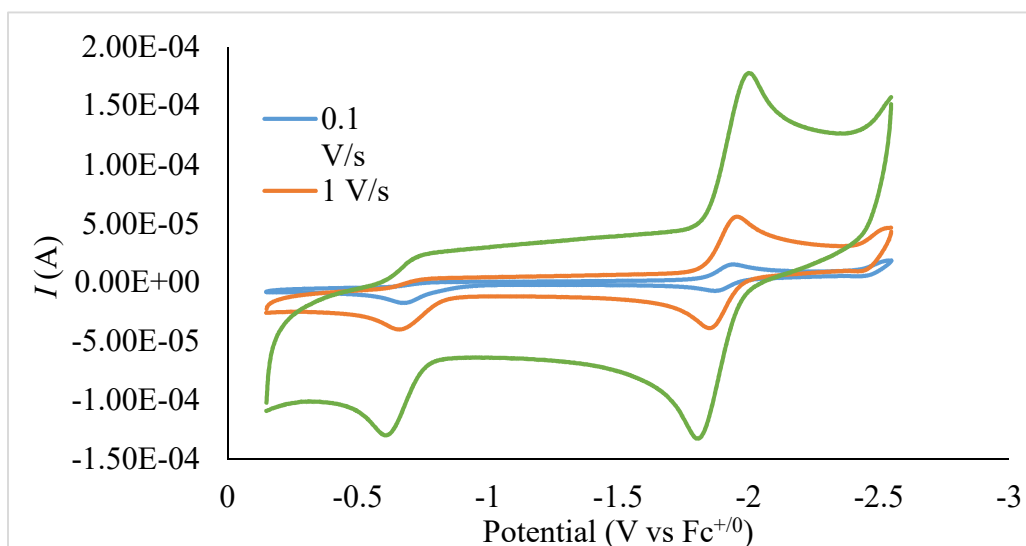
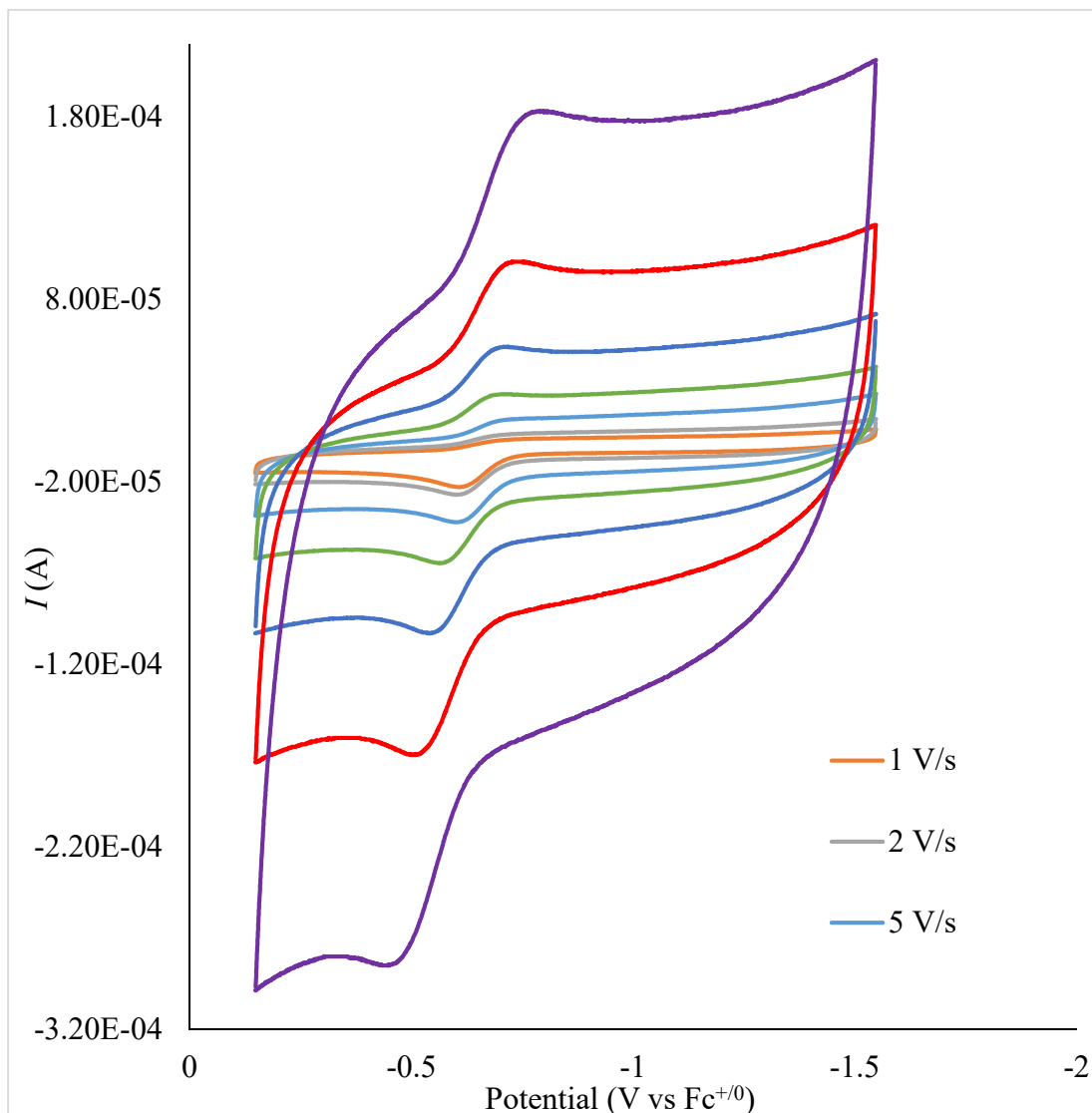


Figure D.31: Cyclic voltammograms of $(\text{Cp}^*)\text{Co}(\text{exo-}\eta^4\text{-C}_5\text{Me}_5\text{H})$ at room temperature at different scan rates in a butyronitrile solution of 0.4 M $[\text{TBA}][\text{PF}_6]$. The quasi-reversible

oxidation event at ~ -0.6 V corresponds to the $(\text{Cp}^*)\text{Co}(\text{exo-}\eta^4\text{-C}_5\text{Me}_5\text{H})^{0/+}$ couple while the highly reversible redox couple at ~ -1.9 V corresponds to the known $\text{Cp}^*_2\text{Co}^{0/+}$ couple observed due to decomposition of $[(\text{Cp}^*)\text{Co}(\text{exo-}\eta^4\text{-C}_5\text{Me}_5\text{H})]^+$ to form $[\text{Cp}^*_2\text{Co}]^+$. There is



the onset of another apparently irreversible reduction event apparent at even more negative potentials. Although this was not explored thoroughly it is in agreement with reports on $\text{Cp}(\eta^4\text{-C}_5\text{H}_5\text{R})\text{Co}$ complexes ($\text{R} = \text{alkyl or H}$) which were found to undergo an irreversible reduction at negative potentials.³⁸

Figure D.32: Cyclic voltammograms of $(\text{Cp}^*)\text{Co}(\text{exo-}\eta^4\text{-C}_5\text{Me}_5\text{H})$ at room temperature at different scan rates in a butyronitrile solution of 0.4 M $[\text{TBA}][\text{PF}_6]$. These demonstrate the increasing reversibility of the couple at extremely high scan rates (maximum $i_c/i_a \sim 0.62$). From the highest scan rate we are able to determine an oxidation potential for $(\text{Cp}^*)\text{Co}(\text{exo-}\eta^4\text{-C}_5\text{Me}_5\text{H})$ of -0.62 V in good agreement with that observed for $(\text{Cp}^*)\text{Co}(\eta^4\text{-C}_5\text{Me}_6)$.

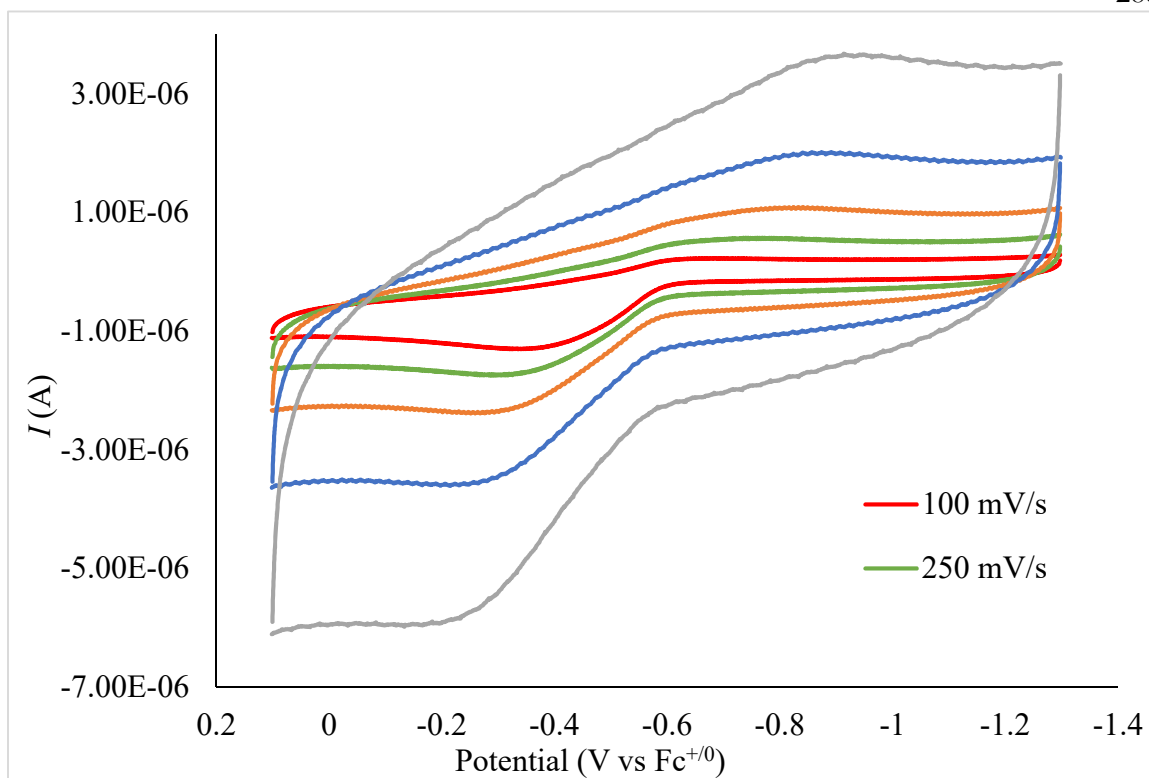


Figure D.33: Cyclic voltammograms of $(\text{Cp}^*)\text{Co}(\text{exo-}\eta^4\text{-C}_5\text{Me}_5\text{H})$ at $-78\text{ }^\circ\text{C}$ at different scan rates in a butyronitrile solution of 0.4 M $[\text{TBA}][\text{PF}_6]$. We can see that a degree of reversibility is achieved at lower scan rates than are necessary at room temperature. A comparison is shown in Figure S15. Attempts to go to the higher scan rates that were used at room temperature were not successful likely due to the increased resistivity at low temperature.

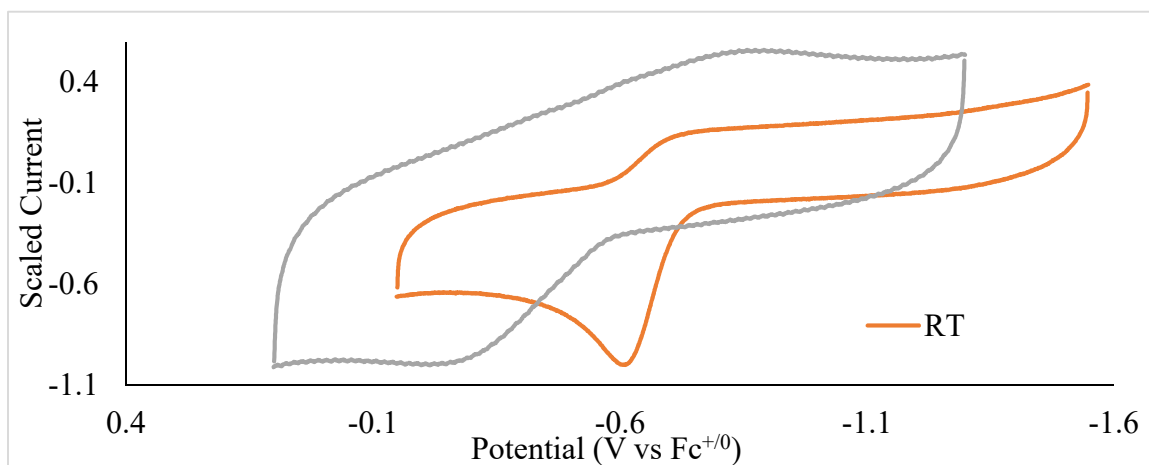


Figure D.34: Comparison of cyclic voltammograms taken at room temperature ($\sim 22\text{ }^\circ\text{C}$) and at $-78\text{ }^\circ\text{C}$. Both voltammograms are taken at a scan rate of 1 V/s with a concentration of analyte of 1 mM and 0.4 M $[\text{TBA}][\text{PF}_6]$ in butyronitrile. This demonstrates that cooling

the cell leads to a significant enhancement of reversibility at a particular scan rate. In order to facilitate the comparison each of the currents have been scaled by dividing them by the absolute value of the peak cathodic current. It is apparent here that the redox couple appears to drift to a slightly more positive potential of -0.56 V when measured at -78 °C. This drift in potential is not uncommon and only represents a $\Delta\text{BDFE} = 23.06 \times 0.05 = 1.4$ kcal mol $^{-1}$. We have used the potential measured at room temperature in our thermodynamic calculations in the main text as that represents the standard state.

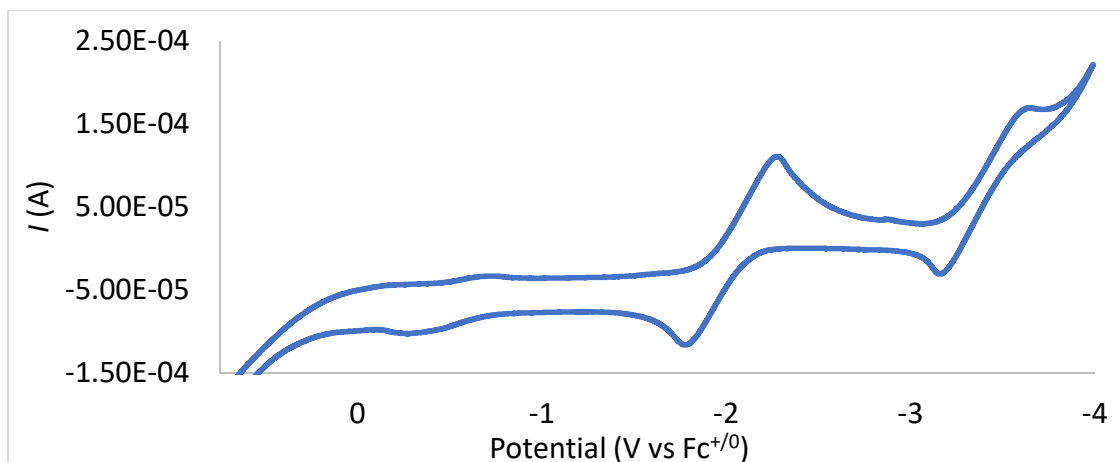


Figure D.35: Cyclic voltammograms of Cp^*_2Co at room temperature in 0.1 M [TBA][PF $_6$] dissolved in THF. The spectrum is referenced to the Cp^*_2Co reduction potential in MeCN of -1.91 V as a reference. After scanning through the reduction of Cp^*_2Co you can then observe the irreversible feature at ~ -0.6 V associated with $\text{Cp}^*(\eta^4\text{-C}_5\text{Me}_5\text{H})\text{Co}^{0/+}$. This suggests that there is a small amount of available proton source, likely water.

D.8 X-ray Crystallography

Table D.2: Crystallographic details for $(\text{Cp}^*)\text{Co}(\text{exo-}\eta^4\text{-C}_5\text{Me}_5\text{H})$ and $(\text{Cp}^*)\text{Co}(\eta^4\text{-C}_5\text{Me}_6)$.

Compound	$(\text{Cp}^*)\text{Co}(\text{exo-}\eta^4\text{-C}_5\text{Me}_5\text{H})$	$\text{Cp}^*(\text{C}_5\text{Me}_6)\text{Co}$
Chemical Formula	$\text{C}_{20}\text{H}_{31}\text{Co}$	$\text{C}_{21}\text{H}_{33}\text{Co}$
Formula Weight	330.38	344.43
Crystal System	Monoclinic	Monoclinic
Space Group	$\text{P2}_1/\text{n}$	$\text{P2}_1/\text{c}$
a [Å]	8.0700(6)	12.8973(5)

b [Å]	8.4605(6)	9.6767(4)
c [Å]	12.8684(10)	15.1146(6)
α [°]	90	90
β [°]	93.611(2)	92.956(2)
γ [°]	90	90
V [Å ³]	876.86(11)	1883.84(13)
Z	2	4
D _{calcd} [g cm ⁻³]	1.251	1.214
F ₀₀₀	356.0	984.0
μ [mm ⁻¹]	0.971	0.93
Temperature [K]	100(2)	100(2)
Wavelength [Å]	0.71073	0.71073
Measured Reflections	38760	117581
Unique Reflections	5620	8739
Data/Restraints/Parameter	5620/0/115	8739/0/210
s		
R(F) (I>2 σ (I))	0.0382	0.0471
wR(F ²) (all)	0.0838	0.0897
GOOF	1.016	1.045

D.9 IR Spectroscopy

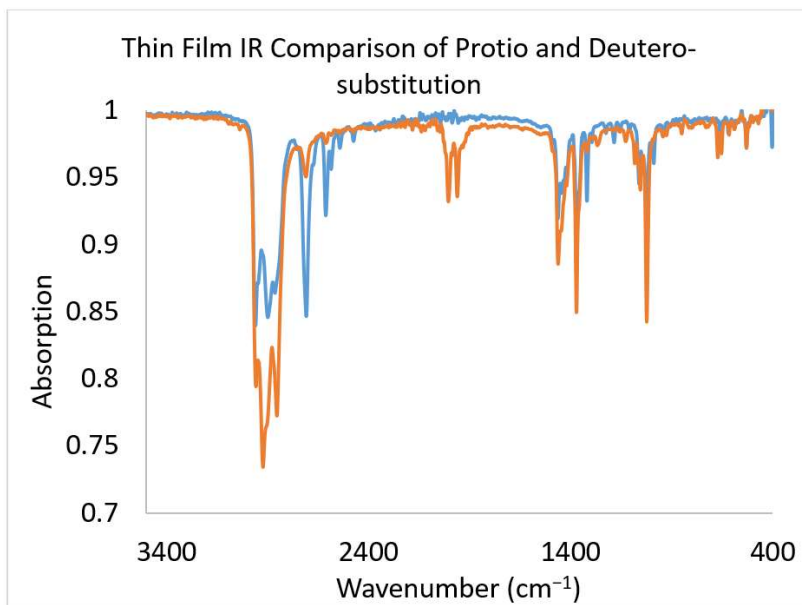


Figure D.36: Thin film IR spectra of $(\text{Cp}^*)\text{Co}(\text{exo-}\eta^4\text{-C}_5\text{Me}_5\text{H})$ (blue) and $(\text{Cp}^*)\text{Co}(\text{exo-}\eta^4\text{-C}_5\text{Me}_5\text{D})$ (orange). C–H vibrations at 2708 cm^{-1} and 2612 cm^{-1} shift to 2005 cm^{-1} and 1962 cm^{-1} . The predicted shift for deuterium substitution based on a simple harmonic oscillator model would be to 1987 cm^{-1} and 1917 cm^{-1} .

It is unclear why there are two stretches visible for this C–H/D mode. It is clear from solution NMR studies that these molecules consist of only one regioisomer (*exo* with no *endo*-contamination) but this phenomenon persists in the solution IR (Figure S37). Similar behavior was observed for $(\text{Cp})\text{Co}(\eta^4\text{-C}_5\text{H}_6)$ and $(\text{Cp})\text{Co}(\text{exo-}\eta^4\text{-C}_5\text{H}_5\text{D})$ by Wilkinson and no regioisomerism is possible in that molecule.³⁹ We have not found other examples of Cp–H or Cp*–H species in the literature that have been characterized by IR spectroscopy. We suggest that the different stretches arise from conformational isomers relating to the eclipsed or staggered nature of the ring that are causing the different stretching frequencies. This has been observed before for Cp* species of M–H.⁴⁰

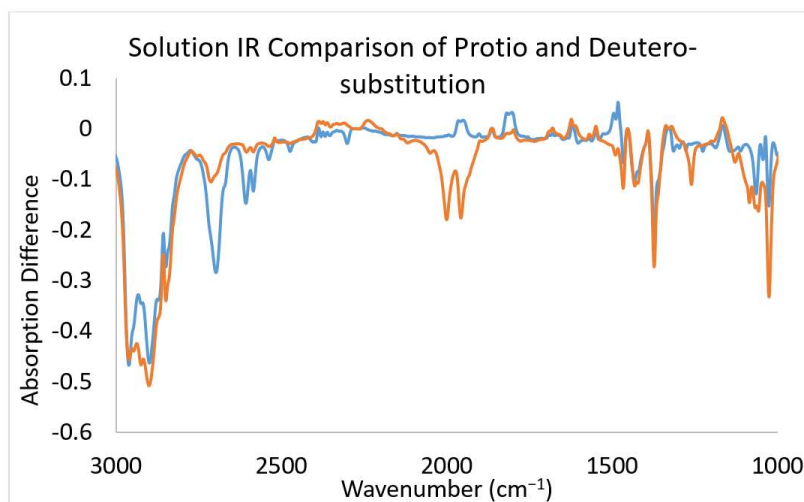


Figure D.37: Solution state IR spectra of $(\text{Cp}^*)\text{Co}(\text{exo-}\eta^4\text{-C}_5\text{Me}_5\text{H})$ (blue) and $(\text{Cp}^*)\text{Co}(\text{exo-}\eta^4\text{-C}_5\text{Me}_5\text{D})$ (orange) in C_6D_6 . This spectra demonstrates the same behavior as the thin film IR does demonstrating that the observed behavior is not only a solid state phenomenon.

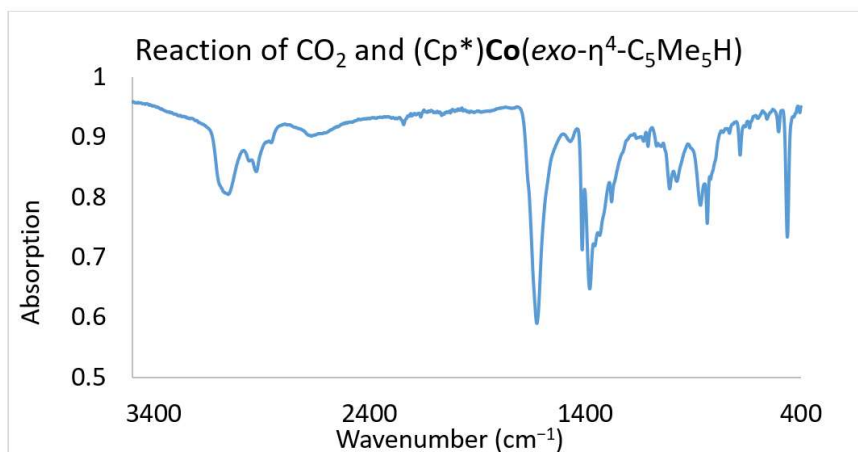


Figure D.38: Thin film IR spectrum of the reaction between $(\text{Cp}^*)\text{Co}(\text{exo-}\eta^4\text{-C}_5\text{Me}_5\text{H})$ and CO_2 demonstrating the formation of $[\text{Cp}^*_2\text{Co}][\text{HCO}_2]$. The features demonstrated here are similar to those previously characterized for tetramethylammonium formate.⁴¹ In particular the unusually low C–H stretch (2666 cm^{-1}) and the C=O (1626 cm^{-1}) stretch are diagnostic for this species.

D.10 Thermochemistry

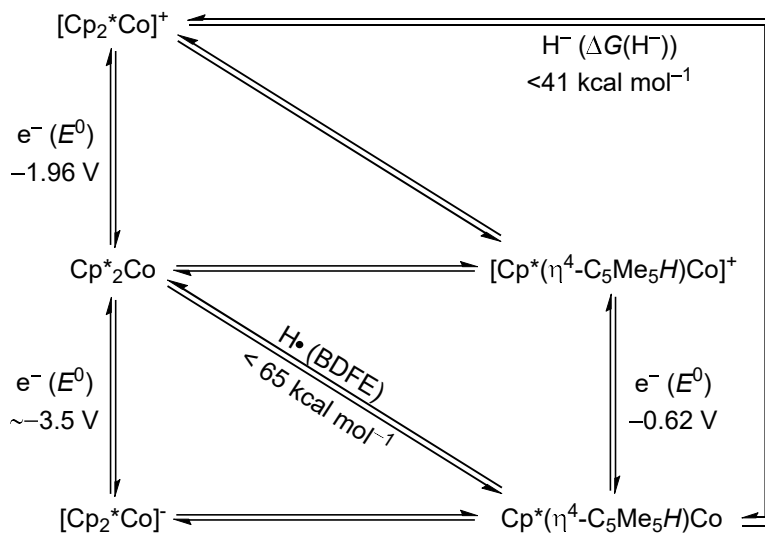


Figure D.39: Measured thermochemical parameters in acetonitrile. Potentials in V vs $\text{Fc}^{+/0}$.

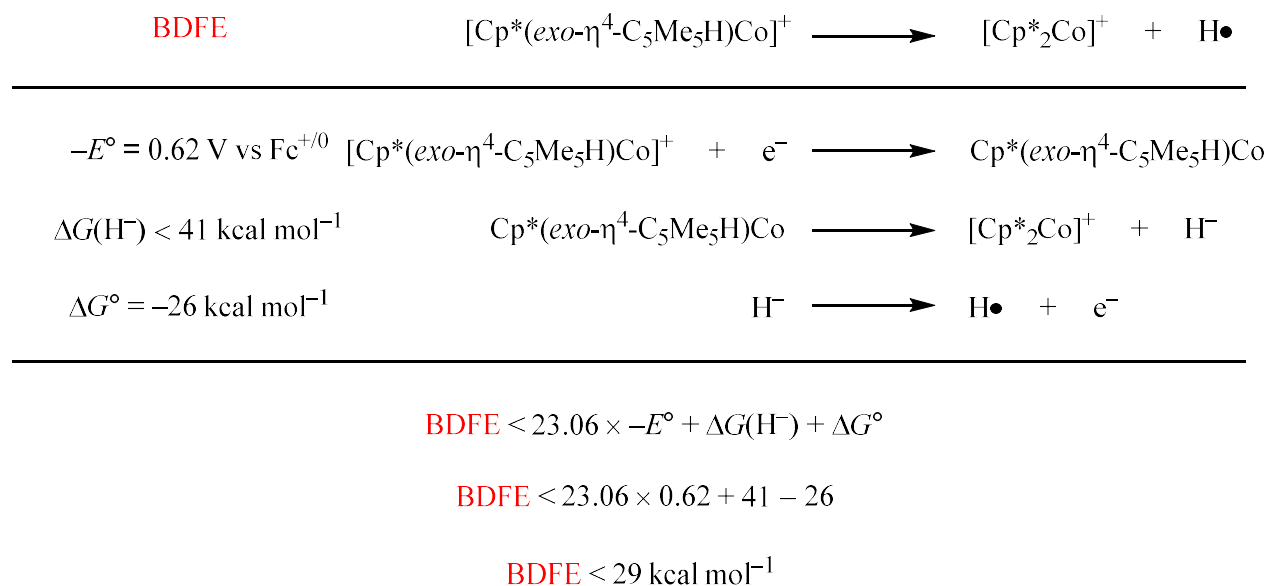
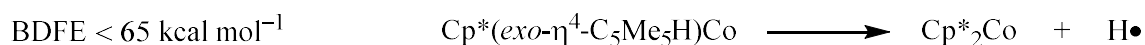
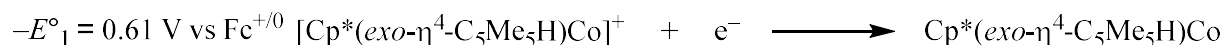


Figure D.40: Describes the process of determining the C–H BDFE in $[(\text{Cp}^*)\text{Co}(\text{exo-}\eta^4\text{-C}_5\text{Me}_5\text{H})]^+$ using the measured hydricity of $(\text{Cp}^*)\text{Co}(\text{exo-}\eta^4\text{-C}_5\text{Me}_5\text{H})$ and the redox potential of $(\text{Cp}^*)\text{Co}(\text{exo-}\eta^4\text{-C}_5\text{Me}_5\text{H})$. There is some disagreement over the hydricity of $[\text{HPt}(\text{dmpe})_2][\text{PF}_6]$ in the literature so we have chosen to use the more conservative value of $\Delta G(\text{H}^-) = 41 \text{ kcal mol}^{-1}$.^{42,43}



$$\text{BDFE} < 23.06 \times -E^\circ_1 + \text{BDFE} + 23.06 \times E^\circ_2$$

$$\text{BDFE} < 23.06 \times 0.61 + 65 + 23.06 \times -1.96$$

$$\text{BDFE} < 34 \text{ kcal mol}^{-1}$$

Figure D.41: Describes the process of determining the C–H BDFE in $[(\text{Cp}^*)\text{Co}(\text{exo-}\eta^4\text{-C}_5\text{Me}_5\text{H})]^+$ using the measured BDFE C–H of $(\text{Cp}^*)\text{Co}(\text{exo-}\eta^4\text{-C}_5\text{Me}_5\text{H})$ and the redox potential of $(\text{Cp}^*)\text{Co}(\text{exo-}\eta^4\text{-C}_5\text{Me}_5\text{H})$ and Cp^*_2Co .

D.11 DFT Calculations

D.11.1 Comparison of Isomer Stability

Table D.3: Thermochemistry for the structures optimized with different functionals. In the B3LYP, TPSSH, and BP86 structures the Co–H has a small negative frequency which could affect the relative energies but given the magnitude likely would not affect the relative ordering.

Functional for Optimization	Species	Spin State	Absolute Energy (Hartrees)	Relative Energy (kcal mol ⁻¹)
TPSSH	Co–H	<i>S</i> = 1/2	-2162.647	18.42
TPSSH	<i>endo</i> -C–H	<i>S</i> = 1/2	-2162.676	0
TPSSH	<i>exo</i> -C–H	<i>S</i> = 1/2	-2162.673	1.82
BP86	Co–H	<i>S</i> = 1/2	-2162.773	16.93
BP86	<i>endo</i> -C–H	<i>S</i> = 1/2	-2162.800	0
BP86	<i>exo</i> -C–H	<i>S</i> = 1/2	-2162.796	2.10
B3LYP	Co–H	<i>S</i> = 1/2	-2161.879	20.91
B3LYP	<i>endo</i> -C–H	<i>S</i> = 1/2	-2161.913	0
B3LYP	<i>exo</i> -C–H	<i>S</i> = 1/2	-2161.911	1.02
TPSS	Co–H	<i>S</i> = 1/2	-2162.785	15.72
TPSS	Co–H	<i>S</i> = 3/2	-2162.725	46.73

TPSS	<i>endo</i> -C–H	$S = 1/2$	-2162.810	0
TPSS	<i>endo</i> -C–H	$S = 3/2$	-2162.746	33.61
TPSS	<i>exo</i> -C–H	$S = 1/2$	-2162.809	0.51
TPSS	<i>exo</i> -C–H	$S = 3/2$	-2162.744	34.92

Table D.4: Thermochemistry for the different potential isomers of neutral, H-functionalized Co species. Note that both of the Co–H structures have small imaginary frequencies ($\sim 80 \text{ cm}^{-1}$) indicating that they may be transition states representing transfer of the hydride between the two rings but they have been included here for completeness.

Species	Spin State	Absolute Energy (Hartrees)	Relative Energy (kcal mol^{-1})
(Cp*)Co(<i>exo</i> - η^4 -C ₅ Me ₅ H)	$S = 0$	-2162.995	0
(Cp*)Co(<i>exo</i> - η^4 -C ₅ Me ₅ H)	$S = 1$	-2162.954	26.18
(Cp*)Co(<i>endo</i> - η^4 -C ₅ Me ₅ H)	$S = 0$	-2162.995	0.22
(Cp*)Co(<i>endo</i> - η^4 -C ₅ Me ₅ H)	$S = 1$	-2162.955	25.29
Cp* ₂ Co–H	$S = 0$	-2162.940	34.44
Cp* ₂ Co–H	$S = 1$	-2162.940	34.46

Table D.5: Thermochemistry for the different potential isomers resulting from the protonation of (Cp*)Co(*exo*- η^4 -C₅Me₅H).

Species	Spin State	Absolute Energy (Hartrees)	Relative Energy (kcal mol^{-1})
[(Cp*)Co(<i>exo</i> - η^4 -C ₅ Me ₅ H)–H] ⁺	$S = 0$	-2163.381	0
[(Cp*)Co(<i>exo</i> - η^4 -C ₅ Me ₅ H)–H] ⁺	$S = 1$	-2163.354	17.34
[(<i>exo</i> - η^4 -C ₅ Me ₅ H)Co(<i>endo</i> - η^4 -C ₅ Me ₅ H)] ⁺	$S = 0$	-2163.358	14.38
[(<i>exo</i> - η^4 -C ₅ Me ₅ H)Co(<i>endo</i> - η^4 -C ₅ Me ₅ H)] ⁺	$S = 1$	-2163.342	24.60
[(<i>exo</i> - η^4 -C ₅ Me ₅ H)Co(<i>exo</i> - η^4 -C ₅ Me ₅ H)] ⁺	$S = 0$	-2163.357	15.18
[(<i>exo</i> - η^4 -C ₅ Me ₅ H)Co(<i>exo</i> - η^4 -C ₅ Me ₅ H)] ⁺	$S = 1$	-2163.340	26.12

D.11.2 Determination of Thermochemical Parameters via DFT

To determine the DFT-predicted gas-phase BDFE's (Main Text Figure 1) we followed a protocol that has been published previously.⁴⁴ In this protocol, the ΔG for a series

of small molecules with known gas-phase BDFE's are calculated (**Eq D.8**). A correlation between ΔG and the BDFE is then established (**Eq D.9**). This allows for accurate gas-phase BDFE's to be calculated. Because of the large differences between how acetonitrile solvation effects X–H bond strengths⁴⁵ no efforts have been made to calculate solution state BDFE values but it can be anticipated that they would be stronger (5-10 kcal mol⁻¹) than those in the gas phase with larger errors being encountered for more acidic species in which H-bonding plays a more noticeable role.

$$\text{Eq D.8) } \Delta G = (G(X\bullet) + G(H\bullet)) - G(X-H)$$

$$\text{Eq D.9) } \text{BDFE} = 0.996 \times \Delta G + 4.376$$

To determine redox potentials, Ferrocene and ferrocenium were optimized using the same input parameters used for all of the thermochemical calculations. By creating a square scheme and taking the known Fc⁺⁰ couple as 0 V we were then able to determine the DFT-predicted redox potential. The energies used in this case were after the solvation correction as described in the general methods.

To determine the gas-phase pK_a we again used a square scheme by calculating the ΔG for a conjugate acid/base pair with a known pK_a in acetonitrile. All calculated ΔG values could then be referenced using this to generate an absolute pK_a value. We chose aniline and anilinium as our pair due to its catalytic relevance. The energies used in this case were after the solvation correction as described in the general methods.

To determine the solution-phase hydricity we again used a square scheme by calculating the ΔG for a hydride donor/acceptor pair with a known hydricity in acetonitrile.

In this case we chose CO₂ and formate given their relevance to this report. Based on the ΔG of this reaction, we then determined the hydricity of the desired compound. The energies used in this case were after the solvation correction as described in the general methods.

Table D.6: Gas phase Gibbs Free Energies for species necessary for determining the thermochemical parameters.

Species	Energy (Hartrees)
Cp* ₂ Co ⁻ (<i>S</i> = 0)	-2162.408
Cp* ₂ Co ⁻ (<i>S</i> = 1)	-2162.384
Cp* ₂ Co	-2162.409
Cp* ₂ Co ⁺	-2162.258
Cp*(η^4 -C ₅ Me ₄ CH ₂)Co	-2161.81
Cp ₂ Fe	-1650.623
Cp ₂ Fe ⁺	-1650.37969
Aniline	-287.363
Anilinium	-287.714
CO ₂	-188.484
Formate	-189.069
H•	-319.972
Cp* ₂ Ni ⁺	-2287.758
Cp* ₂ Ni ²⁺	-2287.426
[(Cp*)Ni(<i>exo</i> - η^4 -C ₅ Me ₅ H)] ⁺	-2288.343
[(Cp*)Ni(<i>exo</i> - η^4 -C ₅ Me ₅ H)] ²⁺	-2287.977

Table D.7: Particular thermochemical properties of interest.

Species	BDFE (kcal mol ⁻¹)	Oxidation Potential (V vs Fc ⁺⁰)	Hydricity (kcal mol ⁻¹)	p <i>K</i> _a
[Cp* ₂ Co] ⁻	N/A	-3.28	N/A	N/A
Cp* ₂ Co	62.4	-2.16	N/A	N/A
(Cp*)Co(<i>exo</i> - η^4 -C ₅ Me ₅ H)	52.6	-0.88	37	49.8
(Cp*)Co(<i>endo</i> - η^4 -C ₅ Me ₅ H)	52.3	-0.98	37	49.6
(Cp*) ₂ Co(H)	7.3	-1.63	4	25.2
[(Cp*)Co(<i>exo</i> - η^4 -C ₅ Me ₅ H)] ⁺	22.1	N/A	N/A	9.3

$[(\text{Cp}^*)\text{Co}(\text{endo-}\eta^4\text{-C}_5\text{Me}_5\text{H})]^+$	24.2	N/A	N/A	10.8
$[(\text{Cp}^*)_2\text{Co}(\text{H})]^+$	18.3	N/A	N/A	-2.6
$[(\text{Cp}^*)\text{Ni}(\text{exo-}\eta^4\text{-C}_5\text{Me}_5\text{H})]^+$	51.4	N/A	N/A	N/A
$[(\text{Cp}^*)\text{Ni}(\text{exo-}\eta^4\text{-C}_5\text{Me}_5\text{H})]^{2+}$	30.1	N/A	N/A	N/A

D.11.3 EPR Predictions by DFT

Table D.8: Effect of functional on structure optimization. EPR parameters calculated for structures optimized with different functionals but the same basis sets (def2-SVP(C and H)/def2-TZVP(Co)). Each structure was then used as the input for the calculation of EPR parameters using the same exact conditions (TPSSH/def2-TZVP (C and H)/CP(PPP) (Co)). More detail provided in the general methods section.

Functional for Optimization	Species	A _x	A _y	A _z	a _{iso}	T _x	T _y	T _z	ΔT
TPSSH	Co-H	-62.3	-70.9	-15.8	-49.7	-12.7	-21.2	33.9	55.1
TPSSH	<i>endo</i> -C-H	29.4	41.4	26.7	32.5	-3.1	8.9	-5.8	14.7
TPSSH	<i>exo</i> -C-H	110.5	117.0	111.6	113.1	-2.5	3.9	-1.41	6.5
BP86	Co-H	-62.5	-70.4	-15.8	-49.6	-13.0	-20.8	33.78	54.6
BP86	<i>endo</i> -C-H	27.7	39.3	25.2	30.8	-3.0	8.6	-5.59	14.2
BP86	<i>exo</i> -C-H	121.9	116.9	115.8	118.2	3.8	-1.3	-2.45	6.2
B3LYP	Co-H	-64.2	-72.0	-15.4	-50.5	-13.7	-21.5	35.16	56.5
B3LYP	<i>endo</i> -C-H	25.4	28.3	40.4	31.4	-5.9	-3.1	9.04	15.0
B3LYP	<i>exo</i> -C-H	100.8	95.5	94.6	97.0	3.9	-1.4	-2.42	6.3
TPSS	Co-H	-62.6	-70.5	-16.3	-49.8	-12.8	-20.7	33.50	54.2
TPSS	<i>endo</i> -C-H	28.6	40.3	26.0	31.6	-3.0	8.7	-5.67	14.4
TPSS	<i>exo</i> -C-H	120.1	114.9	113.8	116.3	3.9	-2.5	-1.37	6.4

Table D.9: Effect of functional on the calculation of EPR parameters. Structures were optimized using (TPSS/def2-SVP(C and H)/def2-TZVP(Co)). Each structure was then used

as the input for the calculation of EPR parameters using different functionals but otherwise the same conditions (def2-TZVP (C and H)/CP(PPP) (Co)).

Functional for EPR Calculation	Species	A_x	A_y	A_z	a_{iso}	T_x	T_y	T_z	ΔT
TPSSH	Co-H	-62.6	-70.5	-16.3	-49.8	-12.8	-20.7	33.5	54.2
TPSSH	<i>endo</i> -C-H	28.6	40.3	26.0	31.6	-3.0	8.7	-5.7	14.4
TPSSH	<i>exo</i> -C-H	120.1	114.9	113.8	116.3	3.9	-2.5	-1.4	6.4
BP86	Co-H	-49.2	-57.5	-8.8	-38.5	-10.7	-19.0	29.7	48.7
BP86	<i>endo</i> -C-H	30.3	40.1	26.9	32.4	-2.1	7.7	-5.5	13.2
BP86	<i>exo</i> -C-H	118.9	112.8	111.6	114.5	4.5	-1.6	-2.8	7.3
B3LYP	Co-H	-91.9	-99.9	-40.5	-77.4	-14.4	-22.5	36.9	59.4
B3LYP	<i>endo</i> -C-H	26.9	38.9	24.1	29.9	-3.1	8.9	-5.4	14.8
B3LYP	<i>exo</i> -C-H	99.9	107.3	101.6	102.8	-2.8	4.5	-1.7	7.4
TPSS	Co-H	-45.0	-53.0	-4.2	-34.1	-10.9	-18.9	29.9	48.8
TPSS	<i>endo</i> -C-H	30.8	41.2	27.8	33.3	-2.5	7.9	-5.5	13.5
TPSS	<i>exo</i> -C-H	128.2	123.0	121.8	124.4	3.9	-1.4	-2.5	6.4

We can see when we optimize the isomers with different functionals and then do a single point EPR prediction under the same conditions that the results are nearly identical (**Table D.8**). When we use different functionals for the single point calculation we see larger differences (**Table D.9**). However, the ΔT and the large disparity in the a_{iso} ($a_{iso} = (A_x + A_y + A_z)/3$) for the *endo*- and *exo*-isomer persist regardless. The performance of TPSSH in predicting the magnitude of a_{iso} was the best so it was selected for use at the higher level of theory (**Table D.10**).

In **Table D.10**, it can be seen that a_{iso} and ΔT are again similar. However, at this level of theory we now also capture that $|T_y|$ is larger than $|T_x|$ or $|T_z|$ in accordance with

experiment. The absolute signs of the individual T components are not relevant because we have not determined the absolute sign of the ^1H hyperfine tensors experimentally. Switching the sign of the hyperfine tensor would switch all of the signs of the components of T as well.

Table D.10: Higher level EPR calculations. Structures were optimized using (TPSS/def2-SVP(C and H)/def2-TZVP(Co)). Then a single point calculation was done with CP(PPP) on Co and EPR-III on C and H with grid 7.

Functional for EPR Calculation	Species	A_x	A_y	A_z	a_{iso}	T_x	T_y	T_z	ΔT
TPSSH	Co-H	-64.2	-72.0	-17.8	-51.3	-12.9	-17.7	33.6	51.3
TPSSH	endo-C-H	28.3	40.1	25.8	31.4	-3.1	8.7	-5.6	14.3
TPSSH	exo-C-H	116.3	122.6	117.4	118.8	-2.4	3.8	-1.3	5.1

D.12 References

- (1) Robbins, J. L.; Edelstein, N.; Spencer, B.; Smart, J. C. *J. Am. Chem. Soc.* **1982**, *104*, 1882–1893.
- (2) Koelle, U.; Khouzami, F. *Angew. Chem. Int. Ed.* **1980**, *19*, 640–641.
- (3) Del Castillo, T. J.; Thompson, N. B.; Peters, J. C. *J. Am. Chem. Soc.* **2016**, *138*, 5341–5350.
- (4) Manson, J. L.; Buschmann, W. E.; Miller, J. S. *Inorg. Chem.* **2001**, *40*, 1926–1935.
- (5) Cazelles, J.; Robert, A.; Meunier, B. *J. Org. Chem.* **2002**, *67*, 609–619.
- (6) Hyde, J. S.; Pasenkiewicz-Gierula, M.; Jesmanowicz, A.; Antholine, W. E. *Appl. Magn. Reson.* **1990**, *1*, 483–496.
- (7) Stoll, S.; Britt, R. D. *Phys. Chem. Chem. Phys.* **2009**, *11*, 6614–6625.
- (8) Sheldrick, G. M. *Acta Crystallogr., Sect. C: Struct. Chem.* **2015**, *71*, 3–8.

- (9) Dolomanov, O. V.; Bourhis, L. J.; Gildea, R. J.; Howard, J. a. K.; Puschmann, H. *J. Appl. Cryst.* **2009**, *42*, 339–341.
- (10) Neese, F. *Wiley Interdiscip. Rev.: Comput. Mol. Sci.* **2012**, *2*, 73–78.
- (11) Neese, F. *Wiley Interdiscip. Rev.: Comput. Mol. Sci.* **2018**, *8*, e1327.
- (12) Tao, J.; Perdew, J. P.; Staroverov, V. N.; Scuseria, G. E. *Phys. Rev. Lett.* **2003**, *91*, 146401–146404.
- (13) Weigend, F.; Ahlrichs, R. *Phys. Chem. Chem. Phys.* **2005**, *7*, 3297–3305.
- (14) Grimme, S.; Antony, J.; Ehrlich, S.; Krieg, H. *J. Chem. Phys.* **2010**, *132*, 154104–154119.
- (15) Becke, A. D. *Phys. Rev. A* **1988**, *38*, 3098–3100.
- (16) Perdew, J. P. *Phys. Rev. B* **1986**, *33*, 8822–8824.
- (17) Becke, A. D. *J. Chem. Phys.* **1993**, *98*, 5648–5652.
- (18) Lee, C.; Yang, W.; Parr, R. G. *Phys. Rev. B* **1988**, *37*, 785–789.
- (19) Staroverov, V. N.; Scuseria, G. E.; Tao, J.; Perdew, J. P. *J. Chem. Phys.* **2003**, *119*, 12129–12137.
- (20) Zhao, Y.; Truhlar, D. G. *J. Chem. Phys.* **2006**, *125*, 194101.
- (21) Chalkley, M. J.; Del Castillo, T. J.; Matson, B. D.; Roddy, J. P.; Peters, J. C. *ACS Cent. Sci.* **2017**, *3*, 217–223.
- (22) Neese, F. *Inorg. Chim. Acta* **2002**, *337*, 181–192.
- (23) Barone, V. *Recent Advances in Density Functional Methods*; Recent Advances in Computational Chemistry; WORLD SCIENTIFIC, 1995; Vol. Volume 1, pp 287–334.
- (24) Klamt, A.; Schüürmann, G. *J. Chem. Soc., Perkin Trans. 2* **1993**, *5*, 799–805.

- (25) Barone, V.; Cossi, M. *J. Phys. Chem. A* **1998**, *102*, 1995–2001.
- (26) Cossi, M.; Rega, N.; Scalmani, G.; Barone, V. *J. Comput. Chem.* **2003**, *24*, 669–681.
- (27) Ribeiro, R. F.; Marenich, A. V.; Cramer, C. J.; Truhlar, D. G. *J. Phys. Chem. B* **2011**, *115*, 14556–14562.
- (28) Wang, T.; Brudvig, G.; Batista, V. S. *J. Chem. Theory Comput.* **2010**, *6*, 755–760.
- (29) Wu, A.; Mader, E. A.; Datta, A.; Hrovat, D. A.; Borden, W. T.; Mayer, J. M. *J. Am. Chem. Soc.* **2009**, *131*, 11985–11997.
- (30) Ohki, Y.; Murata, A.; Imada, M.; Tatsumi, K. *Inorg. Chem.* **2009**, *48*, 4271–4273.
- (31) Bauer, J.; Braunschweig, H.; Hörl, C.; Radacki, K.; Wahler, J. *Chem. - Eur. J.* **2013**, *19*, 13396–13401.
- (32) Yoshida, Z.; [UNK]Osawa, E. *J. Am. Chem. Soc.* **1966**, *88*, 4019–4026.
- (33) Cerichelli, G.; Illuminati, G.; Ortaggi, G.; Maria Giuliani, A. *Journal of Organometallic Chemistry* **1977**, *127*, 357–370.
- (34) Chalkley, M. J.; Del Castillo, T. J.; Matson, B. D.; Peters, J. C. *J. Am. Chem. Soc.* **2018**, *140*, 6122–6129.
- (35) Werner, H.; Lippert, F.; Peters, K.; Schnering, H. G. V. *Chem. Ber.* **1992**, *125*, 347–352.
- (36) Fang, M.; Wiedner, E. S.; Dougherty, W. G.; Kassel, W. S.; Liu, T.; DuBois, D. L.; Bullock, R. M. *Organometallics* **2014**, *33*, 5820–5833.
- (37) Koelle, U. *Inorg. Chim. Acta* **1981**, *47*, 13–18.
- (38) Murr, N. E.; Laviron, E. *Can. J. Chem.* **1976**, *54*, 3350–3356.
- (39) Green, M. L. H.; Pratt, L.; Wilkinson, G. *J. Chem. Soc.* **1959**, *0*, 3753–3767.

- (40) Belkova, N. V.; Epstein, L. M.; Filippov, O. A.; Shubina, E. S. *Spectroscopic Properties of Inorganic and Organometallic Compounds*; 2012; pp 1–28.
- (41) Albert, B.; Jansen, M. Z. *Anorg. Allg. Chem.* **1995**, *621*, 1735–1740.
- (42) Berning, D. E.; Noll, B. C.; DuBois, D. L. *J. Am. Chem. Soc.* **1999**, *121*, 11432–11447.
- (43) Curtis, C. J.; Miedaner, A.; Ellis, W. W.; DuBois, D. L. *J. Am. Chem. Soc.* **2002**, *124*, 1918–1925.
- (44) Matson, B. D.; Peters, J. C. *ACS Cat.* **2018**, *8*, 1448–1455.
- (45) Warren, J. J.; Tronic, T. A.; Mayer, J. M. *Chem. Rev.* **2010**, *110*, 6961–7001.

Appendix E.
Supplementary Information for Chapter 6

E.1 Experimental Details

E.1.1 General Considerations

All manipulations were carried out using standard Schlenk or glovebox techniques under an N₂ atmosphere. Solvents were deoxygenated and dried by thoroughly sparging with N₂ followed by passage through an activated alumina column in a solvent purification system by SG Water, USA LLC. Non-halogenated solvents were tested with sodium benzophenone ketyl in tetrahydrofuran (THF) in order to confirm the absence of oxygen and water. Deuterated solvents were purchased from Cambridge Isotope Laboratories, Inc., degassed, and dried over activated 3-Å molecular sieves prior to use.

Cobaltocenium hexafluorophosphate, trifluoromethanesulfonimide, triflic acid and tetrabutylammonium hexafluorophosphate were all used as purchased. Ferrocenium triflate¹ and 4-lithiodimethylaniline² were synthesized as described previously.

E.1.2 Computational Details

All calculations were performed using the ORCA 4.0 program.^{3,4} In cases where crystal structures were available these coordinates were used as the input. The calculations were performed using the TPSS (meta-GGA)⁵ functional with def2-TZVPP^{6,7} on all atoms, Grimme-d3 dispersion correction,⁸ and SMD⁹ solvent modelling acetonitrile. That optimized structures represented true stationary points was checked by doing a single-point frequency calculations on the optimized structure and ensuring that there were no negative frequencies (≤ -50 cm⁻¹).

Reduction potentials were determined via exchange reactions with ferrocene/ferrocenium. The p*K*_a values were determined via exchange reactions with 2-

chloroanilinium/2-chloroaniline.¹⁰ The hydricity values were determined via exchange reactions with $\text{CO}_2/\text{HCO}_2^-$ (formate).¹¹ The bond dissociation free energies (BDFEs) were calculated directly using the free energy of $\text{H}\cdot$.

E.1.3 EPR Spectroscopy

X-band (9.4 GHz) CW EPR spectra were acquired using a Bruker EMX spectrometer equipped with a Super High-Q (SHQE) resonator using Bruker Win-EPR software (ver. 3.0). Spectra were acquired at 77 K using a vacuum-insulated quartz liquid nitrogen immersion dewar inserted into the EPR resonator.

E.1.4 X-ray Crystallography

XRD studies were carried out at the Beckman Institute Crystallography Facility on a Bruker Kappa Apex II diffractometer (Mo $K\alpha$ radiation). Structures were solved using SHELXS or SHELXT and refined against F^2 on all data by full-matrix least squares with SHELXL.¹² All of the solutions were performed in the Olex2 program.¹³ The crystals were mounted on a glass fiber under Paratone N oil.

E.1.5 Electrochemistry

A CHI instruments 600B electrochemical analyzer was used for data collection. Cyclic Voltammetry (CV), Linear Sweep Voltammetry (LSV) and Differential Pulse Voltammetry (DPV) experiments were carried out in a one-compartment three-electrode cell using a glassy carbon (GC) disk or a boron doped diamond (BDD) disk as the working electrode (3 mm diameter), a Pt wire as the counter electrode, and a Ag/AgOTf (5 mM)

reference electrode. Details for the CVs and LSVs are noted as they appear. DPVs were obtained with the following parameters: amplitude= 50 mV, step height=4 mV, pulse width= 0.05 s, pulse period= 0.5 s and sampling width= 0.0167 s. $E_{1/2}$ values for the reversible waves were obtained from the half potential between the oxidative and reductive peaks, and the one for irreversible processes are estimated according to the potential at the I_{\max} in DPV measurements. All the measurements were done applying IR compensation at 85% of the total resistance. All the reported potentials are referenced to the ferrocenium/ferrocene couple ($\text{Fc}^{+/0}$) used as an internal standard.

Controlled potential electrolyses (CPEs) were carried out in a gas-tight single compartment cell using a BDD plate (dimensions 1x2 cm) working electrode, a Ag/AgOTf (5 mM) reference electrode, and a GC plate (dimensions 1x5 cm) counter electrode. GC electrodes were pre-treated by polishing with 1, 0.3 and 0.05 μm alumina paste followed by rinsing with water and acetone. The BDD electrode was pre-treated according to a literature procedure.¹⁴ A fresh DME solution of 5 mM AgOTf was used in the reference electrode for each experiment.

In a typical CPE experiment, 7 ml of a 200 mM of [TBA][PF₆] DME solution was added to the gas-tight single compartment electrochemical cell. Then 120.5 mg of toluenesulfonic acid (100 mM) was added and a CV's were performed to ensure a stable HER background. Then, 40 μL of acetophenone (50 mM) was added. For the experiments using a catalyst, either 3.2 mg of [CpCp^NCo][OTf] or 2.3 mg of [CpCpCo][PF₆] were then

added to generate a 1 mM solution of the catalyst. The solution was then electrolyzed at -1.45 V vs $\text{Ag}^{+/0}$ with stirring throughout the CPE.

E.1.6 Analysis of Products from CPE

Upon completion of the CPE, the headspace was analyzed for H_2 via gas chromatography with a thermal conductivity detector (GC-TCD). A 100 μL Hamilton syringe was used to sample the headspace and for the injection into the GC-TCD. GC-TCD was performed in the Environmental Analysis Center (Caltech) using a HP 5890 Series II instrument with N_2 as carrier gas. Calibration curve was obtained by direct injection of hydrogen (**Figure E.35**).

The solution was then analyzed via electrochemical methods (CV and DPV) with the BDD plate working electrode and in some cases additionally with a glassy carbon disk electrode (3 mm diameter) prior to working up. The work up procedure consisted first of quenching the solution with an ethereal 2 M HCl solution. This step was found to be necessary to help remove the acid, not to pronate the pinacol product. After 5 min of stirring, the solvent was then removed under reduced pressure with a rotavap until dryness. Then, the organics products were extracted from the resulting solid by extraction with ether (3x10 ml) and filtration through a medium frit. The resulting filtrate was washed with an aqueous solution containing 100 mM Na_2CO_3 (20 ml). This aqueous phase was then further washed with ether (5x20 ml) and the organic phases were combined and evaporated until dryness. The resulting solid was extracted with 4 ml of ethyl acetate and filtered through filter paper. The resulting filtrate was used as analysis solution for detection and

quantification of products and remaining substrate. We verified that work-up via this procedure of a DME solution containing tosic acid, pinacol, ketone, and [TBA][PF₆] led to >95% recovery of the pinacol and ketone.

To the ethyl acetate solution was then added dodecane as an internal standard and the solution was then analyzed via gas chromatography coupled to either mass spectrometry (GC-MS, for products identification) or flame ionization detector (GC-FID, for product identification and quantification). The products were verified by analysis of the compounds (acetophenone, 1-phenylethanol, and 2,3-diphenyl-2,3-butanediol) obtained from commercial sources. Calibration curves (GC-FID, **Figure E.36-Figure E.37**) were obtained by comparing integration areas of known concentrations of the pure compounds with dodecane which was added as an internal standard. GC-MS was performed in an Agilent 5975C instrument in the Center for Catalysis and Chemical Synthesis (Caltech). GC-FID was performed using an Agilent 6850 instrument equipped with an Agilent HP-5 5% phenyl methyl siloxane capillary column (J&W Scientific).

E.1.7 IR Spectroscopy

Spectra were obtained using a Bruker Alpha Platinum ATR spectrometer with OPUS software in a glovebox under an N₂ atmosphere.

E.1.8 UV-Vis Spectroscopy

Measurements were taken on a Cary 50 UV/Visible spectrophotometer using a 1 cm quartz cell connected to a round-bottom flask and sealed with a Teflon stopcock.

Variable temperature measurements were collected with a Unisoku CoolSpek cryostat mounted within the Cary spectrophotometer. The 2-MeTHF:THF mixture was used to achieve low temperature solutions that are mixable as has been noted previously.¹⁵

E.1.9 NMR Spectroscopy

¹H and ¹³C chemical shifts are reported in ppm relative to tetramethylsilane, using residual solvent resonances as internal standards. Solution phase magnetic measurements were performed by the method of Evans.¹⁶

E.1.10 X-ray Photoelectron Spectroscopy

The BDD working electrode used in the CPE experiment was analyzed by X-ray photoelectron spectroscopy using a Kratos AXIS Ultra XPS instrument with a x-ray source consisting in monochromatic Al K alfa line at 1486.6 eV, with 0.2 eV resolution at full width half maximum. XPS results were analyzed using CasaXPS, Casa Software Ltd. The XPS instrument was calibrated to the Au 4f7/2 peak at 84 eV. Samples were calibrated to the adventitious carbon peak at 284.5 eV.

E.2 Synthetic Details

To synthesize (Cp)Co(η^4 -C₅H₅PhNMe₂) a suspension of [Cp₂Co][PF₆] (399 mg, 1.2 mmol) was stirred in THF (6 mL) at -78 °C. To this was added dropwise a room temperature, THF (10 mL) solution of 4-lithiodimethylaniline (152 mg, 1.2 mmol, 1 eq.) causing the reaction mixture to go orange. The suspension was allowed to stir at -78 °C for three hours and then allowed to warm slowly to room temperature at which point the

reaction became homogeneous. The reaction was then evaporated to dryness and the solid was extracted with pentane (3x 100 mL). The pentane was then filtered through an alumina plug and the solution was evaporated. (Yield: 148 mg, 40%)

^1H NMR (C_6D_6 , 400 MHz, 298 K): δ 6.90 (2H, “d”, $J = 8.5$ Hz), 6.58 (2H, “d”, $J = 8.5$ Hz), 5.13 (2 H, t, $^3J_{\text{H-H}} = 2$ Hz), 4.63 (5H, s, Cp), 3.94 (1H, t, $^3J_{\text{H-H}} = 2.4$ Hz), 2.93 (2H, dt $^3J_{\text{H-H}} = 2.4, 2.0$ Hz), 2.51 (6H, s, NMe_2). $^{13}\text{C}\{^1\text{H}\}$ NMR (CD_3CN 100 MHz, 298 K): δ 149.57, 135.96, 126.35, 113.05, 79.42, 75.01, 56.35, 45.99, 40.67. Elemental Analysis: (calculated) C: 69.90%, H: 6.52%, N: 4.53%; (observed) C: 70.33%, H: 6.85%, N: 4.51%.

To synthesize $(\text{Cp})\text{Co}(\text{Cp}^{\text{N}})$, $(\text{Cp})\text{Co}(\eta^4\text{-C}_5\text{H}_5\text{PhNMe}_2)$ (50 mg, 0.16 mmol) was dissolved in 5:1 methylcyclohexane:benzene. The solution was brought to reflux and went from orange to dark red. The solution was refluxed for 18 hours at which point the solution was cooled to room temperature. The solvent was removed under reduced pressure. The solid was extracted with pentane and filtered through celite. The solution was then concentrated by slow evaporation of pentane to yield crystalline $(\text{Cp})\text{Co}(\text{Cp}^{\text{N}})$. (Yield: 29.4 mg, 59%).

^1H NMR (C_6D_6 , 400 MHz, 298 K): δ 11.32 (2H), 4.99 (6H), -2.82 (2H), -41.49 (2H), -47.45 (2H), -50.12 (5H). μ_{eff} (C_6D_6 , 298 K): 1.75. Elemental Analysis: (calculated) C: 70.13%, H: 6.21%, N: 4.54%; (observed) C: 70.01%, H: 6.30%, N: 4.62%

To synthesize $[(\text{Cp})\text{Co}(\text{Cp}^{\text{N}})][\text{OTf}]$, $(\text{Cp})\text{Co}(\text{Cp}^{\text{N}})$ (43.7 mg, 0.147 mmol) was dissolved in THF (3 mL) and added dropwise to a stirring a THF suspension (3 mL) of ferrocenium triflate (50 mg, 0.149 mmol) was added dropwise. The solution was allowed

to stir for thirty minutes and then the solvent was evaporated. The solid was washed with pentane to remove ferrocene and then the solid was redissolved in THF. The solution was then layered with diethyl ether and cooled to $-35\text{ }^{\circ}\text{C}$. Overnight crystalline material of $[(\text{Cp})\text{Co}(\text{Cp}^{\text{N}})][\text{OTf}]$ was deposited. (Yield: 48 mg, 74 %)

^1H NMR (CD_3CN , 400 MHz, 298 K): δ 7.61 (2H, d, $^3J_{\text{H,H}} = 8.5$ Hz), 6.78 (2H, d, $^3J_{\text{H,H}} = 8.5$ Hz), 6.07 (2 H, s), 5.69 (2H, s), 5.39 (5H, s, Cp), 3.01 (6H, s, NMe_2). ^{19}F NMR (CD_3CN , 376 MHz, 298 K): δ 76.6. $^{13}\text{C}\{^1\text{H}\}$ NMR (CD_3CN 100 MHz, 298 K): δ 153.10, 129.91, 113.21, 86.11, 84.52, 78.99, 68.25, 40.30, 26.22.

$[(\text{Cp})\text{Co}(\text{Cp}^{\text{NH}})][\text{OTf}]_2$: A dimethoxyethane (5 mL) solution of $[(\text{Cp})\text{Co}(\text{Cp}^{\text{N}})][\text{OTf}]$ (37 mg, 0.08 mmol) was stirred. To this a dimethoxyethane (1 mL) solution of HOTf (60.8 mg, 39 μL , 0.40 mmol) was added dropwise. This caused the reaction to turn yellow and then over thirty minutes a yellow solid precipitated. The solvent was removed and the solid residue was extracted with acetonitrile. The acetonitrile solution was filtered through celite and then concentrated. Layering with toluene at $-35\text{ }^{\circ}\text{C}$ led to the precipitation of crystalline material of $[(\text{Cp})\text{Co}(\text{Cp}^{\text{NH}})][\text{OTf}]_2$ overnight. (Yield: 25 mg, 50%)

^1H NMR (C_6D_6 , 400 MHz): δ 10.08 (1H, br s, NHMe_2) 7.96 (2H, "d", $^3J_{\text{H,H}} = 8.6$ Hz), 7.73 (2H, "d", $^3J_{\text{H,H}} = 8.6$ Hz), 6.26 (2 H, tt, $J = 2.3, 2.3$ Hz), 5.83 (2H, tt, $J = 2.3, 2.3$ Hz), 5.54 (5H, s, Cp), 3.29 (6H, s, NHMe_2). ^{19}F NMR (CD_3CN , 376 MHz, 298 K): δ 76.5. ^{13}C NMR (C_6D_6 , 100 MHz): δ 144.31, 130.72, 122.69, 102.76, 86.93, 86.12, 82.57, 66.16,

47.73. Elemental Analysis: (calculated) C: 39.55%, H: 3.32%, N: 2.31%; (observed) C:

39.23%, H: 3.44%, N: 2.35%

E.3 NMR Spectroscopy of New Complexes

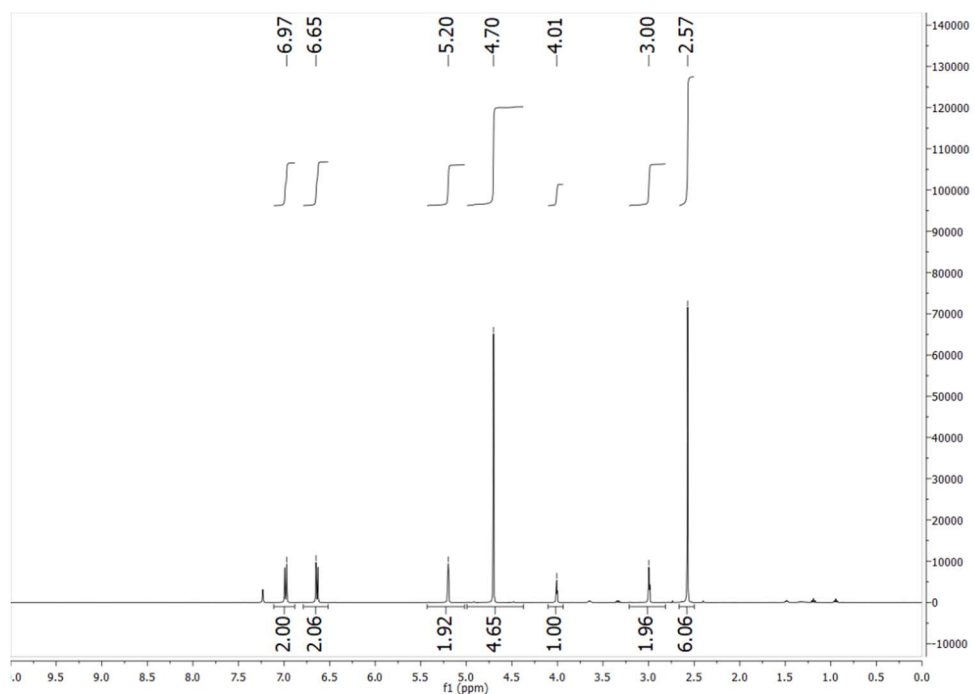


Figure E.1: ^1H NMR spectrum of $\text{Cp}(\eta^4\text{-C}_5\text{H}_5\text{PhNMe}_2)\text{Co}$ in C_6D_6 , 400 MHz, 298 K.

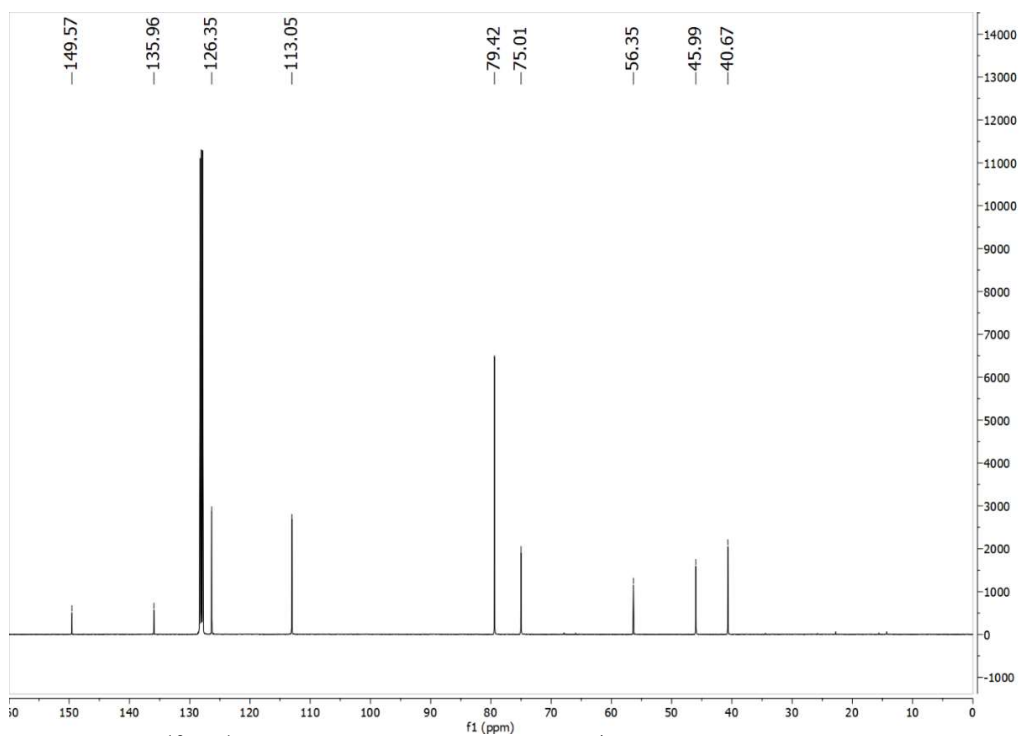


Figure E.2: $^{13}\text{C}\{^1\text{H}\}$ NMR spectrum of $\text{Cp}(\eta^4\text{-C}_5\text{H}_5\text{PhNMe}_2)\text{Co}$ in C_6D_6 , 100 MHz, 298 K.

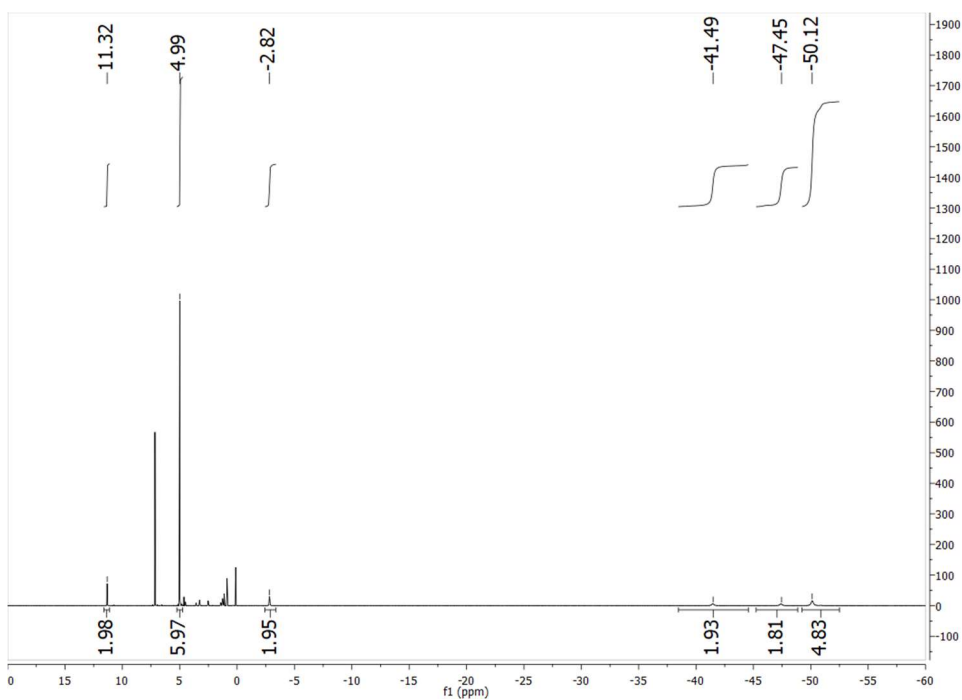


Figure E.3: ^1H NMR spectrum of $(\text{Cp})\text{Co}(\text{Cp}^{\text{N}})$ in CD_3CN , 400 MHz, 298 K.

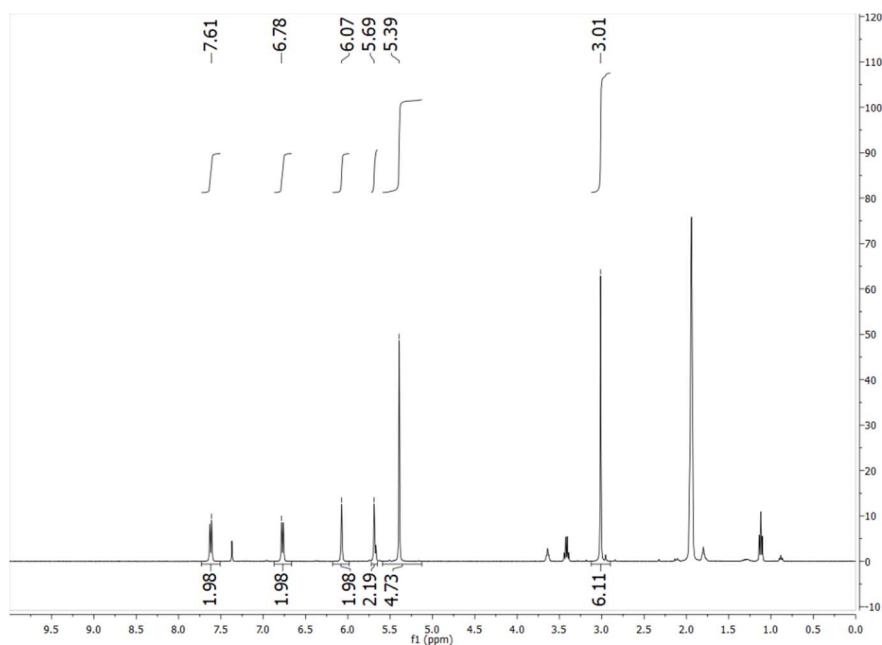


Figure E.4: ^1H NMR spectrum of $[(\text{Cp})\text{Co}(\text{Cp}^{\text{N}})][\text{OTf}]$ in CD_3CN , 400 MHz, 298 K.

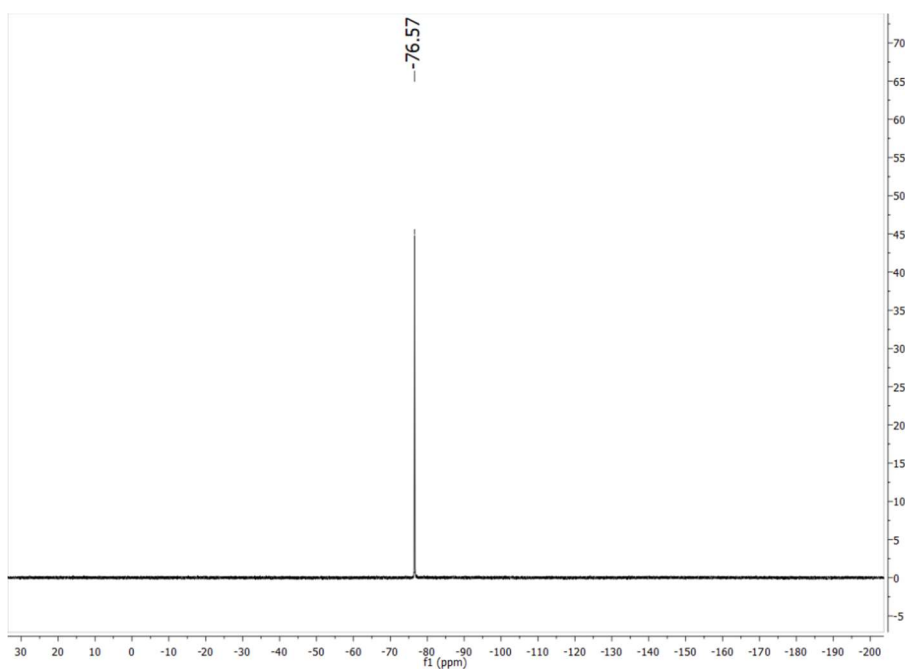


Figure E.5: ^{19}F NMR spectrum of $[(\text{Cp})\text{Co}(\text{Cp}^{\text{N}})][\text{OTf}]$ in CD_3CN , 376 MHz, 298 K.

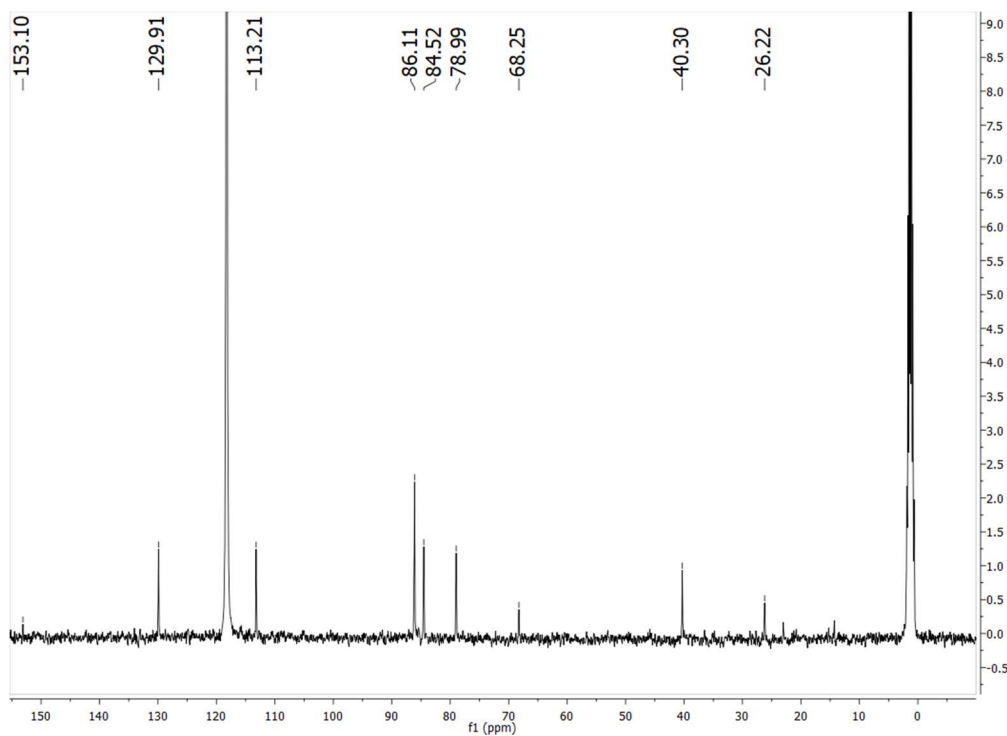


Figure E.6: $^{13}\text{C}\{^1\text{H}\}$ NMR spectrum of $[(\text{Cp})\text{Co}(\text{Cp}^{\text{N}})][\text{OTf}]$ in CD_3CN , 100 MHz, 298 K.

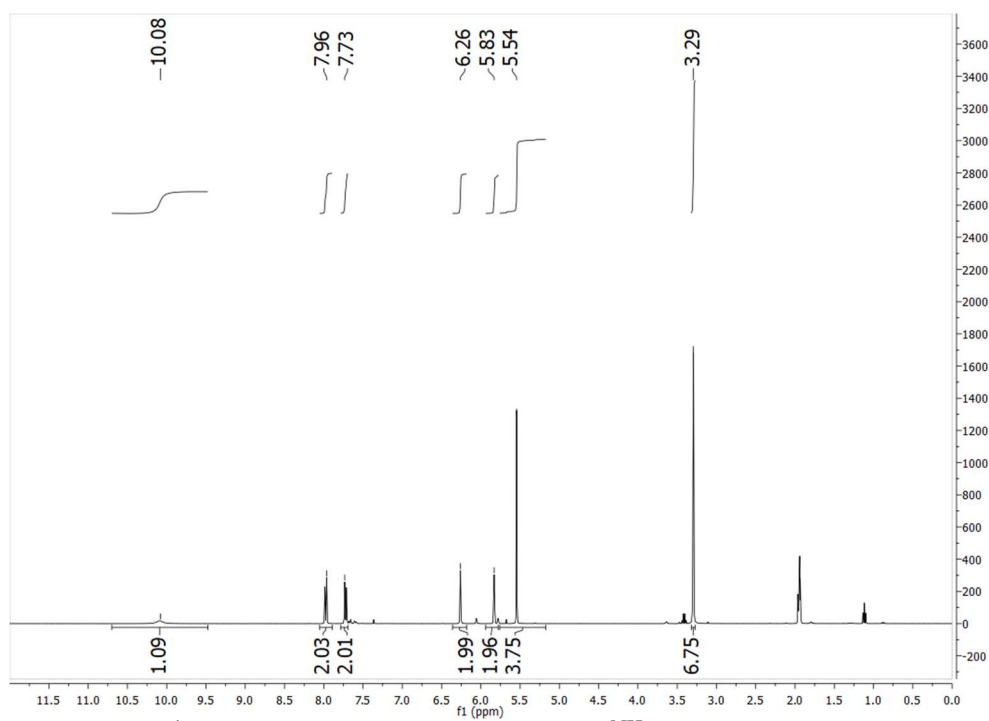


Figure E.7: ^1H NMR spectrum of $[(\text{Cp})\text{Co}(\text{Cp}^{\text{NH}})]_2[\text{OTf}]_2$ in CD_3CN , 400 MHz, 298 K.

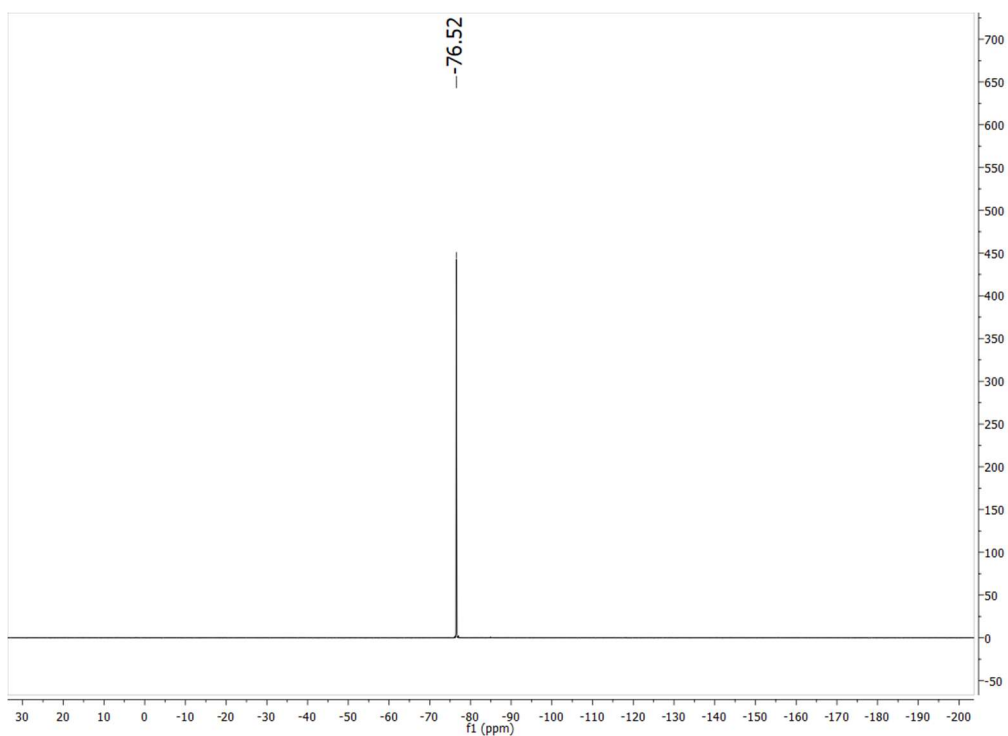


Figure E.8: ^{19}F NMR spectrum of $[(\text{Cp})\text{Co}(\text{Cp}^{\text{NH}})][\text{OTf}]_2$ in CD_3CN , 376 MHz, 298 K.

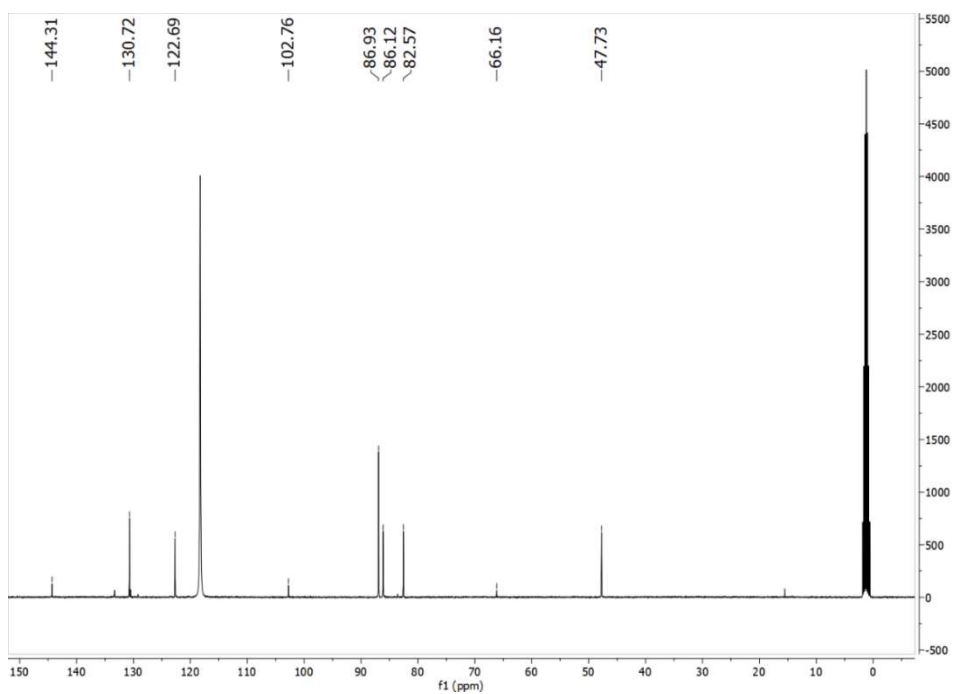


Figure E.9: $^{13}\text{C}\{^1\text{H}\}$ NMR spectrum of $[(\text{Cp})\text{Co}(\text{Cp}^{\text{NH}})][\text{OTf}]_2$ in CD_3CN , 100 MHz, 298 K.

E.4 UV-Vis Spectroscopy

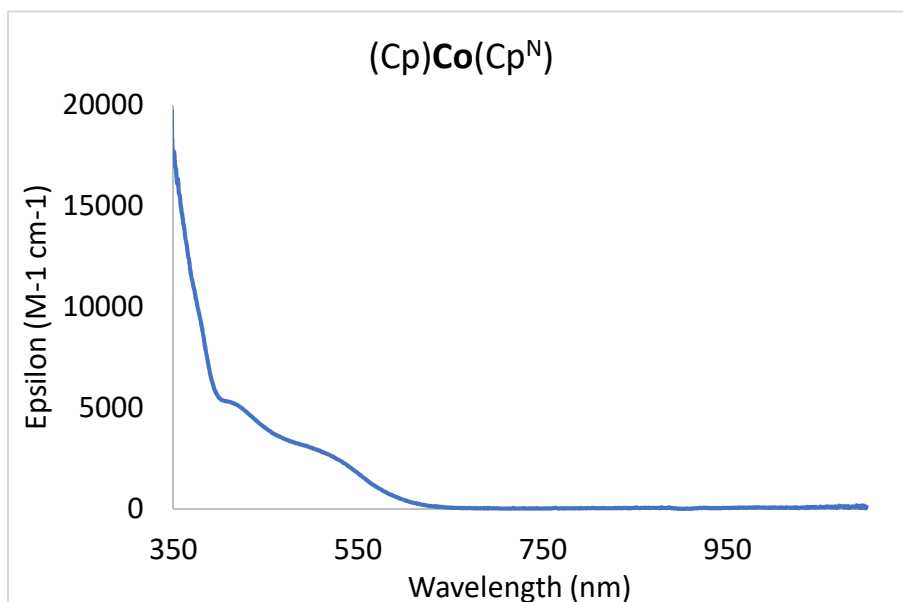


Figure E.10: UV-Vis spectrum at room temperature for [(Cp)Co(Cp^{NH})] [OTf]₂ in 2-MeTHF:THF solution (4:1).

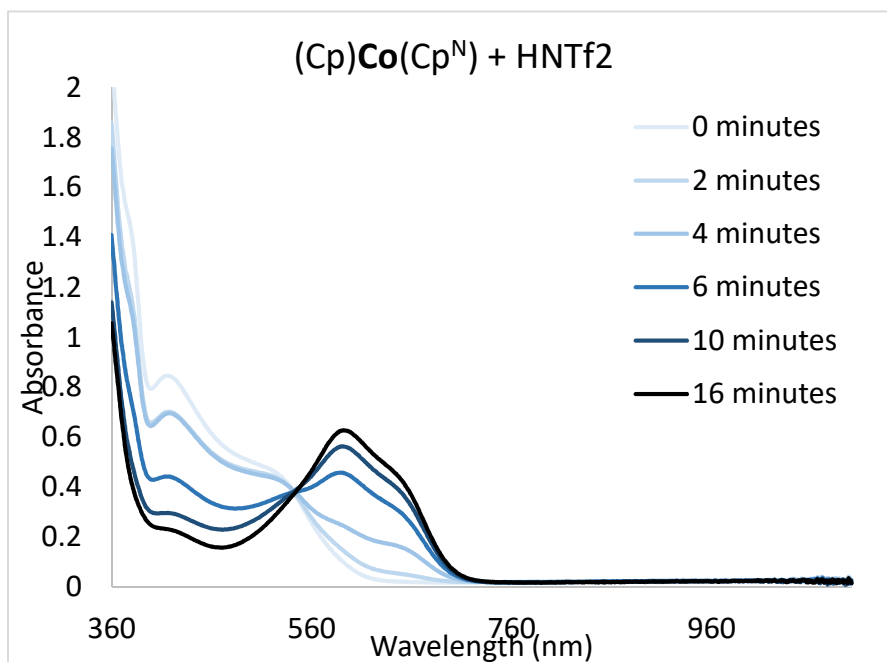


Figure E.11: UV-Vis spectra of the reaction of trifluoromethanesulfonimide and (Cp)Co(Cp^N) at -130 °C in 2-MeTHF:THF solution (4:1) showing conversion to [(Cp)Co(Cp^{NH})] [NTf₂].

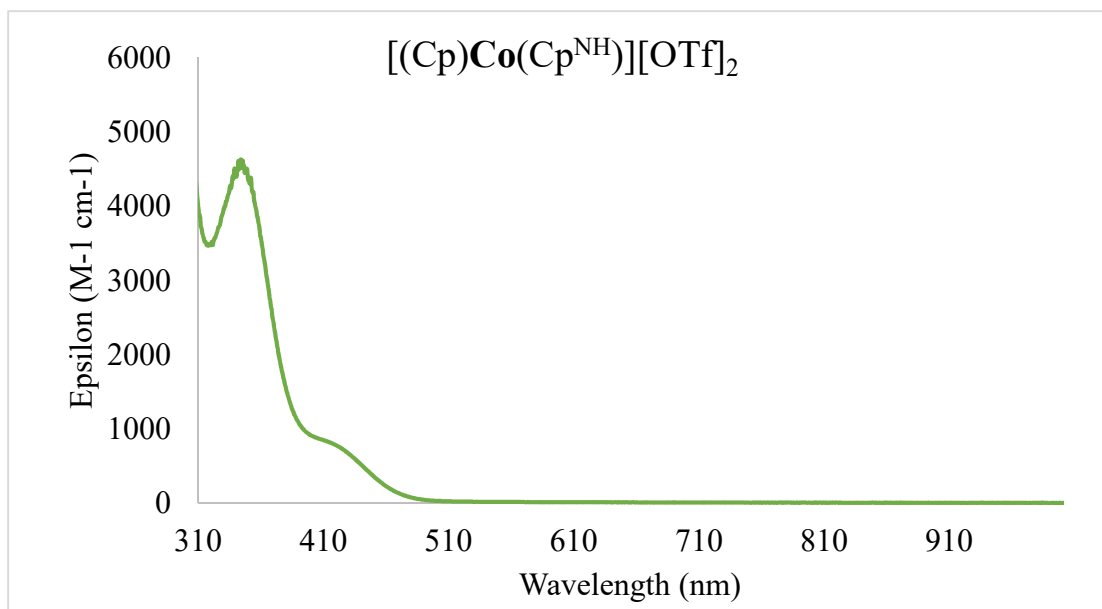


Figure E.12: UV-Vis spectrum at room temperature for $[(\text{Cp})\text{Co}(\text{Cp}^{\text{NH}})][\text{OTf}]_2$ in acetonitrile.

E.5 EPR Spectroscopy

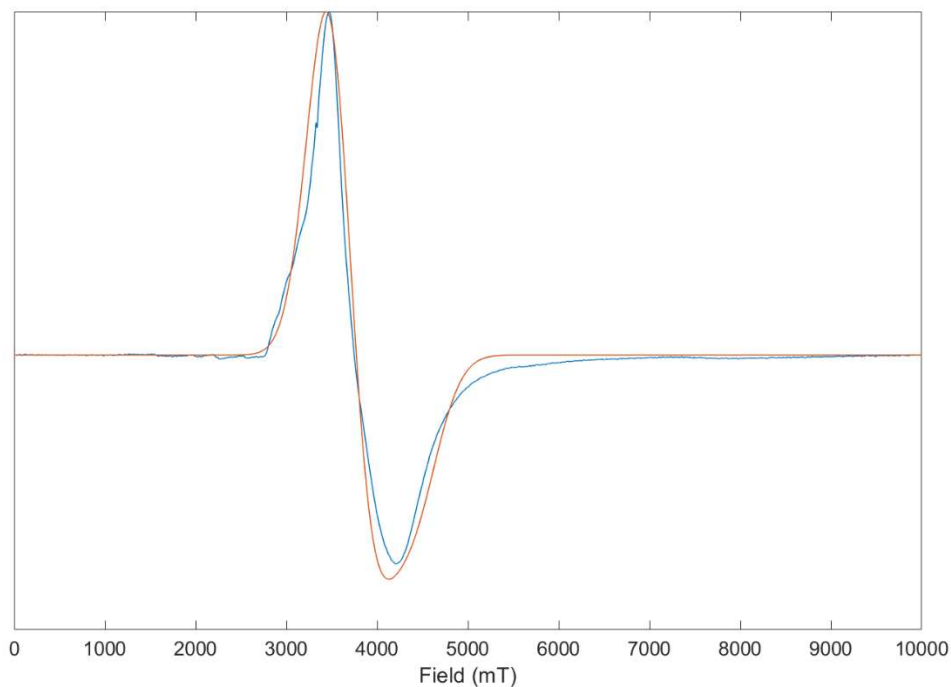


Figure E.13:(blue) X-band EPR spectrum of a 1 mM solution of $(\text{Cp})\text{Co}(\text{Cp}^{\text{N}})$ in a 2-methyltetrahydrofuran glass at 77 K. (orange) Spectral simulation with the following parameters: $g = [1.8669 \ 1.8654 \ 1.5172]$, $lw = 61.42$ Hz, $H\text{strain} = [0.0965 \ 19.3818 \ 510.669]$ Hz.

Sample Preparation for [(Cp)Co(Cp^{NH})]⁺[OTf]⁻:

Protonation: In a glovebox cold well, a 2 mM solution of (Cp)Co(Cp^N) in 2-methyltetrahydrofuran (0.5 mL) was layered on a frozen solution of 2-chloroanilinium triflate in 2-methyltetrahydrofuran (2 mM, 0.5 mL). The layers were thawed were briefly allowed to thaw and agitated with a pre-chilled spatula. The solution turned a dark blue color. It was then rapidly transferred with a prechilled pipette to an X-band EPR tube. The solution was then frozen, brought out of the glovebox, and analyzed by continuous wave X-band EPR.

Reduction: In a glovebox cold well, a 2 mM solution of [(Cp)Co(Cp^{NH})]⁺[OTf]⁻ in acetonitrile (0.5 mL) was added to a vial. This was frozen and on this was layered a 2 mM solution of SmI₂ in acetonitrile (0.5 mL). The layers were thawed and quickly mechanically mixed with a pre-chilled spatula. The solution turned a dark blue color and then transferred with a pre-chilled pipette to an X-band EPR tube. The solution was then frozen, brought out of the glovebox, and analyzed by continuous wave X-band EPR.

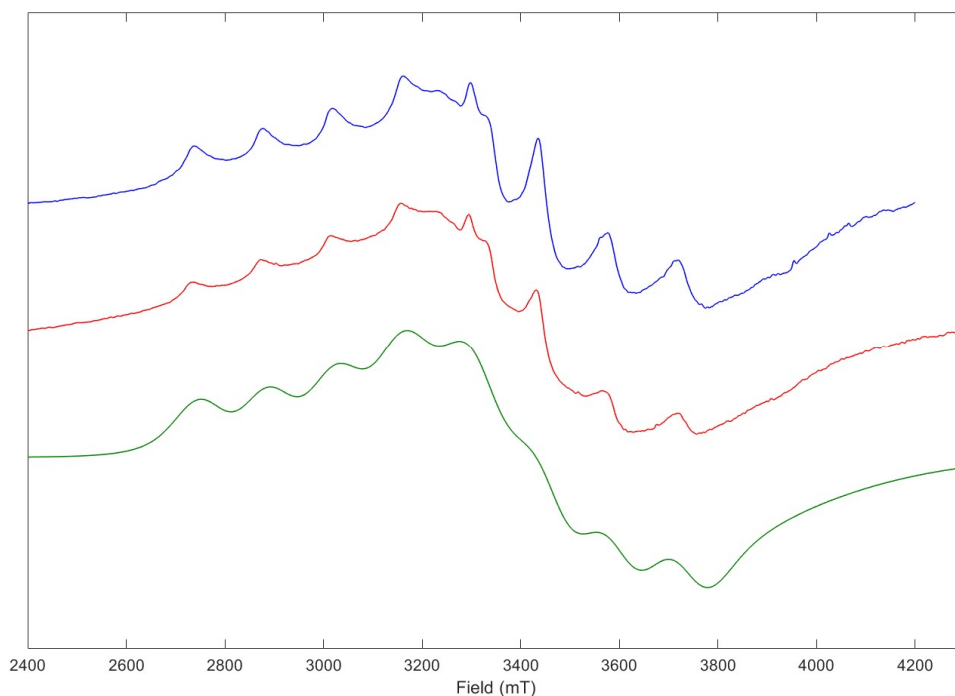


Figure E.14: (blue) X-band EPR spectrum of a 1 mM solution of $[(\text{Cp})\text{Co}(\text{Cp}^{\text{NH}})][\text{OTf}]$ in a 2-methyltetrahydrofuran glass at 77 K generated via protonation of $(\text{Cp})\text{Co}(\text{Cp}^{\text{N}})$. (red) X-band EPR spectrum of a 1 mM solution of $[(\text{Cp})\text{Co}(\text{Cp}^{\text{NH}})][\text{OTf}]$ in frozen acetonitrile at 77 K generated via reduction of $[(\text{Cp})\text{Co}(\text{Cp}^{\text{NH}})][\text{OTf}]_2$. (green) Simulation of these data. $g = [2.0555 \ 1.9932 \ 1.7959]$, $A(^{59}\text{Co}) = [401.1050 \ 27.8926 \ 41.6297]$, $\text{HStrain} = [220.0820 \ 656.3320 \ 1885.5]$, $g\text{Strain} = [0.0307 \ 0.0305 \ 0.0342]$

The high degree of strain in the simulation is suggestive of a variety of conformations or hydrogen bonding interactions, or poor homogeneity of the solution. The broadness of $(\text{Cp})\text{Co}(\text{Cp}^{\text{N}})$ in 2Me-THF glass supports the possibility of the variety of conformations. Indeed the g -values of many cobaltocenes display high sensitivity to their local environment.^{17–19} The increased broadness of the acetonitrile sample relative to the 2-MeTHF sample provides support for poor solution homogeneity.

E.6 IR Spectroscopy

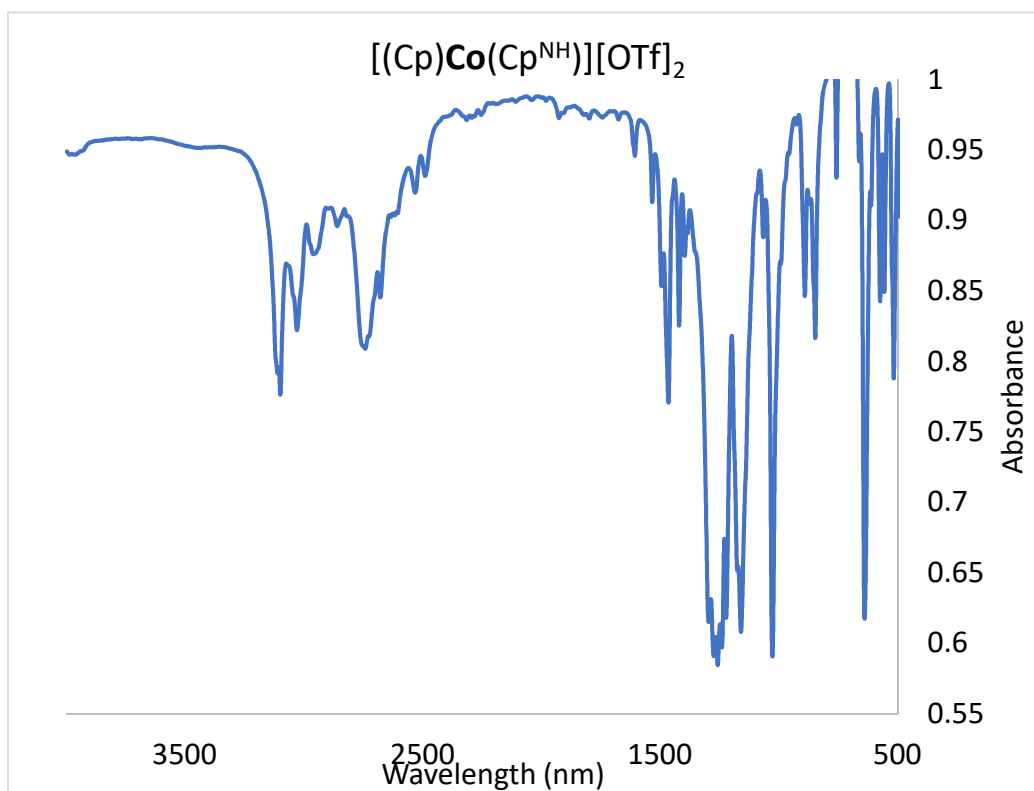


Figure E.15: IR spectrum of $[(\text{Cp})\text{Co}(\text{Cp}^{\text{NH}})][\text{OTf}]_2$ in a KBr pellet. Weak N–H vibration is evident at 3430 cm^{-1} .

E.7 X-ray Crystallography

Table E.1: X-ray crystallography details for $(\text{Cp})\text{Co}(\text{Cp}^{\text{N}})$, $[(\text{Cp})\text{Co}(\text{Cp}^{\text{NH}})][\text{OTf}]$, and $[(\text{Cp})\text{Co}(\text{Cp}^{\text{N}})][\text{OTf}]$

Compound	$(\text{Cp})\text{Co}(\text{Cp}^{\text{N}})$	$[(\text{Cp})\text{Co}(\text{Cp}^{\text{NH}})][\text{OTf}]_2$	$[(\text{Cp})\text{Co}(\text{Cp}^{\text{N}})][\text{OTf}]$
Chemical Formula	$\text{C}_{18}\text{H}_{19}\text{CoN}$	$\text{C}_{20}\text{H}_{20}\text{CoNF}_6\text{O}_6\text{S}_2$	$\text{C}_{19}\text{H}_{19}\text{CoNF}_3\text{O}_3\text{S}$
Formula Weight	308.27	607.42	457.34
Crystal System	Triclinic	Triclinic	Triclinic
Space Group	P –1	P –1	P –1
a (Å)	13.3390(15)	8.2326(5)	10.5419(7)

b (Å)	10.8922(13)	12.5729(7)	11.6519(8)
c (Å)	9.6039(11)	12.9491(8)	16.4972(10)
α (°)	90	67.614(3)	89.708(2)
β (°)	90	76.729(3)	79.981(2)
γ (°)	90	81.730(3)	67.013(2)
V (Å ³)	1395.4(3)	1203.85(13)	1832.6(2)
Z	4	2	4
D _{calcd} (g·cm ⁻³)	9.518	1.676	1.658
F ₀₀₀	644.0	616.0	936.0
μ (mm ⁻¹)	9.518	7.997	1.101
Temperature (K)	100(2)	100(2)	100(2)
Wavelength (Å)	0.71073	1.54178	
Measured Reflections	1457	4716	12299
Unique Reflections	1314	4491	10976
Data/Restraints/ Parameters	1457/0/509	4716/0/327	10976/0/509
R(F) (I>2 σ (I))	0.0543	0.0411	0.0297
wR(F ²) (all)	0.1400	0.0970	0.0793
GOOF	1.068	1.046	1.033

E.8 Cyclic Voltammetry

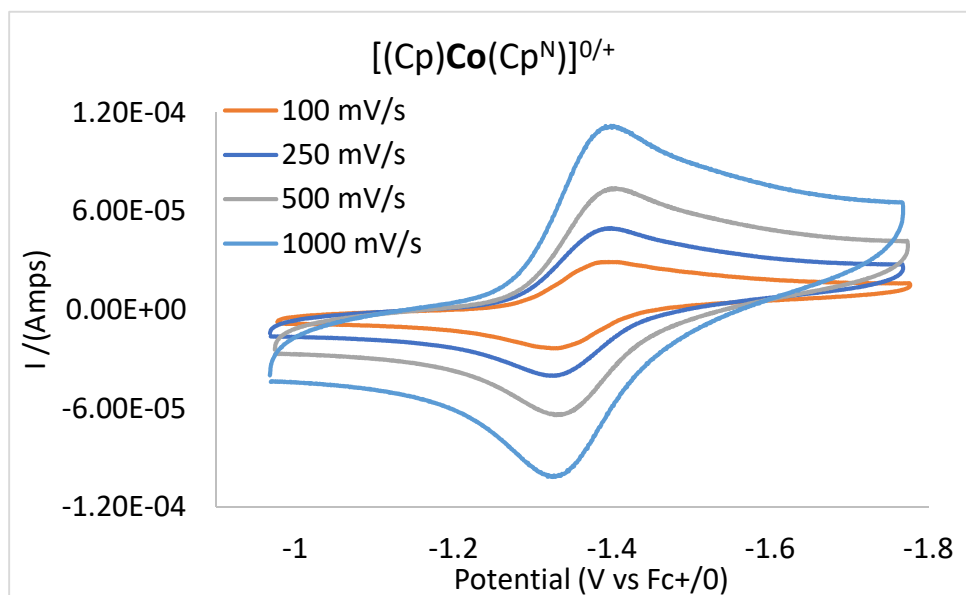


Figure E.16: Variable scan rate cyclic voltammograms with a glassy carbon working electrode of a 1 mM solution of the $(\text{Cp})\text{Co}(\text{Cp}^{\text{N}})^{0/+}$ in acetonitrile with 100 mM $[\text{TBA}][\text{PF}_6]$.

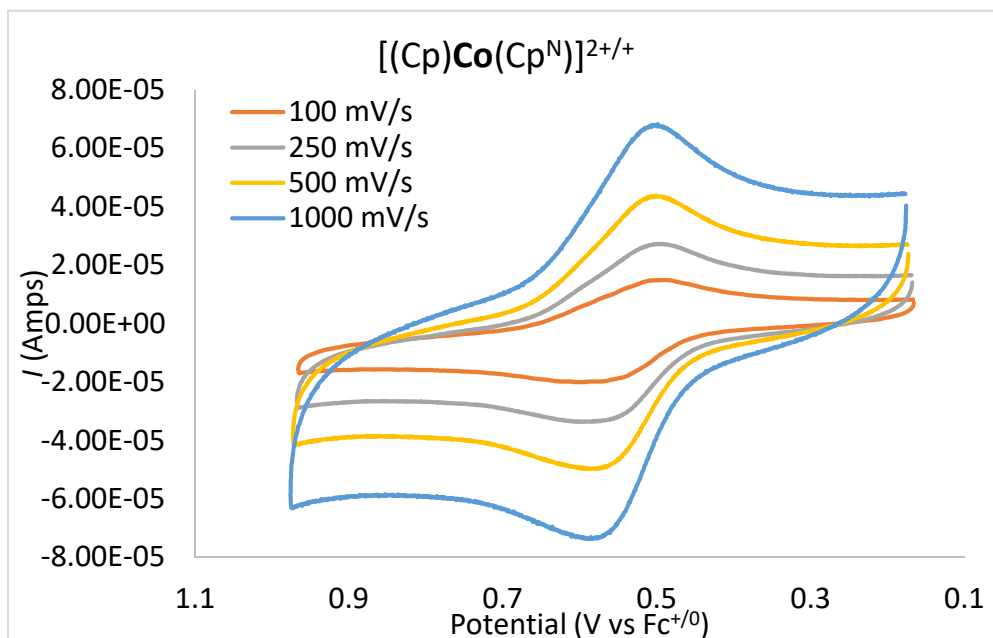


Figure E.17: Variable scan rate cyclic voltammograms with a glassy carbon working electrode of a 1 mM solution of the $[(\text{Cp})\text{Co}(\text{Cp}^{\text{N}})]^{2+/+}$ in acetonitrile with 100 mM $[\text{TBA}][\text{PF}_6]$.

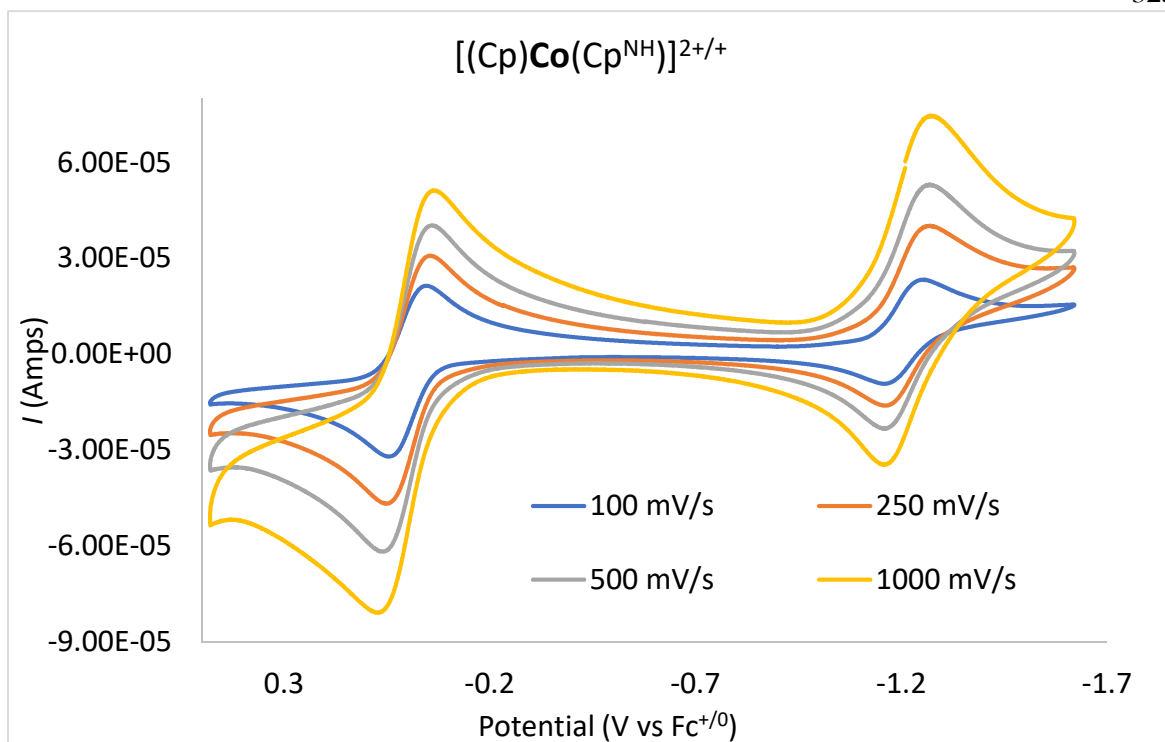


Figure E.18: Variable scan rate cyclic voltammograms with a boron doped diamond working electrode of a 1 mM solution of $[(\text{Cp})\text{Co}(\text{Cp}^{\text{NH}})]\text{[OTf]}_2$ and 1 mM solution of ferrocene in acetonitrile with 100 mM $[\text{TBA}][\text{PF}_6]$.

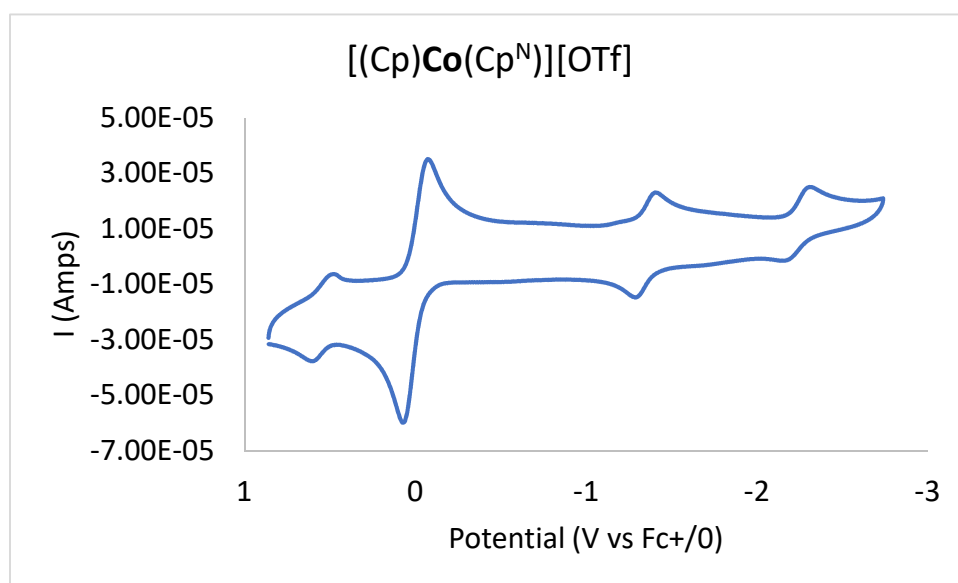


Figure E.19: Cyclic voltammogram of a glassy carbon working electrode of a 1 mM solution of the $(\text{Cp})\text{Co}(\text{Cp}^{\text{N}})^{+/0}$ in DME with 100 mM $[\text{TBA}][\text{PF}_6]$.

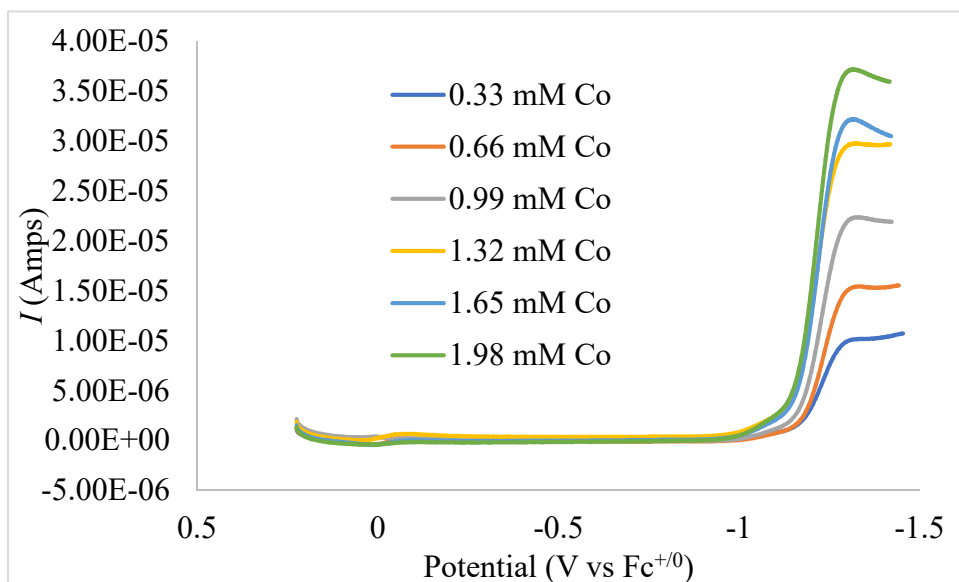


Figure E.20: Cathodic scan of CV's at 100 mV/s of different concentrations of $[(\text{Cp})\text{Co}(\text{Cp}^{\text{N}})]\text{[OTf]}$ on a BDD working electrode of a DME solution of 100 mM $[\text{C}^{\text{N}}\text{PhNH}_3]\text{[OTf]}$, 50 mM acetophenone, and 200 mM $[\text{TBA}]\text{[PF}_6]$.

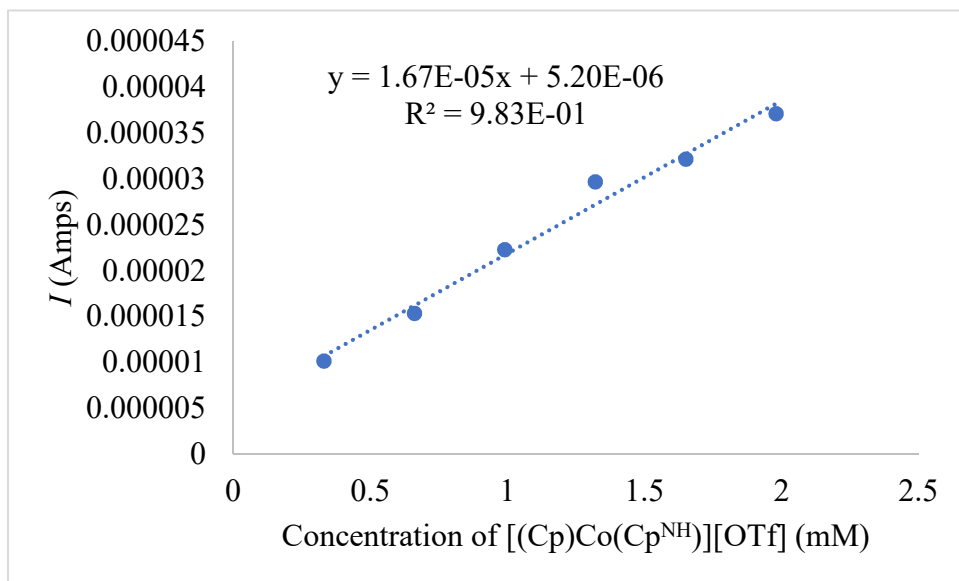


Figure E.21: Plot of plateau current (-1.314 V vs $\text{Fc}^{+/0}$) against concentration of $[(\text{Cp})\text{Co}(\text{Cp}^{\text{NH}})]\text{[OTf]}$ for the CV's shown in **Figure E.20** with a line of best fit.

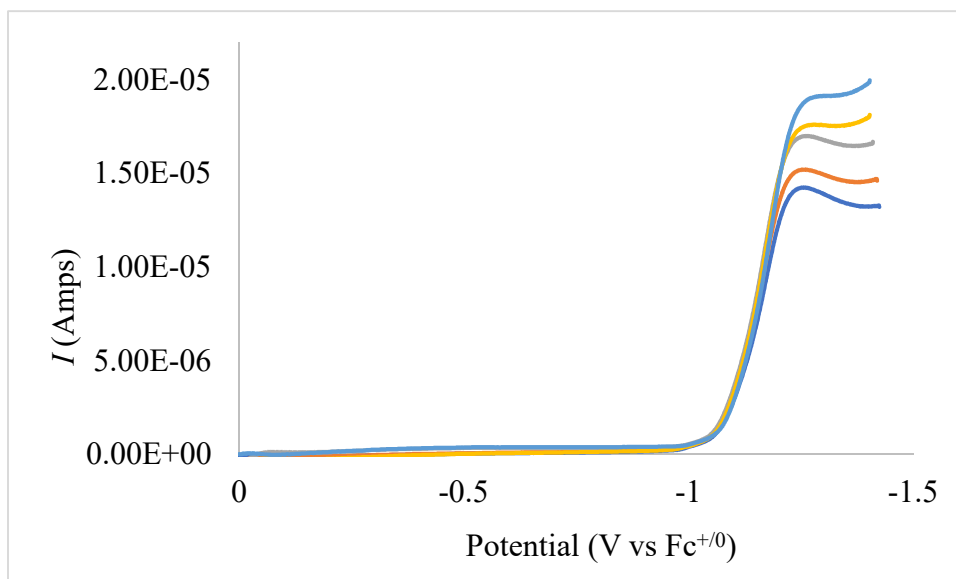


Figure E.22: Cathodic scan of CV's at 10 mV/s of different concentrations of acetophenone on a BDD working electrode of a DME solution of 100 mM [⁴-CNPhNH₃][OTf], 1 mM [(Cp)Co(Cp^N)] [OTf], and 200 mM [TBA][PF₆].

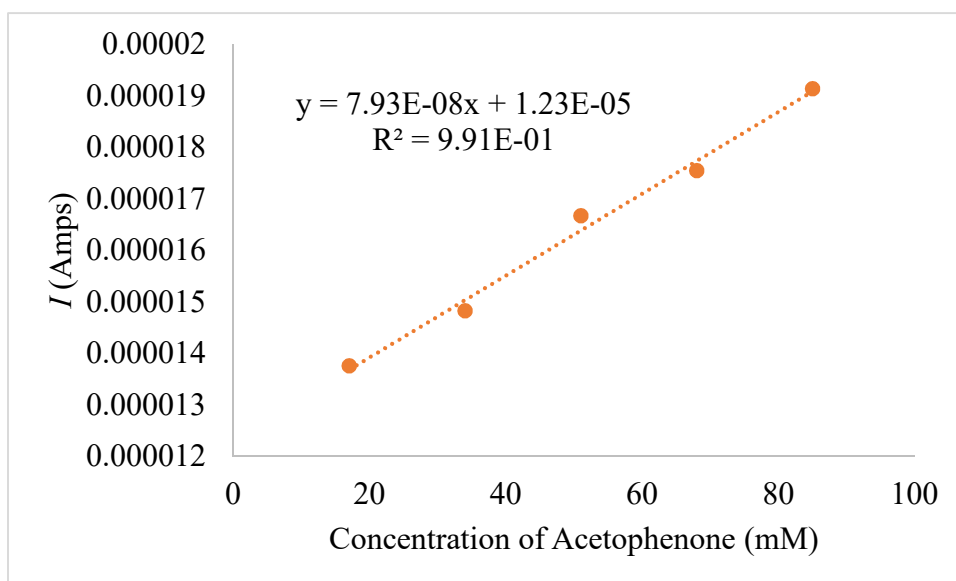


Figure E.23: Plot of plateau current (-1.314 V vs Fc⁺⁰) against concentration of acetophenone for the CV's shown in **Figure E.22** with a line of best fit.

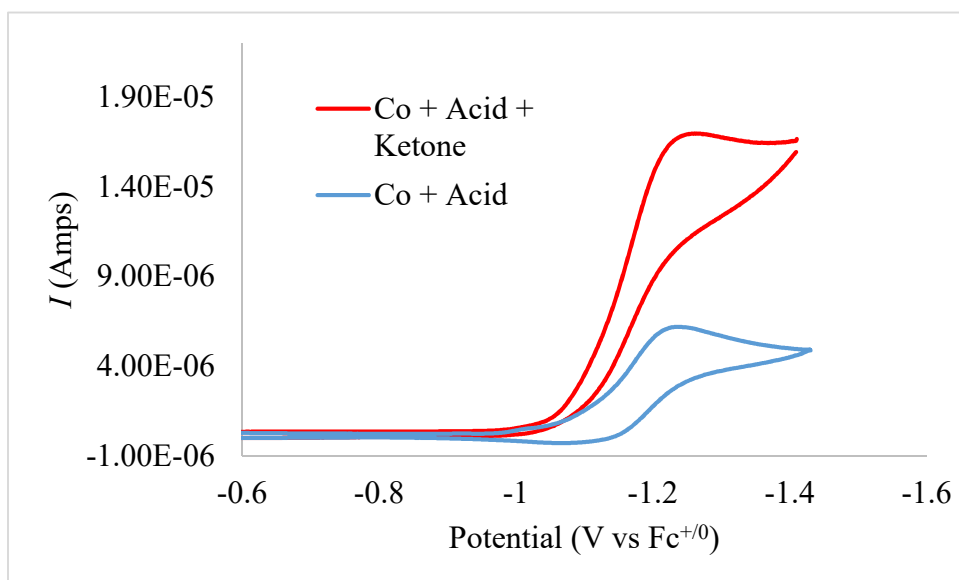


Figure E.24: Comparison of CV's on BDD working electrode at 10 mV/s with 1 mM [(Cp)Co(Cp^N)] [OTf], 100 mM [⁴CNPhNH₃] [OTf], and 200 mM [TBA] [PF₆] with variable amount of acetophenone (0 mM, blue) vs (50 mM, red).

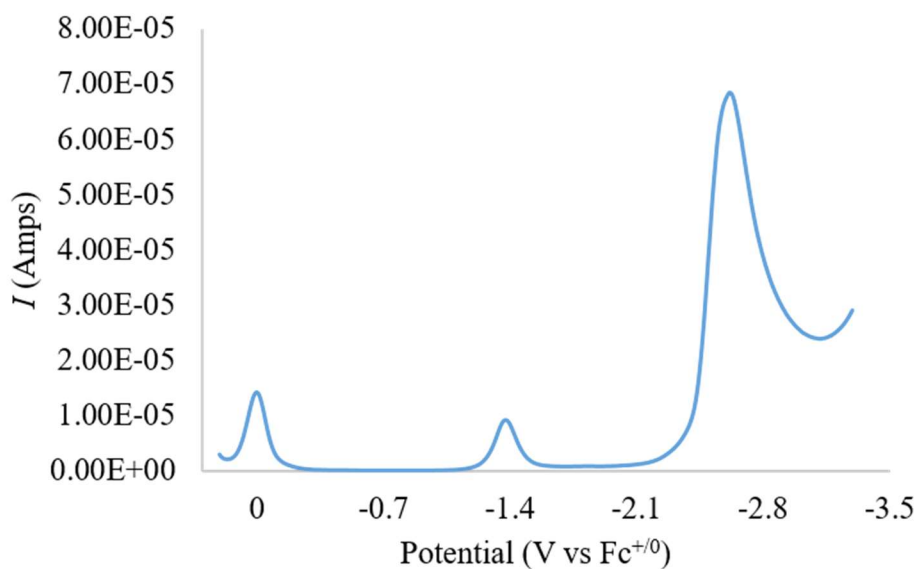


Figure E.25: Differential pulse voltammogram of a DME solution containing 1 mM ferrocene, 1 mM [(Cp)Co(Cp^N)] [OTf], 50 mM acetophenone, and 200 mM [TBA] [PF₆].

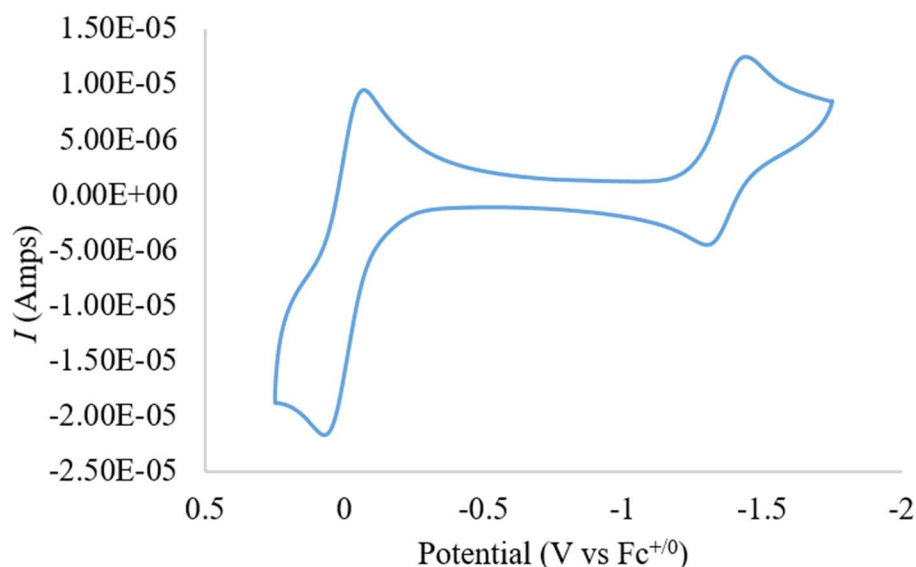


Figure E.26: CV at 100 mV/s of a DME solution containing 1 mM ferrocene, 1 mM [(Cp)Co(Cp^N)] [OTf], 50 mM acetophenone, and 200 mM [TBA][PF₆].

E.9 pK_a Determination

Experiments for pK_a determination were performed in MeCN-*d*₃ using equilibria constants determined using ¹H NMR spectroscopy on a 400 MHz spectrometer. In a standard experiment a cobalt containing starting material was dissolved in MeCN-*d*₃ and added to a J-Young NMR tube. An initial NMR was taken to verify purity and then aliquots of acid (or base) were added to the tube from a stock solution. Although care was taken to add exact amounts of acid (or base) the relative integrals of the species was used to evaluate the amounts of the species rather than an absolute amount as determined by the concentrations/volumes. In all cases, the counterion used was triflate to simplify the analysis. The relative concentration of the protonated/deprotonated species was determined by the chemical shift (CS) of each peak (**Eq B.1-Eq E.3**). For each component (*i.e.*, acid/base and [(Cp)Co(Cp^N)] [OTf]/ [(Cp)Co(Cp^{NH})] [OTf]₂) the average of each of these

25 μL	7.84 (0.66)	7.42 (0.67)	6.19 (0.61)	5.78 (0.64)	5.49 (0.64)	3.2 (0.68)	0.65	0.02
50 μL	7.75 (0.40)	7.17 (0.41)	6.14 (0.33)	5.74 (0.36)	5.45 (0.36)	3.12 (0.39)	0.38	0.03
75 μL	7.70 (0.26)	7.04 (0.27)	6.12 (0.22)	5.72 (0.21)	5.43 (0.21)	3.08 (0.25)	0.24	0.02
100 μL	7.67 (0.17)	6.97 (0.11)	6.10 (0.11)	5.71 (0.14)	5.42 (0.14)	3.06 (0.18)	0.16	0.03

Table E.4: NMR data for the aniline/anilinium during titration of $[(\text{Cp})\text{Co}(\text{Cp}^{\text{NH}})][\text{OTf}]_2$ with 4-chloroaniline. Relative integral is determined by setting the most downfield aryl peaks in the cobalt center to an integral of 1 and integrating the acid peaks in comparison and taking the average of those integrals.

Volume	Shift 1	Shift 2	Average	Std. Dev.	Relative Integral
25 μL	7.49 (0.92)	7.35 (0.91)	0.92	0.003	0.35
50 μL	7.42 (0.78)	7.23 (0.76)	0.77	0.007	0.77
75 μL	7.34 (0.61)	7.11 (0.61)	0.61	0.0001	1.09
100 μL	7.28 (0.49)	7.01 (0.49)	0.49	0.001	1.54

Table E.5: Equilibrium Constants derived from data in Table E.3 and Table E.4.

Volume	K_{eq}
25 μL	0.17
50 μL	0.18
75 μL	0.20
100 μL	0.19

Table E.6: NMR data for the cobalt center during second titration of $[(\text{Cp})\text{Co}(\text{Cp}^{\text{NH}})][\text{OTf}]_2$ with 4-chloroaniline. All chemical shifts are in ppm. In parentheses is the fraction of $[(\text{Cp})\text{Co}(\text{Cp}^{\text{NH}})][\text{OTf}]_2$ indicated by that chemical shift.

Volume	Shift 1	Shift 2	Shift 3	Shift 4	Shift 5	Shift 6	Average	Std. Dev.
25 μL	7.85 (0.69)	7.43 (0.68)	6.19 (0.61)	5.78 (0.64)	5.49 (0.64)	3.20 (0.68)	0.66	0.03
100 μL	7.68 (0.2)	6.11 (0.17)	5.72 (0.21)	5.72 (0.21)	5.43 (0.21)	3.07 (0.21)	0.21	0.02
125 μL	7.67 (0.17)	6.94 (0.17)	6.10 (0.11)	5.71 (0.14)	5.42 (0.14)	3.06 (0.18)	0.15	0.02

Table E.7: NMR data for the aniline/anilinium during second titration of $[(\text{Cp})\text{Co}(\text{Cp}^{\text{NH}})][\text{OTf}]_2$ with 4-chloroaniline. Relative integral is determined by setting the most downfield aryl peaks in the cobalt center to an integral of 1 and integrating the acid peaks in comparison and taking the average of those integrals.

Volume	Shift 1	Shift 2	Average	Std. Dev.	Relative Integral
25 μL	7.50 (0.94)	7.35 (0.91)	0.93	0.01	0.37
100 μL	7.33 (0.59)	7.08 (0.58)	0.58	0.01	1.54
125 μL	7.29 (0.51)	7.02 (0.50)	0.51	0.01	1.85

Table E.8: Equilibrium Constants derived from data in Table E.6 and Table E.7.

Volume	K_{eq}
25 μL	0.15
100 μL	0.18
125 μL	0.18

Table E.9: NMR data for the cobalt center during titration of $[(\text{Cp})\text{Co}(\text{Cp}^{\text{NH}})]\text{[OTf]}_2$ with 2-chloroaniline. All chemical shifts are in ppm. In parentheses is the fraction of $[(\text{Cp})\text{Co}(\text{Cp}^{\text{NH}})]\text{[OTf]}_2$ indicated by that chemical shift.

Volume	Shift 1	Shift 2	Shift 3	Shift 4	Shift 5	Shift 6	Average	Std. Dev.
10 μL	7.90 (0.83)	7.57 (0.83)	6.22 (0.78)	5.81 (0.86)	5.52 (0.86)	3.25 (0.86)	0.83	0.03
20 μL	7.88 (0.77)	7.52 (0.78)	6.21 (0.72)	5.80 (0.79)	5.51 (0.79)	3.23 (0.79)	0.78	0.02
40 μL	7.85 (0.69)	7.44 (0.69)	6.19 (0.61)	5.79 (0.71)	5.49 (0.64)	3.21 (0.71)	0.68	0.04
80 μL	7.81 (0.57)	7.35 (0.60)	6.17 (0.50)	5.77 (0.57)	5.48 (0.57)	3.18 (0.60)	0.57	0.03

Table E.10: NMR data for the aniline/anilinium during titration of $[(\text{Cp})\text{Co}(\text{Cp}^{\text{NH}})]\text{[OTf]}_2$ with 4-chloroaniline. Relative integral is determined by setting the most downfield aryl peak of the Co complex to 1 and then taking the average of the integrals from the acid/base system.

Volume	Shift 1	Shift 2	Shift 3	Shift 4	Average	Std. Dev.	Relative Integral
10 μL	7.33 (0.30)	7.19 (0.29)	7.05 (0.35)	6.91 (0.33)	0.32	0.02	0.28
20 μL	7.30 (0.23)	7.16 (0.22)	7.00 (0.28)	6.85 (0.26)	0.25	0.02	0.51
40 μL	7.27 (0.16)	7.13 (0.16)	6.94 (0.17)	6.78 (0.17)	0.17	0.01	0.90
80 μL	7.25 (0.12)	7.11 (0.11)	6.90 (0.13)	6.73 (0.11)	0.12	0.01	1.62

Table E.11: Equilibrium Constants derived from data in Table E.9 and Table E.10.

Volume	K_{eq}

10 μL	10.9
20 μL	10.3
40 μL	10.2
80 μL	10.3

Table E.12: Final equilibrium constants from data in **Table E.5**, **Table E.8**, and **Table E.11**

Experiment #	K_{eq}	Std. Dev.	$\text{p}K_{\text{a}}$
1 ($^4\text{-ClPhNH}_2$)	0.19	0.01 (6%)	8.83
2 ($^4\text{-ClPhNH}_2$)	0.17	0.01 (7%)	8.88
3 ($^2\text{-ClPhNH}_2$)	10.3	0.4 (3%)	8.87

Final $\text{p}K_{\text{a}}$ is 8.86 ± 0.02

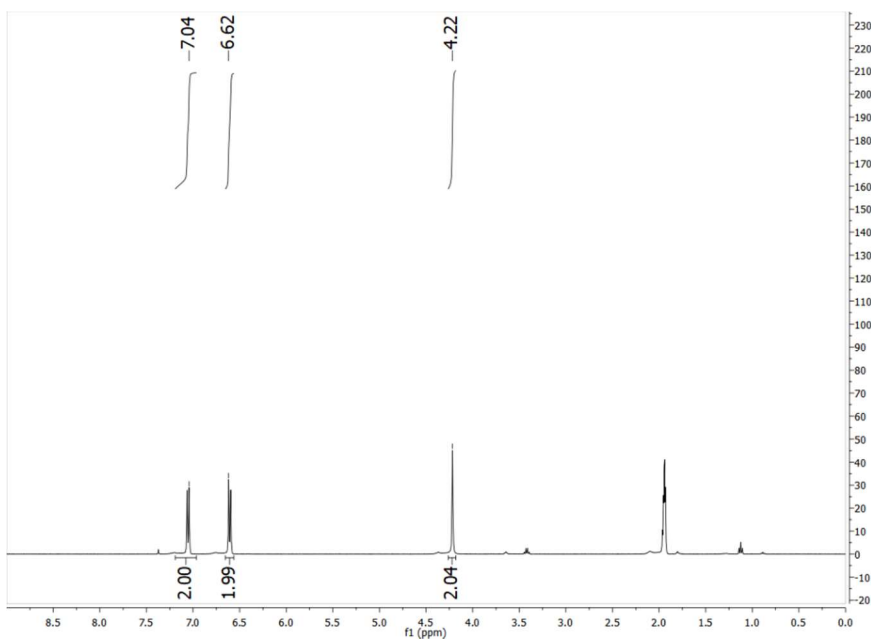


Figure E.27: 400 MHz ^1H NMR spectrum of 4-chloroaniline ($^4\text{-ClPhNH}_2$) in $\text{MeCN-}d_3$ at room temperature.

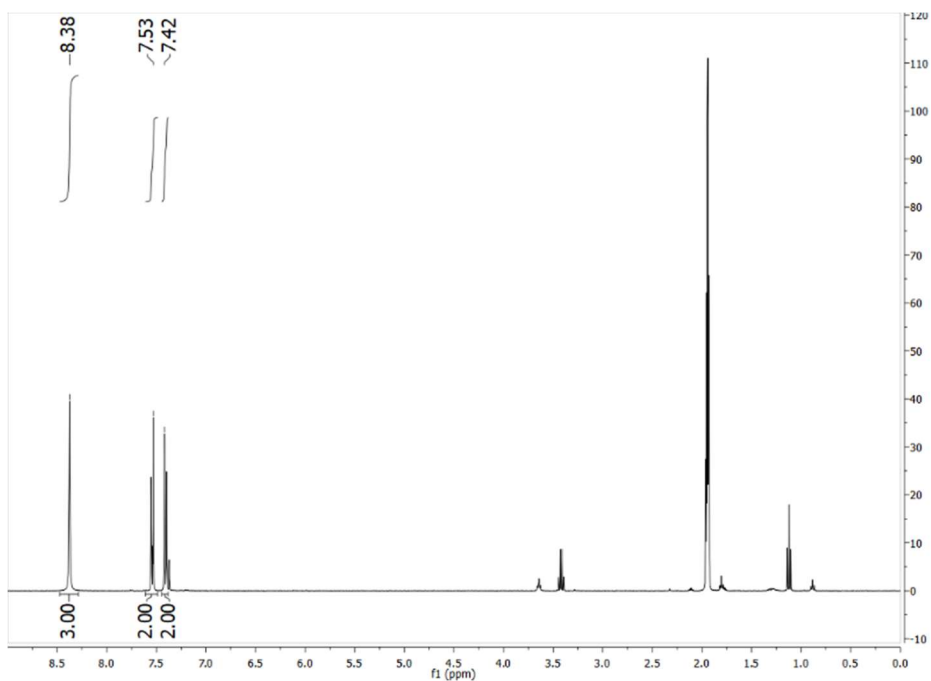


Figure E.28: 400 MHz ^1H NMR spectrum of 4-chloroanilinium triflate ($[\text{}^4\text{-ClPhNH}_3][\text{OTf}]$) in $\text{MeCN-}d_3$ at room temperature.

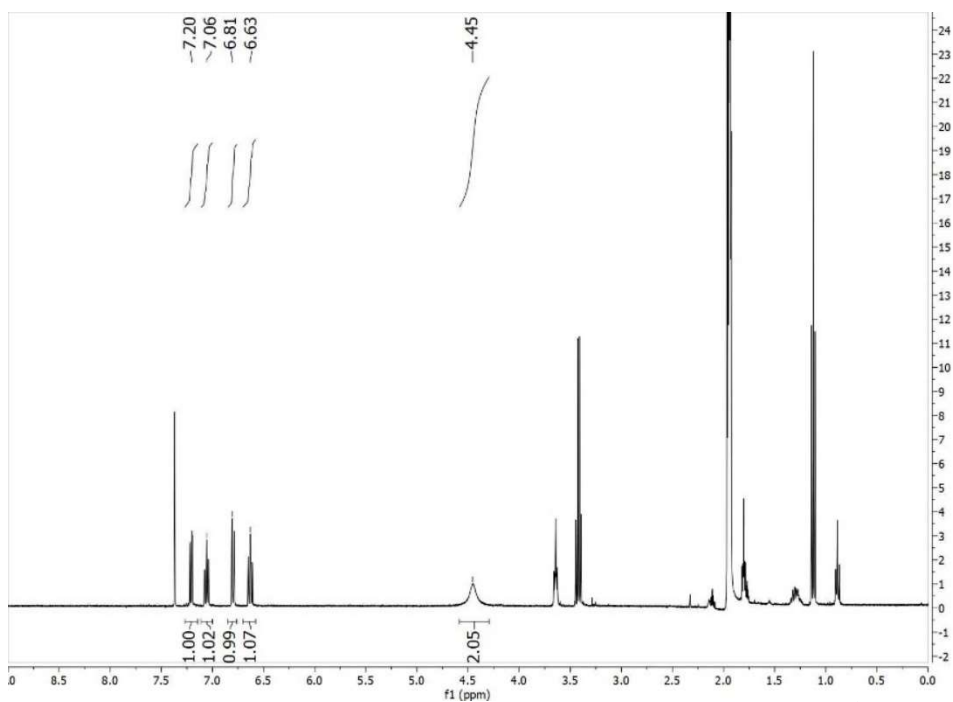


Figure E.29: 400 MHz ^1H NMR spectrum of 2-chloroaniline (${}^2\text{-ClPhNH}_2$) in $\text{MeCN-}d_3$ at room temperature.

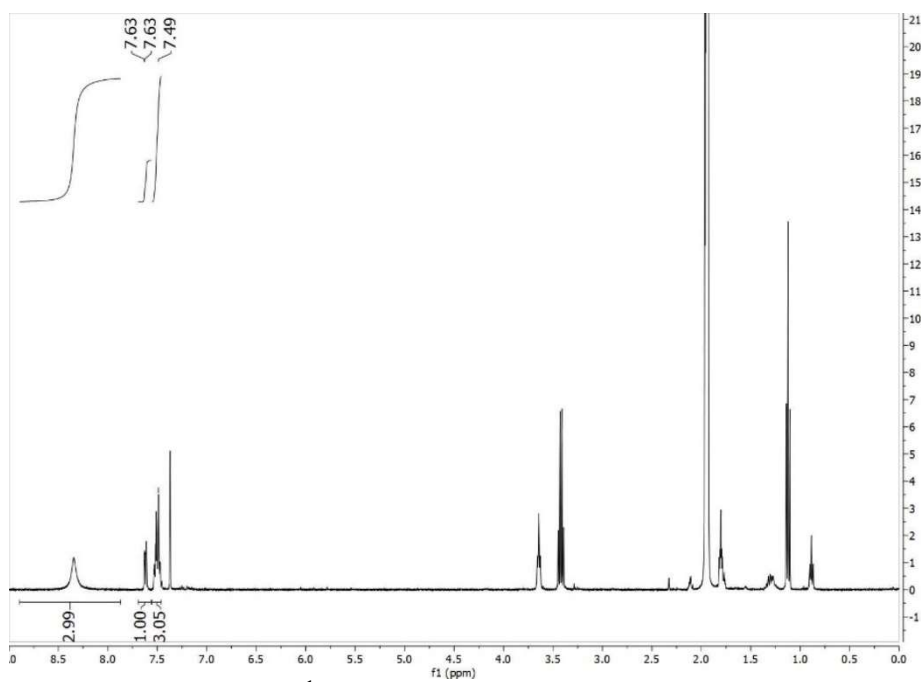


Figure E.30: 400 MHz ^1H NMR spectrum of 2-chloroanilinium triflate ($[\text{}^2\text{-ClPhNH}_3][\text{OTf}]$) in $\text{MeCN-}d_3$ at room temperature.

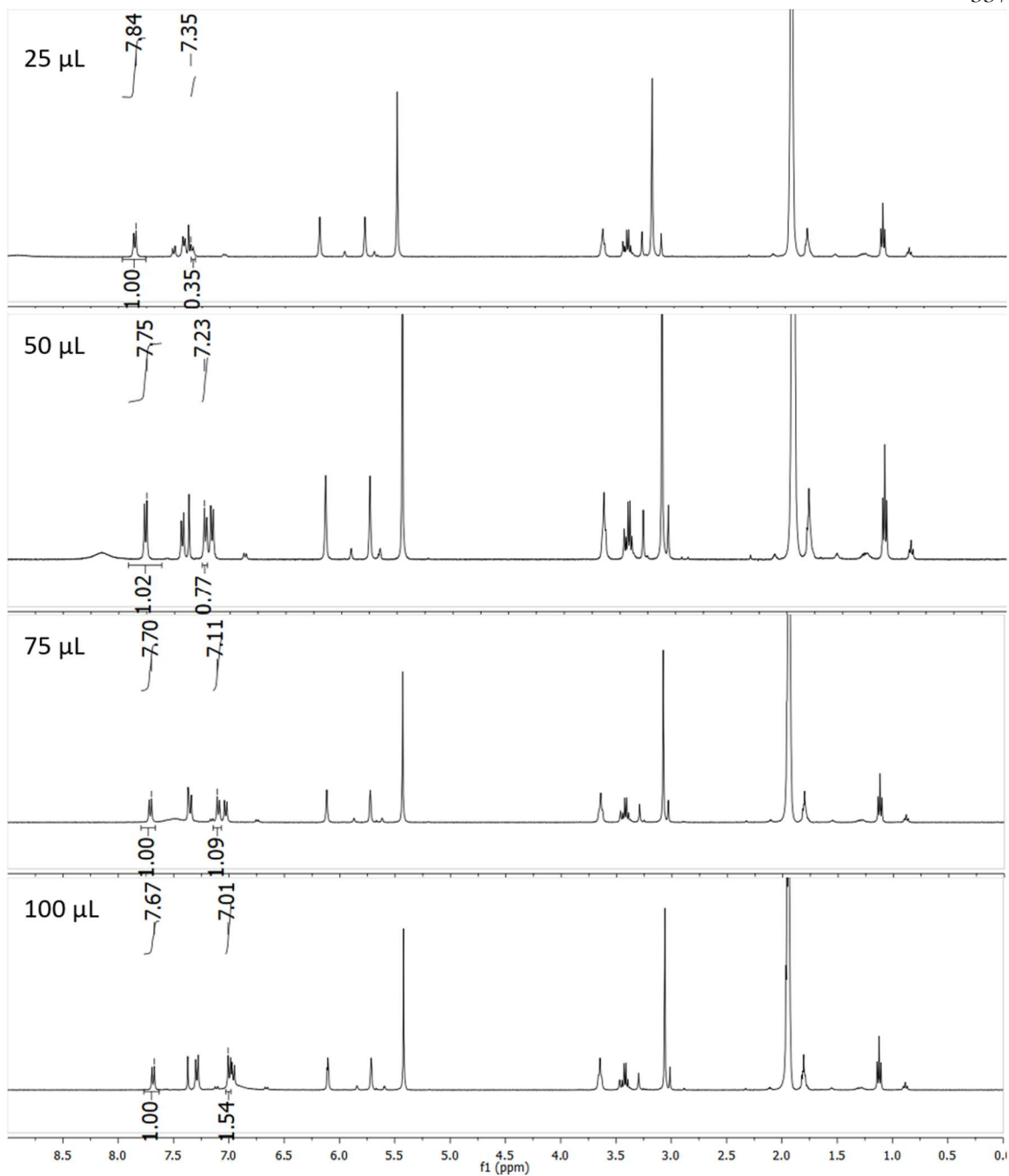


Figure E.31: 400 MHz ^1H NMR spectra of titration experiments of $[(\text{Cp})\text{Co}(\text{Cp}^{\text{NH}})][\text{OTf}]_2$ with 4-chloroaniline in $\text{MeCN-}d_3$ at room temperature. Only one integral and peak pick for both Co and the aniline are shown for clarity, but all the data shown in the above tables was used to determine the equilibrium constants (Experiment #1).

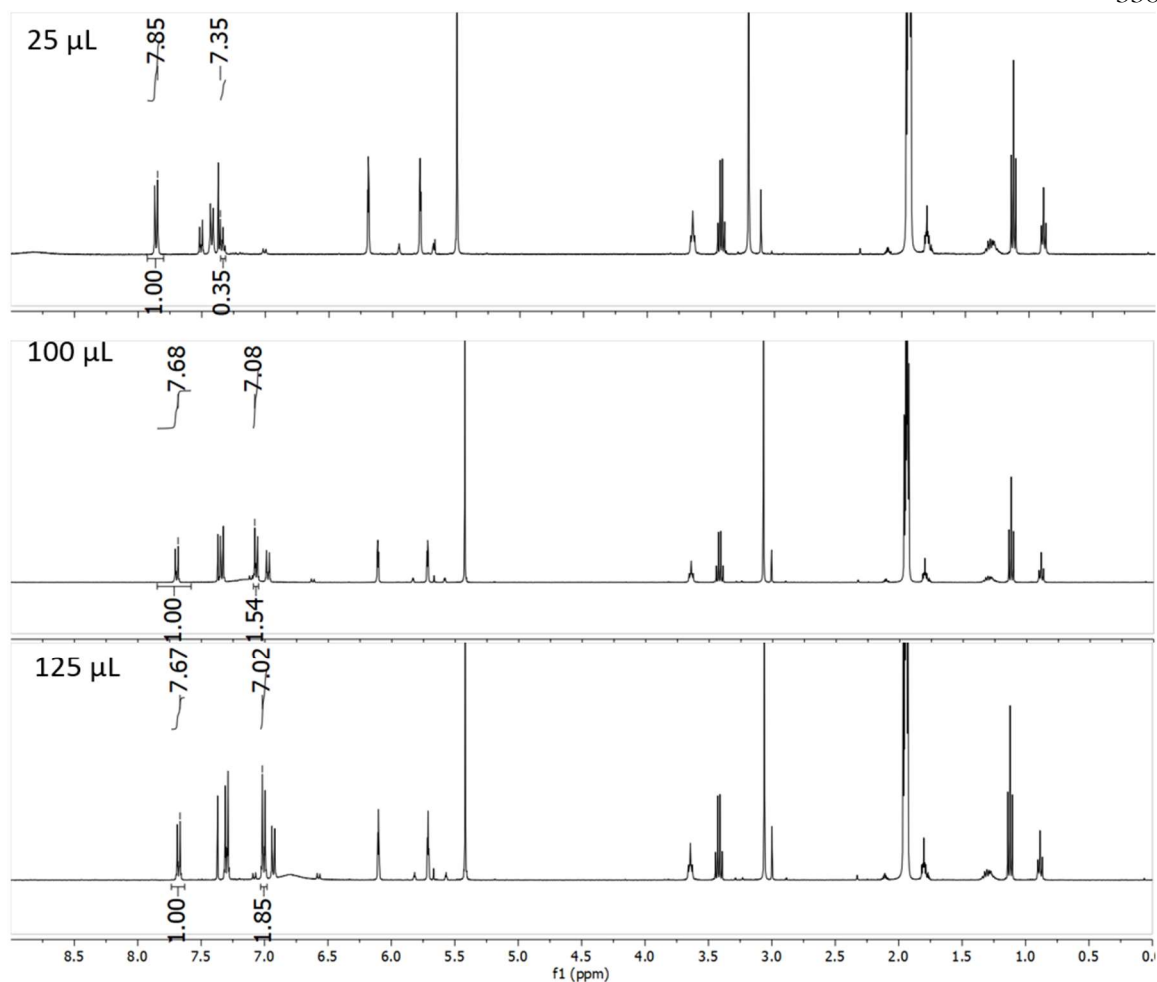


Figure E.32: 400 MHz ^1H NMR spectra of titration experiments of $[(\text{Cp})\text{Co}(\text{Cp}^{\text{NH}})][\text{OTf}]_2$ with 4-chloroaniline in $\text{MeCN-}d_3$ at room temperature. Only one integral and peak pick for both Co and the aniline are shown for clarity, but all the data shown in the above tables was used to determine the equilibrium constants (Experiment #2).

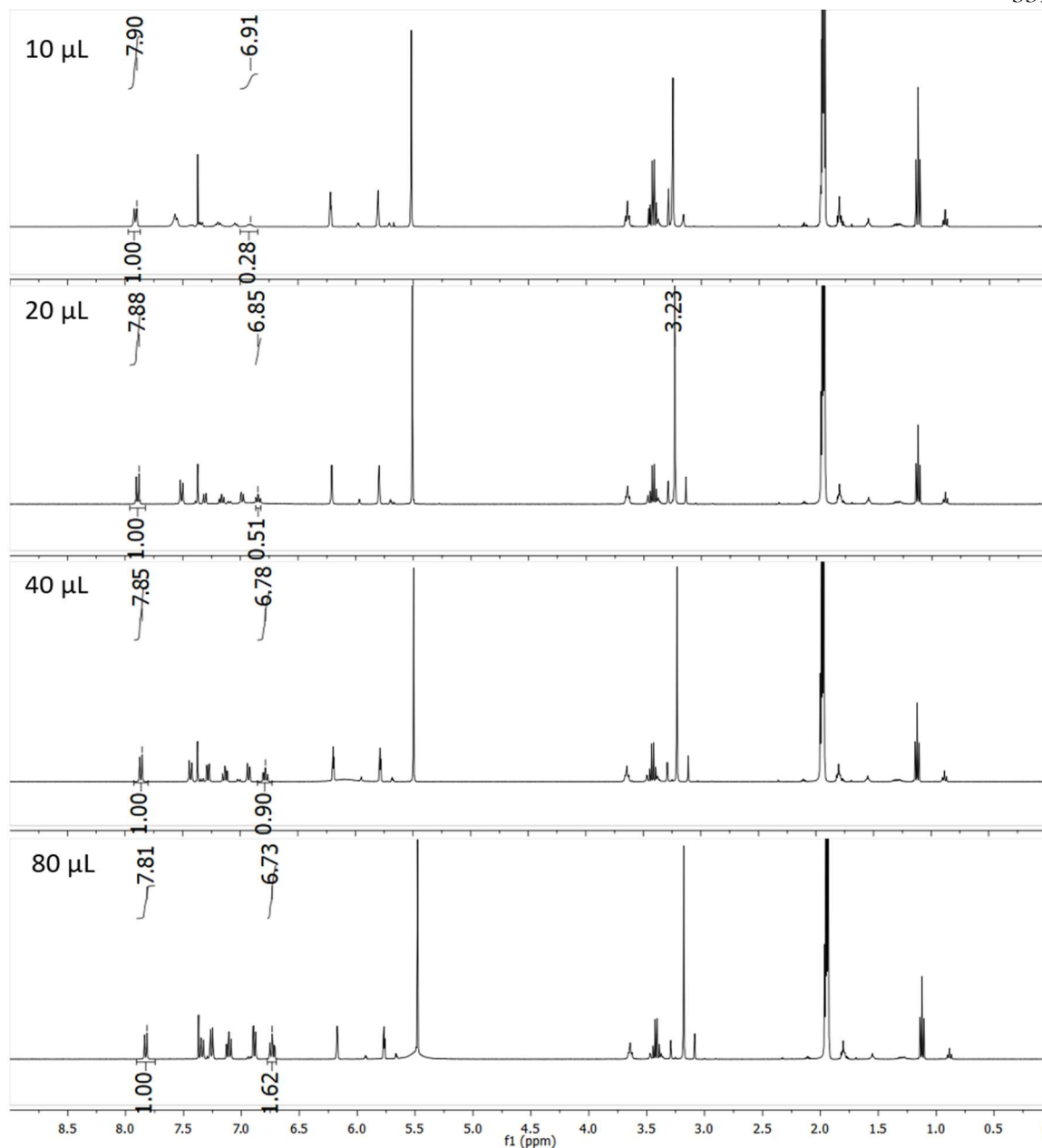


Figure E.33: 400 MHz ^1H NMR spectra of titration experiments of $[(\text{Cp})\text{Co}(\text{Cp}^{\text{NH}})][\text{OTf}]_2$ with 2-chloroaniline in $\text{MeCN-}d_3$ at room temperature. Only one integral and peak pick for both Co and the aniline are shown for clarity, but all the data shown in the above tables was used to determine the equilibrium constants (Experiment #3).

E.10 Application of Hess's Law to $[(\text{Cp})\text{Co}(\text{Cp}^{\text{NH}})]^{n+}$

BDFE = bond dissociation free energy

C_G = solvent-dependent thermodynamic constant accounting for the energy of formation of H^\cdot from one proton and one electron

$\Delta G(H^-)$ = hydricity

C_{Hyd} = solvent-dependent thermodynamic constant accounting for the energy of formation of H^- from one proton and two electrons

Calculation of the Homolytic N–H Bond Strength for [(Cp)Co(Cp^{NH})] [OTf]:

$$\text{Eq E.7) } BDFE = 1.37 \times pK_a + 23.06 \times E^\circ_1 + C_G$$

$$\text{Eq E.8) } BDFE_1 = 1.37 \times 8.6 + 23.06 \times -1.21 + 54.9$$

$$\text{Eq E.9) } BDFE_1 = 38.8 \text{ kcal} \cdot \text{mol}^{-1}$$

Calculation of the Homolytic N–H Bond Strength for [(Cp)Co(Cp^{NH})] [OTf]₂:

$$\text{Eq E.10) } BDFE = 1.37 \times pK_a + 23.06 \times E^\circ_2 + C_G$$

$$\text{Eq E.11) } BDFE_2 = 1.37 \times 8.6 + 23.06 \times 0.54 + 54.9$$

$$\text{Eq E.12) } BDFE_2 = 79.1 \text{ kcal} \cdot \text{mol}^{-1}$$

Calculation of the Heterolytic N–H Bond Strength for [(Cp)Co(Cp^{NH})] [OTf]:

$$\text{Eq E.13) } \Delta G(H^-) = 1.37 \times pK_a + 23.06 \times E^\circ_1 + 23.06 \times E^\circ_2 + C_{Hyd}$$

$$\text{Eq E.14) } \Delta G(H^-) = 1.37 \times 8.6 + 23.06 \times 0.54 + 23.06 \times -1.21 + 79.6$$

$$\text{Eq E.15) } \Delta G(H^-) = 75.9 \text{ kcal} \cdot \text{mol}^{-1}$$

Calculation of the pK_a of [(Cp)Co(Cp^{NH})] [OTf]

$$\text{Eq E.16) } BDFE = 1.37 \times pK_a + 23.06 \times E^\circ_3 + C_G$$

$$\text{Eq E.17) } pK_a = (BDFE - 23.06 \times E^\circ - C_G) / 1.37$$

$$\text{Eq E.18) } pK_a = (38.8 - 23.06 \times -1.35 - 54.9) / 1.37$$

$$\text{Eq E.19) } pK_a = 11.0$$

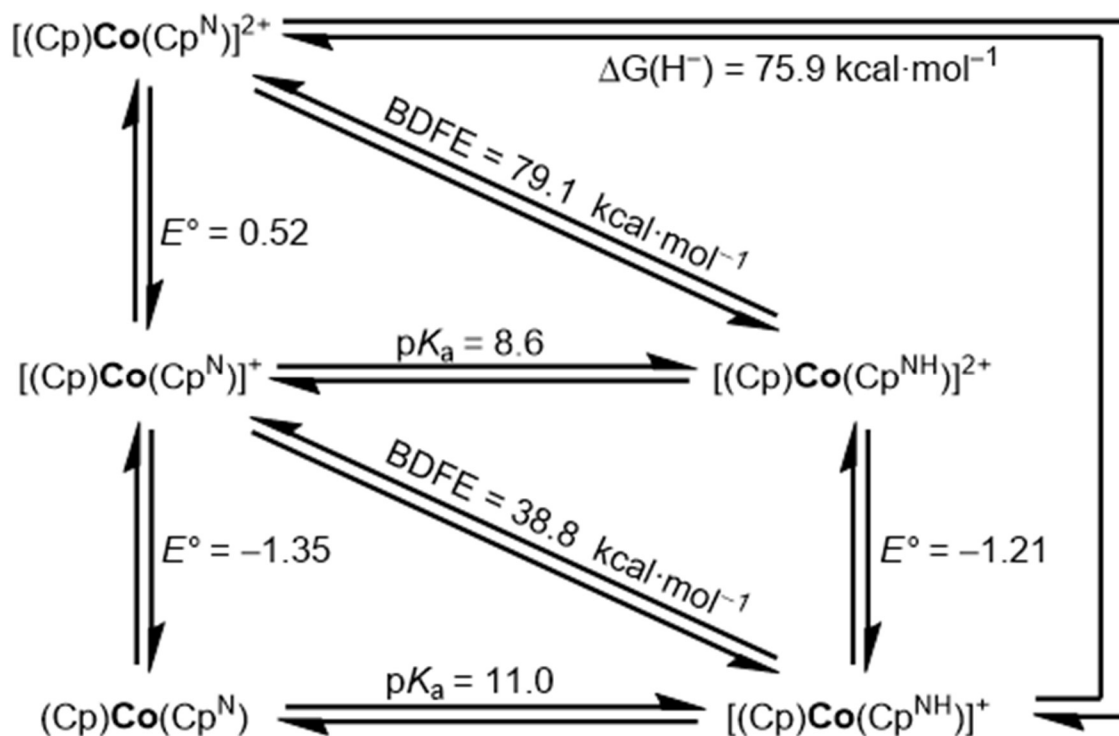


Figure E.34: Thermochemical relationships in acetonitrile for cobaltocene species in this study. Potentials are reported vs $\text{Fc}^{+/0}$.

E.11 Thermochemistry from DFT

In cases, where an experimental spin state was known this was used for the calculation. In cases, where the experimental spin state was unknown the singlet, triplet and quintet or doublet and quartet states were calculated. The lowest energy state was used for the thermochemical calculations and is indicated. Both Co^1 species, $[(\text{Cp})\text{Co}(\text{Cp}^{\text{N}})]^-$ and $\text{CpCp}^{\text{NH}}\text{Co}$, were calculated to be triplets consistent with the known spin state of the isoelectronic nickelocene.²⁰

Table E.13: DFT calculated thermochemical parameters for parent cobaltocene and base-appended cobaltocenes.

Species	Reduction Potential (V vs $\text{Fc}^{+/0}$)	$\text{p}K_{\text{a}}$	BDFE ($\text{kcal}\cdot\text{mol}^{-1}$)	Hydricity ($\text{kcal}\cdot\text{mol}^{-1}$)
$[(\text{Cp})\text{Co}(\text{Cp}^{\text{N}})]^{2+}$ ($S = 1/2$)	0.42	N/A	N/A	N/A
$[(\text{Cp})\text{Co}(\text{Cp}^{\text{N}})]^+$	-1.58	N/A	N/A	N/A

$(\text{Cp})\text{Co}(\text{Cp}^{\text{N}})$	-2.28	N/A	N/A	N/A
$[(\text{Cp})\text{Co}(\text{Cp}^{\text{NH}})]^{2+}$	-1.19	7.9	75.6	N/A
$[(\text{Cp})\text{Co}(\text{Cp}^{\text{NH}})]^{+}$		14.5	38.5	70.8
$[\text{Cp}_2\text{Co}]^{+}$	-1.45	N/A	N/A	N/A
Cp_2Co	-2.20	N/A	N/A	N/A
$[(\text{Cp})\text{Co}(\eta^4\text{-C}_5\text{H}_6)]^{+}$ ($S = 1/2$)	-0.42	9.0	33.8	N/A
$(\text{Cp})\text{Co}(\eta^4\text{-C}_5\text{H}_6)$	N/A		57.8	46.8

E.13 Controlled Potential Electrolyses

To set-up the bulk electrolyses a single-compartment cell was used. The reference electrode contained a silver wire in a DME solution of 5 mM AgOTf and a silver. The counter electrode was a glassy carbon plate. The working electrode was a BDD plate that had been treated as previously described in the literature to generate a clean, H-terminated surface.¹⁴ Additionally, repeated CV's at 100 mV/s were taken with the BDD plate in a 100 mM DME solution of tosic acid and [TBA][PF₆] were taken until a stable HER background was observed. The electrodes were then placed into a fresh solution of DME containing 100 mM tosic acid and 200 mM [TBA][PF₆]. A CV at 100 mV/s was taken to confirm the stable HER background. To this was then added via syringe a sufficient amount of acetophenone to generate a 0.05 M solution. Another CV was taken to evaluate the current. Finally, enough catalyst was added to generate a 1 mM solution and a final CV was taken. Controlled potential electrolyses at -1.45 V with stirring until sufficient charge had passed to consume all of the acid or in the case of the control experiment without catalyst until the same amount of time had passed.

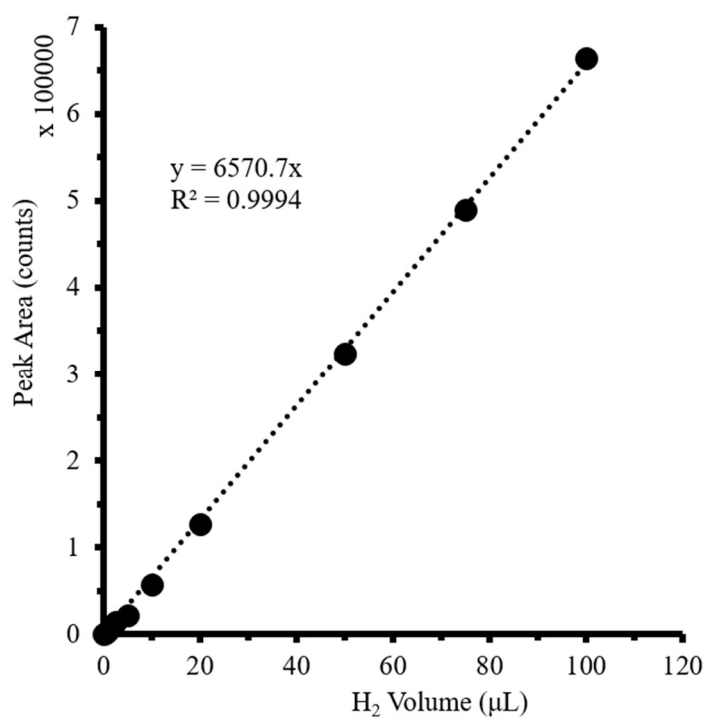


Figure E.35: Calibration curve used for GC-TCD detection of H₂.

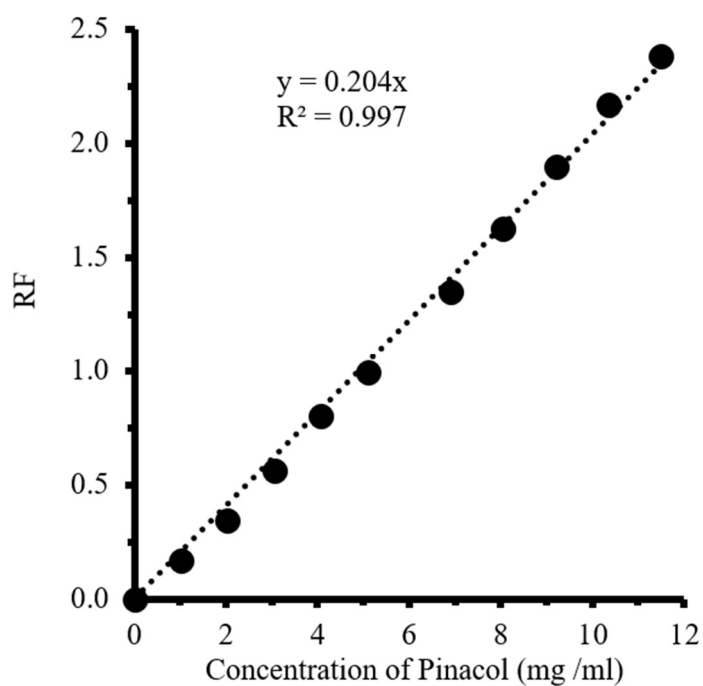


Figure E.36: Calibration curve used for GC-FID quantification of pinacol (2,3-diphenylbutanediol).

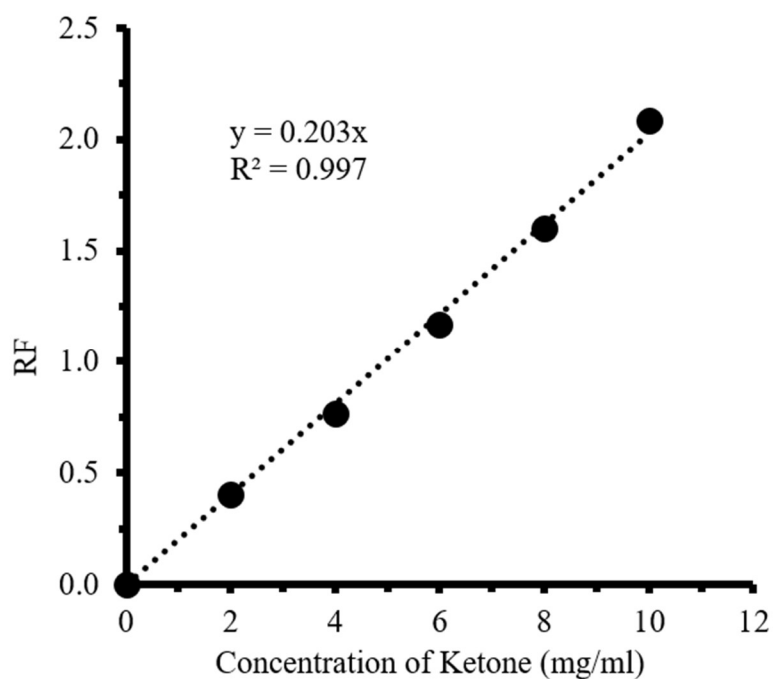


Figure E.37: Calibration curve used for GC-FID quantification of ketone (acetophenone).

Table E.14: Results from CPE experiments under the standard conditions described using the procedures described in Sections E.1.5 and E.1.6

Catalyst	Counter Electrode	Pinacol Yield	Ketone Recovery	Pinacol TON (FE)	H ₂ Yield (FE)	Q (C)
1 mM [(Cp)Co(Cp ^N)] [OTf]	Pt			10.5	11.8%	
		21.9%	5.4%	(35.7%)	(38.4%)	20.7
1 mM [(Cp)Co(Cp ^N)] [OTf]	Glassy			41.5	47.7%	
	Carbon	83.2%	10.8%	(39.0%)	(44.9%)	71.6
1 mM [Cp ₂ Co] [PF ₆]	Glassy				65.8%	
	Carbon	5.6%	0%	2.8		71.6

				(2.6%)	(62.0%)	
none	Glassy			N/A	1.0%	
	Carbon	10.4%	0%	(46.6%)	(7.5%)	7.5

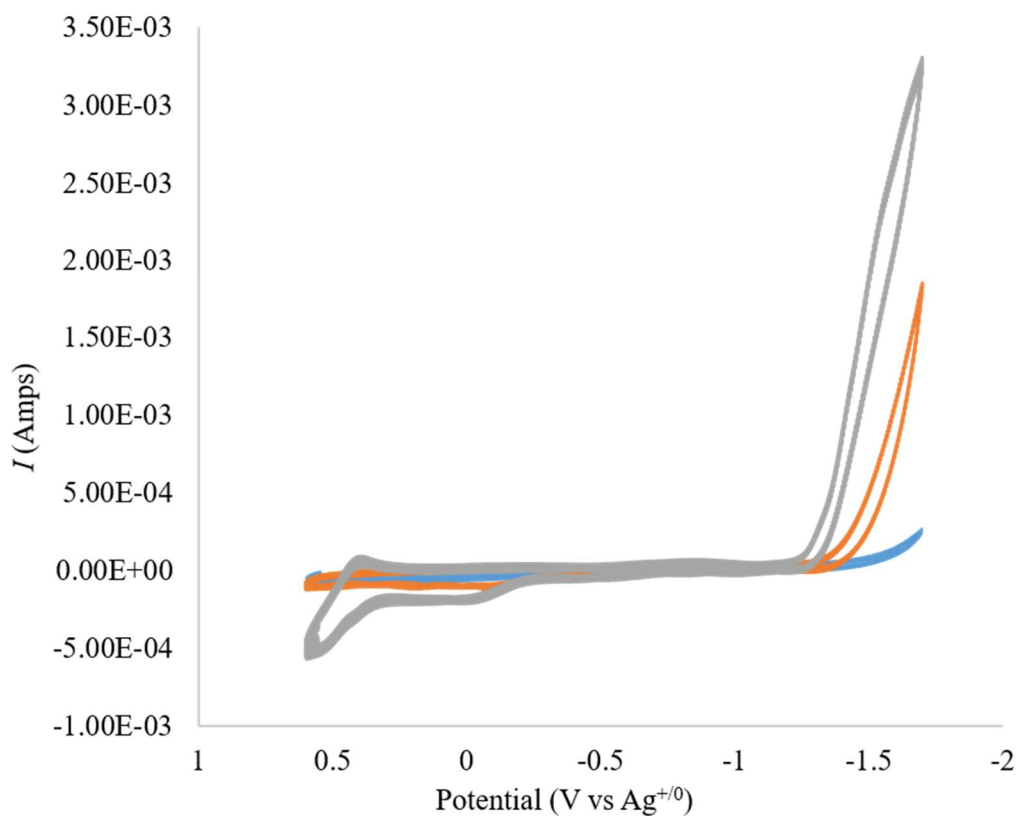


Figure E.38: CV's relevant to the set-up of Entry 1 in **Table E.14**. In blue is toxic acid only. In orange is toxic acid with acetophenone (50 mM) added. In gray is toxic acid and acetophenone with $[(\text{Cp})\text{Co}(\text{Cp}^{\text{N}})][\text{OTf}]$ (1 mM) added. Similar CV's are consistently observed during the set-up.

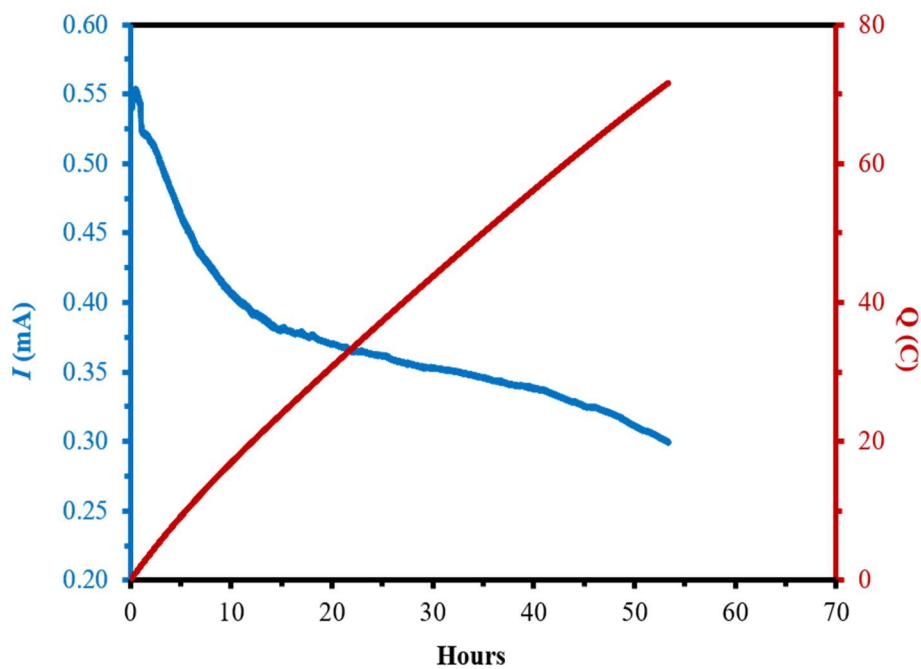


Figure E.39: Current (left axis) and charge passed (right axis) with respect to time during the CPE experiment (Table E.14, Entry 1).

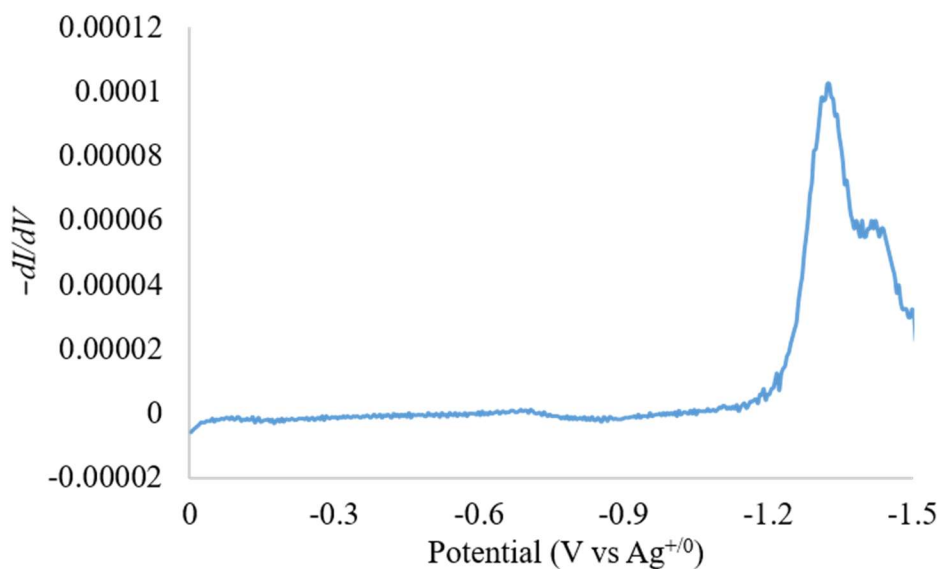


Figure E.40: Negative first derivative of DPV taken after the CPE experiment (Table E.14, Entry 1). Peak at -1.33 V corresponds to the reduction of $[(\text{Cp})\text{Co}(\text{Cp}^{\text{N}})][\text{OTf}]$

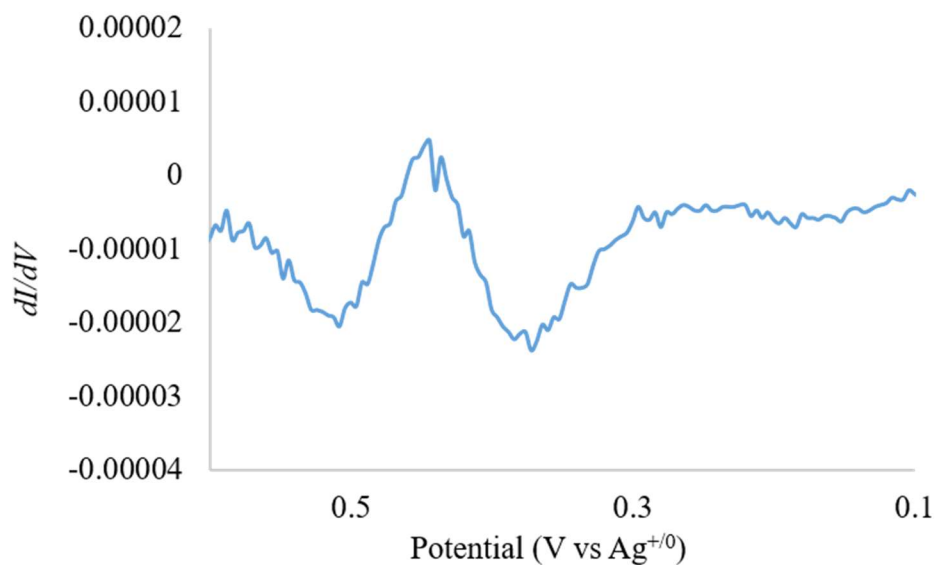


Figure E.41: First derivative of DPV taken after the CPE experiment (Table E.14, Entry 1). Peak at 0.45 V corresponds to the reduction of $[(Cp)Co(Cp^N)][OTf]$

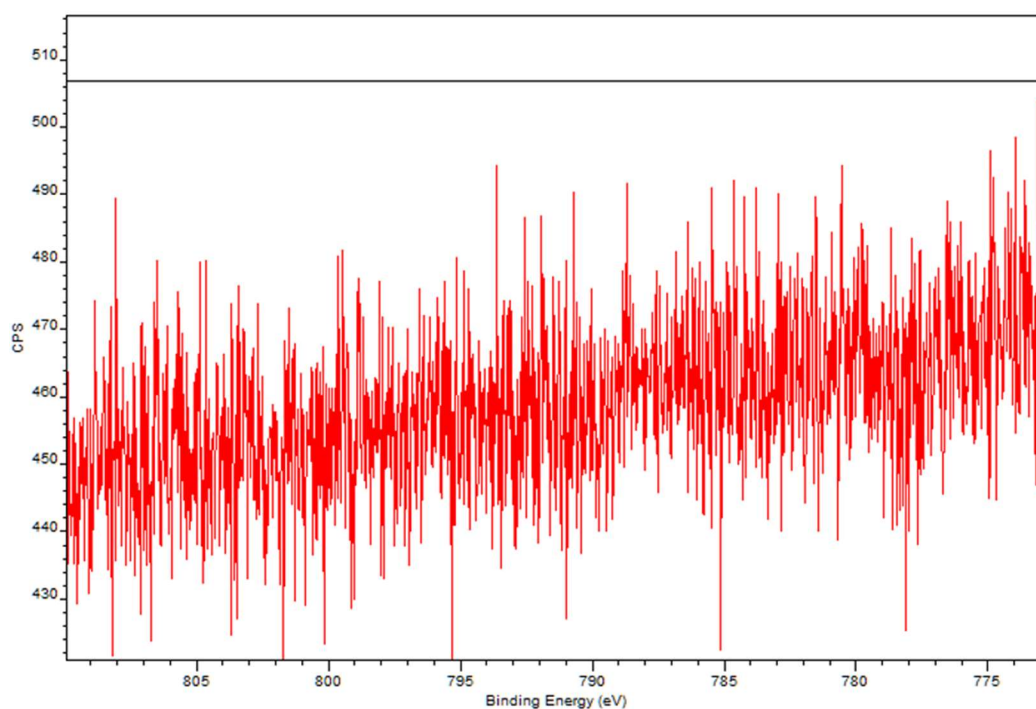


Figure E.42: XPS of the BDD electrode in the Co 2p region, showing no evidence of Co deposition after the CPE experiment with $[(Cp)Co(Cp^N)][OTf]$ (Table E.14, Entry 1).

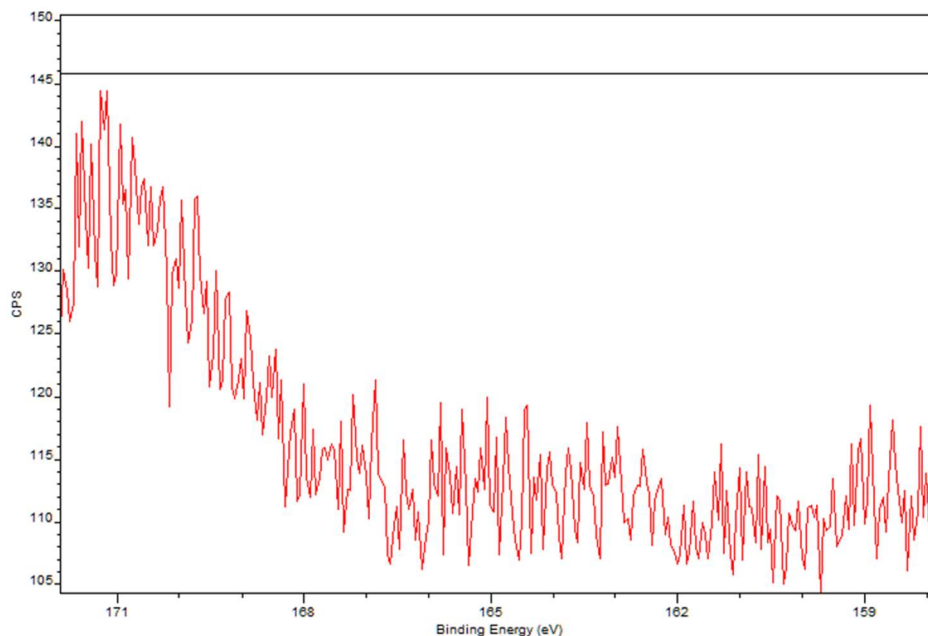


Figure E.43: XPS of the BDD electrode in the S 2p region, showing no evidence of S deposition after the CPE experiment (**Table E.14**, Entry 1). Sulfur is found in both the triflate counteranion and the tosic acid.

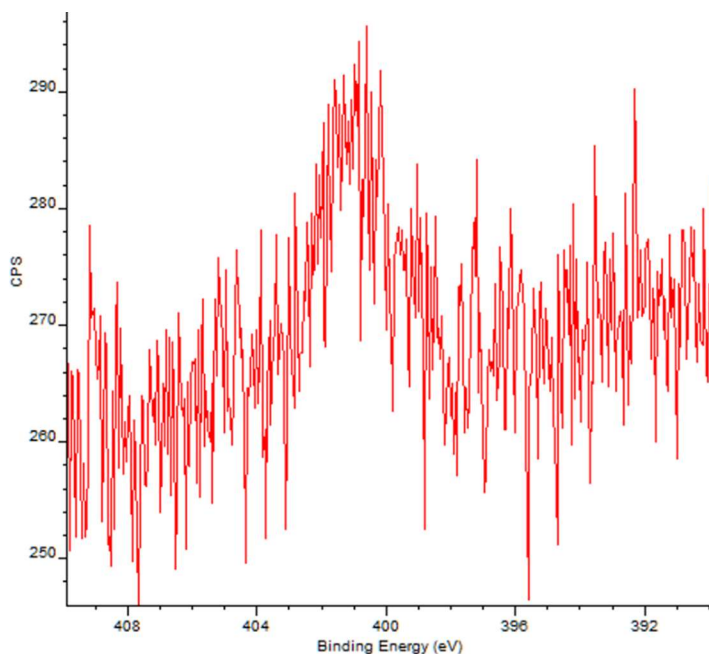


Figure E.44: XPS of the BDD electrode in the N 1s region, showing no minimal evidence of N deposition after the CPE experiment (**Table E.14**, Entry 1). The likeliest source of nitrogen given the lack of adsorbed Co is either environmental contamination or the $[\text{TBA}]^+$.

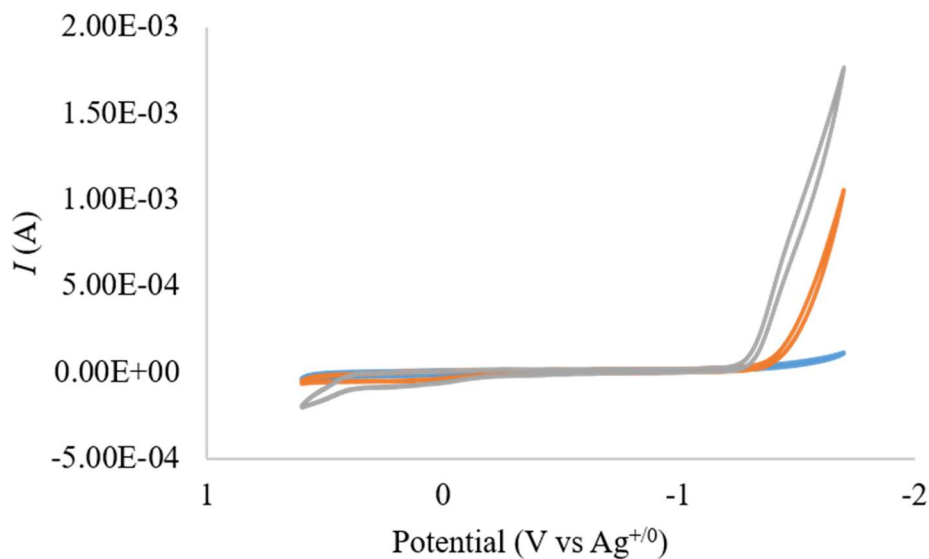


Figure E.45: CV's relevant to the set-up of Entry 2 in **Table E.14**. In blue is toxic acid only. In orange is toxic acid with acetophenone (50 mM) added. In gray is toxic acid and acetophenone with $[(\text{Cp})\text{Co}(\text{Cp}^{\text{N}})][\text{OTf}]$ (1 mM) added. Similar CV's are consistently observed during the set-up.

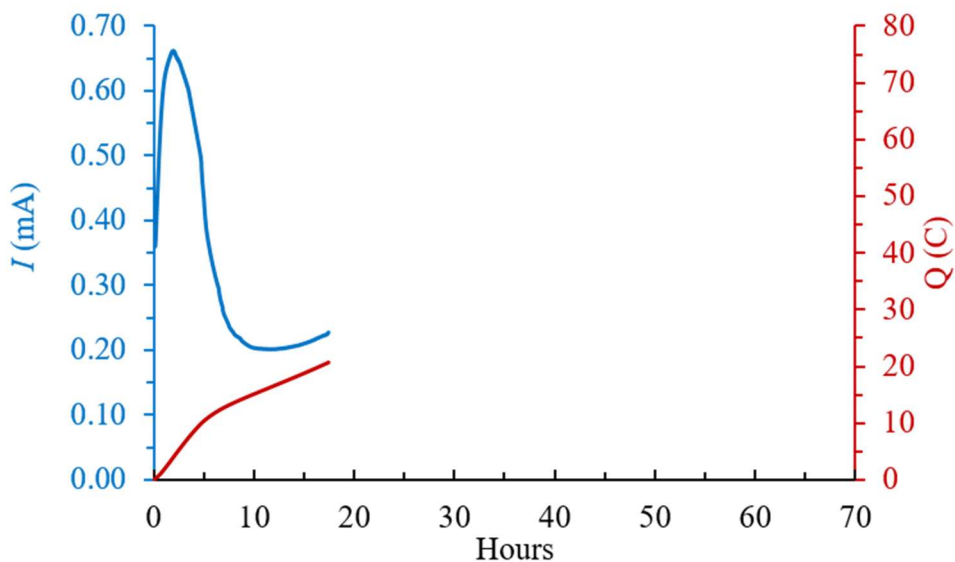


Figure E.46: Current (left axis) and charge passed (right axis) with respect to time during the CPE experiment (**Table E.14**, Entry 2).

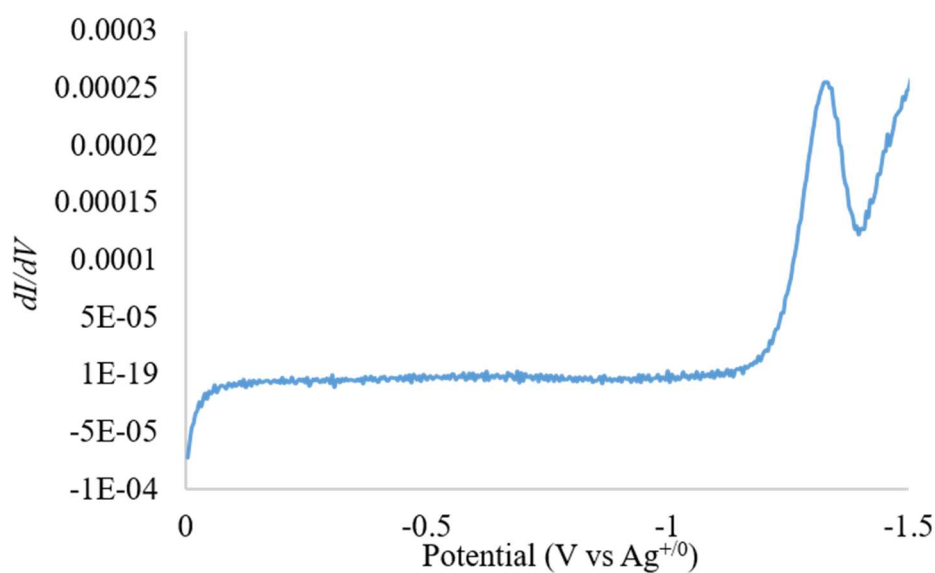


Figure E.47: Negative first derivative of DPV taken after the CPE experiment (Table E.14, Entry 2). Peak at -1.33 V corresponds to the reduction of $[(\text{Cp})\text{Co}(\text{Cp}^{\text{N}})][\text{OTf}]$

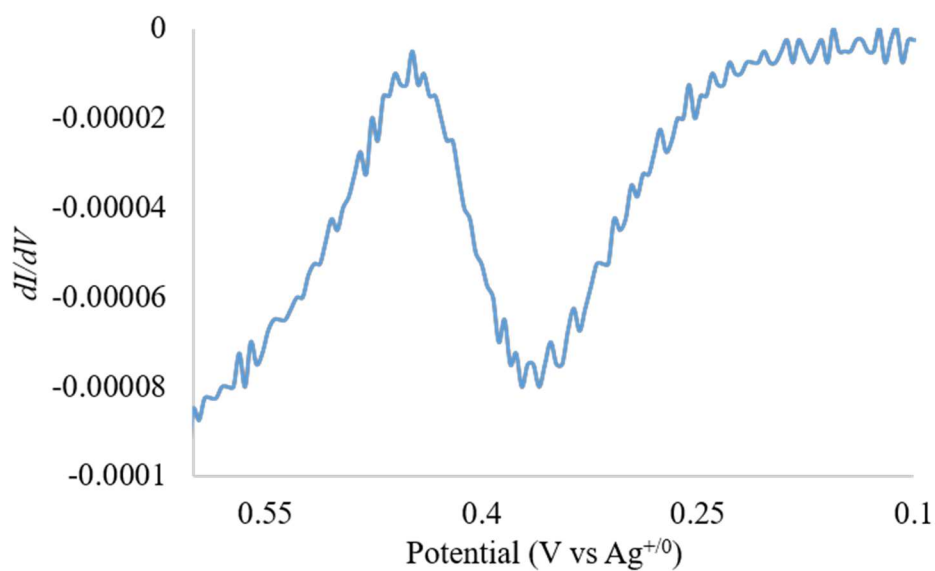


Figure E.48: First derivative of DPV taken after the CPE experiment (Table E.14, Entry 2). Peak at 0.45 V corresponds to the reduction of $[(\text{Cp})\text{Co}(\text{Cp}^{\text{N}})][\text{OTf}]$.

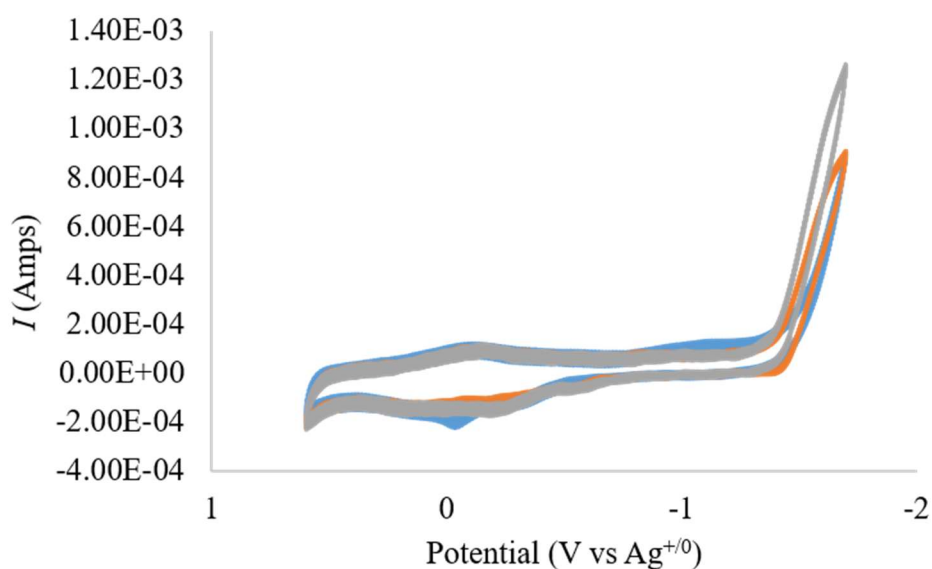


Figure E.49: CV's relevant to the set-up of Entry 3 in **Table E.14**. In blue is tosic acid only. In orange is tosic acid with $[\text{Cp}_2\text{Co}][\text{PF}_6]$ (1 mM) added. In gray is tosic acid and $[\text{Cp}_2\text{Co}][\text{PF}_6]$ with acetophenone (50 mM) added.

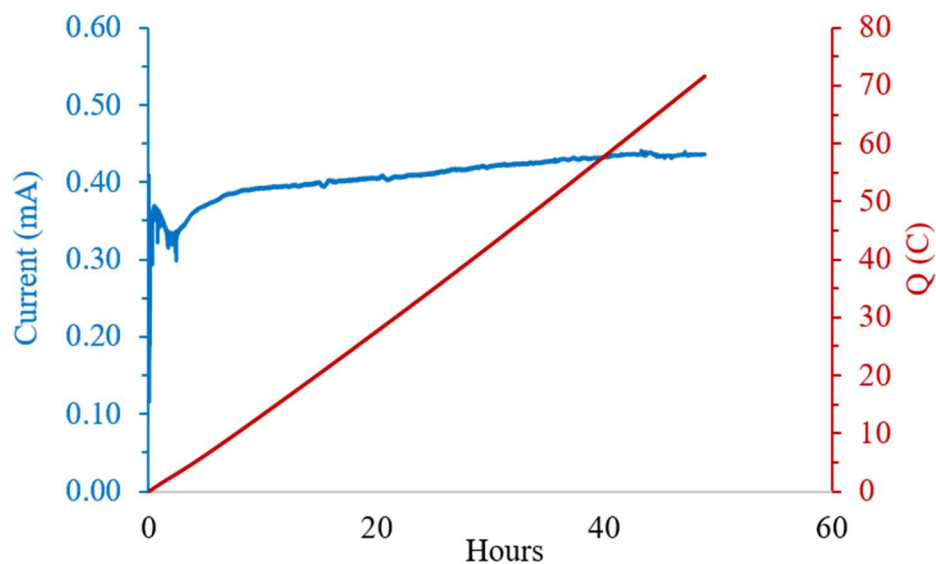


Figure E.50: Current (left axis) and charge passed (right axis) with respect to time during the CPE experiment (**Table E.14**, Entry 3).

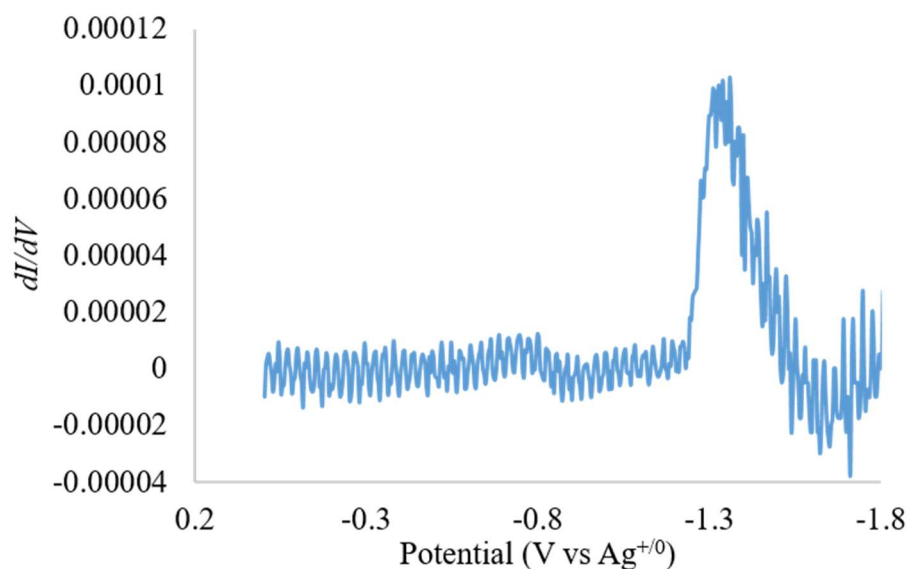


Figure E.51: Negative first derivative of DPV taken after the CPE experiment (Table E.14, Entry 4) with a fresh glassy carbon disk electrode. Peak at -1.31 V corresponds to the reduction of $[\text{Cp}_2\text{Co}][\text{PF}_6]$

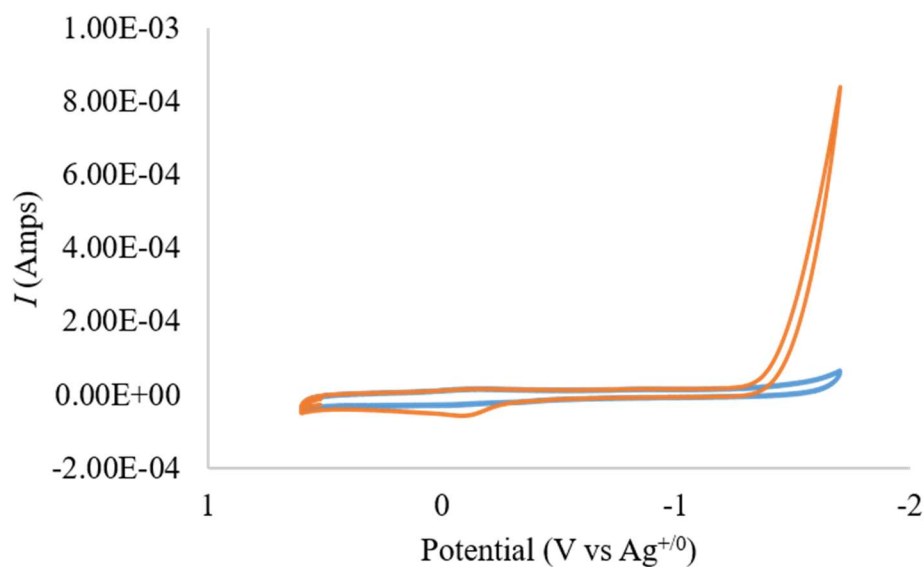


Figure E.52: CV's relevant to the set-up of Entry 4 in Table E.14. In blue is tosic acid only. In orange is tosic acid with acetophenone (50 mM) added.

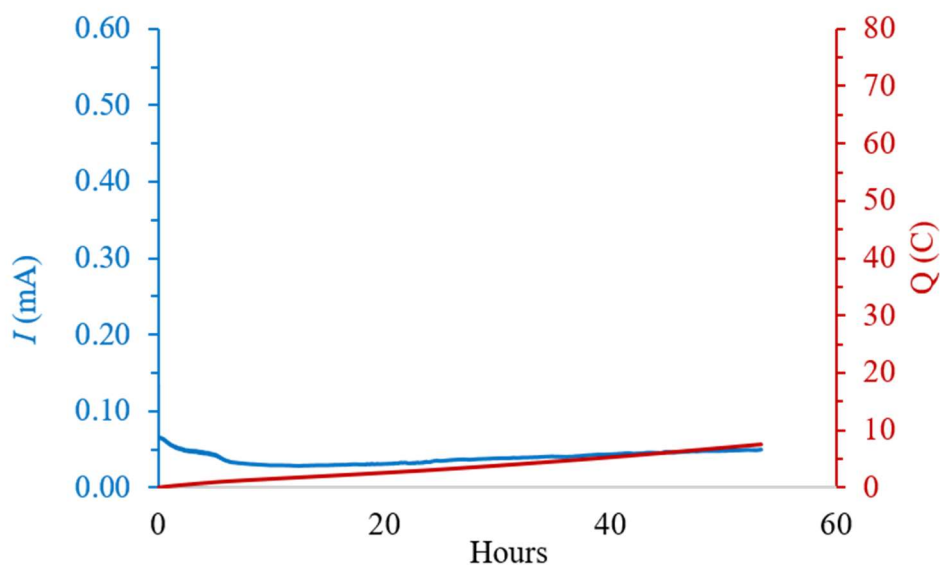


Figure E.53: Current (left axis) and charge passed (right axis) with respect to time during the CPE experiment (Table E.14, Entry 4).

E.14 References

- (1) Tanabe, Y.; Nakajima, K.; Nishibayashi, Y. *Chem. – Eur. J.* **2018**, *24*, 18618–18622.
- (2) Kato, K.; Kim, W.; Kim, D.; Yorimitsu, H.; Osuka, A. *Chem. – Eur. J.* **2016**, *22*, 7041–7045.
- (3) Neese, F. *Wiley Interdiscip. Rev. Comput. Mol. Sci.* **2012**, *2*, 73–78.
- (4) Neese, F. *Wiley Interdiscip. Rev. Comput. Mol. Sci.* **2018**, *8*, e1327.
- (5) Tao, J.; Perdew, J. P.; Staroverov, V. N.; Scuseria, G. E. *Phys. Rev. Lett.* **2003**, *91*, 146401.
- (6) Weigend, F.; Ahlrichs, R. *Phys. Chem. Chem. Phys.* **2005**, *7*, 3297–3305.
- (7) Weigend, F. *Phys. Chem. Chem. Phys.* **2006**, *8*, 1057–1065.

- (8) Grimme, S.; Antony, J.; Ehrlich, S.; Krieg, H. *J. Chem. Phys.* **2010**, *132*, 154104–154119.
- (9) Marenich, A. V.; Cramer, C. J.; Truhlar, D. G. *J. Phys. Chem. B* **2009**, *113*, 6378–6396.
- (10) Kaljurand, I.; Kütt, A.; Sooväli, L.; Rodima, T.; Mäemets, V.; Leito, I.; Koppel, I. *A. J. Org. Chem.* **2005**, *70*, 1019–1028.
- (11) Wiedner, E. S.; Chambers, M. B.; Pitman, C. L.; Bullock, R. M.; Miller, A. J. M.; Appel, A. M. *Chem. Rev.* **2016**, *116*, 8655–8692.
- (12) Sheldrick, G. M. *Acta Crystallogr. Sect. C Struct. Chem.* **2015**, *71*, 3–8.
- (13) Dolomanov, O. V.; Bourhis, L. J.; Gildea, R. J.; Howard, J. a. K.; Puschmann, H. *J. Appl. Crystallogr.* **2009**, *42*, 339–341.
- (14) Macpherson, J. V. *Phys. Chem. Chem. Phys.* **2015**, *17*, 2935–2949.
- (15) Chiang, L.; Keown, W.; Citek, C.; Wasinger, E. C.; Stack, T. D. P. *Angew. Chem. Int. Ed.* **2016**, *55*, 10453–10457.
- (16) Evans, D. F. *J. Chem. Soc. Resumed* **1959**, No. 0, 2003–2005.
- (17) Ammeter, J. H. *J. Magn. Reson. 1969* **1978**, *30*, 299–325.
- (18) Ammeter, J. H.; Swalen, J. D. *J. Chem. Phys.* **1972**, *57*, 678–698.
- (19) Hulliger, J.; Zoller, L.; Ammeter, J. H. *J. Magn. Reson. 1969* **1982**, *48*, 512–518.
- (20) Wilkinson, G.; Pauson, P. L.; Cotton, F. A. *J. Am. Chem. Soc.* **1954**, *76*, 1970–1974.